

PB2001107670


US Department of Transportation Federal Highway Administration
Research, Development, and Technology Turner-Fairbank Highway
Research Center 6300 Georgetown Pike McLean, VA 22101-2296

A Predictive Approach for Long-Term Performance of Recycled
Materials Using Accelerated Aging, Volume 1: Main Report

FHWA-RD-01-022

June 2001

REPRODUCED BY:
U.S. Department of Commerce
National Technical Information Service
Springfield, Virginia 22161

NTIS




FOREWORD

There is increasing interest in the use of recycled materials in the highway environment on the part of States, municipalities, the private sector and the public. As stewards of the Nation's highways, FHWA desires to maintain a quality infrastructure and good roads. Use of recycled materials must promote this concept. Substitution of alternative materials must provide the same economic, engineering, and environmental benefits as traditional materials.

Using recycled materials in a proposed highway application frequently requires assessment of both the physical and environmental performance; however, future behavior is often difficult to predict and long-term results of actual field installations are often unavailable. The objective of this research was to investigate an approach to predicting long-term physical and environmental performance of candidate recycled materials in typical highway applications using accelerated aging. The project was geared specifically towards the use of recycled materials in Portland cement concrete, but similar approaches may be possible for other materials.

The accelerated aging methodology investigated in this project allows the researcher or materials engineer to explore the phenomenon of aging, the complex interactions between physical and environmental performance that occur during aging, and the potential compatibility of candidate recycled materials in a portland cement concrete matrix under controlled conditions. Such aging methods could eventually become standard practices for predicting future behavior.



T. Paul Teng, P.E.
Director, Office of Infrastructure
Research and Development

NOTICE

This document is disseminated under the sponsorship of the Department of Transportation in the interest of information exchange. The United States Government assumes no liability for its contents or use thereof. This report does not constitute a standard, specification, or regulation.

The United States Government does not endorse products or manufacturers. Trade and manufacturers' names appear in this report only because they are considered essential to the object of this document.

1. Report No. FHWA-RD-01-022		2. Government Accession No.		3. Recipient's Catalog No.	
4. Title and Subtitle A Predictive Approach for Long-Term Performance of Recycled Materials Using Accelerated Aging Volume 1: Main Report			5. Report Date June 2001		
			6. Performing Organization Code 480017		
7. Author(s) T.T Eighmy, R.A. Cook, A. Coviello, J.C.M. Spear, K.C. Hover, et. al.			8. Performing Organization Report No.		
9. Performing Organization Name and Address University of New Hampshire Recycled Materials Resource Center 120 Nesmith Hall Durham, NH 03824			10. Work Unit No. (TRAVIS)		
			11. Contract or Grant No. DTFH61-97-X-00021		
12. Sponsoring Agency Name and Address Federal Highway Administration Office of Infrastructure R&D 6300 Georgetown Pike McLean, VA 22101			13. Type of Report and Period Covered Final Report Sept. 1997 - Jan. 2001		
			14. Sponsoring Agency Code		
15. Supplementary Notes Agreement Officer's Technical Representative (AOTR): Marcia Simon (HRDI-12)					
16. Abstract Use of recycled materials in a proposed highway application frequently requires the assessment of physical and environmental performance. Future behavior is often difficult to predict. As an alternative to field demonstrations, there is a need to develop strategies to predict long-term physical and environmental performance. Accelerated aging is one means of exploring the long-term physical and environmental performance of recycled materials in a highway. Coal fly ash (CFA) use in portland cement concrete (PCC) was selected as a model system to develop an accelerated aging approach. Three types of accelerated aging were chosen for this project: Arrhenius aging (AA), cyclic loading (CL), and freeze-thaw exposure (FT). This approach, incorporated in an experimental design, allowed a systematic exploration of the separate effects and combined interactions of both developmental and degradative accelerated aging variables. A slab from U.S. Route 20 in northwest Iowa was used as a both the basis for the concrete mixes and as a field verification site. The aging protocol impacted both physical and chemical properties of the prism monoliths. Generally speaking, the main effects were more important than the interactive effects, which was unexpected. It took about 9 months of elapsed time to age specimens to an equivalent age of up to 4 years. The equivalent ages matched well with the time frame seen in the field in Iowa for the onset of early distress and also matched well the chronological age of the field pavement. AA significantly reduced the compressive strength of the concrete, possibly indicating the onset of a deleterious reaction in the mix. CL affected the microcracking in the concrete. All aging variables affected the fine pore structure of the concrete. CL affected the Ca diffusional leaching from the monoliths. Logically, there appears to be a linkage between strength loss, microcracking, and leaching behavior of a major matrix constituent in the concrete (notably Ca). Most response variables from the aged laboratory prisms and the field samples were similar, suggesting that the method did a reasonable job of producing a laboratory pavement of similar age and distress to the field pavement. Certain field aging phenomena (microcracking from unknown sources, road salting, and carbonation) could not be recreated in the laboratory specimens.					
17. Key Words recycled materials, accelerated aging, Arrhenius aging, cyclical loading, freeze-thaw distress, coal fly ash, portland cement concrete, physical properties, leaching, geochemical modeling			18. Distribution Statement No restrictions. This document is available to the public through the National Technical Information Service, Springfield, Virginia, 22161		
19. Security Classif. (of this report) Unclassified		20. Security Classif. (of this page) Unclassified		21. No. of Pages 423	22. Price

SI* (MODERN METRIC) CONVERSION FACTORS

APPROXIMATE CONVERSIONS TO SI UNITS

APPROXIMATE CONVERSIONS FROM SI UNITS

Symbol	When You Know	Multiply By	To Find	Symbol	When You Know	Multiply By	To Find	Symbol
LENGTH								
in	inches	25.4	millimeters	mm	millimeters	0.039	inches	in
ft	feet	0.305	meters	m	meters	3.28	feet	ft
yd	yards	0.914	meters	m	meters	1.09	yards	yd
mi	miles	1.61	kilometers	km	kilometers	0.621	miles	mi
AREA								
in ²	square inches	645.2	square millimeters	mm ²	square millimeters	0.0016	square inches	in ²
ft ²	square feet	0.093	square meters	m ²	square meters	10.764	square feet	ft ²
yd ²	square yards	0.836	square meters	m ²	square meters	1.195	square yards	yd ²
ac	acres	0.405	hectares	ha	hectares	2.47	acres	ac
mi ²	square miles	2.59	square kilometers	km ²	square kilometers	0.386	square miles	mi ²
VOLUME								
fl oz	fluid ounces	29.57	milliliters	mL	milliliters	0.034	fluid ounces	fl oz
gal	gallons	3.785	liters	L	liters	0.264	gallons	gal
ft ³	cubic feet	0.028	cubic meters	m ³	cubic meters	35.71	cubic feet	ft ³
yd ³	cubic yards	0.765	cubic meters	m ³	cubic meters	1.307	cubic yards	yd ³
NOTE: Volumes greater than 1000 l shall be shown in m ³ .								
MASS								
oz	ounces	28.35	grams	g	grams	0.035	ounces	oz
lb	pounds	0.454	kilograms	kg	kilograms	2.202	pounds	lb
T	short tons (2000 lb)	0.907	megagrams (or "metric ton")	Mg (or "t")	megagrams (or "metric ton")	1.103	short tons (2000 lb)	T
TEMPERATURE (exact)								
°F	Fahrenheit temperature	5(F-32)/9 or (F-32)/1.8	Celsius temperature	°C	Celsius temperature	1.8C + 32	Fahrenheit temperature	°F
ILLUMINATION								
fc	foot-candles	10.76	lux	lx	lux	0.0929	foot-candles	fc
fl	foot-Lamberts	3.426	candela/m ²	cd/m ²	candela/m ²	0.2919	foot-Lamberts	fl
FORCE and PRESSURE or STRESS								
lbf	poundforce	4.45	newtons	N	newtons	0.225	poundforce	lbf
lbf/in ²	poundforce per square inch	6.89	kilopascals	kPa	kilopascals	0.145	poundforce per square inch	lbf/in ²

* SI is the symbol for the International System of Units. Appropriate rounding should be made to comply with Section 4 of ASTM E380. (Revised September 1993)

TABLE OF CONTENTS

<u>Section</u>	<u>Page</u>
CHAPTER 1. TECHNICAL SUMMARY	1
CHAPTER 2. INTRODUCTION AND PURPOSE	6
2.1. Need to Predict Long-Term Performance for Recycled Materials	6
2.2. Use of Accelerated Aging to Predict Long-Term Performance	7
2.2.1 Development of Systematic Aging Protocols that Can Be Generally Applied	7
2.2.2 The Concept of Accelerated Aging	9
2.2.3 Application of the Systematic Approach to Coal Fly Ash Use in Portland Cement Concrete	11
2.3 Scope of the Project	13
2.3.1 Use of a Field Reference Site	13
2.3.2 U.S. 20 Pavement Slab for Field versus Laboratory Verification	14
2.3.3 Materials for Laboratory Prism Study	14
2.3.4 Component Materials Characterization	15
2.3.5 Effects of Accelerated Aging on CFA-C Prism Mixes	16
2.3.6 Effects of Accelerated Aging on CFA-C, CFA-F and PCC Control Prism Mixes	16
2.3.7 Comparison of Aged CFA-C Mixes to the U.S. 20 Slab	16
2.3.8 U.S. 20 Slab and Laboratory Prism Physical and Environmental Properties of Interest	17
CHAPTER 3: MATERIALS COLLECTION AND CHARACTERIZATION	21
3.1. U.S. 20 Slab Collection and Processing	21
3.2. Mixture Components Collection and Processing	27
3.2.1 Coarse Aggregate	27
3.2.2 Fine Aggregate	27
3.2.3 Cement	27
3.2.4 Ottumwa Class C Coal Fly Ash	27
3.2.5 Brayton Point Class F Coal Fly Ash	27
3.2.6 Air-Entraining Admixture	27
3.2.7 Water Reducing Admixture	29
3.2.8 Water	29
3.3. Mix Component Characterization	29
3.3.1 Elemental and Oxide Composition	29
3.3.2 Mercury Intrusion Porosimetry	31
3.3.3 BET-N ₂ Adsorption Surface Area Analysis	33
3.3.4 Morphology	33
3.3.5 Mineralogy	35

TABLE OF CONTENTS
(continued)

<u>Section</u>	<u>Page</u>
3.3.6. pH- Dependent Leaching and Solid Phase Control	36
3.3.6.1 Measurement of Alkalinity and Constituent Solubility as a Function of pH	36
3.3.6.2 pH-Stat Leaching	37
3.3.6.3 Geochemical Modeling	37
3.3.7. Availability Leaching	39
 CHAPTER 4: EXPERIMENTAL PLAN AND PROCEDURES	 40
4.1 Experimental Designs	40
4.1.1 Selection of Aging Methods	40
4.1.2 Response Variable Methods for Both Laboratory Prism and Slab Samples	40
4.1.2.1 Compressive Strength	40
4.1.2.2 Microcracking Using Neutron Radiography and Crack Density Analysis Procedures	41
4.1.2.3 Relative Dynamic Modulus	43
4.1.2.4 Effective Pore Size and Pore Size Distribution	43
4.1.2.5 Effective Surface Area	43
4.1.2.6 Mineralogy	45
4.1.2.7 Determination of the Carbonation Extent	46
4.1.2.8 Measurement of Matrix Alkalinity and Constituent Solubility as a Function of pH	47
4.1.2.9 pH-Stat Leaching	47
4.1.2.10 Geochemical Modeling	47
4.1.2.11 Availability Leaching	47
4.1.2.12 Low Liquid-Solid Ratio Leaching	48
4.1.2.13 Monolithic Leaching	49
4.1.2.14 Release Modeling	53
4.1.3 Factorial Experiment for the Aged CFA-C Laboratory Prisms	57
4.1.4 Comparison of Aged CFA-C, CFA-F, and PCC Control Laboratory Prisms	59
4.1.5 Comparison of CFA-C Aged Laboratory Prisms to the U.S. 20 Field Slab	59
4.2 Laboratory Prism Fabrication	59
4.2.1. Slab Mix Design	59
4.2.2. Prism Mix Design	59
4.2.3. Sample ID and Labeling System	59
4.2.4. Mixing	61
4.2.5. Specifications	61
4.2.6. Casting and Curing	61
4.2.7. Prism and Cylinder Mini-Study	64
4.3 Aging Procedures	64
4.3.1 Selection of Order of Application of Aging Methods	64
4.3.2 AA as an Experimental Variable	64

TABLE OF CONTENTS
(continued)

<u>Section</u>	<u>Page</u>
4.3.2.1 Estimate of Equivalent Age for Experimental Design	65
4.3.3 CL as an Experimental Variable	68
4.3.3.1 $f'_{c(28)}$ Determination and Cyclic Loading Selection	70
4.3.3.2 Determination of Cycles for Experimental Design	70
4.3.4 FT as an Experimental Variable	71
4.3.4.1 FT Procedure	71
4.3.4.2 Relative Dynamic Modulus	72
4.4 Assessment of Leaching From Heterogeneous Monoliths	73
4.4.1 Experimental Program	73
4.4.2 Model Development	73
 CHAPTER 5: RESULTS AND DISCUSSION	 76
5.1 Mix Components Characterization	76
5.1.1 Elemental and Oxide Composition	76
5.1.1.1 CFAs	76
5.1.1.2 Portland Cement	77
5.1.1.3 Aggregates	80
5.1.1.4 Relative Contributions of Constituents of Concern from Mix Components to Overall Prism Composition	80
5.1.1.5 Conclusions	83
5.1.2 Effective Pore Size and Pore Size Distribution	83
5.1.3 Effective Surface Area	85
5.1.4 CFA Morphology	85
5.1.5 Mineralogy	88
5.1.5.1 CFAs	88
5.1.5.2 Portland Cement Paste	88
5.1.5.3 Combined Aggregates	89
5.1.5.4 Conclusions	89
5.1.6 pH-Dependent Leaching and Solid Phase Control	89
5.1.6.1 Mix Components Alkalinity and Constituent Solubility as a Function of pH	89
5.1.6.2 pH-Stat Leaching	96
5.1.6.3 Geochemical Modeling	100
5.1.6.4 Conclusions	107
5.1.7 Availability Leaching	108
5.2 Prism Casting	110
5.2.1 Air Content and Slump Tests	110
5.3 Slab Characterization	110
5.3.1 Compressive Strength	113
5.3.2 Microcracking	113
5.3.3 Effective Pore Size and Pore Size Distribution	115
5.3.4 Effective Surface Area	121

TABLE OF CONTENTS
(continued)

<u>Section</u>	<u>Page</u>
5.3.5	Elemental Composition 123
5.3.6	Mineralogy 123
5.3.6.1	Statistical Comparison by Sample Location in the Slab 125
5.3.7	Evaluation of Carbonation of the Slab 128
5.3.8	pH-Dependent Leaching and Solid Phase Control 129
5.3.8.1	Slab Alkalinity and Constituent Solubility as a Function of pH . . . 129
5.3.8.2	pH-Stat Leaching 132
5.3.8.3	Geochemical Modeling 136
5.3.8.4	Conclusions 144
5.3.9	Low Liquid-Solid Ratio Leaching 144
5.3.10	Slab Constituent Availability 149
5.3.11	Monolithic Leaching 149
5.3.11.1	pH and Conductivity 151
5.3.11.2	Leaching Behavior of Major Species 151
5.3.11.3	Leaching Behavior of Trace Metals 154
5.3.11.4	Conclusions 154
5.3.12	Release Modeling 159
5.4	Evaluation of 2 ³ + 3 Experimental Design for Aged CFA-C Prisms 165
5.4.1	Compressive Strength 165
5.4.1.1	ANOVA 167
5.4.1.2	Main Effects 167
5.4.1.3	Interactions 167
5.4.1.4	Conclusions 169
5.4.2	Microcracking 169
5.4.2.1	ANOVA 169
5.4.2.2	Main Effects 169
5.4.2.3	Interactions 169
5.4.2.4	Conclusions 171
5.4.3	Relative Dynamic Modulus 171
5.4.3.1	ANOVA 171
5.4.3.2	Main Effects 171
5.4.3.3	Interactions 172
5.4.3.4	Conclusions 172
5.4.4	Effective Pore Size and Pore Size Distribution 172
5.4.4.1	ANOVA 172
5.4.4.2	Main Effects 176
5.4.4.3	Interactions 178
5.4.4.4	Conclusions 184
5.4.5	Effective Surface Area 185
5.4.5.1	ANOVA 185
5.4.5.2	Main Effects 185
5.4.5.3	Interactions 185

TABLE OF CONTENTS
(continued)

<u>Section</u>	<u>Page</u>
5.4.5.4 Conclusions	185
5.4.6 Mineralogy	185
5.4.6.1 ANOVA	187
5.4.6.2 Main Effects	187
5.4.6.3 Interactions	187
5.4.6.4 Conclusions	189
5.4.7 pH-Dependent Leaching and Solid Phase Control	189
5.4.7.1 Prism Alkalinity and Constituent Solubility as a Function of pH ..	189
5.4.7.2 pH-Stat Leaching	192
5.4.7.3 ANOVA	196
5.4.7.4 Main Effects	198
5.4.7.5 Interactions	198
5.4.7.6 Geochemical Modeling	199
5.4.7.7 Conclusions	203
5.4.8 Low Liquid-Solid Ratio Leaching	204
5.4.9 Prism Constituent Availability Leaching	209
5.4.10 Monolithic Leaching	209
5.4.10.1 C(XXX)13, C(HNN)13, C(NHN)13, C(NNH)13, C(HHH)13 ...	209
5.4.10.2 CFA-C Samples with Other Levels of Aging	214
5.4.10.3 ANOVA Analysis	217
5.4.10.4 Main Effects	217
5.4.10.5 Interactions	219
5.4.10.6 Conclusions	219
5.4.11 Release Modeling	219
5.4.11.1 Release Modeling for C(XXX)13, C(HNN)13, C(NHN)13, C(NNH)13, C(HHH)13	219
5.4.11.2 Release Modeling for CFA-C Samples with Other Levels of Aging	226
5.4.11.3 ANOVA	234
5.4.11.4 Main Effects	234
5.4.11.5 Interactions	234
5.4.11.6 Conclusions	234
5.5 Evaluation of Three Center Points Experimental Design Between CFA-C, CFA-F, and PCC Mixes	234
5.5.1 Compressive Strength	234
5.5.1.1 ANOVA	234
5.5.1.2 Tukey-Kramer Comparisons	235
5.5.1.3 Conclusions	235
5.5.2 Microcracking	235
5.5.2.1 ANOVA	235
5.5.2.2 Tukey-Kramer Comparisons	237
5.5.2.3 Conclusions	237

TABLE OF CONTENTS
(continued)

<u>Section</u>	<u>Page</u>
5.5.3 Relative Dynamic Modulus	237
5.5.3.1 ANOVA	237
5.5.3.2 Tukey-Kramer Comparisons	239
5.5.3.3 Conclusions	239
5.5.4 Effective Pore Size and Pore Size Distribution	239
5.5.4.1 ANOVA	241
5.5.4.2 Tukey-Kramer Comparisons	250
5.5.4.3 Conclusions	250
5.5.5 Effective Surface Area	250
5.5.5.1 ANOVA	250
5.5.5.2 Tukey-Kramer Comparisons	250
5.5.5.3 Conclusions	252
5.5.6 Elemental Composition	252
5.5.7 Mineralogy	252
5.5.7.1 ANOVA	255
5.5.7.2 Tukey-Kramer Comparisons	255
5.5.7.3 Conclusions	256
5.5.8 pH-Dependent Leaching and Solid Phase Control	256
5.5.8.1 C(XXX)02, F(XXX)02, and P(XXX)02 Alkalinity and Constituent Solubility as a Function of pH	256
5.5.8.2 pH-Stat Leaching	260
5.5.8.3 ANOVA	264
5.5.8.4 Tukey-Kramer Comparisons	264
5.5.8.5 Geochemical Modeling	264
5.5.8.6 Comparison of the Three 28-d Cured Material Types with the Combined Aggregates	270
5.5.8.7 Conclusions	270
5.5.9 Low Liquid-Solid Ratio Leaching	273
5.5.9.1 Low LS of CFA-C Mix, CFA-F Mix, and PCC Control After 28-ds' Cure.	273
5.5.9.2 Conclusions	278
5.5.10 Availability Leaching	279
5.5.10.1 Availability of C(XXX)02, F(XXX)02, and P(XXX)02	279
5.5.10.2 Conclusions	279
5.5.11 Monolithic Leaching on C(XXX)02, F(XXX)02, and P(XXX)02	279
5.5.11.1 pH and Conductivity	279
5.5.11.2 Leaching Behavior of Major Species	282
5.5.11.3 Leaching Behavior of Trace Metals	285
5.5.11.4 Conclusions	285
5.5.12 Monolithic Leaching on F(XXX)02, F(LL)13, F(LL)30, and F(LL)47	287
5.5.12.1 pH and Conductivity	287
5.5.12.2 Leaching Behavior of Major Species	287

TABLE OF CONTENTS
(continued)

<u>Section</u>	<u>Page</u>
5.5.12.3 Conclusions	290
5.5.13 Monolithic Leaching of P(XXX)02, P(LL)13, P(LL)23, and P(LL)39	290
5.5.13.1 pH and Conductivity	290
5.5.13.2 Leaching Behavior of Major Species	292
5.5.13.3 Conclusions	294
5.5.14 Monolithic Leaching of Coarse Aggregates	294
5.5.14.1 pH and Conductivity	294
5.5.14.2 Leaching Behavior of Major Species	296
5.5.14.3 Conclusions	299
5.5.15 Release Modeling	299
5.5.15.1 Release Modeling for C(XXX)02, F(XXX)02, and P(XXX)02 ..	299
5.5.15.2 Release Modeling for F(XXX)02 and the CFA-F Center Points .	306
5.5.15.3 Release Modeling for P(XXX)02 and the PCC Center Points ...	311
5.5.15.4 Release Modeling for Coarse Aggregates	316
5.5.15.5 ANOVA	318
5.5.15.6 Tukey-Kramer Comparisons	318
5.5.15.7 Conclusions	319
5.6 Comparisons Between Slab and CFA-C Prism Specimens	319
5.6.1 Comparison of Materials Used	319
5.6.1.1 Portland Cement	320
5.6.1.2 CFA-C	320
5.6.1.3 Coarse and Fine Aggregates	320
5.6.1.4 Conclusions	320
5.6.2 Elemental Composition Analysis	320
5.6.3 Microcracking	326
5.6.4 Effective Pore Size and Pore Size Distribution	326
5.6.5 Effective Surface Area	328
5.6.6 Mineralogy	328
5.6.7 pH-Dependent Leaching and Solid Phase Control	332
5.6.7.1 Alkalinity and Constituent Solubility as a Function of pH	332
5.6.7.2 pH-Stat Leaching	332
5.6.7.3 Geochemical Modeling	336
5.6.7.4 Conclusions	341
5.6.8 Low Liquid-Solid Ratio Leaching	342
5.6.9 Availability Leaching	346
5.6.10 Monolithic Leaching	348
5.6.10.1 pH and Conductivity	348
5.6.10.2 Leaching Behavior of Major Species	348
5.6.10.3 Conclusions	351
5.6.11 Release Modeling	352
5.7 Modeling of Heterogeneous Materials	352
5.7.1 Effect of the Volume Fraction of Material Occupied by the Aggregates ...	356

TABLE OF CONTENTS
(continued)

<u>Section</u>	<u>Page</u>
5.7.2 Effect of Aggregate Size	356
5.7.3 Effect of Differences in Mass Transfer Rate Between the Components ...	356
5.7.4 Conclusions	356
 CHAPTER 6. CONCLUSIONS	 360
6.1 Summary of Findings	360
6.2 Conclusions.	385
6.3 Suggestions for Future Work	385
 CHAPTER 7. REFERENCES	 387

PROTECTED UNDER INTERNATIONAL COPYRIGHT
ALL RIGHTS RESERVED
NATIONAL TECHNICAL INFORMATION SERVICE
U.S. DEPARTMENT OF COMMERCE

LIST OF TABLES

<u>Table</u>		<u>Page</u>
1	Inventory of Iowa samples	26
2	Fine aggregate sieve analyses (percent passing)	28
3	Chemical analysis of cements used in U.S. 20 (1987) and the accelerated aging project (1997) (percent)	28
4	Physical analysis of cement used in the accelerated aging project (1997)	28
5	Water reducing admixture dosage	30
6	AutoPore III specifications	32
7	TriStar specifications	34
8	Coarse aggregate used in laboratory prism BET-N ₂ surface area analysis	34
9	Leaching time intervals used for the monolithic leaching tests carried out on U.S. 20 slab samples	51
10	Leaching time intervals used for the monolithic leaching tests carried out on CFA-C mix	52
11	Leaching time intervals used for the monolithic leaching tests carried out on CFA-F mix	54
12	Leaching time intervals used for the monolithic leaching tests carried out on PCC control mix	54
13	Leaching time intervals used for the monolithic leaching test carried out on the coarse aggregates	55
14	Material quantities used in U.S. 20 (1987) mix design	60
15	Material quantities used in the accelerated aging mix design (1997)	60
16	Batching quantities for CFA-C and PCC batches	62
17	Batching quantities for CFA-C batches	62
18	Mixing procedure	63

LIST OF TABLES
(continued)

<u>Table</u>	<u>Page</u>
19	Average equivalent ages (in yr) at 20°C at the end of thermal age treatment 69
20	Oxide analysis of coal fly ashes 78
21	Estimated oxide content of the portland cement 79
22	Surface elemental composition of CFA-C and CFA-F (+/- standard deviation) . . . 87
23	Geochemical modeling species for the hydrated portland cement paste 106
24	Air content and slump results on freshly mixed concrete 111
25	U.S. 20 slab core compressive strengths 114
26	Crack density results (in percent) for slab specimens 114
27	U.S. 20 slab first peak nine highest $\Delta P/\Delta \log(d)$ values and their corresponding pore widths 117
28	U.S. 20 slab second peak nine highest $\Delta P/\Delta \log(d)$ values and their corresponding pore widths 118
29	MIP results on U.S. 20 slab samples 119
30	U.S. 20 slab cores BET-N ₂ surface area analysis 122
31	Common concrete mineral phases identified in the U.S. 20 slab 124
32	Average mineral concentrations in the U.S. 20 slab 126
33	Geochemical modeling species for U.S. 20 slab 142
34	Physical properties of U.S. 20 slab, southeast region (sample O-SC) and chemical properties of leachates and pore water 148
35	Major species and trace metal concentrations in contact solutions of U.S. 20 slab samples – comparison with ground water 158
36	Parameter estimates for the release of Na from the one-dimensional diffusion model – U.S. 20 slab samples 160

LIST OF TABLES
(continued)

<u>Table</u>	<u>Page</u>
37	Parameter estimates for the release of K from the one-dimensional diffusion model – U.S. 20 slab samples 161
38	Parameter estimates for the release of Cl from the one-dimensional diffusion model – U.S. 20 slab samples 162
39	Parameter estimates for the release of Ca from the one-dimensional diffusion model – U.S. 20 slab samples 163
40	Post-treatment compressive strength of laboratory-created concrete 166
41	Average compressive strength change from cyclic loading of CFA-C concrete samples 168
42	Crack density results (in %) for CFA-C prism specimens 170
43	CFA-C prism first peak nine highest $\Delta P/\Delta \log(d)$ values and their corresponding pore widths 174
44	CFA-C prism second peak nine highest $\Delta P/\Delta \log(d)$ values and their corresponding pore widths 175
45	MIP results on CFA-C prism samples 177
46	Results from BET-N ₂ adsorption analysis of CFA-C prisms 186
47	Example table of crystalline phases identified by XRPD sample C(NNN)09 186
48	Mineral phases quantified by XRPD 188
49	Summary of significant differences in species concentration in CFA-C leachate due to main effects 197
50	Summary of significant differences in species concentration in CFA-C leachate due to interaction effects 200
51	Geochemical modeling species for CFA-C prisms 201
52	Physical properties of 28-d cured and high temperature-aged CFA-C prisms and chemical properties of leachates and pore water 208

LIST OF TABLES
(continued)

<u>Table</u>	<u>Page</u>
53 ANOVA on the effects of accelerated aging on Na cumulative release at 22 d of leaching - CFA-C prisms	218
54 ANOVA on the effects of accelerated aging on K cumulative release at 22 d of leaching - CFA-C prisms	218
55 ANOVA on the effects of accelerated aging on Ca cumulative release at 22 d of leaching - CFA-C prisms	218
56 Parameter estimates for the release of Na from the one-dimensional diffusion model – 28-d cured and high level aged CFA-C prisms	221
57 Parameter estimates for the release of K from the one-dimensional diffusion model – 28-d cured and high level aged CFA-C prisms	222
58 Parameter estimates for the release of Cl from the one-dimensional diffusion model – 28-d cured and high level aged CFA-C prisms	223
59 Parameter estimates for the release of Ca from the one-dimensional diffusion model – 28-d cured and high level aged CFA-C prisms	224
60 Parameter estimates for the release of Na from the one-dimensional diffusion model – CFA-C prisms with other levels of aging	228
61 Parameter estimates for the release of K from the one-dimensional diffusion model – CFA-C prisms with other levels of aging	229
62 Parameter estimates for the release of Ca from the one-dimensional diffusion model – CFA-C prisms with other levels of aging	230
63 Parameter estimates for the release of Na from the one-dimensional diffusion model – the three center point replicates of CFA-C prisms	231
64 Parameter estimates for the release of K from the one-dimensional diffusion model – the three center point replicates of CFA-C prisms	232
65 Parameter estimates for the release of Ca from the one-dimensional diffusion model – the three center point replicates of CFA-C prisms	233
66a Post-treatment compressive strength of CFA-C prisms	236
66b Post-treatment compressive strength of CFA-F prisms	236

LIST OF TABLES
(continued)

<u>Table</u>	<u>Page</u>
66c Post-treatment compressive strength of PCC prisms	236
67 Crack density results (in %) for prism specimens	238
68 Summary of RDM values for prisms subjected to LLL treatments	240
69 CFA-F first peak nine highest $\Delta P/\Delta \log(d)$ values and their corresponding pore widths	245
70 PCC first peak nine highest $\Delta P/\Delta \log(d)$ values and their corresponding pore widths	246
71 CFA-F second peak nine highest $\Delta P/\Delta \log(d)$ values and their corresponding pore widths	247
72 PCC concrete second peak nine highest $\Delta P/\Delta \log(d)$ values and their corresponding pore widths	248
73 MIP results on CFA-C, CFA-F and PCC low treated concrete samples	249
74 Results from BET-N ₂ adsorption analysis of laboratory prisms	251
75 Mineral concentrations in the three types of experimental prisms quantified by XRPD	253
76 Summary table of ANOVA for leaching of three types of concrete	265
77 Summary table of Tukey-Kramer tests for leaching of three types of concrete	266
78 Geochemical modeling species for three types of concrete mixes	268
79 Physical properties of the three 28-d cured material types (CFA-C, CFA-F and PCC) and chemical properties of leachates and pore water	277
80 Major species and trace metal concentrations in contact solutions of C(XXX)02, F(XXX)02 and P(XXX)02 – comparison with ground water	286
81 Parameter estimates for the release of Na from the one-dimensional diffusion model – comparison between the three 28-d cured material types (CFA-C, CFA-F and PCC)	301

LIST OF TABLES
(continued)

<u>Table</u>	<u>Page</u>
82	Parameter estimates for the release of K from the one-dimensional diffusion model – comparison between the three 28-d cured material types (CFA-C, CFA-F and PCC) 302
83	Parameter estimates for the release of Cl from the one-dimensional diffusion model – comparison between the three 28-d cured material types (CFA-C, CFA-F and PCC) 302
84	Parameter estimates for the release of Ca from the one-dimensional diffusion model – comparison between the three 28-d cured material types (CFA-C, CFA-F and PCC) 304
85	Parameter estimates for the release of Na from the one-dimensional diffusion model – CFA-F 307
86	Parameter estimates for the release of K from the one-dimensional diffusion model – CFA-F 308
87	Parameter estimates for the release of Cl from the one-dimensional diffusion model – CFA-F 309
88	Parameter estimates for the release of Ca from the one-dimensional diffusion model – CFA-F 310
89	Parameter estimates for the release of Na from the one-dimensional diffusion model – PCC 312
90	Parameter estimates for the release of K from the one-dimensional diffusion model – PCC 313
91	Parameter estimates for the release of Cl from the one-dimensional diffusion model – PCC 314
92	Parameter estimates for the release of Ca from the one-dimensional diffusion model – PCC 315
93	Parameter estimates from the one-dimensional diffusion model – coarse aggregates 317
94	Oxide analysis of cements used in Iowa and laboratory concretes 321
95	Oxide analyses of CFA-C used in Iowa and in laboratory concretes 322

LIST OF TABLES
(continued)

<u>Table</u>	<u>Page</u>
96 Total elemental composition (+/- standard deviation) of major elements in CFA-C prism and U.S. 20 slab concrete (>10,000 ppm)	323
97 Total elemental composition (+/- standard deviation) of minor elements in CFA-C prism and U.S. 20 slab concrete (1,000 - 10,000 ppm)	323
98 Total elemental composition (+/- standard deviation) of trace elements in CFA-C prism and U.S. 20 slab concrete (<1,000 ppm)	324
99 Phases identified in both CFA-C prism and U.S. 20 slab	329
100 Geochemical modeling species for the CFA-C prism and U.S. 20 slab	339
101 Physical properties of 28-d cured CFA-C, high temperature-aged CFA-C and U.S. 20 slab concrete samples and chemical properties of leachates and pore water	345
102 Parameter estimates for the release of Na from the one-dimensional diffusion model – comparison between CFA-C and U.S. 20 slab	353
103 Parameter estimates for the release of K from the one-dimensional diffusion model – comparison between CFA-C and U.S. 20 slab	353
104 Parameter estimates for the release of Cl from the one-dimensional diffusion Model – Comparison Between CFA-C Mix and U.S. 20 Slab	354
105 Parameter estimates for the release of Ca from the one-dimensional diffusion model – comparison between CFA-C mix and U.S. 20 Slab	354
106 Summary of results of response variables in the 2 ³ + 3 experimental design for the CFA-C prisms	366
107 Summary of results of Tukey-Kramer comparisons in the three center point experimental design for the CFA-C, CFA-F and PCC prisms	372
108 Summary of results of comparing the CFA-C prisms to the U.S. 20 Slab	377

LIST OF FIGURES

<u>Figure</u>		<u>Page</u>
1	Schematic of development of mechanical and transport properties over time	8
2	Examples of development of compressive strength and permeability over time. . .	8
3	Schematic of degradation of properties over time and of cumulative effects of degradation	10
4	Schematic of development and degradation of mechanical properties over time . .	10
5	U.S. 20 slab saw cut at shoulder and cold joint	22
6	Contractors remove slab on 5 November 1997	22
7	Slab is visually inspected at UNH	23
8	Crack running in direction of traffic along whole length of slab	23
9	Crack is 100 mm deep at cold joint	24
10	Removing bricks from the joint/cut corner	24
11	Final core and brick locations	25
12	Orientation of saw cuts for microcrack analyses of road cores	42
13	Typical neutron radiograph.	42
14	Typical microcrack trace	42
15	Orientation of saw cuts for prism samples	44
16	Geometric representation of factorial experiment	58
17	Labeling scheme	63
18	Curing Tank	66
19	Prism samples in curing tank	66
20	Dummy prisms and temperature probe	67
21	Conceptual model for a heterogeneous porous material	74

LIST OF FIGURES
(continued)

<u>Figure</u>	<u>Page</u>
22	Total content of trace metals as determined by calculation – prisms 81
23	Total content of major species as determined by calculation – prisms 82
24	MIP results for coarse aggregate: (a) cumulative porosity vs. pore width; (b) average differential pore size distribution vs. pore width 84
25a	FESEM micrograph of a CFA-C 86
25b	FESEM micrograph of a CFA-F 86
26	Acid neutralization capacity curves 91
27	Constituent solubility as a function of pH 92
28	pH-dependent leaching of the portland cement paste: (a) Ca, (b) Mg, (c) Al, (d) Si 97
29	pH-dependent leaching of portland cement paste: (a) Ba, (b) Zn, (c) Fe, (d) Cr ... 98
30	pH-dependent leaching of portland cement paste: (a) K, (b) Cl, (c) CO ₃ ²⁻ , (d) SO ₄ ²⁻ 99
31	Ca modeling in cement paste. 101
32	Mg modeling in cement paste. 101
33	Al modeling in cement paste. 102
34	Si modeling in cement paste. 102
35	Ba modeling in cement paste. 103
36	Zn modeling in cement paste. 103
37	Fe modeling in cement paste. 104
38	Cr modeling in cement paste. 104
39	CO ₃ ²⁻ modeling in cement paste. 105
40	SO ₄ ²⁻ modeling in cement paste. 105

LIST OF FIGURES
(continued)

<u>Figure</u>	<u>Page</u>
41	Comparison between total content, maximum of solubility at pH<3 and availability using EDTA extractions at pH 7 109
42	Sampling diagram of the U.S. 20 slab 112
43	MIP results for 1-C(4): (a) cumulative porosity vs. pore width; (b) average differential pore size distribution vs. pore width 116
44	Cumulative porosity vs. pore width plot for Iowa U.S. 20 concrete 120
45	Average differential pore size distribution vs. pore width of U.S. 20 slab. 122
46	Vertical sectioning of core material from the U.S. 20 slab 124
47	Acid neutralization capacity curves for the U.S. 20 concrete samples 130
48	Concentration and solubility as a function of pH for the U.S. 20 concrete samples 131
49	pH-dependent leaching of U.S. 20 slab concrete: (a) Ca, (b) Mg, (c) Al, (d) Si ... 133
50	pH-dependent leaching of U.S. 20 slab concrete: (a) Ba, (b) Zn, (c) Fe, (d) Cr ... 134
51	pH-dependent leaching of U.S. 20 slab concrete: (a) K, (b) Cl, (c) CO ₃ ²⁻ , (d) SO ₄ ²⁻ 135
52	Ca modeling in the U.S. 20 slab. 137
53	Mg modeling in the U.S. 20 slab. 137
54	Al modeling in the U.S 20 slab. 138
55	Si modeling in the U.S. 20 slab. 138
56	Ba modeling in the U.S. 20 slab. 139
57	Zn modeling in the U.S. 20 slab. 139
58	Fe modeling in the U.S. 20 slab. 140
59	Cr modeling in the U.S. 20 slab 140

LIST OF FIGURES
(continued)

<u>Figure</u>	<u>Page</u>
60	CO ₃ ²⁻ modeling in the U.S. slab. 141
61	SO ₄ ²⁻ modeling in the U.S. 20 slab. 141
62	A) pH and B) conductivity as a function of LS ratio in the U.S. 20 concrete sample, southeast region (sample O-SC) 146
63	Major species concentration as a function of LS ratio: A) Na, B) K, C) Cl, D) SO ₄ ²⁻ , and E) Ca in the U.S. 20 sample 147
64	Comparison between total content, maximum of solubility at pH<3, and availability using EDTA extraction at pH 7 in the U.S. 20 samples, two locations 150
65	A) Leachate pH and B) leachate conductivity obtained after each leaching interval of three samples representing the bulk of the U.S. 20 slab and a sample representing the surface 152
66	Na release for three samples representing the bulk of the U.S. 20 slab and a sample representing the surface: A) cumulative mass released in mg/m ² ; B) flux released in mg/m ² s 152
67	Cd release from samples representing the bulk of the U.S. 20 slab: A) cumulative mass released in μg/m ² ; B) flux released in μg/m ² s and C) leachate concentrations in μg/l 155
68	Cu release from samples representing the bulk of the U.S. 20 slab: A) cumulative mass released in μg/m ² ; B) flux released in μg/m ² s and C) leachate concentrations in μg/l 156
69	Pb release from samples representing the bulk of the U.S. 20 slab: A) cumulative mass released in μg/m ² ; B) flux released in μg/m ² s and C) leachate concentrations in μg/l 157
70	MIP results for C(NNN)09: (a), cumulative porosity vs. pore width; (b), average differential pore size distribution vs. pore width 173
71	Average differential pore size distribution vs. pore width plots of all Type-C concrete samples with high and no levels of heat treatment 179
72	Average differential pore size distribution vs. pore width plot for C(NNN)09 and C(NNH)09 180

LIST OF FIGURES
(continued)

<u>Figure</u>		<u>Page</u>
73	Average differential pore size distribution vs. pore width plot for C(HNN)09 and C(HNH)09	181
74	Average differential pore size distribution vs. pore width plot for C(NHN)09 and C(NHH)09	182
75	Average differential pore size distribution vs. pore width plot for C(HHN)09 and C(HHH)09	183
76	Acid neutralization capacity curves for CFA-C mix	190
77	Solubility as a function of pH for CFA-C mix	191
78	pH-dependent leaching of the experimental CFA-C prisms: (a) Ca, (b) Mg, (c) Al, (d) Si	193
79	pH-dependent leaching of the experimental CFA-C prisms: (a) Ba, (b) Zn, (c) Fe, (d) Cr	194
80	pH-dependent leaching of the experimental CFA-C prisms: (a) K, (b) Cl, (c) CO ₃ ²⁻ , (d) SO ₄ ²⁻	195
81	A) pH and B) conductivity as a function of LS ratio	205
82	Major species concentration as a function of LS ratio: A) Na, B) K, C) Cl, D) SO ₄ ²⁻ , and E) Ca	206
83	A) Leachate pH, B) leachate pH and C) leachate conductivity for CFA-C mix. ...	211
84	Na release for 28-d cured and high level aged samples: A) cumulative mass released in mg/m ² ; B) flux released in mg/m ² s	212
85	A), Leachate pH, B) leachate pH and C) leachate conductivity for CFA-C mix: comparison between 28-d cured and aged samples	215
86	Na release for 28-d cured and aged samples: A) cumulative mass released in mg/m ² ; B) flux released in mg/m ² s	216
87	MIP results for C(LL)09: (a), cumulative porosity vs. pore width; (b) average differential pore size distribution vs. pore width	242

LIST OF FIGURES
(continued)

<u>Figure</u>	<u>Page</u>
88 Cumulative porosity vs. pore width plot for CFA-C concrete low treatment samples	243
89 Average differential pore size distribution vs. pore width plot of CFA-C low treatment samples	244
90 Average differential pore size distribution vs. pore width plot for the low treatment CFA-C, CFA-F, and PCC prisms	251
91 Acid neutralization capacity curves	257
92 Solubility as a function of pH: A) Cd, B) Cu, C) Pb, D) Ni, E) Zn	259
93 pH-dependent leaching of three types of concrete: (a) Ca, (b) Mg, (c) Al, (d) Si ..	261
94 pH-dependent leaching of three types of concrete: (a) Ba, (b) Zn, (c) Fe, (d) Cr ..	262
95 pH-dependent leaching of three types of concrete: (a) K, (b) Cl, (c) CO ₃ ²⁻ , (d) SO ₄ ²⁻	263
96 Acid neutralization capacity curves	271
97 Solubility as a function of pH: A) Cd, B) Cu, C) Pb, D) Ni, E) Zn	272
98 A) pH and B) conductivity as a function of LS ratio	274
99 Major species concentration as a function of LS ratio: A) Na, B) K, C) Cl, D) SO ₄ ²⁻ and E) Ca	275
100 Comparison between constituent total content, solubility at pH<3 and availability using EDTA extraction at pH 7	280
101 A) Leachate pH, B) leachate pH and C) leachate conductivity	281
102 Na release from the three 28-d cured material types: A) cumulative mass released in mg/m ² ; B) flux released in mg/m ² s	283
103 A) Leachate pH, B) leachate pH, and C) leachate conductivity obtained after each leaching interval for CFA-F mix	288
104 Na release for CFA-F mix: A) cumulative mass released in mg/m ² ; B) Flux released in mg/m ² s	289

LIST OF FIGURES
(continued)

<u>Figure</u>	<u>Page</u>
105 A) Leachate pH and B) leachate conductivity obtained after each leaching interval for PCC control	291
106 Na release for PCC control: A) cumulative mass released in mg/m ² ; B) flux released in mg/m ² s	293
107 A) Leachate pH and B) leachate conductivity obtained after each leaching interval for the coarse aggregates	295
108 Na release from the coarse aggregates: A) cumulative mass released in mg/m ² ; B) flux released in mg/m ² s	297
109 Comparison between the three 28-d cured material types and the coarse aggregates: A) Na flux; B) K flux; C) SO ₄ ²⁻ flux; D) Ca flux	298
110 Average differential pore size distribution vs. pore width plot for laboratory-created CFA-C and Iowa U.S. 20 concrete.	327
111 Comparison of mineral concentrations in U.S. 20 concrete and CFA-C prisms: (a) ettringite, (b) gypsum	330
112 Comparison of mineral concentrations in U.S. 20 concrete and experimental CFA-C prisms: (a) albite, (b) calcite, (c) portlandite, (d) quartz	331
113 Acid neutralization capacity curves	333
114 Solubility as a function of pH: A) Cd, B) Cu, C) Pb, D) Ni, E) Zn	334
115 Comparison of pH-dependent leaching of the experimental CFA-C prism concrete and the U.S. 20 slab concrete: (a) Ca, (b) Mg, (c) Al, (d) Si	335
116 Comparison of pH-dependent leaching of the experimental CFA-C prism concrete and the U.S. 20 slab concrete: (a) Ba, (b) Zn, (c) Fe, (d) Cr	337
117 Comparison of pH-dependent leaching of the experimental CFA-C prism concrete and the U.S. 20 slab concrete: (a) K, (b) Cl, (c) CO ₃ ²⁻ , (d) SO ₄ ²⁻	338
118 A) pH and B) conductivity as a function of LS ratio	343
119 Major species concentration as a function of LS ratio: A) Na, B) K, C) Cl, D) SO ₄ ²⁻ , E) Ca	344

LIST OF FIGURES
(continued)

<u>Figure</u>		<u>Page</u>
120	Comparison between total content, maximum of solubility at pH<3, and availability using EDTA extractions at pH 7	347
121	A) Leachate pH, B) leachate pH and C) leachate conductivity	349
122	Na release: A) cumulative mass released in mg/m ² ; B) flux released in mg/m ² s	350
123	Release flux as a function of volume fraction of material occupied by the aggregates: A) model system 1 and B) model system 2	357
124	Release flux as a function of aggregate size: A) model system 1 and B) model system 2	357
125	Release flux when diffusion in the aggregates was A) much slower than in the binder; B) much faster than in the binder; and C) the same as in the binder	358

CHAPTER 1: TECHNICAL SUMMARY

Need to Predict Long-term Performance

Use of recycled materials in a proposed highway application frequently requires the assessment of physical and environmental performance. Future behavior is often difficult to predict. Field-scale demonstrations are frequently employed to provide useful information.

As an alternative to field demonstrations, there is a need to develop strategies to predict long-term physical and environmental performance, particularly approaches that involve cost-effective laboratory procedures, experimental methods, data evaluation, and predictive models that are available to practitioners and decision makers.

Use of Accelerated Aging to Predict Long-term Performance

Accelerated aging is one means of exploring the long-term physical and environmental performance of recycled materials in a highway application. Accelerated aging methods require an understanding of both developmental and degradative aging mechanisms and the factors influencing them.

Purpose

The project had a two principal objectives:

- Develop and verify an accelerated aging method that allows examination of the effects of developmental and degradative aging variables on highway concrete pavement performance.
- Examine the interrelation between physical and environmental behavior, especially as it relates to aging.

Scope of the Project

Coal fly ash (CFA) use in portland cement concrete (PCC) was selected as a model system to develop an accelerated aging approach. CFA is widely used in the highway environment and its use as a cementitious replacement material is well understood. The PCC matrix possesses time-dependent physicochemical strength development properties that make it useful for the study of developmental and degradative aging mechanisms.

Three types of accelerated aging were chosen for this project: Arrhenius aging (AA), cyclic loading (CL), and freeze-thaw exposure (FT). AA was intended to accelerate chemical reactions leading to development and maturation of the microstructure in PCC and to accelerate possibly deleterious reactions between components, while CL and FT exposure were intended to rapidly degrade the monolithic material. This approach allowed us to systematically explore the separate and combined interactions of both developmental and degradative accelerated aging

variables.

To conduct this study, a field verification site was needed. After a preliminary review of literature on early distress, it was decided to use pavements from U.S. 20 in northwest Iowa. This pavement, constructed in 1987, experienced early distress. Numerous early distress or failure mechanisms have been hypothesized for U.S. 20, including low initial air contents (either low in the mix or low after placement), high alkali contents in the mixes, alkali silica reaction, freeze-thaw damage, and the appearance of ettringite ($\text{Ca}_6\text{Al}_2(\text{SO}_4)_3(\text{OH})_{12}\cdot 26\text{H}_2\text{O}$) in air voids.

The study had five major experimental components:

- Characterize the component materials that would be used to recreate the job mix from the U.S. 20 project.
- Use a factorial experiment to investigate both the individual and interactive effects of the three accelerated aging variables (AA, CL, FT) on a variety of physical and environmental response variables of the class C coal fly ash (CFA-C) mix.
- Use a designed experiment to compare the CFA-C mix to two controls: one containing a class F coal fly ash (CFA-F) and one containing just PCC.
- Compare the response variables of the aged CFA-C samples with those observed in a slab from the U.S. 20 field site.
- Develop a heterogeneous monolithic leaching model to better describe leaching from multi-component matrices such as concrete pavement slabs containing recycled materials, aggregates, and binder.

Methodology

To compare the properties of the component materials with those used in the original mix in 1987, a series of physical and environmental characterizations were conducted on the coal fly ashes, cements (or mortars made from the cement), and aggregates.

Methods were developed to expose the CFA-C, CFA-F and PCC prisms to various levels of AA, CL, and FT to conform to the experimental designs that were used.

A variety of physical and environmental response variables were used to examine the U.S. 20 pavement slab and the aged laboratory prisms. For physical testing, these included compressive strength, microcracking, relative dynamic modulus, porosity, effective pore size, and effective surface area. For environmental testing, response variables included total elemental composition, mineralogy, acid neutralizing capacity, low liquid-to-solid ratio (LS) leaching, pH-dependent leaching, pH-stat leaching, geochemical modeling of controlling solids, availability leaching, and monolithic diffusional leaching. A high degree of potential interaction between the physical and environmental methods was expected.

Results

An accelerated aging protocol was developed to look at the individual and interactive effects of one developmental and two degradative aging methods on the physical and environmental performance of PCC made with coal fly ash.

The aging protocol impacted both physical and chemical properties of the monoliths. Generally speaking, the main effects were more important than the interactive effects, which was unexpected.

It took about 9 mo of elapsed time to age specimens to an equivalent age of up to 4 yr. The equivalent ages matched well with the time frame seen in the field for the onset of early distress and also matched well the chronological age of the field pavement.

The use of a factorial design was useful in exploring the possibilities of this method; however, given the limited interactions that were seen, the use of experimental variables themselves may be appropriate.

AA significantly reduced the compressive strength of the concrete, possibly indicating the onset of a deleterious reaction in the mix. CL affected the microcracking in the concrete. All aging variables affected the fine pore structure of the concrete. CL affected the Ca diffusional leaching from the monoliths.

Logically, there appears to be a linkage between strength loss, microcracking, and leaching behavior of a major matrix constituent in the concrete (Ca).

Most response variables from the aged laboratory prisms and the field samples were similar, suggesting that the method did a reasonable job of producing a pavement of similar age and distress.

Certain field aging phenomena could not be recreated in the laboratory specimens. These phenomena include more extensive microcracking from unknown sources, road salting, and carbonation.

Conclusions

The accelerated aging method appeared successful in recreating the phenomena that may have contributed to the failure of the field slab. The AA treatment produced an unexpected loss of strength that suggests the accelerated aging promoted the onset of a deleterious reaction.

The use of both physical and environmental response variables shows the linkage between such variables as compressive strength, microcracking, fine pore structure, Cl diffusive leaching (an efflux related to road salting that increases the concentration of Cl in the monolith) and Ca diffusive leaching (related to change in matrix structure and loss of Ca).

The use of CFA as a model recycled material in a portland cement matrix was only

partially useful in exploring the interaction of physical and environmental performance: The trace metal content and contaminants of concern were present in similar concentrations in the CFA, portland cement, and the aggregates. These constituents leached at very low levels. It was impossible to describe which source term contributed to the low signals that were measured.

When evaluating field specimens that have undergone early distress and field aging, it is important to consider samples that have been exposed to additional aging phenomena related to road traffic, road salting, CO₂ uptake, etc. These sub-samples may behave very differently from bulk samples that have aged less drastically.

Comparisons with earlier accelerated aging methods for bituminous asphaltic pavements is useful: In hydrophobic monoliths with little chemical reactivity, loss of tortuosity dramatically impacts the diffusive leaching behavior of many constituents of concern contained in recycled materials. In portland cement concrete, the matrix is hydrophilic, contains a much more elaborate fine pore structure, and the matrix is chemically reactive (e.g., sorption, acid-base reactions, and exchange reactions can occur). Despite significant aging, the matrix may be able to still control contaminant release. Aging in a portland cement matrix is a much more complex system to describe and model.

A diffusion model that explored monolith heterogeneity was developed and proved useful in evaluating diffusive leaching data. Care should be taken in using diffusion models in which components of widely different tortuosity are present.

Suggestions for Future Work

As further data are developed about the failure of the U.S. 20 pavement, it will be important to relate that work to this work.

This proposed accelerated aging method can be further evaluated with other recycled materials in a portland cement matrix, particularly ones that might contribute a more significant signature for contaminants of concern.

To make this approach as useful as possible to the highway and recycling community, it may be useful to explore means to speed up the accelerated aging approach to make it more utilitarian. A method that takes 1 or 2 months may be more useful than one that takes many months.

It may be useful to further explore the importance of other aging phenomena (Cl intrusion/release, carbonation, etc.) as these aging variables may also contribute to environmental behaviors (either beneficial or detrimental).

If an accelerated aging method is to be adopted, then this approach needs to be shared and evaluated by other researchers. Perhaps then a consensus can be reached about a method.

If an accelerated aging method is to be used, it will be necessary to develop a short list of physical and environmental response variable test methods that may be coupled with an aging

protocol to be used in an accelerated aging procedure or method for evaluating future uses of recycled materials in portland cement matrices.

Given the need for accelerated aging, it will be useful to consider development of an accelerated aging protocol for other highway applications such as flowable fill, stabilized base, and granular fill, in which other developmental and degradative aging methods will be occurring.

CHAPTER 2: INTRODUCTION AND PURPOSE

2.1 Need to Predict Long-term Performance for Recycled Materials

Recycled materials are used widely in the highway environment as aggregate substitutes in portland cement concrete (PCC) and bituminous asphalt pavements; as aggregate substitutes in base course, sub-base and embankments; and as components in flowable fill, concrete and asphalt. Some of these uses are so mature they are considered standard practice. However, new recycled materials applications are being proposed, which raises new questions about potential performance.

New recycled materials applications frequently require the assessment of physical and environmental properties. However, the future behaviors of the product in the application, both physical and environmental, are often difficult to predict. Such information is critical for gaining approval from both highway practitioners and environmental regulators.

Full-scale or mini-scale demonstrations are frequently employed to provide useful information on performance. However, these demonstrations are both costly and require long periods of time (frequently decades) to provide quantifiable results showing that the application is suitable. If the performance of the application is unsuitable, then the material must be removed and the application must be re-engineered.

There is, and will always be, a need for such demonstrations. However, there is also a need to develop alternative strategies to predict long-term physical and environmental performance, particularly if the predictive approach involves cost-effective laboratory procedures, experimental methods, data evaluation, and predictive models that are available to practitioners and decision makers (OECD, 1997; Eighmy and van der Sloot, 1994).

The ability to accurately predict both the long-term physical and environmental performance of a waste utilization application is desirable for a number of reasons.

First, it could provide timely and valuable information to decision makers who need to assure the public that a road constructed with waste materials will remain functional and durable over its design life. Second, it could also provide valuable information to decision makers that the product will have acceptable environmental performance over time. Third, in many cases, it may reduce or eliminate the need to conduct costly and lengthy large-scale field-scale demonstrations. Fourth, it could allow correlation between physical and environmental performances over time, as these are typically interrelated (Eighmy and van der Sloot, 1994; Eighmy et al., 1995; Eighmy et al., 1997; van der Wegen and van der Plas, 1994; Fuhrmann et al., 1989). Fifth, it also could provide source term estimates for fluxes of waste constituents from the product over the design life of the application (Eighmy et al., 1995; Kosson et al., 1996); these source term estimates are required for health risk assessments conducted by regulators performing beneficial use determinations.

2.2 Use of Accelerated Aging to Predict Long-term Performance

As part of our early efforts to understand the long-term performance of pavements made with waste materials, we have studied bituminous asphalt pavements made with municipal solid waste bottom ash. We found that asphalt monolith properties (e.g., aggregate substitution rate, asphalt cement content) and monolith accelerated aging (e.g., change in voids, degree of microcracking, bituminous polymer aging, field aging) dramatically influence monolithic diffusional leaching (Eighmy et al.; 1996; Eighmy et al., 1997). Aging resulting in microcracking plays a major role in controlling the environmental behavior of the product. The long-term environmental behavior has also been modeled and partially verified (Eighmy et al., 1996, 1997; Kosson et al., 1996).

This earlier work represented just one recycled material in one application in the highway environment. Further, it focused on bituminous asphalt pavements—a hydrophobic matrix with differing physicochemical properties than many applications in the highway environment.

We desired to expand this concept to develop an approach that would be more wide ranging, more generally applicable, and more systematic in its application of accelerated aging principles.

2.2.1 Development of Systematic Aging Protocols That Can Be Generally Applied

Aging is a natural process that all materials experience over time. One definition for aging is as follows: Aging is the totality of irreversible chemical and physical alterations that may occur within a material in the course of time (Sasse and Schrage, 1983).

For many highway construction materials, the concept of aging has two main components: the development or maturation process in which the material forms an internal microstructure, and the degradation process in which it loses integrity (figures 1 and 2). While both processes involve physicochemical reactions, degradation often involves mechanical processes as well.

For many materials used in the highway environment, the time-dependent development of useful mechanical properties such as hardness, toughness, compressive, tensile, or shear strength, or modulus of elasticity follows a pattern schematically illustrated on the left of figure 1. Similarly, for the same materials, microstructural characteristics such as porosity, or transport properties such as permeability, diffusivity, or absorptivity might change with time in the manner indicated on the right of figure 1.

The use of PCC as a model application to develop an accelerated aging approach is particularly interesting as it allows for the evaluation of both maturation and degradation processes. In the specific case of PCC, the degree of hydration of the portland cement follows a pattern over time indicated by curve 1 on the left in figure 1. The time-dependent development of the microstructure of the hardened cement paste (HCP) therefore manifests itself

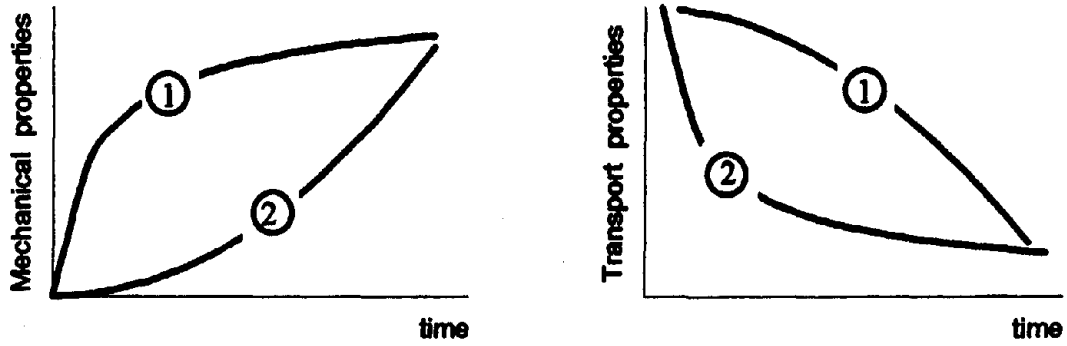


Figure 1: Schematic of development of mechanical and transport properties over time.

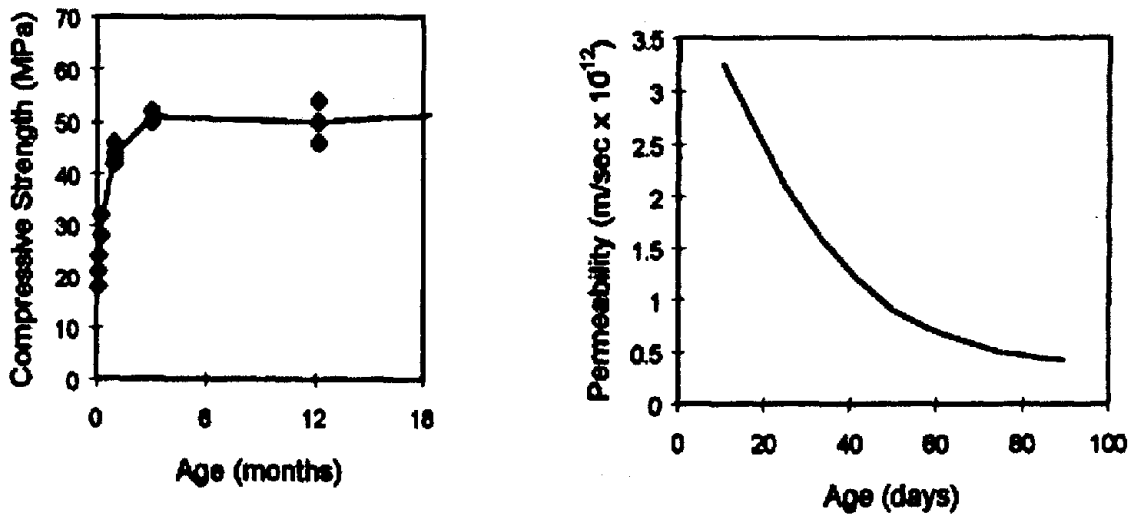


Figure 2: Examples of development of compressive strength and permeability over time.

in the development of mechanical properties such as compressive strength, tensile strength, or modulus of elasticity in the same general manner, as seen in figure 2. As the hardened paste microstructure becomes denser as a result of continued hydration, the capillary porosity of the paste is reduced over time as indicated by curve 2 on the right in figure 1. As a consequence, permeability and other transport properties such as absorptivity and diffusivity can diminish over time as shown on the right in figure 2.

The time dependent degradation of materials such as PCC can be represented by graphs such as those in figures 3 or 4. In figure 3, the first of these patterns indicates the reduction in mechanical properties such as strength or stiffness (elastic or dynamic modulus) as a function of time, while figure 4 shows a more direct measure of the extent of degradation via cumulative mass loss, depth of penetration, and increased volume of cracking. Note that in both cases the degradation may ultimately stabilize or it may become increasingly severe.

The reduction in modulus of elasticity that accompanies repeated cycles of freezing and thawing of non-frost-resistant concrete is indicated by curve 1 on the left of figure 3. Surface scaling of concrete can be tracked by plotting cumulative mass of material lost as a function of the number of freeze-thaw cycles, as indicated in curve 1 on the right of figure 3.

2.2.2 The Concept of Accelerated Aging

Accelerated or “artificial” aging is the process in which one or more of the development and/or degradation mechanisms of a material is intentionally accelerated. In this work “accelerated aging” is an umbrella term incorporating both accelerated development (constructive aging) and accelerated degradation (destructive aging), and refers to processes or exposures designed to modify the character of the material.

Figure 4 schematically describes the purpose of accelerated aging techniques, in which an accelerated development process and accelerated degradation process are shown by the dotted lines. These figures present a natural and an accelerated development and/or degradation curve over time, by plotting any specific property reflective of material behavior. The long-term behavior P_L occurs at time t_L . The goal of accelerated aging techniques is to produce P_L at a shorter time t_s .

To design a quantitatively meaningful exposure, accelerated aging methods require an understanding of the development/degradation mechanisms and the factors influencing them. Thus, accelerated methods must isolate the influential factors and suitably intensify their impact so as to accelerate the actual development and /or degradation mechanisms without triggering anomalous material responses or reactions that would never have developed under actual service conditions, regardless of duration of exposure.

Three types of accelerated aging were chosen for this project: Arrhenius aging (AA), cyclic loading (CL), and freeze-thaw exposure (FT). AA was intended to enhance the development or maturation of microstructure and possibly deleterious reactions between

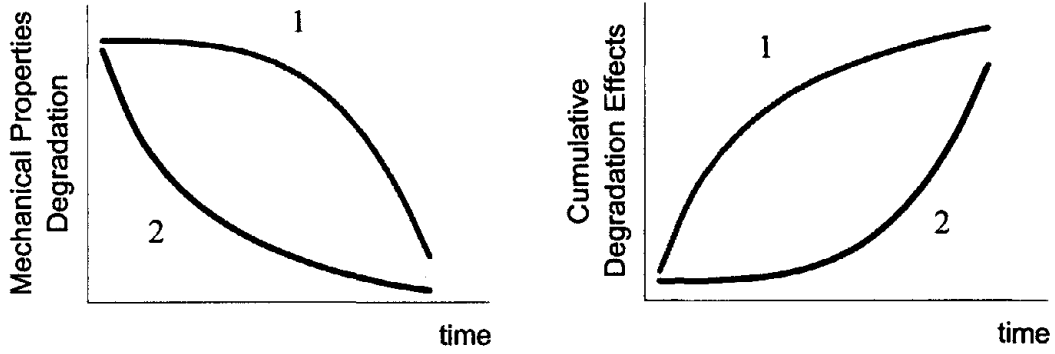


Figure 3: Schematic of degradation of properties over time and of cumulative effects of degradation.

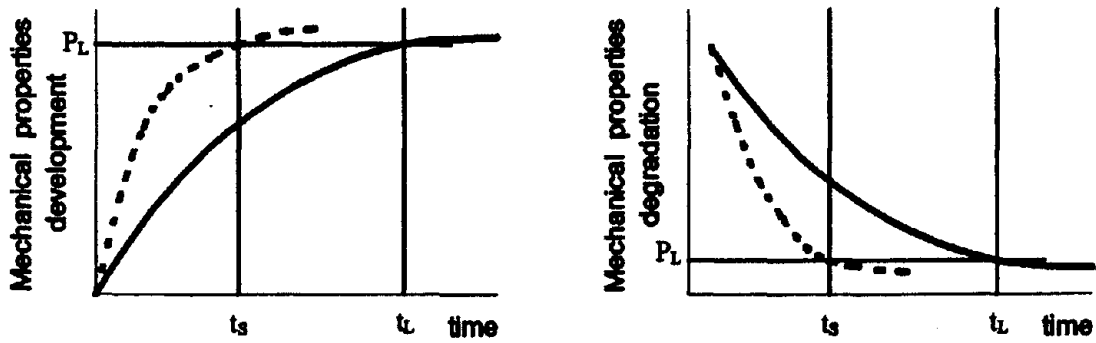


Figure 4: Schematic of development and degradation of mechanical properties over time.

components, while CL and FT exposure were intended to rapidly degrade the material. This approach allowed us to systematically explore the separate and combined interactions of both developmental and degradative accelerated aging variables.

2.2.3 Application of the Systematic Approach to Coal Fly Ash Use in Portland Cement Concrete

CFA use in PCC pavement is a useful model to develop accelerated aging tests and predictive models. First, CFA use presently is considered acceptable to most jurisdictions even though it may not be extensively used or specified (FHWA, 1995). Second, a reasonably large database exists on (i) the physical and environmental properties of CFA (Malhotra and Ramezaniapour, 1994, van der Sloot et al., 1985), (ii) its proper mix formulation when used as a cement replacement in PCC, (iii) the short term environmental behavior of the product (van der Sloot, 1991), and (iv) the longer term environmental performance of the product in actual pavements (Schreurs et al., 1997). Third, there are also some existing long-term demonstration projects for CFA in which field verification of historical physical and environmental performance could be conducted (FHWA, 1995; FHWA, 1997).

CFA use in PCC was not selected for use in this research because significant long-term environmental problems are likely. Rather, it represents a fairly well-defined recycled materials application where cause, effect, and their interaction in a laboratory setting can be further studied.

CFA use in PCC is an interesting model. During natural aging conditions, both development and degradation mechanisms can proceed simultaneously. In the presence of moisture and sufficient heat, the hydration of the cement and the pozzolanic reaction of the CFA, if any, will continue over time, with the consequent increase in mechanical properties and decrease in porosity and transport properties. A variety of mechanisms of degradation may be at work at the same time, so that the behavior after any given duration of exposure is the net result of constructive and destructive processes. For example, were one to conduct CL of an immature concrete specimen continuously immersed in warm water, fatigue cracking would accumulate over time even while the elastic modulus and modulus of rupture of the uncracked concrete were on the increase.

CFA has been widely used as a mineral cement replacement in PCC pavements and infrastructure, stabilized road bases, flowable fill, grouts in PCC sub-sealing, and structural fill/embankments (FHWA, 1995). The performance of these products is usually high, though concern must be given to mix design evaluation, air content, low early strength, seasonal limitations (in the case of freeze-thaw susceptibility or deicer sensitivity), SO_4^{2-} attack, and possible interactions during early distress associated with alkali silicate reactivity (FHWA, 1995; FHWA, 1997; Malhotra and Ramezaniapour, 1994).

A great deal of information is available on the physical, mineralogical, and leaching properties of CFA and CFA used in PCC (FHWA, 1995; Malhotra and Ramezaniapour, 1994; van der Sloot et al., 1985). The Electric Power Research Institute (EPRI) has conducted exhaustive studies during the last 20 years on CFA and has concluded that the physical, chemical, and mineralogical properties are dependent mainly upon the coal source, combustor

type, and the operation of the combustor (EPRI, 1983; 1984).

CFA is typically composed of spherical particles and cenospheres with sizes ranging from 1 to 100 μm . These particles have high specific surface areas up to 900 m^2/kg , in part due to their small size and interior pore structure in the cenospheres. Major elements (greater than 10,000 mg/kg , in decreasing abundance) in CFA are typically O, Si, Al, Fe, and Ca. Minor elements (1,000 to 10,000 mg/kg in decreasing abundance) are typically Ba, Mg, K, Sr, Na, and S. Significant trace elements (less than 1,000 mg/kg in decreasing abundance) are typically As, Mn, Ni, Zn, Pb, B, Cl, Cu, Cr, V, Sb, Mo, Se, Co, and Cd. (EPRI, 1987). There is a clear particle size dependence on composition; more volatile trace elements (i.e. Cd, Pb, Zn, etc.) are typically associated with smaller particles. These same elements are also surface-enriched; supporting the theory that, at low flue gas temperatures, the more volatile elements condensate and precipitate more volatile elements on the relatively larger surface areas associated with smaller particles (EPRI, 1987; 1993).

CFA is composed of three major mineral phases (in decreasing abundance): amorphous glass (Al-Si-O), crystalline mullite ($\text{Al}_6\text{Si}_{12}\text{O}_{13}$), and crystalline, magnetic spinel (Fe_2AlO_4). Minor mineral phases include crystalline quartz (SiO_2), rutile (TiO_2), lime (CaO), anhydrite (CaSO_4), zircon (ZrSiO_4), chromite ($\text{Fe}_{0.6}\text{Cr}_{0.4}$) $_2\text{O}_3$, trevorite (NiFe_2O_4), and donathite ($(\text{Fe},\text{Mg})(\text{Cr},\text{Fe})_2\text{O}_4$) (EPRI, 1981; 1987; 1993). Generally, alkalis, alkaline earths, lanthanides, Pb, Cd, and As are found incorporated in the glassy phase; V, Cr, Zr, Fe, and Ti occupy the Al^{3+} valence sites in the mullite; and V, Cr, Mn, Fe, Co, Ni, Cu, and Zn are enriched in the magnetic spinel (EPRI, 1981).

Observed variability in major element chemical composition is frequently due as much to sampling methods and methods of analysis as it is to shorter-term temporal effects at any one coal combustion facility (EPRI, 1983; 1984). Minor and trace element compositional variability is usually higher yet (EPRI, 1987; 1989). This relates more to the subtle influence of temperature effects in the downstream sections of the boilers and the role that temperature effects play in influencing condensation and precipitation.

In terms of leachability, many studies have been conducted on CFA from both a regulatory and mechanistic basis. In terms of regulatory leaching, CFA will leach detectable and modest levels of regulated analytes (Ag, As, Ba, Cd, Cr, Hg, Pb, and Se) in both the older Extraction Procedures Toxicity Test and the newer Toxicity Characteristics Leaching Procedure; however, these values are below the regulatory levels. The analytical laboratory, the laboratory procedure, and the quantification method all influence the results (EPRI, 1981; 1987). In terms of mechanistic leaching, operationally defined extractions will yield significant fractions of the major (Al, Ca), minor (Mg, K), and trace (As, B, Cr, Cu, Mo, Ni, Se, V) elements from the CFA (EPRI, 1985; 1986; 1987; 1993; van der Sloot et al., 1985).

The largest database on mechanistic leaching as well as diffusional leaching from CFA-PCC is the work by van der Sloot et al. (1985). Many of the cationic elements (e.g., Ca, Sr, Zn) exhibit pH-dependent leaching with minima in the neutral region and maxima at both low and high pH. Numerous mineral phases have been modeled to show solid phase control of leaching of these elements (EPRI, 1987). Therefore, higher fractional availabilities are expected in a fresh

PCC matrix where pH is alkaline (greater than 12). Many of the anionic elements (e.g., AsO_4^{3-} , MoO_4^{3-} , etc.) are more soluble at mildly alkaline pH values (7-10). Some mineral phases and sorption processes have been modeled to show control of leaching of these elements (EPRI, 1987; van der Hoek, 1995). Therefore, higher fractional availabilities of the anionic elements are expected in more aged PCC specimens (which exhibit lower pH values than fresh specimens) or cracked specimens where CO_2 (g) uptake and formation of CaCO_3 surface precipitates controls porewater pH in the mildly alkaline region.

Clearly, PCC aging will influence the leaching behavior of different classes of elements in the products. This is in part borne out by the monolith diffusional leaching studies conducted by van der Sloot et al. (1985). Effective diffusion coefficients (pD_e in m^2/s) from CFA-PCC monoliths have been quantified for Ca, Mg, Na, K, SO_4^{2-} , Pb, Cd, Zn, B, V, As, Sb, Mo, Se, Cr, Ba, and Sr. Values range from immobile (pD_e greater than $14 \text{ m}^2/\text{s}$ for Ca, Mg, SO_4^{2-}) to moderately immobile (pD_e less than $11 \text{ m}^2/\text{s}$ for V, As, Se, Cr). The coefficients for many of the elements show a dependency upon pH, mainly from changes in chemical retention reaction (e.g., localized carbonation). These data indicate that CFA trace constituents of concern can leach out of PCC products containing CFA, but at low levels. This has been documented in the field (Schreurs et al., 1997). It is important to note that the physical integrity of a pavement product containing CFA has not been related to environmental performance in the long term.

For PCC pavements constructed with CFA, the in-place hydraulic regime is not well defined. For intact pavements, percolation regimes (except at slab joints) are unlikely. Rather, contact with water is at monolith exterior surfaces, either from periodic precipitation, localized intermittent groundwater, or periodic condensation of soil water vapor. Assumptions can be made about the types of surfaces that are wetted and the wetting/drying cycles that the to which the surfaces are exposed (Kosson et al., 1996). Nevertheless, from a conceptual approach, diffusional leaching and cumulative release have been verified for CFA constituents in bituminous shoreline protection monoliths (van der Wegen and van der Plas, 1994), nuclear wastes in bituminous asphalt-stabilized monoliths (Fuhrmann et al., 1989), and pavement material made with municipal solid waste incineration bottom ash (Eighmy et al., 1996; Eighmy et al.; 1997; Kosson et al., 1996).

2.3 Scope of the Project

2.3.1 Use of a Field Reference Site

To develop an accelerated aging protocol, it was desired to be able to field-verify the results from our developed protocol.

Ideally, a candidate field pavement would be (i) made with PCC with CFA as a cementitious substitute, (ii) constructed 5 to 15 yr ago, with clear evidence of field aging (including either early distress and/or failure); (iv) well documented so that the original mix design was available, so that component materials (fine aggregates, coarse aggregates, cement, and additives) were still available from suppliers, and so that any research or information as to the cause of the early distress or failure was available; (v) available for study (including collection of a pavement slab and sub-grade soils); and (vi) facilitated by a State Department of

Transportation (DOT) willing to work with the research team to study and obtain the field slab and sub-grade soils.

2.3.2 U.S. 20 Pavement Slab for Field versus Laboratory Verification

After a preliminary review of literature on early distress (FHWA, 1997), it was decided to contact the Iowa DOT about U.S. 20 in northwest Iowa. This pavement, constructed in 1987, had experienced early distress (FHWA, 1997) and the Iowa DOT was willing to work with the research team. It was decided to collect a pavement slab and sub-grade soils on a section of County Road P73, a feeder road to U.S. 20 that crosses U.S. 20 in a north-south direction, which was placed at the same time as U.S. 20 by the same contractor using the same concrete mixture and materials.

The P73 section adjacent to U.S. 20 had apparently undergone the same early distress as had U.S. 20 even though truck traffic was presumably a small fraction of that occurring on U.S. 20. It also was a suitable field site because the logistics of slab cutting, extraction, and replacement were easier than they would have been for U.S. 20.

A great deal of information has been published on the early distress and failure of U.S. 20 (see FHWA, 1997; Jones and Putherickal, 1991; Marks and Debberke, 1995, 1996; Schlorholtz and Amenson, 1995; Cody et al., 1994). There are numerous hypothesized early distress or failure mechanisms, some of which include low initial air contents (either low in the mix or low after placement), high alkali contents in the mixes, alkali silica reaction, freeze-thaw damage, and the appearance of ettringite ($\text{Ca}_6\text{Al}_2(\text{SO}_4)_3(\text{OH})_{12}\cdot 26\text{H}_2\text{O}$) in air voids. These mechanisms are likely to be interrelated.

It was not the intent of this research to ascertain the failure mechanism(s) of the U.S. 20 pavements. Rather, the U.S. 20 field site afforded a location that met all of our criteria. It would allow the research team to recreate the field mix design in the laboratory and subject the laboratory samples to an aging protocol. This site selection allowed us the opportunity to study the individual and combined effects of AA, CL, and FT on pavement physical and environmental performance, compare our job mix (and the U.S. 20 job mix) to suitable controls, and see if we could recreate the early distress in laboratory specimens and then examine possible interactions between loss of physical performance and change in environmental performance.

2.3.3 Materials for Laboratory Prism Study

To be able to recreate the U.S. 20 job mix, the mix design for the U.S. 20 job was required and the same materials used in the original mix were needed. These would be used to manufacture laboratory prisms that could be subjected to accelerated aging experimental variables and then tested to see how physical and environmental properties responded to the treatments.

The job mix was obtained from the Iowa DOT. The original materials that were used [portland cement, class c coal fly ash (CFA-C), coarse aggregate, fine aggregate, air entrainment admixture, water reducing admixture] were identified and the suppliers were contacted. It was

learned that the same type of portland cement could be obtained, but from a different plant. It was not clear if the same feedstocks were used at this plant, but an oxide analysis would help compare the original cement with the new cement. The same CFA-C could be obtained, but it could not be established that the raw coal and coal combustion conditions were identical to those seen in 1987. The coarse aggregates that were used originally could be obtained from the same supplier. The fine aggregates that were used could be obtained from a different supplier, but from the same geologic formation where the original materials were mined. The supplier for the air entrainment agent and water reducing agent had gone out of business. New suppliers who could provide American Society of Testing and Materials (ASTM) specified admixtures were identified.

Given the difficulty in securing all component materials from the original 1987 job mix, it was decided to proceed with the laboratory mix design and, wherever possible, compare characteristics of the original mix to that of the new mix so that potential differences could be highlighted.

2.3.4 Component Materials Characterization

To compare the properties of the component materials with those used in the original mix in 1987 or to accepted standards, a series of physical and environmental characterizations were conducted on the coal fly ashes, cements (or mortars made from the cement) and aggregates.

These tests included:

- *Elemental Composition:* This method identifies the elemental composition of the material. It reports composition as mg of an element per gram dry weight of material (e.g., 45 mg of As per gram dry weight). This was performed on the coal fly ashes, aggregates, and cement.
- *Oxide Composition:* This method identifies the oxide equivalent (e.g., percent CaO) of the material. This was performed on the coal fly ashes and cements.
- *Grain Size Distribution:* This method looks at mass percent distributions as a function of particle diameter or sieve size. This was performed on the aggregates.
- *Morphology and Elemental Distribution:* The morphology and elemental distribution of the coal fly ash can be indicative of coal combustion conditions.
- *Mineralogy:* The crystalline mineralogy is indicative of the mineral components. It was performed on the coal fly ashes, cements, and aggregates.
- *Alkalinity:* The inherent pH and buffering capacity of a material is also indicative of combustion conditions or mineralogy. This was performed on the coal fly ashes, cements, and aggregates.
- *Constituent Solubility as a Function of pH:* The pH-dependent leaching behavior is indicative of environmental behavior. This was conducted on the coal fly ashes and

aggregates.

- *pH-Stat Leaching*: The leaching of major, minor and trace components under pH-static conditions can also be indicative of environmental behavior. This was conducted on the coal fly ashes, a cement mortar, and aggregates.
- *Geochemical Modeling of Leaching*: Coupled with pH-stat leaching, the identity of mineral phases controlling leaching can be indicative of environmental behavior. This was conducted on the coal fly ashes, a cement mortar, and aggregates.
- *Availability Leaching*: This leaching method looks at the fraction of an element that can be leached under environmental conditions. It is indicative of the mobilization/immobilization potential of an element. This was conducted on the coal fly ashes and aggregates.

2.3.5 Effects of Accelerated Aging on CFA-C Prism Mixes

We employed a designed experiment to better understand how the three main aging variables, AA, CL and FT, individually and collectively influenced the physical and environmental response of the laboratory CFA-C prisms.

By using various levels of aging for each main factor (AA, CL, FT), we could see how increased accelerated aging influenced physical and environmental performance.

A $2^3 + 3$ full factorial design with center points was employed for this project. A full factorial design allowed us to examine the effects of individual experimental variables as well as the interactions of two or three of the variables using a powerful analysis of variance (ANOVA) statistical test for significance.

2.3.6 Effects of Accelerated Aging on CFA-C, CFA-F, and PCC Control Prism Mixes

To better understand how well we aged the CFA-C laboratory prisms, some controls were run. These included mixes where a class F coal fly ash (CFA-F) was used instead of the CFA-C. We also ran a PCC control that did not contain coal fly ash. These controls were subjected to the same intermediate level of aging as the CFA-C prisms.

ANOVA and multiple comparison statistical analyses could then be used to compare and contrast performance of the CFA-C with that of the CFA-F and PCC.

2.3.7 Comparison of Aged CFA-C Mixes to the U.S. 20 Slab

The physical and environmental response variables from the aged CFA-C laboratory specimens was compared with data from the U.S. 20 slab.

This comparison allowed us to see how well the accelerated aging protocol produced

concrete with the same physical and environmental properties.

Ideally, an appropriate accelerated aging protocol will create an aged material over a short time frame comparable to that of a field aged material subjected to aging over a longer time frame.

2.3.8 U.S. 20 Slab and Laboratory Prism Physical and Environmental Properties of Interest

It was desired to examine how aging would influence the physical and environmental performance of laboratory prisms. These same experimental response variables were also evaluated in the U.S. 20 pavement slab so comparisons could be made.

The goal of making a variety of measurements was to develop an integrated picture of the effects of the accelerated aging treatment scheme on physical and environmental performance. This would also allow for the study of the interrelation between physical and environmental performance.

The following experimental response variables were measured:

- *Compressive Strength*: This variable was selected to see if the effects of the experimental design resulted in a change in strength of the prisms. Compressive strength provides some indication of the physical integrity of the experimental prisms. This analysis was conducted by the University of New Hampshire (UNH). [Compressive strength would be expected to be directly related to microcracking, relative dynamic modulus, uniformity indicators, weighted average threshold pore widths, porosity, effective surface area, cumulative fluxes, and observed diffusion coefficients.]
- *Microcracking*: This variable was used to see if the experimental design produced any loss of monolith integrity in the experimental prisms as evidenced by damage that can be discerned through the use of neutron radiography. Cornell University conducted this analysis. [Microcracking would be expected to be related to compressive strength, relative dynamic modulus, uniformity indicators, weighted average threshold pore widths, porosity, effective surface area, cumulative fluxes, and observed diffusion coefficients.]
- *Relative Dynamic Modulus*: The loss of monolith integrity was also assessed through measurement of the relative dynamic modulus (RDM). The procedure measures compression or P-wave velocity through the prisms prior to and after freeze-thaw cycling. Decreases in RDM reflect damage and loss of integrity in the prisms. The Cold Regions Research and Engineering Laboratory (CRREL) conducted this work. [RDM would be expected to be related to compressive strength, microcracking, uniformity indicators, weighted average threshold pore widths, porosity, effective surface area, cumulative fluxes, and observed diffusion coefficients.]
- *Uniformity Indicators*: The uniformity indicator is derived from mercury intrusion porosimetry (MIP). It describes the relative shape of the two peaks (for larger and smaller

pores) derived from the differential plot of the intrusion data. It is a general measure of the uniformity of pore sizes in the prisms. UNH conducted this analysis. [Uniformity indicators would be expected to be related to microcracking, relative dynamic modulus, weighted average threshold pore widths, effective surface area, cumulative fluxes, and observed diffusion coefficients.]

- *Weighted Average Threshold Pore Widths:* The weighted average threshold pore widths are also derived from MIP. These weighted pore widths give an indication of the size of interconnecting pores in the concrete. It is a general measure of the type of porosity in the prisms and therefore related to monolith integrity. UNH conducted this analysis. [Weighted average threshold pore widths would be expected to be related to compressive strength, microcracking, relative dynamic modulus, uniformity indicators, porosity, effective surface area, cumulative fluxes, and observed diffusion coefficients.]
- *Porosity:* The porosity is derived from MIP that gives the pore volume (in percent) of the sample. UNH conducted this analysis. [Porosity would be expected to be related to compressive strength, relative dynamic modulus, effective surface area, cumulative fluxes, and observed diffusion coefficients.]
- *Effective Surface Area:* The effective surface area is obtained from gas adsorption isotherms. It measures the surface area (m^2/g) within monolith samples. It is a general measure of the type of porosity in the prisms. UNH conducted this analysis. [Effective surface area would be expected to be related to compressive strength, microcracking, relative dynamic modulus, weighted average threshold pore widths, porosity, cumulative fluxes, and observed diffusion coefficients.]
- *Mineralogy:* This variable is obtained through the use of x-ray powder diffraction (XRPD). The method can identify as well as quantify the concentration of crystalline minerals within the prism samples. It may detect changes in the presence and abundance of minerals as a result of the experimental design. UNH conducted these analyses. [Mineralogy would be expected to be related to alkalinity and constituent leaching as a function of pH, pH-stat leaching, geochemical modeling, availability leaching, cumulative fluxes, and observed diffusion coefficients.]
- *Alkalinity and Constituent Leaching as a Function of pH:* The alkalinity is a measure of the buffer capacity of a sample. It can also be used to infer the chemical species providing the buffer (e.g., CO_3^{2-}). The constituent leaching as a function of pH gives a sense of the pH-dependent leaching behavior of elements of interest (e.g., Ca or Zn). Both are derived from a titration procedure on ground-up monolith samples developed and conducted by Rutgers University. [Alkalinity and constituent leaching as a function of pH would be expected to be related to mineralogy, pH-stat leaching, geochemical modeling, availability leaching, cumulative fluxes, and observed diffusion coefficients.]
- *pH-Stat Leaching:* The equilibrium leaching of ground-up monolith samples at predetermined pH values of interest gives an indication of pH-dependent leaching behavior. This variable might reflect changes in the mineralogy in the experimental

prisms as a result of the experimental design. This analysis was conducted by UNH. [pH-stat leaching would be expected to be related to mineralogy, alkalinity, and constituent leaching as a function of pH, geochemical modeling, availability leaching, cumulative fluxes, and observed diffusion coefficients.]

- *Geochemical Modeling:* Data from pH-stat leaching are used in a geochemical thermodynamic equilibrium source code (MINTEQA2) to identify possible mineral phases that may control the equilibrium leaching of elements of interest (e.g., Cu, Cr) from ground-up prism monoliths. This variable might reflect changes in the mineralogy in the experimental prisms as a result of the experimental design. This analysis was conducted by UNH. [Geochemical modeling would be expected to be related to mineralogy, alkalinity, and constituent leaching as a function of pH, pH-stat leaching, availability leaching, cumulative fluxes, and observed diffusion coefficients.]
- *Availability Leaching:* This operationally defined leaching protocol uses a chelating agent (EDTA) to extract elements of interest (e.g., Ca, Pb) from ground-up monolith prism specimens. It is used to describe the amount of an element that would be available for leaching over some long period (e.g., 10,000 yr). It is directly related to possible changes in mineralogy that produce in changes in solubility (increasing or decreasing) for an element of interest. The procedure is a Rutgers University method. [Availability leaching area would be expected to be related to mineralogy, alkalinity and constituent leaching as a function of pH, pH-stat leaching, cumulative fluxes, and observed diffusion coefficients.]
- *Leaching at Low Liquid-Solid Ratios:* This operationally defined leaching protocol uses a reverse serial batch procedure to extract elements of interest (e.g., SO_4^{2-} , Cl) into leachates of increasing ionic strength. It can then be used to predict what prism monolith pore water constituent concentrations might be. The procedure is a Rutgers University method. [Leaching at low liquid-solid ratios would be expected to be related to pH-stat leaching, cumulative flux, and observed diffusion coefficients.]
- *Cumulative Fluxes from Monolith Leaching:* This operationally defined protocol uses monolith tank leaching tests to look at the cumulative flux (mg/m^2) of an element of interest (e.g., Cd, Ca) from the experimental prisms. Changes in mineralogy or changes in monolith integrity might change the flux that is observed. This method was developed by Rutgers University. [Cumulative flux would be expected to be related to compressive strength, microcracking, relative dynamic modulus, uniformity indicators, weighted average threshold pore widths, porosity, effective surface area, mineralogy, and observed diffusion coefficients.]
- *Tortuosity:* Monolith tortuosity (τ) or matrix tortuosity reflects the tortuous diffusion pathway that a solute must travel to diffuse from the monolith. Tortuosity can be estimated by a number of means, most notably by the ratio of observed diffusivity (D_{obs}) to molecular diffusivity (D) of the solute in water. Another method is the Millington-Quirk relationship where $\tau_{\text{MQ}} = \varepsilon^{-4/3}$, where τ_{MQ} and ε are matrix tortuosity and matrix porosity, respectively. Tortuosity is perhaps the best measure to relate physical changes in

monolith integrity (e.g., microcracking, MIP porosity) to changes in fluxes of constituents of interest leaching via diffusional processes from the slab and prism samples. [Tortuosity would be expected to be related to compressive strength, microcracking, relative dynamic modulus, uniformity indicators, mineralogy, weighted average threshold pore widths, porosity, effective surface area, observed diffusion coefficients, and cumulative fluxes.]

- *Observed Diffusion Coefficients from Monolith Leaching:* This operationally defined protocol uses monolith tank leaching tests to look at the observed diffusion coefficient (D_{obs} , m^2/s) of an element of interest (e.g., Cd, Ca) from the experimental prisms. The D_{obs} is obtained via diffusion modeling using a variety of assumptions about the initial concentration of an element in the prism as well as the assumption of homogeneous or heterogeneous diffusion within the monolith. Changes in mineralogy or changes in monolith integrity might change the D_{obs} that is observed. This method was developed by Rutgers University. [Cumulative flux would be expected to be related to compressive strength, microcracking, relative dynamic modulus, uniformity indicators, mineralogy, weighted average threshold pore widths, porosity, effective surface area, and cumulative fluxes.]

CHAPTER 3: MATERIALS COLLECTION AND CHARACTERIZATION

3.1. U.S. 20 Slab Collection and Processing

Iowa County Road P73 is a north-south feeder road that intersects U.S. 20 approximately 10 miles east of Fort Dodge. It was constructed by the same contractor using the same job mix and materials as U.S. 20. The actual section of P73 that crosses U.S. 20 (from station 22155+36 to 22159+50 (126 m) was constructed on May 1, 1987. The pavement experienced cracking from an unknown mechanism shortly thereafter. The soil sub-grade was moistened before the concrete was placed with a slip-form paver. The pavement was 7.3 m wide and 170 to 200 mm thick. The surface was textured with an Astro-grass drag and saw-cut, transverse grooves prior to sealing for curing. No precautions were taken for cold weather, as the temperatures for that day were 12 to 24°C with a minimum temperature of 8°C on the following night.

On November 5, 1997, at an age of 3,841 d or approximately 10.5 yr, a 1.2- by 1.8-m section of concrete pavement was removed from County Road P73. To minimize saw cutting, it was removed from the shoulder of the roadway at a cold joint (see figure 5). Holes were drilled at opposing corners and eyebolts with expansive anchors were attached. Chains were attached to the eyebolts and connected to the bucket of a large front-end loader. The loader lifted the slab onto a pallet in the rear of a Ryder truck (see figure 6). It was then transported to the UNH for sawing, coring, and subsequent analysis of bricks and cores.

Once at UNH, the slab was visually inspected (see figure 7). Surface damage was evident. The transverse grooves were especially damaged due to spalling of the thin ridges between the grooves. After cleaning the surface with tap water and brushes, a crack was discovered running the full length of the slab (parallel to the direction of traffic) to a depth of 10 cm (see figure 8). The crack was roughly 0.75 m from the shoulder (see figures 7, 8, and 9). This corresponded to the tire path for the right side of a vehicle. Chalk lines were drawn on the slab every 150 mm in each direction for indexing.

The slab was then cored with a 100-mm-diameter tap water-cooled Milwaukee coring drill. Cores were removed from the shoulder, the cold joint, and cut side opposite the shoulder (see figure 10).

Prismatic specimens or “bricks” were removed from three corners of the slab with a 460-mm-diameter wet saw. Intersecting sides designate the three corners: Joint/Cut (JC), Cut/Cut (CC), and Shoulder/Cut (SC). Core and brick locations are shown in figure 11. The samples were then designated first by their number (for cores) or letter (for bricks) and then by their location. When only a portion of the sample was used for a test, a number follows in parenthesis indicating the depth (in) from which the portion was removed. For example, 1-C would be a core from the cut side and A-CC(4) would be a portion of a brick, 4 in (100 mm) from the surface, from the Cut/Cut corner (see figure 11).

A list of the Iowa slab samples used for the work described herein is provided in table 1.

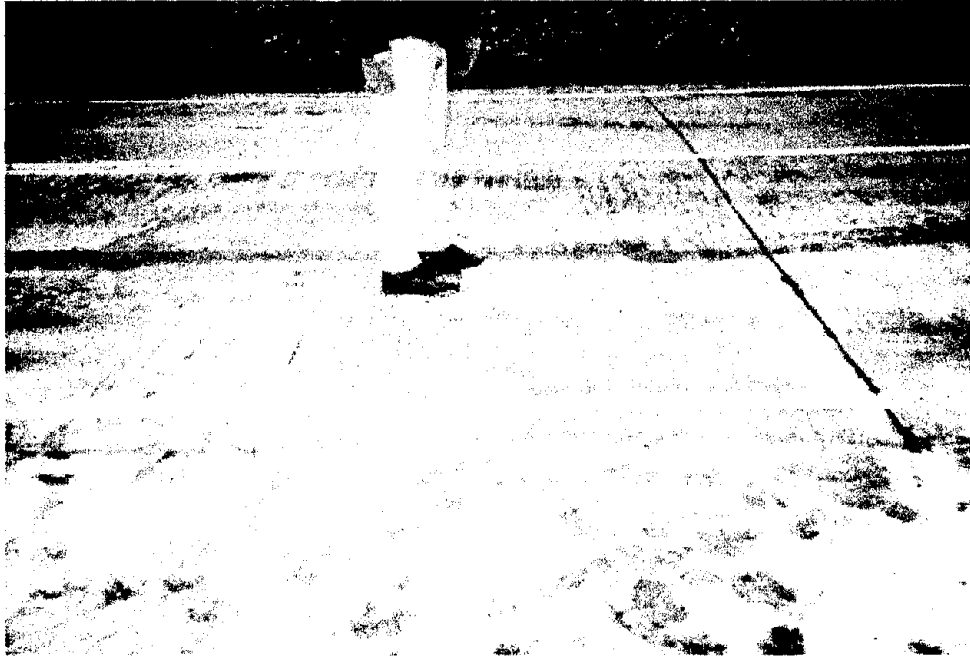


Figure 5: U.S. 20 slab saw cut at shoulder and cold joint.



Figure 6: Contractors remove slab on 5 November 1997.

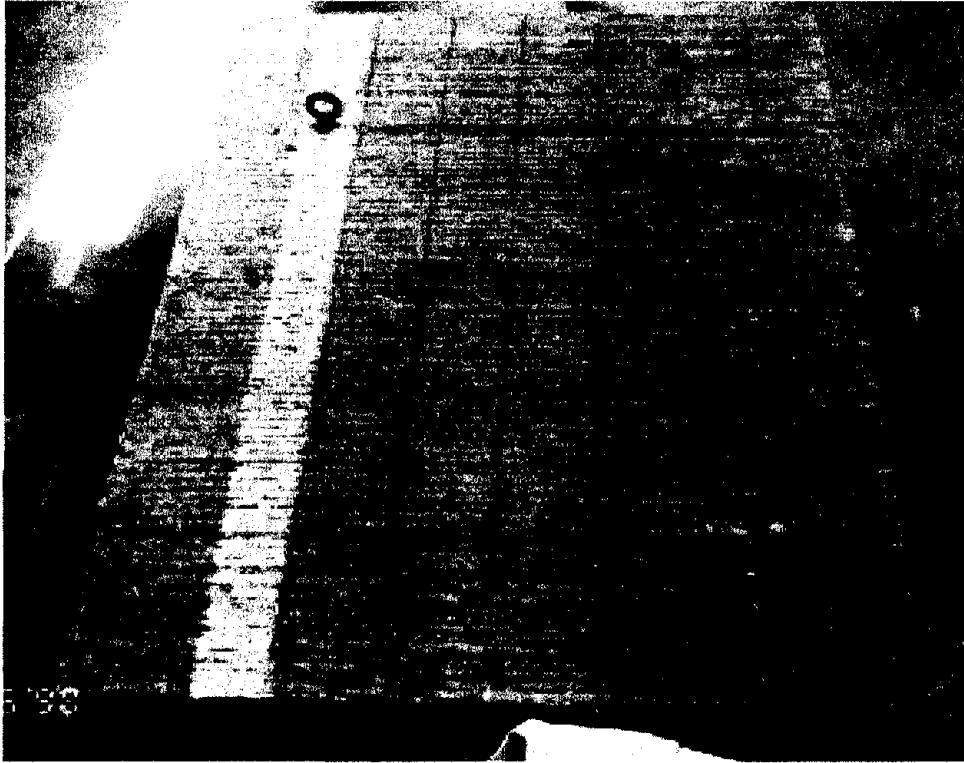


Figure 7: Slab is visually inspected at UNH.

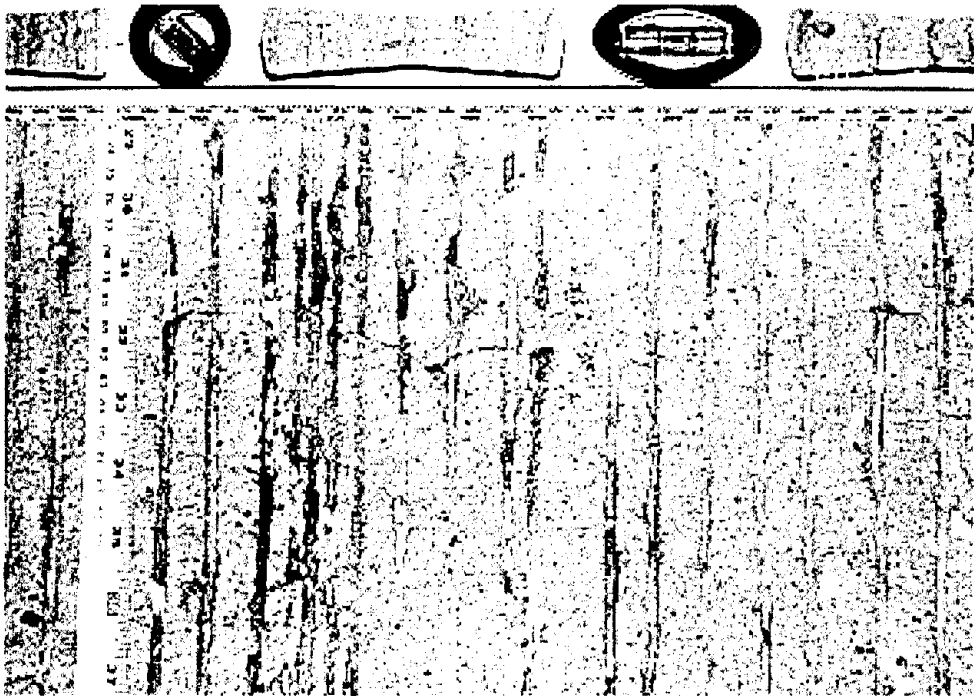


Figure 8: Crack running in direction of traffic along whole length of slab.



Figure 9: Crack is 100 mm deep at cold joint.

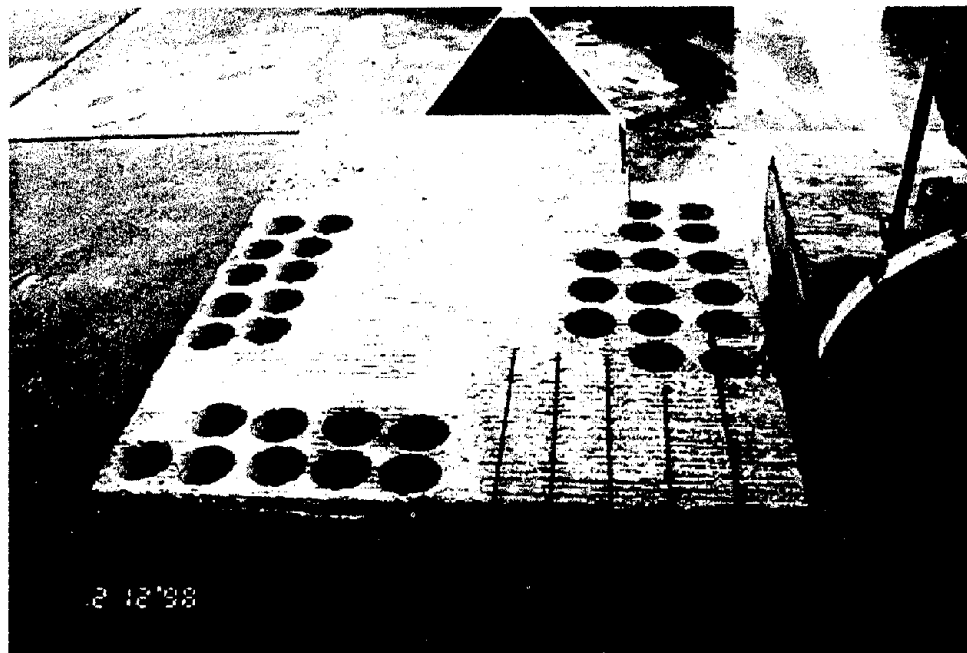


Figure 10: Removing bricks from the joint/cut corner.

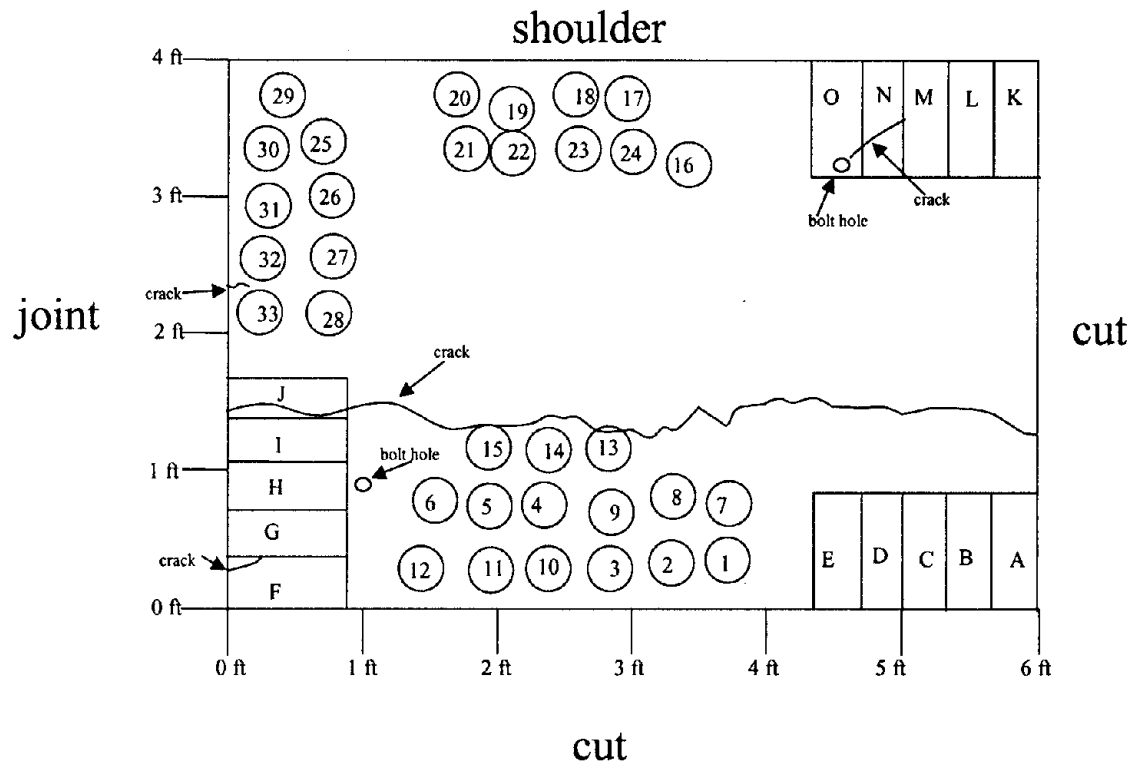


Figure 11: Final core and brick locations.

Table 1: Inventory of Iowa samples.

Sample ID	Test performed on sample
1-C	MIP pore structure, BET Surface Area, XRPD Mineralogy, pH-Stat Leaching, Geochemical Modeling
4-C	Neutron Radiography
5-C	MIP pore structure, BET Surface Area, XRPD Mineralogy, pH-Stat Leaching
6-C	Neutron Radiology
7-C	Monolithic Leaching, Release Modeling
8-C	Monolithic Leaching, Release Modeling
9-C	Monolithic Leaching, Release Modeling
13-C	Compressive Strength Testing
14-C	Neutron Radiology
15-C	MIP pore structure, BET Surface Area, XRPD Mineralogy, pH-Stat Leaching
16-S	Compressive Strength Testing
17-S	MIP pore structure, BET Surface Area, XRPD Mineralogy, pH-Stat Leaching
19-S	Neutron Radiology
22-S	Neutron Radiology
24-S	Neutron Radiology
26-J	MIP pore structure, BET Surface Area, XRPD Mineralogy, pH-Stat Leaching
27-J	Neutron Radiology
30-J	Neutron Radiology
31-J	Neutron Radiology
32-J	Compressive Strength Testing
35-S	Compressive Strength Testing
36-C	Compressive Strength Testing
39-J	Compressive Strength Testing
B-CC	Carbonation
I-JC	NAA/XRF elemental composition
J-JC	Carbonation, Slab Alkalinity and Solubility as a Function of pH, Slab Constituent Availability
N-SC	Carbonation
O-SC	NAA/XRF elemental composition, Slab Alkalinity and Solubility as a Function of pH, Low Liquid-Solid Ratio Leaching, Slab Constituent Availability

3.2. Mixture Components Collection and Processing

3.2.1. Coarse Aggregate

Martin Marietta Materials of Fort Dodge, Iowa, provided the coarse aggregate for the three mix designs. The aggregate was acquired from its mining location in Fort Dodge, by Iowa DOT employees and sent by motor freight to UNH. Martin Marietta was also the coarse aggregate supplier for U.S. 20 in 1987. It classified the aggregate as Size 57 stone (ASTM C 33). At UNH, a standard sieve test was performed in 1997 on the aggregate supplied (ASTM C 136). A contemporary sieve analysis was also obtained from the Iowa DOT (see table 2). This coarse aggregate consists primarily of a crushed limestone aggregate.

3.2.2. Fine Aggregate

Automated Sand and Gravel of Fort Dodge, Iowa provided the fine aggregate on U.S. 20 in 1987 and also the fine aggregate for the three laboratory mix designs. The fine aggregate for the laboratory mixes, however, was mined from a different pit within the same geologic formation because the original mine was not in service at the time materials were collected for the laboratory concrete. The fine aggregate for the laboratory mixes was collected by Iowa DOT employees and shipped with the coarse aggregate. The fine aggregate is primarily a natural deposit of rounded sand.

3.2.3. Cement

Type I portland cement was used originally and obtained for the laboratory mixes from Lehigh portland Cement Company (see tables 3 and 4). The cement used in 1987 came from Lehigh's local plant in Mason City, Iowa, while that for the laboratory mixes came from Lehigh's plant in Helena, Montana.

3.2.4. Ottumwa Class C Coal Fly Ash

The CFA-C, tan in color, was collected from Ottumwa Power Station in Chillicothe, Iowa, in January 1998. It was shipped to UNH from Midwest Fly Ash and Materials by UPS.

3.2.5. Brayton Point Class F Coal Fly Ash

The source of the Class F CFA (CFA-F), gray in color, was the Brayton Point Plant in Somerset, Massachusetts. It was collected in November 1997 and sent to UNH by US Generating via UPS. This was used as a control CFA.

3.2.6. Air-Entraining Admixture

Darex II air-entraining admixture (AEA) (which complies with ASTM C260), was produced and donated by W.R. Grace & Co. of Cambridge, Massachusetts, and was used as the

Table 2: Fine aggregate sieve analyses (percent passing).

Sieve size	1987 U.S. 20 aggregate*	1997 aggregate†
9.5 mm (3/8 in.)	100	100
4.75 mm (No. 4)	97	98
2.36 mm (No. 8)	86	92
1.18 mm (No. 16)	70	70
0.6 mm (No. 30)	40	48
0.3 mm (No. 50)	6.5	16
0.15 mm (No. 100)	1.0	3.0
0.075 mm (No. 200)	0.5	0.0

* Performed by Iowa DOT

† Performed by the authors

Table 3: Chemical analysis of cements used in U.S. 20 (1987) and the accelerated aging project (1997)* (percent).

Material	MgO	SO ₃	Al ₂ O ₃	C ₃ A	Na ₂ O	K ₂ O	Na ₂ O _e †	SiO ₂	Fe ₂ O ₃
1987 Cement	2.58	3.38	4.87	9.05	0.07	1.06	0.77	‡	‡
1997 Cement	3.9	3.0	5.4	11	‡	‡	0.52	21.2	2.4

* Results provided by the supplier

† Equivalent alkali content equal to Na₂O + 0.658 K₂O

‡ Test was not performed or results are unavailable

Table 4: Physical analysis of cement used in the accelerated aging project (1997)*.

Fineness, Blaine Specific Surface (m ² /kg)	403
Time of Set (min): Gilmore	
Initial:	170
Final:	290

* Results provided by the cement supplier

AEA for the laboratory mixes. Its recommended dosage, per manufacturer's instructions, is 30 to 320 ml/100 kg of cement. This recommendation is for an air content ranging from 4 to 7 percent by volume. This project required a low air content value for desired high freeze-thaw susceptibility. For this reason, an air content of 3 to 4 percent was chosen and a dosage of 28 ml/100 kg of cementitious material was used for mixes containing both CFA-C and CFA-F. For PCC control mixes, a dosage of 20 ml/100 kg of cement was used. These values were obtained after evaluating trial batches.

3.2.7. Water Reducing Admixture

Plastocrete 161 (a Type A water reducer as defined by ASTM C 494) by Sika, of Lyndhurst, New Jersey, was donated and used for the water-reducing admixture for the laboratory mixes. The manufacturer's recommendation for dosage is 195–390 ml/100 kg of cementitious material. Different amounts were used for each mix design based on trial batch experience. The dosages used are listed in table 5.

3.2.8. Water

Reagent grade water was used for all three mixes. Water was prepared at UNH in accordance with ASTM D 1193, the Standard Specification for Reagent Water, using a Milli-Q Water System.

3.3. Mix Component Characterization

3.3.1. Elemental and Oxide Composition

Elemental analyses of the CFA-C, CFA-F, portland cement, fine aggregate, coarse aggregate and a combined sample of fine and coarse aggregate were performed under the direction of Dr. Sheldon Landsberger, University of Texas at Austin, using neutron activation analysis and X-ray fluorescence (NAA/XRF). Analysis was performed for the following elements: Ag, Al, As, Au, Ba, Br, Ca, Cd, Ce, Cl, Co, Cr, Cs, Cu, Dy, Eu, Fe, Hf, Hg, I, In, K, La, Lu, Mg, Mn, Mo, Na, Nd, Ni, P, Pb, Rb, S, Sb, Sc, Se, Si, Sm, Sr, Ta, Tb, Th, Ti, U, V, W, Yb, Zn, Zr. References, provided by the analyst, explain the methodology of the NAA/XRF work that was conducted (Landsberger, 1994; Markowicz and Grieken, 1990).

Sample preparation of the fine and coarse aggregates involved grinding the material to a grain size less than 300 μm . The CFA materials and the portland cement already met this requirement. For all materials needing grinding, a requirement was imposed that at least 90 percent of the initial mass of the material was to be recovered in order to best preserve the chemical distribution of the material.

Initially, coarse aggregate was fractured into pieces smaller than 7 mm in diameter using a proctor hammer, while fine aggregate needed no initial crushing. The material was then put through a Weber Brothers and White pulverizing hammer mill several times using progressively smaller screens until most of the material passed a No. 50 sieve (300 μm). When less than 10 g

Table 5: Water reducing admixture dosage*.

Mix PCC	Mix CFA-C	Mix CFA-F
228 ml	98 ml	114 ml

* per 100 Kg .

remained on the sieve the remaining material was ground by hand using a mortar and pestle until it was smaller than 300 μm and would pass the No. 50 sieve.

The fine aggregate also was put through a Weber Brothers and White pulverizing mill several times using progressively smaller screens until most of the material passed a No. 50 sieve. All material was ground by hand using a mortar and pestle until it was less than 300 μm .

Oxide analyses were performed on the CFA-C and CFA-F at the Materials Analysis and Research Laboratory at Iowa State University using an XRF procedure. The samples were ignited at 750°C to a constant weight and then fused in a borate flux.

3.3.2. Mercury Intrusion Porosimetry

MIP is a method used to study and characterize a material's interconnected pores (pore network). These interconnected pores are an important characteristic of aggregates and concrete. Relationships have been determined as to how the performance and durability of concrete is affected by its pore structure (Powers and Brownyard, 1948; Young, 1974; and Rößler and Odler, 1985). MIP was chosen as a test procedure to compare pore structures of certain mix components.

A Micromeritics (Norcross, GA) AutoPore III 9405 porosimeter was used for mercury intrusion porosimetry. The machine was configured to perform two sets of pressure ranges, low and high. Low-pressure ranges from 13.79 to 138.5 kPa and high pressure ranges from 138.5 to 207,000 kPa. The porosimeter's specifications are listed in table 6.

Samples were allowed to dry on a countertop until the surface was noticeably dry. At this time, they were weighed on a Sartorius (Göttingen, Germany) BP121S analytical balance (± 0.1 mg). Samples were then placed inside a Labconco (Kansas City, MO) FreeZone 6-Liter Freeze Dry System (Model 77530) at -40°C and $30\text{--}130 \times 10^{-3}$ mbar. Copeland and Hayes (1956) chose 3 to 4 d for the drying time of their ground cement pastes. Powers, who also used crushed pastes, recommended longer drying times for larger samples (Powers, 1949). For this study, samples were dried until weight changes of less than 1 mg were recorded. This was found to correspond to a maximum required drying time of 14 d.

After drying, samples were processed per standard Micromeritics procedures. An initial vacuum of 6.66 Pa was applied for drying prior to mercury immersion and mercury was introduced at a filling pressure of 13.8 kPa. Pressure and volume measurements were taken in logarithmic pressure increments until the pressure reached 138.5 kPa, at which time the low-pressure analysis was terminated, the penetrometer assembly was weighed, and the samples were transferred back to the porosimeter for high-pressure intrusion.

Appendix A in volume II provides background on how pore size uniformity, threshold pore diameters and porosity are calculated.

Table 6: AutoPore III specifications.

Low Pressure	
Measurement:	0–345 kPa
Resolution:	69 Pa
High Pressure	
Measurement:	Atmospheric–228 MPa
Resolution	
Atmospheric–21 MPa:	140 Pa
21–228 MPa:	1400 Pa
Transducer	
Accuracy:	±0.1% of full scale (transducer manufacturer's specifications)

3.3.3. BET-N₂ Adsorption Surface Area Analysis

A Micromeritics TriStar 3000 automated gas adsorption analyzer was used for all sorptometry experiments in this project. The TriStar allows three samples to be analyzed simultaneously. The sorptometer's specifications are listed in table 7.

Once the samples were allowed to air-dry, they were ground with a mortar and pestle until the largest samples passed a No. 4 (4.75 mm) sieve. The crushed portion of the samples that remained on a No. 30 (0.6 mm) sieve were then placed into the freeze dryer for a minimum of 14 d prior to testing. Once the samples had finished drying, they were placed inside a glass penetrometer of known weight. This assembly was then weighed and the sample weight determined. This process was repeated for two remaining penetrometers. The three penetrometers were placed onto the TriStar's ports with compression fittings. A dewar of liquid nitrogen (LN) was then placed beneath the samples on an elevator that raises and submerges the penetrometers during the analysis. A liquid nitrogen temperature of 77.3 °K (-195.9°C) was used in all analyses. Saturation pressure, P_o , was determined through the course of each experiment by the sorptometer.

The sorptometer begins the experiment with a leak test. The sample tubes are evacuated at 50 mm Hg/s until a pressure of 5 mm Hg is reached. The samples are left at this pressure for 30 min, at which time the ports are sealed and the pressure monitored. If the pressure holds to a tolerance of $\pm 1\%$ for 120 s then the experiment will continue; otherwise, the vacuum is repeated for 30 min and the leak test is performed again.

Once the three sample ports have passed the leak test, a cryogenic bath of liquid nitrogen is elevated to submerge the sample tubes. The $P/[V_o(P_o-P)]$ readings were taken at eight partial pressure increments (0.025, 0.03, 0.05, 0.10, 0.15, 0.20, 0.25, and 0.30). Trial experimental runs showed that the first two points lie on the first section of the isotherm. Therefore, only the last six readings were used in the BET surface area calculations.

Coarse aggregate surface areas were measured on samples from the same source used in laboratory-created concretes. Results are presented in table 8.

Appendix B in volume II provides backg round on BET adsorption theory and methods to calculate surface area.

3.3.4. Morphology

Field emission scanning electron microscopy (FESEM) was used to examine the morphology of the CFA-C and CFA-F. An AMRAY 2000 FESEM was used. Au-Pd plated samples were mounted for the purpose of taking micrographs of the materials. An accelerating voltage of 7keV was used. Micrographs were taken of multiple particles at varying magnifications. Additional ash samples were mounted for examination of surface composition. An accelerating voltage of 20keV was used for this analysis. The extractor current of the gun was

Table 7: TriStar specifications.

Pressure measurement	
Range:	0 to 999 mmHg
Resolution:	Within 0.05 mmHg
Accuracy:	Within 0.5% of full scale
Linearity:	Within 0.25% of full scale (transducer manufacturer's specification)
Manifold temperature	
Accuracy:	$\pm 0.25^{\circ}\text{C}$
Resolution:	Within 0.1°C

Table 8: Coarse aggregate used in laboratory prism
BET-N₂ surface area analysis.

Core ID	Weighted surface area m ² /g
CA-1	0.340
CA-2	0.360
CA-3	0.354

116 mA with a working distance of 26 mm. The size of particles and the magnification used varied. Particle surfaces were analyzed for elemental composition for C, O, Na, Mg, Al, Si, P, S, K, Ca, Ti, and Fe.

3.3.5. Mineralogy

X-ray powder diffraction (XRPD) was used to identify and quantify crystalline phases in samples. Powdered aggregate samples were used; the grinding procedure for these samples was described as follows.

The powdering of aggregate samples was accomplished with either a Weber Brothers and White pulverizing hammer mill or a BICO Inc. pulverizing mill. A requirement of greater than 90 percent mass recovery was maintained throughout the grinding of all samples. Samples were generally broken into pieces smaller than 21 mm in diameter using a proctor hammer and then ground to smaller than 300 μm by the mill. Any material not passing the No. 50 sieve after processing through the mill was ground by hand with a mortar and pestle until it would pass the No. 50 sieve. CFA-C and CFA-F were analyzed in the condition in which they were received from the distributors and used in the concrete specimens.

A portland cement paste was created for analysis of the mineral phases of hydrated portland cement. To make the paste, portland cement was mixed with Milli-Q™ Type II water at a water/cement ratio of 0.48 according to ASTM C 305 (ASTM, 1998). The fresh paste was poured into a 250-ml HDPE bottle and set on a sample rotator for 24 h. After the first 24 h, the bottle was cut away from the hardened paste and the paste was placed in a high humidity environment (97 percent \pm 2 relative humidity) until day 28. It was powdered as described above.

Specimens were analyzed on a Rigaku-Geigerflex goniometer from 6 to 90 degrees 2θ by a step-scan analysis with a step size of 0.02 and a dwell time of 4 s/step. A Cu-K α X-ray source (45 kV, 35 mA) was used. A divergence slit of 1°, a scattering slit of 1°, a receiving slit (crystal) of 0.3°, and a receiving slit (monochromator) of 0.6° were employed to optimize a combination of peak definition and peak intensity. Data were collected using Datascan 3.1, a Materials Data Inc. (MDI) product. Qualitative and quantitative analyses were performed using Jade 5, also by MDI. Samples were run in triplicate with elemental tungsten (W) added as an internal standard and 2θ correction.

Jade 5 uses a search/match procedure to identify crystalline phases in the diffractogram. It employs the Release 1998, sets 1-48 and 70-85, CD-ROM database from the International Centre for Diffraction Data (ICDD) to compare the sample diffractogram with diffractograms of pure phases. Jade 5 assigns a figure of merit (FOM) to each identified phase based on how well the peak location and intensity of the pure phase compares with to the location and intensity of peaks in the sample diffractogram. A lower FOM indicates higher confidence in the identification of a phase in the sample. Jade 5 designates phases as major, minor, or trace based on the relative intensity of the phases in the diffractogram. If a diffractogram had a high level of backg round noise, then trace phases were considered unidentifiable.

Three diffractograms were taken for each sample. Each diffractogram was put through the search/match phase and assigned a list of identified phases with FOM. These three lists were then combined into a final list for the specimen with a new FOM for each phase. The final FOM of a phase was a weighed average, based on the original FOMs and in how many diffractograms a phase was identified.

$$\text{Avg FOM} = \left(\frac{\sum \text{FOMs}}{n} \right) * \left(\frac{1}{0.5 * n} \right) \quad (1)$$

where:

- n is the number of diffractograms of the samples in which the mineral phase was identified.

Jade 5 was also used for quantitative analysis of crystalline phases in a sample. Selected phases were compared, based on the ICDD database, with specific peaks in the sample diffractogram. W peaks were also identified and assigned to the W phase. The known weight percent of W, added as an internal standard, was specified to the program. The calculated weight percents of the selected phases were based on the relative intensity of the peaks belonging to that phase, the relative intensity of the W peaks, the weight percent of W in the sample, the reference intensity ratio (RIR) of the phase in question, and the RIR of W. The RIR is a constant retrieved from the ICDD database, relating to the expected peak intensity of a pure phase. This procedure was followed for each of the three diffractograms of the samples in which the mineral phase was identified. The mean of the three weight percent values for each value was used as the final result.

3.3.6. pH- Dependent Leaching and Solid Phase Control

3.3.6.1 Measurement of Alkalinity and Constituent Solubility as a Function of pH

Determinations of alkalinity and constituent solubility and release as a function of pH for mix components were carried out using the RU-SR002.0 (Solubility and Release as a Function of pH) protocol [Garrabrants, 1998]. Eleven aliquots of crushed materials (e.g., size reduction less than 300 μm , 15 g minimum) were contacted, at room temperature ($20 \pm 2^\circ\text{C}$), with HNO_3 or KOH solutions of varying acidity or basicity using a liquid-solid ratio of 5 ml/g of dry sample. After a contact time of 24 h under agitation, the leachate pH of each extract was measured prior to filtration through 0.45- μm pore size polypropylene membranes. The test was carried out in duplicate for each of the mix components. The filtered leachates were preserved with nitric acid to a pH less than 2 for chemical analyses. The leachate composition was first screened using flame atomic absorption spectrometry (FAAS) to determine the primary trace contaminants. The primary contaminants of interest found for the two CFAs were As, Cd, Cr, Cu, Pb, Ni, and Zn. The primary contaminants of interest found for the combined aggregates were Cd, Cu, Pb, Ni, and Zn. The concentration of these contaminants in the leachates was then measured by FAAS.

The acid neutralization behavior of the materials was evaluated by plotting the pH of each

extract as a function of milli-equivalents of acid added per gram of dry sample. Equivalents of base are presented as the negative of acid equivalents (e.g., 5 mEq/g of KOH corresponds to - 5 mEq/g of acid). The constituent concentration in each extract was plotted as a function of extract final pH to provide extract concentration and solubility as a function of pH. Plateaus in extract concentrations at the extremes of pH (acid and alkali) are interpreted as release being limited by either availability or total content of the species of interest, rather than solubility in the extract solution.

3.3.6.2 pH-Stat Leaching

The pH-dependent leaching involved leaching a powdered sample at a constant pH for 24 h. The leachate was analyzed for specific elements or compounds using a variety of analysis methods depending on the analytes.

Each sample was leached at four different pH points, 5.0, 7.3, 9.7, and 12.0, using a liquid to solid ratio (LS) ratio of 10.0. Fifty grams of powdered sample, as prepared in section 3.3.5, was placed in a 1000-ml Teflon® vessel with 500 ml Milli-Q™ Type II water. The samples were mixed by overhead stirring for the duration of the leaching. An Orion pH controller, equipped with a Beckman pH probe, was used to monitor pH.

By adding Omni Trace® HNO₃ (14.54 N), in increments of 1 ml or less, the solution was brought within range of the desired pH. Diluted solutions of the Omni Trace® HNO₃ were automatically added, 2 N HNO₃ for pH values of 12.0 and 9.7, 4.3 N HNO₃ for pH values of 7.3 and 5.0. Addition of the acid was controlled by the Orion pH controller, which is designed to keep the pH of the solution within +/- 0.1 pH units of the desired pH.

After 24 h of leaching at a constant pH, the leachate was filtered from the solid using a Kontes glass vacuum filtration apparatus. The fritted-glass filter was equipped with a 0.2-µm Nucleopore™ polycarbonate filter. The filtered leachate was separated for analysis: 250 ml of leachate was preserved with concentrated HNO₃ to a pH less than 2 and stored in a 250-ml HDPE bottle at 4°C until analysis; 125 ml of filtered leachate was stored, unpreserved in a 125-ml HPDE bottle at 4°C until analysis; and 50 ml of filtered leachate was preserved with concentrated H₂SO₄ to a pH less than 2 and stored in a 125-ml HPDE bottle at 4°C until analysis. Leachate samples that were nitric preserved were sent to Resource Lab, Inc. (RLI) in Portsmouth, NH, to be analyzed for Al, Ba, Ca, Cr, Fe, K, Mg, and Zn in accordance with EPA method 200.7 (Martin et al., 1994). Leachate samples that were preserved with sulfuric acid were sent to RLI to be analyzed for NO₃, in accordance with the same EPA method, 200.7. The 125-ml unpreserved filtered leachate samples were sent to RLI for analysis of Cl, Si, and SO₄²⁻ in accordance with EPA method 300.0 (Pfaff, 1993). A total of 50 ml of filtered leachate was titrated for alkalinity measurement with 0.02 N H₂SO₄ manufactured by JT Baker, in accordance with Standard Methods section 2320 (APHA, 1995). Any remaining leachate was stored unpreserved at 4°C.

3.3.6.3 Geochemical Modeling

A geochemical equilibrium modeling program, MINTEQA2 version 4, was used in conjunction with the pH-dependent leaching data to determine which solid phases controlled the

leachate composition (Allison Geoscience Consultants and HydroGeoLogic, 1998; Allison et al., 1991).

The results of the pH-dependent leachate analysis were input into a MINTEQA2 file. Comparison of measured conductivities and calculated conductivities, based on the leachate analyses, confirmed that all major ionic components had been accounted for. Since each sample was leached at four pH points, four MINTEQA2 files were created for each sample. Each input file contained the results of the leachate analysis, the fixed pH point of the leachate, and temperature was fixed at 25°C. Initially no solids were permitted to precipitate, no redox reactions were specified, and no sorption reactions were designated.

The initial output files, based on the information given above, contained data listing solids phases that were likely to be controlling leaching behavior at the stated conditions, pH, temperature and analyte concentrations. Each of the solid phases listed was assigned a saturation index (SI) number. If the SI is closer to zero, then the solid phase is more likely to be controlling the leaching behavior. The SI is calculated and assigned by MINTEQA2 based on the logarithmic ratio of the ion activity product (IAP) and the formation constant (K) for that species (Allison Geoscience Consultants and HydroGeoLogic, 1998; Allison et al., 1991).

$$SI = \log \frac{IAP}{K} \quad (2)$$

A list of solids phases with a SI of zero (+/- 1) was compiled. Final selection of mineral phases used for geochemical modeling was based on MINTEQA2 SI values, XRPD mineralogy results, and relevance to concrete chemistry.

Each phase selected for geochemical modeling was added to each MINTEQA2 input file as an infinite solid; no solids were allowed to precipitate. In the original input file, inorganic carbon concentration was entered as alkalinity (mg/L CaCO₃), but alkalinity cannot be used in conjunction with an infinite solid in this program. Instead inorganic carbon was re-entered as total dissolved carbonate (mg/L CO₃²⁻). The total dissolved carbonate concentration entered was calculated by MINTEQA2 based on alkalinity and other analyte concentrations and it was displayed as part of the initial output file for each sample. The equation used for total inorganic carbonate concentration is below (Allison Geoscience Consultants and HydroGeoLogic, 1998; Allison et al., 1991).

$$T_{CO_3^{2-}} = \text{alk} - \text{excrb} - \text{noncrb} + [H_2CO_3] \quad (3)$$

where:

- alk is the input alkalinity value converted to eq/L,
- excrb is the total number of excess equivalents of acid consumed per mole of carbonate containing species (summed over all such species), and
- noncrb is the total number of equivalents of non-carbonate alkalinity (summed over all species contributing to non-carbonate alkalinity).

Each solid phase input file results in altered MINTEQA2 output data of calculated concentrations of each analyte in the leachate. The solid phases finally determined to be the most likely to be controlling the solubility of the analytes resulted in calculated concentration close to or mimicking the actual leachate concentrations over part or all of the pH range measured.

3.3.7. Availability Leaching

The constituent availability defines the fraction of specific constituent that may be released over an infinite time period or under extreme environmental conditions. The RU-AV002.0 (availability at pH 7.0 with EDTA) protocol (Garrabrants, 1998; Garrabrants et al., 2000), a one-step extraction, was used. An aliquot of crushed material (e.g., size reduction less than 300 μm) was contacted, at room temperature ($20 \pm 2^\circ\text{C}$), with a solution of 50 mM ethylenediamine-tetraacetic acid (EDTA) using an LS of 100. The required endpoint pH value of 7.0 (e.g., pH of the optimized extraction of cations and anions) was obtained by addition of a pre-determined equivalent of acid or base. After a contact time of 24 h under agitation, the leachate pH was measured prior to filtration through 0.45- μm pore size polypropylene membranes. The filtered leachate was saved for subsequent chemical analyses. The primary contaminants of interest were Cd, Cu, Pb, Ni, and Zn. Analyses were carried out using FAAS.

CHAPTER 4: EXPERIMENTAL PLAN AND PROCEDURES

4.1 Experimental Designs

Three basic experimental designs were prepared. The first was an experimental design where three accelerated aging methods would be applied to the CFA-C laboratory prisms to allow for examination of the effects of the individual and combined aging methods on the mix. The second was an experimental design where the three accelerated aging methods would be applied to the CFA-C, CFA-F, and PCC controls to allow for examination of the effects of the individual and combined aging methods on the three mixes and for comparisons between the three mix types. The third was a design to compare the results from the accelerated aging of the CFA-C mix to the field slab for verification purposes.

In all cases, a variety of physical and environmental response variables were measured to examine how the laboratory prisms had aged and how they compared with a field pavement that had undergone early distress in the field.

4.1.1 Selection of Aging Methods

As indicated in section 2.2, it was desired to subject the laboratory prisms to both developmental and degradative aging phenomena. The aging methods that were selected were chosen for their general applicability to PCC pavements exposed to harsh environmental conditions (precipitation, freezing and thawing cycles) and repeated vehicular loadings over time.

AA (using elevated storage temperature) was the principal means of accelerating the chemical aging of the concrete. This increased the rate of the cement-water hydration reaction and the rate of the pozzolanic reaction (a CFA reaction in which amorphous silica, calcium-hydroxide, and water are the reactants).

As a result of this acceleration, thermally treated test specimens had a more advanced degree of hydration and a more advanced extent of pozzolanic reaction at the end of the thermal treatment period than did their counterparts stored at normal temperature.

Following this artificially accelerated development of the material, cycled compressive stress loading (CL) was applied to accelerate the degradation via formation of microcracks, and freeze-thaw treatment (FT) was then used to accelerate the degradation of the material in response to rapid cycles of freezing and thawing.

4.1.2 Response Variable Methods for Both Laboratory Prism and Slab Samples

4.1.2.1 Compressive Strength

Cored cylinders were tested for compressive strength per ASTM C 39. Prisms were tested for compressive strength per ASTM C 39 modified as necessary for the prism shape.

4.1.2.2 Microcracking Using Neutron Radiography and Crack Density Analysis Procedures

Neutron radiography was used to visually assess the crack density and patterns of a given specimen. A slice of concrete is treated with a neutron absorbing/attenuating material (gadolinium nitrate) that will fill the existing cracks in the sample. These treated cracks are visible in the neutron radiograph, which is created during the radiography procedure.

Each specimen was sliced into one transverse and two longitudinal slices (about 0.28 cm thick) using a kerosene-cooled saw, as illustrated in figure 12. The slices were washed with soap to remove the excess kerosene, polished briefly with No. 240 polishing grit to remove rough edges and create a fairly smooth surface, and then rewashed to remove the polishing remains. Once clean and smooth, the slices were labeled and then left to dry for at least 4 d in desiccating containers.

All slices were then coated (on one side only) with a thin layer of gadolinium nitrate to fill the cracks and returned to the desiccating containers for at least 1 d. Once the applied solution had dried, the remaining powder deposits on the slice surfaces were removed with sandpaper and kerosene. Since gadolinium nitrate is water soluble, the use of kerosene as a solvent minimized the possibility of dissolving any gadolinium nitrate in the cracks below the free surface.

The prepared slices were then mounted (up to six at a time) on a thin aluminum plate and positioned inside the neutron radiography equipment, in front of a loaded film cassette. After a 15-min exposure to the neutron beam, the film and the plate were removed from the testing set-up, and the film was developed in an adjacent darkroom. The image on the film was then digitized using a transparent scanner hooked up to a computer. Sized at about 36- by 43-cm, each radiograph yielded a final digitized image size on the order of 20 MB when scanned using the highest possible resolution (300 dpi). For analysis purposes, therefore, each scanned radiograph image was divided into smaller files, one for each slice. An example of a scanned and digitized radiograph is shown in figure 13.

The crack density for each digital slice image was assessed using Adobe Photoshop. For each image, the contrast was first increased to enhance the visibility of the cracks. Then, using a 5-pixel-wide pencil tool in white, the cracks were traced freehand. Once the crack tracing was complete, the crack density of the image was evaluated by dividing the number of white crack pixels by the total number of pixels in the image. A sample traced radiograph is shown in figure 14.

It is important to note that the crack density analysis yields relative and not absolute results. All the crack densities reported and discussed are based on a crack tracing procedure using a 5-pixel-wide pen. If the size of the pen size were altered, so too would the resulting crack densities. In addition, the combined neutron radiography procedure and crack density analysis contains some inherent variability, despite efforts to standardize the radiography preparation process and crack tracing method. Finally, since concrete is naturally a non-

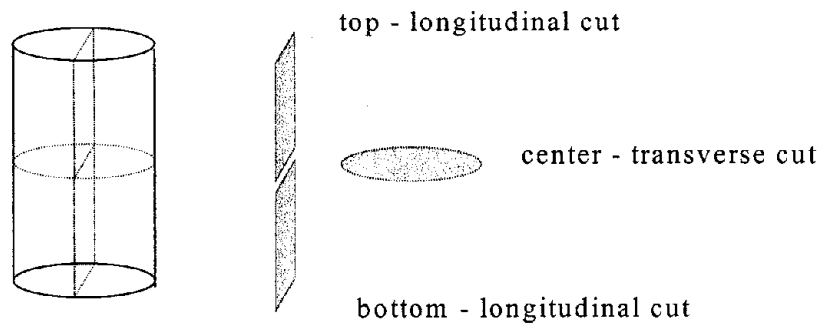


Figure 12: Orientation of saw cuts for microcrack analyses of road cores.



Figure 13: Typical neutron radiograph.



Figure 14: Typical microcrack trace.

homogeneous material, it too is subject to variation; no two samples, even from the same batch, can be expected to perform identically.

The neutron radiography and crack density analysis procedures were performed on nine slab cores (4-C, 6-C, 14-C, 19-S, 22-S, 24-S, 27-J, 30-J, and 31-J) to assess the condition of the slab at various locations.

The neutron radiography and crack density analysis procedures used for the prism specimens were nearly identical to those described for the slab specimens. The one difference was that all prism specimen slices were all rectangular or square, as shown in figure 15, since the specimens were not cylindrical cores, but rectilinear prisms.

The neutron radiography and crack density analysis procedures were performed on two sets of concrete prism samples: 28-d prism specimens from the three primary mixes (PCC, CFA-C, and CFA-F), and artificially aged samples subjected to AA, CL, and FT. The 28-d samples were assessed to provide baseline data prior to any aging, and the artificially aged specimens were assessed to identify the effects of the artificial aging processes.

4.1.2.3 Relative Dynamic Modulus

The concrete obtained from Iowa had already experienced freezing and thawing in the field. If prisms had been cut from the slab, there would be no way of knowing what the original (prior to free-thaw cycling) fundamental frequency of these prisms had been. Therefore, it was not possible to determine a relative dynamic modulus for potential prisms cut from the slab.

Laboratory prisms were tested for fundamental frequency at CRREL. ASTM C 597 was used. Subsequently they were subjected to 0, 30, or 60 cycles of FT (corresponding to N, L, or H FT treatments, respectively, as described later in section 4.1.3). Prisms that experienced FT were tested again for fundamental frequency, and the corresponding relative dynamic modulus of elasticity was subsequently calculated.

4.1.2.4 Effective Pore Size and Pore Size Distribution

Two parameters were developed to define the location and shape of the peaks in the differential mercury intrusion curve: the weighted average threshold pore width, d_{wgt} , and a peak shape uniformity indicator as described in section 3.3.2 and in appendix A in volume II. Additionally, the total porosity of a sample was calculated as the corrected mercury intrusion at maximum pressure divided by the bulk volume of the unintruded sample. This was applied to both slab and laboratory prism samples.

4.1.2.5 Effective Surface Area

The surface area of each sample, s_m , was estimated from the Langmuir and BET equations and results from adsorption experiments, as described in section 3.3.3 and in appendix B in volume II. This was conducted on both slab and laboratory prism specimens.

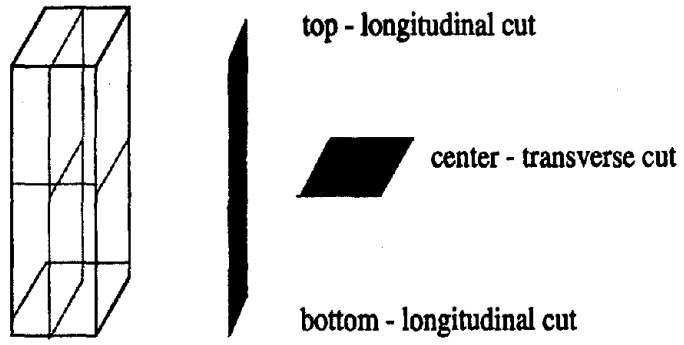


Figure 15: Orientation of saw cuts for prism samples.

4.1.2.6 Mineralogy

Methods for conducting XRPD are described in section 3.3.5.

Samples from each of the three cored regions of the slab were analyzed. Three cores from the cut region of the slab, 5-C (mid), 15-C (mid), and 17-C (mid), were analyzed to examine the heterogeneity in samples from a similar location in the slab. One core was sampled from each of the other two regions, 17-S (mid) and 26-J (mid). All of the aforementioned samples were taken from a middle slice of the cores measured along the vertical axis. Sample material was also analyzed from the top and bottom of the slab to examine variability within the road slab along the vertical axis. For these examinations, material from two neighboring cores, 5-C and 15-C, were combined to have enough material for the desired analyses. The resulting samples were labeled 5/15-C (top) and 5/15-C (mid). These samples were compared with the sampled 5-C and 15-C taken from the middle of the slab, or to the average of the same samples. All samples were ground to smaller than 300 μm and analyzed with XRPD according to the procedure found in section 3.3.5.

XRPD analysis was performed on one prism for each of the CFA-C corner points, on three prisms for the CFA-C center point, on three prisms for the CFA-F mix design, and on three prisms for the PCC mix design. In each case a square slice of the prism was taken from the middle of the prism, as measured along its longest axis. Each prism slice was separately ground into a powder smaller than 300 μm .

In addition to identification of mineral phases in the concrete samples, quantification of six mineral phases, albite ($\text{NaAlSi}_3\text{O}_8$), calcite (CaCO_3), gypsum ($\text{CaSO}_4 \cdot 2\text{H}_2\text{O}$), ettringite ($\text{Ca}_6\text{Al}_2(\text{SO}_4)_3(\text{OH})_{12} \cdot 26\text{H}_2\text{O}$), portlandite ($\text{Ca}(\text{OH})_2$), and quartz (SiO_2) was performed. The quantification work used the same computer program used for mineral identification, Jade 5.0. The six phases selected for quantification were selected on the basis of (i) occurrence of the mineral phase in the ICDD database, (ii) relevance to concrete chemistry, and (iii) presence of an RIR value on the ICDD powder diffraction file (PDF). The RIR value is a constant based on the relative intensity of the 100 percent peak of the mineral phase of interest and the relative intensity of the 100-percent peak of the mineral phase corundum in a 50:50 mixture of the two phases:

$$\text{RIR}_{a,c} = \frac{I_a^{100}}{I_c^{100}} \quad (4)$$

where:

- a refers to the mineral phase in question, and
- c refers to the mineral phase corundum (Al_2O_3).

To quantify the chosen mineral phases in the samples, an internal standard of known weight percent was added to the sample prior to the XRPD analysis. Tungsten (W) was used as the internal standard. Selection of a standard was based on (i) presence of an RIR value in the ICDD PDF and (ii) presence of major peaks of the standard in the diffractogram that were not overlapping with peaks present in the sample. W was typically added in quantities of 5 to 7.5

weight percent of the total sample.

The result of the quantification program is a calculated weight percent of the mineral phase(s) in question:

$$\text{wt}\% \text{ X} = \left(\frac{I_X}{I_W} \right) \left(\frac{I_W^{\text{rel}}}{I_X^{\text{rel}}} \right) \left(\frac{\text{RIR}_{W,c}}{\text{RIR}_{X,c}} \right) (\text{wt}\% \text{ W}) \quad (5)$$

where:

- X refers to the mineral being quantified,
- I_X refers to the intensity of the selected peak of mineral phase “X”,
- I_X^{rel} refers to the relative intensity in the sample diffractogram of the 100% peak of phase X, and
- $\text{RIR}_{X,c}$ refers to the RIR value listed in the ICDD PDF for phase X, which is based on corundum.

The final weight percent is based on averaged values of equation 5 resulting from four W peaks and a varying number of peaks for phase “X”. Peaks selected for quantification had to be well resolved and non-overlapping. Peak selection was done by the researcher rather than the program. The number and location of peaks varied for each mineral and diffractogram. The more peaks selected for quantification calculations, the greater the certainty of the final weight percent. Trace phases often had only one peak usable for quantification, which increased the uncertainty associated with the result.

Three diffraction analyses were performed for each sample. For final quantification results the mean mineral content of the three diffractograms of a sample was reported as the mineral phase weight percent as described in section 3.3.5.

4.1.2.7 Determination of the Carbonation Extent

The primary objective was to evaluate the depth of carbonation within the slab. This evaluation was carried out on bricks cut from the field slab that were 10-cm wide by 25-cm long by about 23-cm deep. For each of the three locations (e.g., northwest region, southeast region and southwest region), the carbonation extent was determined as a function of the brick depth as well as of the brick length. The method of testing consisted of determining the depth of the carbonated layer on the surface of the samples using a pH indicator dye. Carbon dioxide that penetrates the exposed surface of concrete reacts with alkaline components in the cement paste, mainly $\text{Ca}(\text{OH})_2$ and therefore causes a decrease of the pH in the pore water solution to less than 9. The resulting change in pH can be made visible by the color change of a suitable indicator. A solution of 1 percent phenolphthalein in isopropanol solution is suitable for this purpose. The visual transition interval of phenolphthalein is colorless at pH 8 to red at pH 10. Therefore, phenolphthalein turns pink to red for non-carbonated concrete and remains colorless in carbonated concrete. Carbonation depths less than 0.5 mm cannot be differentiated (RILEM Recommendations CPC-18, 1988).

To test, the surfaces of samples were cleared of dust and then sprayed with indicator

solution. When a weak coloration or none at all appeared on the treated surface, the spray test was repeated after the surface had dried. Precautions were taken to avoid the formation of flow channels on the test surface.

4.1.2.8 Measurement of Matrix Alkalinity and Constituent Solubility as a Function of pH

Determination of matrix alkalinity and constituent solubility and release as a function of pH were carried out as described in section 3.3.6.1.

The acid neutralization behavior of the materials was evaluated using methods described in section 3.3.6.1.

This method was used on only two locations of the U.S. 20 slab (e.g., northwest region and southeast region). For each of the two locations, samples were taken from the core of the bricks (e.g., non-carbonated zone with no likely metals depletion).

This method was used on the three 28-d cured material mixes prior to any aging (e.g., C(XXX)02, F(XXX)02, and P(XXX)02) and the high temperature-aged CFA-C mix (e.g., C(HNN)13).

4.1.2.9 pH-Stat Leaching

For slab specimens, the methods described in section 3.3.6.2 were used. A slight variation on the methodology for the leaching of the slab samples occurred as follows: for the leaching of samples at constant pH points of 12.0 and 9.7, 1N HNO₃ was used to maintain the pH at the desired level, while at constant pH points of 7.3 and 5.0, 2N HNO₃ was used.

For prisms specimens, pH-stat leaching was conducted as described in section 3.3.6.2.

4.1.2.10 Geochemical Modeling

Geochemical modeling on pH-stat leachates for both slab and prism specimens was conducted as described in section 3.3.6.3.

4.1.2.11 Availability Leaching

The constituent availability defines the fraction of a specific constituent that may be released over an infinite time period or under extreme environmental conditions. The methods used were described previously in section 3.3.7.

For slab specimens, this procedure was carried out on only two locations of the U.S. 20 slab (e.g., northwest region and southeast region). For each of the two slab locations, samples were taken from the core of the bricks (e.g., non-carbonated zone with no likely metals depletion).

This method was carried out on the three 28-d cured material types prior to any aging (e.g., C(XXX)02, F(XXX)02, and P(XXX)02).

4.1.2.12 Low Liquid-Solid Ratio Leaching

The RU-SR003.0 (Solubility and Release as a Function of LS Ratio) protocol (Garrabrants, 1998) was used. This protocol was designed to show the effect of liquid-solid ratios (e.g., LS ratios) on the release and solubility of material constituents and to provide an estimate of constituent release and solubility in the pore solution of the material. The range of LS ratios was chosen to correspond with test conditions of common extraction protocols while approaching the LS ratio of typical cement-based materials. Five aliquots of crushed material (e.g., size reduction smaller than 300 μm) were contacted, at room temperature ($20 \pm 2^\circ\text{C}$), with demineralized water at different LS ratios (e.g., 10, 5, 2, 1, and 0.5 ml/g of dry material). The amount of demineralized water required to reach each specified LS ratio was added to a minimum 15-g dry equivalent mass of size-reduced material. After a contact time of 24 h under agitation, extracts were filtered through 0.45- μm pore size polypropylene filtration membranes. Leachate pH and conductivity were then measured, and leachate aliquots were preserved for subsequent chemical analysis. Samples for anion analysis were not preserved. The test was carried out in duplicate. The primary constituents of interest were Na, K, Cl, SO_4^{2-} , and Ca. Analyses were carried out on preserved aliquots using FAAS for Na, K, and Ca and ion chromatography for SO_4^{2-} and Cl on unpreserved aliquots.

pH and concentrations of constituents of concern (e.g., Na, K, Cl, SO_4^{2-} , and Ca) as a function of LS then were extrapolated to the LS for the pore water within the slab. The LS for the pore water is defined by the porosity of the matrix as:

$$L/S = \frac{\varepsilon}{\rho_{\text{dry}}} \quad (6)$$

where:

- L/S is the liquid to solid ratio on a dry weight basis [ml/g dry],
- ε is the porosity [cm^3/cm^3] estimated from the moisture content of the material, and
- ρ_{dry} is the density on a dry basis [g dry/ cm^3].

The resulting concentrations then were used to estimate the pore water ionic strength and activity coefficients as a function of the ion charge number.

For slab specimens, this procedure was carried out only on the southeast region of the U.S. 20 slab. Samples were taken from the core of the bricks (e.g., non-carbonated zone with no likely metals depletion).

This procedure was carried out on the three 28-d cured material types prior to any aging (e.g., C(XXX)02, F(XXX)02 and P(XXX)02) and the high temperature-aged CFA-C mix (e.g., C(HNN)13).

4.1.2.13 Monolithic Leaching

The constituent release rates were determined using modifications of the RU-MT001.0 (Mass Transfer Rates in Monolithic Materials) protocol (Garrabrants, 1998). Modifications were made to account for the size of the monolithic samples and the duration of the refresh intervals. Thus, contact intervals were extended beyond the specified 8 d to a cumulative leaching period of 20 mo for the three samples representing the bulk of the slab and 10 mo for the sample representing the surface of the slab.

For all tests, at the end of each leaching interval, the leachates were filtrated through 0.45- μm pore size polypropylene membranes and pH and conductivity were measured. The filtered leachates then were preserved with HNO_3 to pH less than 2 and analyzed using FAAS for Na, K, and Ca, graphite furnace for Cd, Cu, and Pb and ion chromatography for SO_4^{2-} and Cl on unpreserved aliquots. Flux and cumulative release as a function of time for each constituent of interest were plotted.

Specific procedures were used for slab specimens, laboratory prisms and the coarse aggregates. These are outlined below.

For the three samples representing the bulk of the slab, monolithic samples of 10-cm diameter by 10-cm height were contacted, at room temperature ($20 \pm 2^\circ\text{C}$), with demineralized water using a liquid-solid ratio (LS_a) of 10 ml of leachant per cm^2 exposed surface area (e.g., LS_a of 10 cm). The leachant was refreshed with an equal volume of demineralized water at cumulative leaching times of 3, 6, and 12 h, 1, 2, 4, and 8 d, then refreshed every wk or every other wk up to a cumulative leaching period of 50 d, then refreshed about every mo or every 2 mo up to a cumulative leaching period of 8 m. At this point, the leachant was refreshed and the samples were left in contact with the leachant without any renewals for a leaching interval of 6 m, resulting in a cumulative leaching period of 14 m. The leachant was then refreshed about every mo or every 2 mo up to a cumulative leaching period of 20 mo (e.g., 1 yr and 8 mo). This schedule resulted in 21 extracts. Duration of the refresh intervals is given in table 9.

For the sample representing the surface of the slab, a monolithic sample of 10-cm diameter by 4-cm height was contacted, at room temperature ($20 \pm 2^\circ\text{C}$), with demineralized water using a liquid-solid ratio (LS_a) of 10 ml of leachant per cm^2 exposed surface area (e.g., LS_a of 10 cm). The leachant was refreshed with an equal volume of demineralized water at cumulative leaching times of 3, 6, and 12 h, 1, 2, 4, and 8 d, then refreshed every wk or every other wk up to a cumulative leaching period of 1 mo and then refreshed every mo or every 2 mo up to a cumulative leaching period of approximately 10 m. This schedule resulted in 16 extracts. Duration of the refresh intervals is presented in table 9.

For slab specimens, this procedure was carried out on cores (e.g., 7-C, 8-C, and 9-C) taken from the west central location of the U.S. 20 slab. Three samples taken respectively from the middle part of cores 7-C, 8-C, and 9-C (e.g., non-carbonated zone with no likely constituent depletion) and one sample taken from the surface of the core 9-C (e.g., surface exposed to traffic and climatic conditions over 10 y) were examined. With the slab labeling scheme used, these samples are referred as 7-C(2.5-6.5 in from top), 8-C(2.5-6.5 in from top) and 9-C(2.5-6.5 in

from top) for the three samples representing the bulk of the slab and 9-C(0-1.6 in from top) for the sample representing the top of the slab.

For the three 28-d cured material types (e.g., CFA-C mix, CFA-F mix, and PCC control), fresh cut, monolith samples of 7- by 7- by 10-cm were contacted with demineralized water using an LS_a of 10 ml of leachant per cm^2 exposed surface area (e.g., LS_a of 10 cm). Only one replicate of each material (e.g., C(XXX)02, F(XXX)02, and P(XXX)02) was carried out. The leachant was refreshed with an equal volume of demineralized water at cumulative leaching times of 3, 6, and 12 h, 1, 2, 4, and 8 d, then refreshed about every wk or every other wk up to a cumulative leaching period of 1 mo and then refreshed about every mo or every 2 mo up to a cumulative leaching period of 7 mo. At this point, the leachant was refreshed and the samples were left in contact with the leachant without any renewals for a leaching interval of 6 mo, resulting in a cumulative leaching period of 14 mo. The leachant was then refreshed about every mo or every 2 mo up to a cumulative leaching period of 20 mo (e.g., 1 yr and 8 mo). This schedule resulted in 18 extracts. Duration of the refresh intervals is given in table 10 for C(XXX)02, F(XXX)02, and P(XXX)02.

For the four high-level aged CFA-C mix samples (e.g., C(HNN)13, C(NHN)13, C(NNH)13, and C(HHH)13), fresh cut, monolith samples of 7- by 7- by 10-cm were contacted with demineralized water using an LS_a of 10 ml of leachant per cm^2 exposed surface area (e.g., LS_a of 10 cm). Only one replicate of each sample was carried out. The leachant was refreshed with an equal volume of demineralized water at cumulative leaching times of 3, 6, and 12 h, 1, 2, 4, and 8 d, then refreshed about every wk or every other wk up to a cumulative leaching period of 1 mo and then refreshed about every mo or every 2 mo up to a cumulative leaching period of approximately 10 mo. This schedule resulted in 16 extracts. Duration of the refresh intervals is given in table 10.

For samples of CFA-C mix submitted to other levels of aging (e.g., C(NNN)14, C(NHH)14, C(HHN)13, C(HNH)12, C(LL)16, C(LL)30, and C(LL)47), fresh cut, monolith samples of 7- by 7- by 10-cm were contacted with demineralized water using an LS_a of 10 ml of leachant per cm^2 exposed surface area (e.g., LS_a of 10 cm). Only one replicate of each sample was carried out. The leachant was refreshed with an equal volume of demineralized water at cumulative leaching times of 3, 6, and 12 hr, 1, 2, 4, and 8 d, then refreshed about every wk up to a cumulative leaching period of 1 mo and then refreshed about every mo up to a cumulative leaching period of 3.5 mo. This schedule resulted in 12 extracts. Duration of the refresh intervals is given in table 10.

In all cases, it was desired to leach the monolithic specimens for as long a period as practical to allow for surface wash off and surface dissolution to occur. These can be artifacts of monolithic leaching that can affect diffusional leaching in the short term.

No attempts were made to routinely monitor pH in the monolithic leach tests. It is possible for pH gradients to develop at the surface of the monoliths when incubated for long periods.

Table 9: Leaching time intervals used for the monolithic leaching tests carried out on the U.S. 20 slab samples.

	<u>Road bulk</u> 7-C(2.5-4.5 in from top) 8-C(2.5-4.5 in from top) 9-C(2.5-4.5 in from top)	<u>Road surface</u> 9-C(0-1.6 in from top)
Extract (n)	Leaching intervals [d]	Leaching intervals [d]
1	0.125	0.125
2	0.125	0.125
3	0.250	0.250
4	0.500	0.500
5	1	1
6	2	2
7	4	4
8	7	7
9	7	7
10	7	14
11	7	29
12	14	47
13	38	50
14	34	49
15	35	29
16	78	49
17	186 (6.2 mo)	-
18	48	-
19	37	-
20	61	-
21	36	-
Cumulative leaching time	603 d (20.1 mo)	289 d (9.7 mo)

Table 10: Leaching time intervals used for the monolithic leaching tests carried out on CFA-C mix.

	<u>28-d cured CFA-C mix</u> C(XXX)02	<u>High-level aged CFA-C mix</u> C(HNN)13, C(NHN)13, C(NNH)13, C(HHH)13	<u>Other level aged CFA-C mix</u> C(NNN)14, C(NHH)14, C(HHN)13, C(HNH)12, C(LL)16, C(LL)30, C(LL)47
Extract (n)	Leaching intervals [d]	Leaching intervals [d]	Leaching intervals [d]
1	0.125	0.125	0.125
2	0.125	0.125	0.125
3	0.25	0.250	0.250
4	0.5	0.500	0.500
5	1	1	1
6	2	2	2
7	4	4	4
8	7	7	6
9	8	7	8
10	38	14	19
11	41	29	30
12	32	47	35
13	78	50	-
14	189 (6.3 mo)	49	-
15	48	29	-
16	37	49	-
17	61	-	-
18	36	-	-
Cumulative leaching time	603 d (20.1 mo)	289 d (9.7 mo)	106 d (3.6 mo)

For samples of CFA-F mix and PCC control submitted to low levels of aging (e.g., F(LLL)13, F(LLL)30, F(LLL)47, P(LLL)13, P(LLL)23, and P(LLL)39), fresh cut, monolith samples of 7- by 7- by 10-cm were contacted with demineralized water using an LS_a of 10 ml of leachant per cm^2 exposed surface area (e.g., LS_a of 10 cm). Only one replicate of each sample was carried out. For F(LLL)13 and P(LLL)13, the leachant was refreshed with an equal volume of demineralized water at cumulative leaching times of 3, 6, and 12 h, 1, 2, 4, and 8 d, then refreshed about every wk or every other wk up to a cumulative leaching period of 1 mo and then refreshed about every mo or every 2 mo up to a cumulative leaching period of approximately 10 mo. This schedule resulted in 16 extracts. For F(LLL)30, F(LLL)47, P(LLL)23, and P(LLL)39, the leachant was refreshed with an equal volume of demineralized water at cumulative leaching times of 3, 6, and 12 h, 1, 2, 4, and 8 d, then refreshed about every wk up to a cumulative leaching period of 1 mo and then refreshed about every mo up to a cumulative leaching period of 3.5 mo. This schedule resulted in 12 extracts. Duration of the refresh intervals is given in tables 11 and 12 for CFA-F mix samples and PCC control samples, respectively.

The coarse aggregates were also subjected to monolithic leaching tests. For coarse aggregates with an average surface area of 60 cm^2 , each were contacted with demineralized water using an LS_a of 10 ml of leachant per cm^2 exposed surface area (e.g., LS_a of 10 cm). Four replicates were used in order to ensure representativeness. For each replicate, two coarse aggregates were used. The leachant was refreshed with an equal volume of demineralized water at cumulative leaching times of 3, 6, and 12 h, 1, 2, 4, and 8 d, then refreshed about every wk or every other wk up to a cumulative leaching period of 1 mo and then refreshed at cumulative leaching time of 3 mo. This schedule resulted in 11 extracts. Duration of the refresh intervals is given in table 13.

In all cases, it was desired to leach the monolithic specimens for as long a period as practical to allow for surface wash off and surface dissolution to occur. These can be artifacts of monolithic leaching that can affect diffusional leaching in the short term.

4.1.2.14 Release Modeling

The diffusion model (de Groot et al., 1992; Kosson et al., 1996; Barna et al., 1997) was used to interpret the leaching behavior of Na, K, Cl and Ca from the three samples representing the bulk of the slab and from the sample representing the surface of the slab.

This model, based on Fick's second law, assumes that the species of interest is initially present throughout the homogeneous porous medium at uniform concentration and considers that mass transfer takes place in response to concentration gradients in the pore water solution of the porous medium. Two parameters characterize the magnitude and rate of the release: C_D , the initial leachable concentration (e.g., available release potential) and D_{obs} , the observed diffusivity of the species in the porous medium.

When the species of concern is not depleted over the time period of interest, the cumulative mass release can be described by a one-dimensional semi-infinite diffusion model and calculated considering that the concentration at the solid-liquid interface is equal to zero (e.g., case of a sufficient water renewal) as (Crank, 1986) noted:

Table 11: Leaching time intervals used for the monolithic leaching tests on CFA-F mix.

Extract (n)	<u>28-d cured CFA-F mix</u>	<u>Low-level aged CFA-F mix</u>	
	F(XXX)02	F(LL)13	F(LL)30, F(LL)47
	Leaching intervals [d]	Leaching intervals [d]	Leaching intervals [d]
1	0.125	0.125	0.125
2	0.125	0.125	0.125
3	0.25	0.250	0.250
4	0.5	0.500	0.500
5	1	1	1
6	2	2	2
7	4	4	4
8	7	7	6
9	8	7	8
10	38	14	19
11	41	29	30
12	32	47	35
13	78	50	-
14	189 (6.3 mo)	49	-
15	48	29	-
16	37	49	-
17	61	-	-
18	36	-	-
Cumulative leaching time	603 d (20.1 mo)	289 d (9.7 mo)	106 d (3.6 mo)

Table 12: Leaching time intervals used for the monolithic leaching tests on PCC control mix.

Extract (n)	<u>28-d cured PCC control</u>	<u>Low -level aged PCC control</u>	
	P(XXX)02	P(LL)13	P(LL)23, F(LL)39
	Leaching intervals [d]	Leaching intervals [d]	Leaching intervals [d]
1	0.125	0.125	0.125
2	0.125	0.125	0.125
3	0.25	0.250	0.250
4	0.5	0.500	0.500
5	1	1	1
6	2	2	2
7	4	4	4
8	7	7	6
9	8	7	8
10	38	14	19
11	41	29	30
12	32	47	35
13	78	50	-
14	189 (6.3 mo)	49	-
15	48	29	-
16	37	49	-
17	61	-	-
18	36	-	-
Cumulative leaching time	603 d (20.1 mo)	289 d (9.7 mo)	106 d (3.6 mo)

Table 13: Leaching time intervals used for the monolithic leaching test on the coarse aggregates.

Extract (n)	Coarse aggregates	
	Leaching intervals [d]	
1		0.125
2		0.125
3		0.25
4		0.5
5		1
6		2
7		4
8		7
9		10
10		14
11		48
Cumulative leaching time	87 d (2.9 mo)	

$$M_t = 2\rho C_0 \left(\frac{D_{\text{obs}} t}{\pi} \right)^{1/2} \quad (7)$$

where:

- M_t is the cumulative mass of the constituent released per unit surface area at time t [mg/m^2],
- C_0 is the initial leachable concentration [mg/kg],
- ρ is the sample density [kg/m^3],
- t is the Time interval [s], and
- D_{obs} is the observed diffusivity of the species of concern [m^2/s].

After log transformation, equation 7 becomes:

$$\log M_t = \log \left[2\rho C_0 \left(\frac{D_{\text{obs}}}{\pi} \right)^{1/2} \right] + \frac{1}{2} \log t \quad (8)$$

Thus, when the release mechanism is diffusion and the species of concern is not depleted over the time period of interest, the logarithm of the cumulative release plotted versus the logarithm of time is expected to be a straight line with a slope of 0.5.

From tank leaching test results and by determining on the log-log cumulative release versus time plot the position of the "most representative" straight line with a slope of 0.5, an observed diffusivity of the species of concern can be determined by:

$$D_{\text{obs}} = \pi \left(\frac{10^b}{2\rho C_0} \right)^2 \quad (9)$$

where:

- D_{obs} is the observed diffusivity of the species of concern [m^2/s],
- b is the intercept from the graph logarithm of the cumulative release versus the logarithm of time,
- C_0 is the initial leachable concentration (e.g., available release potential) [mg/kg], and
- ρ is the sample density [kg/m^3].

However, since the slope may change over different time intervals, it is more accurate to examine the slope over each leaching interval. An observed diffusivity can then be determined for each leaching interval where the slope is 0.5 ± 0.15 by [De Groot et al., 1992]:

$$D_{i,\text{obs}} = \pi \left(\frac{M_{t_i}}{2\rho C_0 (\sqrt{t_i} - \sqrt{t_{i-1}})} \right)^2 \quad (10)$$

where:

- $D_{i,\text{obs}}$ is the observed diffusivity of the species of concern for leaching interval i [m^2/s],

- M_i is the mass released during leaching interval i [mg/m^2],
- t_i is the contact time after leaching interval i [s],
- t_{i-1} is the contact time after leaching interval $i-1$ [s],
- C_0 is the initial leachable concentration (e.g., available release potential) [mg/kg], and
- ρ is the sample density [kg/m^3].

The overall observed diffusivity is then determined by taking the average of the interval observed diffusivities.

4.1.3 Factorial Experiment for the Aged CFA-C Laboratory Prisms

A $2^3 + 3$ full factorial design with center points was employed. Three main experimental variables (AA, CL, and FT) were tested at three levels: no treatment (-1), low or medium (0), and high (+1). The 2^3 factorial design can be depicted geometrically by the eight corner points of a cube (see figure 16). The cube contains three axes, one for each experimental variable, giving each corner point a geometric coordinate that describes the treatment scheme each sample underwent. For example, a sample corresponding to the corner (+1, -1, +1) underwent high AA, no CL, and high FT. A full factorial design allows the experimenter to examine the effects of individual experimental variables as well as the interactions of two or three of the variables.

The $2^3 + 3$ experimental design is a factorial design with triplicate center points, as indicated by the “+ 3” in the design description. Samples corresponding to the center point underwent treatment of the three experimental variables at a median level (0) of treatment. The geometric coordinate, which describes these samples, is (0,0,0).

The triplicate center points allow for analysis of error between samples that received the same treatment, termed pure error. Triplicate center points also allow for analysis of linearity between the (-1) and (+1) treatment levels.

The designations (-1), (0), and (+1) are statistical designations needed to understand the experimental design and to perform statistical analysis of the response variables. Common shorthand representation of the above designations are (-), (0), and (+), respectively. The reader must understand that for the purpose of this project the three statistical designations above correspond to selected treatment levels as follows: (-) means that no treatment was performed, (0) means that a low or median level of treatment was performed, and (+) means that a high level of treatment was performed. To minimize confusion the sample labeling system developed for the project adopted alternative representation to explain a treatment scheme: (N) means no treatment was performed, (L) means a low level of treatment was performed, and (H) means that a high level of treatment was performed. Wherever possible, the N-L-H representation is used, but at times, for the purpose of statistical analysis, the -, 0, + designation may be used instead.

Appendix C in volume II provides useful ANOVA definitions and ANOVA theory for the evaluation of data from the full factorial experimental design.

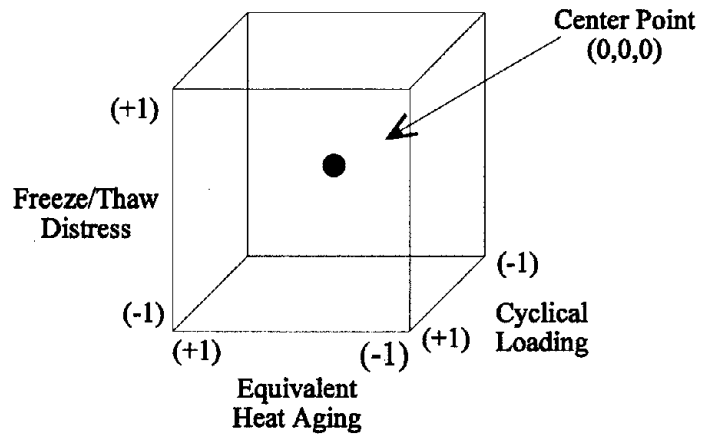


Figure16:Geometric representation of factorial experiment.

4.1.4 Comparison of Aged CFA-C, CFA-F, and PCC Control Laboratory Prisms

The choice of CFA-C as the recycled material of interest was dictated by the design of U.S. 20. In this research, a PCC control and a CFA-F control were chosen for comparative analysis to the CFA-C.

The second experimental design involved the following. The center point conditions (LLL) for the CFA-C, where the low levels of AA, CL, and FT were applied, were also used to create triplicate aged prism specimens of the CFA-F and the PCC. This allowed for comparison between all three mixes at the LLL level using ANOVA and Tukey-Kramer comparisons of means.

Appendix D in volume II provides background on the use of Tukey-Kramer multiple comparisons.

4.1.5 Comparison of CFA-C Aged Laboratory Prisms to the U.S. 20 Field Slab

This third experimental design involved comparison of the aged CFA-C laboratory prisms to the field slab. Here, where possible, replicates of all the experimental variables were obtained so that the range of values observed in the aged CFA-C laboratory prisms could be compared with a range of values obtained from the slab. No statistical tests methods were used to make these comparisons.

4.2 Laboratory Prism Fabrication

4.2.1. Slab Mix Design

The mix design for the overall U.S. 20 1987 paving operation was used as the basis for the prism mixes. The Iowa County P73 road adjacent to U.S. 20 (where the slab was obtained) was paved by the same contractor with the same materials using the same job mix as U.S. 20. The Iowa DOT provided a daily inspection report that described the materials used, placement methods, curing conditions, and tests performed on the roadway pavement. A summary of the U.S. 20 mix design is provided in table 14.

4.2.2. Prism Mix Design

Three concrete mixes were designed, the first of which (designated as CFA-C) was intended to match the 1987 mixture used in the U.S. 20 pavement. The CFA-C mixture contained portland cement, CFA-C fly ash, coarse aggregate, fine aggregate, an air-entrainment admixture, a water-reducing admixture, and water. The second mix, the CFA-F mix, employed CFA-F fly ash as a control. The third mixture was a PCC control without CFA. Table 15 summarizes the material quantities in the mixes.

4.2.3. Sample ID and Labeling System

Table 14: Material quantities used in the U.S. 20 (1987) mix design.*

Material	1987 mix kg
Cement	221
Coal fly ash	39
Fine aggregate [†]	621
Coarse aggregate [†]	765
Water added from materials	26.3
Water	93.4

* Values are per 0.765 m³ of fresh concrete

[†] Values correspond to the saturated surface dry (SSD) condition

Table 15: Material quantities used in the accelerated aging mix design (1997).*

	1997 CFA [‡] mixes kg	1997 PCC mix kg
Cement	221	260
Coal fly ash	39	None
Fine aggregate [†]	621	621
Coarse aggregate [†]	765	765
Water added from materials	-6.80	-6.80
Water	(279)	(279)
Total water	(264)	(264)

* Values are per 0.765 m³ of fresh concrete

[†] Values correspond to the saturated surface dry (SSD) condition

[‡] Coal fly ash

Concrete batches were assigned one of four colors: red, green, yellow, or black (see tables 16 and 17). Labels were printed on colored Dymo embossing tape and attached to the bottom of each mold. The elevated surface of the characters on the tape made a reverse imprint of the label on the concrete surface. Label paper covered with clear tape was also affixed to the samples by Dacron string. The sample numbers were chosen based on the treatment scheme that samples were to receive (see figure 17).

The first letter describes the mix type, C for CFA-C, F for CFA-F, and P for PCC. The three letters in parentheses indicate the level of treatment a sample received for equivalent aging, cyclic stress, and freeze-thaw cycles, respectively. The letters "N", "L", and "H" correspond to the assigned None, Low, and High treatment levels. The letter "T" implies that the sample was removed at this point in the treatment scheme for preliminary testing. The letter "X" was used where no treatment was applied because the sample had been removed from the process. The number on the right of the label is the replicate number.

For example, C(LHH)03 is third in the series of samples made from the CFA-C mix and treated with low AA, high CL, and high FT. In all, there were 17 groups of samples for the AA method; 11 for CFA-C, and 3 for both CFA-F and PCC mixes. For each group, there were 16 replicates. Over 400 samples (plus extra samples for initial testing, labeled XXX) were created.

4.2.4. Mixing

Each concrete mix was divided up into the smallest number of batches that could be adequately mixed by the largest, locally available, rotary drum mixer. A 0.255-m³ rotating steel drum mixer was used. The mixer was a Whiteman, model 62-P, driven by an 8-hp gasoline engine. Although the mixer's size was listed as 0.255 m³, it could only adequately mix 0.113 m³ of fresh concrete per batch.

There were eight batches divided evenly into 2 d. The first day of batching was on Thursday, March 5, 1998. The PCC mix was batched first. The PCC mix was divided into two 0.113-m³ batches. The actual quantities used are listed in table 16. The mixing procedure described in table 18 was followed on all batches. The CFA-F mix was batched second. This was also divided into two-0.113 m³ batches. The next and last day of batching was on Tuesday, March 10, 1998. On this day, the CFA-C mix was prepared in four batches, each 0.113 m³.

4.2.5. Specifications

Goals for slump and total air content were set for the properties of the freshly mixed concrete. Values of 3.5 percent total air and 50-mm slump were decided upon. Total air and slump were measured in accordance with ASTM C 231 and ASTM C 143, respectively.

4.2.6 Casting and Curing

Samples were cast five samples to a mold. The molds were made from a particle board surfaced with a low-pressure melamine resin laminate with water-resistant properties. Fresh

Table 16: Batching quantities for CFA-C and PCC batches.

	Red	Green	Yellow	Black
Cement	32.8 kg	32.8 kg	38.6 kg	38.6 kg
Coal fly ash F	5.78 kg	5.78 kg	N/A	N/A
Water	18.73 kg	18.73 kg	18.73 kg	18.73 kg
Water reducer	44.03 ml	44.03 ml	88.71 ml	88.71 ml
Air entrainment	11.23 ml	11.23 ml	7.54 ml	7.54 ml
Coarse aggregate	112 kg	112 kg	112 kg	112 kg
Fine aggregate	92.1 kg	92.1 kg	92.1 kg	92.1 kg
Time of day	12:04 pm	12:56 pm	10:14 am	11:01 am
Day	3/5/98	3/5/98	3/5/98	3/5/98

Table 17: Batching quantities for CFA-C batches.

	Red	Green	Yellow	Black
Cement	32.8 kg	32.8 kg	32.8 kg	32.8 kg
Fly Ash C	5.78 kg	5.78 kg	5.78 kg	5.78 kg
Water	18.73 kg	18.73 kg	18.73 kg	18.73 kg
Water reducer	37.74 ml	37.74 ml	37.74 ml	37.74 ml
Air entrainment	11.31 ml	11.31 ml	11.31 ml	11.31 ml
Coarse aggregate	112 kg	112 kg	112 kg	112 kg
Fine aggregate	92.1 kg	92.1 kg	92.1 kg	92.1 kg
Time of day	8:56 am	10:03 am	11:07 am	11:57 am
Day	3/10/98	3/10/98	3/10/98	3/10/98

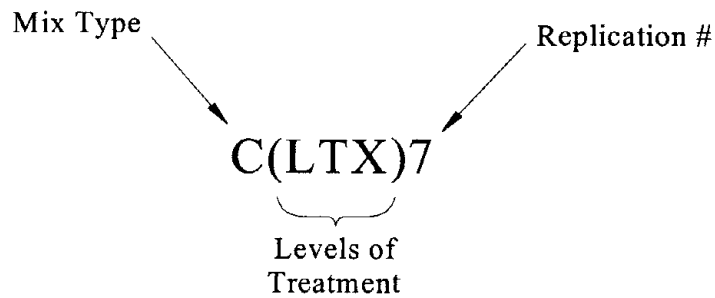


Figure 17: Labeling scheme.

Table 18: Mixing procedure.

Procedure	Time
1. Wet down the mixer with hot water	
2. Empty all free water from mixer	
3. Add coarse aggregate	
4. Start mixer	
5. Add fine aggregate	
6. Cover mixer with plastic and mix aggregates together	6.5 – 8 min
7. Remove cover and add air entrainment admixture*	
8. Add portland cement and fly ash if applicable	
9. Cover mixer with plastic and mix components	2.5 – 4.5 min
10. Remove cover; add combination of water and water-reducing admixture with mixer rotating†	
11. Cover mixer and mix	1 – 4 min
12. Stop mixer; remove cover; manually scrape dry material from bottom	
13. Start mixer and mix	5 – 7 min
14. Stop mixer: empty into wheelbarrow‡	
15. Insert thermometer; start air and slump tests	
16. Record temperature	
17. Record air and slump test results	
18. Begin filling molds with concrete	

* Darex II AEA by W.R. Grace & Co

† Plastocrete 161 by Sika

‡ Total mixing time with water (10 – 13 min.)

concrete was consolidated in two lifts with a 10-mm stainless steel rod. Surface finishes were prepared with hand trowels

Samples were cured in a fog room for 24 h at 98 percent relative humidity and $22 \pm 2^\circ\text{C}$. After 24 h, the samples were stripped from their molds. The samples were labeled with a Dacron string, wrapped with foam sheets, secured with rubber bands, and placed inside a clear plastic bag. The wrapped prisms were then loaded into a 5-gal bucket lined with foam fabric. Each bucket held five prisms. The voids between the plastic bags were packed with Perlite to act as a cushion and filler during transportation. Lime-saturated distilled water was poured into and around the tops of the five plastic bags. The plastic bags were closed with cable ties and each bucket was capped with a rubber gasket and plastic lid.

4.2.7. Prism and Cylinder Mini-Study

There is currently no ASTM protocol for compressive strength testing of prisms of the size described previously. For this reason, cylinders were cast along with the prisms. A mini-study was performed to create a relationship between the compressive strengths of prisms to the ASTM standard cylinder shape. These procedures are discussed in appendix E in volume II.

4.3 Aging Procedures

4.3.1 Selection of Order of Application of Aging Methods

The first treatment the samples were subjected to was AA, performed at Cornell University (Ithaca, NY). The subsequent treatments were CL, conducted at UNH (Durham, NH), followed by FT conducted at Cold Regions Research and Engineering Laboratory (Hanover, NH).

The goal of the treatment scheme was to induce developmental and degradative aging of the concrete on an accelerated time line (on the order of months) in a manner that approximated typical aging of concrete in a natural environment (on the order of yr).

AA was applied first to allow for the development of microstructure and possible deleterious reactions under a developmental aging scenario. CL was applied second to produce some microcracking (but not loss of monolith integrity) as a degradative aging scenario. FT was applied third to produce some loss of material integrity (but not complete loss of monolith integrity) as a degradative aging scenario.

4.3.2 AA as an Experimental Variable

Tanks were built to provide an accelerated aging environment for some of the specimens by curing at 60°C at high relative humidity and a normal curing environment at room temperature at high relative humidity for the other specimens. The specimens were divided between the tanks and cured for designated lengths of time, according to the experimental specifications.

Each curing tank, as pictured in figure 18, was composed of a large aluminum tank, a

composite plywood/styrofoam insulation cover, a plastic top sheet, and additional insulation around the sides. The tanks were filled with about 25 cm of water. Large stainless steel wire racks were placed on wooden beams that ran across supports just above the water line, such that the specimens could sit on the racks without being immersed in the water, as seen in figure 19. The room-temperature tank was positioned on the ground, whereas the two 60°C tanks were raised on supports to allow for heating coils to be attached to the underside of the tanks. The heating coils were regulated by a feedback control system, which would turn them on and off as necessary to maintain the set temperature.

All three tanks were also outfitted with temperature and relative humidity probes. While the relative humidity probe was attached to one end of the tank near the top of the specimens, the temperature probes were taped directly to several “dummy” specimens in the middle and ends of the tanks, as shown in figure 20. Temperature and relative humidity readings were performed every 15 min until the specified curing times were achieved. The typical temperature profile for the tanks fluctuated between about 58 and 63°C for the 60°C tank, and remained a nearly constant 30 C for the room temperature tank. The relative humidity measurements remained above 98 percent for all tanks throughout the curing process.

After the designated 100 d, the “low” aging specimens were removed from the 60°C tanks and transferred to the room temperature tank. After 200 d, the heat aging of the “high” aging samples was stopped by turning off the heating elements in the 60°C tanks. At this point, the specimens were individually removed from their respective tanks, rewrapped in their (same) initial packing materials, and placed back in their initial buckets for shipping.

4.3.2.1 Estimate of Equivalent Age for Experimental Design

The extensive calibration of the AA procedure to produce equivalent aging is described in appendix F in volume II.

The purpose of the calibration tests was to assess the equivalent age of the concrete prisms after the temperature aging. Mortar specimens were subjected to four curing temperatures (5, 25, 45, and 65°C). The development of compressive strength, non-evaporable water content, and ultrasonic pulse velocity were measured at various ages for each of these different curing temperatures. The apparent activation energy was calculated for each property based on two development models: a linear hyperbolic (ASTM C 1074) and a parabolic hyperbolic.

Tables F-9 and F-15 in appendix F of volume II present the equivalent ages for the concrete prisms at the end of the various thermal treatments for each property based on the two models. The results show a wide range of equivalent ages depending on the extent of the thermal aging, mixture type, property measured, and type of model. For example, for the PCC mixture subjected to high thermal aging, equivalent ages of 4.6 to 8.0 yr were estimated from different properties using the linear hyperbolic model. Likewise, for the CFA-F mixture at high thermal aging, equivalent ages of 2.8 to 20.1 yr were estimated from different properties using the parabolic hyperbolic model.



Figure 18: Curing tank.

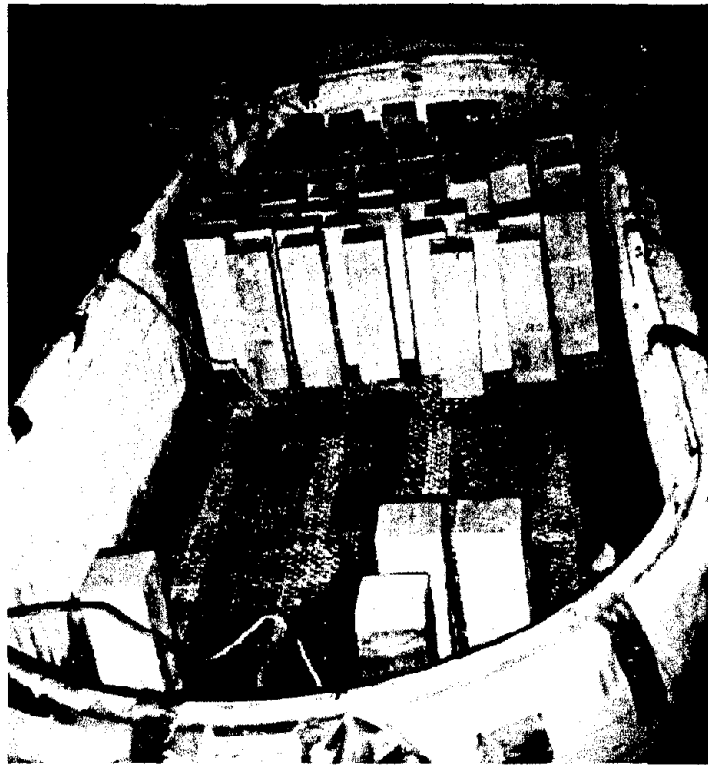


Figure 19: Prism samples in curing tank.



Figure 20: Dummy prisms and temperature probe.

This wide range of results, however, may be narrowed down when the following sequence of analysis is performed. First, analyze both hyperbolic models to indicate which one is more applicable to each property development for each mixture. Second, evaluate the application of each property to the main goal of the present study. Finally, obtain the most appropriate equivalent age for each mixture after each thermal aging process.

Regarding the two models for development of concrete property with time, they both seem to satisfactorily fit the data. However, as shown in these tables, the best-fit parabolic-hyperbolic curve yielded a higher dof-adjusted- R^2 and a lower fit-standard- error for all mixtures and all properties. These data suggest that the parabolic-hyperbolic equation better models the development of the concrete properties studied here, and thus the equivalent ages presented in table F-15 are more appropriate than those in table F-9 for the mixtures studied.

The main goal of this project was to predict long-term environmental performance of concrete pavements based on monolith integrity and product leaching. Monolith integrity is related to two of the three concrete properties studied: compressive strength and ultrasonic pulse velocity. An internal crack in a concrete specimen causes a decrease in its compressive strength and a decrease in the ultrasonic pulse velocity through the specimen.

Product leaching, on the other hand, is related to both internal microcracking and also the extent of the internal chemical reaction, since the extent of cement hydration greatly affects permeability and porosity, which in turn influence leaching. The non-evaporable water content indicates the extent of the cement hydration, e.g., degree of hydration.

Given the complications of transforming non-evaporable water measurements to degree of hydration in the mixtures with fly ash, as already discussed, w_p/c measurements in such mixtures might not reflect the correct development of cement hydration. Therefore, the equivalent ages from w_p/c for the fly ash mixtures, as presented in tables F-9 and F-15, were not considered at this time.

From the arguments above, an estimate of the thermal aging effects on the mixtures studied is more likely to be reflected by the values presented in table F-15, not including the equivalent ages from w_p/c measurements for the ash mixtures. As such, table 19 presents values of equivalent ages at the end of the thermal aging process for each mixture based on the average of the mean values of table F-15.

4.3.3 CL as an Experimental Variable

CL is a process of continuous load reversal resulting in the fatigue of a material. Fatigue failure in concrete is a complicated result of microcrack propagation, still not fully understood. Concrete fatigue failure can occur under applied compressive stresses, tensile stresses, or a combination of the two. The research of interest in this work was limited to compressive stress fatigue aging.

Table 19: Average equivalent ages (in yr) at 20°C at the end of thermal aging treatment.

Thermal aging	Equivalent age		
	PCC	CFA-C	CFA-F
None	1.2	1.0	1.0
Low	3.7	1.9	2.2
High	6.2	2.9	3.4

Research in the area of fatigue failure began with the development of the highway system in the late 1920s. Numerous amounts of research have been performed on this topic since then. It would be beyond the scope of this project to present the development of current theories.

4.3.3.1 $f'_{c(28)}$ Determination and Cyclic Loading Selection

The work of Hsu (1981) was used as the basis for determining cyclic fatigue parameters in this project. Prior to Hsu's paper, the fatigue of concrete was thought to be controlled by the compressive strength, f_c , number of cycles, N_{cyc} , and the ratio of maximum applied stress to that of the compressive strength, f_{max}/f_c . The compressive strength of concrete is defined by the procedure of ASTM C 39. Per ASTM instructions, the load shall be applied in a short amount of time (0.14 to 0.34 MPa/s). Research has shown that under a sustained static load, concrete specimens will fail at a load as low as 75 percent of their ASTM 28-d strengths due to creep (Rusch, 1960). Hsu applied a load duration variable to his formula for predicting the fatigue life of concrete,

$$\frac{f_{max}}{f_c} = 1 - \left[0.0662(1 - 0.556R) \log N_{cyc} \right] - 0.0294 \log T \quad (11)$$

where:

- T is the period of loading (inverse of frequency), and
- R is the ratio of the minimum applied stress to the maximum, f_{min}/f_{max} .

To apply equation 11 to this work it was necessary to determine the compressive strength of the laboratory-created prisms. A mini-study was performed (described in section 4.2.7) to create a relationship between the compressive strengths of prisms to the ASTM standard cylinder shape.

4.3.3.2 Determination of Cycles for Experimental Design

The goal of the CL phase of the accelerated aging process was to induce microcracking. The level of loading required to produce microcracking is close to the loading responsible for fatigue failure. It was necessary to avoid the destruction of any samples before the FT phase, where complete samples were required to measure resonant frequency. The parameters used in equation 11 were, therefore, chosen conservatively.

The process of AA created concrete samples of varying compressive strengths (see table E-1 in appendix E of volume II). It was decided to use the smallest of these prism compressive strengths to ensure that all samples remained intact. The samples that received the "high" level of AA had the lowest mean prism compressive strength at 35.4 kPa.

The period of cyclic load, T, was determined by the testing machine's capabilities. Trial runs were performed on an Instron® 1100 MN load frame. The best results were with a period of 0.25 s (frequency equals 4 Hz).

The maximum stress limit was set at 75 percent of the mean prism compressive strength of those samples that had received high CL (26.6 kPa). The lower limit was changed until the predicted life of the specimen by Hsu's equation was determined to be 2 h. Thus, a minimum applied stress of 12.5 percent of the mean prism compressive strength (4.43 kPa) was applied. The duration of cyclic loading was then shortened to reduce the chance of failure. The "high" samples were loaded for 1 h and the "low" for 1/12 h.

4.3.4 FT as an Experimental Variable

4.3.4.1 FT Procedure

FT distress was one of three experimental variables selected to accelerate the aging of the concrete prisms in this study. Freezing and thawing was done according to the American Association of State Highway And Transportation Officials (AASHTO) TP17-93, "Standard Test Method for Resistance of Concrete to Rapid Freezing and Thawing," (Procedure C), where each freeze-thaw cycle consists of alternately cooling the center of each prism from 4.4 to -17.8°C in air and by warming it back to 4.4°C in water. Strict adherence to the standard requires that the prisms be within ± 1.7 °C of these temperatures at the end of the cooling and heating periods. Further, the time to cool from 2.8 to -16.1°C should be at least half of the cooling time, and the time to warm from -16.1 to 2.8°C should be at least half of the thawing time. Thawing time should constitute at least 25 percent of each cycle.

Soon after the prisms arrived at CRREL, those to which nothing was to be done were separated from those which were to be freeze-thaw aged. The prisms to be freeze-thaw aged were then submerged in lime-saturated water for 24 h, surfaced dried, and measured for fundamental transverse frequency to document their as-received condition. Each prism was then wrapped in wet cotton terry cloth and sealed in individual plastic bags to keep them wet during freezing and to avoid leaching anything out of them during thawing.

According to plan, some prisms were to be subjected to a high (H) number of freeze-thaw cycles while others were to be subjected to exactly half or to a low (L) number of cycles. The high number of freeze-thaw cycles was to be determined during the aging process as the point where one or more of the prisms started to develop visible surface cracks. To make this determination and to not over-expose any of the prisms, the "H" prisms were the first to be cycled. Once cracking became evident in those prisms, the high level was set, the low level was determined as half this, and the "L" prisms were cycled.

All freezing and thawing was done in a Scientemp Corp. apparatus modified to accommodate 65 concrete prisms. Since there were 63 H prisms, all could be accommodated in a single load by the freeze-thaw apparatus. Once cracking became evident, the high number of freeze-thaw cycles was set and the H prisms were unloaded from the apparatus. The L prisms, randomly distributed into three loads, were then cycled to half that number of cycles.

Each freeze-thaw cycle was closely monitored by embedding thermocouples in two dummy prisms placed at the far ends of the apparatus. Each freeze-thaw cycle ran 3 h and essentially satisfied the AASHTO requirements. The primary differences between these cycles

and the AASHTO requirements were that the temperatures at the end of the cooling and heating periods were a degree or two lower than specified, and that the time to cool from 2.8 to -16.1°C comprised only 45 percent, rather than the specified minimum 50 percent, of the cooling period.

The freeze-thaw cycles remained consistent throughout this study, ensuring that each prism was subjected to identical freeze-thaw environments.

The prisms were removed from the freeze-thaw apparatus once every 15 to 30 cycles, read for fundamental transverse frequency, and returned to random positions, turned end-for-end in the chamber to ensure that each prism was evenly subjected to conditions in all parts of the chamber. Uniformity between cycles was ensured by maintaining the chamber at full load capacity by placing dummy prisms into empty spaces as needed.

4.3.4.2 Relative Dynamic Modulus

The effect of freezing and thawing on the integrity of each prism was assessed by measuring the change in relative dynamic modulus (RDM) of elasticity according to the following equation.

$$P_c = (n_c^2/n^2)100 \quad (12)$$

where:

- P_c is the relative dynamic modulus of elasticity, after C cycles of freezing and thawing, in percent,
- n is the fundamental transverse frequency at 0 cycles of freezing and thawing, and
- n_c is the fundamental transverse frequency at C cycles of freezing and thawing.

Fundamental transverse frequencies were measured according to ASTM C 215⁽²⁾ with an accelerometer mounted on the end of each prism that was read with a Rion Model SA-77 signal analyzer. Prism vibrations were excited by tapping the prisms lightly with a slender metal rod.

As previously mentioned, the prisms were subjected to either a high or a low number of freeze-thaw cycles. All prisms were closely monitored for cracking. The range of cracking increased across concrete types.

The high number of freeze-thaw cycles occurred at 60 cycles when two prisms [C(HHH)11 and C(HHH)15] started to exhibit surface cracks. The low number of freeze-thaw cycles, therefore, was established at 30 cycles.

Appendix G in volume II provides detailed information about determination of FT cycles for the experimental design.

4.4 Assessment of Leaching from Heterogeneous Monoliths

4.4.1 Experimental Program

An experimental program was developed to examine leaching of constituents of concern from heterogeneous concrete monoliths. This work, conducted by the Netherlands Energy Research Foundation, is presented in appendix H in volume II.

Results for leaching and spectroscopic evaluations of concrete specimens using Pb/Zn slag as an aggregate (as a partial sand replacement) or doped with various Pb and Zn compounds showed:

1. The leachability from the concrete containing Pb/Zn slag as aggregate based on tank leaching was not significantly different from regular portland cement over the period of testing. The only element that is significantly increased relative to portland cement was Mo.
2. Based on the experimental and modeling results, significantly longer periods of tank leaching than 64 d may be required to observe differences in constituent release, when present, that are a consequence of the heterogeneity of the matrix in comparison with a homogeneous matrix.
3. The pH at the interface between the leaching solution and the external boundary of the concrete matrix is the most important factor controlling short-term release of constituents of interest, when the solubility of the constituent is strongly dependent on pH.
4. Geochemical speciation modeling revealed that for Cr, the Ba (SO₄,CrO₄) solid solution determines the solubility of Cr. In concrete containing Pb/Zn slag as aggregate, the Cr leachability is much lower than in ordinary portland cement due to reduction of Cr VI to Cr III by the reducing properties of the slag.
5. MIP on the concrete cubes was consistent with SEM observations, both of which indicated that the concrete was more porous when Pb/Zn slag (<125 mm) was used as a partial sand replacement.

4.4.2 Model Development

The heterogeneous porous materials were assumed to consist of two distinct physical components (e.g., aggregates and binder). Constituents of interest may be present in either or both components. Model development was adapted from the approach used by Massry (1997) to describe the fate of volatile organic carbon in soils and based on the conceptual diagram shown in figure 21. The porous solid matrix was modeled as two distinct homogeneous compartments: (i) a compartment made of binder in that mass transport of the species of interest toward the leaching solution occurred by diffusion and (ii) a compartment made of a uniform distribution of

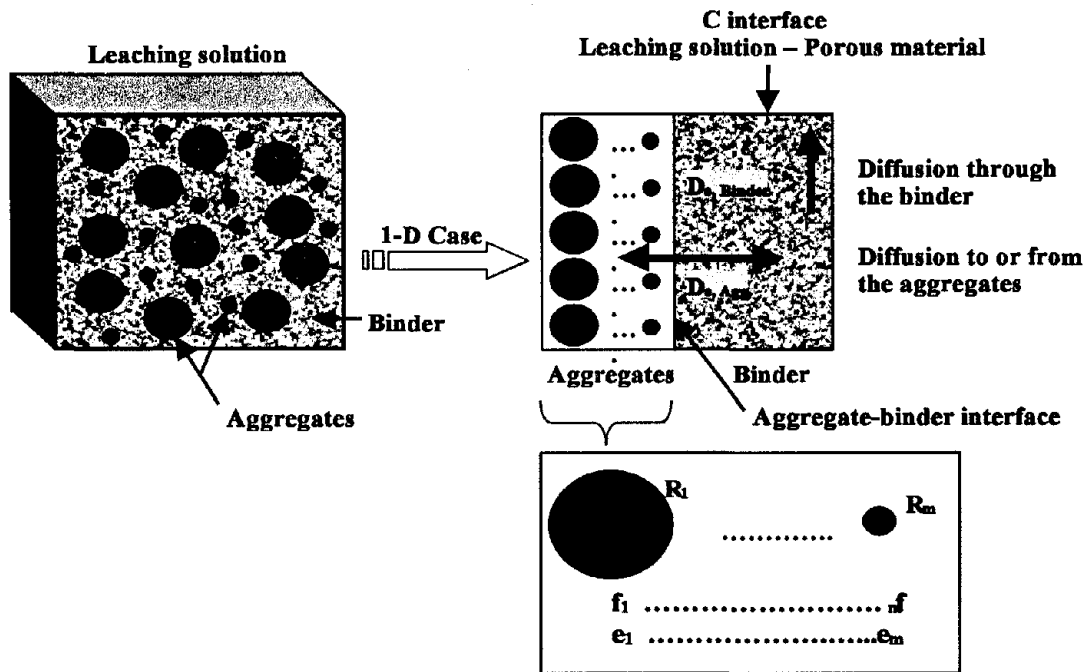


Figure 21: Conceptual model for a heterogeneous porous material.

aggregates which acted as sources or sinks for the species of interest. The aggregates were modeled as spheres within which transport occurred by diffusion. The model assumed that there is no interface reaction between the aggregates and the binder. In this stage of development, the model is only valid to describe the release of species from the model porous material when leaching behavior is not a function of pH (e.g., Na, Cl) or when no pH gradient within the material is generated during the leaching. Indeed, in those cases, species release is only controlled by diffusion.

Using the conservation principle and Fick's law, mass transport of the species of interest within the binder in one-dimension is given by:

$$\frac{\partial C_{\text{Binder}}}{\partial t} = D_{e, \text{Binder}} \frac{\partial^2 C_{\text{Binder}}}{\partial x^2} + \frac{1}{(1 - \sum_{j=1}^m f_{\text{Agg},j})} \sum_{j=1}^m f_{\text{Agg},j} q_{\text{Agg},j} \quad (13)$$

where:

- C_{Binder} is the species concentration in the binder [mass/m³ binder],
- $D_{e, \text{Binder}}$ is the effective diffusivity of the species of interest in the binder [m²/s],
- $q_{\text{Agg},j}$ is the flux from aggregate type j [mass/m³ aggregate s],
- $f_{\text{Agg},j}$ is the volume fraction of aggregate type j [m³ aggregate/m³ porous material],
- m is the total number of aggregate types,
- t is the time [s], and
- x is the linear coordinate [m].

Mass transport of the species of interest within an aggregate of radius R is given by:

$$\frac{\partial C_{\text{Agg},j}}{\partial t} = D_{e, \text{Agg},j} \frac{1}{r^2} \frac{\partial}{\partial r} \left(r^2 \frac{\partial C_{\text{Agg},j}}{\partial r} \right) \quad (14)$$

where:

- $C_{\text{Agg},j}$ is the species concentration in aggregate type j [mass/m³ aggregate],
- $D_{e, \text{Agg},j}$ is the effective diffusivity of the species of interest in aggregate type j [m²/s],
- t is the time [s], and
- r is the radial coordinate [m].

The model is accomplished by dividing the computation into two stages: (i) calculation of the flux to or from the aggregates using diffusion through spheres of radius R and, (ii) calculation of species transport by diffusion through the binder by plugging the aggregate flux into the binder equation. The obtained concentration profile within the binder then is used as the boundary conditions for the aggregate equation. These two steps are repeated until the convergence of the solution is obtained. The overall release flux of the species of concern then is calculated.

CHAPTER 5: RESULTS AND DISCUSSION

5.1. Mix Components Characterization

Environmental characterization was performed on the four component materials used to create the experimental concrete: CFA-C, CFA-F, portland cement and combined samples of the fine and coarse aggregate.

CFA is typically divided into two categories; Class C CFA (CFA-C) and Class F CFA (CFA-F). CFA-C typically results from the burning of subbituminous or lignite coal, has a high Ca content (greater than 10 percent CaO), and has cementitious and pozzolanic properties. CFA-F typically results from the burning of anthracite or bituminous coal, has a low Ca content (less than 10 percent CaO), and has pozzolanic properties, but no cementitious properties (ASTM C 618; Malhotra and Ramezani pour, 1994).

Portland cement is created from the high temperature burning of calcium materials like limestone or chalk and silaceous materials like clays (Neville, 1996). Ca, Si, and Al oxides combine in various ratios to make up the bulk of the portland cement matrix. Portland cement was used in the concrete with a water to cement (w/c) ratio of 0.485 (table 16). The same w/c ratio used for the creation of the experimental concrete prisms was used for the creation of the hydrated paste.

The total aggregate content of the experimental concrete was 45 percent fine aggregate and 55 percent coarse aggregate (table 16). The combined samples used for environmental characterization utilized this same ratio of fine to coarse aggregate. The fine aggregate used in the experimental concrete mixes was a quartz-based (SiO_2) aggregate. The coarse aggregate was a limestone aggregate (CaCO_3).

5.1.1. Elemental and Oxide Composition

5.1.1.1 CFAs

The results of the elemental analyses of the CFA-C and the CFA-F by neutron activation analysis and X-ray fluorescence (NAA/XRF) can be found in tables I-1 through I-6 in appendix I in volume II. The elemental data have been divided into three groups: major (greater than 10,000 ppm), minor (1,000 to 10,000 ppm) and trace components (less than 1,000 ppm) and are compared with elemental data of other CFAs. In these tables, the elemental composition of the CFA-C is presented for comparison with elemental composition of 12 subbituminous and lignite CFA samples (EPRI, 1987). The elemental composition of the CFA-F is compared with the range of elemental composition of 21 bituminous CFA samples (EPRI, 1987).

Chemical composition of CFA depends on the composition of coal burned in power plants as well as the conditions under which the power plant operates (Malhotra and Ramezani pour, 1994). For the CFA-C used here, several minor element concentrations were outside the range found in the EPRI samples for the corresponding elements (EPRI, 1987), but the differences were not overwhelming. The CFA-F analysis did indicate that some

concentrations were significantly different from the EPRI bituminous samples (EPRI, 1987).

Major elements Al, Si, and Ti were considerably higher in concentration in the CFA-F used in this experimental concrete than the highest concentration in the ERPI samples. Fe, a major element, and Ca, a minor element, were lower in concentration in this CFA-F than in lowest EPRI bituminous sample.

Table 20 compares the results of the oxide analysis performed on the CFA-C and CFA-F used in this project with typical oxide data of similar materials (FWHA, 1995). Oxide contents of the CFA-C and CFA-F are close to typical oxide contents and meet ASTM oxide requirements for use with concrete (FHWA, 1995; ASTM C 618).

MgO concentrations above 5 percent in CFA-C have been shown to cause deleterious reactions in concrete through the formation of $Mg(OH)_2$ (Malhotra and Ramezaniapour, 1994). The oxide analysis of the CFA-C used in the experimental concrete showed a MgO content of 5.6 percent.

In conclusion:

1. The elemental composition of the CFA-C used here was in line with published values.
2. The elemental composition of the CFA-F used here is higher in Al, Si, and Ti and lower in Fe and Ca.
3. MgO concentrations were found to be about 5 percent in the CFA-C. Such concentrations have been shown to cause deleterious reactions in concrete through the formation of $Mg(OH)_2$.

5.1.1.2 Portland Cement

Total elemental analysis was performed by NAA/XRF on the unhydrated portland cement. These results are presented in tables I-7 through I-9 in appendix I of volume II. The tables of elemental composition are divided into major, minor and trace concentrations.

An estimate of oxide content was made based on the elemental composition data. This estimated oxide content, in table 21, is compared with typical oxide concentrations in portland cement.

Calculation of the oxide compounds was based on the percent composition of the cation in the total elemental data, the molecular weight of the cation, the molecular weight of the oxide species, and the mole ratio of the cation to the oxide.

Most oxide species were within or close to the typical values cited. SO_3 content was found to be much greater in the experimental prism concrete than the typical values given for SO_3 content in portland cement. This difference may reflect a difference in calculation methods

Table 20: Oxide analysis of coal fly ashes.

wt %	CFA-C	Typical CFA-C ¹	ASTM requirements ²
LOI	0.19		6% maximum
SiO ₂	32.8	39.9	50% total minimum
Al ₂ O ₃	18.8	16.7	
Fe ₂ O ₃	6.3	5.8	
SO ₃	2.2	3.3	5% maximum
CaO	26.8	24.3	
MgO	5.6	4.6	
Na ₂ O	2.0		
K ₂ O	0.34		
P ₂ O ₅	1.13		
TiO ₂	1.5		
SrO	0.35		
BaO	0.83		

wt %	CFA-F	typical CFA-F ¹	ASTM requirements ²
LOI	0.91		6% maximum
SiO ₂	59.9	54.9	70% total minimum
Al ₂ O ₃	28.8	25.8	
Fe ₂ O ₃	3.3	6.9	
SO ₃	0.1	0.6	5% maximum
CaO	0.8	8.7	
MgO	0.8	1.8	
Na ₂ O	0.4		
K ₂ O	2.4		
P ₂ O ₅	0.11		
TiO ₂	1.51		
SrO	0.07		
BaO	0.09		

1 (FHWA, 1995)

2 (ASTM C 618)

Table 21: Estimated oxide content of the portland cement.

Species	Calculated oxide %	Soroka, 1979	Neville, 1996
SiO ₂	21.2%	17 - 25	20
Al ₂ O ₃	6.4%	3 - 8	6
Fe ₂ O ₃	2.3%	0.5 - 6	3
SO ₃	9.0%	1 - 3	2
CaO	70.9%	60 - 67	63
MgO	0.6%	0.1 - 5.5	1.5
Na ₂ O	0.1%	0.5 - 1.3	1
K ₂ O	0.7%		
TiO ₂	0.2%	0.1 - 0.4	

rather than an actual difference in SO₃ concentration. Higher SO₃ content in the portland cement can lead to a deleterious reaction by forming ettringite (Ca₆Al₂(SO₄)₃(OH)₁₂•26H₂O).

In conclusion:

1. There are indications that the portland cement used for these experiments was unusually high in sulfates. A high level of sulfates can result in a deleterious reaction by forming ettringite.

5.1.1.3 Aggregates

NAA/XRF was performed on a combined sample of 45 percent fine aggregate and 55 percent coarse aggregate. The results of the total elemental analysis are presented in tables I-10 through I-12 in appendix I in volume II. Results are divided into major, minor, and trace concentrations.

The most significant species identified in the total elemental composition were Ca and Si. Since the aggregates were limestone and quartz-based (SiO₂) it is expected that these would be the highest elemental components in the NAA/XRF analysis.

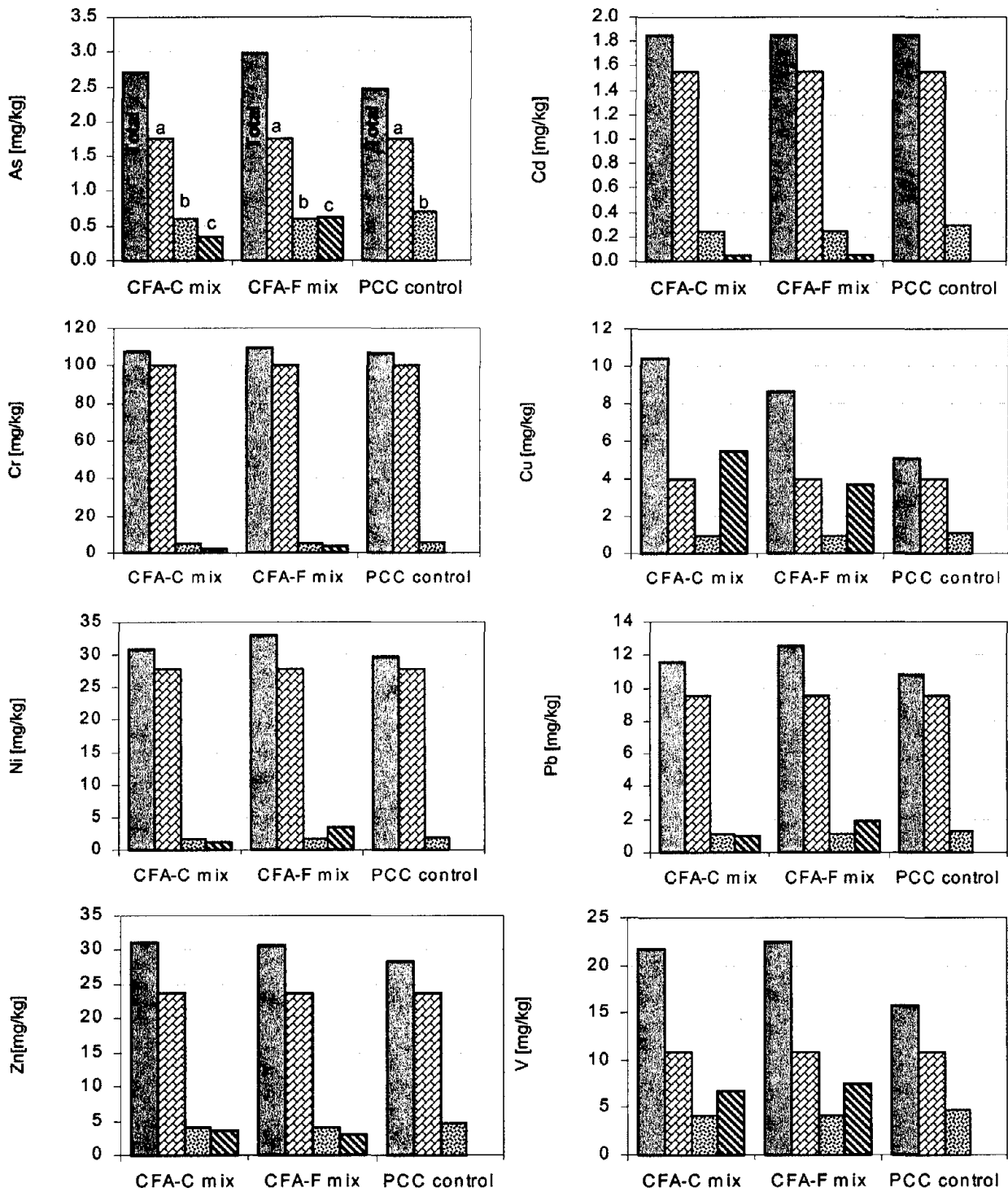
In conclusion:

1. The elemental composition of the aggregates was as expected for limestone- and quartz-based aggregates.

5.1.1.4 Relative Contributions of Constituents of Concern from Mix Components to Overall Prism Composition

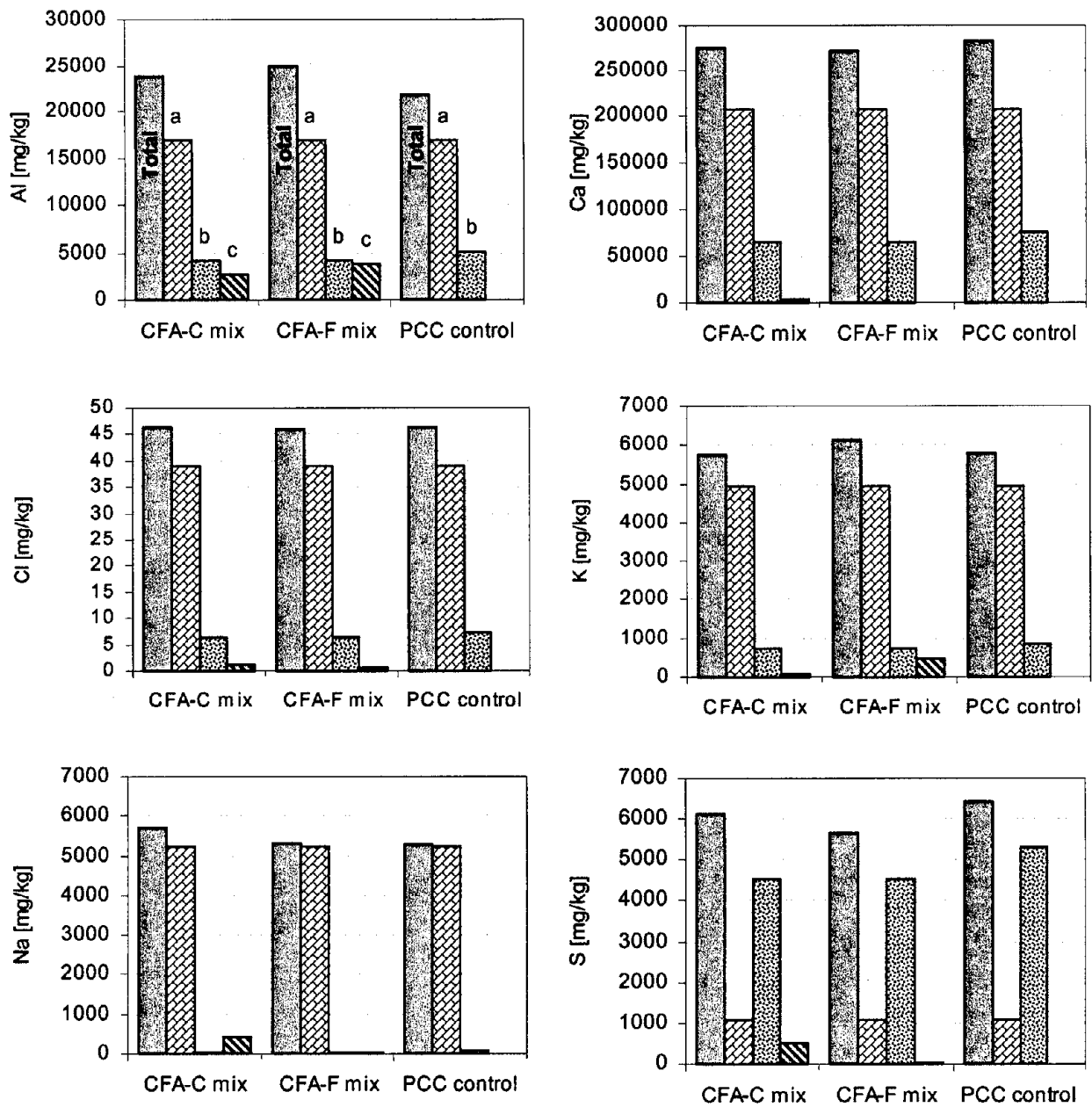
Total constituent content of trace metals (e.g., As, Cd, Cr, Cu, Pb, Ni, V, and Zn) and major species (e.g., Al, Ca, Cl, K, Na, and S) present in the CFA-C mix, CFA-F mix, and PCC mix are presented in figure 22 and figure 23, respectively. These values were mass balance calculations using the NAA/XRF total constituent contents of individual mix components and each mix design. Relative contributions of constituents of concern from individual mix components to the overall product composition are shown.

The constituents of concern (e.g., As, Cd, Cr, Cu, Pb, V, and Zn) were present in each of the concrete product components (e.g., CFA-C, CFA-F, portland cement and aggregates). The CFA-C mix, CFA-F mix, and PCC control resulted in similar total contents for both trace metals and major species. Results indicated that (i) the trace metals were present in the three materials at concentrations less than 0.01 wt percent and (ii) Na, K, and S were present at concentrations less than 1 wt percent. In addition, the largest percentage of the total content for the constituents of concern was provided by the aggregates. In all cases, this resulted from the combination of (i) a high percentage of aggregates (e.g., approximately 78 percent), (ii) a low percentage of CFA (i.e., approximately 2 percent) and (iii) comparable orders of magnitude for the total content of each species in the individual concrete product components.



a Contribution of specific element from aggregates to the total concrete product composition.
 b Contribution of specific element from cement to the total concrete product composition.
 c Contribution of specific element from coal fly ash to the total concrete product composition.

Figure 22: Total content of trace metals as determined by calculation – prisms.



- a Contribution of specific element from aggregates to the total concrete product composition.
- b Contribution of specific element from cement to the total concrete product composition.
- c Contribution of specific element from coal fly ash to the total concrete product composition.

Figure 23: Total content of major species as determined by calculation – prisms.

5.1.1.5 Conclusions

In conclusion:

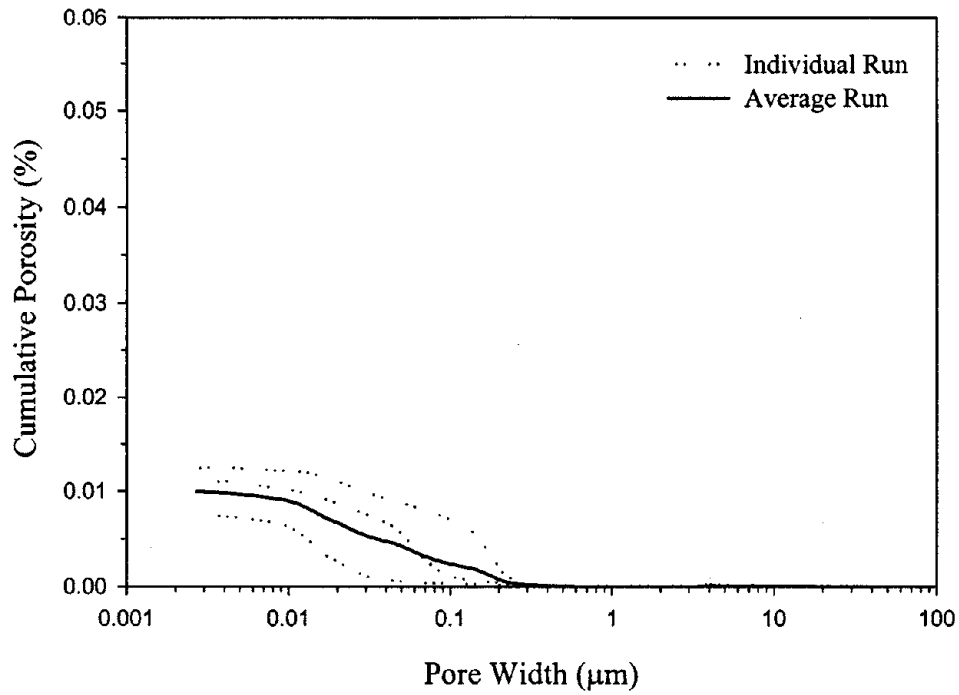
1. The CFA-C was typical compared with other Class C ashes.
2. The CFA-F was enriched in Al, Si, and Ti and lower in Fe and Ca compared with other Class F ashes.
3. MgO concentrations were found to be about 5 percent in the CFA-C. (Such concentrations have been shown to cause deleterious reactions in concrete through the formation of Mg.)
4. The oxide content of the portland cement was high in SO₃. (A high level of sulfates can result in a deleterious reaction by forming ettringite.)
5. The elemental composition of the aggregates was as expected for limestone- and quartz-based aggregates.
6. The aggregates were the greatest source of the trace metals and major species of concern.
7. The trace metals of concern were present at low concentrations (e.g., less than 0.01 wt percent).

5.1.2. Effective Pore Size and Pore Size Distribution

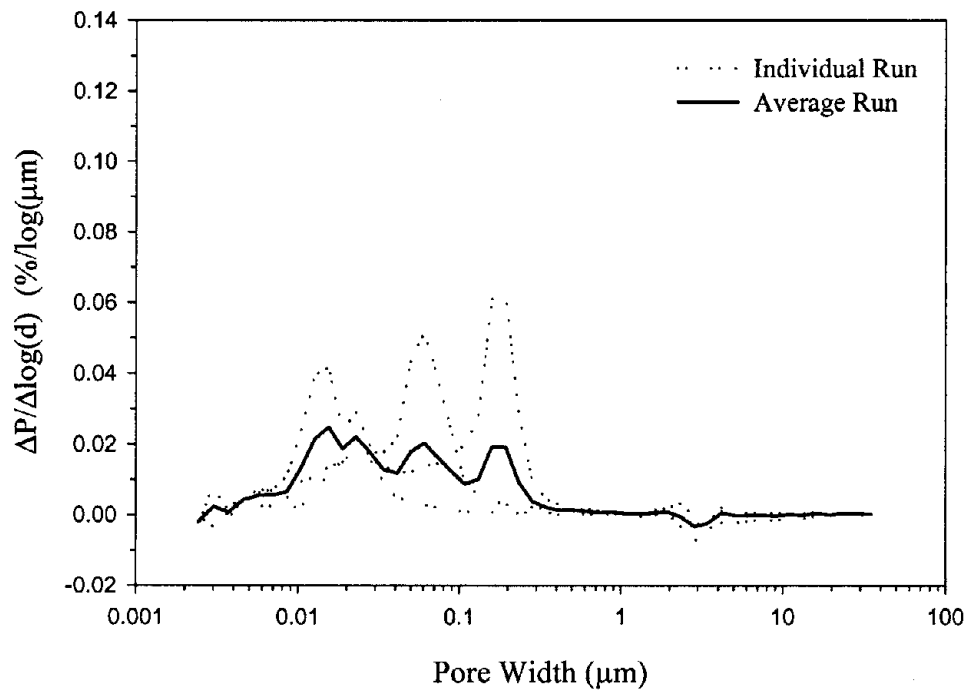
Samples of coarse aggregate were analyzed using MIP. Samples were of the same sizes used for the prism samples. Results of these tests are shown in figure 24.

A total average porosity was found to be approximately 1 percent which is about 1/10th that found in the concrete samples. Furthermore, as coarse aggregate comprised less than half the volume of the concrete, the coarse aggregate's contribution to the intrusion of the concrete as a whole would be less than 0.5 percent. Similar arguments apply to the fine aggregates. As such, the affect of coarse and fine aggregate porosity on the pore size distribution of the concretes was expected to be negligible. Furthermore, pore size distributions were used to compare the effects of treatments and compare laboratory results with field samples. As the same aggregates were used for all laboratory samples, aggregate porosities cannot affect the relative differences found between laboratory samples. Also, as the laboratory aggregates were quite similar to the aggregates used in the U.S. 20 job mix, and as aggregate effects are necessarily minor when compared with other differences between laboratory and field samples, potential differences in aggregates were not expected to have an effect on the comparison between laboratory and U.S. 20 slab concretes. As such, no further characterization of aggregates was undertaken.

In conclusion:



(a)



(b)

Figure 24: MIP results for coarse aggregate: (a) cumulative porosity vs. pore width; (b) average differential pore size distribution vs. pore width.

1. Coarse aggregate porosity was found to be approximately 1 percent which would contribute less than 0.5 percent of the concrete porosity
2. Coarse and fine aggregate porosity and pore size distributions do not substantially affect those of the concrete as a whole.
3. Coarse and fine aggregate porosity and pore size distributions are consistent between all concretes examined here and therefore do not have any effect on differences noted between the concretes.

5.1.3. Effective Surface Area

The surface area of the crushed limestone coarse aggregate used in this project was measured to be $0.35 \pm 0.012 \text{ m}^2/\text{g}$. This compared well with values found by Potgieter and Strydom (1996). The surface areas internal to aggregates were also found to be 12 to 25 percent of the surface areas of the concretes. Furthermore, fine aggregate surface area was not expected to have any effect on the relative comparisons made in this research. As such fine aggregate surface areas were not determined.

In conclusion:

1. Surface areas of the aggregates were found to be 12 to 25 percent of the surface areas of the concretes.
2. Surface areas of the aggregates are consistent between all concretes examined here and therefore do not have any effect on differences noted between the concretes.

5.1.4. CFA Morphology

Field emission scanning electron microscopy (FESEM) images were made of CFA-C and CFA-F samples (see figures 25a and 25b). CFA particles typically range from 1 to 150 μm in diameter. Particles are spherical in nature, some appearing solid and other as thin, hollow spheres. The larger hollow spheres are often broken or incomplete spheres that reveal many smaller spherical particles contained within the larger particle (Malhotra and Ramezani-pour, 1994). CFA-C has been found to be a finer material than CFA-F, on average (Malhotra and Ramezani-pour, 1994). No particle size survey was performed but particles examined for surface chemical composition fell within the typical range, with one exception of a CFA-C particle estimated at 275 μm .

Elemental surface composition analyses were performed by FESEM. Table 22 details the average surface composition of 10 particles for both the CFA-C and the CFA-F. There was no observed relationship between the size of the particle examined and the chemical composition of the particle surface.

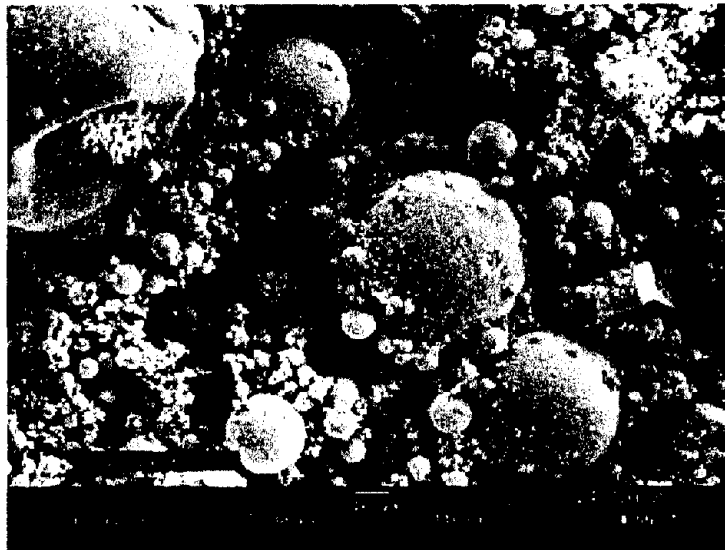


Figure 25a: FESEM micrograph of a CFA-C.

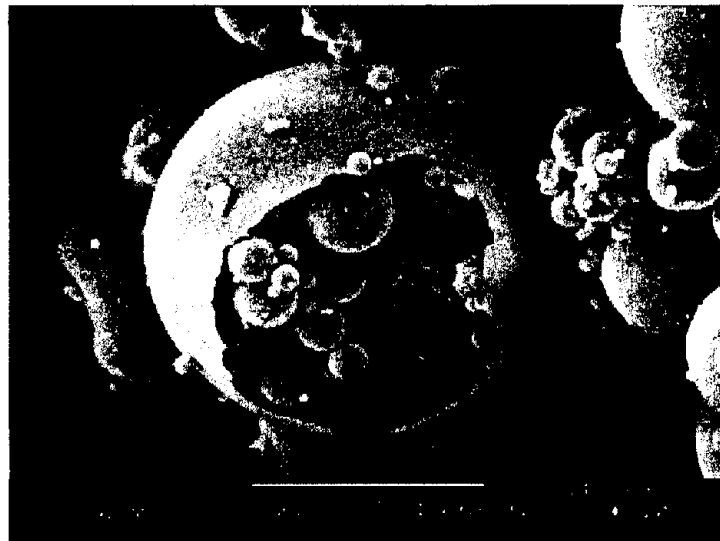


Figure 25b: FESEM micrograph of a CFA-F.

Table 22: Surface elemental composition of CFA-C and CFA-F (+/- standard deviation).

Element	CFA-C (%wt)	CFA-F (%wt)
C	1.12 +/- 1.41	0.57 +/- 0.32
O	13.17 +/- 1.54	14.85 +/- 2.67
Na	2.27 +/- 1.37	0.17 +/- 0.06
Mg	2.81 +/- 1.26	0.63 +/- 0.41
Al	24.24 +/- 4.51	35.63 +/- 4.98
Si	34.94 +/- 13.16	44.79 +/- 3.19
P	0.62 +/- 1.1	0.01 +/- 0.04
S	0.59 +/- 0.47	0.03 +/- 0.05
K	0.42 +/- 0.24	1.27 +/- 0.39
Ca	17.4 +/- 11.94	0.32 +/- 0.52
Ti	0.89 +/- 0.28	0.72 +/- 0.31
Fe	1.56 +/- 0.53	1.04 +/- 0.39

Elemental analysis of the surface of the CFA particles by FESEM was found to have a large relative standard deviation for the average concentration of most elements in the ten particles analyzed for both ash types. Chemical composition of CFA measured by FESEM was in general agreement with total elemental composition measured by NAA/XRF for Ca, K, Na, P, and Ti for both CFA-C and CFA-F. The estimates of Al, Si, and Mg concentrations by FESEM were 1.5 to 3.7 times the reported NAA/XRF concentrations. FESEM elemental analysis found Fe and S to be 20 to 50 percent of the NAA/XRF concentrations. These differences in reported concentration may have to do with the tendency of certain elements to be found on the interior or exterior of particles, based on the rates of volatilization and condensation.

In conclusion:

1. Surface concentrations of elements vary widely from particle to particle.
2. Compared with analysis by NAA/XRF, surface concentrations of Al, Si, and Mg were higher and Fe and S were lower than bulk concentrations.

5.1.5. Mineralogy

5.1.5.1 CFAs

CFA-C and CFA-F samples were analyzed for bulk phase mineralogy by XRPD. Mineral phases identified in the CFA-C sample can be found in table I-13 of appendix I in volume II. Some common CFA-C mineral phases identified in the CFA-C sample include Ca_2SiO_4 , anhydrite (CaSO_4), periclase (MgO), quartz (SiO_2), and CaO (EPRI; 1981; Tishmack et al., 1999; Malhotra and Ramezani pour, 1994). Mineral phases identified in the CFA-F can be found in table I-14 of appendix I in volume II. Mullite ($\text{Al}_6\text{Si}_2\text{O}_{13}$), hematite (Fe_2O_3), and quartz (SiO_2) phases are typical CFA-F phases that were identified in this CFA-F sample (EPRI, 1981).

In conclusion:

1. Expected, typical mineral phases were found in both CFA samples.

5.1.5.2 Portland Cement Paste

XRPD was performed on the hydrated portland cement paste. Table I-15 of appendix I in volume II presents phases identified in this paste that are considered typical hydration products of portland cement. Several typical phases of unhydrated portland cement were identified in the cement paste: $3\text{CaO}\cdot\text{SiO}_2$, $2\text{CaO}\cdot\text{SiO}_2$, $3\text{CaO}\cdot\text{Al}_2\text{O}_3$ and gypsum ($\text{CaSO}_4\cdot 2\text{H}_2\text{O}$). $3\text{CaO}\cdot\text{SiO}_2$ and $2\text{CaO}\cdot\text{SiO}_2$ have been shown to persist in unhydrated grain in portland cement paste for months (Neville, 1996). Gypsum is added to react quickly with $3\text{CaO}\cdot\text{Al}_2\text{O}_3$ to prevent immediate stiffening of the cement paste, known as flash set (Neville, 1996). Gypsum is reported to react completely in the cement paste within 24 h and should no longer be detectable after this point (Taylor, 1997). Detection of gypsum in the month-old cement paste may be explained by detection of a trace and unexpected amount of gypsum remaining in the paste. The unexpected presence of the sulfate bearing gypsum may also correspond to the higher than expected level of

sulfates found in the cement by NAA/XRF.

In conclusion:

1. Typical cement mineral phases were found in month-old hydrated cement paste.
2. Gypsum was also detected in the paste, but this was unexpected as gypsum is expected to have completely reacted by the age of 1 month.
3. The presence of gypsum in the hydrated paste may correspond to the unexpectedly high level of sulfates detected in the portland cement.

5.1.5.3 Combined Aggregates

A sample of mixed coarse and fine aggregates was subjected to XRPD for identification of mineral phases. Table I-16 of appendix I in volume II details the mineral phases identified in the combined aggregate sample. Calcite (CaCO_3) and dolomite ($\text{CaMg}(\text{CO}_3)_2$) are typical limestone minerals that were identified in the aggregate mix (EPRI, 1986). Quartz, the expected primary fine aggregate component, was identified with high certainty in the mixed aggregate sample. Several other mineral phases were identified in the mixed aggregate sample, including arcanite (K_2SO_3), albite ($\text{NaAlSi}_3\text{O}_8$), and MgFe oxide. Detection of these three additional phases is supported by the total elemental composition data of the aggregate where the elements that make up these phases occur as major and minor components of the aggregate.

5.1.5.4 Conclusions

In conclusion:

1. The CFA-C and CFA-F contained typical mineral phases.
2. Typical cement mineral phases were found in month-old hydrated cement paste.
3. Unexpectedly, gypsum was found in the month-old hydrated cement paste. This unexpected mineral may correspond to the unexpectedly high levels of sulfate in the source cement.
4. The combined aggregates contained the expected calcite and quartz phases.

5.1.6. pH-Dependent Leaching and Solid Phase Control

5.1.6.1 Mix Components Alkalinity and Constituent Solubility as a Function of pH

Acid neutralization capacity curves for the CFA-C, CFA-F, and the combined aggregates are compared in figure 26. These curves provide information on the amount of acid required to

neutralize the matrix alkalinity and decrease the pH to defined levels.

Acid neutralization capacity curves for the CFA-C, CFA-F, and the combined aggregates are compared in figure 26. These curves provide information on the amount of acid required to neutralize the matrix alkalinity and decrease the pH to defined levels.

The pH titration curve of CFA-C exhibited a rapid drop from a pH 12 to a pH 10 followed by a quasi-linear slope to a pH 3 with no discernible plateaus. The CFA-C buffering capacity was relatively high with a natural pH around 12 and a pH¹ less than 3 achieved upon addition of 16 mEq of acid/g of dry sample. This behavior was consistent with the cementitious character of CFA-C as defined by ASTM.

In contrast, the pH titration curve of CFA-F exhibited an extremely rapid drop from a pH of 12 to a pH of 2. The CFA-F buffering capacity was low with a natural pH around 4 and a pH less than 2 upon addition of 0.4 mEq of acid/g of dry sample. This behavior seemed to indicate that a significant fraction of the CFA-F was inert.

The pH titration curve of the combined aggregates (limestone type) showed a rapid decrease from a pH of 12 to a pH of 6 below which a plateau was reached. This plateau was consistent with the buffering capacity of CaCO₃ and reflected 9 mEq of acid/g of dry sample. This plateau was followed by a rapid decrease to a pH less than 2 upon additional acid addition of 2 mEq of acid/g of dry sample. The natural pH of the combined aggregates was around pH 9; this is typical for weathered limestones.

As, Cd, Cr, Cu, Pb, Ni, and Zn solubility as a function of pH obtained for CFA-C and CFA-F is compared in figure 27. Cd, Cu, Pb, Ni, and Zn solubility obtained for the combined aggregates is also shown. Horizontal lines on each of the figures are used to indicate the FAAS detection limits.

Different solubility levels as well as behaviors could be observed according to the type of CFA. The observed differences most likely can be attributed to different speciation as well as to the degree of encapsulation of these trace contaminants in the different mineral phases of the CFA.

Different solubility behaviors could also be observed for the combined aggregates with solubility levels of the same order of magnitude or higher than the ones obtained for CFA-C or CFA-F and solubility levels limited by the total content for pH less than 4.

The individual pH-dependent leaching behaviors of elements shown in figure 27 are described below.

¹ Natural pH is used to refer to the pH when the material equilibrates with demineralized water.

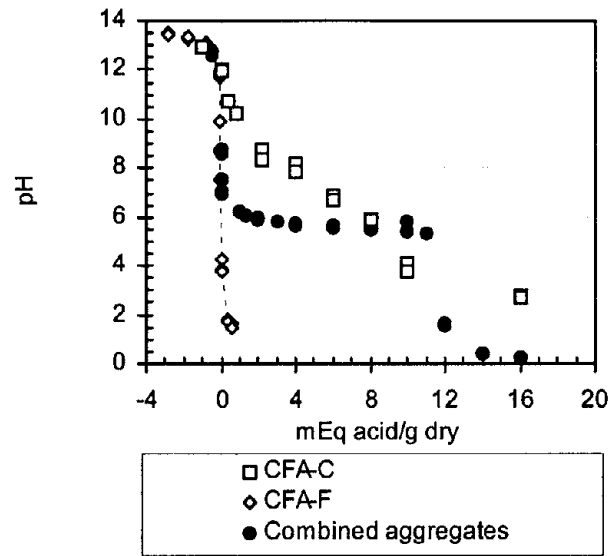


Figure 26: Acid neutralization capacity curves.

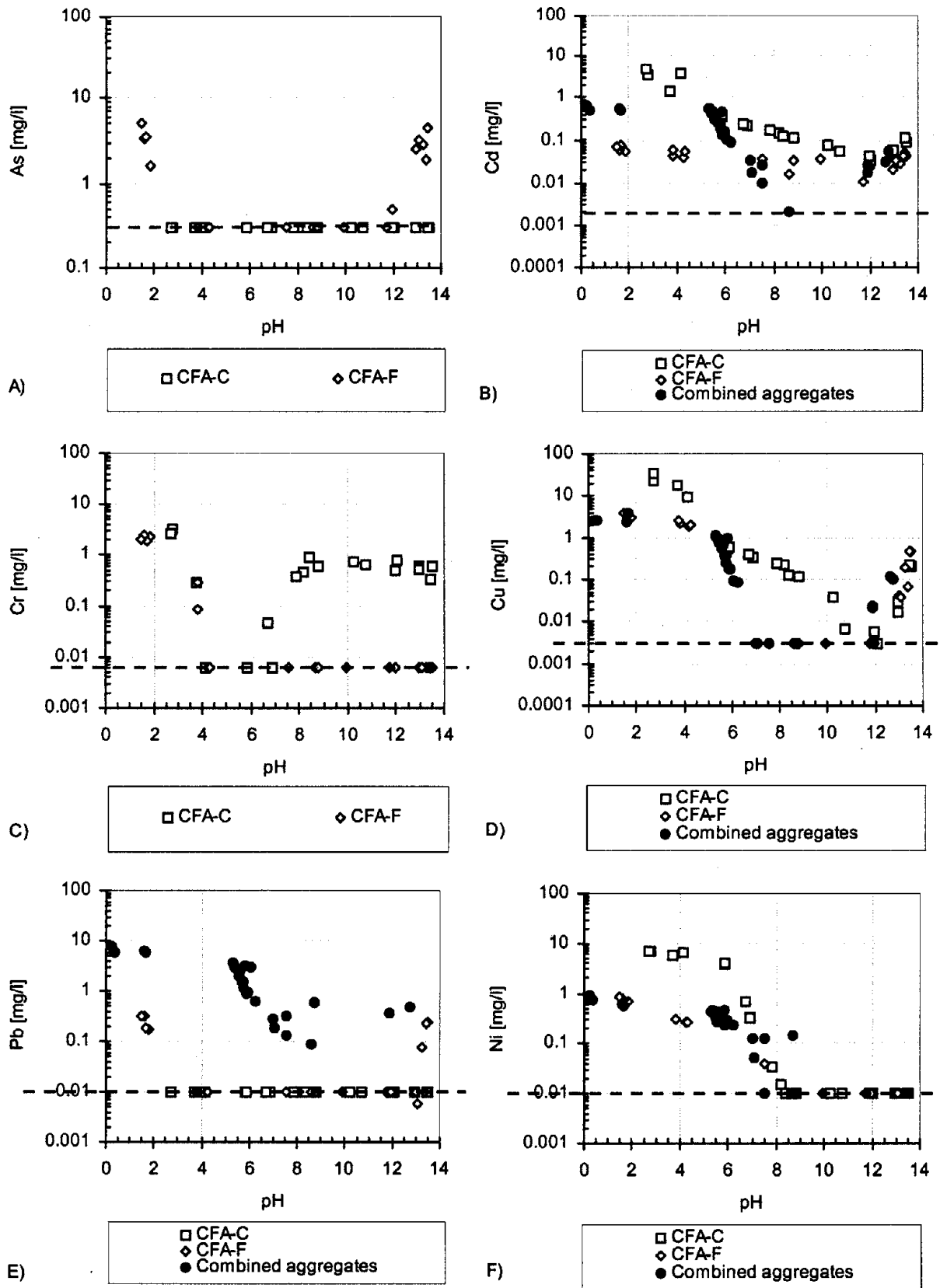
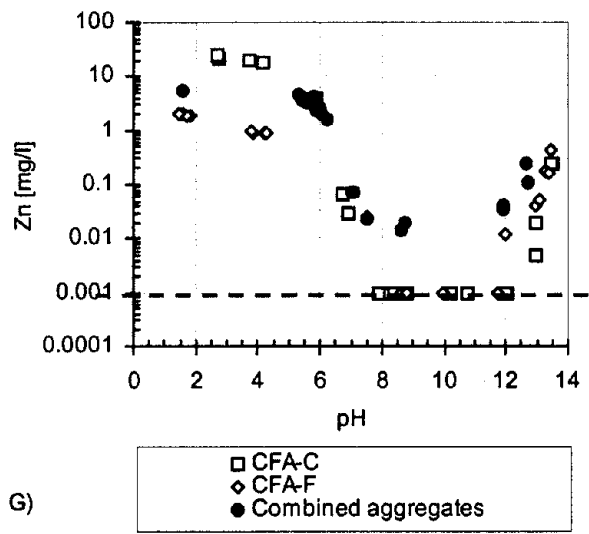


Figure 27: Constituent solubility as a function of pH.



Dashed line indicates analytical detection limits

G)

Figure 27 (continued): Constituent solubility as a function of pH.

As. As solubility in CFA-C remained below FAAS detection limit (e.g., 0.3 mg/l) over all the pH range. As solubility of CFA-F was below FAAS detection limit for a pH between 3 and 12. At a pH less than 3 and greater than 12, As solubility increased up to 5 mg/l. As behavior can be related to the dissolution of the CFA glassy phase that can occur at high and low pH, releasing constituents of interest.

Cd. Cd solubility in CFA-C, CFA-F, and the combined aggregates exhibited an amphoteric behavior with a minimum of solubility reached for high pH. For CFA-C, Cd solubility increased from 0.04 mg/l to 5 mg/l as pH decreased from 12 to 2. A minimum of solubility of 0.04 mg/l was reached for a pH of about 12. For CFA-F, Cd solubility slightly varied between 0.01 mg/l and 0.07 mg/l. For the combined aggregates, Cd solubility varied between 0.01 mg/l and 0.1 mg/l for a pH greater than 11 and between 0.01 mg/l and 0.9 mg/l for a pH lower than 8. For a pH less than 6, Cd solubility was limited by the total content of Cd in the material (e.g., maximum release of 3 mg/kg while the Cd total content was less than 2 mg/kg) and did not reflect solubility.

Cr. Cr solubility in CFA-C remained fairly constant at 0.6 mg/l between a pH 8 and a pH 13, reflecting Cr⁺⁶ content. For a pH between 8 and 4, Cr solubility decreased up to a value below FAAS detection limit (e.g., 0.006 mg/l). For a pH less than 4, Cr solubility increased up to a maximum of 4 mg/l. Cr solubility of CFA-F remained below FAAS detection limit (e.g., 0.006 mg/l) over the entire pH range.

Cu. Cu solubility in CFA-C, CFA-F, and the combined aggregates exhibited an amphoteric behavior. For CFA-C, the minimum of solubility was reached for a pH of 11. For CFA-F and the combined aggregates, the minimum of solubility was reached between a pH of 8 and a pH of 11. For a pH less than 12, Cu solubility of CFA-C was an order of magnitude greater than Cu solubility of CFA-F and the combined aggregates. For a pH less than 8, Cu solubility of CFA-F and the combined aggregates were similar. For a pH greater than 12, Cu solubility of the combined aggregates was slightly greater than for CFA-C and CFA-F. For a pH less than 3, Cu solubility of both CFAs seemed to be limited by an available concentration of Cu in the material (e.g., maximum release of 150 mg/kg for CFA-C and 20 mg/kg for CFA-F while the Cu total content was 247 mg/kg and 167 mg/kg , respectively). For a pH less than 3, Cu solubility of the combined aggregates reached a plateau for a value exceeding the total content in Cu (e.g., maximum release of 12 mg/kg while the Cu total content was 5 mg/kg) indicating that Cu solubility was limited by the total content of Cu in the material and did not reflect solubility. The conflicting result that the maximum of solubility indicated a value exceeding the total content is attributable to either (i) analytical errors associated with measurement of trace metals or (ii) possible sample heterogeneity.

Pb. Pb solubility in CFA-C and CFA-F remained below FAAS detection limit (e.g., 0.01 mg/l) from a pH of 2 to a pH of 12. The Pb leaching behavior for both CFAs can be related to the dissolution of the CFA glassy phase that can occur at high and low pH, releasing the pollutants. Over the entire pH range, Pb solubility of the combined aggregates was one to two orders of magnitude greater than that obtained for CFA-C and CFA-F. For a pH less than 3, Pb solubility of the combined aggregates reached a plateau for a value exceeding the total content in Pb (e.g., maximum release of 38 mg/kg while the Pb total content was 12 mg/kg) indicating that Pb

solubility was limited by the total content of Pb in the material and did not reflect solubility. The conflicting result that the maximum of solubility indicated a value exceeding the total content is attributable to either (i) analytical errors associated with measurement of trace metals or (ii) sample heterogeneity.

Ni. Ni solubility in CFA-C, CFA-F, and the combined aggregates remained below FAAS detection limit (e.g., 0.01 mg/l) as pH decreased from 12 to 8. For a pH less than 8, Ni solubility increased to a maximum of 10 mg/l for CFA-C and 1 mg/l for CFA-F and the combined aggregates. For a pH less than 3, Ni solubility of CFA-C, CFA-F, and the combined aggregates seemed to be limited by an available concentration of Ni in the material (e.g., maximum release of 35 mg/kg for CFA-C, 4 mg/kg for CFA-F and 5 mg/kg for the combined aggregates while the Ni total content was 60 mg/kg, 160 mg/kg and 36 mg/kg, respectively).

Zn. Zn solubility in CFA-C, CFA-F, and the combined aggregates exhibited amphoteric behavior with a minimum of solubility between a pH of 10 and a pH of 11. For a pH less than 3, Zn solubility of CFA-C and CFA-F seemed to be limited by an available concentration of Zn in the material (e.g., maximum release of 130 mg/kg for CFA-C and 10 mg/kg for CFA-F while the Zn total content was 161 mg/kg and 137 mg/kg, respectively). For a pH less than 3, Zn solubility of the combined aggregates seemed to be limited by the total content of Zn in the material (e.g., maximum release of 28 mg/kg while the Zn total content was 30 mg/kg).

In conclusion:

1. CFA-C provides a relatively high pH buffering capacity consistent with its cementitious properties.
2. CFA-F exhibits no pH buffering capacity indicating it is substantially inert.
3. The combined aggregates exhibit significant buffering capacity consistent with the CaCO_3 component.
4. As was released only by the CFA-F at pH levels below 2 and above 12 which would correspond to the dissolution of a glassy phase in the CFA.
5. Cd release was detectable for both CFAs and the combined aggregate. Cd release was greatest at lower pHs and greatest for the CFA-C followed by the combined aggregates.
6. Cr release was detectable from both ashes below a pH of 4. Cr release was also consistent and detectable from the CFA-C at pH above 6.
7. Cu release was greatest from the CFA-C, varying from a maximum release at pH below 4 to a minimum release at pH of 11 and increasing again to a pH of 14. Cu release from the CFA-F and combined aggregates was similar being greatest below a pH of 5, varying to a minimum at a pH of 7, being undetectable from 7 to 11, and then increasing with higher pH.

8. Pb release occurred predominantly from the combined aggregates decreasing gradually from the lowest to the highest pH values. Pb release was similar for both CFAs, being evident only at pH values below 2 or above 13 at which pH values glassy phases can be expected to dissolve.
9. Ni was released only below a pH of 9. Ni was released predominantly from the CFA-C reaching a maximum below a pH of 6. Ni release from the CFA-F and combined aggregates was similar in behavior but lower in magnitude.
10. Zn was released in a similar manner by both CFAs and the combined aggregates being greatest at lower pH values, decreasing from pH 6 to pH 9, being undetectable until pH 12, and then increasing. Zn was predominantly released by the combined aggregates and the CFA-C at the lower pH values.

5.1.6.2 pH-Stat Leaching

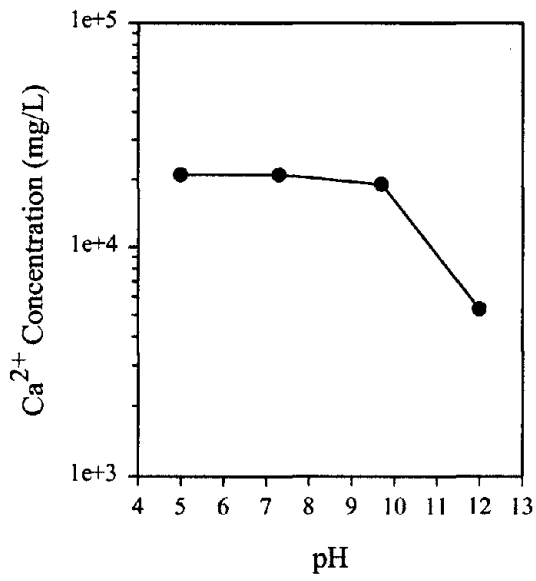
Portland Cement Paste. A hydrated portland cement paste was ground to less than 300 μm and leached. Four samples were leached for 24 h, each at a different pH. Leaching occurred at a pH of 5.0, 7.3, 9.7, and 12.0. Figures 28 through 30 show the leaching of each analyte as a function of pH.

Ca, Mg, Al, and Si leaching behaviors are depicted in figure 28. Ca leaching was relatively constant in the acidic and neutral pH ranges, but then decreased in leachability from a pH of 9.7 to a pH of 12.0. Si leaching decreased with increasing pH over the entire pH range. Similar leaching for Ca and Si has been demonstrated (van der Sloot et al., 1994a,b,c). Mg leaching exhibited changes in behavior throughout the pH range, demonstrating two local minimums in leaching at a pH of 7.3 and a pH of 12.0. The leaching of Al decreased from a pH of 5.0 to a pH of 7.3, remained relatively constant until a pH of 9.7, and then decreased again between a pH of 9.7 and a pH of 12.0.

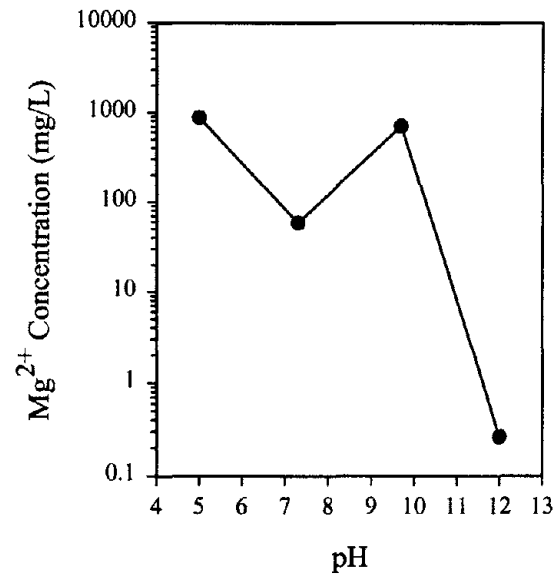
Zn and Fe (see figure 29) showed nearly identical leaching behaviors to Mg and Al, respectively. The leached Ba concentration did not vary much throughout the pH range examined, as Ba concentration in the portland cement was low. Cr leaching showed a decrease in leachability with increasing pH.

Figure 30 depicts the leaching of K, Cl, CO_3^{2-} , and SO_4^{2-} . K and CO_3^{2-} leaching varied little over the pH range examined. Cl leaching could not be characterized because the concentrations were below detection (BDL) throughout the pH range. SO_4^{2-} leaching was constant from a pH of 5.0 to a pH of 7.9 and then increased to a maximum at a pH of 9.7.

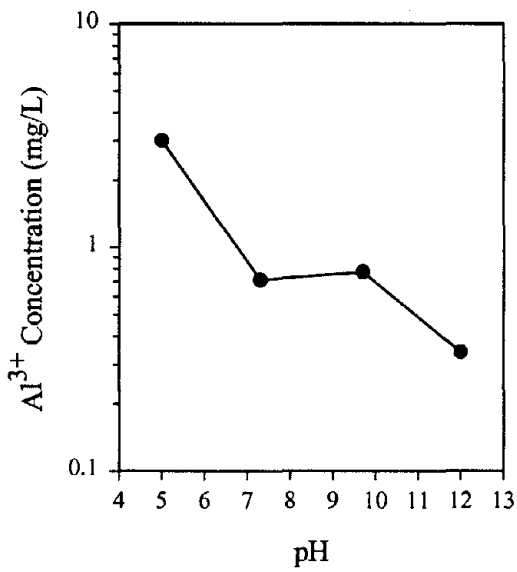
In conclusion:



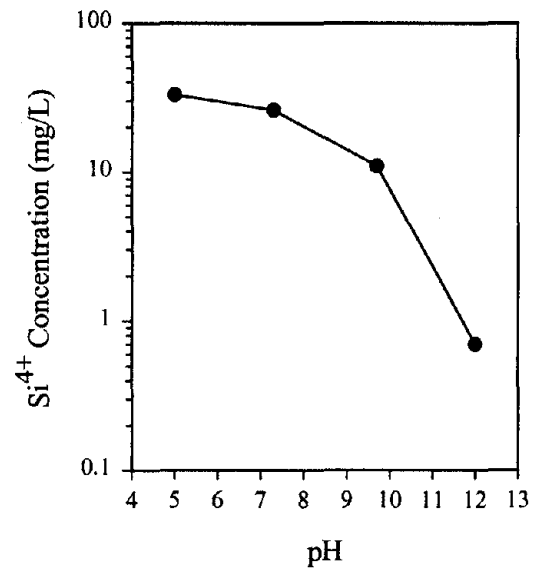
(a)



(b)

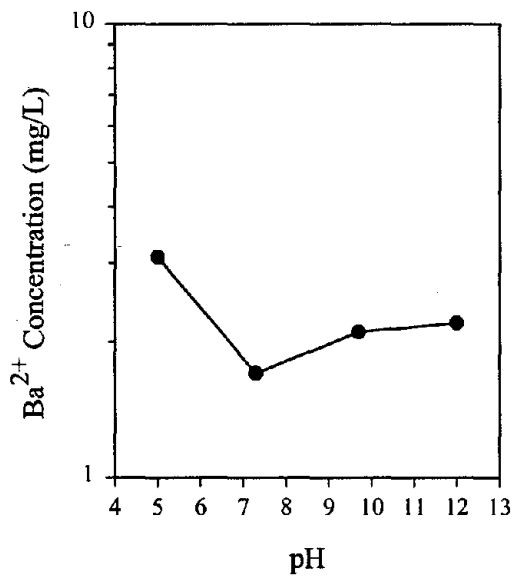


(c)

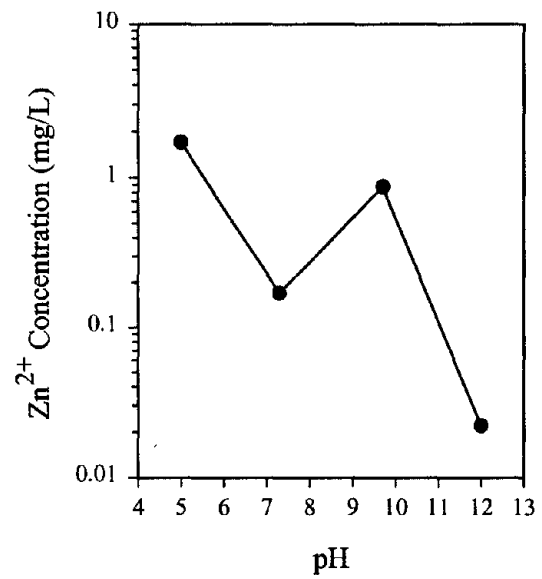


(d)

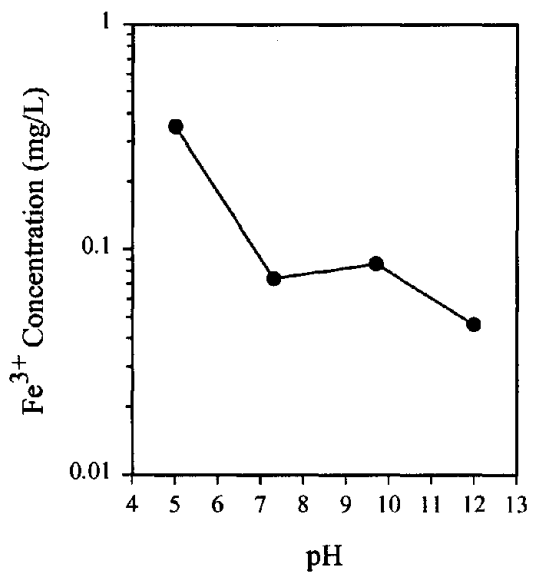
Figure 28: pH-dependent leaching of the portland cement paste:
 (a) Ca, (b) Mg, (c) Al, (d) Si.



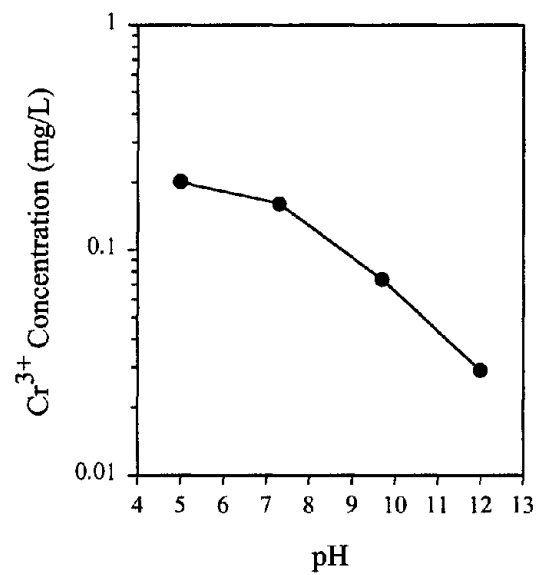
(a)



(b)

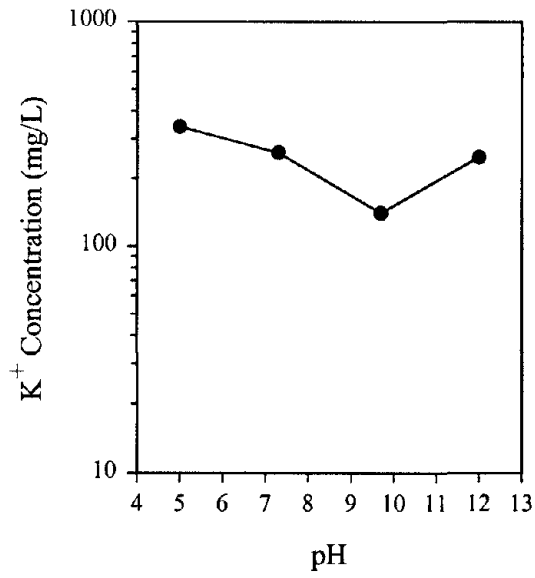


(c)

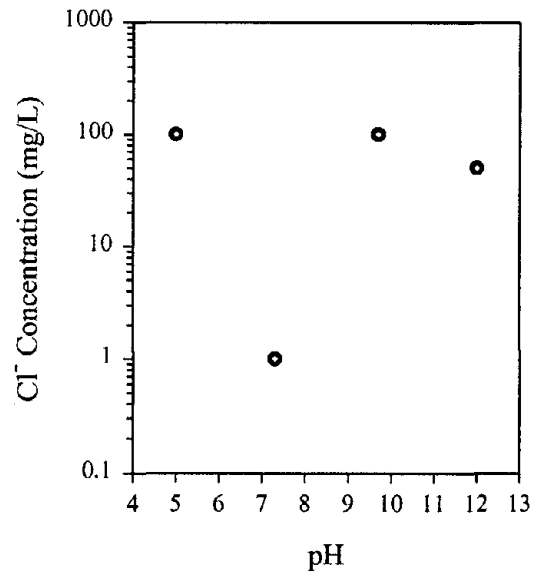


(d)

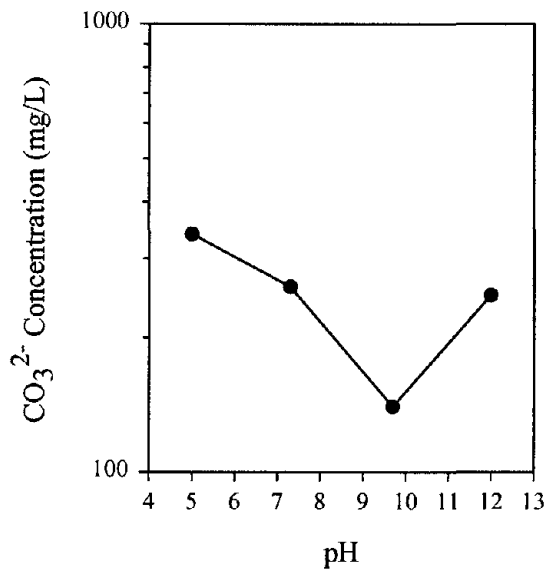
Figure 29: pH-dependent leaching of portland cement paste:
(a) Ba, (b) Zn, (c) Fe, (d) Cr.



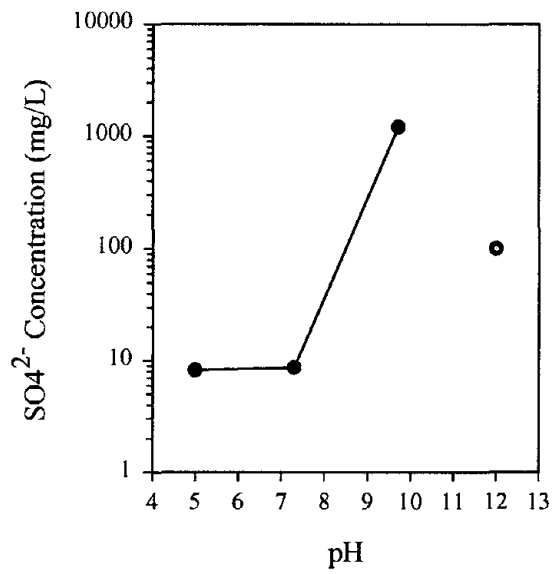
(a)



(b)



(c)



(d)

Figure 30: pH-dependent leaching of portland cement paste:
 (a) K, (b) Cl, (c) CO₃²⁻, (d) SO₄²⁻.

1. When leached from portland cement, Ca, Mg, Al, Si, Zn, Fe, and Cr generally leached less as pH varied from low to high and Ba, K, Cl, and CO_3^{2-} did not vary much with changing pH levels.
2. When leached from portland cement, SO_4^{2-} leaching was constant from a pH of 5.0 to a pH of 7.9 and then increased to a maximum at a pH of 9.7.

5.1.6.3 Geochemical Modeling

Portland Cement Paste. Geochemical modeling of the portland cement paste was performed using the modeling program MINTEQA2. Results of the geochemical modeling are summarized in table 23. Modeled data are shown for 10 species with the experimental leaching data of the paste in figures 31 through 40. Table 23 summarizes the modeling of each solid for each species based on agreement in concentration and shape of the modeled leaching curve.

Ca Modeling. As shown in figure 31, Ca leaching was well modeled over the pH range from 5 to 12 by calcite (CaCO_3), dolomite ($\text{CaMg}(\text{CO}_3)_2$), and gypsum ($\text{CaSO}_4 \cdot 2\text{H}_2\text{O}$). Ettringite ($\text{Ca}_6\text{Al}_2(\text{SO}_4)_3(\text{OH})_{12} \cdot 26\text{H}_2\text{O}$) modeled well as a possible controlling solid at a pH greater than 7. All four of these phases were identified in the cement paste by XRPD. Portlandite (CaOH_2) was also detected by XRPD. Portlandite was only modeled at a pH of 12, where it gave a reasonable approximation of leached Ca concentration. Below a pH of 12, modeled Portlandite concentrations were unreasonably high. Calcite has been shown to be a controlling solid for Ca (EPRI, 1987). Calcite and dolomite are likely controlling solids for Ca leaching from the hydrated cement paste.

Mg Modeling. Mg modeling is depicted in figure 32. Solids modeled for Mg leaching were dolomite ($\text{CaMg}(\text{CO}_3)_2$) and brucite ($\text{Mg}(\text{OH})_2$). Brucite matched well with the experimental concentrations at the higher pH levels, but was unreasonably high at the lower pH range. Dolomite was an excellent match both in modeled concentration and shape of the modeled curve and is therefore a likely controlling solid for Mg leaching.

Al Modeling. Figure 33 shows the modeling of Al with ettringite ($\text{Ca}_6\text{Al}_2(\text{SO}_4)_3(\text{OH})_{12} \cdot 26\text{H}_2\text{O}$), gibbsite ($\text{Al}(\text{OH})_3$), and amorphous $\text{Al}(\text{OH})_3$. Gibbsite was the best match of the three controlling solids, but the range of minimum solubility of the modeled curve at a pH of 7.3 did not match the minimal change in concentration from a pH of 7.3 to a pH of 9.7 in the experimental data. Al leaching in cement-based systems can be controlled by the hydrated Ca species, which are not included in the MINTEQA2 database (Glasser, 1997).

Si Modeling. Si (see figure 34) was modeled for both crystalline and amorphous SiO_2 . Both solids model reasonably well in the lower pH range, but the shape of the model curves diverge from the experimental data between a pH of 7.3 and a pH of 9.7. Poor modeling results for SiO_2 have been reported previously (Eighmy, 1994; Fruchter 1990), largely because Si dissolution can be kinetically controlled. Cement paste is made up of a hydrated Ca-silica gel that varies in Ca:Si mol ratios and cannot be modeled by the current MINTEQA2 database.

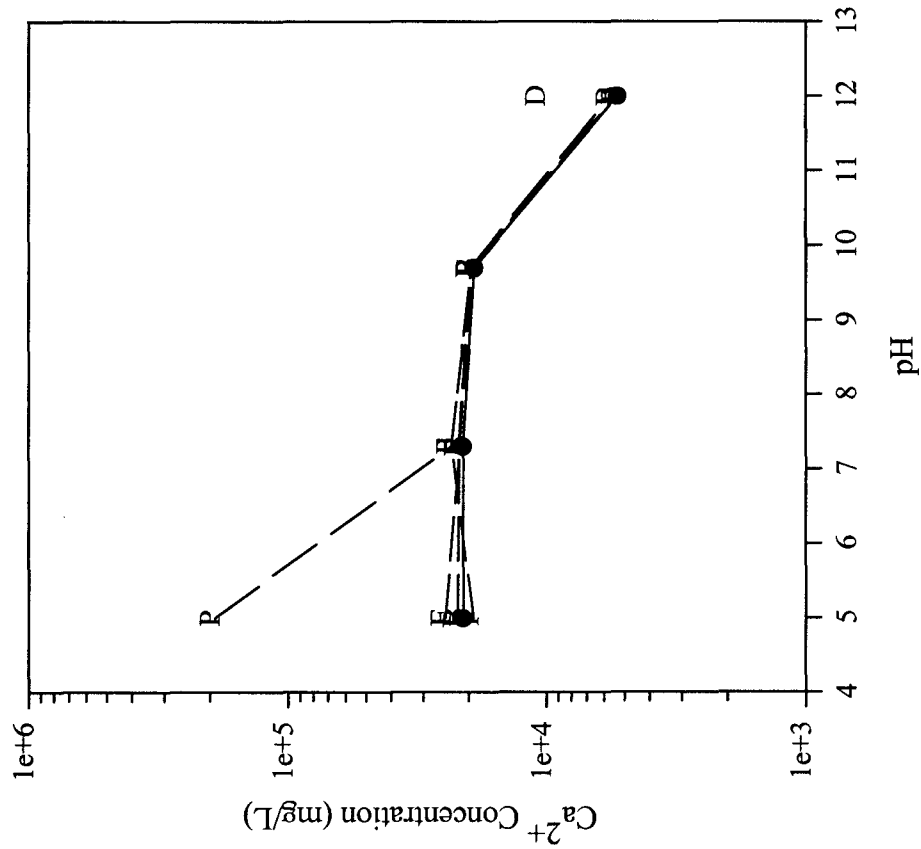


Figure 31: Ca modeling in cement paste.

- Leached Value [B] - Gypsum [D] - Portlandite [E] - Calcite [F] - Dolomite [P] - Ettringite [B], [E], and [F] are completely overlapped

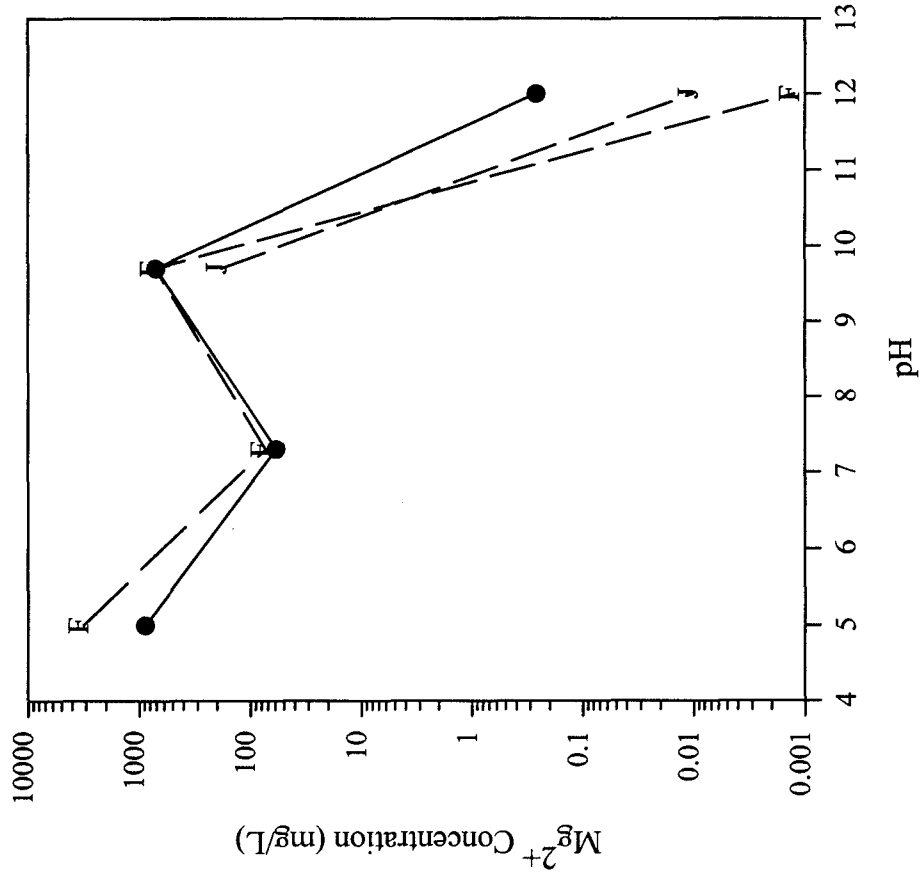


Figure 32: Mg modeling in cement paste.

- Leached Value [F] - Dolomite [J] - Brucite

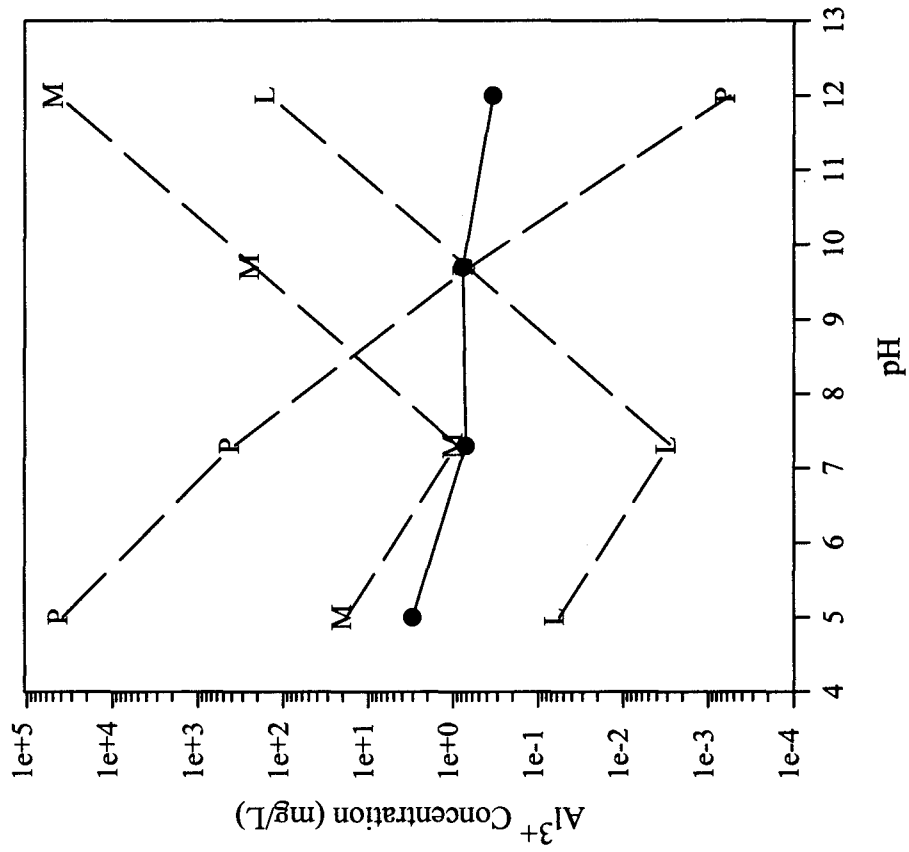


Figure 33: Al modeling in cement paste.
 • Leached Value [L] – Gibbsite
 [M] – $Al(OH)_3$ *amorphous [P] – Etringite

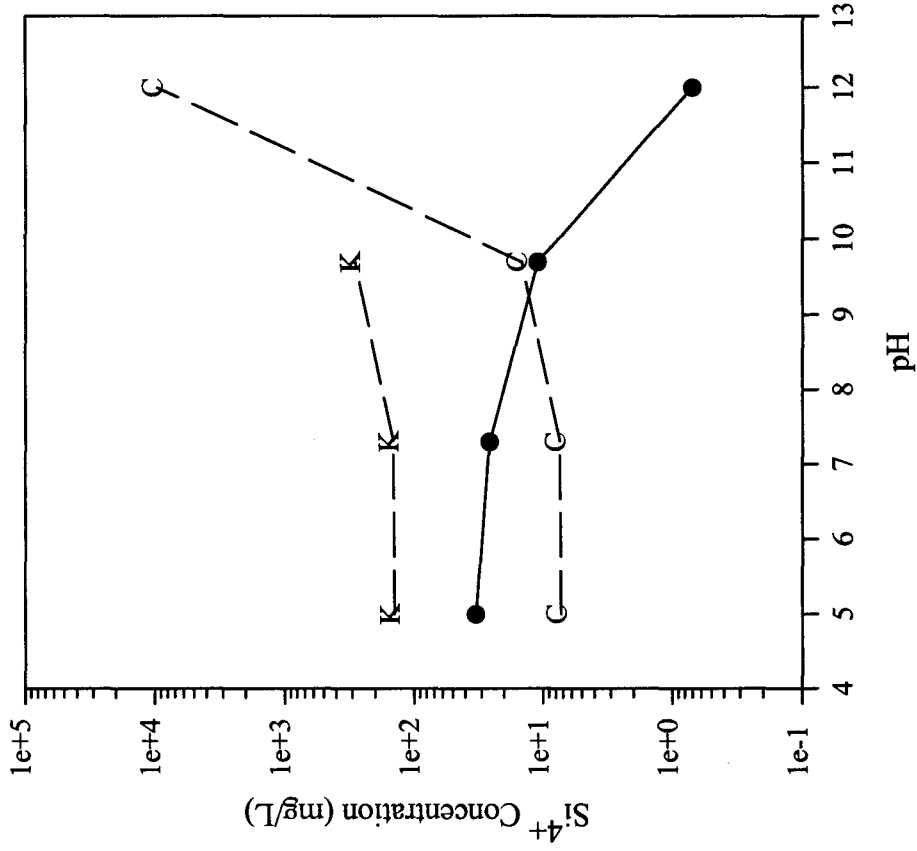


Figure 34: Si modeling in cement paste.
 • Leached Value
 [C] – Quartz [K] – SiO_2 *amorphous

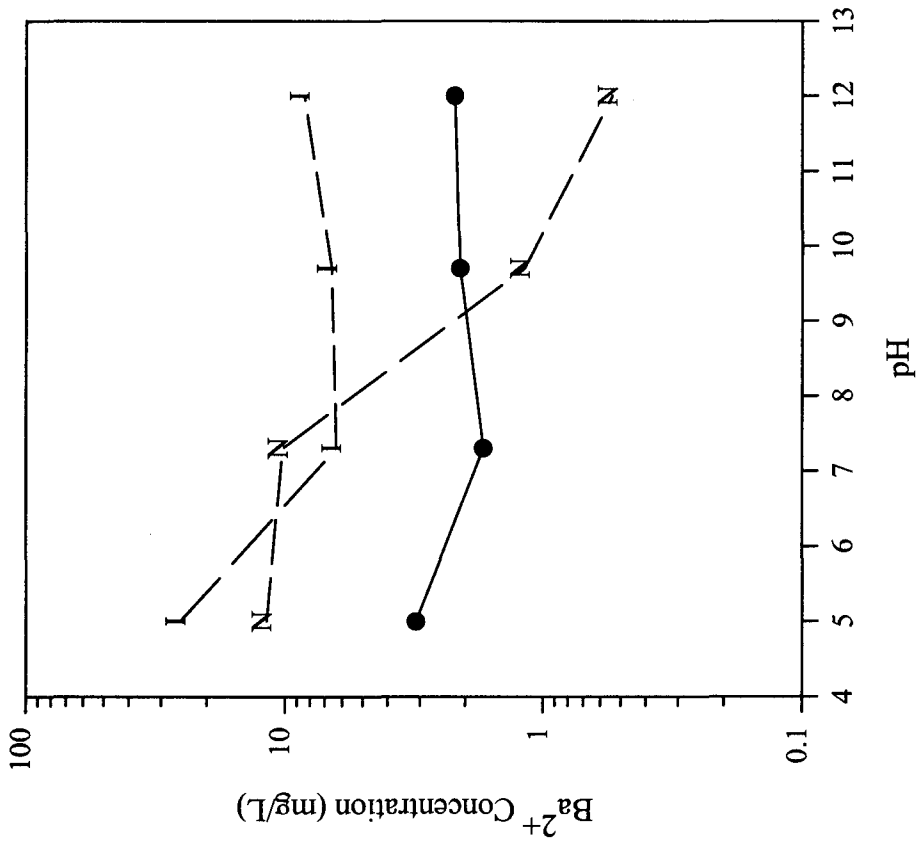


Figure 35: Ba modeling in cement paste.

● Leached Value
[I] - BaCrO₄ [N] - Barite

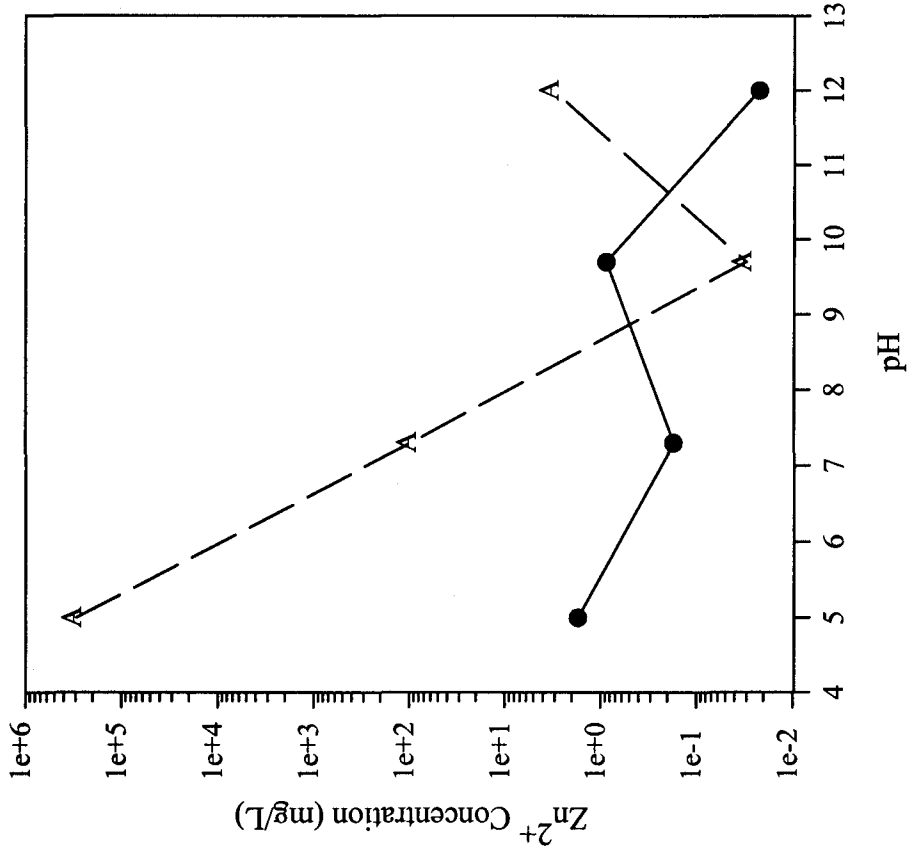


Figure 36: Zn modeling in cement paste.

● Leached Value
[A] - Zincite

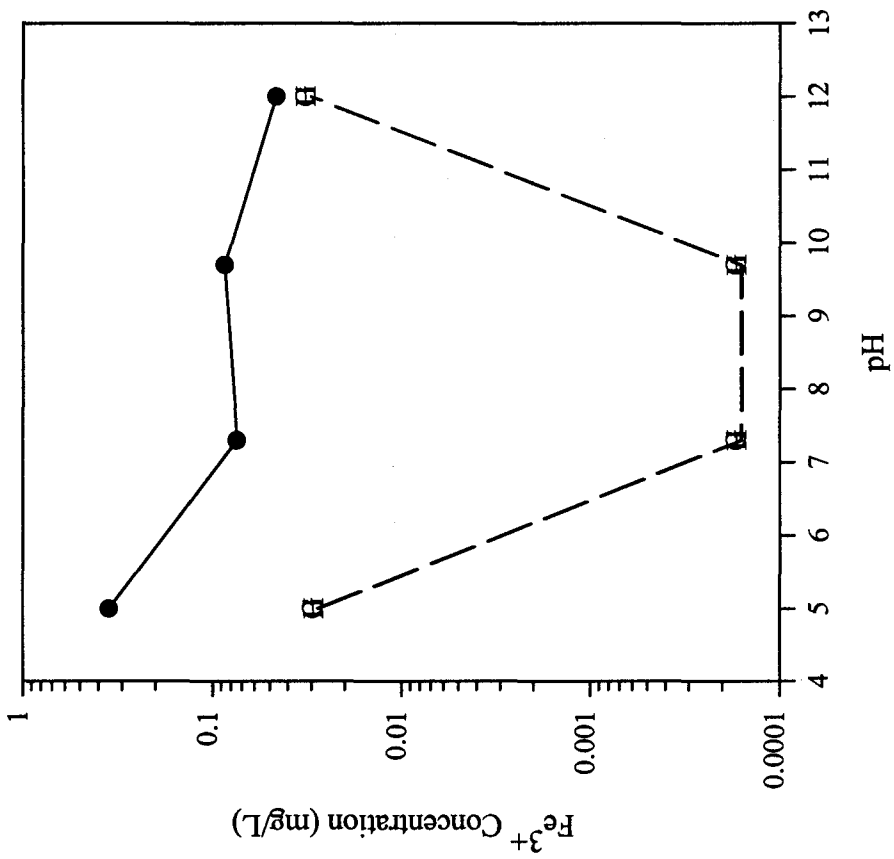


Figure 37: Fe modeling in cement paste.

• Leached Value
 [G] - Ferrihydrate [H] - Maghemite
 [G] and [H] are overlapped

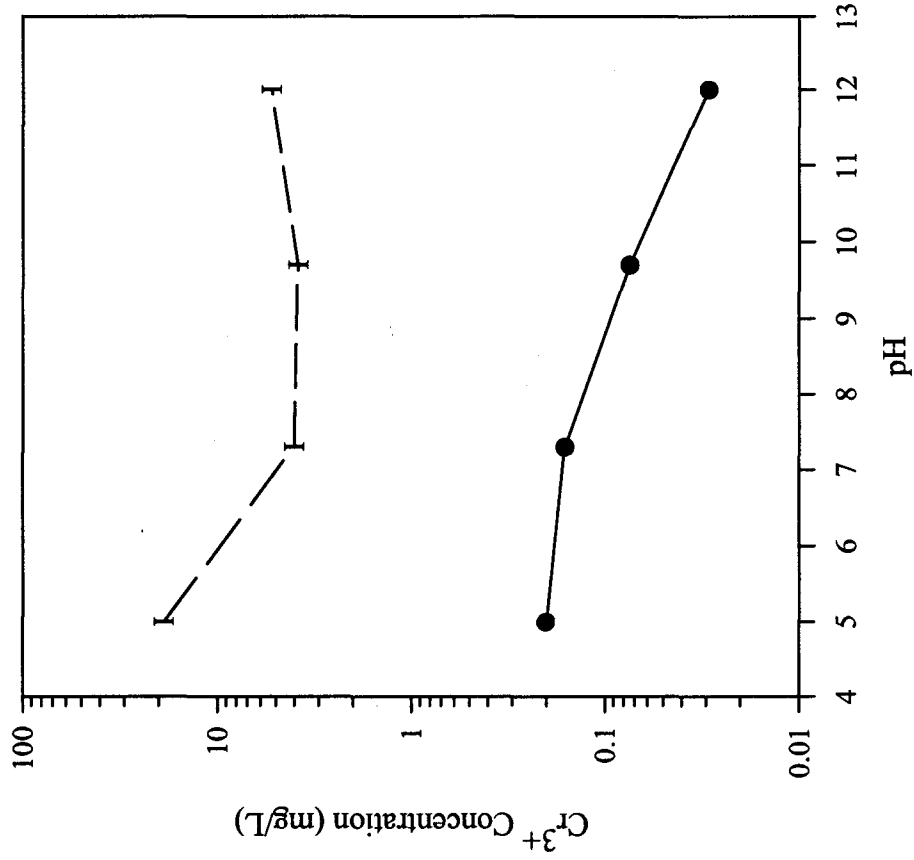


Figure 38: Cr modeling in cement paste.

• Leached Value
 [I] - BaCrO₄

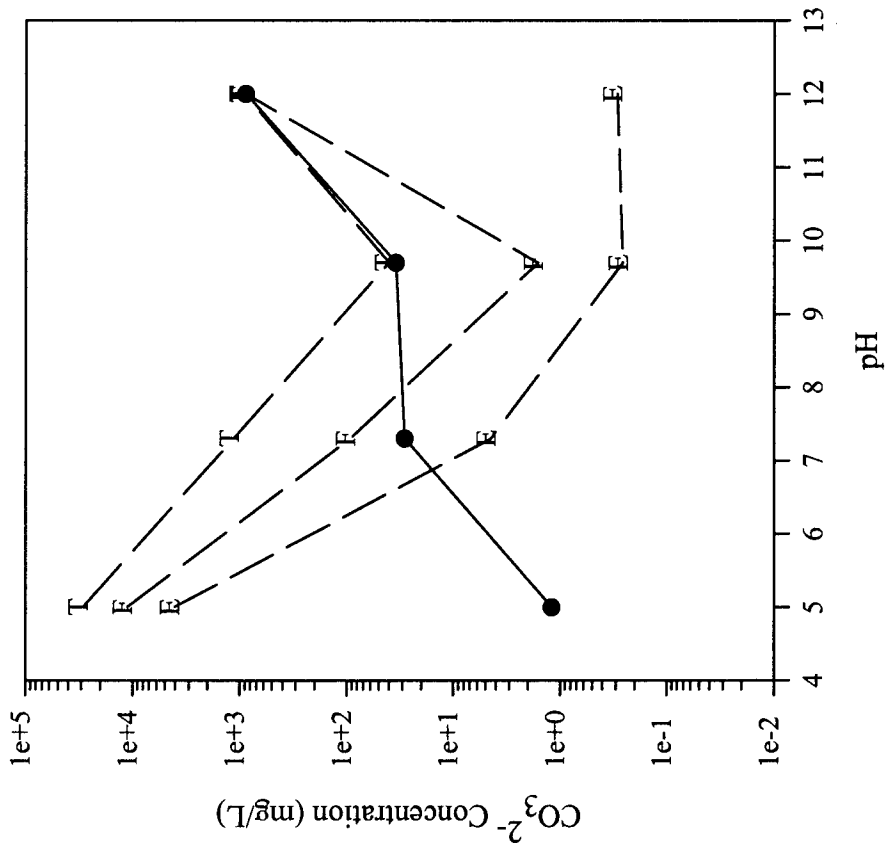


Figure 39: CO_3^{2-} modeling in cement paste.

• Leached Value
 [E] – Calcite [F] – Dolomite [T] – Magnesite

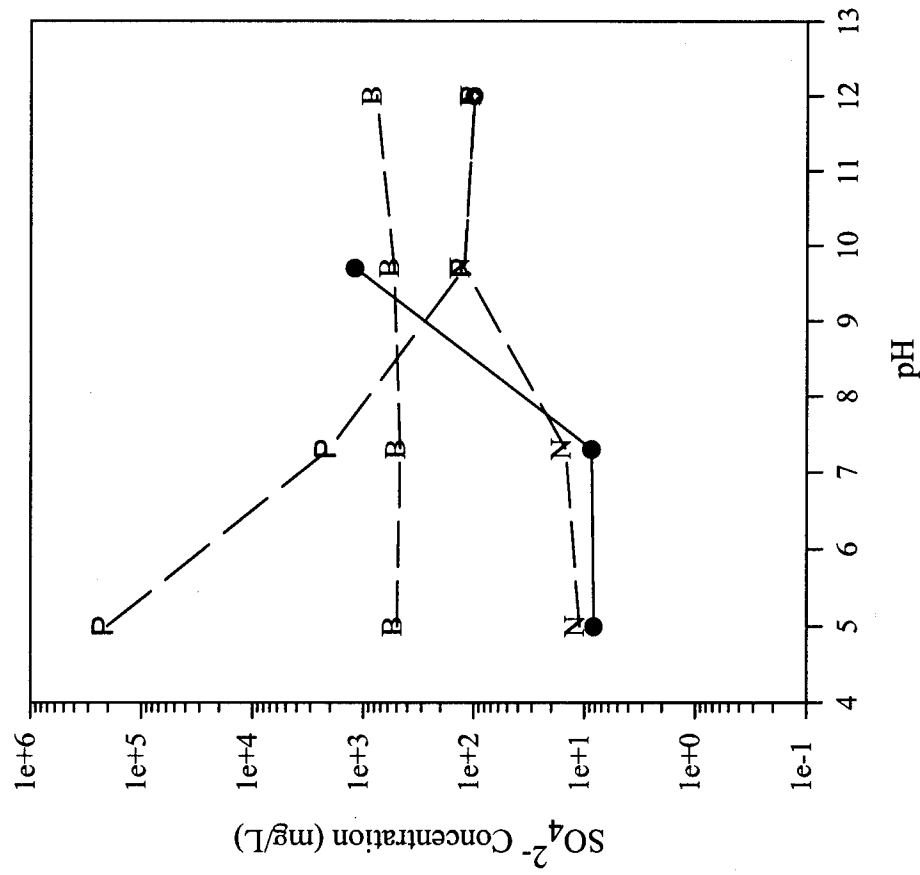


Figure 40: SO_4^{2-} modeling in cement paste.

• Leached Value
 [B] – Gypsum [N] – Barite [P] – Ettringite

Table 23: Geochemical modeling species for the hydrated portland cement paste.

Species	Solid Phase	log K_{sp}	Well modeled pH range
Al	Gibbsite ($Al(OH)_3$)	-8.291	none
	$Al(OH)_3$ amorphous	-10.800	none
	Ettringite ($Ca_6Al_2(SO_4)_3(OH)_{12} \cdot 26H_2O$)	-56.700	none
Ba	$BaCrO_4$	9.670	5 - 12
	Barite ($BaSO_4$)	9.980	none
Ca	Gypsum ($CaSO_4 \cdot 2H_2O$)	4.610	5 - 12
	Portlandite ($Ca(OH)_2$)	-22.804	none
	Calcite ($CaCO_3$)	8.480	5 - 12
	Dolomite ($CaMg(CO_3)_2$)	16.540	5 - 12
	Ettringite ($Ca_6Al_2(SO_4)_3(OH)_{12} \cdot 26H_2O$)	-56.700	7 - 12
CO_3	Calcite ($CaCO_3$)	8.480	none
	Dolomite ($CaMg(CO_3)_2$)	16.540	7 - 12
	Magnesite ($MgCO_3$)	7.46	7 - 12
Cr	$BaCrO_4$	9.670	none
Fe	Ferrihydrite ($Fe(OH)_3$)	-3.191	none
	Maghemite (Fe_2O_3)	-6.386	none
Mg	Dolomite ($CaMg(CO_3)_2$)	16.540	5 - 12
	Brucite ($Mg(OH)_2$)	-16.844	none
Si	Quartz (SiO_2)	4.000	none
	SiO_2 amorphous gel	2.710	none
SO_4	Gypsum ($CaSO_4 \cdot 2H_2O$)	4.610	none
	Barite ($BaSO_4$)	9.980	5 - 12
	Ettringite ($Ca_6Al_2(SO_4)_3(OH)_{12} \cdot 26H_2O$)	-56.700	none
Zn	Zincite ($Zn(OH)_2$)	-11.334	none

Ba Modeling. Ba leaching (see figure 35), which changed little over the pH range, was well modeled by barium chromate (BaCrO_4), matching in the shape of the modeled curve and within one log of the experimental concentration from a pH of 5.0 to a pH of 12.0.

Zn Modeling. Figure 36 shows that the leaching behavior of Zn from the cement paste was not successfully modeled by zincite (Zn(OH)_2). Previous studies have suggested that Zn sorbs to metal oxides which then control the solubility of Zn (EPRI, 1987; van der Sloot et al., 1994).

Fe Modeling. Fe leaching (see figure 37) was not successfully modeled by either ferrihydrite (Fe(OH)_3) or maghemite (Fe_2O_3). In both of these species Fe^{3+} is the only cation present. XRPD identified Fe as part of multiple Ca-iron oxide and Ca-iron-silica oxide. These more complex species found in the cement paste were not part of the MINTEQA2 database. Difficulty in modeling of Fe has been demonstrated in other research (Fruchter, 1990).

Cr Modeling. Cr modeling was only attempted with one solid phase in the MINTEQA2 database, barium chromate ($\text{BaCr}^{6+}\text{O}_4$), and the modeling of this phase to the experimental data was not successful (see figure 38); perhaps because Cr is reduced. Cr^{3+} has been shown to substitute for Al^{3+} in cement hydration products and become part of the Ca Al hydrates matrix (Glasser, 1997). Cr^{3+} solubility is then limited by these cement species rather than more common Cr oxides and hydroxides that would be found in the MINTEQA2 database.

CO_3^{2-} Modeling. Figure 39 depicts the leaching behavior of CO_3^{2-} modeled by controlling solids calcite (CaCO_3), dolomite ($\text{CaMg}(\text{CO}_3)_2$), and magnesite (MgCO_3). In neutral and alkaline pH ranges dolomite and magnesite exhibited leaching curves similar to the experiment data of the portland cement paste. At acidic pHs the models for both of these solids predicted a large increase in the leachability of CO_3^{2-} from neutral pH leaching, but the experimental data showed a significant decrease in CO_3^{2-} concentration at a pH of 5.0.

SO_4^{2-} Modeling. SO_4^{2-} leaching is modeled by gypsum ($\text{CaSO}_4 \cdot 2\text{H}_2\text{O}$), barite (BaSO_4) and ettringite ($\text{Ca}_6\text{Al}_2(\text{SO}_4)_3(\text{OH})_{12} \cdot 26\text{H}_2\text{O}$) (see figure 40). Barite was a good match for the experimental leaching data in both curve shape and concentrations. The shapes of the ettringite and gypsum modeling curves did not resemble the experimental data curve. Barite appears to be a controlling solid for SO_4^{2-} leaching (EPRI, 1987).

5.1.6.4 Conclusions

In conclusion:

1. The CFA-F is alkaline and well buffered, the CFA-C is more acidic and less well buffered, and the aggregates are alkaline and buffered.
2. At their respective natural pH values (e.g., pH 12 for CFA-C, 4 for CFA-F, and 9 for the combined aggregates), CFA-F released greater concentrations of Cu, Ni, and Zn than CFA-C and the combined aggregates; CFA-C released greater concentrations of Cd and

Cr than CFA-F and the combined aggregates; the combined aggregates released greater concentration of Pb than CFA-C and CFA-F.

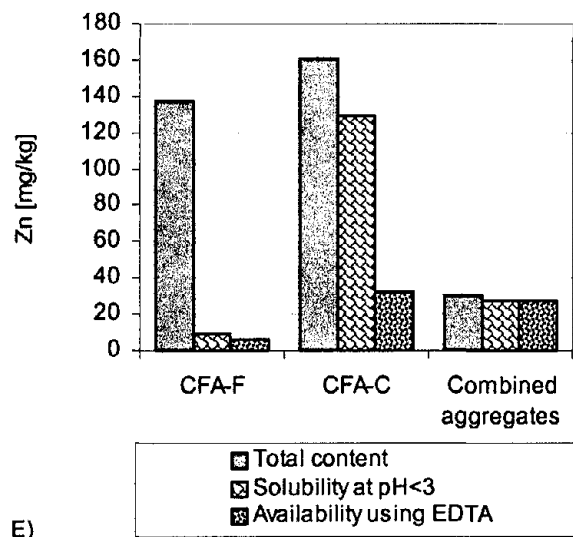
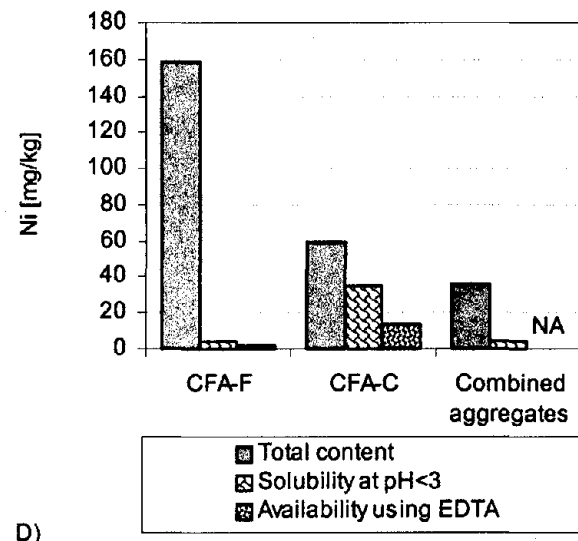
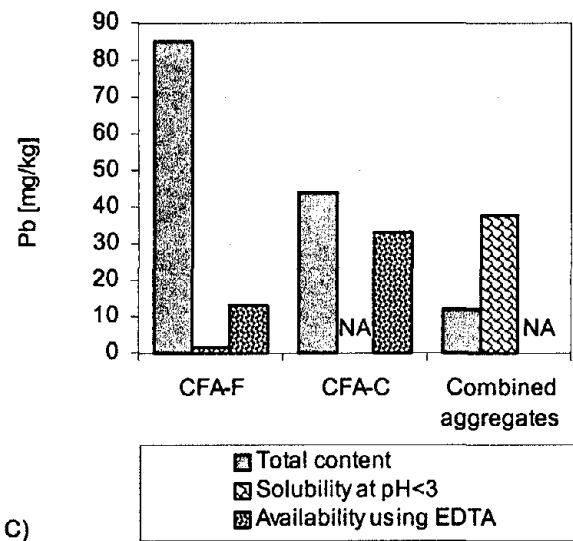
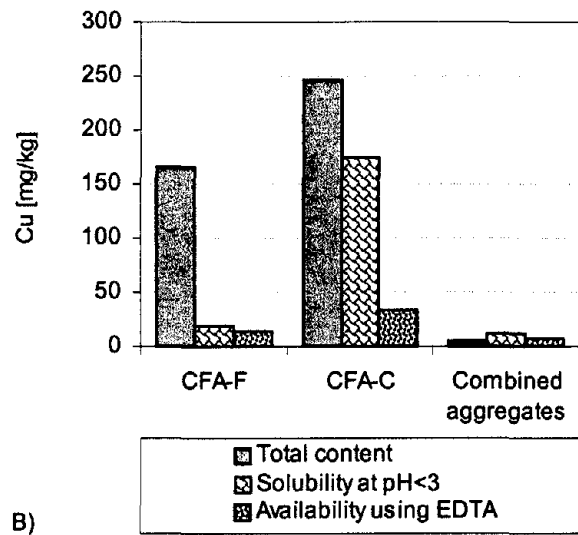
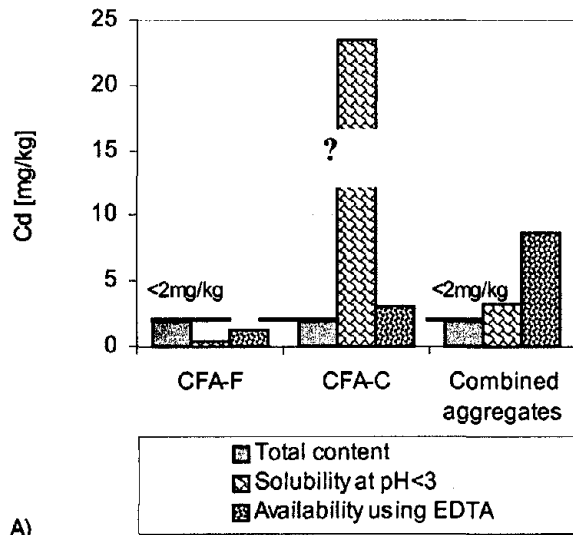
3. Calcite (CaCO_3) and dolomite ($\text{CaMg}(\text{CO}_3)_2$) are likely controlling solids for Ca leaching from the hydrated cement paste.
4. Dolomite is likely a controlling solid for Mg leaching from the hydrated cement paste.
5. Barium chromate (BaCrO_4) is likely a controlling solid for Ba from the hydrated cement paste.
6. Barite (BaSO_4) is likely a controlling solid for SO_4^{2-} leaching from the hydrated cement paste.
7. Geochemical modeling was not successful for Al, Si, Zn, Fe, and Cr.
8. Controlling solids, such as barite and dolomite, appear to be typical of cement-based leaching.

5.1.7. Availability Leaching

Cd, Cu, Ni, Pb, and Zn availability, as determined by the RU-AV002.0 protocol (e.g., EDTA extraction at a pH 7.0), is presented in figure 41 for both CFAs and the combined aggregates. In addition to availability results, total content as determined by neutron activation analyses or X-ray fluorescence (e.g., NAA or XRF) and maximum release (e.g., maximum reached using the RU-SR002.0 protocol for a pH less than 3) are provided for comparison.

Availability of Cu, Ni, Pb and Zn in CFA-F were found to be lower than the total contents. Indeed only 9 percent of Cu, 1 percent of Ni, 15 percent of Pb and 4 percent of Zn were removed under RU-AV002.0 conditions. No significant difference was observed between constituent availability and maximum of solubility data.

Availability of Cu, Ni and Zn in CFA-C were found to be lower than the total contents. Indeed only 14 percent of Cu, 23 percent of Ni and 21 percent of Zn were removed under RU-AV002.0 conditions. However, more than 70 percent of Pb was removed under RU-AV002.0 conditions. Significant differences were found between the availability values and the maximum of solubility for Cd, Cu, and Zn, with a maximum of solubility exceeding the total content for Cd. This could most likely be attributable to analytical errors associated with measurement of trace metals in extracts containing high concentration of total salts and analyses performed near FAAS detection limits (e.g., 2 $\mu\text{g/l}$ for Cd, 3 $\mu\text{g/l}$ for Cu, 1 $\mu\text{g/l}$ for Zn). In addition, in order to obtain values in mg/kg , the low concentrations measured in the leachates have been multiplied by 5 in the case of the solubility data (e.g., liquid-solid ratio of 5 ml/g) and by 100 in the case of the availability data (e.g., liquid-solid ratio of 100 ml/g); therefore, a small variation in the measurement of the leachate concentration can substantially change the results once expressed in mg/kg .



? Questionable analysis result due to analytical difficulties.

NA Not available.

Note Cd total content < 2mg/kg detection limit.

Figure 41: Comparison between total content, maximum of solubility at pH<3 and availability using EDTA extractions at pH 7.

Availability of Zn in the combined aggregates was found to be close to the total content with 91 percent of Zn removed under RU-AV002.0 conditions. Availability values of Cd and Cu exceeded the total content. This might be attributable to analytical errors associated with measurement of trace metals or possible sample heterogeneity. No significant difference between availability values and maximum of solubility was observed.

In conclusion:

1. CFA-F availability of Cu, Ni, Pb, and Zn was found to be far lower when determined by solubility at pH <3 or by EDTA extraction at pH 7.0 than the total concentration found by NAA/XRF (1 to 15 percent of NAA/XRF values).
2. CFA-C availability of Cu, Ni, and Zn was found to be lower when determined by solubility at pH <3 or by EDTA extraction at pH 7.0 than the total concentration found by NAA/XRF (14 to 23 percent of NAA/XRF values).
3. CFA-C availability of Pb was found to be somewhat lower when determined by EDTA extraction at pH 7.0 than the total concentration found by NAA/XRF (70 percent of NAA/XRF values).
4. Availabilities between the methods vary when applied to the coarse aggregates giving consistent values for Zn and Cu, but substantially varying values for Cd, Pb, and Ni.

5.2. Prism Casting

5.2.1. Air Content and Slump Tests

At the time of experimental design, it was determined that it was desirable to have the laboratory concrete susceptible to freeze-thaw deterioration. A typical pavement, designed for cold weather areas, should have a total air content value around 6 to 7 percent as these air contents have been shown to reduce the amount of damage caused by freezing and thawing. The air content for the U.S. 20 roadway was measured to be 6.8 and 7.4 percent at the time of placement. The test most likely performed was ASTM C 231. This method measures the total air content of fresh concrete and not necessarily the content of air aiding in the resistance to freeze-thaw deterioration. Petrographic examination of concrete from U.S. 20 has found air contents as low as 2.85 percent (FHWA, 1997). Other experience indicates that air contents in the range of 3 to 4 percent provide varying amounts of freeze-thaw resistance. As such, a decision was made to try for this latter range in laboratory specimens. The results from the air and slump tests are listed in table 24.

5.3. Slab Characterization

A 1.2- by 1.8-meter slab of distressed pavement was retrieved from County P-73 adjacent to U.S. 20 near Fort Dodge, Iowa (see section 3.1). Figure 42 is a schematic of the concrete slab that shows where each sample used for environmental characterization was taken.

Table 24: Air content and slump results on freshly mixed concrete.

Batch color	Mix type	Slump (mm) [*]	Total air content (%) [†]
Red	CFA-C	57	3.6
Green	CFA-C	32	3.6
Yellow	CFA-C	44	3.6
Black	CFA-C	38	3.8
Red	CAF-F	38	2.9
Green	CFA-F	32	3.2
Yellow	PCC	57	4.1
Black	PCC	38	3.6

* Uncertainty = $\pm \sim 3$ mm

† Uncertainty = $\pm 0.1\%$

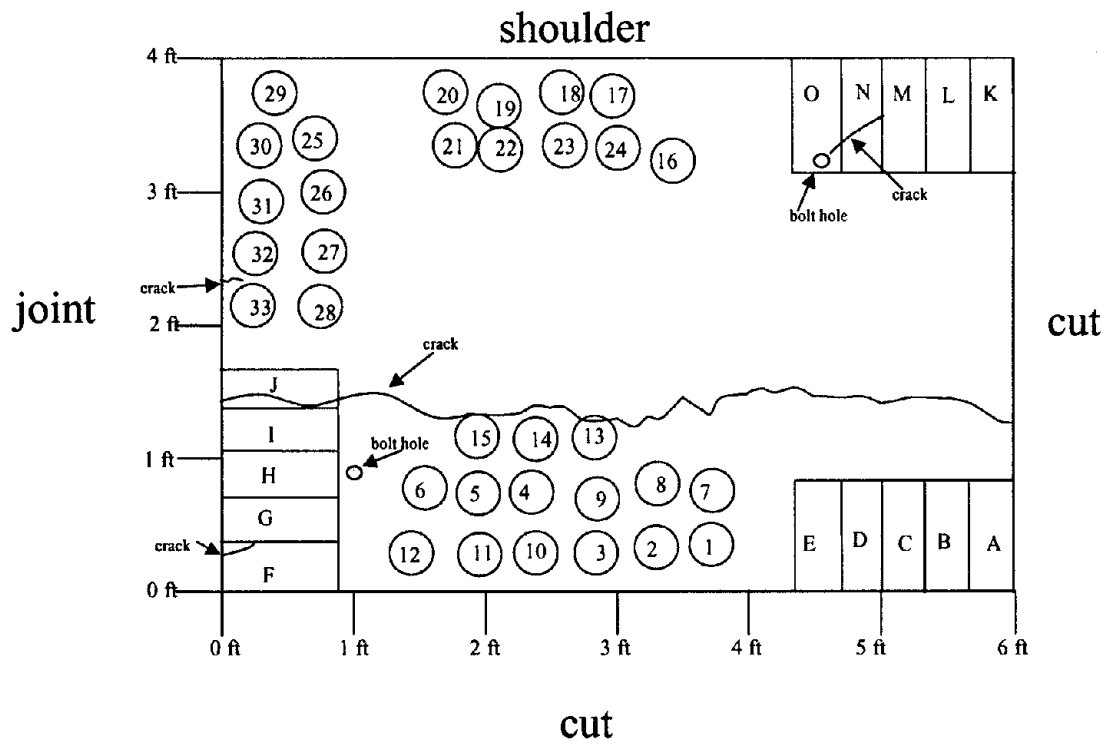


Figure 42: Sampling diagram of the U.S. 20 slab.

5.3.1. Compressive Strength

Cores from the slab had an average compressive strength of 35.1 ± 4.7 MPa (see table 25). This strength exceeds typical strengths as design specifications normally require 24.1 MPa 28-d compressive strengths.

In conclusion:

1. Strength of the slab was in excess of expected values.

5.3.2. Microcracking

As is evident from the results in the table 26, the slab specimens experienced a wide range of cracking. Of the slab specimens analyzed via neutron radiography, core 22 (originally near the highway shoulder) illustrated the least amount of cracking (0.3 to 0.8 percent) whereas core 14 (near the discovered slab crack and near the original tire path) showed the most cracking (3.4 to 6.6 percent).

All nine of the slab cores were taken from three main regions of the slab, three from each region. For the most part, the crack density results can be grouped according to region, with cores 4-C, 6-C, and 14-C having the most cracking; cores 27-J, 30-J, and 31-J having slightly less cracking; and cores 19-S, 22-S, and 24-S having the least cracking of the specimens.

This range of crack densities for the different slab specimens relates to the different patterns of wear across the slab itself. Since the various regions of the slab are not subject to the same stresses (cars, for example, tend to travel in designated lanes), it is not surprising that the cores from the three selected regions would exhibit varying extents of cracking. Furthermore, that all the samples within a given region would exhibit a similar level of cracking is logical.

Within each individual core, the crack patterns are more intense near the top of the specimen than toward the bottom. This is true, without exception, for all of the nine cores analyzed via neutron radiography. In most cases, the transverse section has a crack density equal to or greater than that of the bottom longitudinal slice, but less than the top longitudinal slice.

The bulk of the cracks in all the specimens are primarily transverse cracks, except for a few noticeable vertical cracks on the bottom slices of cores 4-C and 14-C.

This range of cracking from top to bottom within a given slab specimen is evidence of the variation in stresses along it. One reason the top slices depict more cracking than their respective bottom slices in all cases may be a result of the traffic along the top of the slab, which creates

Table 25: U.S. 20 slab core compressive strengths.

Core ID	MPa
13-C	29.2
36-C	30.4
16-S	40.8
35-S	40.0
32-J	40.3
39-J	30.4
Average	35.1 ± 4.7

Table 26: Crack density results (in %) for slab specimens.

Specimen No.	Top	Center	Bottom
4-C	4.7	2.5	2.7
6-C	4.9	4.4	3.5
14-C	6.6	3.4	3.4
19-S	1.1	0.5	0.5
22-S	0.4	0.8	0.3
24-S	2.0	1.3	1.1
27-J	4.2	1.9	1.7
30-J	2.3	1.3	0.7
31-J	3.4	1.0	1.1

localized stresses in the top of the slab that even out further down. Another possibility is that when the slab was placed, concrete nearer the bottom was more densely compacted and experienced less drying, such that the material in the bottom slices was less susceptible to cracking. Furthermore, microcracking may have resulted from cycles of freezing and thawing, wetting and drying, and heating and cooling, all of which occur more often and to a greater degree near the top of the slab. In general, the extent of cracking in all the slab specimens as a whole, regardless of location either on the slab or within the specimen, clearly illustrates the damage in the material itself.

In conclusion:

1. Microcracking was more extensive in cores taken from near the tire path and least in cores taken from near the shoulders. This correlates to the supposition that localized stresses due to traffic contributed to microcracking.
2. Microcracking was more extensive near the top of cores than near the bottom. This corresponds to placement compaction, placement curing, density changes, and cycles of freezing and thawing, heating and cooling, and drying and wetting.

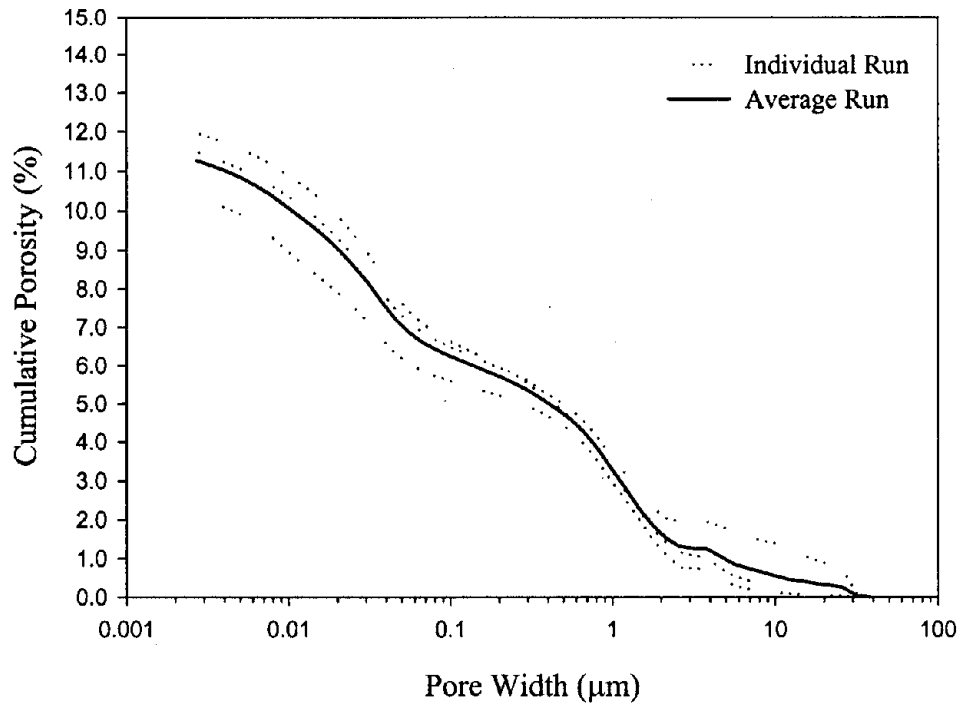
5.3.3. Effective Pore Size and Pore Size Distribution

The results from porosimetry experiments performed on samples from the slab are presented in figures 43 and J-1 through J-7 of appendix J in volume II.

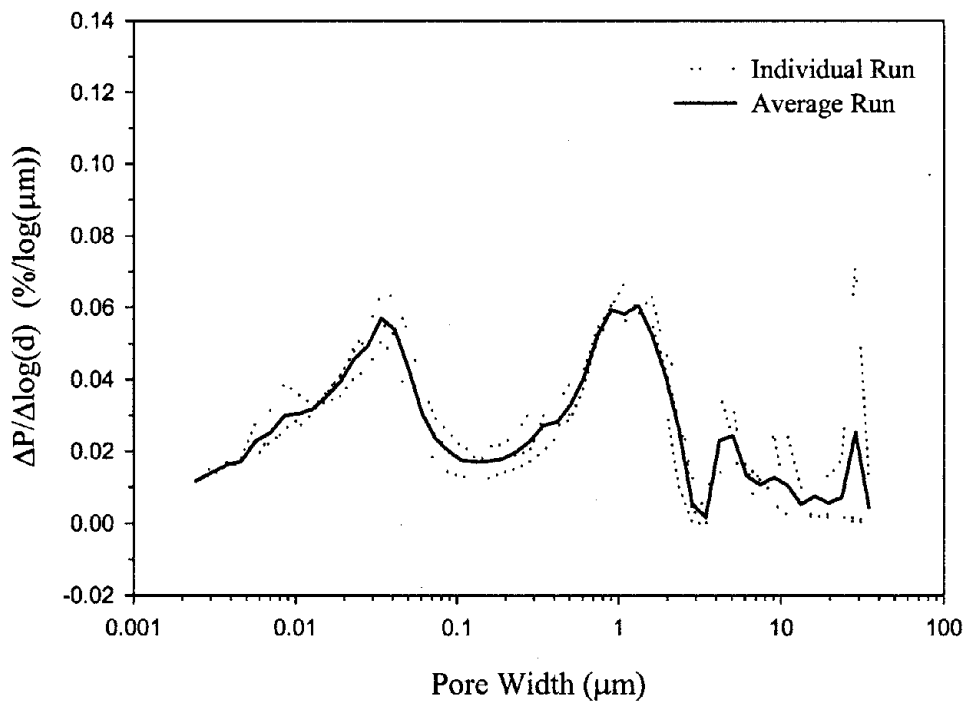
The pore width range of 0.1 to 2.5 μm was used to define the first peaks' boundaries. The second peaks remained well defined and required no pore width restrictions. However, the incremental porosities of the first peaks (indicated by the area beneath the peak) plotted higher than the second peaks. The opposite was true for the laboratory prisms.

Tables 27 and 28 list the nine highest values used in the calculation of uniformity indicators and weighted average threshold pore widths for each peak. Maximum peak (traditionally referred to as the critical threshold) pore widths have been underlined in these tables as well. The calculated uniformity indicators, weighted average threshold pore widths, and porosities are listed in table 29.

Slab porosity measurements ranged from 10 to 13 percent (see table 29 and figure 43). A slight increase of intrusion during the initial phases of the porosimetry runs was observed on five out of the seven samples. This occurred during the first 13 data points, which corresponded to the low-pressure intrusion portion. Once past the changeover pressure and into the high-pressure portion, no further intrusion was noticed in this area. It is thought that some problems existed with the low-pressure portion of the experimental runs. If these 2 percent increases are ignored and slab concrete porosities recalculated, the resulting porosities range from 10 to 11 percent. In either case, slab concrete porosities were generally higher than the laboratory-created concretes (10 to 13 percent as opposed to 8 to 10 percent). This suggests the larger porosities are



(a)



(b)

Figure 43: MIP results for 1-C(4): (a) cumulative porosity vs. pore width; (b) average differential pore size distribution vs. pore width.

Table 27: U.S. 20 slab first peak nine highest $\Delta P/\Delta \log(d)$ values and their corresponding pore widths.

Sample ID	Parameter	1	2	3	4	5	6	7	8	9
1-C(4)	$\Delta P/\Delta \log(d)$ (%/log(μm))	0.0413	0.0524	0.0605	0.0583	0.0592	0.0524	0.0405	0.0329	0.0281
	Pore Width (μm)	1.947	1.606	<u>1.325</u>	1.093	0.902	0.744	0.614	0.506	0.418
5-C(1)	$\Delta P/\Delta \log(d)$ (%/log(μm))	0.0456	0.0559	0.0581	0.0733	0.0729	0.0637	0.0514	0.0446	0.0364
	Pore Width (μm)	1.947	1.606	1.325	<u>1.093</u>	0.902	0.744	0.614	0.506	0.418
5-C(4)	$\Delta P/\Delta \log(d)$ (%/log(μm))	0.0387	0.0506	0.0626	0.0641	0.0712	0.0737	0.0633	0.0495	0.0383
	Pore Width (μm)	1.947	1.606	1.325	1.093	0.902	<u>0.744</u>	0.614	0.506	0.418
5-C(8)	$\Delta P/\Delta \log(d)$ (%/log(μm))	0.0229	0.0553	0.0581	0.0748	0.0709	0.0642	0.0558	0.0375	0.0273
	Pore Width (μm)	1.947	1.606	1.325	<u>1.093</u>	0.902	0.744	0.614	0.506	0.418
15-C(4)	$\Delta P/\Delta \log(d)$ (%/log(μm))	0.0424	0.0414	0.0509	0.0545	0.0523	0.0449	0.0355	0.0292	0.0240
	Pore Width (μm)	1.947	1.606	1.325	<u>1.093</u>	0.902	0.744	0.614	0.506	0.418
17-S(4)	$\Delta P/\Delta \log(d)$ (%/log(μm))	0.0278	0.0741	0.0617	0.0667	0.0641	0.0599	0.0474	0.0361	0.0294
	Pore Width (μm)	1.947	<u>1.606</u>	1.325	1.093	0.902	0.744	0.614	0.506	0.418
26-J(4)	$\Delta P/\Delta \log(d)$ (%/log(μm))	0.0465	0.0534	0.0468	0.0809	0.0785	0.0910	0.0711	0.0516	0.0432
	Pore Width (μm)	1.947	1.606	1.325	1.093	0.902	<u>0.744</u>	0.614	0.506	0.418

Note: Threshold pore widths are underlined

Table 28: U.S. 20 slab second peak nine highest $\Delta P/\Delta \log(d)$ values and their corresponding pore widths.

Sample ID	Parameter	1	2	3	4	5	6	7	8	9
1-C(4)	$\Delta P/\Delta \log(d)$ (μm)	0.0305	0.0430	0.0538	0.0570	0.0493	0.0456	0.0392	0.0353	0.0317
	Pore Width (μm)	0.0607	0.0500	0.0412	<u>0.0339</u>	0.0279	0.0230	0.0189	0.0155	0.0127
5-C(1)	$\Delta P/\Delta \log(d)$ (μm)	0.0421	0.0504	0.0566	0.0579	0.0514	0.0491	0.0448	0.0400	0.0359
	Pore Width (μm)	0.0607	0.0500	0.0412	<u>0.0339</u>	0.0279	0.0230	0.0189	0.0155	0.0127
5-C(4)	$\Delta P/\Delta \log(d)$ (μm)	0.0406	0.0529	0.0598	0.0568	0.0555	0.0469	0.0392	0.0357	0.0322
	Pore Width (μm)	0.0500	0.0412	<u>0.0339</u>	0.0279	0.0230	0.0189	0.0155	0.0127	0.0085
5-C(8)	$\Delta P/\Delta \log(d)$ (μm)	0.0256	0.0330	0.0413	0.0478	0.0451	0.0486	0.0331	0.0290	0.0255
	Pore Width (μm)	0.0607	0.0500	0.0412	0.0339	0.0279	<u>0.0230</u>	0.0189	0.0155	0.0127
15-C(4)	$\Delta P/\Delta \log(d)$ (μm)	0.0311	0.0426	0.0528	0.0522	0.0453	0.0421	0.0394	0.0375	0.0334
	Pore Width (μm)	0.0607	0.0500	<u>0.0412</u>	0.0339	0.0279	0.0230	0.0189	0.0155	0.0127
17-S(4)	$\Delta P/\Delta \log(d)$ (μm)	0.0305	0.0347	0.0366	0.0409	0.0462	0.0470	0.0431	0.0352	0.0299
	Pore Width (μm)	0.0736	0.0607	0.0500	0.0412	0.0339	<u>0.0279</u>	0.0230	0.0189	0.0155
26-J(4)	$\Delta P/\Delta \log(d)$ (μm)	0.0350	0.0425	0.0492	0.0545	0.0585	0.0485	0.0377	0.0330	0.0284
	Pore Width (μm)	0.0500	0.0412	<u>0.0339</u>	0.0279	<u>0.0230</u>	0.0189	0.0155	0.0127	0.0104

Note: Threshold pore widths are underlined

Table 29: MIP results on U.S. 20 slab samples.

Sample	Porosity * (%)	First peak		Second peak	
		Uniformity indicator (μm) [†]	Weighted average threshold pore width (μm)	Uniformity indicator (μm)	Weighted average threshold pore width (μm)
1-C(4)	11.27	0.01198	1.067	0.00946	0.0318
5-C(1)	12.83	0.01272	1.032	0.00746	0.0324
5-C(4)	13.36	0.01317	0.993	0.01009	0.0270
5-C(8)	10.01	0.01854	1.003	0.00928	0.0313
15-C(4)	11.27	0.01049	1.075	0.00752	0.0317
17-S(4)	10.46	0.01724	1.048	0.00636	0.0374
26-J(4)	12.99	0.01788	0.982	0.01030	0.0265

*Porosity as measured by the volume of intrusion recorded at 207 MPa divided by the bulk volume of the sample

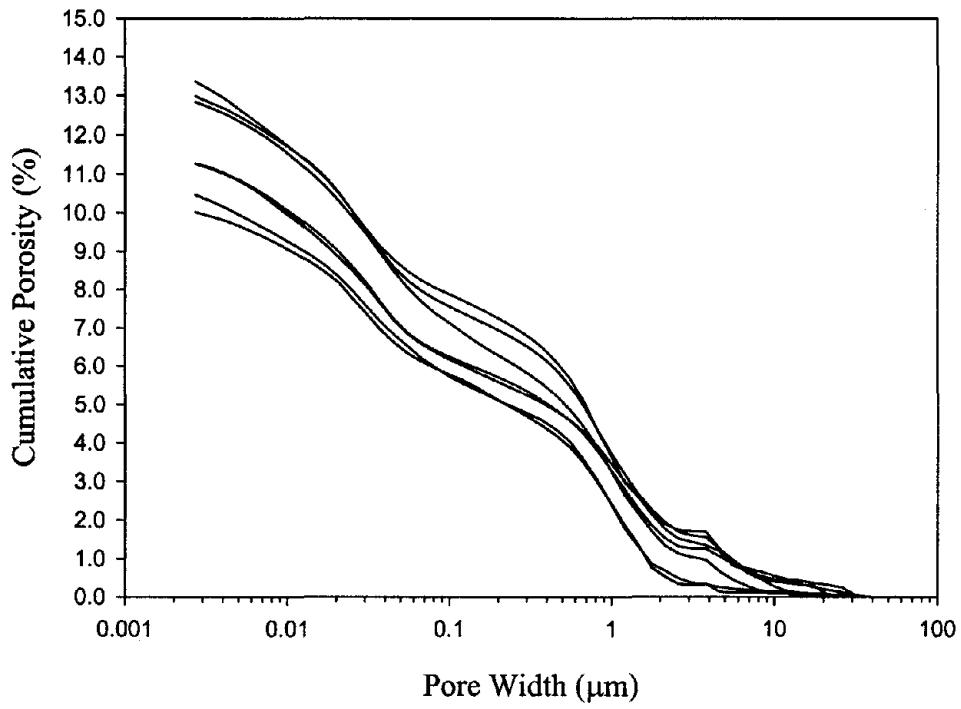


Figure 44: Cumulative porosity vs. pore width plot for Iowa U.S. 20 concrete.

associated with the macrocrack portion of the average differential pore size distribution plots.

The pore size distribution of the U.S. 20 concrete was repeatable with samples from different locations in the slab (figures 44 and 45). This indicates that sample location did not have an effect on the pore structure. The peaks to the right of 3 μm are to be ignored. They occurred prior to the changeover pressure.

The area under the first peak of intrusion was considerably higher than the second peak. This would indicate a larger porosity in the coarse pore sizes. The second peaks were sharp and well defined.

In conclusion:

1. Slab concrete porosities as measured by MIP ranged from 10 to 13 percent .
2. Slab concrete exhibited two distinct pore system microstructures: the first with an interconnecting pore width in the 1- μm range, the second in the 0.03- μm range.
3. Slab concrete had similar pore system characteristics to the laboratory concrete.

5.3.4. Effective Surface Area

The results of surface area analysis for the U.S. 20 concrete cores are presented in table 30. The slab concrete's surface area results varied as much as 50 percent for samples of the same age, materials, and location of removal from the slab. The cause of this variation was attributed to the unknown coarse aggregate content.

Concrete samples used in the surface area experiments were crushed from their original dice-size shapes to pebbles that could fit inside the 12.7-mm-diameter penetrometer tubes used in the testing apparatus. The action of crushing may have increased the surface areas of samples by fracturing on previously nonexistent cracks. However, the magnitude of this increase was determined to be minimal by experiments on the surface areas of the limestone coarse aggregate. The surface area of the crushed limestone coarse aggregate used in this project was measured to be $0.35 \pm 0.012 \text{ m}^2/\text{g}$. This compared well to typical values. Given the good reproducibility of these values, any increase in surface area from the crushing process is likely negligible or uniform throughout.

The more probable source of error is the unknown coarse aggregate content in each sample. Surface area is measured on the mortar fraction and the coarse aggregate fraction. The surface area of cement/fly ash pastes with similar water to cementitious material ratios has been reported from 42.4 to 168.8 m^2/g with good repeatability. Assuming a paste surface area of 42.4 m^2/g , a fine aggregate surface area similar to the coarse aggregate, and the percentage of paste in the mortar to be 35 percent by weight, the surface area of the mortar should be approximately 15 m^2/g . (The repeatability of surface area measurements on

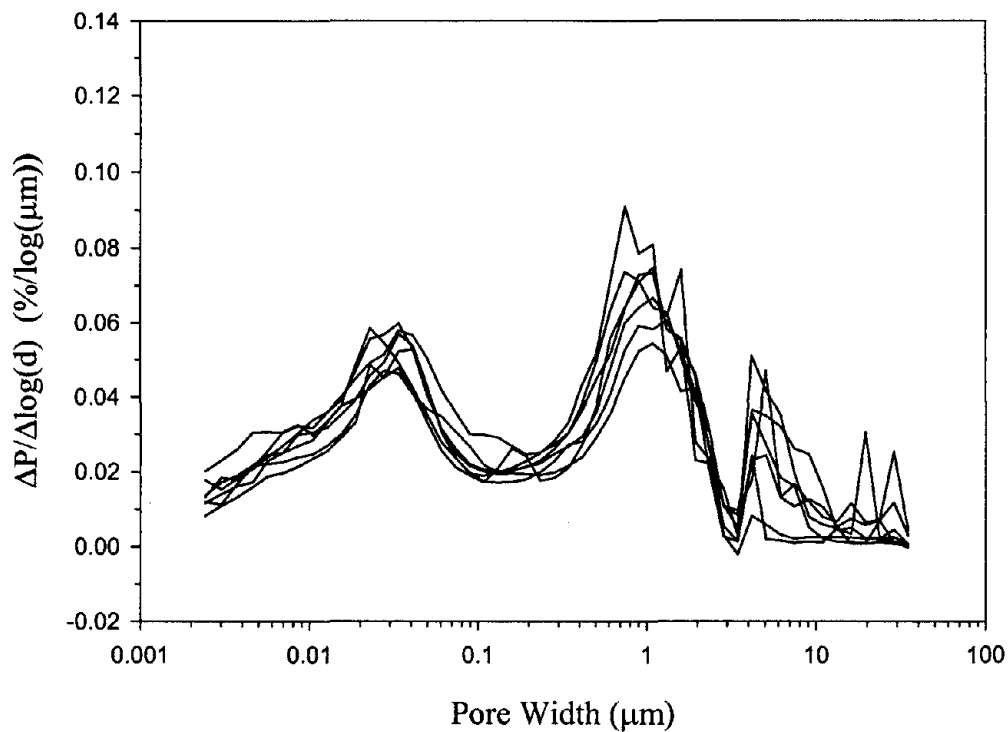


Figure 45: Average differential pore size distribution vs. pore width U.S. 20 slab.

Table 30: U.S. 20 slab cores BET-N₂ surface area analysis.

Core ID	Weighted surface area m ² /g
1-C(4)	2.886
5-C(1)	1.580
5-C(4)	1.882
5-C(8)	1.397
15-C(4)	2.384
17-S(4)	2.633
26-J(4)	2.216

mortars has not been established. It is assumed that the homogeneity of the sample, at this size, would produce consistent results.) Given a mortar and a coarse aggregate content of 15 to 85 percent by weight of each sample, surface area measurements on dice-size concrete samples could range from 2.5 to 12.8 m²/g. This range compares well with the experimental results. With such a large variability due to coarse aggregate content, one can see how repeatability is unlikely.

It may have been possible to calculate the surface areas if coarse aggregate contents were measurable. Methods to do this could consist of scraping away the mortar fraction by hand or dissolving the paste by some other means. The scraping method was not employed due to time constraints. The use of acidic solutions has been applied by some researchers to dissolve the paste. However, this was not a viable option for the concretes in this work as the limestone aggregates would have also been dissolved.

In conclusion:

1. Surface areas of the slab concrete ranged from 1.4 to 2.9 m²/g with poor reproducibility.
2. The surface areas of the slab concrete are low but reasonable when compared with known paste surface areas and probable aggregate fractions.

5.3.5. Elemental Composition

Two slab samples were analyzed by neutron activation analysis/X-ray fluorescence (NAA/XRF) for elemental composition. These samples were I-JC and O-SC. The average elemental concentrations of these samples are divided into tables J-1, J-2 and J-3 in appendix J in volume II for major (greater than 10,000 ppm), minor (1,000 to 10,000 ppm), and trace (less than 1,000 ppm) elements.

5.3.6. Mineralogy

Seven samples from the slab: 1-C(mid), 5-C(mid), 15-C(mid), 5/15-C(top), 5/15-C(bottom), 17-S(mid), and 26-J(mid), were analyzed in triplicate by XRPD to identify crystalline phases and to quantify mineral content for six selected phases. Figure 42 shows the locations of samples from different regions of the slab. Figure 46 indicates the sampling locations of the top, middle, and bottom designations within a concrete core.

Table 31 details what component materials may contribute to the crystalline phases in the slab concrete. All of the phases in table 31 were identified in the slab concrete as well as in the component materials.

Quantification of mineral phases was performed on the seven slab samples. The crystalline phases selected for quantification of mineral concentrations were albite (NaAlSi₃O₈), calcite (CaCO₃), gypsum (CaSO₄•2H₂O), ettringite (Ca₆Al₂(SO₄)₃(OH)₁₂•26H₂O), portlandite

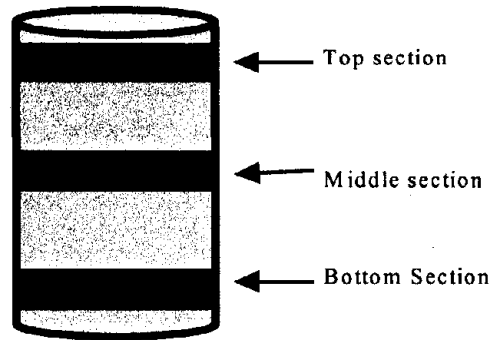


Figure 46: Vertical sectioning of core material from the U.S. 20 slab.

Table 31: Common concrete mineral phases identified in the U.S. 20 slab.

PDF No.	Mineral name	Chemical formula	References
<u>Portland cement paste phases</u>			
02-0083	Calcium Aluminum Oxide Hydrate	$\text{Ca}_3\text{Al}_2\text{O}_6 \cdot x\text{H}_2\text{O}$	1
04-0733	Portlandite, syn	$\text{Ca}(\text{OH})_2$	1, 2
05-0586	Calcite, syn	CaCO_3	
28-0775	Calcium Oxide	CaO	
47-1743	Calcite	CaCO_3	
<u>CFA-C phases</u>			
28-0775	Calcium Oxide	CaO	3
29-1489	Halloysite-10A	$\text{Al}_2\text{Si}_2\text{O}_5(\text{OH})_4 \cdot 2\text{H}_2\text{O}$	
46-1045	Quartz, syn	SiO_2	4
<u>Combined aggregate phases</u>			
05-0586	Calcite, syn	CaCO_3	
05-0613	Arcanite, syn	K_2SO_4	
09-0466	Albite, ordered	$\text{NaAlSi}_3\text{O}_8$	
29-1489	Halloysite-10A	$\text{Al}_2\text{Si}_2\text{O}_5(\text{OH})_4 \cdot 2\text{H}_2\text{O}$	
35-1393	Magnesium Iron Oxide	$\text{Mg}_1-x\text{Fe}_x\text{O}$	
36-0426	Dolomite	$\text{CaMg}(\text{CO}_3)_2$	
46-1045	Quartz, syn	SiO_2	
47-1743	Calcite	CaCO_3	

1 (Cook, 1992)

2 (Glasser, 1993)

3 (FWHA, 1995)

4 (Malhotra and Ramezani pour, 1994)

(Ca(OH)₂), and quartz (SiO₂). Table 32 shows mean concentrations and the concentration range of these phases in the slab concrete samples.

The typical concentration of portlandite (Ca(OH)₂) in cement paste is 20 to 30 percent by weight (Glasser, 1997). Using this range for portlandite concentration in cement paste, a mass balance was performed to estimate a typical concentration of portlandite for this concrete. Assuming the weight percent of the portland cement (12.5 percent) plus the weight percent of water in the concrete (7.2 percent) equals the weight percent of the hydrated cement paste in the concrete (19.7 percent), portlandite concentration could be estimated at 3.9 to 5.9 percent of the concrete.

The mean concentration of portlandite (Ca(OH)₂) in the slab samples was lower than range calculated based on the mass balance of the concrete. This is to be expected since the concrete contained CFA-C and over time the silicates in the CFA-C react with the Ca in the available portlandite, reducing the portlandite concentration and increasing the formation of C-S-H gel (Glasser, 1997). Since this concrete pavement was more than 10 yr old at the time of analysis it would be expected that the portlandite concentration to be lower than the range calculated above.

Both gypsum (CaSO₄•2H₂O) and ettringite (Ca₆Al₂(SO₄)₃(OH)₁₂•26H₂O) were detected at low levels. According to the literature, neither phase is expected to be detected in this concrete. Gypsum concentrations in cement pastes are typically not detectable for XRPD after 24 h (Taylor, 1997). Ettringite is not expected to form in concrete containing CFA-C because this concrete typically has lower SO₄²⁻ concentrations than portland cement concrete. Additionally the detection levels are below those found for trace phases in other quantitative work. The presence of gypsum in the slab concrete matches the high sulfate content in the source cement and the presence of gypsum found in month-old laboratory pastes (see sections 5.1.1.2 and 5.1.5.2).

In conclusion:

1. Expected minerals such as portlandite (Ca(OH)₂), calcite (CaCO₃), and quartz (SiO₂) were found in the slab concrete.
2. Portlandite concentrations in the slab concrete were low as is expected for older concretes containing fly ash.
3. Unexpected amounts of gypsum (CaSO₄•2H₂O) were found in the slab concrete corresponding to high sulfate contents in the source cement and high gypsum content in month-old laboratory pastes.

5.3.6.1 Statistical Comparison by Sample Location in the Slab

The three middle samples from the cut region were compared with a sample from the joint region and the shoulder region to test for significant variations between slab regions (see figure 42 for general locations).

Table 32: Average mineral concentrations in the U.S. 20 slab.

PDFNo.	Mineral name	Chemical formula	RIR value	Mean concentration ²	Concentration range ³
09-0466	Albite	NaAlSi ₃ O ₈	2.10	3.0%	0.9% - 15.8%
05-0586	Calcite	CaCO ₃	2.00	21.7%	15.2% - 36.2%
41-1451	Ettringite	Ca ₆ Al ₂ (SO ₄) ₃ (OH) ₁₂ • 26H ₂ O	1.00 ¹	0.5%	0.0% - 1.8%
33-0311	Gypsum	CaSO ₄ • 2H ₂ O	1.83	0.4%	0.2% - 1.7%
04-0733	Portlandite	Ca(OH) ₂	1.40	1.0%	0.4% - 2.6%
46-1045	Quartz	SiO ₂	3.41	4.4%	1.0% - 18.4%

1 The RIR value for ettringite was assumed to be 1.00

2 This is the mean for all 21 diffractograms of the Iowa slab samples

3 This is the range of concentration found in the 21 Iowa slab diffractograms

comparison, concrete material from the top of 5-C and 15-C was combined into one sample and material from the bottom of 5-C and 15-C was combined into a second sample. The mineral concentrations of the top and bottom samples were compared with mineral concentrations to samples taken from the middle of 5-C and 15-C.

ANOVAs of mineral concentrations in the three regions of the slab showed no statistical difference at a 90 percent confidence level between the cut, shoulder, and joint regions (see tables J-4 through J-7 in appendix J in volume II). The tabular F value for the 90 percent confidence level was 2.70 (Kuehl, 1994). Statistical analysis was not performed on gypsum ($\text{CaSO}_4 \cdot 2\text{H}_2\text{O}$) and ettringite ($\text{Ca}_6\text{Al}_2(\text{SO}_4)_3(\text{OH})_{12} \cdot 26\text{H}_2\text{O}$) since these phase concentrations were considered negligible.

ANOVA of mineral concentration changes in the slab related to depth of samples taken from the slab showed no difference in the concentrations of albite ($\text{NaAlSi}_3\text{O}_8$), calcite (CaCO_3), or portlandite (CaOH_2), with 90 percent confidence (see tables J-8 through J-11 in appendix J of volume II). ANOVA of quartz (SiO_2) concentration changes with changing depth in slab showed a statistical difference existed in the data set at 90 percent confidence (see table J-11). The tabular F value used for these analyses was 3.01 (Kuehl, 1994).

Table J-12 of appendix J in volume II shows a Tukey-Kramer comparison of means performed on the quartz (SiO_2) concentrations from the top, middle, and bottom of the slab samples 5-C and 15-C. At a 90 percent confidence level, the quartz concentration was found to be statistically higher at the top of the concrete slab than the bottom of the slab. The quartz concentration measured in the middle of the slab samples was not found to be statistically different from the top or bottom sections. A higher quartz concentration in the top level of the slab than the bottom section may have been caused by the movement of fine aggregate upwards in the slab as a result of the consolidation process.

Placement procedures for the U.S. 20 concrete may in part describe the behavior of the fine aggregate/ quartz in the samples.

Overall, the mineral concentration of the six quantified mineral phases was not affected by vertical or regional positions in the slab. The mineralogy of the slab has been shown to be relatively uniform.

In conclusion:

1. Quartz (SiO_2) concentrations were found to be higher in the top of the slab than in the bottom, perhaps due to a higher concentration of fine aggregate there.
2. The slab showed no difference in the concentrations of albite ($\text{NaAlSi}_3\text{O}_8$), calcite (CaCO_3), or portlandite (CaOH_2) between the top, middle, and bottom.

5.3.7. Evaluation of Carbonation of the Slab

A phenolphthalein spray was used as a screening test to determine the extent of carbonation within the U.S. 20 slab.

In the northwest region of the slab, the phenolphthalein test was carried out on sample J-JC. This sample had a joint edge where water contact may have occurred and a crack on the upper surface. The cut edges were fully non-carbonated (e.g., pink color). Therefore, there was no detectable carbonation within the slab core in the northwest region. A part of the joint edge, the upper surface, and the lower surface appeared to be carbonated (e.g., colorless). Nevertheless the carbonation depth for each of these surfaces was less than 0.5 mm and could not be clearly differentiated because of the presence of aggregates.

In the southeast region, the phenolphthalein test was carried out on sample N-SC. This sample had a shoulder edge and a crack on the upper surface. The cut edges were fully non-carbonated (e.g., pink color). Therefore, there was no carbonation within the slab core in the southeast region. The shoulder edge, the upper surface, and the lower surface appeared to be carbonated (e.g., colorless). Nevertheless, as with the northwest region, the carbonation depth could not be measured.

In the Southwest region, the phenolphthalein test was carried out on sample B-CC. Only the lower surface and the upper surface were carbonated (e.g., colorless). Similarly to the two previous regions, the carbonation depth was not significant and could not be measured. The cut edges were fully non-carbonated. Therefore, there was no carbonation within the slab core in the southwest region.

The rate of carbonation in concrete materials depends upon many factors that may be categorized into those affecting the character of the material (e.g., mix proportions, cement type, compaction, curing) and those affecting the environment (e.g., temperature, humidity, CO₂) (Sims, 1994). The limited extent of carbonation of the slab, although it was exposed to external conditions for 10 yr, may be a combination of (i) a low percentage of cement, (ii) a low percentage of Ca(OH)₂ produced during the hydration reactions because of the presence of the coal fly ash, (iii) low open porosity, or (iv) the presence within the pore of the slab of a relative humidity lower or higher than the one required for optimal carbonation to proceed (e.g., about 65 percent).

In conclusion:

1. Regardless of slab location, the carbonation depth of the upper surface of the slab was less than 0.5 mm and could not be measured although the slab was exposed to traffic and climatic conditions for more than 10 yr.
2. The same was true for the lower surfaces which had been in contact with the base soils.
3. The failures (e.g., cracks) on the upper surface did not seem to have influenced the carbonation rate.

4. There was no detectable carbonation within the slab core.

5.3.8. pH-dependent Leaching and Solid Phase Control

5.3.8.1 Slab Alkalinity and Constituent Solubility as a Function of pH

Acid neutralization capacity curves of sample I-JC and sample O-SC are compared in figure 47. Differences in pH reached for the same amount of acid added were observed between the two locations within the pH range of 10 to 6. This was likely due to heterogeneity of the slab composition.

The pH titration curve of sample I-JC exhibited a rapid decrease from a pH of 12 to a pH of 6 followed by a plateau around a pH of 6, consistent with the buffering capacity of the aggregates (e.g., limestone type, see also figure 26). This plateau, which lasted from 4 mEq of acid/g dry to 12 mEq of acid/g dry, was followed by a rapid decrease to a pH less than 2 for an acid addition of 4 mEq/g dry. The pH titration curve of sample O-SC presented a quasi-linear decrease from pH 12 to pH 6 with no discernible plateau, followed by a rapid decrease to a pH less than 2 for an acid addition of 4 mEq/g dry. pH 6 was reached for an acid addition (e.g., 12 mEq of acid/g dry) corresponding to the end of the plateau observed for sample I-JC.

This behavior buffering behavior is similar to that observed for the CFA-C (see figure 26).

Based on the acid required to reach a pH of 11.9 (approximately 0.50 mEq/g dry and 0.45 mEq/g dry for sample I-JC and sample O-SC, respectively), the quantity of $\text{Ca}(\text{OH})_2$ produced during the hydration reactions of the cement was estimated at 18.6 g/kg of dry material (e.g., 41 kg /m³ of porous material) for sample I-JC and 16.7 g/kg of dry material (e.g., 37 kg /m³ of porous material) for sample O-SC.

Cd, Cu, Pb, Ni, and Zn solubility as a function of pH for sample I-JC and sample O-SC is presented in figure 48. Horizontal dashed lines on each of the figures are used to indicate the analytical detection limits.

The solubility of the species of concern was not influenced by the sample location. For each of the metals of concern, the solubility increased as the pH decreased and no amphoteric behavior was observed. For pHs greater than 8, Ni solubility remained below the analytical detection limit. Similarly, for a pH greater than 6, Zn solubility remained below the analytical detection limit. At low pH (e.g., less than 3), the concentration of the metals of concern reached a plateau. Leaching then seemed to be limited by an available content in the case of Cd, Ni, and Zn while exceeding the total content in the case of Cu and Pb. Thus, for sample I-JC, only 70 percent of Cd, 3 percent of Ni and 70 percent of Zn have been released at a pH of 3. For sample O-SC, only 70 percent of Cd, 64 percent of Ni and 95 percent of Zn have been released at a pH of 3. The differences observed in the percentage of Ni released between the two

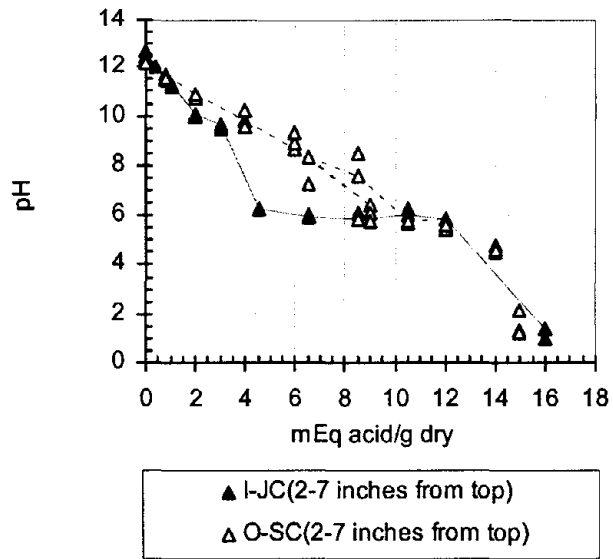
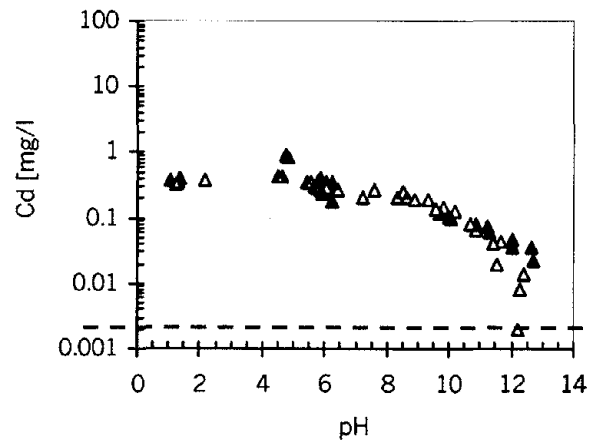
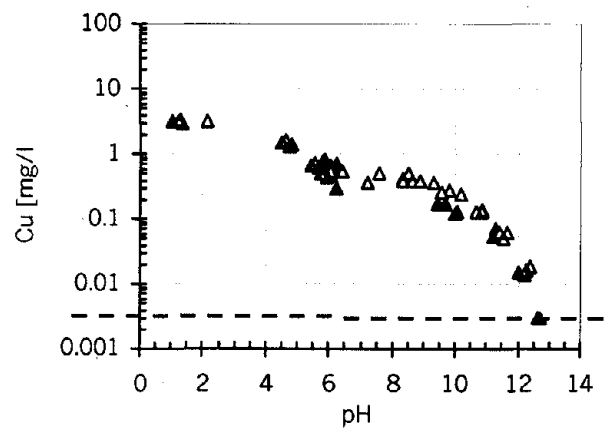


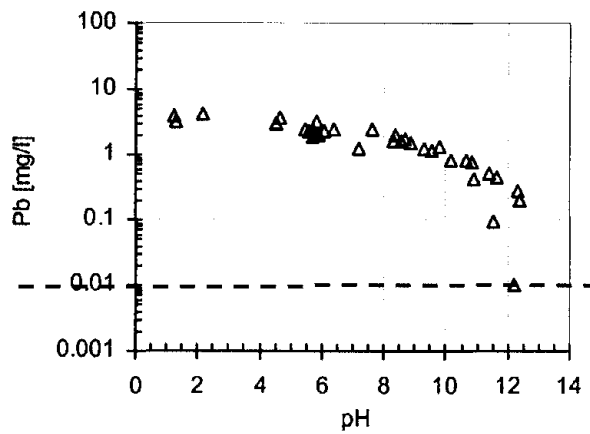
Figure 47: Acid neutralization capacity curves for the U.S. 20 concrete samples.



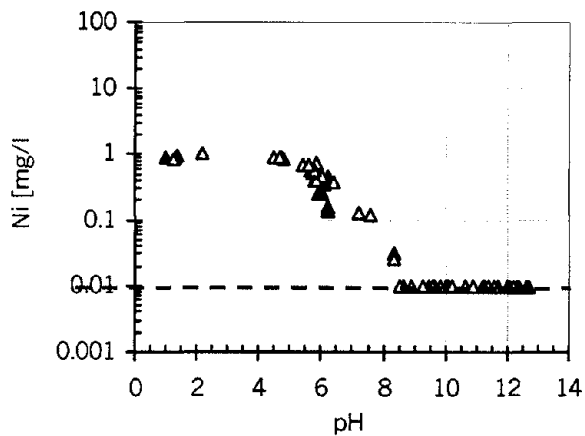
A)
 ▲ I-JC(2-7 inches from top)
 △ O-SC(2-7 inches from top)



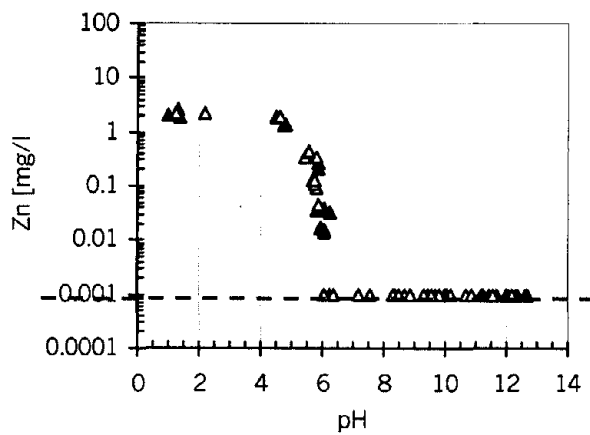
B)
 ▲ I-JC(2-7 inches from top)
 △ O-SC(2-7 inches from top)



C)
 △ O-SC(2-7 inches from top)



D)
 ▲ I-JC(2-7 inches from top)
 △ O-SC(2-7 inches from top)



E)
 ▲ I-JC(2-7 inches from top)
 △ O-SC(2-7 inches from top)

Dashed line indicates analytical detection limits

Figure 48: Concentration and solubility as a function of pH for the U.S. 20 concrete samples.

samples were only due to differences found in their total contents (e.g., total content in Ni of 155 mg/kg for sample I-JC and 3 mg/kg for sample O-SC).

In conclusion:

1. Acid neutralization curves of the slab concrete were very similar to curves obtained for the combined aggregates and the CFA-C source materials.
2. Curves for the solubility of elements as a function of pH for Cd, Cu, Ni, and Zn were similar in shape to but lower in magnitude than those found for the CFA-C.
3. Curves for the solubility of Pb as a function of pH were similar in shape to but lower in magnitude than those found for the combined aggregates.

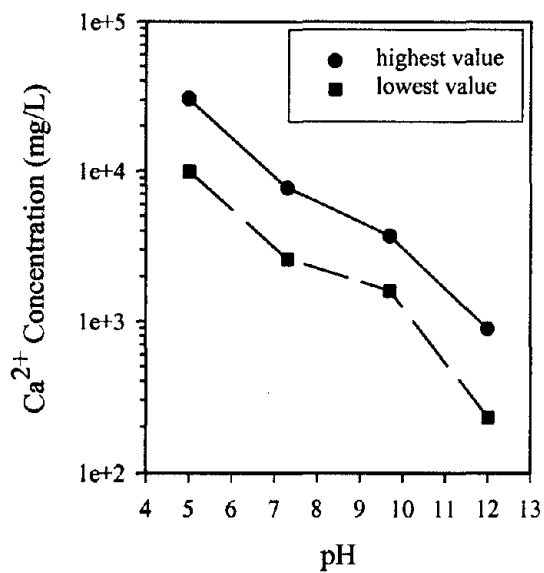
5.3.8.2 pH-Stat Leaching

Seven samples from the slab were subjected to pH-dependent leaching. Those samples were 1-C(mid), 5-C(mid), 15-C(mid), 5/15-C(top), 5/15-C(bottom), 17-S(mid), and 26-J(mid) (see figure 42). Each slab concrete sample was leached at four pH points: 5.0, 7.3, 9.7, and 12.0. The resulting leachates were analyzed for Al, Ba, Ca, Cl, CO_3^{2-} , Cr, Fe, K, Mg, NO_3^- , Si, SO_4^{2-} , and Zn. NO_3^- was added to the leaching system as HNO_3 to maintain a constant pH. NO_3^- was measured for the purposes of geochemical modeling. The remaining 12 species were measured to characterize the pH-dependent leaching behavior of the U.S. 20 slab concrete. Because only one data point was taken at each pH for each sample no statistical analysis was done to examine differences in leaching behavior associated with slab region or depth. Figures 49 through 51 show the range of analyte concentrations leached at each pH.

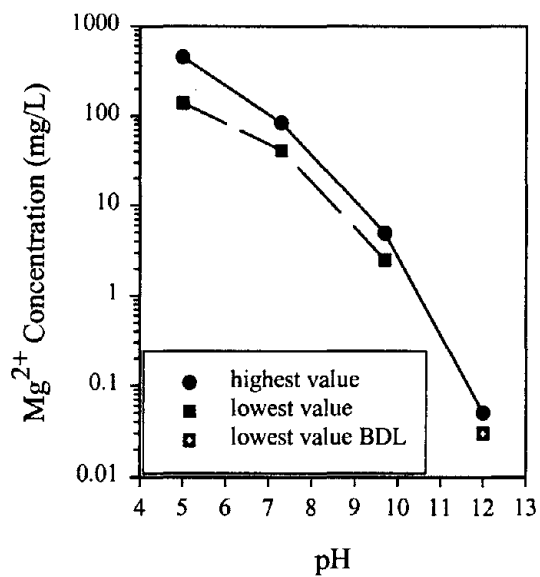
Figure 49 presents the leaching data for Ca, Mg, Al, and Si. Ca, Mg and Si all show a pH-dependent behavior of decreasing leachability with increasing pH with changes in leachate concentration of a factor of 100, 1×10^6 , and 10, respectively. The leaching behaviors of these species agreed with leaching behavior previously studied in cement mortars (van der Sloot, 1998). Al leaching showed amphoteric behavior with a minimum solubility around a pH of 9 to 10.

Figure 50 examines the pH-dependent leaching behaviors of Ba, Zn, Fe, and Cr. Ba, Zn, and Fe exhibit amphoteric behavior. This was similar behavior to what has been shown previously for amphoteric trace metals in cement based waste stabilization (van der Sloot et al., 1994; Glasser, 1997). Cr^{3+} leaching could not be characterized over the entire pH range as it was BDL for every sample at a pH of 5.0. Over the neutral pH range, Cr leaching showed little change and then decreased at a pH of 12.0. The increase in Cr solubility at alkaline pH may be explained by Cr^{3+} substitution for Al^{3+} in Ca hydrates in cement systems and thus the solubility is controlled by the Ca species and does not follow simple Cr solubility diagrams (Glasser, 1997).

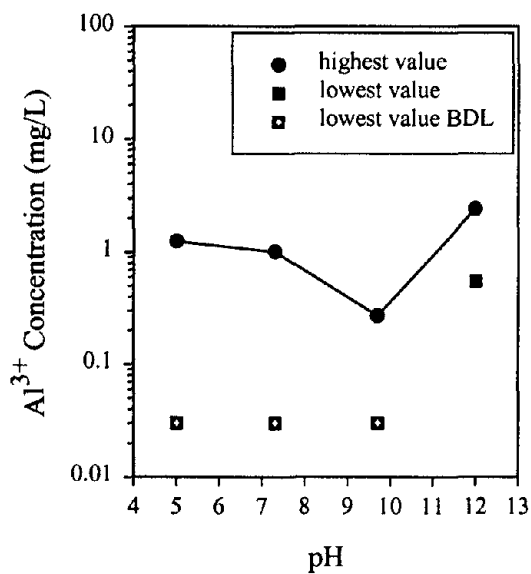
Figure 51 presents the leaching data for K, Cl, CO_3^{2-} , and SO_4^{2-} . K and Cl exhibited characteristic pH-independent leaching behavior for salts over the entire pH range examined. The



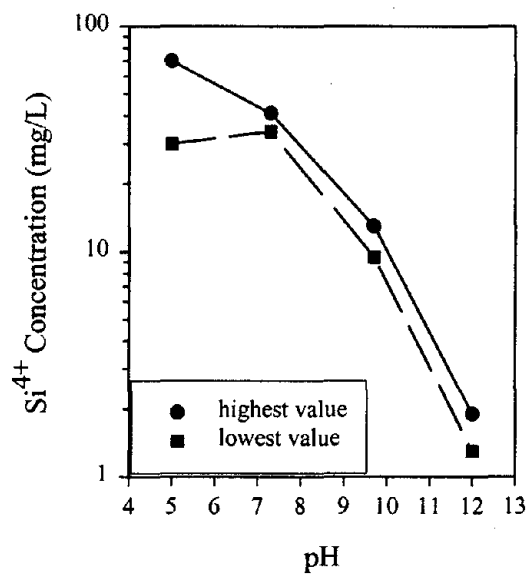
(a)



(b)

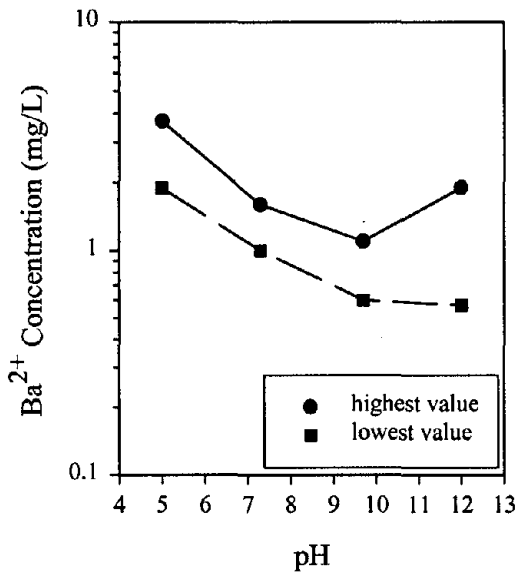


(c)

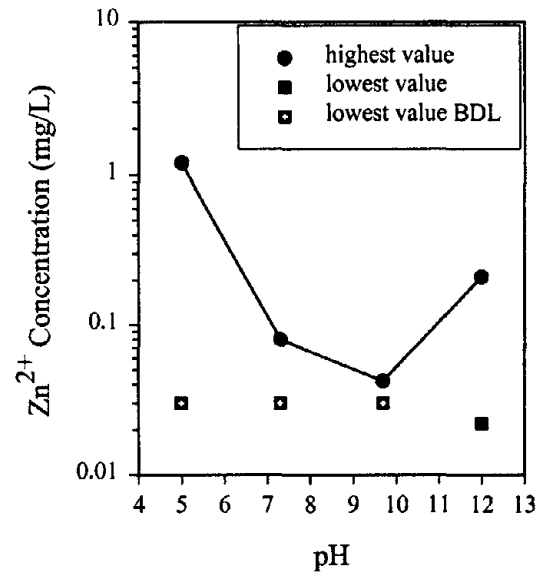


(d)

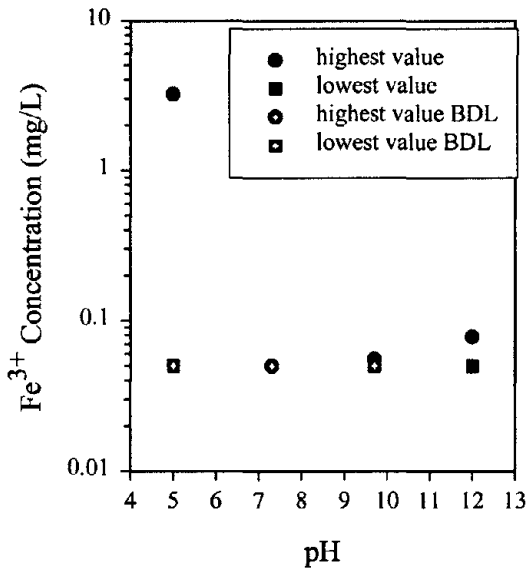
Figure 49: pH-dependent leaching of U.S. 20 slab concrete:
 (a) Ca, (b) Mg, (c) Al, (d) Si.



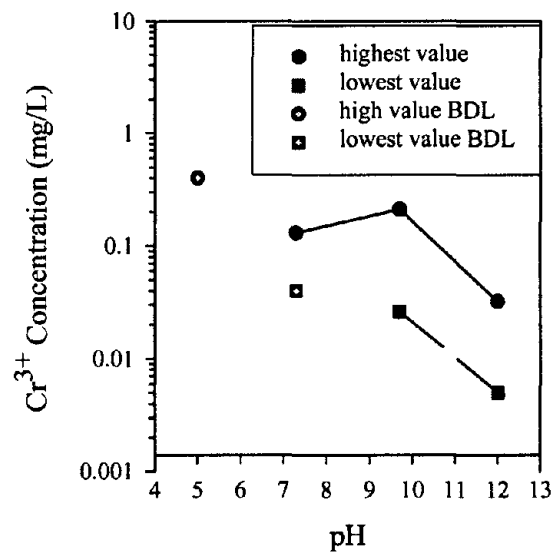
(a)



(b)

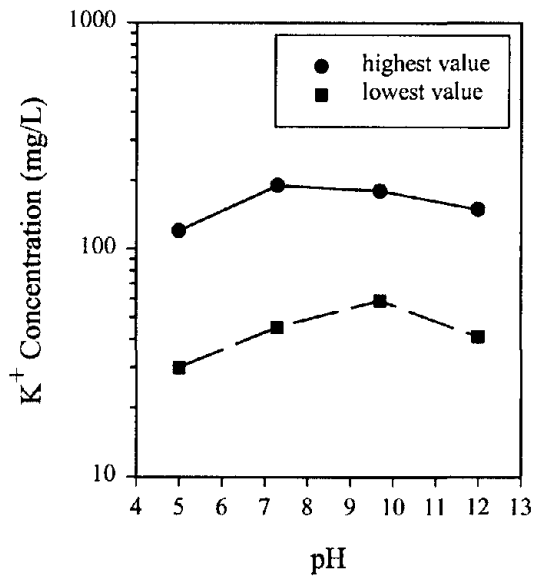


(c)

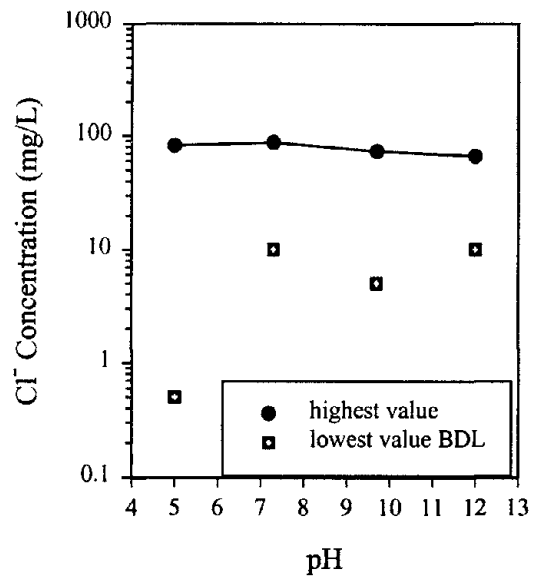


(d)

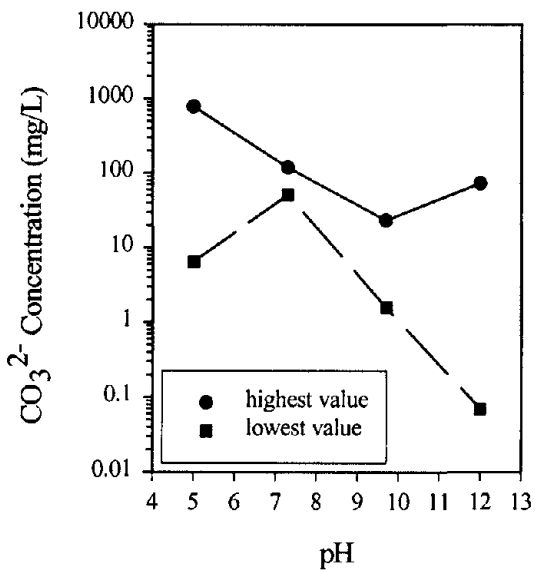
Figure 50: pH-dependent leaching of U.S. 20 slab concrete:
 (a) Ba, (b) Zn, (c) Fe, (d) Cr



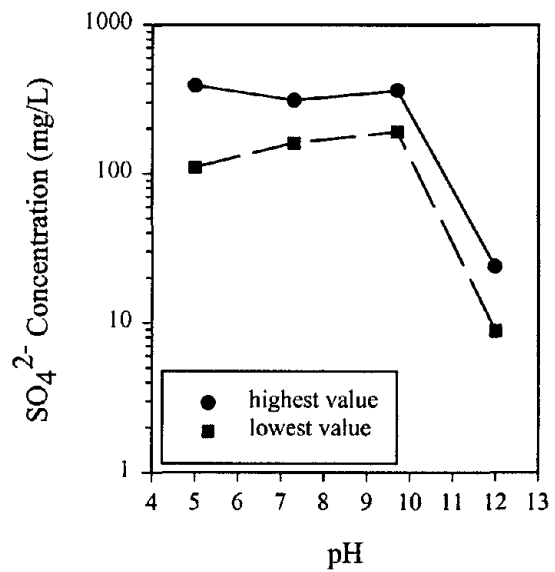
(a)



(b)



(c)



(d)

Figure 51: pH-dependent leaching of U.S. 20 slab concrete:
 (a) K, (b) Cl, (c) CO₃²⁻, (d) SO₄²⁻.

high to low range of CO_3^{2-} concentrations in samples seemed variable, showing wide ranges at a pH of 5.0 and a pH of 12.0. These ranges of values at one pH point may reflect the difficulty experienced in ascertaining accuracy in the alkalinity measurement, on which the CO_3^{2-} value is based. The overall trend for CO_3^{2-} is a decrease from neutral to alkaline pH while remaining, on average, constant between acidic and neutral pH levels. SO_4^{2-} leaching was relatively constant between a pH of 5.0 and a pH of 9.7, but decreased by a factor of 10 between a pH of 9.7 and a pH of 12.0.

5.3.8.3 Geochemical Modeling

Geochemical modeling was performed using the modeling program MINTEQA2 as described in section 3.3.6.3. The leaching data of sample 1-C(mid) was used as representative data for modeling candidate solids in the slab. Modeled leaching data are shown with the range of actual leached concentrations found in all seven of the slab samples. Candidate controlling solids were selected for modeling of the leaching behavior of the analytes based on the XRPD data and the MINTEQA2 saturation indices of each solid. Each candidate solid was individually introduced into the modeling program with leachate data from pH 5.0, 7.3, 9.7, and 12.0. Figures 52 through 61 show the geochemical modeling of selected solids for 10 species analyzed from the slab concrete. Cl and K were not modeled. A successful identification of a controlling solid occurs when (i) the modeled concentrations agree with the experimental leaching data (± 1 log), (ii) the controlling solid describes leaching over the entire pH range examined, and (iii) the shape of the modeled leaching curve matches that of the experimental leaching curve. Table 33 summarizes the modeling of each solid for each species based on agreement in concentration and shape of modeled leaching curve.

Ca Modeling. As shown in figure 52, Ca leaching was well modeled over the 5 to 12 pH range by calcite (CaCO_3) and dolomite ($\text{CaMg}(\text{CO}_3)_2$). Both of these solids were identified in the slab concrete by XRPD. Calcite is typically considered a controlling solid for ash- and cement-based systems (EPRI, 1987). Gypsum ($\text{CaSO}_4 \cdot 2\text{H}_2\text{O}$) models the Ca leaching data well over the range of pH of 5 to 10 and ettringite ($\text{Ca}_6\text{Al}_2(\text{SO}_4)_3(\text{OH})_{12} \cdot 26\text{H}_2\text{O}$) is well modeled from pH of 9 to 12. Both of these species were quantified by XRPD at trace concentrations in the slab concrete slab. Portlandite (CaOH_2), a typical hydrated cement phase, did not model well for the slab concrete leaching. Portlandite was also quantified at low concentrations by XRPD. In the presence of CFA, portlandite concentration is decreased in the concrete over time as the silicate species of the CFA take up Ca from portlandite to form the C-S-H gel (Glasser, 1997). As for the hydrated cement paste (see section 5.1.6.3), Ca leaching from the slab concrete was likely controlled by the calcite or dolomite over the entire pH range examined.

Mg Modeling. Mg modeling is depicted in figure 53. Solids modeled for Mg leaching were dolomite ($\text{CaMg}(\text{CO}_3)_2$) and brucite ($\text{Mg}(\text{OH})_2$). Brucite can be a reaction product of the hydration of the MgO often found in CFA-C. Brucite was not well modeled and should not be considered a controlling solid for Mg leaching. Dolomite, identified by XRPD, well modeled

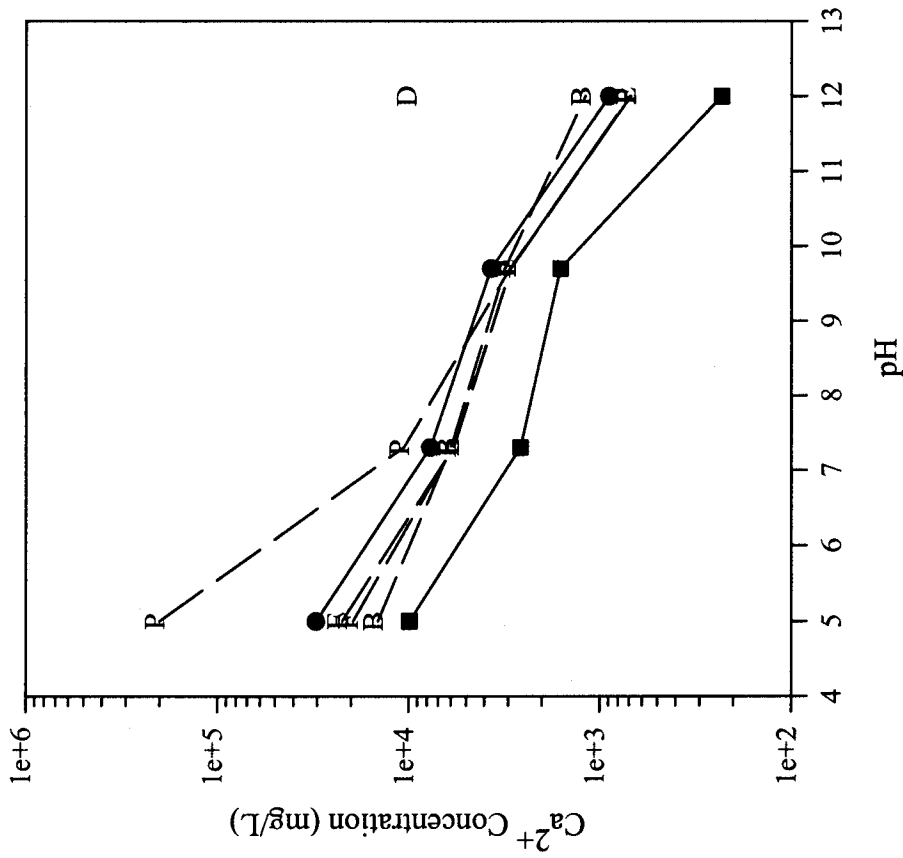


Figure 52: Ca modeling in the U.S. 20 slab.

- Highest Leaching Value
- Lowest Leaching Value
- [B] – Gypsum [D] – Portlandite [E] – Calcite
- [F] – Dolomite [P] – Ettringite
- [E] and [F] are completely overlapped

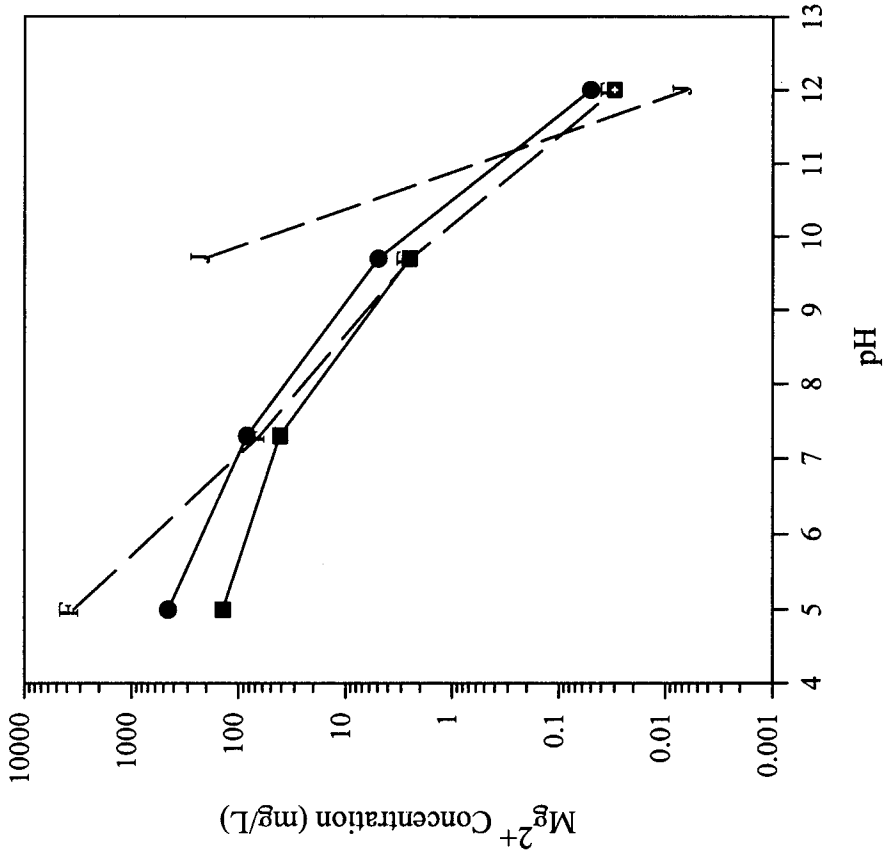


Figure 53: Mg modeling in the U.S. 20 slab.

- Highest Leaching Value
- Lowest Leaching Value
- [F] – Dolomite [J] – Brucite

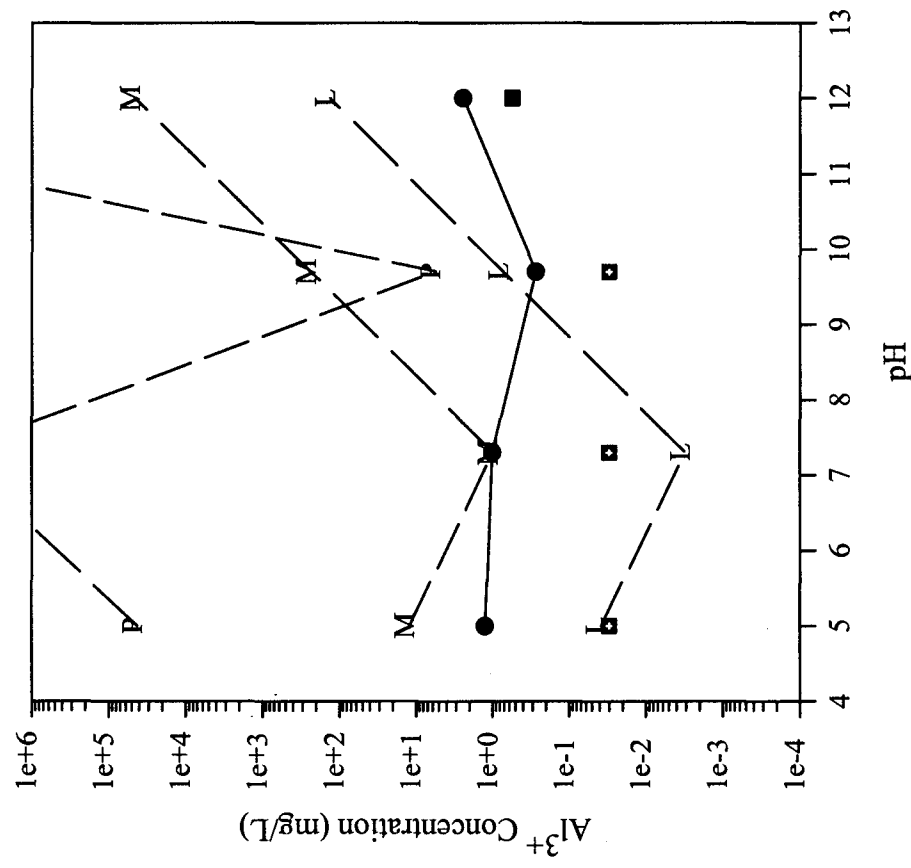


Figure 54: Al modeling in the U.S. 20 slab.
 ● Highest Leaching Value ■ Lowest Leaching Value
 ▣ Lowest Leaching Value BDL
 [L] - Gibbsite [M] - Al(OH)₃*amorphous
 [P] - Ettringite

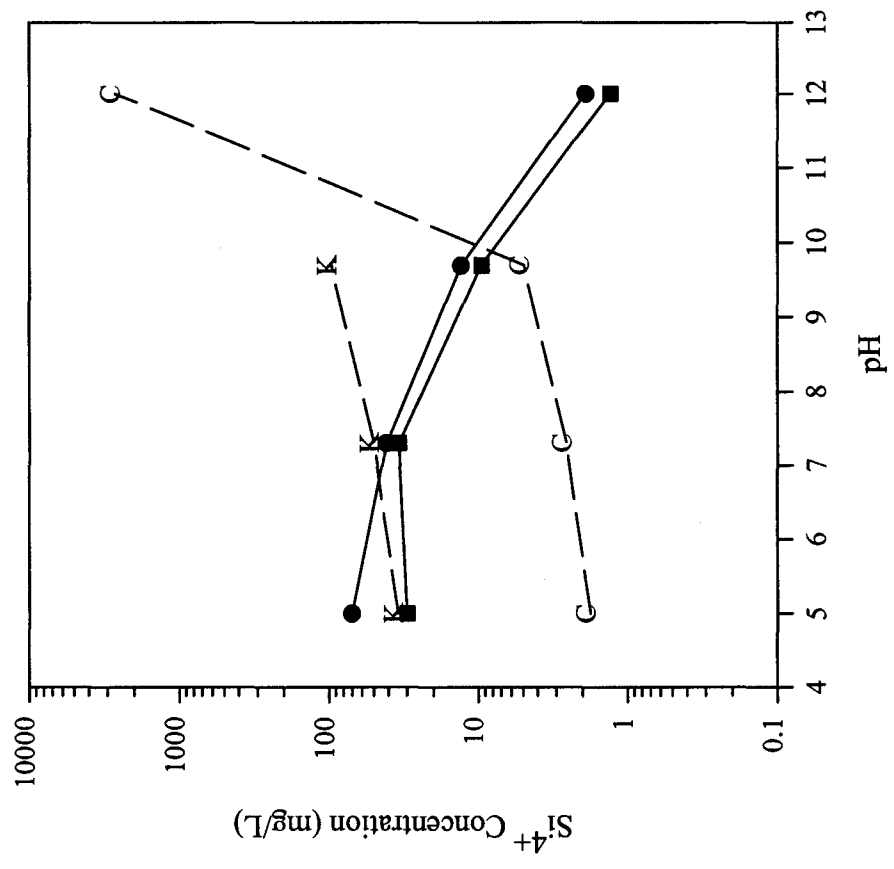


Figure 55: Si modeling in the U.S. 20 slab.
 ● Highest Leaching Value ■ Lowest Leaching Value
 [C] - Quartz [K] - SiO₂*amorphous

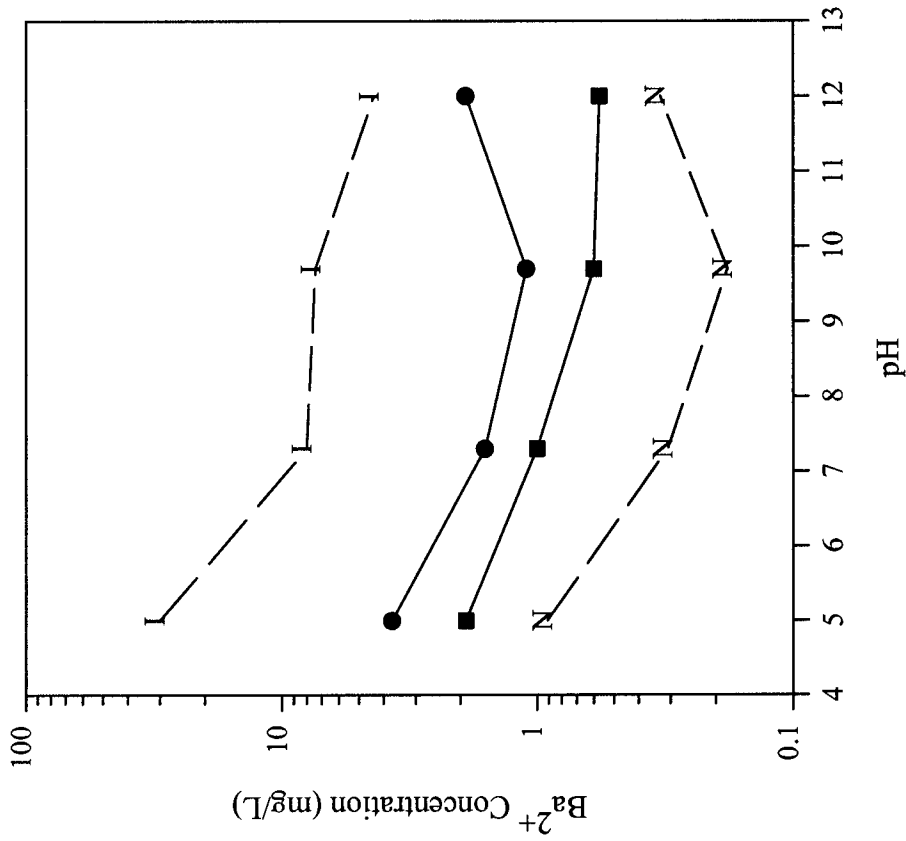


Figure 56: Ba modeling in the U.S. 20 slab.
 • Highest Leaching Value ■ Lowest Leaching Value
 [I] - BaCrO₄ [N] - Barite

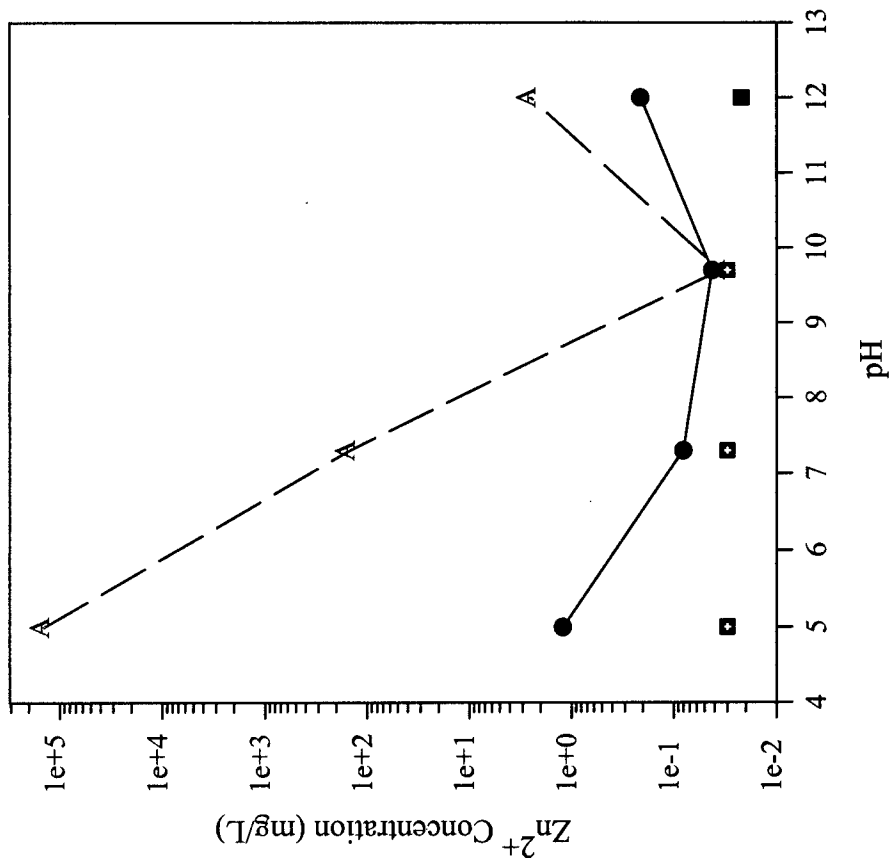


Figure 57: Zn modeling in the U.S. 20 slab.
 • Highest Leaching Value ■ Lowest Leaching Value
 [A] - Zincite

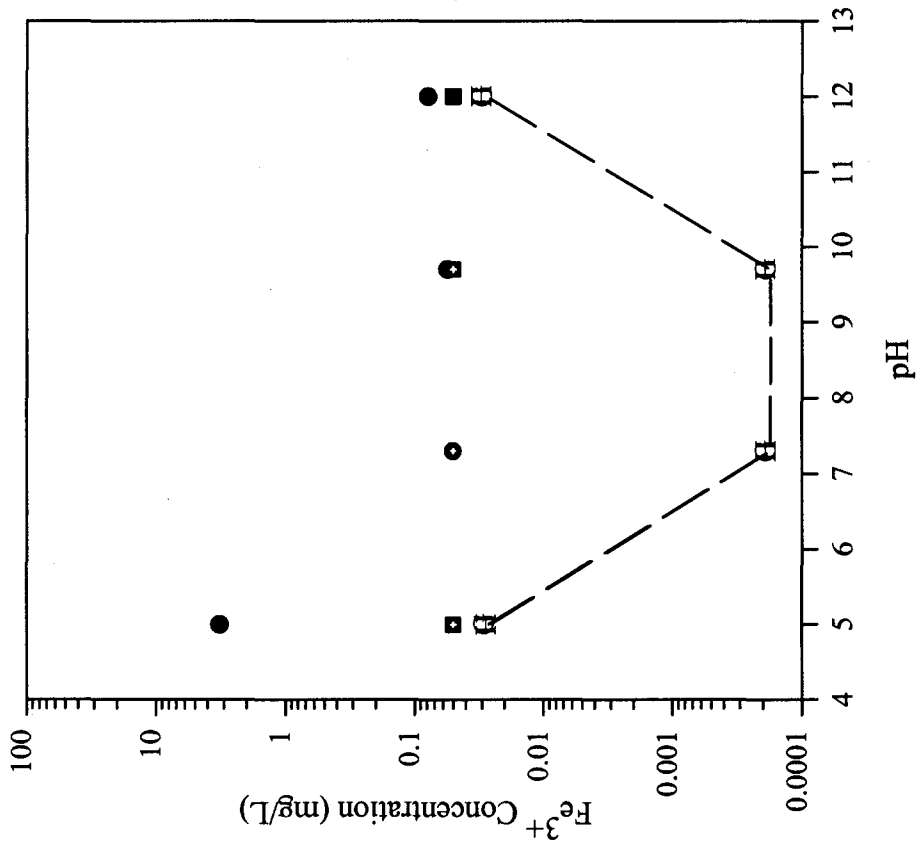


Figure 58: Fe modeling in the U.S. 20 slab.
 • Highest Leaching Value ■ Lowest Leaching Value
 ○ Highest Leaching Value BDL □ Lowest Leaching Value BDL
 [G] – Ferrihydrate [H] – Maghemite (overlapped)

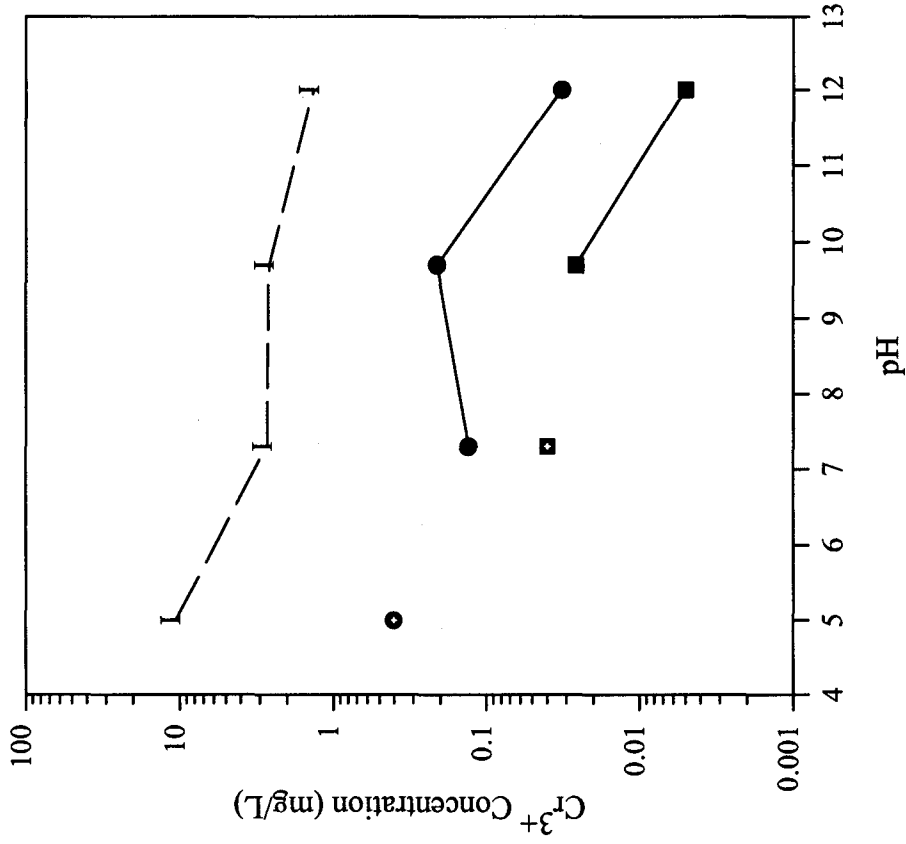


Figure 59: Cr modeling in the U.S. 20 slab.
 • Highest Leaching Value ■ Lowest Leaching Value
 ○ Highest Leaching Value BDL □ Lowest Leaching Value BDL
 [I] – $BaCrO_4$

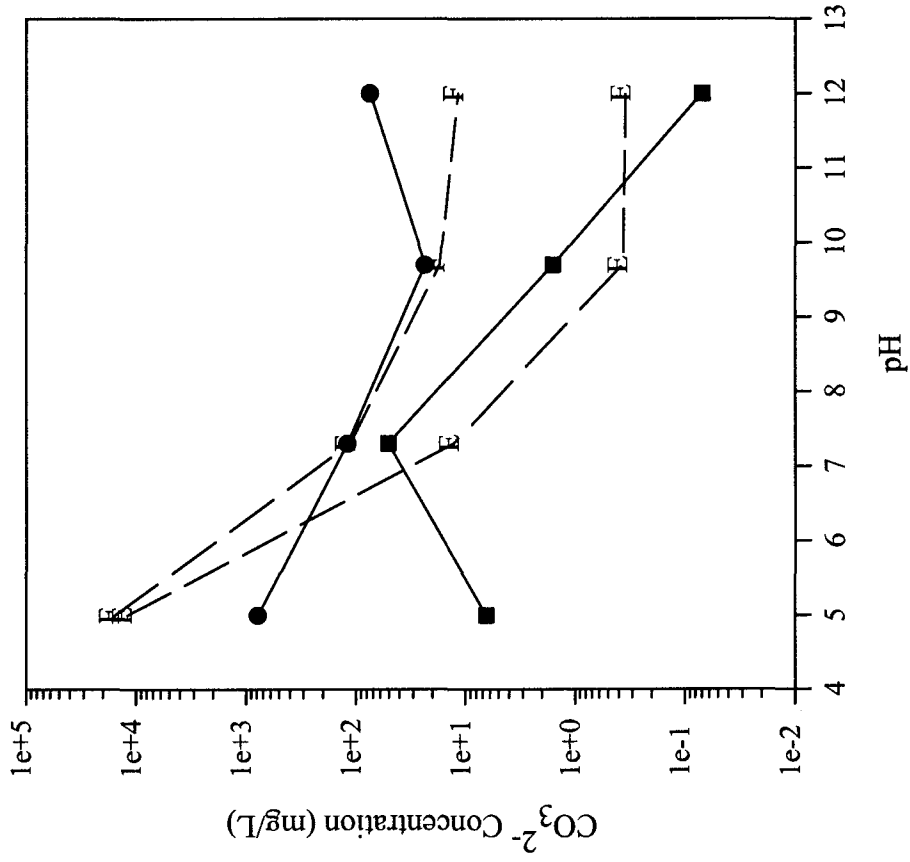


Figure 60: CO_3^{2-} modeling in the U.S. 20 slab.
 • Highest Leaching Value [E] – Calcite [F] – Dolomite
 ■ Lowest Leaching Value

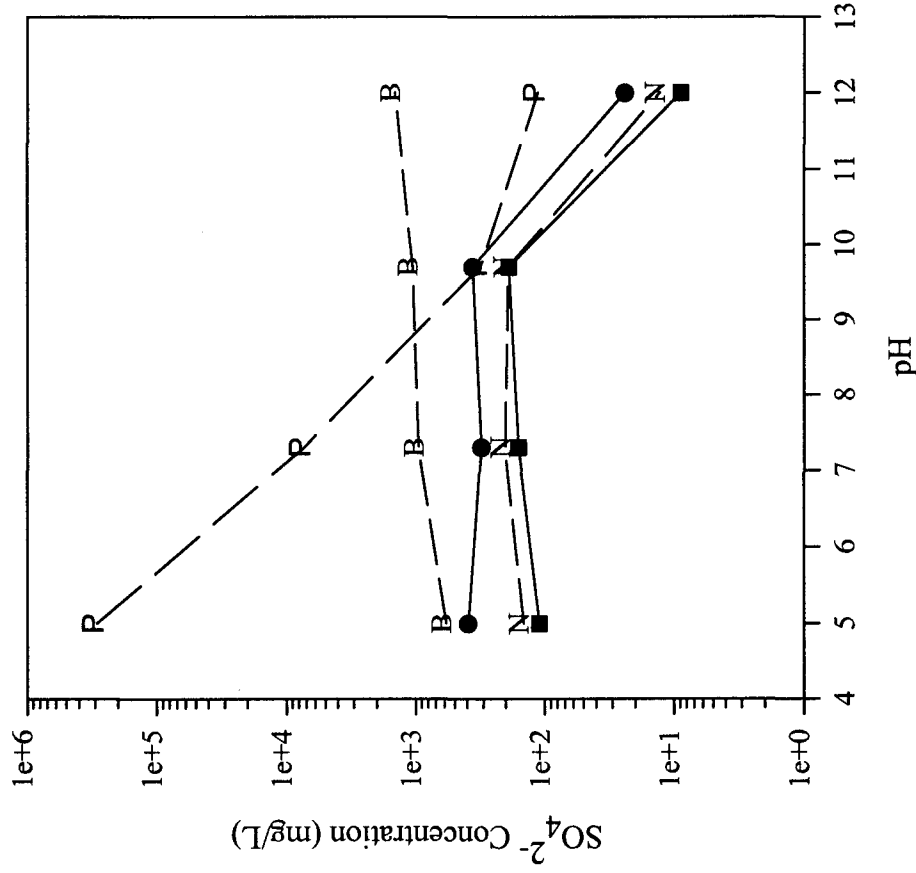


Figure 61: SO_4^{2-} modeling in the U.S. 20 slab.
 • Highest Leaching Value [B] – Gypsum [N] – Barite [P] – Ettringite
 ■ Lowest Leaching Value

Table 33: Geochemical modeling species for U.S. 20 slab.

Species	Solid phase	log K_{sp}	Well modeled pH range
Al	Gibbsite $\text{Al}(\text{OH})_3$	-8.291	none
	$\text{Al}(\text{OH})_3$ amorphous	-10.800	none
	Ettringite $(\text{Ca}_6\text{Al}_2(\text{SO}_4)_3(\text{OH})_{12} \cdot 26\text{H}_2\text{O})$	-56.700	none
Ba	BaCrO_4	9.670	5 - 7
	Barite (BaSO_4)	9.980	5 - 12
Ca	Gypsum ($\text{CaSO}_4 \cdot 2\text{H}_2\text{O}$)	4.610	5 - 10
	Portlandite ($\text{Ca}(\text{OH})_2$)	-22.804	none
	Calcite (CaCO_3)	8.480	5 - 12
	Dolomite ($\text{CaMg}(\text{CO}_3)_2$)	16.540	5 - 12
	Ettringite $(\text{Ca}_6\text{Al}_2(\text{SO}_4)_3(\text{OH})_{12} \cdot 26\text{H}_2\text{O})$	-56.700	7 - 12
CO_3	Calcite (CaCO_3)	8.480	7 - 12
	Dolomite ($\text{CaMg}(\text{CO}_3)_2$)	16.540	7 - 12
Cr	BaCrO_4	9.670	none
Fe	Ferrihydrite ($\text{Fe}(\text{OH})_3$)	-3.191	none
	Maghemite (Fe_2O_3)	-6.386	none
Mg	Dolomite ($\text{CaMg}(\text{CO}_3)_2$)	16.540	5 - 12
	Brucite ($\text{Mg}(\text{OH})_2$)	-16.844	none
Si	Quartz (SiO_2)	4.000	none
	SiO_2 amorphous gel	2.710	none
SO_4	Gypsum ($\text{CaSO}_4 \cdot 2\text{H}_2\text{O}$)	4.610	5 - 10
	Barite (BaSO_4)	9.980	5 - 12
	Ettringite $(\text{Ca}_6\text{Al}_2(\text{SO}_4)_3(\text{OH})_{12} \cdot 26\text{H}_2\text{O})$	-56.700	none
Zn	Zincite ($\text{Zn}(\text{OH})_2$)	-11.334	9 - 12

the Mg leaching behavior from in neutral and alkaline pH ranges and was within one log of the experimental data in the acidic pH range. Similarly, dolomite well modeled Mg leaching for the hydrated cement paste.

Al Modeling. Figure 54 shows the modeling of Al with ettringite ($\text{Ca}_6\text{Al}_2(\text{SO}_4)_3(\text{OH})_{12}\cdot 26\text{H}_2\text{O}$), gibbsite ($\text{Al}(\text{OH})_3$) and amorphous $\text{Al}(\text{OH})_3$. Ettringite was not a good model for the leaching of Al from the slab samples. Gibbsite was the best match of the three controlling solids, but the range of minimum solubility was shifted to a lower pH than was demonstrated for the experimental data. Crystalline Al phases identified by XRPD included albite ($\text{NaAlSi}_3\text{O}_8$), halloysite ($\text{Al}_2\text{Si}_2\text{O}_5(\text{OH})_4\cdot 2\text{H}_2\text{O}$) and other multiple oxide solids that do not exist in the MINTEQA2 database. Al leaching in cement-based systems can be controlled by the hydrated Ca species, which are not included in the MINTEQA2 database (Glasser, 1997).

Si Modeling. Si was modeled for both crystalline and amorphous SiO_2 in figure 55. Neither solid adequately described the leaching behavior of Si observed in the Slab concrete, despite a certain identification of quartz (SiO_2) in the concrete by XRPD. Similar results have been reported previously (Eighmy et al., 1994; Fruchter 1990) The Ca-Al-silicates abundant in the concrete matrix may be the source of controlling solids for Si leaching, but these species are not present in the MINTEQA2 database and therefore were not modeled.

Ba Modeling. Figure 56 depicts the modeling of Ba leaching by barium chromate (BaCrO_4) and barite (BaSO_4). Barite was the best match of the two solids. Although the predicted solubility was lower in the barite model than the experimental data, the shape of the leaching curves was an excellent match. SO_4^{2-} species have been shown to control Ba in other systems (Fruchter, 1990).

Zn Modeling. The leaching behavior of Zn (see figure 57), while exhibiting a typical amphoteric curve, was not successfully modeled. The solid, suggested as most likely to control Zn leaching by MINTEQA2, modeled reasonably well only at the higher end of the tested pH range. Other work has suggested that Zn sorbs to metal oxides which then control the solubility of Zn (EPRI, 1987; van der Sloot et al., 1994).

Fe Modeling. Experimental data for Fe modeling was incomplete because all Fe concentration from the slab sample at a pH of 7.3 were BDL. When all data points were BDL, the detection limit was input into MINTEQA2 as the Fe concentration for that pH. Modeling was attempted for solids ferrihydrite ($\text{Fe}(\text{OH})_3$) and maghemite (Fe_2O_3) (see figure 58). Neither solid adequately modeled the leaching of Fe from the slab concrete. $\text{Fe}(\text{OH})_3$ has been identified as a likely controlling solid based on thermodynamic data (EPRI, 1987), but in modeling applications problems of agreement between observed and predicted data have been shown (Fruchter, 1990).

Cr Modeling. Figure 59 depicts the modeling of Cr with barium chromate ($\text{BaCr}^{6+}\text{O}_4$). The predicted leaching curve of this solid does not match well with the curve of the experimental leaching data, perhaps because Cr is reduced. Cr^{3+} has been shown to substitute for Al^{3+} in cement hydration products and is then part of the Ca Al hydrates matrix (Glasser, 1997). Cr solubility is then limited by these cement species rather than more common Cr oxides and hydroxides that would be found in the MINTEQA2 database.

CO₃²⁻ Modeling. Figure 60 depicts the leaching behavior of CO₃²⁻ modeled by controlling solids calcite (CaCO₃) and dolomite (CaMg(CO₃)₂). In neutral and alkaline pH ranges both calcite and dolomite exhibit leaching curves similar to the experiment data from the slab concrete samples. At acidic pHs the models for both of these solids predict a large increase in the leachability of CO₃²⁻ from neutral pH leaching, but the experimental data show a wide range of results at a pH of 5.0. Some samples increased in leachate concentration from a pH of 7.3 to a pH of 5.0, while others decreased. The modeling of calcite and dolomite remains satisfactory for the higher values of the experimental data at a pH of 5.0.

SO₄²⁻ Modeling. SO₄²⁻ leaching is modeled by gypsum (CaSO₄•2H₂O), barite (BaSO₄), and ettringite (Ca₆Al₂(SO₄)₃(OH)₁₂•26H₂O) (see figure 61). Barite was a good match of the modeling of the leaching data over the entire pH range. Gypsum modeling data were within concentration limits for most of the pH range but did not match well to the shape of the curve. Ettringite was not a well-modeled solid. Barite appears to be a controlling solid for SO₄²⁻ leaching (EPRI, 1987).

5.3.8.4 Conclusions

In conclusion:

1. There was a slight difference in the buffering capacity of the slab according to the sample location (e.g., northwest region or southeast region).
2. There was no influence of sample location with respect to extract concentration and solubility as a function of pH for each of the trace metals of concern.
3. As with the hydrated cement paste, calcite (CaCO₃) and dolomite (CaMg(CO₃)₂) are likely controlling solids for Ca leaching from the slab concrete.
4. As with the hydrated cement paste, dolomite is a likely controlling solid for Mg leaching.
5. Unlike the hydrated cement paste for which barium chromate (BaCrO₄) was better, barite (BaSO₄) is a likely controlling solid for Ba.
6. Modeling was successful only at higher pH values for CO₃²⁻ and indicated dolomite (CaMg(CO₃)₂) and calcite (CaCO₃) as likely controlling solids. (Dolomite and barite were found for the hydrated cement pastes.)
7. Geochemical modeling was not successful for Al, Si, Zn, Fe, and Cr.
8. The controlling solids identified for the slab concrete appear to be typical of cement-based leaching.

5.3.9. Low Liquid-Solid Ratio Leaching

This study was only carried out on sample O-SC (e.g., from the southeast region) because

of the similarity of behavior observed for different locations. pH and conductivity as a function of the liquid-solid ratio (e.g., LS ratio of 10, 5, 2, 1 and 0.5 ml/g of dry material) are presented in figure 62. Concentrations of the species of concern (e.g., Na, K, Cl, SO_4^{2-} and Ca) as a function of the liquid-solid ratio are presented in figure 63.

When LS ratio decreased from 10 to 0.5 ml/g of dry material, pH (see figure 62) increased slightly from 12.2 to 13.0 and conductivity increased from 6 mS/cm to 16 mS/cm, respectively. As with conductivity, Na (see figure 63), K (see figure 63), and Cl (see figure 63) concentration increased when the LS ratio decreased. SO_4^{2-} concentration appeared to be independent of the LS ratio (see figure 62). Ca concentration (see figure 63) decreased with the LS ratio, which was consistent with pH evolution (e.g., increasing pH) and $\text{Ca}(\text{OH})_2$ solubility. In addition, this result confirmed that there was no carbonation of the slab core in the southeast region.

Table 34 provides a comparison of the physical and chemical properties measured at LS of 5 ml/g dry and the estimated values for the pore water.

An open porosity of 7.4 percent was estimated from the moisture content and density of sample O-SC, assuming that the pores were completely filled with water (e.g., moisture of 3.2 percent and matrix density of 2.3 g/cm^3). This resulted in estimated pore water LS ratio of 0.03 ml/g dry. Empirical curve fits were then used to estimate pH and species concentrations to this LS ratio. Extrapolations resulted in estimated pH of 13.7 with concentrations of Na, K, Cl, SO_4^{2-} , and Ca of 12,000 mg/l, 19,800 mg/l, 410 mg/l, 6 mg/l and 110 mg/l, respectively. Charge balances on the pore water of the matrix indicated that anionic species other than OH^- (as obtained from pH measurement), Cl, and SO_4^{2-} were likely present in the matrix pore water.

These anionic species might likely be the CO_3^{2-} due to the large quantities of limestone type aggregates (e.g., 78 percent) present in the sample. If assumed of CO_3^{2-} , the concentration of these species was estimated to be 16,000 mg/l. Therefore, the ionic strength of the pore water was estimated to be 1.3 mol/l, which corresponds to an activity coefficient of 0.74 for ions with a charge number of 1 and 0.30 for ions with a charge number of 2 (Hemond and Fechner, 1994). In contrast, the estimated ionic strength for an LS ratio of 5 (e.g., typical LS ratio for most equilibrium batch tests) was 0.06 mol/l, which corresponds to an activity coefficient of 0.82 for ions with a charge number of 1 and 0.46 for ions with a charge number of 2 (Linde, 1996).

In conclusion:

1. Conductivity and Na, Cl, and K concentrations increase substantially with decreasing LS ratios.
2. pH increases from 12.4 to 13 with decreasing LS ratios.

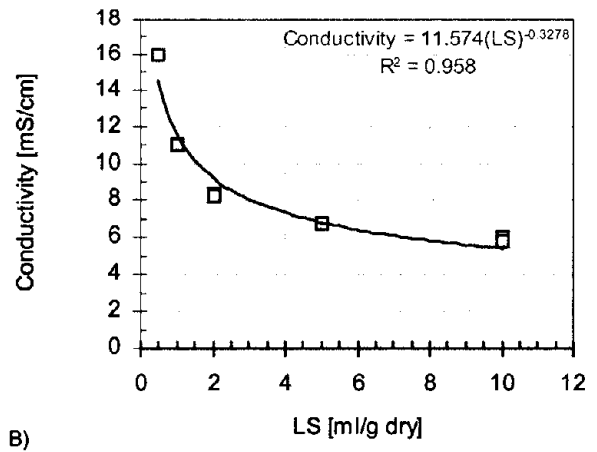
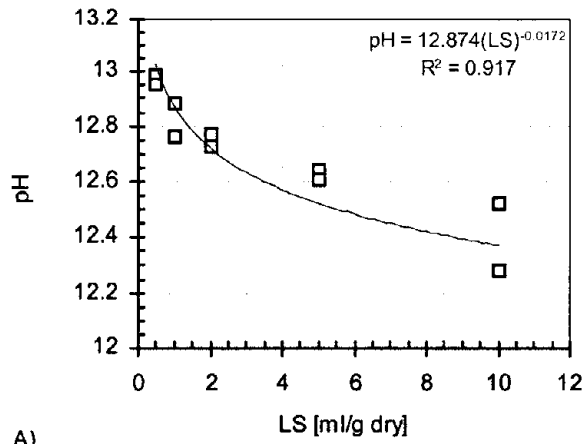
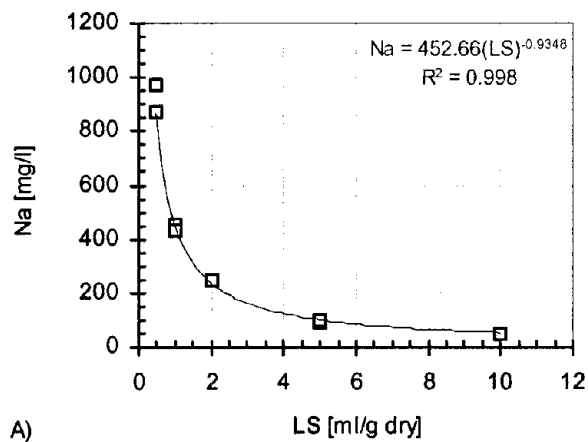
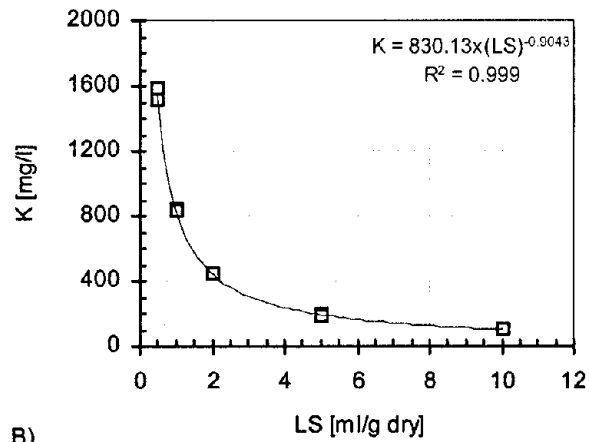


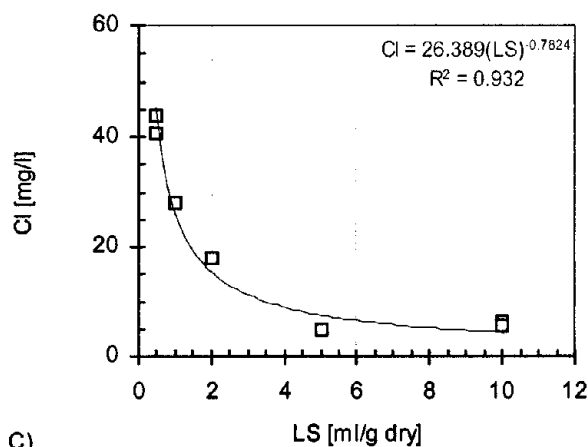
Figure 62: A) pH and B) conductivity as a function of LS ratio in the U.S. 20 concrete sample, southeast region (sample O-SC).



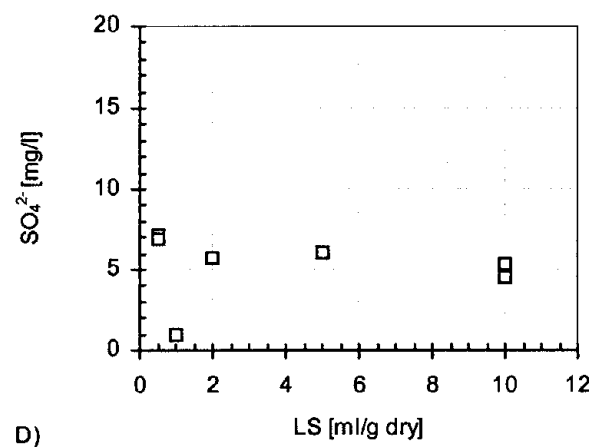
A)



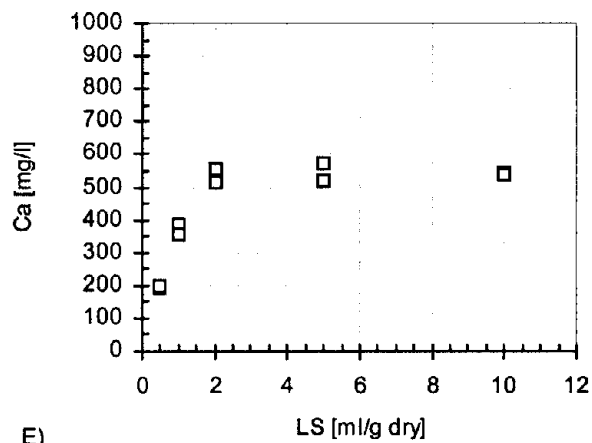
B)



C)



D)



E)

Figure 63: Major species concentration as a function of LS ratio:
A) Na, B) K, C) Cl, D) SO₄²⁻, and E) Ca in the U.S. 20 sample.

Table 34: Physical properties of U.S. 20 slab, southeast region (sample O-SC) and chemical properties of leachates and pore water.

Physical or chemical property	Material type
	O-SC (southeast region)
Moisture content (%)	3.2
Density (g/cm ³)	2.3
Open porosity (%)	7.4
LS estimated for p.w. ^a (ml/g)	0.03
pH (standard units)	
at LS 5	12.6
Estimated for p.w.	13.7
Na (mg/l)	
at LS 5	94
Estimated for p.w.	12,000
K (mg/l)	
at LS 5	193
Estimated for p.w.	19,800
Cl (mg/l)	
at LS 5	4.9
Estimated for p.w.	410
SO ₄ ²⁻ (mg/l)	
at LS 5	6
Estimated for p.w.	6
Ca (mg/l)	
at LS 5	550
Estimated for p.w.	110
Ionic strength (mol/l)	
at LS 5	0.06
Estimated for p.w.	1.3
Activity coefficient	
charge ± 1	
at LS 5	0.82
Estimated for p.w.	0.74
charge ± 2	
at LS 5	0.46
Estimated for p.w.	0.30

^a p.w. – pore water

3. SO_4^{2-} concentration appeared to be independent of the LS ratio.
4. Consistent with pH changes, Ca concentration (see figure 63) decreased with the LS ratio.
5. The estimated LS and pH of the pore water in the slab concrete were 0.03 ml/dry gram and 13.7 respectively.

5.3.10. Slab Constituent Availability

Cd, Cu, Ni, Pb, and Zn availability in sample I-JC (e.g., from the northwest region) and sample O-SC (e.g., from the southeast region), as determined by the RU-AV002.0 protocol (e.g., EDTA extraction at pH 7.0), is presented in figure 64. Similar to the comparisons provided for the mixture components (see section 5.1.7), in addition to availability results, total content as determined by neutron activation analyses or X-ray fluorescence (e.g., NAA or XRF) and maximum release (e.g., maximum reached using the RU-SR002.0 protocol for pH less than 3) are provided for comparison.

Availability values of Cd, Cu, and Pb by EDTA extraction at pH 7.0 exceeded the total content for the two locations as determined by NAA/XRF. This conflicting result most likely is attributable to analytical errors associated with measurement of trace metals in extracts containing high concentration of total salts, analyses performed near FAAS detection limits (e.g., 2 $\mu\text{g/l}$ for Cd, 3 $\mu\text{g/l}$ for Cu, 10 $\mu\text{g/l}$ for Pb) and possible sample heterogeneity. For the two locations, availability of Ni and Zn by EDTA extraction at pH 7.0 were found to be lower than the total contents as determined by NAA/XRF. Less than 2 percent and 25 percent of Ni and less than 70 percent and 84 percent of Zn were removed under RU-AV002.0 conditions for sample I-JC and sample O-SC, respectively.

In conclusion:

1. Availability values of Cd, Cu and Pb by EDTA extraction at pH 7.0 exceeded the total content for the two locations as determined by NAA/XRF.
2. Availability of Ni and Zn by EDTA extraction at pH 7.0 were found to be lower than the total contents as determined by NAA/XRF
3. The relative availabilities of Cu and Pb in the slab concrete differ from those found for the CFA-F and the CFA-C alone.

5.3.11. Monolithic Leaching

This study was carried out on cores (e.g., 7-C, 8-C, and 9-C) taken from the west central location of the slab. Three samples taken respectively from the middle part of cores 7-C, 8-C, and 9-C and one sample taken from the surface of core 9-C (e.g., surface exposed to traffic and climatic conditions) were examined.

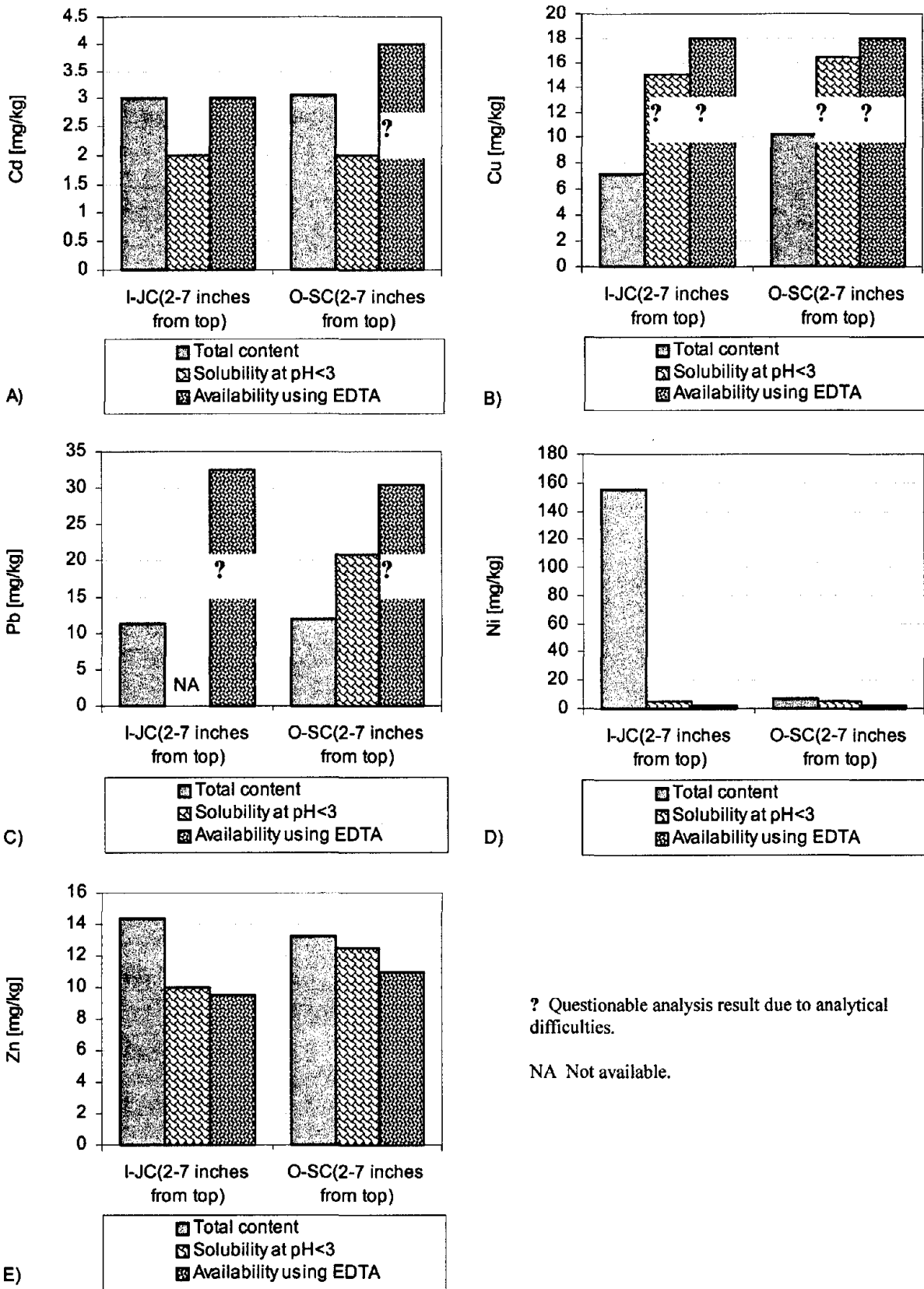


Figure 64: Comparison between total content, maximum of solubility at pH<3 and availability using EDTA extraction at pH 7 in the U.S. 20 samples, two locations.

With the labeling used, these samples are referred to in the following as 7-C (2.5 to 6.5 in from top), 8-C (2.5 to 6.5 in from top) and 9-C (2.5 to 6.5 in from top) for the three samples representing the bulk of the slab and 9-C (0 to 1.6 in from top) for the sample representing the top of the slab.

Results presented here were obtained from a cumulative leaching period of 20 mo with periodic renewals resulting in 21 extracts for the 3 samples from the bulk of the slab. A 10-mo cumulative leaching period resulted in 16 extracts for the sample from the top of the slab.

5.3.11.1 pH and Conductivity

Final leachate pH and conductivity obtained after each leaching interval are shown in figures 65a and 65b, respectively. For the three samples representing the bulk of the slab, final leachate pH ranging from 10.5 to 11.5 was controlled by the release of hydroxides and the duration of the leaching period except for the last extract. The leachate pH of the last renewal was abnormally low and showed scattering between the three samples, suggesting that reaction with atmospheric carbon dioxide infiltrating through leaching vessel seals might have occurred. For the sample representing the top of the slab, after 10 d of leaching, final leachate pHs were as much as 4 pH units lower than the ones obtained for the three samples representing the bulk of the slab, indicating that the surface at the top of the slab was partially carbonated. As with pH, leachate conductivity also was lower for the sample representing the top of the slab.

In conclusion:

1. Leachate pH and conductivity for slab concrete taken from near the top of the slab decreased much earlier than those for the bulk of the slab, indicating partial carbonation despite the lack of carbonation found using phenolphthalein (see section 5.3.7).

5.3.11.2 Leaching Behavior of Major Species

Flux and cumulative release of Na, K, SO_4^{2-} , Cl, and Ca as a function of time obtained for the three samples representing the bulk of the slab and the sample representing the top of the slab are shown in figures 66 and J-8 through J-11 in appendix J of volume II. Overall, good reproducibility was observed between the three samples representing the bulk of the slab.

Na Release. The cumulative release of Na (figure 66) from the three samples representing the bulk of the slab was low. After 17 mo of leaching with periodic renewals, less than 7 percent of the total Na content released for sample 7-C (2.5 to 6.5 in from top) and less than 9 percent for samples 8-C (2.5 to 6.5 in from top) and 9-C (2.5 to 6.5 in from top), indicating significant retention of Na. In addition, the Na flux was diffusion controlled with no depletion observed. A much greater Na flux was seen for the top of the slab with 23 percent of the total content in Na (e.g., total content as determined from the bulk of the slab) released after 10 mo of leaching. Thus, the flux of Na from 9-C (0 to 1.6 in from top) was about 3 times greater than that of 7-C (2.5 to 6.5 in from top), 8-C (2.5 to 6.5 in from top) and 9-C (2.5 to 6.5

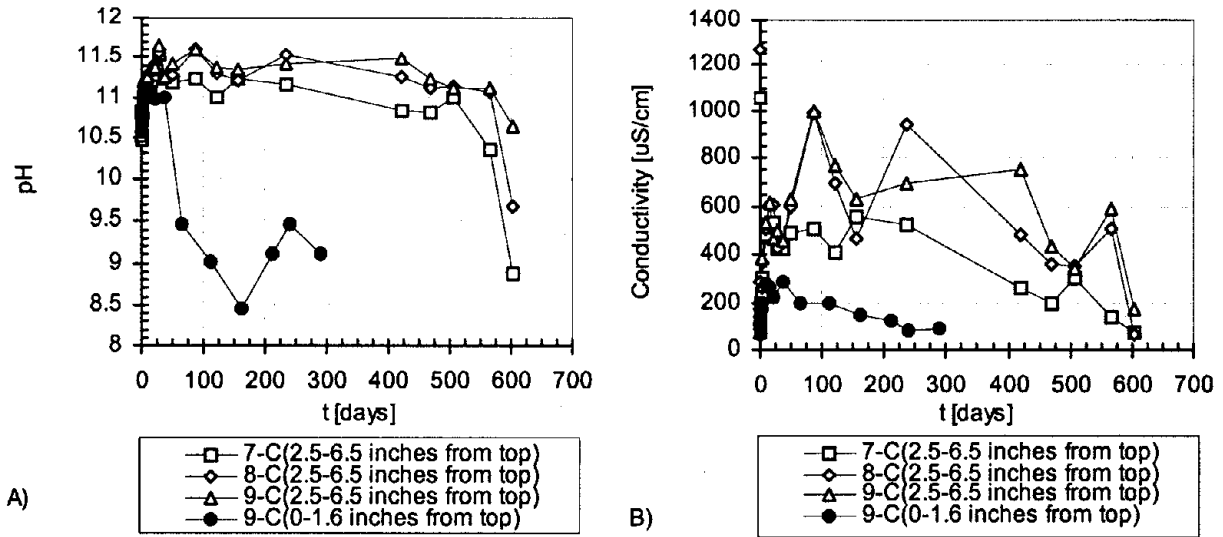


Figure 65: A) Leachate pH and B) leachate conductivity obtained after each leaching interval of three samples representing the bulk of the U.S. 20 slab and a sample representing the surface.

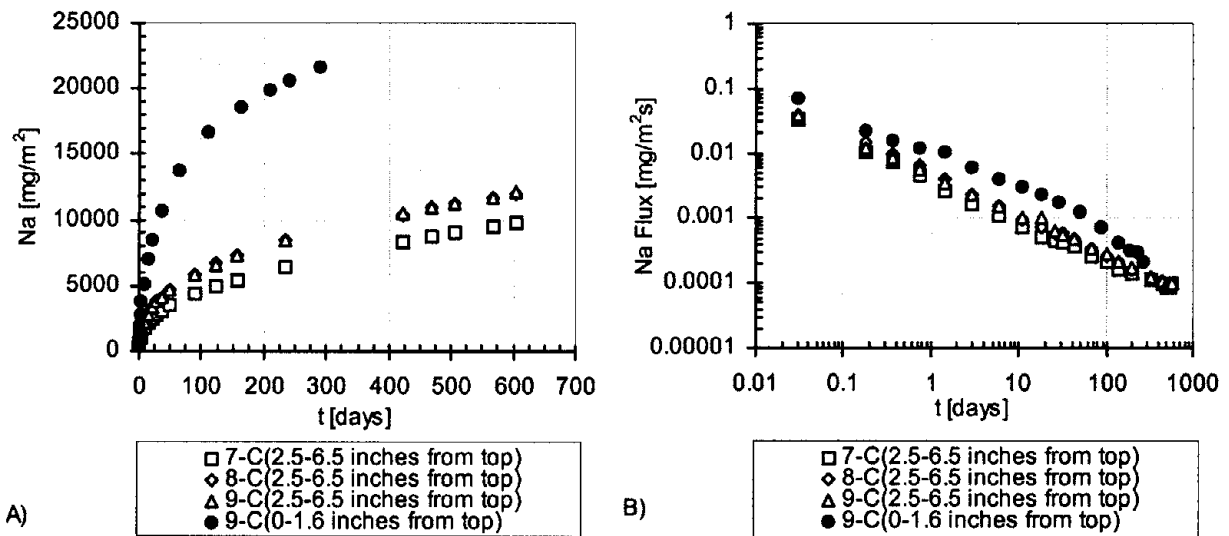


Figure 66: Na release for three samples representing the bulk of the U.S. 20 slab and a sample representing the surface: A) cumulative mass released in mg/m^2 ; B) flux released in $\text{mg}/\text{m}^2\text{s}$.

in from top). The difference observed in Na leaching behavior between the two vertical locations within the slab might indicate (i) Na accumulation at the surface of the slab from road salting activities over the 10 yr of exposure to traffic and climatic conditions and/or (ii) change in porosity at the surface of the slab from aging.

K Release. The cumulative release of K from the three samples representing the bulk of the slab was low. After 17 mo of leaching with periodic renewals, less than 12 percent, 13 percent and 15 percent of the total content in K was released from samples 7-C (2.5 to 6.5 in from top), 8-C (2.5 to 6.5 in from top) and 9-C (2.5 to 6.5 in from top), respectively, indicating significant retention of K in the materials. In addition, the release flux of K seemed to be diffusion controlled with no depletion observed over the 20 mo of leaching. As with Na, a greater release of K was observed from the sample representing the top of the slab with approximately 22 percent of the total content in K released after 10 mo of leaching. However, slight differences in the flux of K could be observed with a flux slightly higher for 9-C (0 to 1.6 in from top). The difference in K leaching behavior observed between the two vertical locations within the slab might indicate (i) K accumulation at the surface of the slab over the 10 yr of exposure to traffic and climatic conditions and/or (ii) change in porosity at the surface of the slab from aging.

Cl Release. The cumulative release of Cl from the sample representing the top of the slab exceeded the Cl total content (e.g., total content as determined from the bulk of the slab) after 8 d of leaching, which represented only 23 percent of the total content after 17 mo of leaching for the three samples representing the bulk of the slab. Thus, the flux of Cl from 9-C (0 to 1.6 in from top) was as much as 30 times higher than that of 7-C (2.5 to 6.5 in from top), 8-C (2.5 to 6.5 in from top) and 9-C (2.5 to 6.5 in from top). This result indicated that significant Cl accumulation at the surface of the slab from road salting activities had occurred over the 10 yr of exposure to traffic and climatic conditions.

SO₄²⁻ Release. As with Na, K, and Cl, the cumulative release of SO₄²⁻ from the sample representing the top of the slab was much greater than that observed from the three samples representing the bulk of the slab (e.g., 150 mg/kg of sample and 50 mg/kg of sample, respectively after 4 mo of leaching). After 15 d of leaching, the release flux of SO₄²⁻ from the sample representing the top of the slab decreased towards the release flux obtained from the three samples representing the bulk of the slab. This result might indicate a surface layer effect.

Ca Release. The cumulative release of Ca from the three samples representing the bulk of the slab was higher than the cumulative release of Ca from the sample representing the top of the slab. This result was in good agreement with pH observations and suggested that the surface of the slab was partially carbonated.

In conclusion:

1. The flux of Na, K, Cl, and SO₄²⁻ from the top of the slab was greater than that from the bulk of the slab.
2. Cl release from the top of the slab exceeded the Cl available in the bulk of the slab indicating greater amounts of Cl in the top of the slab from road salting operations.

3. Increased fluxes from the top of the slab correlates with the greater degree of cracking found there.
4. The release of Ca from the top of the slab was lower than that from the bulk of the slab correlating with the possibility of greater carbonation there in agreement with findings from pH (see section 5.3.8.1) despite the findings of the phenolphthalein testing (see section 5.3.7).

5.3.11.3 Leaching Behavior of Trace Metals

Flux and cumulative release of Cd, Cu, and Pb as a function of time obtained for the three samples representing the bulk of the slab are shown in figures 67 through 69. Cd, Cu, and Pb concentrations measured in the leachates are also shown and compared with graphite furnace detection limits. Only the initial 11 extracts corresponding to a cumulative leaching time of 36 d have been analyzed. Further analysis was not carried out because of the extremely low concentrations observed in the initial extracts. For similar reasons, trace metal concentrations were not measured in extracts from the sample representing the surface of the slab. All the concentrations measured in the leachates were close to or below the GFAAS detection limits and therefore, no interpretation of the results was possible.

Average concentrations of major species and trace metals measured in the leachates are given in table 35. In all cases, the concentrations measured were close to or below average "natural" ground water concentration (e.g., data from (van der Sloot et al., 1985)). Although these ground water results are not from the vicinity of the test slab, they do indicate that the extract concentrations are of the same order of magnitude as unimpacted ground waters.

5.3.11.4 Conclusions

In conclusion:

1. There were significant differences in leaching behavior of major species between the two studied vertical locations within the slab (e.g., bulk and top): much greater release of the highly soluble species (e.g., Na, K, Cl) and less release of Ca obtained for the surface of the slab, suggesting possible species accumulation at the surface, microcracking, change in porosity, and/or partial carbonation of the slab surface.
2. All the concentrations of the trace metals of concern measured in the monolith leach test leachates were close to or below the detection limits.
3. Road salting may have influenced the release behavior of Cl.
4. Surficial carbonation might have a potential effect on trace metal release.

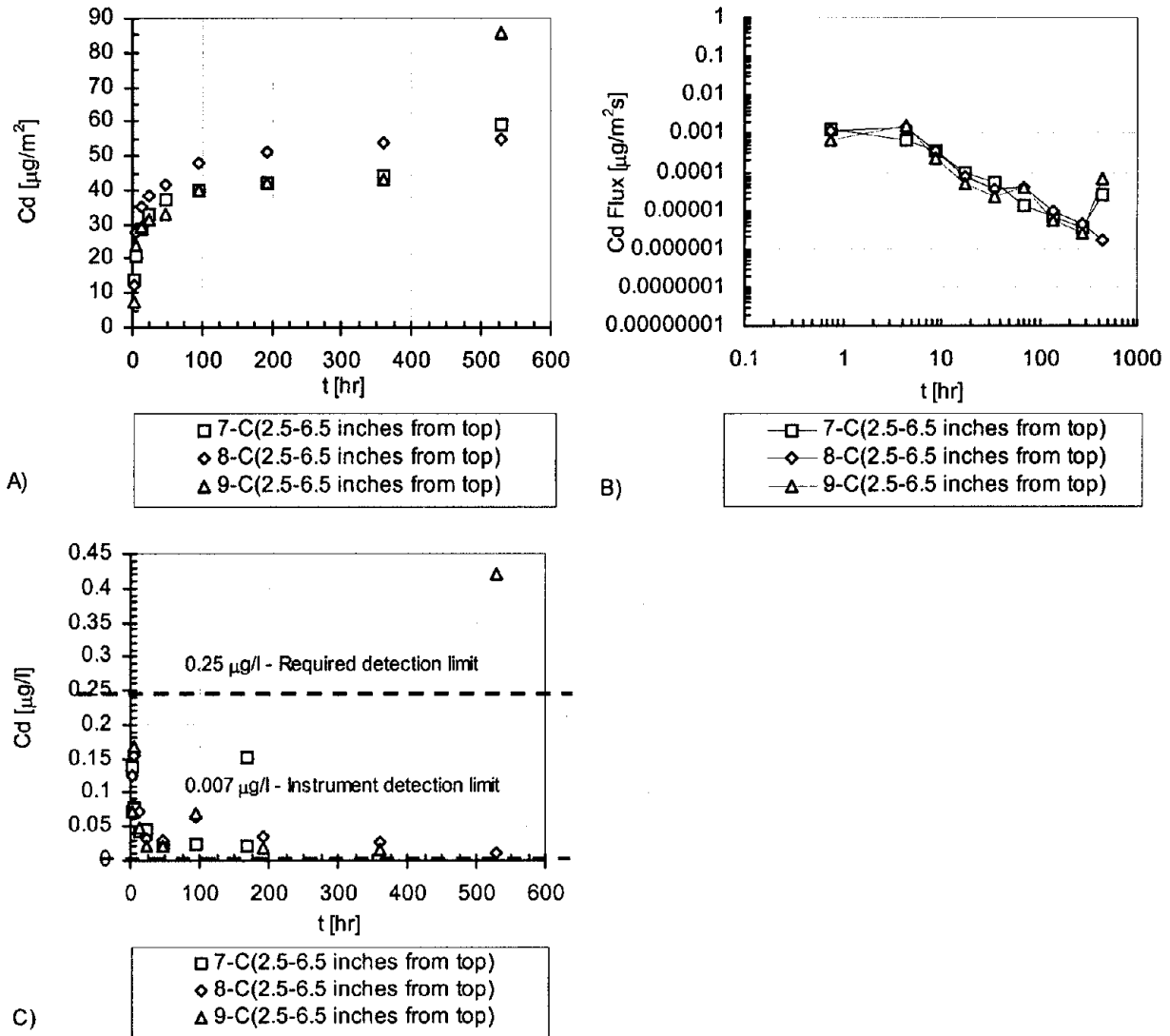


Figure 67: Cd release from samples representing the bulk of the U.S. 20 slab: A) cumulative mass released in $\mu\text{g}/\text{m}^2$; B) flux released in $\mu\text{g}/\text{m}^2\text{s}$; and C) leachate concentrations in $\mu\text{g}/\text{l}$.

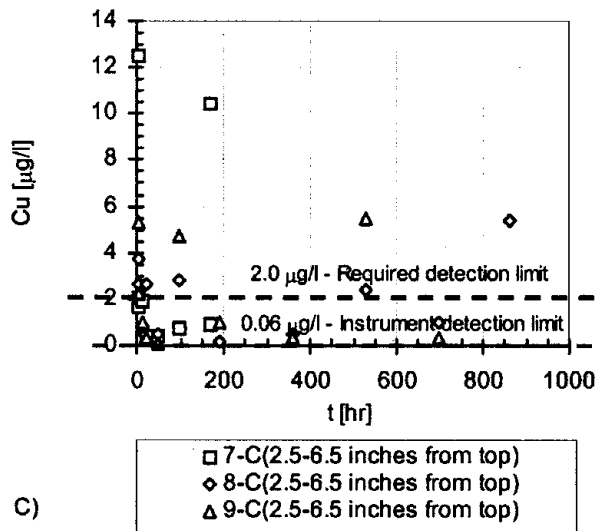
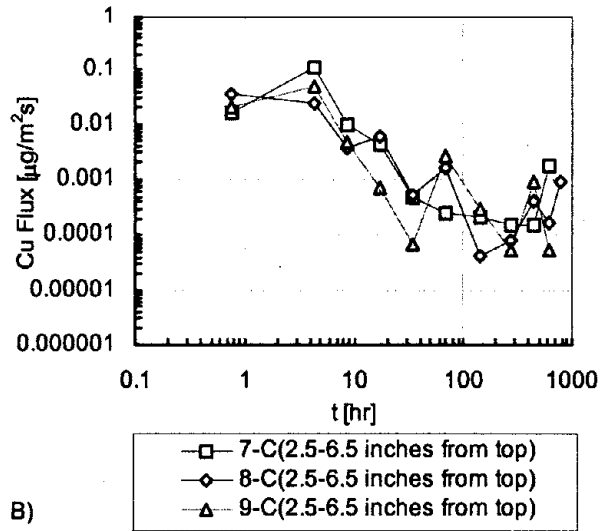
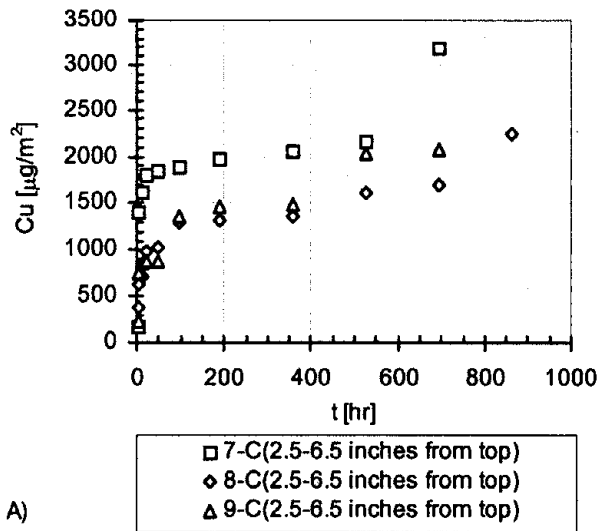
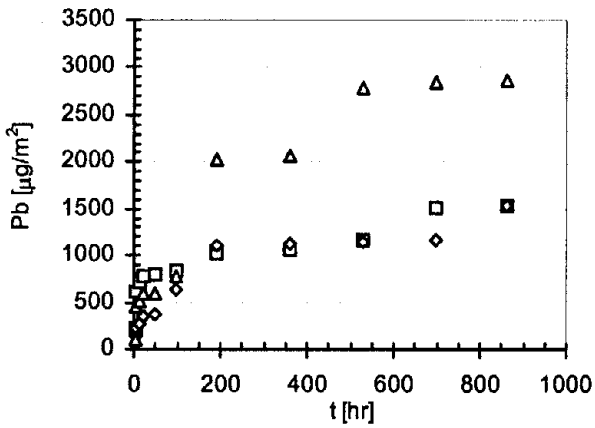
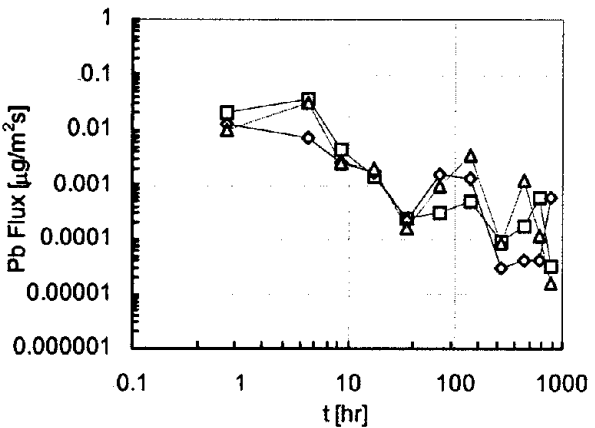


Figure 68: Cu release from samples representing the bulk of the U.S. 20 slab: A) cumulative mass released in $\mu\text{g}/\text{m}^2$; B) flux released in $\mu\text{g}/\text{m}^2\text{s}$; and C) leachate concentrations in $\mu\text{g}/\text{l}$.



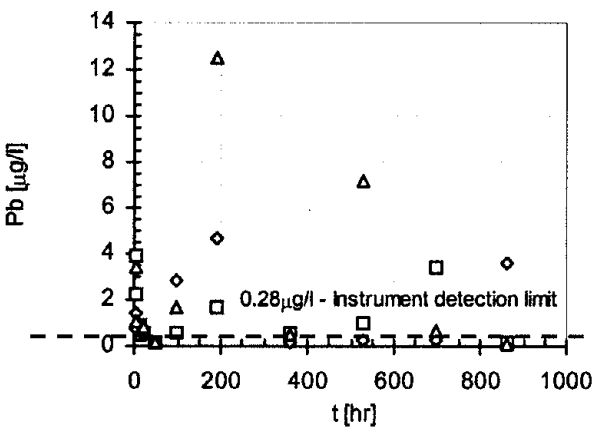
□ 7-C(2.5-6.5 inches from top)
 ◇ 8-C(2.5-6.5 inches from top)
 △ 9-C(2.5-6.5 inches from top)

A)



□ 7-C(2.5-6.5 inches from top)
 ◇ 8-C(2.5-6.5 inches from top)
 △ 9-C(2.5-6.5 inches from top)

B)



□ 7-C(2.5-6.5 inches from top)
 ◇ 8-C(2.5-6.5 inches from top)
 △ 9-C(2.5-6.5 inches from top)

C)

Figure 69: Pb release from samples representing the bulk of the U.S. 20 slab:
 A) cumulative mass released in $\mu\text{g}/\text{m}^2$; B) fFlux released in $\mu\text{g}/\text{m}^2\text{s}$; and
 C) leachate concentrations in $\mu\text{g}/\text{l}$.

Table 35: Major species and trace metal concentrations in contact solutions of U.S. 20 slab samples – comparison with ground water.

	Bulk of the slab	Surface of the slab	Ground water ^c
Ca [mg/l] ^a	5-90	2-20	20-120
Na [mg/l] ^a	1.2-20	2-35	20-70
K [mg/l] ^a	3-35	2-30	2-15
SO ₄ ²⁻ [mg/l] ^a	0.1-1.7	1-10	26-100
Cl [mg/l] ^a	0.6-0.9	2-20	30-100
pH ^a	10.4-11.6	8-11.5	3.2-7.7
Pb [μg/l] ^b	0.2-12	NA	5-10
Cd [μg/l] ^b		NA	
Cu [μg/l] ^b	0.1-13	NA	5-10

NA not available

^a 20 mo (e.g., 21 extracts) for the bulk of the slab; 10 mo (e.g., 16 extracts) for the surface of the slab

^b 36 d, 11 extracts

^c van der Sloot et al., 1985

5.3.12. Release Modeling

The one-dimensional diffusion model was used to interpret the release of Na, K, Cl, and Ca from the U.S. 20 concrete samples. During the time scale of the laboratory testing (e.g., 10 mo for the sample representing the surface of the slab and 20 mo for the samples representing the bulk of the slab), no depletion of these species within the concrete samples was observed. For each species of concern, three different observed diffusivities (e.g., D_{obs1} , D_{obs2} and D_{obs3}) were determined. D_{obs1} was calculated assuming that the initial leachable concentration C_D was the total content of the species of concern. This also implies an assumption of a homogeneous matrix. D_{obs2} was calculated assuming that (i) the initial leachable concentration C_D was the species content provided only by the cement and the CFA-C, and (ii) the U.S. 20 slab had the same mix design and same constituent total content of individual mix components as the CFA-C mix. Finally, D_{obs3} was calculated with the D_{obs2} assumptions and (iii) the aggregates were inert and uniformly distributed within the material and, (iv) the flux was only provided by the fraction of the surface² of the sample not occupied by the aggregates. Thus, while D_{obs1} and D_{obs2} correspond to observed diffusivities through the overall matrix (e.g., binder made of cement and CFA-C and aggregates), D_{obs3} corresponds to an observed diffusivity only through the binder (e.g., cement and CFA-C). Initial leachable concentrations and observed diffusivities of the three samples taken from the bulk of the slab and the sample representing the surface of the slab are compared in tables 36 through 39, for Na, K, Cl, and Ca, respectively. Ratios of observed diffusivity to molecular diffusivity are also compared with estimates of matrix tortuosity calculated using the Millington-Quirk relationship (Millington et al., 1971) (e.g., $\tau_{MQ} = \varepsilon^{-4/3}$, where τ_{MQ} and ε are tortuosity and matrix porosity, respectively).

Na Modeling. Similar Na observed diffusivity were calculated for the three samples representing the bulk of the slab while a greater observed diffusivity (e.g., about 10 times greater) was calculated for the sample representing the surface of the slab (see table 36). The difference in Na observed diffusivity between the two vertical locations within the slab might be the result of change in porosity at the surface of the slab from aging (e.g., 10 yr of exposure to traffic and climatic conditions). Low Na observed diffusivities (e.g., on the order of 10^{-14} m²/s for the three samples representing the bulk of the slab and 10^{-13} m²/s for the sample representing the surface of the slab) were determined from the Na total content, leading to ratios of observed diffusivity to molecular diffusivity for Na as much as three orders of magnitude greater than the estimated tortuosity using the Millington-Quirk relationship (e.g., $\tau_{MQ} = 30$). This comparison indicated that significant retention of Na occurred within the concrete material and the assumption of a homogeneous matrix was not appropriate. When considering only the Na content provided by the cement and the CFA-C, the diffusivity results (e.g., D_{obs2} and D_{obs3}) changed by two orders of magnitude leading to more realistic diffusivity values (e.g., on the order of 10^{-12} m²/s for the three samples representing the bulk of the slab and 10^{-11} m²/s for the sample representing the surface of the slab). Diffusivity results slightly increased (D_{obs3} were 3 times greater than D_{obs2}) when calculations accounted for the surface of the matrix not occupied by the aggregates. Ratios of observed diffusivity to molecular diffusivity for Na were

2 As a first approach, it was assumed that 57.5 percent of the surface of the material was non-occupied by the aggregates (42.5 percent of coarse aggregates were used in the mix design).

Table 36: Parameter estimates for the release of Na from the one-dimensional diffusion model – U.S. 20 slab samples.

	Bulk of the slab			Surface of the slab
	7-C (2.3-6.5 in from top)	8-C (2.3-6.5 in from top)	9-C (2.3-6.5 in from top)	9-C (0-4.2 in from top)
C_0^a [(mg elemental species from <u>cement</u> , <u>aggregates</u> and <u>CFA-C</u>) / (kg of concrete product)]	3600	3600	3600	3600
$D_{obs 1}^b$ [m ² /s]	$3.3 \cdot 10^{-14}$	$5.7 \cdot 10^{-14}$	$5.2 \cdot 10^{-14}$	$41.0 \cdot 10^{-14}$
$\frac{D_{m,Na}^c}{D_{obs 1}}$	40,000	23,200	25,400	3,220
C_0^d [(mg elemental species from <u>cement</u> and <u>CFA-C</u>) / (kg of concrete product)]	500	500	500	500
$D_{obs 2}^e$ [m ² /s]	$1.7 \cdot 10^{-12}$	$2.9 \cdot 10^{-12}$	$2.6 \cdot 10^{-12}$	$21.0 \cdot 10^{-12}$
$\frac{D_{m,Na}}{D_{obs 2}}$	780	460	510	65
$D_{obs 3}^f$ [m ² /s]	$5.0 \cdot 10^{-12}$	$8.8 \cdot 10^{-12}$	$8.0 \cdot 10^{-12}$	$63.0 \cdot 10^{-12}$
$\frac{D_{m,Na}}{D_{obs 3}}$	270	150	165	20
$\tau_{MQ} = \epsilon^{-4/3} g$	30	30	30	30

^a Total content in Na

^b Calculated assuming that the initial leachable concentration C_0 was the total content

^c $D_{m,Na} = 1.32 \cdot 10^{-9}$ m²/s (Linde, 1996)

^d Based on CFA-C mix design and total content of individual mix components (e.g., cement and CFA-C)

^e Calculated assuming that the initial leachable concentration C_0 was the species content provided only by the cement and the CFA-C

^f Calculated assuming that the initial leachable concentration C_0 was the species content provided only by the cement and the CFA-C and the flux was only provided by the fraction of the surface of the sample non-occupied by the aggregates

^g Millington-Quirk relationship (Millington et al., 1971). The porosity was estimated from moisture content and matrix density

Table 37: Parameter estimates for the release of K from the one-dimensional diffusion model – U.S. 20 slab samples.

	Bulk of the slab			Surface of the slab
	7-C (2.3-6.5 in from top)	8-C (2.3-6.5 in from top)	9-C (2.3-6.5 in from top)	9-C (0-4.2 in from top)
C_0^a [(mg elemental species from cement, aggregates and CFA-C) / (kg of concrete product)]	3500	3500	3500	3500
$D_{obs 1}^b$ [m ² /s]	$1.1 \cdot 10^{-13}$	$2.7 \cdot 10^{-13}$	$2.1 \cdot 10^{-13}$	$4.4 \cdot 10^{-13}$
$\frac{D_{m,K}^c}{D_{obs 1}}$	17,800	7,260	9,400	4,460
C_0^d [(mg elemental species from cement and CFA-C) / (kg of concrete product)]	820	820	820	820
$D_{obs 2}^e$ [m ² /s]	$2.0 \cdot 10^{-12}$	$4.9 \cdot 10^{-12}$	$3.8 \cdot 10^{-12}$	$8.1 \cdot 10^{-12}$
$\frac{D_{m,K}}{D_{obs 2}}$	980	400	520	240
$D_{obs 3}^f$ [m ² /s]	$6.1 \cdot 10^{-12}$	$15.0 \cdot 10^{-12}$	$12.0 \cdot 10^{-12}$	$25.0 \cdot 10^{-12}$
$\frac{D_{m,K}}{D_{obs 3}}$	320	130	170	80
$\tau_{MO} = \epsilon^{-4/3} g$	30	30	30	30

^a Total content in K

^b Calculated assuming that the initial leachable concentration C_0 was the total content

^c $D_{m,K} = 1.96 \cdot 10^{-9}$ m²/s (Linde, 1996)

^d Based on CFA-C mix design and total content of individual mix components (e.g., cement and CFA-C)

^e Calculated assuming that the initial leachable concentration C_0 was the species content provided only by the cement and the CFA-C

^f Calculated assuming that the initial leachable concentration C_0 was the species content provided only by the cement and the CFA-C and the flux was only provided by the fraction of the surface of the sample non-occupied by the aggregates

^g Millington-Quirk relationship (Millington et al., 1971). The porosity was estimated from moisture content and matrix density

Table 38: Parameter estimates for the release of Cl from the one-dimensional diffusion model – U.S. 20 slab samples.

	Bulk of the slab			Surface of the slab
	7-C (2.3-6.5 in from top)	8-C (2.3-6.5 in from top)	9-C (2.3-6.5 in from top)	9-C (0-4.2 in from top)
C_0^a [(mg elemental species from cement, aggregates and CFA-C) / (kg of concrete product)]	110	110	110	110
$D_{obs 1}^b$ [m ² /s]	$5.1 \cdot 10^{-12}$	$4.8 \cdot 10^{-12}$	$8.1 \cdot 10^{-12}$	$1.7 \cdot 10^{-10}$
$\frac{D_{m,Cl}^c}{D_{obs 1}}$	400	420	250	12
$\tau_{MO} = \epsilon^{-4/3 d}$	30	30	30	30

^a Total content in Cl

^b Calculated assuming that the initial leachable concentration C_0 was the total content

^c $D_{m,Cl} = 2.03 \cdot 10^{-9}$ m²/s (Linde, 1996)

^d Millington-Quirk relationship (Millington et al., 1971). The porosity was estimated from moisture content and matrix density

Table 39: Parameter estimates for the release of Ca from the one-dimensional diffusion model – U.S. 20 slab samples.

	Bulk of the slab			Surface of the slab
	7-C (2.3-6.5 in from top)	8-C (2.3-6.5 in from top)	9-C (2.3-6.5 in from top)	9-C (0-4.2 in from top)
C_0^a [(mg elemental species from cement, aggregates and CFA-C) / (kg of concrete product)]	372,200	372,200	372,200	372,200
D_{obs1}^b [m ² /s]	$2.9 \cdot 10^{-16}$	$3.3 \cdot 10^{-16}$	$3.6 \cdot 10^{-16}$	$0.7 \cdot 10^{-16}$
$\frac{D_{m,K}^c}{D_{obs1}}$	$2.8 \cdot 10^6$	$2.4 \cdot 10^6$	$2.3 \cdot 10^6$	$11.0 \cdot 10^6$
C_0^d [(mg elemental species from cement and CFA-C) / (kg of concrete product)]	69,100	69,100	69,100	69,100
D_{obs2}^e [m ² /s]	$8.4 \cdot 10^{-15}$	$9.6 \cdot 10^{-15}$	$10.0 \cdot 10^{-15}$	$2.1 \cdot 10^{-15}$
$\frac{D_{m,Ca}}{D_{obs2}}$	$9.4 \cdot 10^4$	$8.3 \cdot 10^4$	$7.7 \cdot 10^4$	$38.0 \cdot 10^4$
D_{obs3}^f [m ² /s]	$2.5 \cdot 10^{-14}$	$2.9 \cdot 10^{-14}$	$3.1 \cdot 10^{-14}$	$0.7 \cdot 10^{-14}$
$\frac{D_{m,Ca}}{D_{obs3}}$	$3.1 \cdot 10^4$	$2.8 \cdot 10^4$	$2.6 \cdot 10^4$	$12.6 \cdot 10^4$
$\tau_{MO} = \epsilon^{-4/3} g$	30	30	30	30

^a Total content in Ca

^b Calculated assuming that the initial leachable concentration C_0 was the total content

^c $D_{m,Ca} = 7.92 \cdot 10^{-10}$ m²/s (Linde, 1996)

^d Based on CFA-C mix design and total content of individual mix components (e.g., cement and CFA-C)

^e Calculated assuming that the initial leachable concentration C_0 was the species content provided only by the cement and the CFA-C

^f Calculated assuming that the initial leachable concentration C_0 was the species content provided only by the cement and the CFA-C and the flux was only provided by the fraction of the surface of the sample non-occupied by the aggregates

^g Millington-Quirk relationship (Millington et al., 1971). The porosity was estimated from moisture content and matrix density

then as much as 10 times greater than the estimated tortuosity using the Millington-Quirk relationship for the three samples representing the bulk of the slab, while relatively close for the sample representing the surface of the slab.

K Modeling. K observed diffusivities of the same order of magnitude were calculated for the three samples representing the bulk of the slab and the sample representing the surface of the slab (see table 37). K observed diffusivity of sample 7-C (2.5 to 6.5 in from top) was 2 times less than that of samples 8-C (2.5 to 6.5 in from top) and 9-C (2.5 to 6.5 in from top). K observed diffusivity of sample 9-C (0 to 1.6 in from top) was 2 times greater than that of samples 8-C (2.5 to 6.5 in from top) and 9-C (2.5 to 6.5 in from top). As with Na, low K observed diffusivities (e.g., of the order of 10^{-13} m²/s) were determined from the K total content, leading to ratios of observed diffusivity to molecular diffusivity for K as much as three orders of magnitude greater than the estimated tortuosity using the Millington-Quirk relationship (e.g., τ_{MQ} of 30). This comparison indicated that significant retention of K occurred within the concrete material and the implied assumption of a homogeneous matrix was not appropriate. When considering only the K content provided by the cement and the CFA-C, the diffusivity results (e.g., $D_{obs 2}$ and $D_{obs 3}$) changed by an order of magnitude. Diffusivity results slightly increased ($D_{obs 3}$ were 3 times greater than $D_{obs 2}$) when calculations were done by accounting only for the surface of the matrix non-occupied by the aggregates. Ratios of observed diffusivity to molecular diffusivity for K were then as much as 10 times greater than the estimated tortuosity using the Millington-Quirk relationship.

Cl Modeling. Similar Cl observed diffusivity on the order of 10^{-12} m²/s were calculated for the 3 samples representing the bulk of the slab while a much greater observed diffusivity (e.g., 2 orders of magnitude greater) was calculated for the sample representing the surface of the slab (see table 38). The significant difference in Cl observed diffusivity between the two vertical locations within the slab can not only be explained by change in porosity at the surface of the slab, but might also result in change of the initial leachable concentration C_D due to road salting activities over the 10 yr of exposure to traffic and climatic conditions. When considering only the Cl provided by the cement and the CFA-C, unrealistic diffusivity data (e.g., diffusivity data greater than the Cl molecular diffusivity³) were obtained. This might be due to a low Cl total content of the material (e.g., 110 mg/kg) and uncertainties in the Cl content of individual mix components. Indeed, it was assumed that the U.S. 20 slab had the same mix design and same constituent total content of individual mix components as the CFA-C mix. However, total contents of individual mix components of the U.S. 20 slab prepared 10 yr ago could have been different.

Ca Modeling. Similar Ca observed diffusivity was calculated for the three samples representing the bulk of the slab while a lower observed diffusivity (e.g., an order of magnitude lower) was calculated for the sample representing the surface of the slab (see table 39). The difference in Ca observed diffusivity between the two vertical locations within the slab might indicate that the surface of the slab was partially carbonated. Low Ca observed diffusivities (e.g., of the order of 10^{-16} m²/s for the 3 samples representing the bulk of the slab and 10^{-17} m²/s for the

3 Cl molecular diffusivity: $2.03 \cdot 10^{-9}$ m²/s [Linde, 1996].

sample representing the surface of the slab) were calculated using the Ca total content, Leading to ratios of observed diffusivity to molecular diffusivity for Ca as much as 6 orders of magnitude greater than the estimated tortuosity using the Millington-Quirk relationship (e.g., τ_{MQ} of 30). When considering only the Ca content provided by the cement and the CFA-C, the diffusivity results (e.g., $D_{obs\ 2}$ and $D_{obs\ 3}$) changed by an order of magnitude. Diffusivity results slightly increased ($D_{obs\ 3}$ were 3 times greater than $D_{obs\ 2}$) when calculations were done by accounting only for the surface of the matrix non-occupied by the aggregates. Ratios of observed diffusivity to molecular diffusivity for Ca were then three orders of magnitude greater than the estimated tortuosity using the Millington-Quirk relationship. This discrepancy was consistent with the large interaction of Ca with the concrete matrix. Indeed Ca is found in the major products of cement hydration that include Ca hydroxide, Ca silicate hydroxide (CSH), and Ca sulfoaluminates and for which solubility differs by orders of magnitude.

In conclusion:

1. Na and K were substantially retained in the bulk of the slab.
2. Cl calculations led to unrealistic diffusivity data, perhaps due to Cl provided by road salting operations.
3. Diffusivity calculations involving Ca confirm its interaction with the concrete matrix.
4. It is inappropriate to assume the matrix is homogeneous when calculating diffusivities.
5. Considering only the Na content provided by the cement and the CFA-C lead to more realistic diffusivity values.
6. There were significant differences in observed diffusivities of major species between the two studied vertical locations within the slab (e.g., bulk and top): much greater Na, K, and Cl observed diffusivities and lower Ca observed diffusivity obtained for the surface of the slab.
7. The three different observed diffusivities calculated for each species of concern showed the importance of correctly selecting the initial leachable concentration, C_D , used in the diffusion model to estimate the observed diffusivity and highlighted the limits of the diffusion model in the case of heterogeneous porous materials.

5.4. Evaluation of $2^3 + 3$ Experimental Design for Aged CFA-C Prisms

5.4.1. Compressive Strength

Results from compressive strength testing on CFA-C prisms are listed in table 40.

Table 40: Post-treatment compressive strength of laboratory-created concrete.

Compressive strength	MPa
C(NNN)01	54.1
C(NNN)02	50.4
C(NNN)03	53.9
C(NHN)01	56.1
C(NHN)02	51.4
C(NHN)03	57.1
C(HNN)01	40.0
C(HNN)02	40.0
C(HNN)04	44.6
C(HHN)01	38.7
C(HHN)02	43.5
C(HHN)03	42.8
C(NNH)01	46.8
C(NNH)02	52.1
C(NNH)03	48.2
C(NHH)01	46.9
C(NHH)02	44.4
C(NHH)03	49.7
C(HNH)01	34.4
C(HNH)02	31.8
C(HNH)03	36.3
C(HHH)01	34.6
C(HHH)02	31.1
C(HHH)03	25.9
C(LL)01	28.6
C(LL)02	29.8
C(LL)03	32.2
C(LL)17	26.1
C(LL)18	34.2
C(LL)19	31.5
C(LL)33	33.9
C(LL)34	27.7
C(LL)35	28.8
(LL) Mean	30.3 ± 1.9

5.4.1.1 ANOVA

Tests on the CFA-C found the C(NHN) samples to have the highest average compressive strengths. The group of C(LLL) prisms had the lowest average compressive strengths. However, C(HHH)03 had the lowest recorded strength for a single sample of the CFA-C mix.

An ANOVA performed on the prism compressive strength data revealed a large negative effect due to AA and FT cycling (see table K-1 in appendix K in volume II). The reference F-values were 4.3 and 7.8 for 95 and 99 percent confidence, respectively. CL had no apparent effect. The curvature effect indicates that the model does not follow a linear relationship.

5.4.1.2 Main Effects

CFA-C concrete showed, with 99 percent confidence, large negative effects from AA and FT. There was no apparent effect from CL.

The negative effect from AA suggests that compressive strengths were decreased due to a deleterious reaction brought about or accelerated by the elevated temperatures. Possible reactions include delayed ettringite formation, alkali-silica reaction (alkali-aggregate reaction), and sulfate attack. The highest compressive strengths were measured on samples that had received no AA.

The negative effect from FT was an expected result for concretes with total air contents of 2.9 to 4.1 percent. The American Concrete Institute (ACI) recommendation for pavements with 19-mm largest nominal aggregate size and severe exposure is a minimum of 6 percent total air (Kosmatka and Panarese, 1988). It is likely that the developed air system was not sufficient to protect against the stresses induced by freeze-thaw cycling.

The lack of effect from CL was probably a result of the varied compressive strengths produced from AA, the first step in the accelerated aging method. CL increased the strengths of some samples and weakened others (table 41 and see section 4.3.3). Samples that received high levels of AA had lower compressive strengths than the samples that received no AA. These lower strength samples were the limiting factor in the determination of cyclic loading parameters. Research has shown that cyclically loading concrete below 50 percent of its capacity can actually increase its compressive strength (Pons and Maso, 1984; Nelson et al., 1988). A 4 percent increase in strength was measured on C(NHN) samples (see table 41). This value correlates well with work by others on low-cycle fatigue loading (Nelson et al., 1988). Therefore, it is likely that CL caused a positive effect on some samples and a negative effect on others. Their sum resulted in a net effect of zero.

5.4.1.3 Interactions

Results from the ANOVA revealed no interactions at a 95 percent confidence level.

Table 41: Average compressive strength change from cyclic loading of CFA-C concrete samples.

Sample	Compressive strength (MPa)	Sample	Compressive strength (MPa)	Change (MPa)	% Change
C(NNN)	52.8	C(NHN)	54.9	+2.1	+4.0
C(NNH)	49.0	C(NHH)	47.0	-2.0	-4.1
C(HNN)	41.5	C(HHN)	41.7	+0.2	+0.4
C(HNH)	34.2	C(HHH)	30.5	-3.7	-10.8

5.4.1.4 Conclusions

In conclusion:

1. AA treatment lowered concrete strength, indicating a deleterious chemical reaction was present in addition to the normal hydration reactions.
2. FT treatment produced an expected decrease in compressive strength.
3. CL treatment had no net effect due to conflicting tendencies for CL to increase strength when applied at low levels and decrease strength when applied at high levels.
4. No interactions between aging treatments on compressive strength were observed.
5. The lack of interaction was unexpected.

5.4.2. Microcracking

5.4.2.1 ANOVA

The numerical results from the crack density traces are listed in table 42. The table includes the results from each of the three slices (two longitudinal and one transverse) for each prism in addition to the average of these three values. Averaging is possible since the specimens were subject to more or less uniform conditions throughout.

The ANOVA for the prism crack density results is presented in table K-2 in appendix K of volume II. The corresponding tabular F values for this experiment are 98.5, 18.5, and 8.5 for 99, 95, and 90 percent confidence levels, respectively.

5.4.2.2 Main Effects

As can be seen from the crack density ANOVA results in table K-2, the main effects of any single type of aging were varied depending on the type of aging. AA has a computed F value of 4.3, whereas CL and FT had computed F values of 9.115 and 0.974, respectively. Of those, only the F value for CL exceeds the tabulated F value at a 90 percent confidence level. Hence, the only single type of aging that is statistically significant at a 90 percent confidence level is CL.

5.4.2.3 Interactions

Also evident from the ANOVA results in table K-2 is that none of the two-way or three-way interaction effects are significant at a 90 percent confidence level. The computed F values

Table 42: Crack density results (in percent) for CFA-C prism specimens.

Specimen Name	Top	Center	Bottom	Average
C(NNN)08	0.4	0.7	0.3	0.50
C(NHN)08	0.5	0.4	0.7	0.53
C(HNN)08	0.3	0.6	0.5	0.47
C(HHN)08	1.1	1.6	1.1	1.27
C(NNH)08	0.5	0.9	0.2	0.54
C(NHH)08	1.0	0.7	0.8	0.83
C(HNH)08	0.5	0.7	0.5	0.57
C(HHH)08	1.3	1.9	1.2	1.50
C(LL)08	1.3	1.5	1.5	1.45
C(LL)24	1.5	0.9	0.7	1.08
C(LL)40	0.8	1.3	0.9	1.00

for the interaction range from 0.000 to 4.312, none of which exceeds the tabular F value of 8.526 for 90 percent confidence. Likewise, the curvature is statistically insignificant even at a 90 percent confidence level, meaning that the linear model of experimental design is adequate to describe the response behavior.

5.4.2.4 Conclusions

In conclusion:

1. Of the aging treatments, only CL produced significant amounts of microcracking. This contrasts with the compressive strength results where CL had no effect (see section 5.4.1.2).

5.4.3. Relative Dynamic Modulus

Freeze-thaw cycling is a form of treatment that results in aging of the concrete prisms. The consequent relative dynamic modulus values, therefore, do not represent the same type of response variable as others in this experimental program. While most response variables are measured after different levels of three distinct types of ageing mechanisms (heat, cyclic stress, and freeze-thaw cycles), the relative dynamic modulus values represent responses to only two types of prior aging treatments (AA and CL). As such, it is not possible to do a $2^3 + 3$ analysis of RDM data. It is, however possible to do a $2^2 + 3$ analysis of RDM data for the low level of freeze-thaw aging.

5.4.3.1 ANOVA

The RDM values in section 4.3.4 have been subjected to ANOVAs to identify any effects resulting from the applied aging treatments (see table K-3 in appendix K of volume II). Reference F values were 6.9 and 3.9 for 99 and 95 percent confidence, respectively.

5.4.3.2 Main Effects

The ANOVAs for RDM found that AA had a significant negative affect on RDM at a 99 percent confidence level. The model also indicated a non-linear relationship due to AA. CL application was not found to have a significant effect.

Freeze-thaw deterioration occurs when freezing causes inhibited water movement in the hydrated cement paste component of the concrete. When water cannot move freely during a freezing cycle, pressures build up that are resisted by the tensile strength of the paste component. If these pressures result in tensile stresses that exceed the strength of the paste, cracks form. Left unchecked, the cracks propagate and join and the concrete breaks down resulting in surface scaling, exposed aggregate, and crumbling.

The most common way of mitigating this potential is through the use of entrained air at levels typically on the order of 6 to 8 percent by volume of concrete. Entrained air bubbles (often taken as those less than 100 micrometers or 0.004 in diameter) provide a well-dispersed void

volume limiting the distance water has to move to find available space. This experimental program intentionally restricted air contents to less than 4 percent by volume so that the concrete would be susceptible to freezing and thawing damage.

From the results here, AA resulted in concrete with a microstructure that further restricts water movement (through a tighter pore structure or the loss of entrained air volume), which reduces the tensile strength of the concrete, or some combination of these effects.

There is no research indicating that air entrainment is changed by hydration and aging of the concrete. Beneficial chemical aging should result in both a tighter pore structure (lowering freeze-thaw resistance) and higher tensile strength (increasing freeze-thaw resistance). The effects are offsetting and there are apparently no studies showing that freeze-thaw resistance changes substantially with age barring deleterious chemical mechanisms.

Here, however, it has already been shown that AA has caused a loss in strength (see section 5.4.1). Thus, AA has apparently accelerated a deleterious chemical mechanism resulting in a loss of strength and consequently freeze-thaw durability. That CL had no significant effects is not surprising in light of previous discussion (see section 5.4.1).

5.4.3.3 Interactions

No significant interactions were found between AA and CL on RDM.

5.4.3.4 Conclusions

In conclusion:

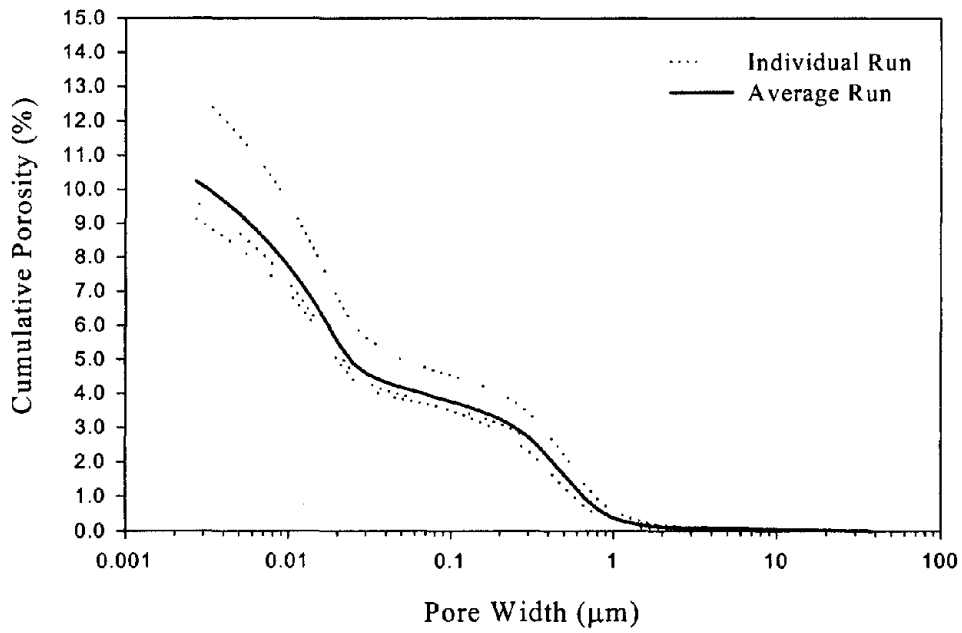
1. AA caused an increase in vulnerability to FT deterioration, which is likely the result of a deleterious chemical reaction during accelerated aging, which also resulted in a loss of tensile strength in the matrix.

5.4.4. Effective Pore Size and Pore Size Distribution

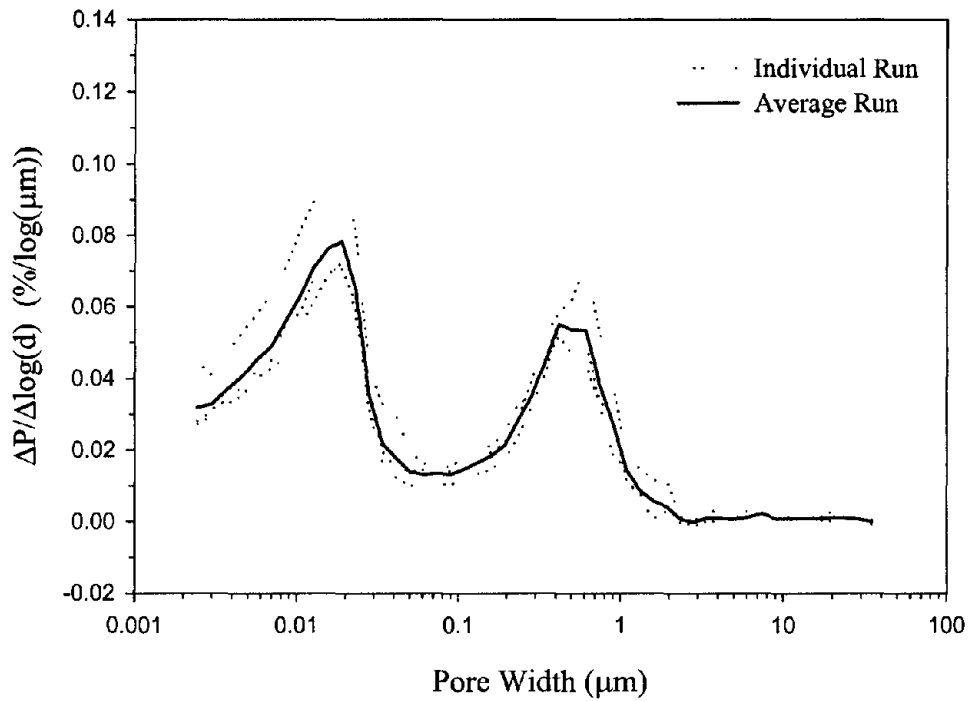
Porosimetry results (see figures 70 and K-1 through K-10 in appendix K of volume II) show two distinct regions in the cumulative porosity and average differential pore size distribution vs. pore widths plots. The cumulative porosity graphs sharply rise in the 0.1- to 1.0- μm region, followed by a flattening of the curve and then a second rise near the 0.01- μm region.

5.4.4.1 ANOVA

Significant intrusions of mercury into the CFA-C concrete occurred in the pore width ranges of 0.1 to 2 μm and approximately 0.01 μm . The nine highest $\Delta P/\Delta \log(d)$ values, used in the determination of each peak's uniformity indicator and average weighted threshold pore width, are listed in tables 43 and 44. The pore widths corresponding to the largest incremental



(a)



(b)

Figure 70: MIP results for C(NNN)09: (a) cumulative porosity vs. pore width; (b) average differential pore size distribution vs. pore width.

Table 43: CFA-C prism first peak nine highest $\Delta P/\Delta \log(d)$ values and their corresponding pore widths.

Sample ID	Parameter	1	2	3	4	5	6	7	8	9
C(NNN)09	$\Delta P/\Delta \log(d)$ (%/log(μm))	0.0274	0.0385	0.0533	0.0536	0.0551	0.0450	0.0350	0.0283	0.0214
	Pore Width (μm)	0.902	0.744	0.614	0.506	<u>0.418</u>	0.344	0.284	0.234	0.193
C(NHN)09	$\Delta P/\Delta \log(d)$ (%/log(μm))	0.0232	0.0263	0.0360	0.0472	0.0466	0.0373	0.0279	0.0253	0.0293
	Pore Width (μm)	0.902	0.744	0.614	<u>0.506</u>	0.418	0.344	0.284	0.234	1.325
C(HNN)09	$\Delta P/\Delta \log(d)$ (%/log(μm))	0.0175	0.0247	0.0272	0.0405	0.0316	0.0316	0.0225	0.0189	0.0183
	Pore Width (μm)	0.614	0.506	0.418	0.344	0.284	0.234	0.193	0.159	0.131
C(HHN)09	$\Delta P/\Delta \log(d)$ (%/log(μm))	0.0295	0.0393	0.0400	0.0492	0.0404	0.0347	0.0268	0.0218	0.0201
	Pore Width (μm)	0.614	0.506	0.418	<u>0.344</u>	0.284	0.234	0.193	0.159	0.131
C(NNH)09	$\Delta P/\Delta \log(d)$ (%/log(μm))	0.0203	0.0273	0.0487	0.0563	0.0613	0.0426	0.0332	0.0278	0.0218
	Pore Width (μm)	0.902	0.744	0.614	0.506	<u>0.418</u>	0.344	0.284	0.234	0.193
C(NHH)09	$\Delta P/\Delta \log(d)$ (%/log(μm))	0.0171	0.0187	0.0313	0.0506	0.0432	0.0415	0.0304	0.0214	0.0170
	Pore Width (μm)	1.325	1.093	0.902	<u>0.744</u>	0.614	0.506	0.418	0.344	0.284
C(HNH)09	$\Delta P/\Delta \log(d)$ (%/log(μm))	0.0210	0.0352	0.0276	0.0336	0.0308	0.0270	0.0235	0.0219	0.0204
	Pore Width (μm)	1.093	<u>0.744</u>	0.614	0.506	0.418	0.344	0.284	0.234	0.193
C(HHH)09	$\Delta P/\Delta \log(d)$ (%/log(μm))	0.0165	0.0321	0.0372	0.0632	0.0325	0.0214	0.0194	0.0175	0.0164
	Pore Width (μm)	0.902	0.744	0.614	0.506	0.418	0.344	0.284	0.234	0.193
C(LL)09	$\Delta P/\Delta \log(d)$ (%/log(μm))	0.0209	0.0169	0.0315	0.0491	0.0325	0.0272	0.0205	0.0173	0.0143
	Pore Width (μm)	1.325	0.902	0.744	<u>0.614</u>	0.506	0.418	0.344	0.284	0.234
C(LL)25	$\Delta P/\Delta \log(d)$ (%/log(μm))	0.0243	0.0216	0.0277	0.0251	0.0229	0.0201	0.0180	0.0167	0.0164
	Pore Width (μm)	1.093	0.902	<u>0.744</u>	0.614	0.506	0.418	0.344	0.284	0.234
C(LL)41	$\Delta P/\Delta \log(d)$ (%/log(μm))	0.0255	0.0332	0.0427	0.0480	0.0367	0.0295	0.0257	0.0211	0.0192
	Pore Width (μm)	0.614	0.506	0.418	0.344	0.284	0.234	0.193	0.159	0.131

Note: Threshold pore widths are underlined

Table 44: CFA-C prism second peak nine highest $\Delta P/\Delta \log(d)$ values and their corresponding pore widths.

Sample ID	Parameter	1	2	3	4	5	6	7	8	9
C(NNN)09	$\Delta P/\Delta \log(d)$	0.0655	0.0782	0.0763	0.0708	0.0627	0.0560	0.0489	0.0453	0.0406
	(%/log(μm))									
C(NHN)09	Pore Width (μm)	0.0230	0.0189	0.0155	0.0127	0.0104	0.0085	0.0070	0.0057	0.0046
	$\Delta P/\Delta \log(d)$	0.0385	0.0544	0.0620	0.0603	0.0548	0.0502	0.0440	0.0396	0.0374
C(HNN)09	(%/log(μm))									
	Pore Width (μm)	0.0279	0.0230	0.0189	0.0155	0.0127	0.0104	0.0085	0.0070	0.0057
C(HNN)09	$\Delta P/\Delta \log(d)$	0.0395	0.0492	0.0600	0.0582	0.0577	0.0546	0.0481	0.0448	0.0399
	(%/log(μm))									
C(HHN)09	Pore Width (μm)	0.0412	0.0339	0.0279	0.0230	0.0189	0.0155	0.0127	0.0104	0.0070
	$\Delta P/\Delta \log(d)$	0.0440	0.0488	0.0552	0.0577	0.0553	0.0525	0.0493	0.0459	0.0462
C(NNH)09	(%/log(μm))									
	Pore Width (μm)	0.0339	0.0279	0.0230	0.0189	0.0155	0.0127	0.0104	0.0085	0.0070
C(NNH)09	$\Delta P/\Delta \log(d)$	0.0446	0.0665	0.0674	0.0614	0.0548	0.0517	0.0489	0.0448	0.0389
	(%/log(μm))									
C(NHH)09	Pore Width (μm)	0.0230	0.0189	0.0155	0.0127	0.0104	0.0085	0.0070	0.0057	0.0046
	$\Delta P/\Delta \log(d)$	0.0426	0.0523	0.0522	0.0497	0.0458	0.0405	0.0374	0.0347	0.0323
C(HNH)09	(%/log(μm))									
	Pore Width (μm)	0.0230	0.0189	0.0155	0.0127	0.0104	0.0085	0.0070	0.0057	0.0046
C(HNH)09	$\Delta P/\Delta \log(d)$	0.0445	0.0444	0.0460	0.0460	0.0446	0.0422	0.0393	0.0396	0.0393
	(%/log(μm))									
C(HHH)09	Pore Width (μm)	0.0339	0.0279	0.0230	0.0189	0.0155	0.0127	0.0104	0.0057	0.0046
	$\Delta P/\Delta \log(d)$	0.0438	0.0446	0.0477	0.0483	0.0476	0.0449	0.0429	0.0424	0.0427
C(LL)09	(%/log(μm))									
	Pore Width (μm)	0.0339	0.0279	0.0230	0.0189	0.0155	0.0127	0.0104	0.0085	0.0070
C(LL)09	$\Delta P/\Delta \log(d)$	0.0405	0.0490	0.0515	0.0510	0.0487	0.0459	0.0466	0.0427	0.0381
	(%/log(μm))									
C(LL)25	Pore Width (μm)	0.0230	0.0189	0.0155	0.0127	0.0104	0.0085	0.0070	0.0057	0.0030
	$\Delta P/\Delta \log(d)$	0.0451	0.0475	0.0466	0.0453	0.0424	0.0405	0.0431	0.0406	0.0398
C(LL)41	(%/log(μm))									
	Pore Width (μm)	0.0230	0.0189	0.0155	0.0127	0.0104	0.0070	0.0057	0.0046	0.0037
C(LL)41	$\Delta P/\Delta \log(d)$	0.0491	0.0580	0.0616	0.0591	0.0565	0.0549	0.0556	0.0557	0.0513
	(%/log(μm))									
C(LL)41	Pore Width (μm)	0.0230	0.0189	0.0155	0.0127	0.0104	0.0085	0.0070	0.0057	0.0046
	$\Delta P/\Delta \log(d)$	0.0491	0.0580	0.0616	0.0591	0.0565	0.0549	0.0556	0.0557	0.0513

intrusion are underlined in these tables. These widths are commonly referred to as the critical threshold pore widths. Each peak's resulting uniformity indicator and weighted average threshold pore width is listed in table 45. The porosity of the samples is also listed in this table.

5.4.4.2 Main Effects

The ANOVAs for porosity, first peak uniformity indicator, and first peak weighted average threshold pore width found no significant effects among the different treatments (see tables K-4 through K-8 in appendix K of volume II). For these ANOVAs the reference F values were 18.5 and 98.5 for 95 and 99 percent confidence, respectively. However, significant effects were identified for the second peak's uniformity indicator and weighted average threshold pore width.

AA and FT were found to affect the second peak's uniformity indicator at a 95 percent confidence level. The model also indicated a non-linear relationship due to one or both of the sources.

The second peak's weighted average threshold pore width revealed that AA and FT had significant effects at the 99 percent confidence level.

The first and second peaks' threshold pore widths (as opposed to the weighted average threshold pore widths) were also analyzed for effects caused by the different aging treatments. ANOVAs performed on both values (see tables K-9 and K-10 in appendix K of volume II) showed no significant effects from the applied treatments. For these ANOVAs the reference F values remain 18.5 and 98.5 for 95 and 99 percent confidence respectively.

Porosity measurements showed no statistically significant effects from AA, CL, or FT. This, in conjunction with the large variance for the low treatment samples, suggests one of two things: (i) the amount of change to porosity from the applied treatments is negligible or (ii) the unknown coarse aggregate content per sample resulted in large variances that masked subtle differences.

The lack of an effect from AA and FT is consistent with published research. Rostásy et al. (1980) found no changes in total porosity for concretes cyclically cooled from $-170\text{ }^{\circ}\text{C}$ to $-20\text{ }^{\circ}\text{C}$ and concretes cyclically heated from $20\text{ }^{\circ}\text{C}$ to $300\text{ }^{\circ}\text{C}$. In both experiments, the concrete samples had been cured for 90 d under normal conditions.

CL was expected to cause an effect. Work by Zhang (1998) found an increase in porosity with increasing fatigue cycles. However, low stress cyclic loading has been found to densify concrete and reduce porosity by as much as 4 percent (Pons and Maso, 1984). Porosity measurements from this work may have been confounded by such a densification effect as was found for compressive strength testing results.

There is also a possibility that trends in porosity results were obscured by the unknown coarse aggregate content in each sample. Tests were performed on dice-size specimens taken

Table 45: MIP results on CFA-C prism samples.

Sample	Porosity * (%)	First peak		Second peak	
		Uniformity indicator (μm) [†]	Weighted average threshold pore width (μm)	Uniformity indicator (μm)	Weighted average threshold pore width (μm)
C(NNN)09	10.24	0.01267	0.482	0.01361	0.01283
C(NHN)09	9.06	0.00906	0.573	0.00950	0.01476
C(HNN)09	8.85	0.00766	0.321	0.00783	0.02124
C(HHN)09	10.10	0.00967	0.340	0.00485	0.01751
C(NNH)09	9.50	0.01514	0.464	0.01011	0.01230
C(NHH)09	8.18	0.01261	0.669	0.00746	0.01248
C(HNH)09	8.91	0.00551	0.502	0.00283	0.01741
C(HHH)09	9.02	0.01523	0.497	0.00232	0.01766
C(LL)09	8.24	0.01095	0.607	0.00469	0.01180
C(LL)25	8.55	0.00394	0.606	0.00281	0.01160
C(LL)41	9.92	0.00974	0.337	0.00382	0.01181

* Porosity as measured by the volume of intrusion recorded at 207 MPa divided by the bulk volume of the sample.

from larger prismatic samples. Coarse aggregate contents were unknown. The author estimates that they could have ranged from 15 percent to as high as 85 percent of the total porosity. The porosity of the limestone coarse aggregate used in this project was determined to be ~2.5 percent by MIP. The remaining mortar fraction porosities could have ranged from 9 to 25 percent depending upon the degree of hydration and the amount of microcracking (Cook, 1991; Sersale et al., 1991). The combination of the two materials of different porosities could have resulted in substantially different total porosities for samples removed from the same prism or cylinder. This made it difficult to determine true differences in porosities due to treatments.

Statistical analysis of CFA-C concrete's uniformity indicators and weighted average threshold pore widths, for the first peaks, found them to be unrelated to the aging treatment types. This corroborates the earlier proposed theory that macrocracks have a large natural variation in size when treatments are applied.

The second peak of the CFA-C prism concrete did change in size and location for the different treatments (see figure 71). AA caused the second peak to shift to the right and flatten. This was indicated by the significant changes to the uniformity indicators and weighted average threshold pore widths at a 99 percent confidence level. It appears that a deleterious reaction caused a breakdown in the pore structure and/or expansive pressures that resulted in a widening of the connective pore system.

CL was found to have no individual significant effect on the second peaks shape or location at a 95 percent confidence level. It is thought that, as before, cyclic loading was either strengthening or deleterious, depending on the prior conditions of the concretes.

FT caused a decrease in the uniformity indicator at a 95 percent confidence level and a decrease in the weighted average threshold pore width at a 99 percent confidence level. This is apparent by the decreased and flattened shape of the second intrusion peak on the average differential pore size distribution plots (see figures 72 through 75). Though the threshold pore width of the second peak did not change, the relative volume of smaller pores increased and pulled the weighted average in their direction.

The action of freezing in concrete first takes place in larger water-filled pores (Powers and Brownyard, 1948). The expansive forces are enough to induce and widen large cracks (Neville 1996). As these large cracks are forced apart, smaller non-frozen pores are crushed and squeezed together. This would require higher pressures for mercury to access these smaller widths, resulting in smaller weighted average threshold pore widths.

The expansion of the large cracks is supported by the movement of the first intrusion peak to the right, for the high freeze-thaw samples that have undergone previous treatments (see figures 73 through 75). The decrease in area underneath the second peak indicates a decrease in the porosity of the smallest pores.

5.4.4.3 Interactions

AA interacted with CL to decrease the second peak's weighted average threshold pore width at a significance of 99 percent. The second peak's weighted average threshold pore width

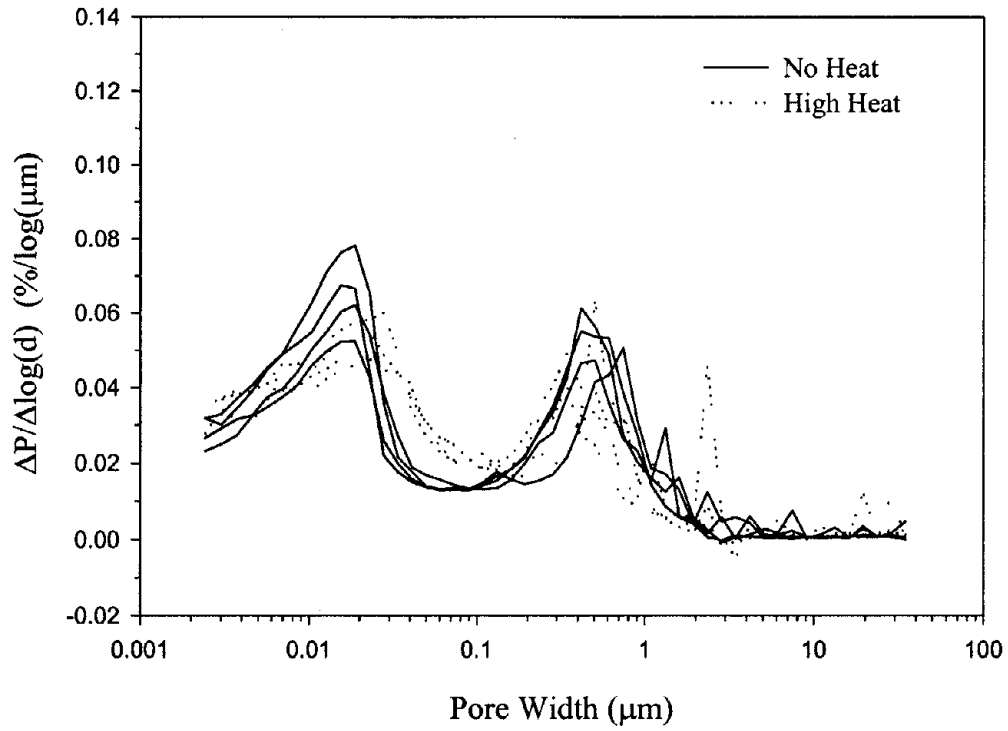


Figure 71: Average differential pore size distribution vs. pore width plots of all CFA-C concrete samples with high and no levels of heat treatment.

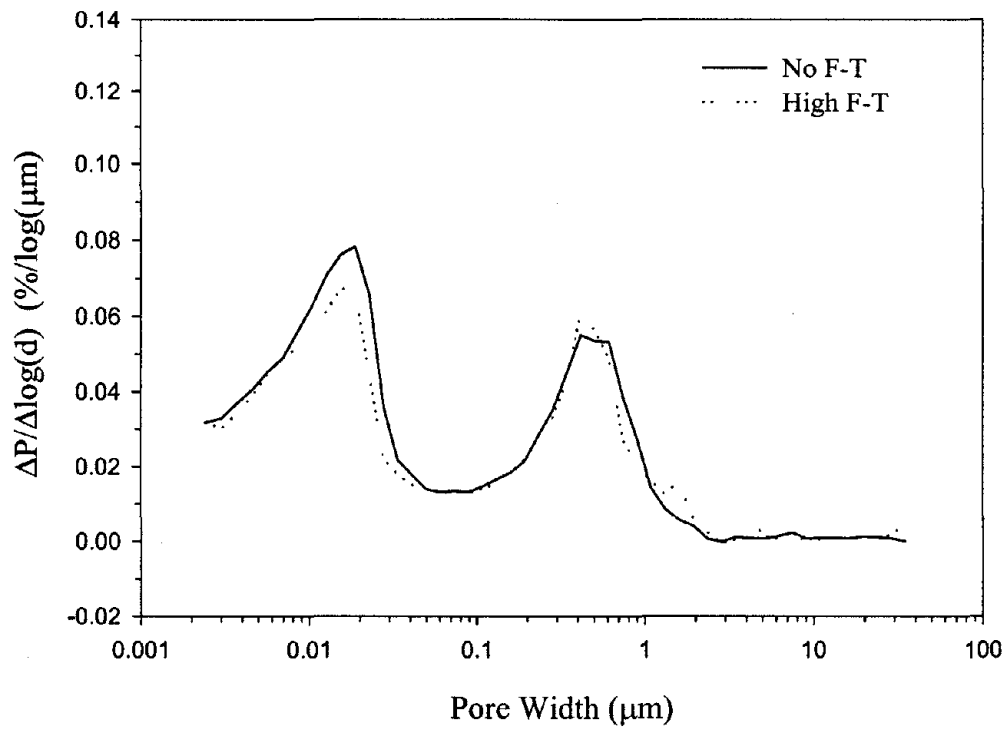


Figure 72: Average differential pore size distribution vs. pore width plot for C(NNN)09 and C(NNH)09.

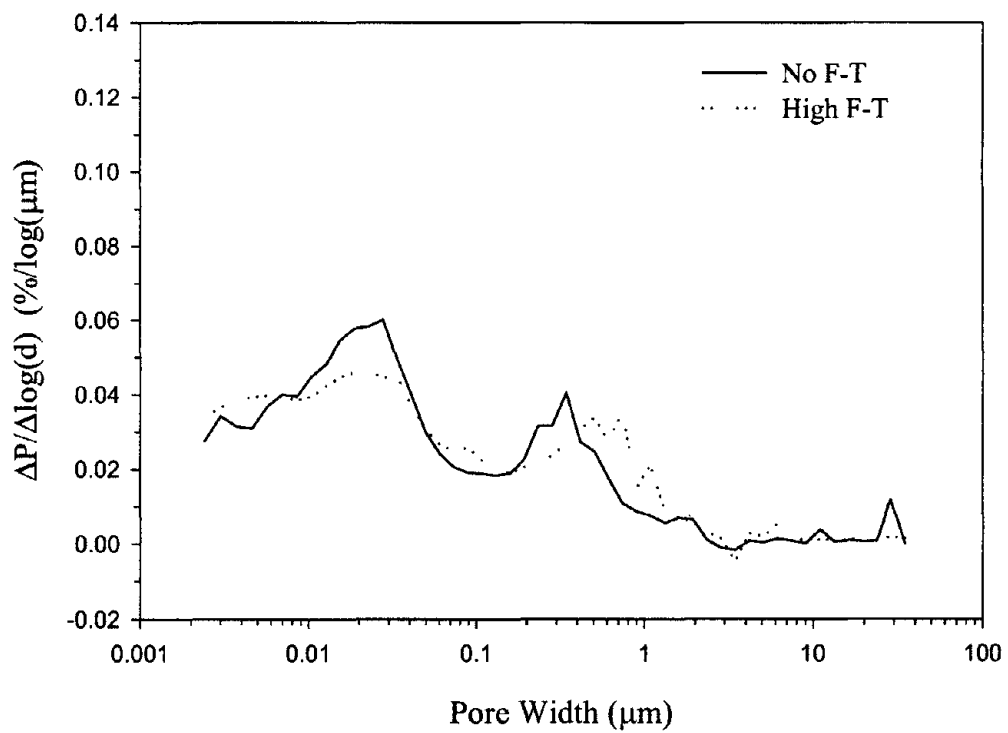


Figure 73: Average differential pore size distribution vs. pore width plot for C(HNN)09 and C(HNH)09.

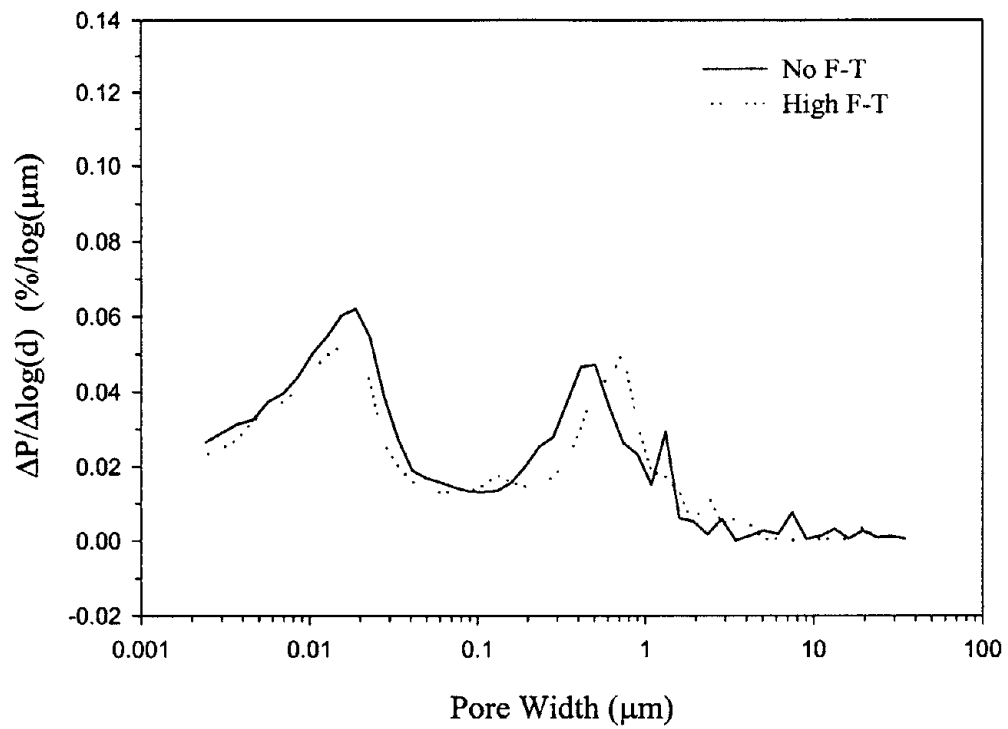


Figure 74: Average differential pore size distribution vs. pore width plot for C(NHN)09 and C(NHH)09.

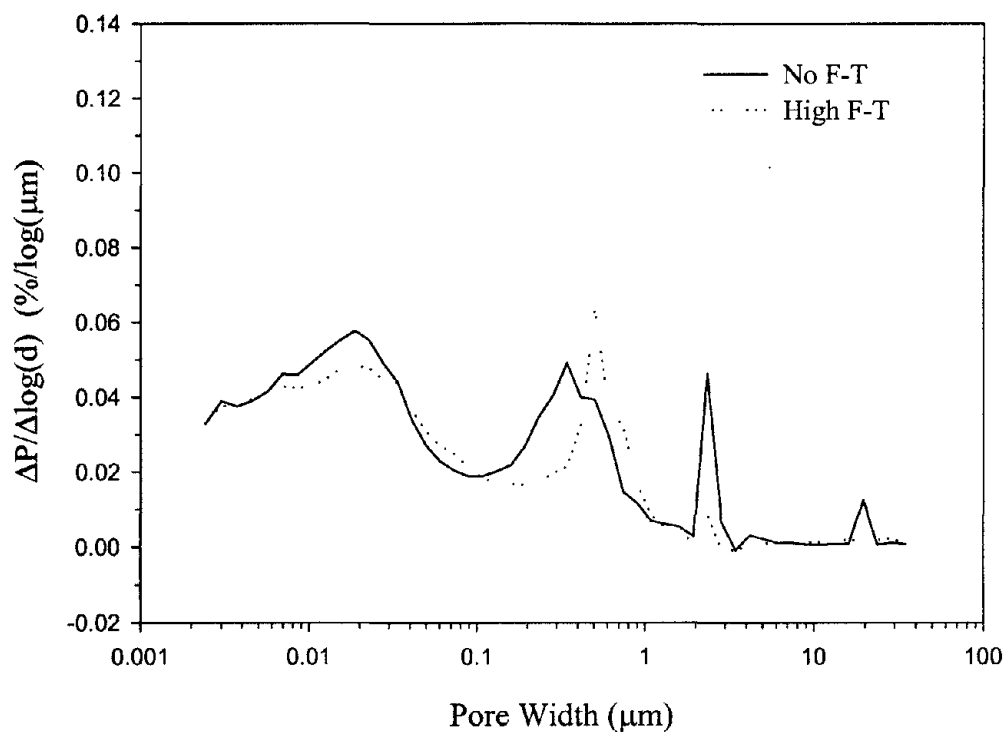


Figure 75: Average differential pore size distribution vs. pore width plot for C(HHN)09 and C(HHH)09.

also increased due to an interaction of CL and FT at the 95 percent confidence level. All three treatments interacted to increase the second peak's weighted average threshold pore width at a 99 percent confidence interval.

AA reduced strengths and opened the pore structure as mentioned earlier. This weakening of the concrete may be what allowed CL to have an interactive effect on the aged samples as CL apparently densified the finer pore system that had been coarsened by AA.

CL allowed FT cycles to coarsen the finer pore system. It has been shown that CL resulted in more microcracking (see section 5.4.2.1). This increased microcracking may have allowed water to enter the matrix more readily, resulting in more damage to the fine pore system.

All three treatments combined and interacted to coarsen the weighted average threshold pore widths. AA aging weakened the matrix (see section 5.4.1.2) and CL introduced microcracking, resulting in a weaker system more accessible to water which finally resulted in more FT damage.

5.4.4.4 Conclusions

In conclusion:

1. Aging treatments either had no effect on porosity or uncertain coarse aggregate fractions obscured effects that were caused. AA and FT were not expected to have an effect; CL was.
2. Concretes exhibited two distinct pore networks: a coarser pore network centered on connection pore widths of approximately 0.5 μm , and a finer network centered on approximately 10 to 20 nm.
3. Aging treatments had no apparent effect on the coarser pore network, probably because large natural variations masked effects if any.
4. AA caused the finer pore network to coarsen and become less uniform apparently due to a deleterious reaction.
5. CL had no apparent effect on the finer pore network.
6. FT aging caused the finer pore network to shift to a smaller average pore width of a less uniformly defined nature. This may be due to expansive pressures in the coarser pores having squeezed and narrowed the finer pores.
7. There were significant interactive effects on the finer pore system between AA and CL, CL and FT, and the three aging treatments.

5.4.5. Effective Surface Area

Results are presented in table 46. For the center point values (LLL), the average was found to be 6.12 and the variance to be 13.3.

5.4.5.1 ANOVA

Results from an ANOVA performed on the CFA-C prism samples found no significant effects due to treatment type or level (see table K-11 in appendix K of volume II). Reference F values for this table were 98.5 and 18.5 for 99 and 95 percent confidence intervals, respectively.

Nitrogen adsorption measurements on laboratory-created concrete were variable and found unrelated to treatment type or mix design. It was hoped that the increased surface areas from microcracks induced by the applied treatments would be measurable with BET-N₂ adsorption. Research on cement pastes and mortars has found surface area measurements useful in determining characteristics for the microstructure of concrete (Mikhail et al. 1964, Mehta 1985, Gimblett et al. 1989, Odler and Köster 1991, and Zhang 1998). This did not appear to be true for the concrete samples used in this project. As with the concrete taken from the slab, it is believed that variations in coarse aggregate content resulted in no apparent differences in surface area.

5.4.5.2 Main Effects

There were no main effects.

5.4.5.3 Interactions

There was no interaction.

5.4.5.4 Conclusions

In conclusion:

1. Surface area measurements were inconclusive due to the heterogeneous nature of concrete and the sample sizes relative to coarse aggregate sizes.

5.4.6. Mineralogy

XRPD analysis was used to examine the bulk phase mineralogy of the CFA-C concrete prisms. XRPD was performed in triplicate on aged samples C(NNN)09, C(NHN)09, C(HNN)09, C(HHN)09, C(NNH)09, C(NHH)09, C(HNH)09, C(HHH)09, C(LL)09, C(LL)25, and C(LL)41. Qualitative analysis resulted in identification of likely mineral phases in the concrete samples. Table 47 contains the crystalline phases identified by XRPD in sample C(NNN)09. A figure of merit (FOM) was assigned by the data analysis program, Jade 5.0. A lower FOM indicates a greater certainty that the phase is in the sample. Six mineral phases were chosen for quantification based on detectability, availability of a standard diffraction pattern, and relevance to the mineralogy of concrete.

Table 46: Results from BET-N₂ adsorption analysis of CFA-C prisms.

Sample ID	Weighted surface area m ² /g
C(NNN)09	7.61
C(NHN)09	6.98
C(HNN)09	2.73
C(HHN)09	2.65
C(NNH)09	6.43
C(NHH)09	2.25
C(HNH)09	2.40
C(HHH)09	11.48
C(LL)09	2.53
C(LL)25	6.02
C(LL)41	9.81

Table 47: Example table of crystalline phases identified by XRPD sample C(NNN)09.

PDF No.	Name	Chemical formula	Replicate FOM			Weighted average FOM
			1	2	3	
04-0733	Portlandite, syn	Ca(OH) ₂	6.6	6.9	10.7	5.4
05-0586	Calcite, syn	CaCO ₃	5.2	0.6	6.4	2.7
06-0711	Iron Oxide	FeO		5.7		11.4
09-0466	Albite, ordered	NaAlSi ₃ O ₈	10.8		10.6	10.7
14-0617	Potassium Iron Silicate	KFeSi ₃ O ₈			8.9	17.8
17-0522	Omphacite	NaCaMgAl(Si ₂ O ₆) ₂			8.2	16.4
19-1184	Albite, ordered	NaAlSi ₃ O ₈			8.9	17.8
20-0669	Nesquehonite, syn	MgCO ₃ • 3H ₂ O			9.6	19.2
21-1258	Ringwoodite, ferroan	(Mg,Fe) ₂ SiO ₄	6.3			12.6
26-1076	Carbon	C	13.9	9.1	8.3	7.0
26-1077	Carbon	C	12.9	9.7		11.3
27-0606	Silicon Oxide Hydrate	H ₂ Si ₂ O ₅			6.8	13.6
28-0775	Calcium Oxide	CaO	6.1		8.5	7.3
32-0827	Potassium Oxide	K ₂ O ₂	9.5			19.0
33-0311	Gypsum, syn	CaSO ₄ • 2H ₂ O	6.9	10.4	7.2	5.4
35-0964	Magnesium Aluminum Hydroxide Hydrate	Mg ₄ Al ₂ (OH) ₁₄ • 3H ₂ O	5.5	5.4		5.5
35-1393	Magnesium Iron Oxide	Mg _{1-x} Fe _x O	4.4	5.3	4.5	3.2
36-0426	Dolomite	CaMg(CO ₃) ₂	11.8	12.6	13.5	8.4
40-0292	Calcium Iron Sulfate Hydroxide Hydrate	Ca ₆ Al ₂ (SO ₄) ₃ (OH) ₁₂ • xH ₂ O	6.4			12.8
43-0596	Silicon Oxide	SiO ₂	7.4			14.8
46-1045	Quartz, syn	SiO ₂	3.7	3.5	3.9	2.5
46-1360	Thaumasite	Ca ₃ Si(OH) ₆ [CO ₃][SO ₄] • 12H ₂ O	7.8			15.6
47-1743	Calcite	CaCO ₃	0.9	2.1	1	0.9

Examination of the identification tables for each sample revealed that the six mineral phases selected for quantification, listed in table 48, occurred with varying frequency and FOM in the samples that were analyzed.

The presence of calcite, here found at a mean concentration of 22.2 percent, was also found by previously described geochemical modeling (see sections 5.1.6.3 and 5.3.8.3). Dolomite, here not chosen as one of the six mineral phases for quantification, had been found by geochemical modeling as a likely controlling phase for leaching.

5.4.6.1 ANOVA

ANOVAs were performed to assess the statistical significance of changes in mineral concentrations caused by the accelerated aging treatment methods (tables K-12 through K-17 in appendix K of volume II). These ANOVA tables contain the statistical analyses for the six mineral phases listed in table 48. The tabular F values used to determine statistical significance in mineral concentration changes were 2.93 at 90 percent confidence, 4.26 at 95 percent confidence, and 7.82 at 99 percent confidence (Kuehl, 1994).

Curvature was assessed in order to determine if the linear model of the experimental design adequately described the changes in mineral concentrations caused by accelerated aging. Curvature was not statistically significant in any changes in mineral concentration. Therefore the linear model of the experimental design was appropriate to relate the changes in mineral concentration attributable to the accelerated aging treatments.

5.4.6.2 Main Effects

The majority of the quantified phases showed no significant change in concentration due to an accelerated aging method (table K-18). FT had a statistical effect on the concentrations of gypsum ($\text{CaSO}_4 \cdot 2\text{H}_2\text{O}$) and crystalline quartz (SiO_2). For both mineral phases, FT treatment caused a decrease in the mineral concentration. AA also decreased the mineral concentration of gypsum.

Accelerated aging methods may increase the incorporation of Si into the cement paste and thereby reduce the concentration of amorphous quartz, but not when crystalline quartz is the source of the Si.

Gypsum ($\text{CaSO}_4 \cdot 2\text{H}_2\text{O}$) is an additive to portland cement, designed to react in the beginning of the curing process (Taylor, 1997). Gypsum, remaining in trace concentrations at later stages of concrete curing, may be dissolved by the freeze-thaw process and the Ca incorporated into the cement paste.

5.4.6.3 Interactions

None of the six phases quantified by XRPD were significantly affected by the interaction of any of the three accelerated aging variables (table K-19 of appendix K in volume II.)

Table 48: Mineral phases quantified by XRPD.

PDFNo.	Mineral Name	Chemical formula	RIR value	Mean concentration	Concentration range ³
09-0466	Albite	NaAlSi ₃ O ₈	2.10	3.1%	0% - 25.3%
05-0586	Calcite	CaCO ₃	2.00	22.2%	12.2% - 34.1%
41-1451	Ettringite	Ca ₆ Al ₂ (SO ₄) ₃ (OH) ₁₂ • 26H ₂ O	1.00 ¹	0.4%	0% - 1.7%
33-0311	Gypsum	CaSO ₄ • 2H ₂ O	1.83	0.3%	0% - 1.4%
04-0733	Portlandite	Ca(OH) ₂	1.40	1.3%	0.7% - 3.2%
46-1045	Quartz	SiO ₂	3.41	5.1%	1.8% - 11.0%

5.4.6.4 Conclusions

In conclusion:

1. Of six mineral phases used to detect the effect of aging, few were affected and no interactions among aging treatments were detected.
2. Gypsum ($\text{CaSO}_4 \cdot 2\text{H}_2\text{O}$) concentrations were reduced by AA and FT treatments, probably due to increased reaction and dissolution during these treatments, respectively.
3. Quartz (SiO_2) concentrations were reduced by FT aging; however, the mechanism is unknown.

5.4.7. pH-dependent Leaching and Solid Phase Control

5.4.7.1 Prism Alkalinity and Constituent Solubility as a Function of pH

Acid neutralization capacity curves of 28-d cured CFA-C mix prior to any aging (e.g., C(XXX)02) and a high AA-aged CFA-C mix (e.g., C(HNN)13) are compared in figure 76. The 28-d cured sample showed a greater acid neutralization capacity than the high AA-aged sample. For the 28-d cured sample, 6 mEq of acid/g of dry material was required to reach a pH of 10 (pH of the limit of stability of the CSH [Brodersen et al., 1990; Stegemann et al., 1997]) while only 2.5 mEq acid/g of dry material was required for the high AA-aged sample. Based on the acid required to reach a pH 11.9, the quantity of $\text{Ca}(\text{OH})_2$ produced during the hydration reactions of the cement was estimated at 22.6 g/kg of dry material (e.g., 57kg /m³ of porous material) for the 28-d cured sample and 12.6 g/kg of dry material (e.g., 30 kg /m³ of porous material) for the high AA-aged sample. Thus, AA changed the $\text{Ca}(\text{OH})_2$ produced during the cement hydration reaction. The pH titration curves presented a plateau around pH 6 due to the buffering capacity of the aggregates (e.g., limestone type, see section 5.1.6.1). However, this plateau was greater for the temperature aged sample (e.g., from 6 to 12 mEq acid/g dry for C(HNN)13 while from 7 to 10 mEq acid/g dry for C(XXX)02). These results might indicate a slight carbonation of the sample during the temperature aging, increasing the amount of CaCO_3 present in the sample and originally only provided by the aggregates.

Cd, Cu, Pb, Ni and Zn solubility as a function of pH for 28-d cured CFA-C mix (e.g., C(XXX)02) and a high AA aged CFA-C mix (e.g., C(HNN)13) is compared in figure 77. Horizontal lines on each of the figures are used to indicate analytical detection limits.

No influence of temperature aging could be observed on Cd, Ni, and Zn solubility (see figure 77). A slight effect of temperature aging was observed on Cu solubility at a pH greater than 8 (see figure 77). Indeed, for a pH greater than 8, decreased Cu solubility was observed for C(HNN)13 relative to C(XXX)02, suggesting a change in Cu speciation during the temperature aging. For a pH less than 8, there was no differences in Cu solubility between the two materials. A significant effect of temperature aging was observed on Pb solubility (see figure 77). Decreased Pb solubility was observed for the C(HNN)13 sample over the entire pH range,

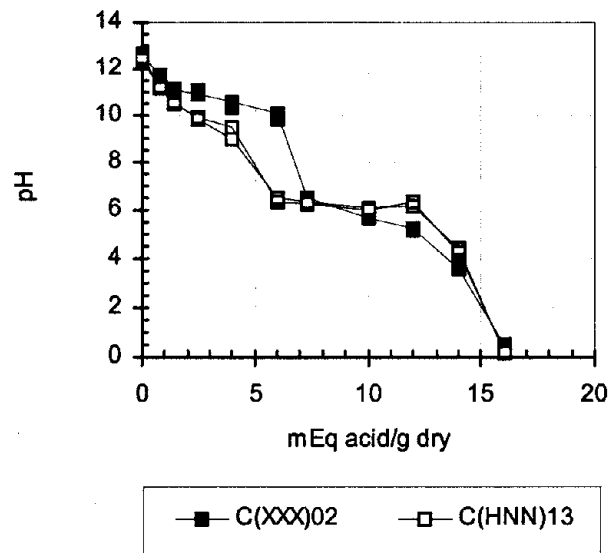


Figure 76: Acid neutralization capacity curves for CFA-C mix.

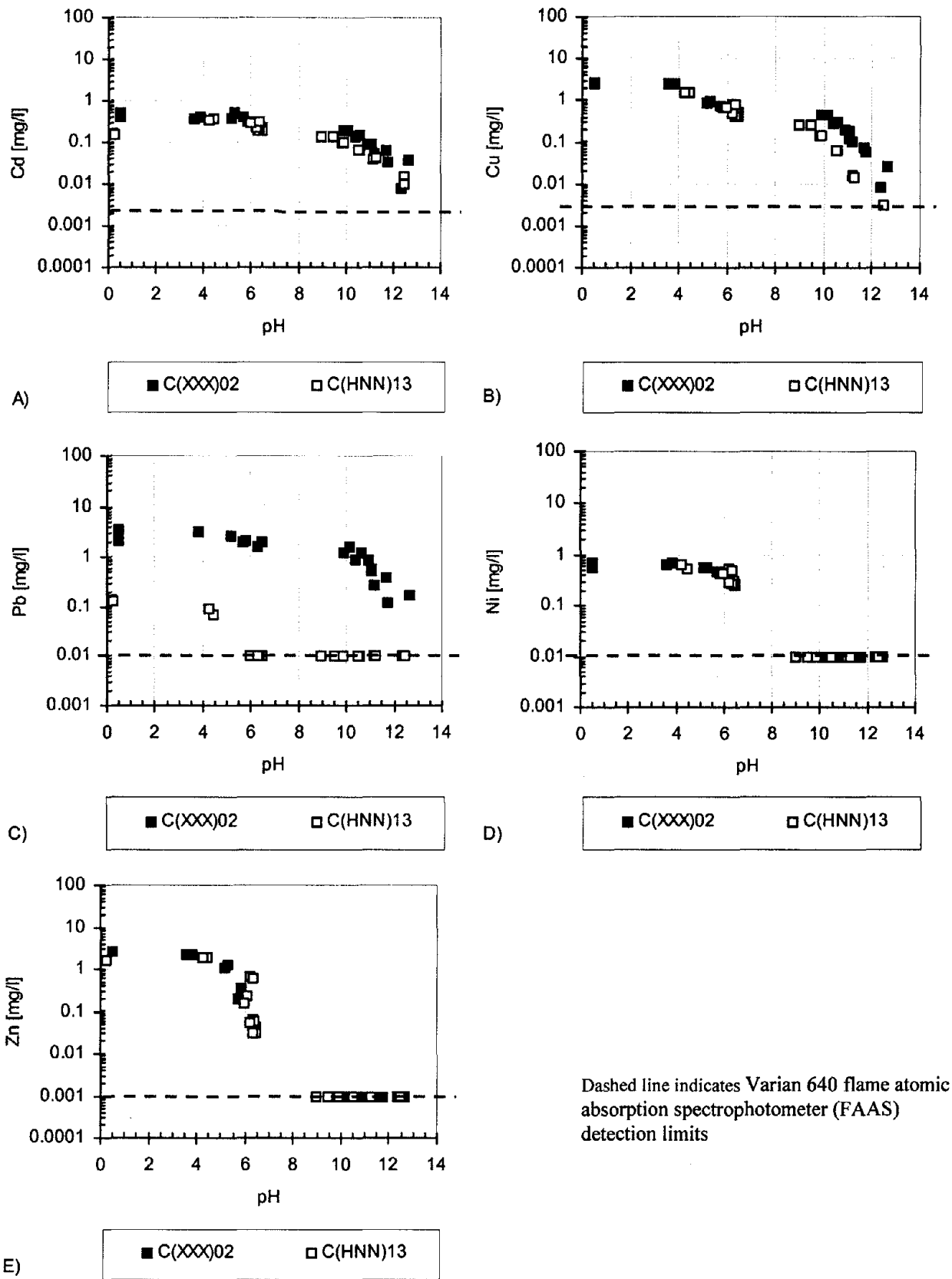


Figure 77: Solubility as a function of pH for CFA-C mix.

indicating a change in Pb speciation during the temperature aging. In addition, at pH greater than 6, Pb solubility of the C(HNN)13 sample was less than the FAAS detection limit.

These results might indicate a carbonation of the material during the temperature aging, decreasing Pb solubility over all the pH range and Cu solubility only for pHs greater than 8. These results are consistent with results that were observed at Rutgers University by Kosson et al. (1996) during a study carried out to examine the effect of intermittent wetting with and without carbonation on the leaching behavior of inorganic contaminants from cement-based waste materials (Gervais et al., 1999; Garrabrants et al., 2000). Indeed, this study showed that carbonation did influence Cu and Pb solubility in a similar way as observed here, while having no effect on Cd and Zn solubility.

Comparing figure 77 for the laboratory concrete with figure 27 for the source components (see section 5.1.6.1), Cd, Cu, and Zn solubility curves match well those of the CFA-C while Pb and Ni solubility curves match well those for the combined aggregates.

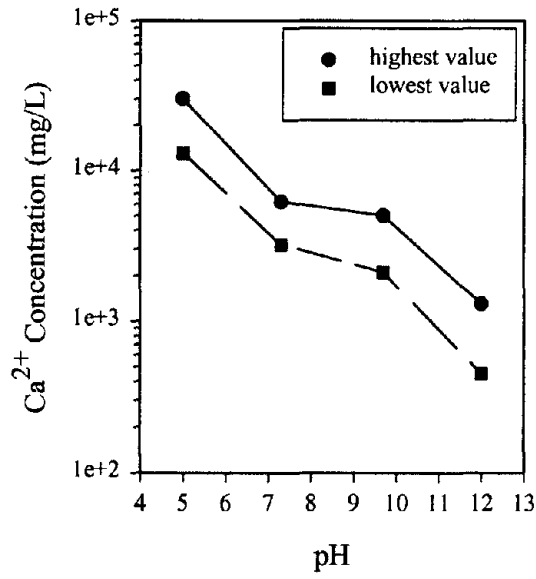
Comparing figure 77 for the laboratory concrete with figure 48 for the slab concrete (see section 5.3.8.1) reveals excellent correspondence in curve shape and solubility magnitudes between the C(XXX)02 samples and the slab concrete. Similarly excellent correspondence occurs between slab and the C(HNN)13 concrete with the exception of lead, which had much lower measured solubilities in the laboratory concrete.

In conclusion:

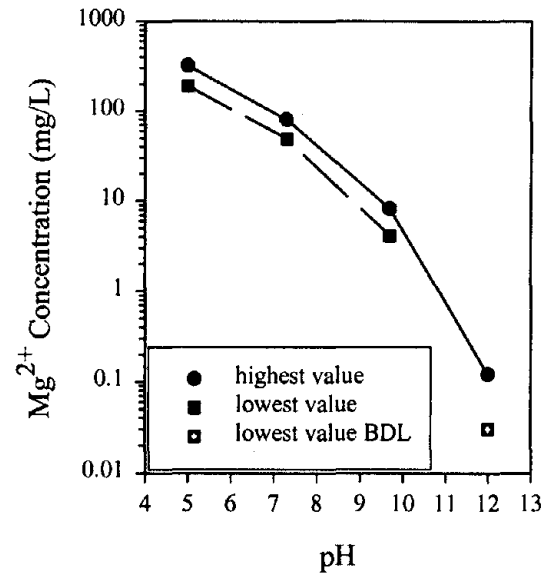
1. Solubility curve shapes and magnitudes between the slab and the C(XXX)02 samples show excellent correspondence.
2. The C(HNN)13 and C(XXX)02 laboratory concrete samples showed excellent correspondence in curve shape and magnitude, with the exception of Pb leaching, which was much lower in the (HNN) laboratory concrete.

5.4.7.2 pH-Stat Leaching

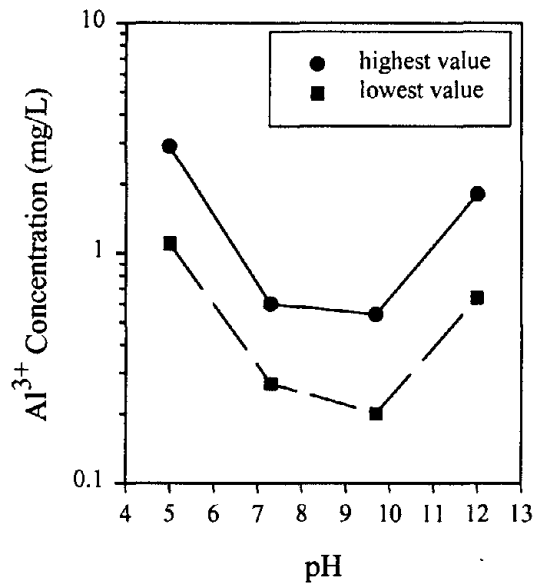
Leaching was performed on the following CFA-C concrete prisms: C(NNN)09, C(NHN)09, C(HNN)09, C(HHN)09, C(NNH)09, C(NHH)09, C(HNH)09, C(HHH)09, C(LLN)09, C(LLN)25, and C(LLN)41. Twelve species were selected to be analyzed in the leachate generated from pH-dependent leaching. Al, Ba, Ca, Cl, CO_3^{2-} , Cr, Fe, K, Mg, Si, SO_4^{2-} , and Zn concentrations were monitored to look for any changes in leachability attributable to the three experimental aging treatments. A thirteenth species analyzed, NO_3^- , was added to the leaching system as HNO_3 . HNO_3 was used to maintain a constant pH in the leachate over the 24-h period. The concentration of this species was quantified for the purposes of geochemical modeling of the system. Figures 78 through 80 show the range of leached concentrations of the 12 analytes. The highest and lowest value of the 11 CFA-C concrete prisms was shown for each of the four pH points where leaching was conducted. In several cases the lowest value indicated was BDL and for Cl concentrations, at a pH of 9.7 and a pH of 7.3, all 11 prisms resulted in



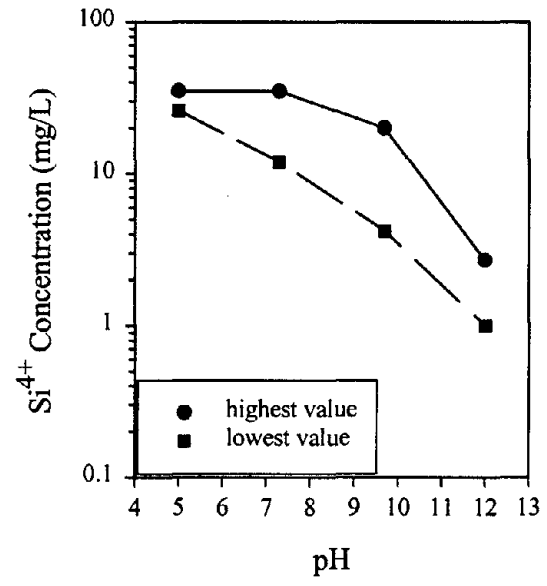
(a)



(b)

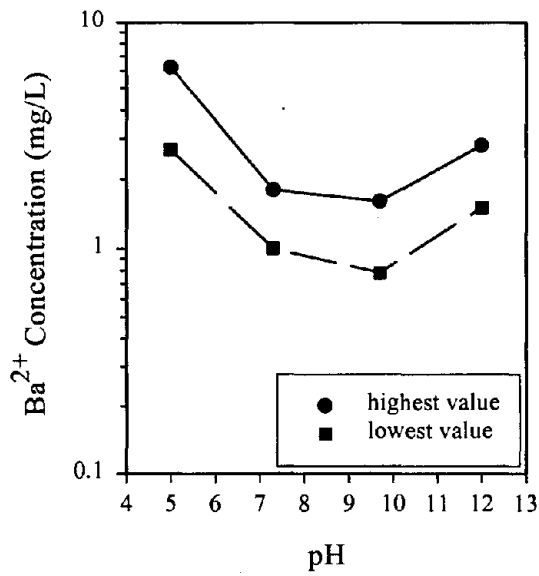


(c)

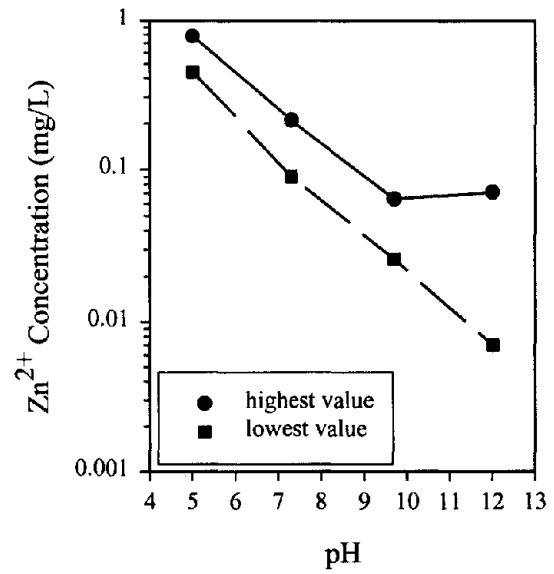


(d)

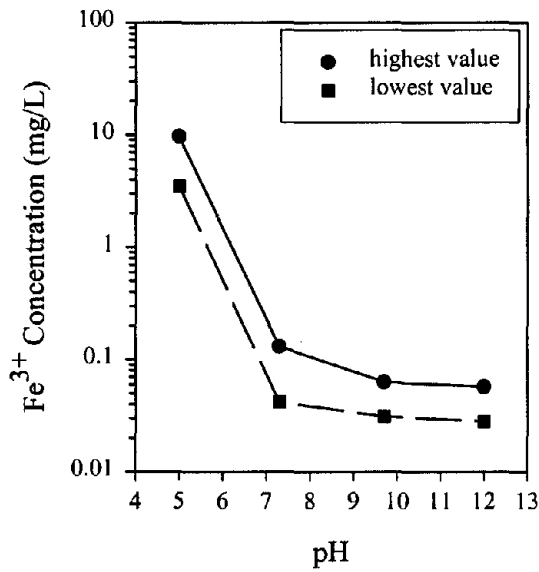
Figure 78: pH-dependent leaching of the experimental CFA-C prisms:
 (a) Ca, (b) Mg, (c) Al, (d) Si.



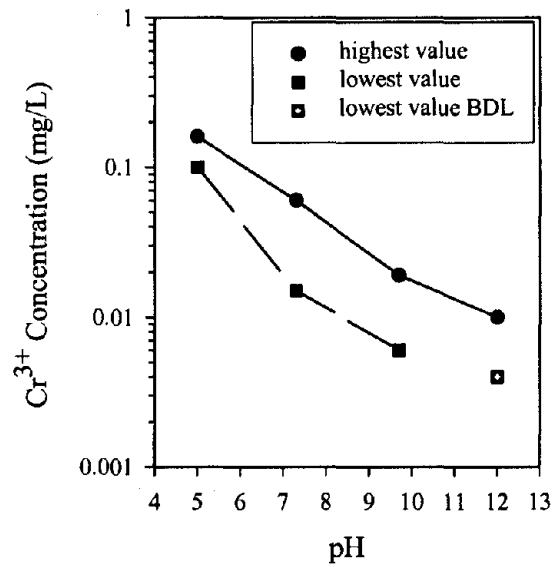
(a)



(b)

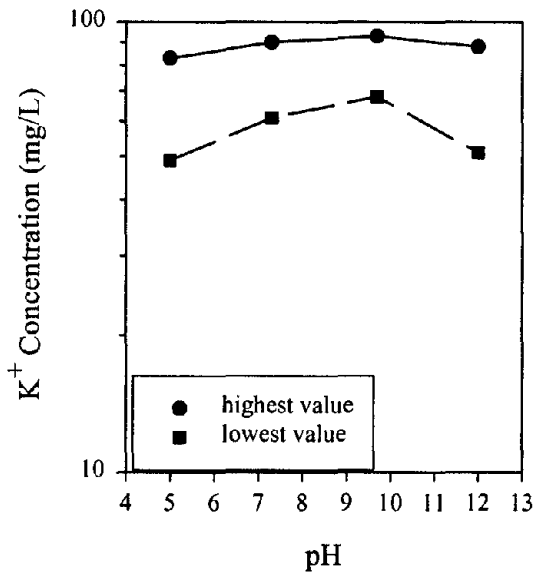


(c)

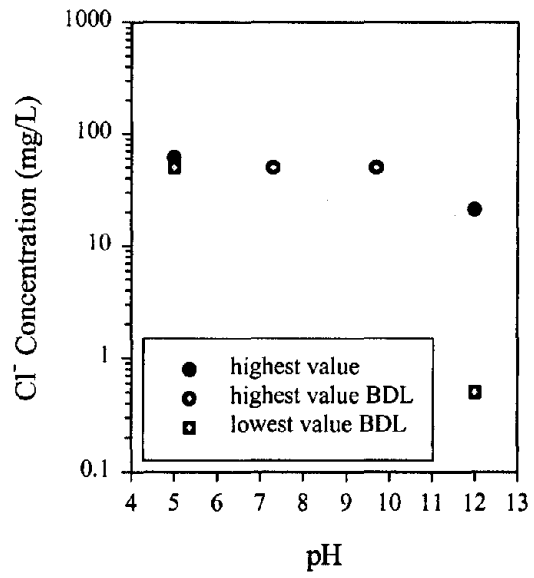


(d)

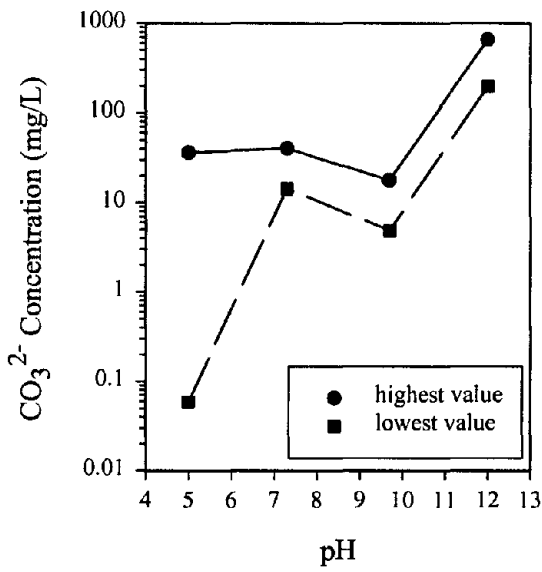
Figure 79: pH-dependent leaching of the experimental CFA-C prisms:
 (a) Ba, (b) Zn, (c) Fe, (d) Cr.



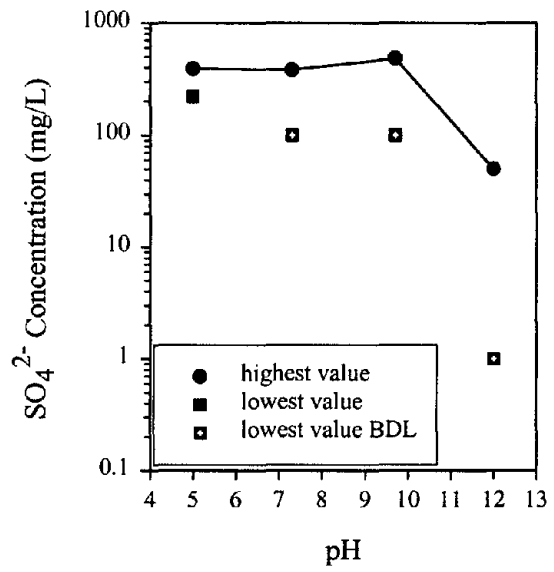
(a)



(b)



(c)



(d)

Figure 80: pH-dependent leaching of the experimental CFA-C prisms:
 (a) K, (b) Cl, (c) CO₃²⁻, (d) SO₄²⁻.

concentrations that were BDL; each of these scenarios is represented in the plots in figures 78 through 80.

Ca, Mg, Al, and Si all exhibited pH-dependent leaching behavior (see figure 78). Ca, Mg, and Si demonstrated a decrease in leachability with increasing pH. Similar behavior for these species has been shown in other literature (van der Sloot, 1998). Al leaching showed amphoteric behavior with a minimum solubility around a pH of 9 to 10.

Figure 79 details the pH-dependent leaching behavior of Ba, Zn, Fe and Cr. Leached concentrations of Ba did not change much over the pH range, but still clearly exhibited typical amphoteric behavior with a minimum solubility around a pH of 9.7. Zn leaching decreased from a pH of 5.0 to a pH of 9.7. At a pH of 12.0 the range of concentrations leached from the 11 prisms was fairly large. Some samples continued to decrease in Zn concentration with increasing pH, while others demonstrated a minimum solubility around a pH of 9.7. Fe leaching decreased with increasing pH through the acidic and neutral pH ranges but leveled off in the basic pH range. Cr decreased in leachability with increasing pH for the entire pH range examined.

Leaching behaviors of K, Cl, CO_3^{2-} , and SO_4^{2-} from the experimental CFA-C prisms are shown in figure 80. K leachate concentration remained relatively constant over the pH range examined. Cl concentrations were BDL over much of the pH range and therefore it was not possible to characterize the leaching behavior. Species such as K and Cl are expected to be pH-independent. CO_3^{2-} demonstrated pH-dependent leaching behavior. A wide range of concentration at a pH of 5.0 made it hard to characterize the behavior of CO_3^{2-} in acidic conditions. The wide range of values at a pH of 5.0 reflects the difficulty experienced in evaluating alkalinity, and in turn CO_3^{2-} concentrations at high and low concentrations. CO_3^{2-} leachate concentrations decreased from a pH of 7.3 to a pH of 9.7 and increased from a pH of 9.7 to a pH of 12.0. SO_4^{2-} leachate concentrations were fairly constant from a pH of 5.0 to a pH of 9.7 and then decreased at the high end of the pH range examined.

5.4.7.3 ANOVA

ANOVA was performed to examine the effects of the experimental treatments on the leachability of selected analytes. Four ANOVA tables were created for each of the 12 selected analytes, one ANOVA for each pH point where leaching was conducted (tables K-20 through K-23 in appendix K of volume II). The F-test was used as the statistical measure of significant change in analyte concentration. The determination of statistical significant changes in concentration requires a confidence level of greater than or equal to 90 percent. The tabular F values used to determine statistical significance in analyte concentration changes were 8.53 at 90 percent confidence, 18.5 at 95 percent confidence, and 98.5 at 99 percent confidence (Kuehl, 1994).

Of the 12 analytes statistically tested, only Cl^- and SO_4^{2-} showed no statistically significant changes in concentration at any pH (see table 49). The other 10 analytes demonstrated significant changes in leachate concentration at one or more pH points that can be attributed to the accelerated aging methods.

Table 49: Summary of significant differences in species concentration in CFA-C leachate due to main effects.

species		Al				Ba				Ca			
pH		5.0	7.3	9.7	12.0	5.0	7.3	9.7	12.0	5.0 ¹	7.3	9.7	12.0
Main Effect	AA	>90%	>95%	99.3%	none	>99%	>99%	>90%	>90%	>99%	none	>95%	>90%
	CL	>95%	>95%	none	none	>90%	none	none	none	>99%	none	>95%	>95%
	FT	>95%	>95%	none	none	none	96.1%	none	none	>99%	none	>95%	none
species		Cl ²				CO ₃				Cr			
pH		5.0	7.3	9.7	12.0	5.0	7.3	9.7	12.0	5.0	7.3	9.7	12.0
Main Effect	AA	--	--	--	none	none	none	>95%	none	none	>95%	>95%	none
	CL	--	--	--	none	none	none	none	none	none	>95%	>95%	none
	FT	--	--	--	none	none	none	>90%	none	none	>95%	none	none
species		Fe				K				Mg			
pH		5.0	7.3	9.7	12.0	5.0	7.3	9.7	12.0	5.0	7.3	9.7	12.0
Main Effect	AA	none	>90%	none	none	none	none	none	>90%	none	none	none	>90%
	CL	none	none	none	none	none	none	none	none	none	none	none	>90%
	FT	none	none	none	none	none	none	none	none	none	none	none	none
species		Si				SO ₄				Zn			
pH		5.0	7.3	9.7	12.0	5.0	7.3	9.7	12.0	5.0	7.3	9.7	12.0
Main Effect	AA	>95%	>99%	>99%	none	none	none	none	none	none	none	none	>95%
	CL	none	none	none	none	none	none	none	none	none	none	none	none
	FT	none	none	>90%	none	none	none	none	none	none	none	none	>95%

- 1 The pure error value for Ca at pH = 5.0 was zero. Therefore all effects and interactions resulting in any variation, no matter how small, were statistically significant
- 2 All or a majority of the Cl concentrations at these pH levels were BDL. Therefore no statistical analysis could be done

Curvature proved statistically significant in some cases and insignificant in others. Out of the 45 ANOVA tables created from the pH-dependent leaching data, there were 25 cases where a treatment effect or interaction produced a significant concentration change of the analyte in question at a given pH. Of these 25 cases of significant concentration change, a linear model proved adequate to describe the leaching behavior in 14 cases, e.g., curvature was not statistically significant. In the remaining 11 cases, curvature was statistically significant. For the analytes, Cr, Fe, Mg, and Si, curvature was not significant at any of the pH levels. For the analytes, Ca and Zn, curvature was significant at every pH that produced concentration changes attributable to a treatment effect or interaction. For analytes Al, Ba, CO_3^{2-} , and K, there were mixed results with respect to the significance of curvature at pH levels where concentration changes proved statistically significant. At pH levels of 5.0 and 12.0 curvature proved statistically significant more often than not for analytes that experienced a concentration change attributable to one or more treatment effects and interactions. At pH levels of 7.3 and 9.7 curvature was more often insignificant for analytes that demonstrated a significant concentration change. Since curvature was not statistically significant in the majority of the ANOVAs, the experimental design proved adequate for describing the effects of accelerated aging on the pH-dependent leaching of the concrete prisms.

5.4.7.4 Main Effects

Of the 45 ANOVA tables produced detailing the pH-dependent leaching results, AA was found to produce significant changes in species concentrations in 20 analyses. FT was determined to have a significant effect 9 out of 45 times and CL was significant just 7 times. No pH level was noticeably more affected by the accelerated aging treatments than another.

Of the three aging methods, AA had the greatest effect on the leaching of selected species from the experimental prisms. Since this aging method was designed to accelerate the chemical reactions involved in the natural aging of concrete, it was not surprising to find this experimental aging method contributed the most to changes in leachability of various analytes. When CL was significant, it may have been due to the increased microcracking caused by CL (see section 5.4.2.2). Increased microcracking would correspond to facilitated species transport. When FT cycling was found to be significant, the cycling, which causes water movement, may have resulted in a “pumping” effect, facilitating species transport.

In conclusion:

1. Species concentrations in leachate were not typically affected by aging mechanisms.
2. When species concentrations were affected, AA had the greatest effect.
3. CL and FT treatments did, in some cases, affect species concentrations.

5.4.7.5 Interactions

Of the 45 pH-dependent leaching tests for which ANOVA tables were developed, the two-way interaction of AA and FT was more often a statistically significant effect, in 13 out of 45 analyses, than the other two-way or three-way interactions (see table 50). The CL and FT interaction was significant 10 of 45 times. The AA and CL interaction was statistically significant in 7 of 45 cases and the three-way interaction was significant in 6 of 45 cases.

The AA and FT interaction had the greatest effect on the leaching of selected species from the experimental prisms. The mechanisms of these two aging methods, more than CL aging, were expected to affect leaching. This compares with the AA/CL, CL/FT, and AA/CL/FT interactions found as affecting the fine pore structure of the concrete (see section 5.4.4.3).

In conclusion:

1. Interactions of aging treatments on leaching tests were found for all combinations, but primarily as AA/FT interactions.
2. With the exception of the AA/FT interaction, interactions match those affecting the fine pore system of the concrete.

5.4.7.6 Geochemical Modeling

The results of the pH-dependent leaching tests were input into a geochemical modeling program, MINTEQA2, in order to determine the controlling solid phases in the CFA-C concrete prisms. Selection of likely controlling solid phases that would be modeled was based on the output of the modeling program as well as a desire to model for phases that were quantified by XRPD. Each candidate solid was individually introduced into the modeling program with leachate data from pH 5.0, 7.3, 9.7, and 12.0. Figures K-11 through K-20 in Appendix K in volume II show the geochemical modeling of selected solids for 10 species leached from the CFA-C concrete prisms. Cl and K were not modeled. A successful identification of a controlling solid occurs when (i) the modeled concentrations agree with the experimental leaching data (± 1 log), (ii) the controlling solid describes leaching over the entire pH range examined, and (iii) the shape of the modeled leaching curve matches that of the experimental leaching curve. Table 51 summarizes the modeling of each solid for each species based on agreement in concentration and shape of modeled leaching curve.

Ca Modeling. As shown in figure K-11, Ca leaching was well modeled over the entire pH range by calcite (CaCO_3), dolomite ($\text{CaMg}(\text{CO}_3)_2$), and gypsum ($\text{CaSO}_4 \cdot 2\text{H}_2\text{O}$). Ettringite ($\text{Ca}_6\text{Al}_2(\text{SO}_4)_3(\text{OH})_{12} \cdot 26\text{H}_2\text{O}$) modeled well as a possible controlling solid at a pH greater than 7.3. All four of these phases were identified in the CFA-C concrete prisms by XRPD. Portlandite (CaOH_2) was also detected by XRPD, but the predicted leaching of portlandite was much higher than the observed data. Calcite has been shown to be a controlling solid for cement-based systems (EPRI, 1987) Calcite, dolomite, and gypsum are likely controlling solids for Ca leaching from the CFA-C concrete prisms. Calcite and dolomite were found to be likely controlling solids for the hydrated cement paste and the slab concrete (see sections 5.1.6.3 and 5.3.8.3).

Mg Modeling. Figure K-12 shows the geochemical modeling of Mg with candidate controlling solids dolomite ($\text{CaMg}(\text{CO}_3)_2$) and brucite ($\text{Mg}(\text{OH})_2$). Brucite can be a reaction product of MgO often found in CFA-C. Brucite modeling was only adequate at a pH of 12.0. At other pHs the predicted Mg concentration was much greater than the observed data. Dolomite modeled showed satisfactory agreement for a pH of 5.0 to a pH of 9.7. The predicted

Table 50: Summary of significant differences inspecies concentration in CFA-C leachate due to interaction effects.

species		Al				Ba				Ca			
pH		5.0	7.3	9.7	12.0	5.0	7.3	9.7	12.0	5.0 ¹	7.3	9.7	12.0
Interactions	AAxCL	none	>95%	none	none	none	>95%	none	none	>99%	none	none	none
	AAxFT	>90%	>95%	none	none	none	>95%	none	none	>99%	none	>95%	none
	CLxFT	none	>95%	>90%	none	none	none	none	none	>99%	none	none	none
	AAxCCxFT	none	none	>95%	none	>95%	none	none	none	>99%	none	none	none
species		Cl ²				CO ₃				Cr			
pH		5.0	7.3	9.7	12.0	5.0	7.3	9.7	12.0	5.0	7.3	9.7	12.0
Interactions	AAxCL	--	--	--	none	>95%	none	>90%	none	none	none	>95%	none
	AAxFT	--	--	--	none	>95%	none	>90%	none	>90%	>95%	>90%	none
	CLxFT	--	--	--	none	>95%	none	none	none	none	>95%	>95%	none
	AAxCLxFT	--	--	--	none	none	none	none	none	none	>90%	none	none
species		Fe				K				Mg			
pH		5.0	7.3	9.7	12.0	5.0	7.3	9.7	12.0	5.0	7.3	9.7	12.0
Interactions	AAxCL	none	none	none	none	none	none	none	none	none	none	none	>95%
	AAxFT	none	none	none	none	none	>90%	none	none	>95%	none	none	none
	CLxFT	none	>95%	none	none	none	none	none	none	none	none	none	>90%
	AAxCLcFT	none	none	none	none	>90%	none	none	none	none	none	none	none
species		Si				SO ₄				Zn			
pH		5.0	7.3	9.7	12.0	5.0	7.3	9.7	12.0	5.0	7.3	9.7	12.0
Interactions	AAxCL	none	none	none	none	none	none	none	none	none	none	none	none
	AAxFT	>90%	none	none	none	none	none	none	none	none	none	none	none
	CLxFT	>90%	none	none	none	none	none	none	none	none	none	none	>90%
	AAxCLxFT	none	none	>90%	none	none	none	none	none	none	none	none	none

- 1 The pure error value for Ca at pH = 5.0 was zero. Therefore all effects and interactions resulting in any variation, no mater how small, were statistically significant
- 2 All or a majority of the Cl concentrations at these pH levels were BDL. Therefore no statistical analysis could be done

Table 51: Geochemical modeling species for CFA-C prisms.

Species	Solid phase	log K _{sp}	Well modeled pH range
Al	Gibbsite Al(OH) ₃	-8.291	none
	Al(OH) ₃ amorphous	-10.800	none
	Ettringite (Ca ₆ Al ₂ (SO ₄) ₃ (OH) ₁₂ • 26H ₂ O)	-56.700	none
Ba	BaCrO ₄	9.670	5 - 10
	Barite (BaSO ₄)	9.980	5 - 12
Ca	Gypsum (CaSO ₄ • 2H ₂ O)	4.610	5 - 12
	Portlandite (Ca(OH) ₂)	-22.804	none
	Calcite (CaCO ₃)	8.480	5 - 12
	Dolomite (CaMg(CO ₃) ₂)	16.540	5 - 12
	Ettringite (Ca ₆ Al ₂ (SO ₄) ₃ (OH) ₁₂ • 26H ₂ O)	-56.700	7 - 12
CO ₃	Calcite (CaCO ₃)	8.480	7 - 10
	Dolomite (CaMg(CO ₃) ₂)	16.540	7 - 10
Cr	BaCrO ₄	9.670	none
Fe	Ferrihydrite (Fe(OH) ₃)	-3.191	none
	Maghemite (Fe ₂ O ₃)	-6.386	none
Mg	Dolomite (CaMg(CO ₃) ₂)	16.540	5 - 10
	Brucite (Mg(OH) ₂)	-16.844	~12
Si	Quartz (SiO ₂)	4.000	none
	SiO ₂ amorphous gel	2.710	5 - 7
SO ₄	Gypsum (CaSO ₄ • 2H ₂ O)	4.610	7 - 10
	Barite (BaSO ₄)	9.980	5 - 12
	Ettringite (Ca ₆ Al ₂ (SO ₄) ₃ (OH) ₁₂ • 26H ₂ O)	-56.700	10 - 12
Zn	Zincite (Zn(OH) ₂)	-11.334	none

concentration of Mg and the shape of the dolomite modeling curve deviated from the observed data at a pH of 12.0. Overall, and similarly to the hydrated cement paste and slab concretes, the leaching behavior of Mg was described by dolomite over most of the pH range, but, only for the laboratory concrete, better matched brucite modeling at the highest pH level.

Al Modeling. Figure K-13 shows the modeling of Al with ettringite ($\text{Ca}_6\text{Al}_2(\text{SO}_4)_3(\text{OH})_{12}\cdot 26\text{H}_2\text{O}$), gibbsite ($\text{Al}(\text{OH})_3$) and amorphous $\text{Al}(\text{OH})_3$. Ettringite was not a good model for the leaching of Al^{3+} from the CFA-C concrete prisms. Gibbsite was the best match of the three controlling solids, but the range of minimum solubility was shifted to a lower pH than was demonstrated for the experimental data. Crystalline Al phases identified by XRPD included albite ($\text{NaAlSi}_3\text{O}_8$), halloysite ($\text{Al}_2\text{Si}_2\text{O}_5(\text{OH})_4\cdot 2\text{H}_2\text{O}$), and other multiple oxide solids that do not exist in the MINTEQA2 database. Al^{3+} leaching in cement-based systems can be controlled by the hydrated Ca species, which are not included in the MINTEQA2 database (Glasser, 1997). Al was also not modeled well for the hydrated cement paste or the slab concrete.

Si Modeling. Si was modeled for both crystalline and amorphous SiO_2 in figure K-14. Neither solid adequately described the leaching behavior of Si observed in the CFA-C concrete prisms, despite a certain identification of quartz (SiO_2) in the concrete by XRPD. Similar results have been reported previously (Eighmy et al., 1994; Fruchter, 1990). The Ca-Al-silicates abundant in the concrete matrix may be the source of controlling solids for Si leaching, but these species are not present in the MINTEQA2 database and therefore were not modeled. Si was also not modeled well for the hydrated cement paste or the slab concrete.

Ba Modeling. Figure K-15 depicts the modeling of Ba leaching by barium chromate (BaCrO_4) and barite (BaSO_4). BaCrO_4 demonstrated a reasonable match in concentration between the predicted and observed data for the entire pH, but the shape of the modeled curve was in good agreement only from a pH of 5.0 to a pH of 9.7. Barite modeling agreed well with the observed leaching data for the entire pH range in both concentration and curve shape. SO_4^{2-} species have been shown to control Ba leaching in other systems (Fruchter, 1990). Barite was also found to be the controlling solid for the slab concrete but not for the hydrated cement paste.

Zn Modeling. Figure K-16 shows that the leaching behavior of Zn was unsuccessfully modeled by zincite ($\text{Zn}(\text{OH})_2$), the solid suggested as most likely to control Zn leaching by MINTEQA2. Other work has suggested that Zn sorbs to metal oxides, which then control the solubility of Zn (EPRI 1987; van der Sloot et al., 1994). Zn was also not modeled well for the hydrated cement paste or the slab concrete.

Fe Modeling. Geochemical modeling of Fe leaching was performed for candidate controlling solids ferrihydrite ($\text{Fe}(\text{OH})_3$) and maghemite (Fe_2O_3) (see figure K-17). Neither solid adequately modeled the leaching of Fe from the CFA-C concrete prisms. $\text{Fe}(\text{OH})_3$ has been identified as a likely controlling solid based on thermodynamic data (EPRI, 1987), but in modeling applications problems of agreement between observed and predicted data have been shown (Fruchter, 1990). Fe was also not modeled well for the hydrated cement paste or the slab concrete.

Cr Modeling. Figure K-18 depicts the modeling of Cr with barium chromate ($\text{BaCr}^{6+}\text{O}_4$). The predicted leaching curve of this solid agreed well with the observed leaching trends of Cr

from the CFA-C concrete prisms, but the predicted concentrations were considerably higher than the observed data. Cr^{3+} has been shown to substitute for Al^{3+} in cement hydration products and is then part of the Ca Al hydrates matrix (Glasser, 1997). Cr^{3+} solubility is then limited by these cement species rather than more common Cr oxides and hydroxides that would be found in the MINTEQA2 database. Cr was also not modeled well for the hydrated cement paste or the slab concrete.

CO_3^{2-} Modeling. Figure K-19 depicts the leaching behavior of CO_3^{2-} modeled by controlling solids calcite (CaCO_3) and dolomite ($\text{CaMg}(\text{CO}_3)_2$). Both calcite and dolomite show reasonable agreement with the observed data at a pH of 7.3 and a pH of 9.7. At a pH of 5.0, the observed CO_3^{2-} concentrations were much lower than the modeled concentrations. At a pH of 12.0, the observed CO_3^{2-} concentrations were higher than the modeled concentrations. CO_3^{2-} leaching was adequately modeled by calcite and dolomite in the middle of the pH range examined, but not at the highest and lowest pH points. Dolomite and calcite were also found as likely controlling solids for the slab concrete, but only at higher pH values. Dolomite and barite were likely controlling solids for the hydrated cement pastes.

SO_4^{2-} Modeling. SO_4^{2-} leaching is modeled by gypsum ($\text{CaSO}_4 \cdot 2\text{H}_2\text{O}$), barite (BaSO_4), and ettringite ($\text{Ca}_6\text{Al}_2(\text{SO}_4)_3(\text{OH})_{12} \cdot 26\text{H}_2\text{O}$) (see figure K-20). Barite was an excellent match of the modeling of the leaching data over the entire pH range. Gypsum modeling data were within concentration limits for most of the pH range but did not match well in the shape of the curve. Ettringite was not a well-modeled solid. As with the slab concrete, barite appears to be a controlling solid for SO_4^{2-} leaching (EPRI, 1987).

5.4.7.7 Conclusions

In conclusion:

1. There was a slight difference between the 28-d cured material and the temperature aged material with respect to buffering capacity, suggesting possible sample carbonation during the temperature aging.
2. There was no difference between the 28-d cured material and the temperature aged material with respect to solubility as a function of pH for Cd, Ni, and Zn.
3. There was a significant decrease of Pb solubility as a function of pH for the temperature-aged material and a slight decrease of Cu solubility for pHs greater than 8, suggesting possible sample carbonation during the temperature aging.
4. Most analytes were successfully modeled over some or part of the pH range examined.
5. The controlling solids identified for the CFA-C concrete prisms appear to be typical of cement-based leaching.
6. There was excellent correspondence of apparent controlling solids between the slab and the laboratory concretes.

5.4.8. Low Liquid-Solid Ratio Leaching

pH and conductivity as a function of the liquid-solid ratio (e.g., LS ratio of 10, 5, 2, 1 and 0.5 ml/g of dry material) of 28-d cured CFA-C mix and high temperature-aged CFA-C mix are compared in figure 81. Concentration of the species of concern (e.g., Na, K, Cl, SO_4^{2-} , and Ca) as a function of the liquid-solid ratio are compared in figure 82.

When LS ratio decreased from 10 to 0.5 ml/g of dry material, pH (see figure 81) increased slightly from 12.3 to 12.5 for C(XXX)02 and from 12.5 to 12.7 for C(HNN)13. The pH data obtained for C(HNN)13 were slightly greater overall (e.g., 0.1 to 0.2 pH unit) than that for C(XXX)02. The pH behavior of C(HNN)13 as a function of the LS ratio did not indicate any material carbonation and therefore did not confirm the results observed on the acid neutralization capacity of the material. When compared to similar data for the slab concrete (see figure 62 and section 5.3.9), the C(HNN) sample produced the most similar results. No significant difference could be observed between the two materials on conductivity data, except at the LS ratio of 10 ml/g of dry material for which a lower conductivity was found for C(HNN)13 (approximately 4 mS/cm for C(HNN)13 and 5.5 mS/cm for C(XXX)13). Here, the C(XXX) laboratory concrete better modeled the slab concrete.

Similar Na behavior as a function of the LS ratio could be observed for the 28-d cured material and the high temperature-aged material (see figure 82). For both materials, Na concentrations greatly increased as LS ratio decreased from 10 to 0.5 ml/g of dry material. No significant differences in Na concentrations could be observed between the two materials for LS ratios greater than 2 ml/g of dry material. At LS ratios less than 2 ml/g of dry material, Na concentrations of C(HNN)13 were slightly lower than that of C(XXX)02 (e.g., at LS 1, 400 mg/l for C(XXX)02 while 300 mg/l for C(HNN)13 and at LS 0.5, 700 mg/l for C(XXX)02 while 550 mg/l for C(HNN)13).

As with Na, K concentrations greatly increased as LS ratio decreased from 10 to 0.5 ml/g of dry material (see figure 82). No significant differences in K concentrations could be observed between the two materials, except for an LS of 0.5 ml/g of dry material. At this LS ratio, K concentration appeared to be slightly greater for C(XXX)02 than for C(HNN)13 (e.g., 700 to 800 mg/l and 600 to 650 mg/l for C(XXX)02 and C(HNN)13, respectively). However, the observed differences were in the same order as that observed between two replicates of the same material. Therefore, these differences could likely be due to material heterogeneity.

Cl concentrations as a function of the LS ratio were overall slightly higher for the temperature-aged material than for the 28-d cured material (see figure 82). For C(XXX)02, Cl concentration increased from 10 mg/l to 35 mg/l as LS ratio decreased from 10 to 0.5 ml/g of dry material. For C(HNN)13, Cl concentration increased from 10 mg/l to 60 mg/l as LS ratio decreased from 10 to 0.5 ml/g dry.

Overall, low SO_4^{2-} concentrations (e.g., less than 10 mg/l) were observed for both materials (see figure 82). When the LS ratio decreased, a slight increase in SO_4^{2-} concentration was first observed, specially for C(XXX)02, followed by a decrease for LS ratio less than 5 ml/g of dry material. At LS ratio of 5, 2 and 1 ml/g of dry material, SO_4^{2-} concentrations obtained for C(HNN)13 were lower than that obtained for C(XXX)02. At LS ratio of 10 and 0.5 ml/g of dry material, there was no significant difference in SO_4^{2-} concentration between the two materials.

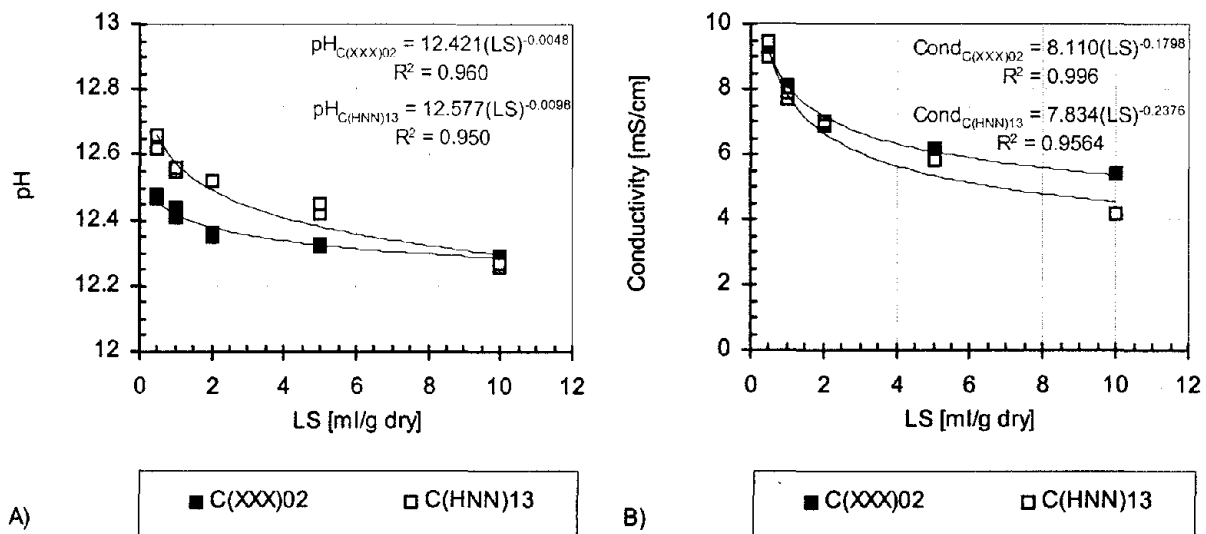


Figure 81: A) pH and B) conductivity as a function of LS ratio.

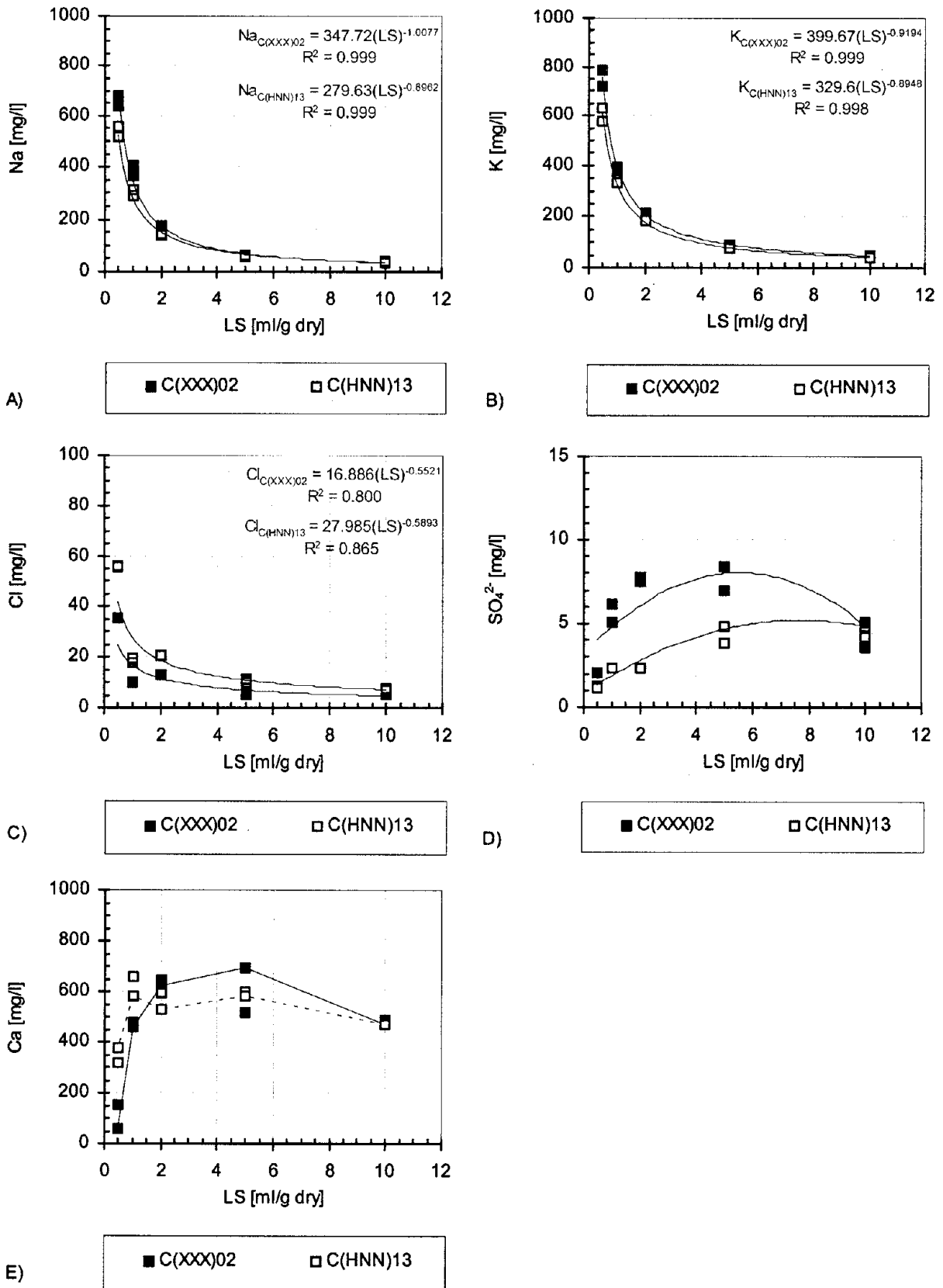


Figure 82: Major species concentration as a function of LS ratio:
 A) Na, B) K, C) Cl, D) SO_4^{2-} , and E) Ca.

Similar Ca behavior as a function of the LS ratio could be observed for both materials (see figure 82) with Ca concentration slightly higher greater for the temperature-aged material at LS ratio of 1 and 0.5 ml/g dry. For C(XXX)02, Ca concentration first increased from 500 mg/l to 600 mg/l when LS ratio decreased from 10 to 2 ml/g dry, followed by a decrease to 50 mg/l when LS decreased from 2 to 0.5 ml/g dry. For C(HNN)13, Ca concentration first increased from 500 mg/l to 700 mg/l when LS ratio decreased from 10 to 2 ml/g dry, followed by a decrease to 300 mg/l when LS decreased from 2 to 0.5 ml/g dry. As with pH data, the Ca behavior of C(HNN)13 as a function of the LS ratio did not indicate any material carbonation.

When compared with the slab concrete (see section 5.3.9 and figure 63), Na, K, Ca, and Cl concentrations of both laboratory concretes match well. The SO_4^{2-} concentrations match moderately better for the C(HNN) laboratory concrete.

Table 52 provides a comparison of the physical and chemical properties measured at LS of 5 ml/g dry for each sample and the estimated values for the pore water in each case.

For the 28-d cured material, an open porosity of 8.0 percent was estimated from the moisture content and density of sample C(XXX)02, assuming that the pores were completely filled with water (e.g., moisture of 3.0 percent and matrix density of 2.7 g wet/cm³). This resulted in an estimated pore water LS ratio of 0.03 ml/g dry. Empirical curve fits were used to estimate pH and species concentrations to this LS ratio. Extrapolations resulted in estimated pH of 12.7 with concentrations of Na, K, Cl, SO_4^{2-} , and Ca of 11,900 mg/l, 10,000 mg/l, 120 mg/l, 0.8 mg/l, and less than 50 mg/l, respectively. Charge balances indicated that anionic species other than OH^- (as obtained from pH measurement), Cl^- , and SO_4^{2-} were likely present in the matrix pore water. These anionic species might likely be CO_3^{2-} due to the large quantities of limestone (e.g., 78 percent). Ionic strength of the pore water was estimated to be 1.2 mol/l, which corresponds to an activity coefficient of 0.73 for ions with a charge number of 1 and 0.29 for ions with a charge number of 2 (Hemond and Fechner, 1994). In contrast, the estimated ionic strength for an LS ratio of 5 (e.g., typical LS ratio for most equilibrium batch tests) was 0.05 mol/l, which corresponds to an activity coefficient of 0.85 for ions with a charge number of 1 and 0.53 for ions with a charge number of 2 (Linde, 1996).

For the high AA aged material, an open porosity of 7.4 percent was estimated from the moisture content and density of sample C(HNN)13, assuming that the pores were completely filled with water (e.g., moisture of 3.0 percent and matrix density of 2.5 g wet/cm³). This resulted in an estimated pore water LS ratio of 0.03 ml/g dry. Empirical curve fits were then used to estimate pH and species concentrations to this LS ratio. Extrapolations resulted in an estimated pH of 13 with concentrations of Na, K, Cl, SO_4^{2-} , and Ca of 6,500 mg/l, 7,600 mg/l, 220 mg/l, 0.8 mg/l, and less than 100 mg/l, respectively. Charge balances on the pore water of the matrix indicated that anionic species other than OH^- (as obtained from pH measurement), Cl^- , and SO_4^{2-} were likely present in the matrix pore water. These anionic species might likely be CO_3^{2-} due to the large quantities of lime stone type aggregates (e.g., 78 percent) present in the sample.

Table 52: Physical properties of 28-d cured and high temperature-aged CFA-C prisms and chemical properties of leachates and pore water.

Physical or Chemical Property	Material type	
	C(XXX)02	C(HNN)13
Moisture content (%)	3	3
Density (g/cm ³)	2.7	2.5
Open porosity (%)	8	7.4
LS estimated for p.w. ^a (ml/g)	0.03	0.03
pH (standard units)		
at LS 5	12.3	12.5
Estimated for p.w.	12.7	13
Na (mg/l)		
at LS 5	63	62
Estimated for p.w.	11,900	6,500
K (mg/l)		
at LS 5	90	80
Estimated for p.w.	10,000	7,600
Cl (mg/l)		
at LS 5	6	11
Estimated for p.w.	120	220
SO ₄ ²⁻ (mg/l)		
at LS 5	8	4.5
Estimated for p.w.	0.8	0.8
Ca (mg/l)		
at LS 5	520	590
Estimated for p.w.	< 50	< 50
Ionic strength (mol/l)		
at LS 5	0.05	0.05
Estimated for p.w.	1.2	0.7
Activity coefficient		
charge ± 1		
at LS 5	0.85	0.85
Estimated for p.w.	0.73	0.71
charge ± 2		
at LS 5	0.53	0.53
Estimated for p.w.	0.29	0.26

^a p.w. – pore water

Therefore, the ionic strength of the pore water was estimated to be 0.7 mol/l, which corresponds to an activity coefficient of 0.71 for ions with a charge number of 1 and 0.26 for ions with a charge number of 2 (Hemond and Fechner, 1994). In contrast, the estimated ionic strength for an LS ratio of 5 (e.g., typical LS ratio for most equilibrium batch tests) was 0.05 mol/l, which corresponds to an activity coefficient of 0.85 for ions with a charge number of 1 and 0.53 for ions with a charge number of 2 (Linde, 1996).

In conclusion:

1. AA did not result in a significant change in the leaching behavior of primary matrix components (e.g., Ca, Na, K, SO_4^{2-} , Cl) as a function of LS ratio.
2. AA did not affect the ionic strength at an LS ratio of 5 ml/g dry (e.g., typical LS ratio for most equilibrium batch tests) but resulted in a decrease in pore water ionic strength.
3. For the slab concrete, the estimated LS concentration and pH of the pore water in the slab concrete were 0.03 ml/dry gram and 13.7, respectively. For the C(XXX) concrete, the values were 0.03 and 12.7, respectively. For the C(HNN) concrete, the values were 0.03 and 13, respectively.
4. There was very good agreement of low LS leaching behaviors between slab and laboratory concretes.

5.4.9. Prism Constituent Availability Leaching

Availability leaching tests were not completed on the aged materials because pH-dependent leaching and low LS leaching did not show significant changes in the leaching chemistry of the major species and trace metals of concern.

5.4.10. Monolithic Leaching

5.4.10.1 C(XXX)13, C(HNN)13, C(NHN)13, C(NNH)13, C(HHH)13

The effect of AA, CL, and FT on the matrix integrity was examined using pH, conductivity, and leaching behavior of primary matrix components (e.g., Ca, Na, K, SO_4^{2-} , Cl). As a first step, only samples of CFA-C mix that were submitted to high levels of aging were tested in order to assess the impact of aging. These samples included C(HNN), C(NHN), C(NNH), and C(HHH). As a baseline, one sample of 28-d cured CFA-C mix was tested (e.g., C(XXX)02). The four aged samples of concern were leached for 10 mo with periodic renewals resulting in 16 extracts. The 28-d cured sample was leached for 20 mo with periodic renewals resulting in 18 extracts. Only one replicate of each sample was carried out.

pH and Conductivity. Final leachate pH and conductivity obtained after each leaching interval for the four aged samples of concern and the 28-d cured sample are compared in figure 83. During the initial 200 d (e.g., approximately 7 mo) of leaching with periodic renewals, leachate pH of C(XXX)02 appeared to be overall slightly greater than that of the four high level

aged samples. After 200 d of leaching an increase in leachate pH of the four aged samples was observed, and leachate pH was then similar to that of C(XXX)02. Between the aged-samples, although slight differences in pH could be observed (the greatest leachate pH seemed to be obtained for C(HHH)13), no clear tendency resulting from aging effects could be observed. As with pH, during the initial 200 d of leaching, leachate conductivity of C(XXX)02 appeared to be slightly higher than that of the four aged samples. After 200 d of leaching, leachate conductivity of the four aged samples increased and was similar to or greater than that of C(XXX)02. Between the aged samples, although the greatest conductivities were obtained for C(HHH)13 and the least for C(NHN)13, no clear tendency resulting from aging effect could be observed. From these results, it seemed that, over the 10 mo of leaching examined, there was no significant effect of the three types of aging on leachate pH and conductivity.

Release and flux plots for major constituents are shown in figures 84 and K-21 through K-24 in appendix K of volume II.

Na Release. During the initial 100 d of leaching (see figure 84), no significant difference in Na cumulative release as well as in the released flux could be observed between the 28-d cured and high level aged samples. Moreover, the release of Na was overall relatively low with less than 3 percent of the total content in Na released after 100 d of leaching with a cumulative release of Na from C(HNN)13, C(NNH)13, and C(HHH)13 slightly greater than that from C(XXX)02 and C(NHN)13. Thus, after 300 d (e.g., 10 mo) of leaching with periodic renewals, approximately 130 mg/kg was released from C(XXX)02 and C(NHN)13, approximately 150 mg/kg from C(HNN)13, approximately 160 mg/kg from C(NNH)13, and approximately 170 mg/kg from C(HHH)13. However, no clear tendency resulting from aging effects could be observed. In addition, no significant difference in Na released flux was observed over the 10 mo of leaching. Therefore, from these results, it seemed that, over the 10 mo of leaching, there was no substantial effect of the three types of aging on the release of Na.

Na release for the laboratory concretes was lower than that for the middle slab portion of the slab concrete though release curve shapes and fluxes matched well (see section 5.3.11 and figure 66)

K Release. The cumulative release of K from C(XXX)02 appeared to be slightly greater than that from C(HNN)13, C(NHN)13, C(NNH)13 and C(HHH)13 (see figure K-21). Between the aged samples, although slight differences in K cumulative release could be observed (e.g., approximately 150 mg/kg released from C(HNN)13 after 10 mo of leaching, approximately 160 mg/kg from C(NHN)13, approximately 190 mg/kg from C(NNH)13 and approximately 160 mg/kg from C(HHH)), no clear tendency resulting from aging effects could be seen.

It is difficult to attribute the observed differences to aging effects because the release of K was low (e.g., less than 6 percent of the total content in K released for all the samples after 10

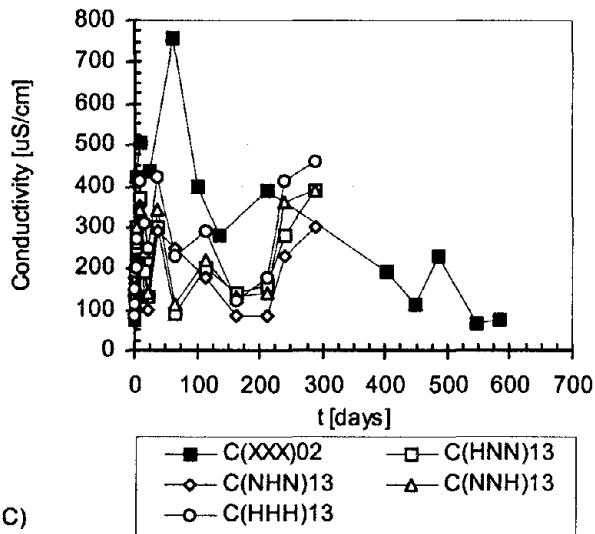
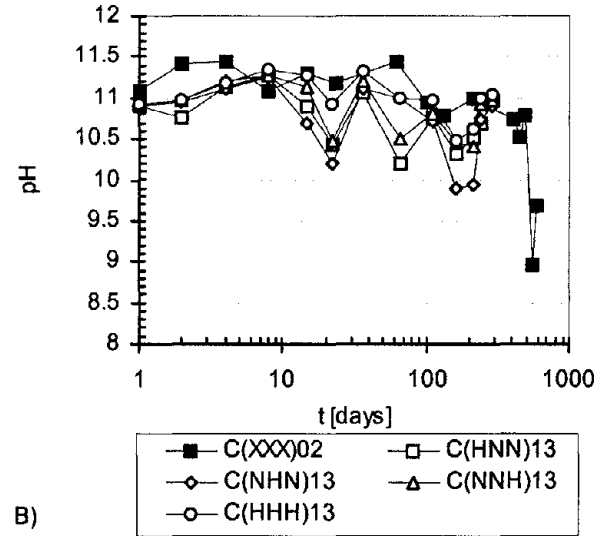
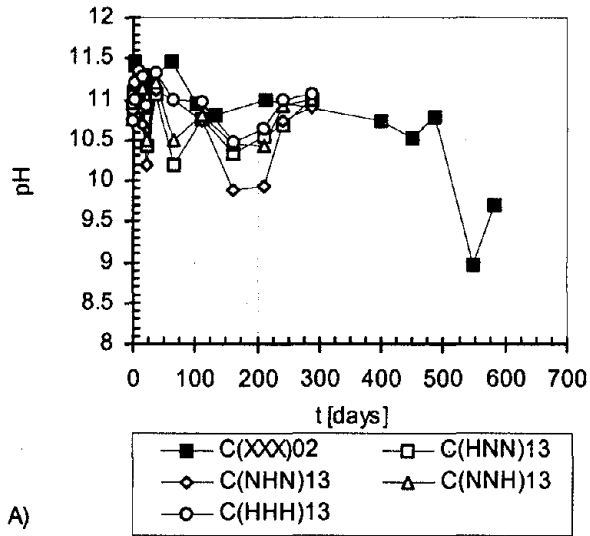


Figure 83: A) leachate pH, B) leachate pH, and C) leachate conductivity for CFA-C mix.

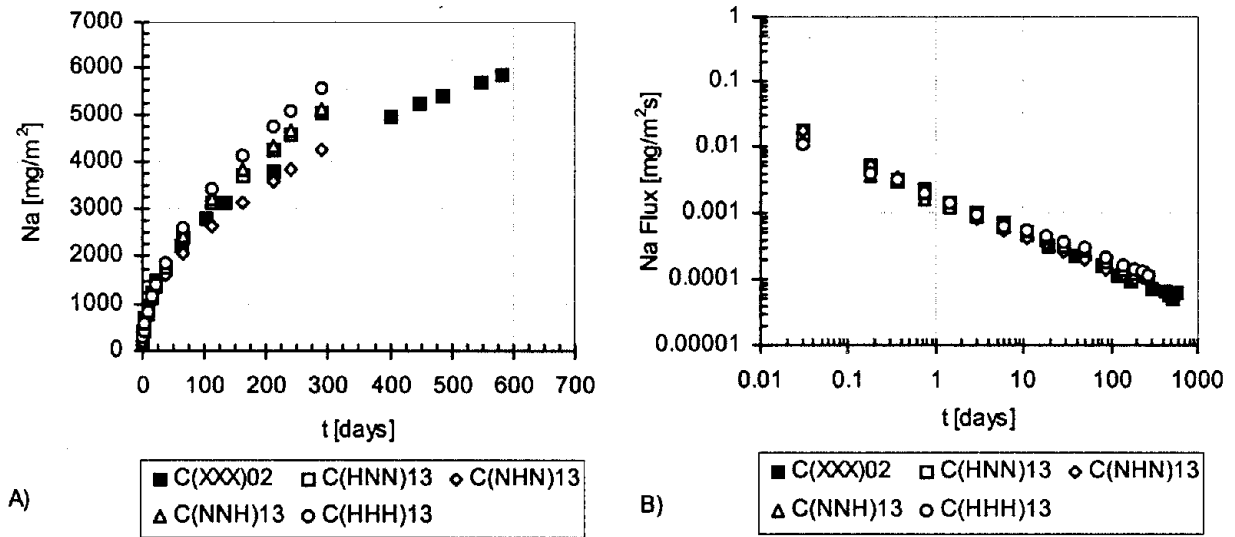


Figure 84: Na release for 28-d cured and high level aged samples: A) cumulative mass released in mg/m^2 ; B) flux released in $\text{mg}/\text{m}^2\text{s}$.

mo of leaching). In addition no significant difference in K released flux was observed. From these results, it seemed that, over the 10 mo of leaching examined, there was no significant effect of the three types of aging on the release of K.

K release for the laboratory concretes was lower than that for the middle slab portion of the slab concrete though release curve shapes and fluxes matched well (see section 5.3.11)

Cl Release. For all samples, all the concentration measured in the leachates was close to or below the Dionex ion chromatograph detection limit (e.g., 1 mg/l). In addition, signals obtained during analyses were noisy. Therefore, no interpretation of the results (see figure K-22) could be done due to large uncertainties on the analyses.

Cl release fluxes match well in curve shape and magnitude to that of the middle slab portions of the slab concrete (see section 5.3.11).

SO₄²⁻ Release. The cumulative release of SO₄²⁻ from C(HNN)13, C(NHN)13, C(NNH)13, and C(HHH)13 was much greater than that from C(XXX)02 (see figure K-23). Thus after 100 d of leaching, 120 mg/kg was released from C(HNN)13, 100 mg/kg from C(NHN)13, 80 mg/kg from C(NNH)13, 115 mg/kg from C(HHH)13, and only 50 mg/kg for C(XXX)02. During the initial 10 d of leaching, the released flux of SO₄²⁻ from the aged samples (e.g., C(HNN)13, C(NHN)13, C(NNH)13, and C(HHH)13) was 4 times greater than the released flux from C(XXX)02. However, after 10 d of leaching (e.g., at longer leaching intervals), no significant differences in SO₄²⁻ released flux could be observed between the 28-d cured and aged samples, suggesting that the initial difference could be due to surface wash-off.

SO₄²⁻ release of the C(XXX) concrete best matched the middle slab portion of the slab concrete in release curve shape and magnitude and in flux curves.

Ca Release. The cumulative release of Ca from C(XXX)02 appeared to be slightly greater than the cumulative release from C(HNN)13, C(NHN)13, C(NNH)13, and C(HHH)13 (see figure K-24). The difference started to be seen only after 10 d of leaching. Thus, after 100 d of leaching, 1,100 mg/kg was released from C(XXX)02, 800 mg/kg from C(HNN)13, 760 mg/kg from C(NHN)13, 820 mg/kg from C(NNH)13, and 975 mg/kg from C(HHH)13. In addition, after 36 d of leaching, the cumulative release of Ca from C(HHH)13 appeared to be slightly greater than the one from C(HNN)13, C(NHN)13, C(NNH)13, and C(HHH)13, consistent with leachate pH. However, no significant differences in Ca released flux could be observed between the samples. From these results, it seemed that, over the 10 mo of leaching examined, there was no substantial effect observed from the three types of aging on the release of Ca.

Ca release of the C(XXX) sample best matched that of the slab concrete in the middle slab portion (see section 5.3.11).

5.4.10.2 CFA-C Samples with Other Levels of Aging

The other levels of aging and the 3 center point replicates of CFA-C mix were tested for an overall cumulative leaching time of 4 mo with periodic renewals resulting in 12 extracts. These samples included C(NHH), C(HNH), C(HHN), C(NNN), and C(LLl). Results of pH, conductivity, and leaching behavior of primary matrix components (e.g., Na, K, and Ca) are presented in figures 85 and 86 as well as K-25 through K-26 in appendix K of volume II. The 4-mo results obtained for the four high level aged and the 28-d cured CFA-C mix samples are also shown for comparison. In all 12 materials were examined. For each material only one replicate was carried out.

pH and Conductivity. Final leachate pH and conductivity obtained after each leaching interval for the seven aged samples of concern, the four high level aged samples, and the 28-d cured sample are compared in figure 85.

Leachate pH of C(XXX)02 appeared to be overall slightly greater than that of the 11 aged samples. During the initial 10 d of leaching, final leachate pH of the four high level aged samples were slightly greater than that of the other aged samples. This behavior was reversed after 40 d of leaching. Although slight differences in pH could be observed between the aged samples, no clear tendency resulting from aging effects could be observed. Leachate conductivity of the four high level aged samples was, after 10 d of leaching, less than that of the other level aged samples. The greatest leachate conductivity was observed for the three center point replicates. As with pH, no clear tendency resulting from aging effect could be observed on leachate conductivity.

Na Release. After 4 mo of leaching, a much greater Na cumulative release was observed for the three center point replicates (figure 86). In addition, after 5 d of leaching, significant differences in Na cumulative release were observed between these samples indicating poor reproducibility between the center point replicates. Thus, after 4 mo of leaching, Na cumulative release of C(LLl)16 (e.g., 180 mg/kg) was greater than that of C(LLl)47 (e.g., 160 mg/kg), and was much greater than that of C(LLl)30 (e.g., 120 mg/kg). During the initial 40 d of leaching, no significant difference in Na cumulative release (figure 86 A) could be observed between the 28-d cured sample, the four high level aged samples, and the other aged samples except for the three center point replicates for which the cumulative release of Na was already much greater. After 40 d of leaching, slight differences in Na cumulative release between the aged samples could be observed with nevertheless no clear tendency resulting from aging effects. It is difficult to attribute the observed differences to aging effects because much greater differences were observed between the three center point replicates. Therefore it seemed that the observed differences in Na cumulative release between the aged samples were on the order of uncertainties, indicating that there was no substantial effect observed from the three types of aging (e.g., AA, CL, and FT) on the release of Na. In addition, although a slightly greater flux of Na was observed for C(LLl)16 and slightly less for C(NNN)14, no substantial difference in Na release flux (figure 86 B) could be observed between the samples over the 4 mo of leaching examined.

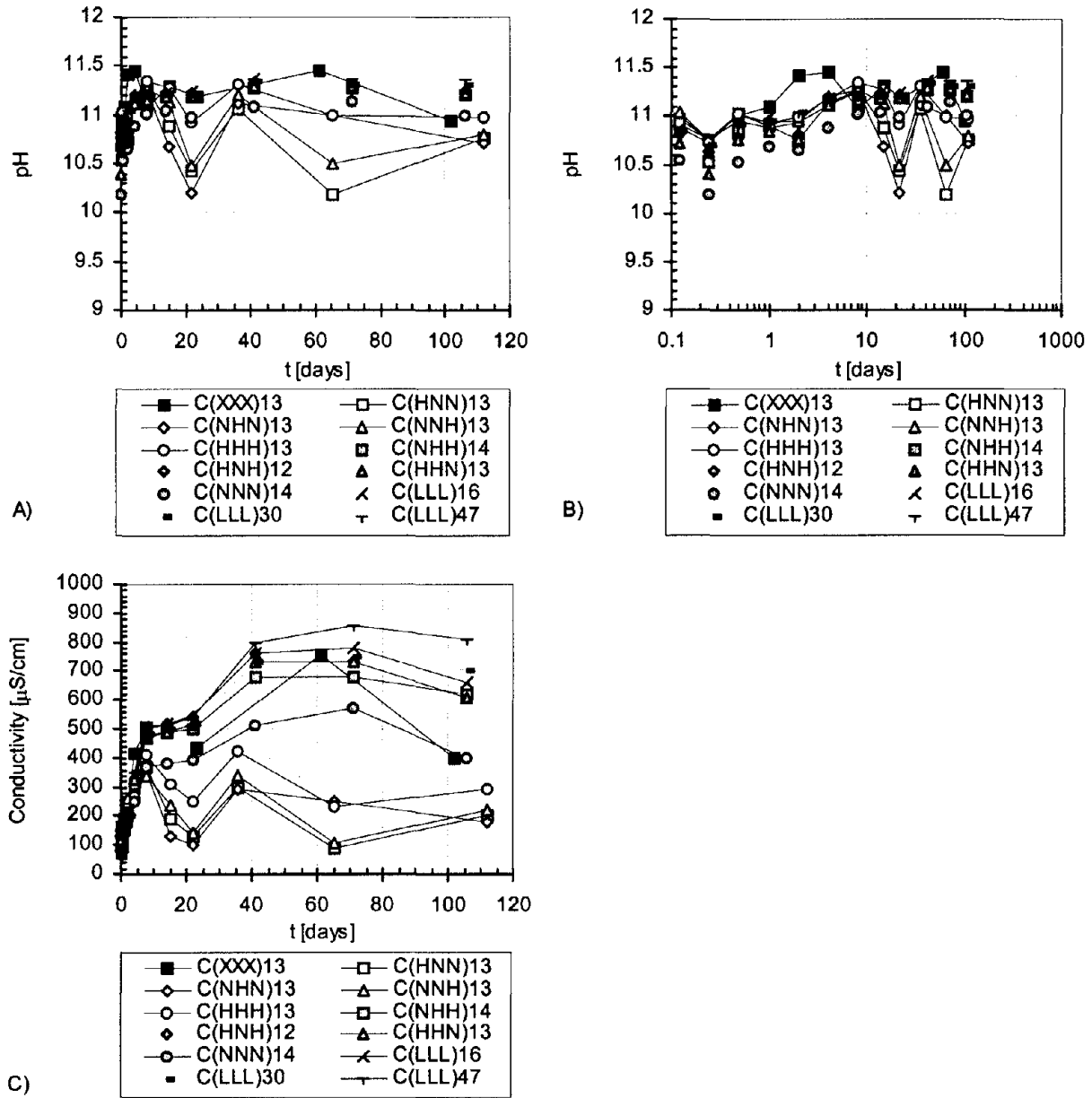


Figure 85: A) leachate pH, B) leachate pH, and C) leachate conductivity for CFA-C mix. Comparison between 28-d cured and aged samples.

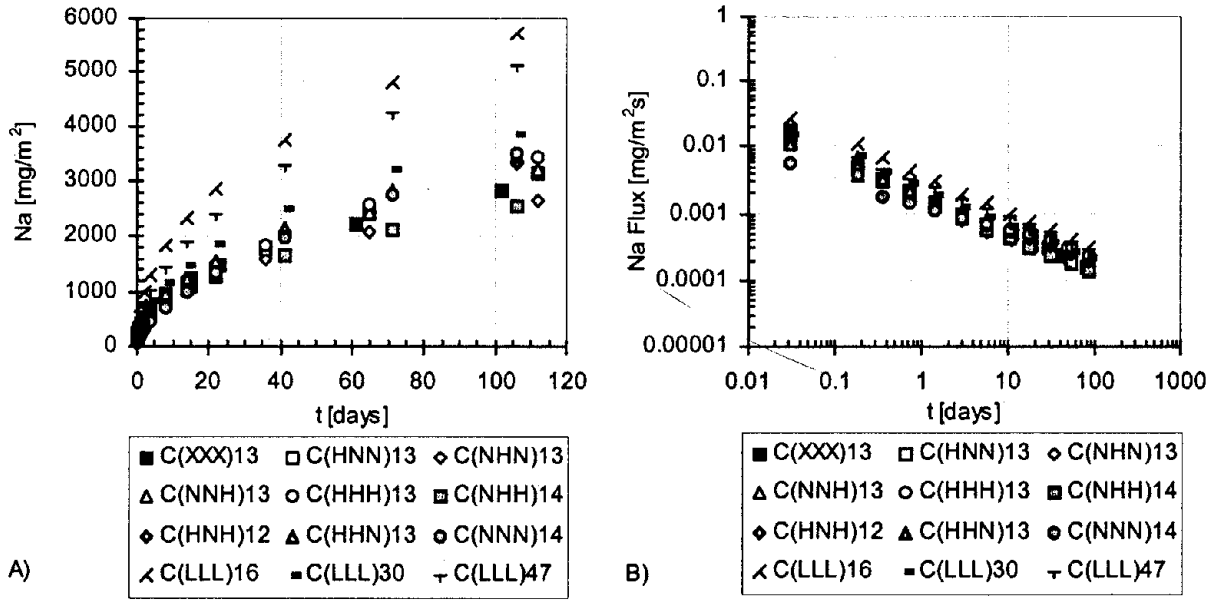


Figure 86: Na release for 28-d cured and aged samples.
 A) cumulative mass released in mg/m²; B) flux released in mg/m²s.

K Release. As with Na, after 4 mo of leaching a much greater K cumulative release was observed for the three center point replicates (figure K-25). In addition, after 15 d of leaching, differences in K cumulative release were observed between these samples, indicating poor reproducibility between the center point replicates. Thus, after 4 mo of leaching with periodic renewals, K cumulative release of C(LL)16 (e.g., 180 mg/kg) was much greater than that of C(LL)47 (e.g., 150 mg/kg), which was slightly greater than that of C(LL)30 (e.g., 145 mg/kg). Although slight differences in K cumulative release could be observed between the aged samples, no clear tendency resulting from aging effects could be observed. As with Na, it is difficult to attribute the observed differences to aging effects because much greater differences were observed between the three center point replicates. Therefore it seemed that the observed differences in K cumulative release between the aged samples were on the order of uncertainties, indicating that there was no substantial effect observed from the three types of aging (e.g., AA, CL, and FT) on the release of K. In addition, no significant difference in K release flux (see figure K-25) could be observed between the samples over the 4 mo of leaching examined.

Ca Release. In contrast with Na and K cumulative release, there was no significant difference in Ca cumulative release between the three center point replicates over the 4 mo of leaching. During the initial 20 d of leaching with periodic renewals, there was no significant difference in Ca cumulative release between the 11 aged samples and the 28-d cured CFA-C mix sample (see figure K-26). After 20 d of leaching, the cumulative release of Ca from the four high level aged samples was less than that from the other aged samples and the 28-d cured sample. Slight differences in Ca cumulative release could be observed after 40 d of leaching between the aged samples. Differences in Ca release flux were not apparent between the samples over the 4 mo of leaching examined.

5.4.10.3 ANOVA Analysis

ANOVA was carried out on the cumulative release of Na, K and Ca obtained at 22 d of leaching.⁴ Calculated F values and tabulated F values at 99 percent, 95 percent, and 90 percent are compared in tables 53, 54, and 55.

5.4.10.4 Main Effects

ANOVA carried out on the cumulative release of Na and K at 22 d of leaching provided calculated F values that were much less than the tabulated F values at 99 percent, 95 percent and 90 percent. These results indicated that the experimental variable of interest (e.g., AA, CL, or FT) did not have any statistically significant effect on the cumulative release of Na and K.

For the cumulative release of Ca at 22 d of leaching, when considering the three types of aging individually, much greater calculated F values than the tabulated ones were obtained.

4 Twenty-two days of leaching were chosen for ANOVA because that represented the greatest cumulative leaching time common to all samples.

Table 53: ANOVA on the effects of accelerated aging on Na cumulative release at 22 d of leaching - CFA-C prisms.

Source	Effect	Sum of squares	DF	Mean square	F ratio	Significant at
AA	50.425	5085.3612	1	5085.3612	0.021	none
CL	103.125	21269.531	1	21269.531	0.087	none
FT	45.125	4072.5313	1	4072.5313	0.017	none
AAxCL	-3.525	24.85125	1	24.85125	0.000	none
AAxFT	-147.525	43527.251	1	43527.251	0.177	none
CLxFT	35.075	2460.5113	1	2460.5113	0.010	none
AAxCLxFT	-57.175	6537.9612	1	6537.9612	0.027	none
Curvature		2086571.9	1	2086571.9	8.499	none
Pure Error		491040.67	2	245520.33		
Total		2.66E+06	10			

Table 54: ANOVA on the effects of accelerated aging on K cumulative release at 22 d of leaching - CFA-C prisms.

Source	Effect	Sum of squares	DF	Mean square	F ratio	Significant at
AA	-289.675	167823.21	1	167823.21	0.889	none
CL	108.975	23751.101	1	23751.101	0.126	none
FT	109.725	24079.151	1	24079.151	0.128	none
AAxCL	-126.875	32194.531	1	32194.531	0.171	none
AAxFT	-139.125	38711.531	1	38711.531	0.205	none
CLxFT	-59.375	7050.7813	1	7050.7813	0.037	none
AAxCLxFT	-282.925	160093.11	1	160093.11	0.849	none
Curvature		1810720.2	1	1810720.2	9.597	>90%
Pure Error		377345.79	2	188672.89		
Total		2.64E+06	10			

Table 55: ANOVA on the effects of accelerated aging on Ca cumulative release at 22 d of leaching - CFA-C prisms.

Source	Effect	Sum of squares	DF	Mean square	F ratio	Significant at
AA	2243.35	10065238	1	10065238	995.365	>99%
CL	798.65	1275683.6	1	1275683.6	126.154	>99%
FT	2171.15	9427784.6	1	9427784.6	932.326	>99%
AAxCL	235.3	110732.18	1	110732.18	10.950	>90%
AAxFT	-976	1905152	1	1905152	188.403	>99%
CLxFT	-231.3	106999.38	1	106999.38	10.581	>90%
AAxCLxFT	-7091.75	100585836	1	100585836	9947.067	>99%
Curvature		45680794	1	45680794	4517.434	>99%
Pure Error		20224.22	2	10112.11		
Total		1.69E+08	10			

5.4.10.5 Interactions

ANOVA carried out on the cumulative release of Na and K at 22 d of leaching showed that the experimental variable of interest (e.g., AA, CL, or FT) did not have any statistically significant effect on the cumulative release of Na and K.

When AA and FT interactions were considered, a much greater calculated F value was obtained. Similarly, when the three-way interaction was considered, a much greater calculated F value was obtained. However, when AA and CL interactions were considered or when the CL and the FT were considered, the calculated F values were less than the tabulated ones at 99 percent and 95 percent but slightly greater than the tabulated one at 90 percent.

5.4.10.6 Conclusions

In conclusion:

1. For leachate pH and conductivity, no clear tendency resulting from any aging treatment was observed.
2. The experimental variables (AA, CL, and FT) did not significantly affect cumulative release of Na or K.
3. The experimental variables (AA, CL, and FT) did significantly affect cumulative release of Ca.
4. The interactions of AA and FT as well as AA, CL, and FT significantly affected Ca cumulative release.

5.4.11. Release Modeling

The effect of AA, CL, and FT on the release modeling was explored. Release modeling allowed for examination of the effects of the experimental design on the diffusivity of components leaching from the monoliths.

5.4.11.1 Release Modeling for C(XXX)13, C(HNN)13, C(NHN)13, C(NNH)13, C(HHH)13

The one-dimensional diffusion model was used to interpret the release of Na, K, Cl, and Ca from the 28-d cured CFA-C mix sample (e.g., C(XXX)02) and the four high level aged CFA-C mix samples (e.g., C(HNN)13, C(NHN)13, C(NNH)13, and C(HHH)13). During the time scale of the laboratory testing (e.g., 7 mo for the four aged samples and 20 mo for the 28-d cured sample), no depletion of these species within the matrices was observed. For each species of concern, three different observed diffusivities (e.g., $D_{\text{obs } 1}$, $D_{\text{obs } 2}$ and $D_{\text{obs } 3}$) were determined. $D_{\text{obs } 1}$ was calculated assuming that the initial leachable concentration C_D was the total content of the species of concern. $D_{\text{obs } 2}$ was calculated assuming that the initial leachable concentration C_D was the species content provided only by the cement and the CFA-C. $D_{\text{obs } 3}$ was calculated assuming

that (i) the initial leachable concentration C_D was the species content provided only by the cement and the CFA-C, (ii) the aggregates were inert and uniformly distributed within the matrix, and (iii) the flux was only provided by the fraction of the surface⁵ of the sample non-occupied by the aggregates. Thus, while D_{obs1} and D_{obs2} correspond to observed diffusivities through the overall matrix (e.g., binder and aggregates), D_{obs3} corresponds to an observed diffusivity only through the binder (e.g., cement and CFA-C). Initial leachable concentrations and observed diffusivities of the 28-d cured and the four high level aged CFA-C mix samples are compared in tables 56 through 59 for Na, K, Cl, and Ca, respectively. Ratios of observed diffusivity to molecular diffusivity are also compared with estimate of matrix tortuosity calculated using the Millington-Quirk relationship [Millington et al., 1971] (e.g., τ_{MQ} of $\epsilon^{-4/3}$, where τ_{MQ} and ϵ are tortuosity and matrix porosity, respectively).

Na Modeling. Low Na observed diffusivities (e.g., on the order of 10^{-15} m²/s) were calculated using the Na total content for the 28-d cured CFA-C mix sample (e.g., C(XXX)02) and the four high level aged CFA-C mix samples (e.g., C(HNN)13, C(NHN)13, C(NNH)13 and C(HHH)13) (see table 56). This resulted in ratios of observed diffusivity to molecular diffusivity for Na as much as five orders of magnitude greater than the estimated tortuosity using the Millington-Quirk relationship (e.g., τ_{MQ} of 30). This comparison indicated that significant retention of Na occurred within the concrete materials and the assumption of a homogeneous matrix was not appropriate. Na observed diffusivity of the 28-d cured CFA-C mix sample (e.g., $6.5 \cdot 10^{-15}$ m²/s) was slightly lower than that of the four high level aged materials for which the observed diffusivity ranged from $8.0 \cdot 10^{-15}$ m²/s to $11.0 \cdot 10^{-15}$ m²/s. Within the four high level aged materials, the sample that was submitted to the three high levels of aging (e.g., C(HHH)13) provided the greatest value of Na observed diffusivity (i.e., $11.0 \cdot 10^{-15}$ m²/s) while the sample that was only submitted to the high level of cyclical mechanical stress provided the least value (e.g., $8.0 \cdot 10^{-15}$ m²/s). When considering only the Na content provided by the cement and the CFA-C, the diffusivity results (e.g., D_{obs2} and D_{obs3}) changed by two orders of magnitude. However, much greater ratios of observed diffusivity to molecular diffusivity for Na than the estimated tortuosity using the Millington-Quirk relationship were obtained (e.g., 3000 for ratios and 30 for estimated tortuosity). Diffusivity slightly increased (D_{obs3} were 3 times greater than D_{obs2}) when calculations were done by accounting only for the surface of the matrix not occupied by the aggregates. In that case, no significant difference in Na observed diffusivity could be observed between the 28-d cured and the four high level aged CFA-C mix samples. Indeed, Na observed diffusivities ranged from $1.1 \cdot 10^{-12}$ m²/s for C(XXX)02 to $1.8 \cdot 10^{-12}$ m²/s for C(HHH)13.

K Modeling. As with Na, low K observed diffusivities (e.g., on the order of 10^{-14} m²/s) were calculated using the K total content for the 28-d cured CFA-C mix sample (e.g., C(XXX)02) and the four high level aged CFA-C mix samples (e.g., C(HNN)13, C(NHN)13, C(NNH)13, and C(HHH)13) (see table 57). This resulted in ratios of observed diffusivity to molecular diffusivity for K as much as four orders of magnitude greater than the estimated

5 As a first approach, it was assumed that 57.5 percent of the surface of the material was non-occupied by the aggregates (42.5 percent of coarse aggregates were used in the mix design).

Table 56: Parameter estimates for the release of Na from the one-dimensional diffusion model – 28-d cured and high level aged CFA-C prisms.

	28-d cured CFA-C mix	High level aged CFA-C mix			
	C(XXX)02	C(HNN)13	C(NHN)13	C(NNH)13	C(HHH)13
C_0^a [(mg elemental species from <u>cement, aggregates</u> and <u>CFA-C</u>) / (kg of concrete product)]	3770	3770	3770	3770	3770
$D_{obs 1}^b$ [m ² /s]	$6.5 \cdot 10^{-15}$	$9.6 \cdot 10^{-15}$	$7.9 \cdot 10^{-15}$	$9.3 \cdot 10^{-15}$	$11.0 \cdot 10^{-15}$
$\frac{D_{m,Na}^c}{D_{obs 1}}$	$2.1 \cdot 10^5$	$1.5 \cdot 10^5$	$1.8 \cdot 10^5$	$1.5 \cdot 10^5$	$1.3 \cdot 10^5$
C_0^d [(mg elemental species from <u>cement and CFA-</u> <u>C</u>)/(kg of concrete product)]	500	500	500	500	500
$D_{obs 2}^e$ [m ² /s]	$3.6 \cdot 10^{-13}$	$5.3 \cdot 10^{-13}$	$4.4 \cdot 10^{-13}$	$5.2 \cdot 10^{-13}$	$5.9 \cdot 10^{-13}$
$\frac{D_{m,Na}}{D_{obs 2}}$	3670	2490	3000	2540	2240
$D_{obs 3}^f$ [m ² /s]	$1.1 \cdot 10^{-12}$	$1.6 \cdot 10^{-12}$	$1.3 \cdot 10^{-12}$	$1.6 \cdot 10^{-12}$	$1.8 \cdot 10^{-12}$
$\frac{D_{m,Na}}{D_{obs 3}}$	1200	825	1015	825	735
$\tau_{MO} = \epsilon^{-4/3} g$	30	30	30	30	30

^a Total content in Na

^b Calculated assuming that the initial leachable concentration C_0 was the total content

^c $D_{m,Na} = 1.32 \cdot 10^{-9}$ m²/s (Linde, 1996)

^d Based on CFA-C mix design and total content of individual mix components (e.g., cement and CFA-C)

^e Calculated assuming that the initial leachable concentration C_0 was the species content provided only by the cement and the CFA-C

^f Calculated assuming that the initial leachable concentration C_0 was the species content provided only by the cement and the CFA-C and the flux was only provided by the fraction of the surface of the sample non-occupied by the aggregates

^g Millington-Quirk relationship (Millington et al., 1971). The porosity was estimated from moisture content and matrix density

Table 57: Parameter estimates for the release of K from the one-dimensional diffusion model – 28-d cured and high level aged CFA-C prisms.

	28-d cured	High level aged CFA-C mix			
	CFA-C mix	C(HNN)13	C(NHN)13	C(NNH)13	C(HHH)13
C_0^a					
[(mg elemental species from <u>cement</u> , <u>aggregates</u> and <u>CFA-C</u>) / (kg of concrete product)]	3150	3150	3150	3150	3150
$D_{obs 1}^b$ [m ² /s]	$2.2 \cdot 10^{-14}$	$1.4 \cdot 10^{-14}$	$2.2 \cdot 10^{-14}$	$2.1 \cdot 10^{-14}$	$1.4 \cdot 10^{-14}$
$\frac{D_{m,K}^c}{D_{obs 1}}$	$0.9 \cdot 10^5$	$1.4 \cdot 10^5$	$0.9 \cdot 10^5$	$0.9 \cdot 10^5$	$1.4 \cdot 10^5$
C_0^d	820	820	820	820	820
[(mg elemental species from <u>cement</u> and <u>CFA-C</u>)/(kg of concrete product)]					
$D_{obs 2}^e$ [m ² /s]	$3.3 \cdot 10^{-13}$	$2.0 \cdot 10^{-13}$	$3.2 \cdot 10^{-13}$	$3.2 \cdot 10^{-13}$	$2.1 \cdot 10^{-13}$
$\frac{D_{m,K}}{D_{obs 2}}$	5940	9800	6125	6125	9340
$D_{obs 3}^f$ [m ² /s]	$10.0 \cdot 10^{-13}$	$6.2 \cdot 10^{-13}$	$9.7 \cdot 10^{-13}$	$9.6 \cdot 10^{-13}$	$6.5 \cdot 10^{-13}$
$\frac{D_{m,K}}{D_{obs 3}}$	1960	3160	2020	2040	3020
$\tau_{MO} = \epsilon^{-4/3} g$	30	30	30	30	30

^a Total content in K

^b Calculated assuming that the initial leachable concentration C_0 was the total content

^c $D_{m,K} = 1.96 \cdot 10^{-9}$ m²/s (Linde, 1996).

^d Based on CFA-C mix design and total content of individual mix components (e.g., cement and CFA-C)

^e Calculated assuming that the initial leachable concentration C_0 was the species content provided only by the cement and the CFA-C

^f Calculated assuming that the initial leachable concentration C_0 was the species content provided only by the cement and the CFA-C and the flux was only provided by the fraction of the surface of the sample non-occupied by the aggregates

^g Millington-Quirk relationship (Millington et al., 1971). The porosity was estimated from moisture content and matrix density

Table 58: Parameter estimates for the release of Cl from the one-dimensional diffusion model – 28-d cured and high level aged CFA-C prisms.

	28-d cured CFA-C mix	High level aged CFA-C mix			
	C(XXX)02	C(HNN)13	C(NHN)13	C(NNH)13	C(HHH)13
C_0^a [(mg elemental species from cement, aggregates and CFA-C)/(kg of concrete product)]	120	120	120	120	120
$D_{obs 1}^b$ [m ² /s]	1.5 10 ⁻¹¹	1.9 10 ⁻¹¹	2.1 10 ⁻¹¹	2.6 10 ⁻¹¹	1.5 10 ⁻¹¹
$\frac{D_{m, Cl}^c}{D_{obs 1}}$	140	110	100	80	140
$\tau_{MO} = \epsilon^{-4/3 d}$	30	30	30	30	30

^a Total content in Cl

^b Calculated assuming that the initial leachable concentration C_0 was the total content

^c $D_{m, Cl} = 2.03 \cdot 10^{-9}$ m²/s (Linde, 1996)

^d Millington-Quirk relationship (Millington et al., 1971). The porosity was estimated from moisture content and matrix density

Table 59: Parameter estimates for the release of Ca from the one-dimensional diffusion model – 28-d cured and high level aged CFA-C prisms.

	28-d cured CFA-C mix	High level aged CFA-C mix			
	C(XXX)02	C(HNN)13	C(NHN)13	C(NNH)13	C(HHH)13
C_0^a	$370.0 \cdot 10^3$	$370.0 \cdot 10^3$	$370.0 \cdot 10^3$	$370.0 \cdot 10^3$	$370.0 \cdot 10^3$
[(mg elemental species from <u>cement</u> , <u>aggregates</u> and <u>CFA-C</u>)/(kg of concrete product)]					
$D_{obs\ 1}^b$ [m ² /s]	$3.5 \cdot 10^{-16}$	$3.9 \cdot 10^{-16}$	$3.0 \cdot 10^{-16}$	$3.6 \cdot 10^{-16}$	$3.1 \cdot 10^{-16}$
$\frac{D_{m,Ca}^c}{D_{obs\ 1}}$	$2.3 \cdot 10^6$	$2.1 \cdot 10^6$	$2.7 \cdot 10^6$	$2.3 \cdot 10^6$	$2.6 \cdot 10^6$
C_0^d	$68.1 \cdot 10^3$	$68.1 \cdot 10^3$	$68.1 \cdot 10^3$	$68.1 \cdot 10^3$	$68.1 \cdot 10^3$
[(mg elemental species from <u>cement</u> and <u>CFA-C</u>)/(kg of concrete product)]					
$D_{obs\ 2}^e$ [m ² /s]	$1.0 \cdot 10^{-14}$	$1.1 \cdot 10^{-14}$	$0.9 \cdot 10^{-14}$	$1.0 \cdot 10^{-14}$	$0.9 \cdot 10^{-14}$
$\frac{D_{m,Ca}}{D_{obs\ 2}}$	$7.9 \cdot 10^4$	$7.2 \cdot 10^4$	$9.3 \cdot 10^4$	$7.8 \cdot 10^4$	$9.0 \cdot 10^4$
$D_{obs\ 3}^f$ [m ² /s]	$3.1 \cdot 10^{-14}$	$3.3 \cdot 10^{-14}$	$2.6 \cdot 10^{-14}$	$3.1 \cdot 10^{-14}$	$2.6 \cdot 10^{-14}$
$\frac{D_{m,Ca}}{D_{obs\ 3}}$	$2.6 \cdot 10^4$	$2.4 \cdot 10^4$	$3.1 \cdot 10^4$	$2.6 \cdot 10^4$	$3.1 \cdot 10^4$
$\tau_{MO} = E_{4/3, g}$	30	30	30	30	30

^a Total content in Ca

^b Calculated assuming that the initial leachable concentration C_0 was the total content

^c $D_{m,Ca} = 7.92 \cdot 10^{-10}$ m²/s (Linde, 1996)

^d Based on CFA-C mix design and total content of individual mix components (e.g., cement and CFA-C)

^e Calculated assuming that the initial leachable concentration C_0 was the species content provided only by the cement and the CFA-C

^f Calculated assuming that the initial leachable concentration C_0 was the species content provided only by the cement and the CFA-C and the flux was only provided by the fraction of the surface of the sample non-occupied by the aggregates

^g Millington-Quirk relationship (Millington et al., 1971). The porosity was estimated from moisture content and matrix density

tortuosity using the Millington-Quirk relationship (e.g., τ_{MQ} of 30). This comparison indicated that significant retention of Na occurred within the concrete materials. Similar K observed diffusivity was obtained for the 28-d cured CFA-C mix sample (e.g., C(XXX)02), the sample that was submitted only to the high level of cyclical mechanical stress (e.g., C(NHN)13) and the sample that was submitted only to the high level of freeze-thaw deterioration (e.g., C(NNH)13). Slightly lower K observed diffusivities (e.g., 1.5 times lower) were obtained for the sample that was submitted to the three high levels of aging (e.g., C(HHH)13) and the sample that was submitted only to the high level of temperature aging (e.g., C(HNN)13). However, it is difficult to attribute the observed differences in K observed diffusivity to aging effects because these differences were small (e.g., K observed diffusivities were $1.4 \cdot 10^{-14} \text{ m}^2/\text{s}$ for C(HNN)13 and C(HHH)13 and $2.2 \cdot 10^{-14} \text{ m}^2/\text{s}$ for C(XXX)02, C(NHN)13, and C(NNH)13). When considering only the K content provided by the cement and the CFA-C, the diffusivity results (e.g., $D_{\text{obs } 2}$ and $D_{\text{obs } 3}$) changed by an order of magnitude, leading to K observed diffusivity on the order of $10^{-13} \text{ m}^2/\text{s}$. Diffusivity results slightly increased ($D_{\text{obs } 3}$ were 3 times greater than $D_{\text{obs } 2}$) when calculations were done by accounting only for the surface of the matrix non-occupied by the aggregates. However, as with Na, much greater ratios (e.g., 2 orders of magnitude greater) of observed diffusivity to molecular diffusivity for K than the estimated tortuosity using the Millington-Quirk relationship were obtained.

Cl Modeling. No significant difference in Cl observed diffusivity (see table 58) could be observed between the 28-d cured CFA-C mix sample (e.g., C(XXX)02), the sample that was submitted to the three high levels of aging (e.g., C(HHH)13), and the sample that was submitted only to the high level of temperature aging (e.g., C(HNN)13). Slightly greater Cl observed diffusivities were obtained for the sample that was submitted only to the high level of cyclical mechanical stress (e.g., C(NHN)13) and the sample that was submitted only to the high level of freeze-thaw deterioration (e.g., C(NNH)13). However, it is difficult to attribute the observed differences in Cl observed diffusivity to aging effects because of the large uncertainties in the determination of these coefficients due to low Cl concentrations measured in the leachates (e.g., close to or below 1 mg/l, the instrument detection limit). In addition, when considering only the Cl provided by the cement and the CFA-C, unrealistic diffusivity data (e.g., diffusivity data greater than the Cl molecular diffusivity⁶) were obtained. This might be due to a low Cl total content of the material (e.g., 120 mg/kg) and uncertainties in the Cl content of individual mix components. Indeed, when considering the CFA-C mix design and Cl content of individual mix components, Cl total content of CFA-C mix was 50 mg/kg with 40 mg/kg from the aggregates while 120 mg/kg was found by NAA/XRF analyses.

Ca Modeling. No significant difference in Ca observed diffusivities (see table 59) could be observed between the 28-d cured CFA-C mix sample (e.g., C(XXX)02) and the four high level aged CFA-C mix samples (e.g., C(HNN)13, C(NHN)13, C(NNH)13, and C(HHH)13). Low Ca observed diffusivities (e.g., on the order of $10^{-16} \text{ m}^2/\text{s}$) were calculated from the Ca total content, leading to ratios of observed diffusivity to molecular diffusivity for Ca as much as 5 orders of magnitude greater than the estimated tortuosity using the Millington-Quirk relationship (e.g., τ_{MQ} of 30). This comparison indicated that significant retention of Ca occurred within the

6 Cl molecular diffusivity: $2.03 \cdot 10^{-9} \text{ m}^2/\text{s}$ (Linde, 1996).

concrete materials. When considering only the Ca content provided by the cement and the CFA-C, the diffusivity results (e.g., $D_{obs,2}$ and $D_{obs,3}$) changed by two orders of magnitude, leading to Ca observed diffusivity on the order of 10^{-14} m²/s. Diffusivity results slightly increased ($D_{obs,3}$ were 3 times greater than $D_{obs,2}$) when calculations were done by accounting only for the surface of the matrix non-occupied by the aggregates. However, much greater ratios (e.g., 2 orders of magnitude greater) of observed diffusivity to molecular diffusivity for Ca than the estimated tortuosity using the Millington-Quirk relationship were obtained. This discrepancy was consistent with the large interaction of Ca with the concrete matrix. Indeed, Ca is found in the major products of cement hydration that include Ca hydroxide, Ca silicate hydroxide (CSH), and Ca sulfoaluminates and for which solubility differs by orders of magnitude.

In conclusion:

1. After 4 mo of leaching examined there was no significant effect from the three types of aging on the Na, K, Cl, and Ca observed diffusivities

5.4.11.2 Release Modeling for CFA-C Samples with Other Levels of Aging

The one-dimensional diffusion model was used to interpret the release of Na, K, and Ca from CFA-C mix samples with other levels of aging (e.g., C(NHH)14, C(HNH)12, C(HHN)13, C(NNN)14) and the three center point replicates (e.g., C(LL)16, C(LL)30 and C(LL)47). During the time scale of the laboratory testing (e.g., 4 mo), no depletion of these species within the matrices was observed. For each species of concern, three different observed diffusivities (e.g., $D_{obs,1}$, $D_{obs,2}$, and $D_{obs,3}$) were determined. $D_{obs,1}$ was calculated assuming that the initial leachable concentration C_0 was the total content of the species of concern. $D_{obs,2}$ was calculated assuming that the initial leachable concentration C_0 was the species content provided only by the cement and the CFA-F. $D_{obs,3}$ was calculated assuming that (i) the initial leachable concentration C_0 was the species content provided only by the cement and the CFA-F, (ii) the aggregates were inert and uniformly distributed within the matrix and, (iii) the flux was only provided by the fraction of the surface⁷ of the sample not occupied by the aggregates. Thus, while $D_{obs,1}$ and $D_{obs,2}$ correspond to observed diffusivities through the overall matrix (e.g., binder and aggregates), $D_{obs,3}$ corresponds to an observed diffusivity only through the binder (e.g., cement and CFA-C).

Initial leachable concentrations and observed diffusivities of the four aged CFA-C mix samples of concern (e.g., C(NHH)14, C(HNH)12, C(HHN)13, C(NNN)14) are compared in tables 60, 61, and 62 for Na, K, and Ca, respectively. Initial leachable concentrations and observed diffusivities of the three center point replicates of CFA-C mix (e.g., C(LL)16, C(LL)30, and C(LL)47) are compared in tables 63, 64, and 65 for Na, K, and Ca, respectively. Ratios of observed diffusivity to molecular diffusivity are also compared with estimate of matrix tortuosity calculated using the Millington-Quirk relationship (Millington et al., 1971) (e.g., $\tau_{MQ} = \epsilon^{-4/3}$ where τ_{MQ} and ϵ are tortuosity and matrix porosity, respectively).

7 As a first approach, it was assumed that about 57.5 percent of the surface was not occupied by aggregate (42.5 percent of coarse aggregates were used in the mix design).

Na Modeling. Na observed diffusivities of the same order of magnitude were calculated for the four aged CFA-C mix samples of concern (e.g., C(NHH)14, C(HNH)12, C(HHN)13, C(NNN)14). No significant difference in Na observed diffusivities could be observed between C(NHH)14 and C(HNH)12 while slightly greater Na observed diffusivities were calculated for C(HHN)13 and less Na observed diffusivities for C(NNN)14. Na observed diffusivities of the three center point replicates were approximately 4 times less than that of the 4 aged materials of concern, with greater Na observed diffusivities obtained for C(LL)16 and less for C(LL)47. In addition, no significant difference in Na observed diffusivities could be observed between the four aged CFA-C mix samples of concern (table 60), the four high level aged, and the 28-d cured CFA-C mix samples (table 56).

K Modeling. There was no significant difference in K observed diffusivities between the four aged samples of concern although slightly greater K observed diffusivities were calculated for C(NHH)14. K observed diffusivities of the three center point replicates were greater than that of the four aged samples of concern. In addition, greater K observed diffusivities were calculated for C(LL)16 compared with C(LL)30 and C(LL)47, for which K observed diffusivities were similar. As with NA, there was no significant difference in K observed diffusivities between the four aged CFA-C mix samples of concern (table 61), the four high level aged, and the 28-d cured samples (table 57).

Ca Modeling. There was no significant difference in Ca observed diffusivities between the four aged samples of concern although slightly greater Ca observed diffusivities were calculated for C(HNH)12. Slightly greater Ca observed diffusivities were obtained for C(LL)16 compared with the two other center point replicates and the four aged samples of concern. As with Na and K, there was no significant difference in Ca observed diffusivities between the four aged CFA-C mix samples of concern (table 62), the four high level aged, and the 28-d cured samples (table 58).

The results showed greater differences in Na, K, and Ca observed diffusivities between the three center point replicates than between the aged samples. This indicated that the slight differences observed from one aged sample to another aged sample were more likely the result of experimental uncertainties than aging effect. In addition, no clear tendency resulting from aging effect could be observed. Indeed, while slightly less Na observed diffusivities and slightly greater K observed diffusivities were obtained for the three center point replicates compared with the other aged samples, there was no significant difference in Na, K, and Ca observed diffusivities between the aged samples (e.g., C(NHH)14, C(HNH)12, C(HHN)13), the non-aged sample (e.g., C(NNN)14) and the 28-d cured sample (e.g., C(XXX)02).

Therefore, from the obtained results, it seemed that over the 4 mo of leaching examined there was no substantial effect from the three types of aging (AA, Cl, FT) on Na, K and Ca observed diffusivities.

Table 60: Parameter estimates for the release of Na from the one-dimensional diffusion model – CFA-C prisms with other levels of aging.

	C(NNN)14	C(NHH)14	C(HNH)12	C(HHN)13
C_0^a [(mg elemental species from <u>cement</u> , <u>aggregates</u> and <u>CFA-C</u>) / (kg of concrete product)]	3770	3770	3770	3770
$D_{obs 1}^b$ [m ² /s]	$7.7 \cdot 10^{-15}$	$11.0 \cdot 10^{-15}$	$11.0 \cdot 10^{-15}$	$9.7 \cdot 10^{-15}$
$\frac{D_{m,Na}^c}{D_{obs 1}}$	$1.8 \cdot 10^5$	$1.3 \cdot 10^5$	$1.3 \cdot 10^5$	$1.4 \cdot 10^5$
C_0^d [(mg elemental species from <u>cement</u> and <u>CFA-C</u>) / (kg of concrete product)]	500	500	500	500
$D_{obs 2}^e$ [m ² /s]	$4.3 \cdot 10^{-13}$	$6.2 \cdot 10^{-13}$	$6.0 \cdot 10^{-13}$	$5.4 \cdot 10^{-13}$
$\frac{D_{m,Na}}{D_{obs 2}}$	3260	2225	2330	2560
$D_{obs 3}^f$ [m ² /s]	$1.3 \cdot 10^{-12}$	$1.9 \cdot 10^{-12}$	$1.8 \cdot 10^{-12}$	$1.6 \cdot 10^{-12}$
$\frac{D_{m,Na}}{D_{obs 3}}$	1080	740	770	845
$\tau_{MO} = \epsilon^{4/3} g$	30	30	30	30

^a Total content in Na

^b Calculated assuming that the initial leachable concentration C_0 was the total content

^c $D_{m,Na} = 1.32 \cdot 10^{-9}$ m²/s (Linde, 1996)

^d Based on CFA-C mix design and total content of individual mix components (e.g., cement and CFA-C)

^e Calculated assuming that the initial leachable concentration C_0 was the species content provided only by the cement and the CFA-C

^f Calculated assuming that the initial leachable concentration C_0 was the species content provided only by the cement and the CFA-C and the flux was only provided by the fraction of the surface of the sample non-occupied by the aggregates

^g Millington-Quirk relationship (Millington et al., 1971). The porosity was estimated from moisture content and matrix density

Table 61: Parameter estimates for the release of K from the one-dimensional diffusion model – CFA-C prisms with other levels of aging.

	C(NNN)14	C(NHH)14	C(HNH)12	C(HHN)13
C_0^a [(mg elemental species from <u>cement, aggregates and CFA-C</u>) / (kg of concrete product)]	3150	3150	3150	3150
$D_{obs 1}^b$ [m ² /s]	$2.0 \cdot 10^{-14}$	$3.2 \cdot 10^{-14}$	$2.2 \cdot 10^{-14}$	$1.6 \cdot 10^{-14}$
$\frac{D_{m,Na}^c}{D_{obs 1}}$	$9.9 \cdot 10^4$	$6.2 \cdot 10^4$	$8.9 \cdot 10^4$	$12.0 \cdot 10^4$
C_0^d [(mg elemental species from <u>cement and CFA-C</u>) / (kg of concrete product)]	820	820	820	820
$D_{obs 2}^e$ [m ² /s]	$2.9 \cdot 10^{-13}$	$4.7 \cdot 10^{-13}$	$3.2 \cdot 10^{-13}$	$2.4 \cdot 10^{-13}$
$\frac{D_{m,Na}}{D_{obs 2}}$	6640	4150	6030	8010
$D_{obs 3}^f$ [m ² /s]	$0.9 \cdot 10^{-12}$	$1.4 \cdot 10^{-12}$	$1.0 \cdot 10^{-12}$	$0.7 \cdot 10^{-12}$
$\frac{D_{m,Na}}{D_{obs 3}}$	2200	2000	1370	2650
$\tau_{MO} = \varepsilon^{-4/3} g$	30	30	30	30

^a Total content in K

^b Calculated assuming that the initial leachable concentration C_0 was the total content

^c $D_{m,K} = 1.96 \cdot 10^{-9}$ m²/s (Linde, 1996)

^d Based on CFA-C mix design and total content of individual mix components (e.g., cement and CFA-C)

^e Calculated assuming that the initial leachable concentration C_0 was the species content provided only by the cement and the CFA-C

^f Calculated assuming that the initial leachable concentration C_0 was the species content provided only by the cement and the CFA-C and the flux was only provided by the fraction of the surface of the sample non-occupied by the aggregates

^g Millington-Quirk relationship (Millington et al., 1971). The porosity was estimated from moisture content and matrix density

Table 62: Parameter estimates for the release of Ca from the one-dimensional diffusion model – CFA-C prisms with other levels of aging.

	C(NNN)14	C(NHH)14	C(HNH)12	C(HHN)13
C_0^a [(mg elemental species from <u>cement</u> , <u>aggregates</u> and <u>CFA-C</u>) / (kg of concrete product)]	370.0 10 ³	370.0 10 ³	370.0 10 ³	370.0 10 ³
$D_{obs 1}^b$ [m ² /s]	3.1 10 ⁻¹⁶	3.4 10 ⁻¹⁶	4.0 10 ⁻¹⁶	3.1 10 ⁻¹⁶
$\frac{D_{m,Na}^c}{D_{obs 1}}$	2.6 10 ⁶	2.3 10 ⁶	2.0 10 ⁶	2.0 10 ⁶
C_0^d [(mg elemental species from <u>cement</u> and <u>CFA-C</u>) / (kg of concrete product)]	68.1 10 ³	68.1 10 ³	68.1 10 ³	68.1 10 ³
$D_{obs 2}^e$ [m ² /s]	8.8 10 ⁻¹⁵	9.8 10 ⁻¹⁵	11.0 10 ⁻¹⁵	8.8 10 ⁻¹⁵
$\frac{D_{m,Na}}{D_{obs 2}}$	8.9 10 ⁴	8.0 10 ⁴	7.0 10 ⁴	9.0 10 ⁴
$D_{obs 3}^f$ [m ² /s]	2.7 10 ⁻¹⁴	3.0 10 ⁻¹⁴	3.4 10 ⁻¹⁴	2.7 10 ⁻¹⁴
$\frac{D_{m,Na}}{D_{obs 3}}$	3.0 10 ⁴	2.7 10 ⁴	2.0 10 ⁴	3.0 10 ⁴
$\tau_{MO} = \epsilon^{-4/3} g$	30	30	30	30

^a Total content in Ca

^b Calculated assuming that the initial leachable concentration C_0 was the total content

^c $D_{m,Ca} = 7.92 \cdot 10^{-10}$ m²/s (Linde, 1996)

^d Based on CFA-C mix design and total content of individual mix components (e.g., cement and CFA-C)

^e Calculated assuming that the initial leachable concentration C_0 was the species content provided only by the cement and the CFA-C

^f Calculated assuming that the initial leachable concentration C_0 was the species content provided only by the cement and the CFA-C and the flux was only provided by the fraction of the surface of the sample non-occupied by the aggregates

^g Millington-Quirk relationship (Millington et al., 1971). The porosity was estimated from moisture content and matrix density

Table 63: Parameter estimates for the release of Na from the one-dimensional diffusion model –the three center point replicates of CFA-C prisms.

	C(LL)16	C(LL)30	C(LL)47
C_0^a [(mg elemental species from <u>cement</u> , <u>aggregates</u> and <u>CFA-C</u>) / (kg of concrete product)]	3770	3770	3770
$D_{obs 1}^b$ [m ² /s]	$3.7 \cdot 10^{-14}$	$1.8 \cdot 10^{-14}$	$2.6 \cdot 10^{-14}$
$\frac{D_{m,Na}^c}{D_{obs 1}}$	$3.8 \cdot 10^4$	$7.8 \cdot 10^4$	$5.4 \cdot 10^4$
C_0^d [(mg elemental species from <u>cement</u> and <u>CFA-C</u>) / (kg of concrete product)]	500	500	500
$D_{obs 2}^e$ [m ² /s]	$2.1 \cdot 10^{-12}$	$1.0 \cdot 10^{-12}$	$1.4 \cdot 10^{-12}$
$\frac{D_{m,Na}}{D_{obs 2}}$	680	1390	980
$D_{obs 3}^f$ [m ² /s]	$6.2 \cdot 10^{-12}$	$3.0 \cdot 10^{-12}$	$4.3 \cdot 10^{-12}$
$\frac{D_{m,Na}}{D_{obs 3}}$	225	460	320
$\tau_{MO} = \varepsilon^{-4/3 g}$	30	30	30

^a Total content in Na

^b Calculated assuming that the initial leachable concentration C_0 was the total content

^c $D_{m,Na} = 1.32 \cdot 10^{-9}$ m²/s (Linde, 1996)

^d Based on CFA-C mix design and total content of individual mix components (e.g., cement and CFA-C)

^e Calculated assuming that the initial leachable concentration C_0 was the species content provided only by the cement and the CFA-C

^f Calculated assuming that the initial leachable concentration C_0 was the species content provided only by the cement and the CFA-C and the flux was only provided by the fraction of the surface of the sample non-occupied by the aggregates

^g Millington-Quirk relationship (Millington et al., 1971). The porosity was estimated from moisture content and matrix density

Table 64: Parameter estimates for the release of K from the one-dimensional diffusion model – the three center point replicates of CFA-C prisms.

	C(LL)16	C(LL)30	C(LL)47
C_0^a [(mg elemental species from <u>cement</u> , <u>aggregates</u> and <u>CFA-C</u>) / (kg of concrete product)]	3150	3150	3150
$D_{obs 1}^b$ [m ² /s]	$6.0 \cdot 10^{-14}$	$3.8 \cdot 10^{-14}$	$3.9 \cdot 10^{-14}$
$\frac{D_{m,Na}^c}{D_{obs 1}}$	$3.3 \cdot 10^4$	$5.2 \cdot 10^4$	$5.0 \cdot 10^4$
C_0^d [(mg elemental species from <u>cement</u> and <u>CFA-C</u>) / (kg of concrete product)]	820	820	820
$D_{obs 2}^e$ [m ² /s]	$8.9 \cdot 10^{-13}$	$5.6 \cdot 10^{-13}$	$5.8 \cdot 10^{-13}$
$\frac{D_{m,Na}}{D_{obs 2}}$	2200	3490	3370
$D_{obs 3}^f$ [m ² /s]	$2.7 \cdot 10^{-12}$	$1.7 \cdot 10^{-12}$	$1.8 \cdot 10^{-12}$
$\frac{D_{m,Na}}{D_{obs 3}}$	730	1160	1115
$\tau_{MQ} = \epsilon^{-4/3 g}$	30	30	30

^a Total content in K

^b Calculated assuming that the initial leachable concentration C_0 was the total content

^c $D_{m,K} = 1.96 \cdot 10^{-9}$ m²/s (Linde, 1996)

^d Based on CFA-C mix design and total content of individual mix components (e.g., cement and CFA-C)

^e Calculated assuming that the initial leachable concentration C_0 was the species content provided only by the cement and the CFA-C

^f Calculated assuming that the initial leachable concentration C_0 was the species content provided only by the cement and the CFA-C and the flux was only provided by the fraction of the surface of the sample non-occupied by the aggregates

^g Millington-Quirk relationship (Millington et al., 1971). The porosity was estimated from moisture content and matrix density

Table 65: Parameter estimates for the release of Ca from the one-dimensional diffusion model – the three center point replicates of CFA-C prisms.

	C(LL)16	C(LL)30	C(LL)47
C_0^a [(mg elemental species from <u>cement, aggregates and CFA-C</u>) / (kg of concrete product)]	$370.0 \cdot 10^3$	$370.0 \cdot 10^3$	$370.0 \cdot 10^3$
D_{obs1}^b [m ² /s]	$3.6 \cdot 10^{-16}$	$3.9 \cdot 10^{-16}$	$3.7 \cdot 10^{-16}$
$\frac{D_{m,Na}^c}{D_{obs1}}$	$2.2 \cdot 10^6$	$2.0 \cdot 10^6$	$2.2 \cdot 10^6$
C_0^d [(mg elemental species from <u>cement and CFA-C</u>) / (kg of concrete product)]	$68.1 \cdot 10^3$	$68.1 \cdot 10^3$	$68.1 \cdot 10^3$
D_{obs2}^e [m ² /s]	$1.0 \cdot 10^{-14}$	$1.1 \cdot 10^{-14}$	$1.1 \cdot 10^{-14}$
$\frac{D_{m,Na}}{D_{obs2}}$	$7.7 \cdot 10^4$	$7.1 \cdot 10^4$	$7.5 \cdot 10^4$
D_{obs3}^f [m ² /s]	$3.1 \cdot 10^{-14}$	$3.4 \cdot 10^{-14}$	$3.2 \cdot 10^{-14}$
$\frac{D_{m,Na}}{D_{obs3}}$	$2.5 \cdot 10^4$	$2.4 \cdot 10^4$	$2.5 \cdot 10^4$
$\tau_{MQ} = \varepsilon^{-4/3} g$	30	30	30

^a Total content in Ca

^b Calculated assuming that the initial leachable concentration C_0 was the total content

^c $D_{m,Ca} = 7.92 \cdot 10^{-10}$ m²/s (Linde, 1996)

^d Based on CFA-C mix design and total content of individual mix components (e.g., cement and CFA-C)

^e Calculated assuming that the initial leachable concentration C_0 was the species content provided only by the cement and the CFA-C

^f Calculated assuming that the initial leachable concentration C_0 was the species content provided only by the cement and the CFA-C and the flux was only provided by the fraction of the surface of the sample non-occupied by the aggregates

^g Millington-Quirk relationship (Millington et al., 1971). The porosity was estimated from moisture content and matrix density

5.4.11.3 ANOVA

ANOVA analysis was carried out on Na, K and Ca observed diffusivities.⁸ Calculated F values and tabulated F values at 99 percent, 95 percent and 90 percent are compared in tables K-24, K-25 and K-26 in appendix K of volume II.

5.4.11.4 Main Effects

Much lower calculated F values than the tabulated ones were obtained for Na and K observed diffusivities, indicating that AA, CL, or FT did not have any statistically significant effect on Na and K observed diffusivities.

Similarly, calculated F values for Ca observed diffusivities were less than the tabulated ones except for CL which was slightly greater than the tabulated F value at 90 percent.

5.4.11.5 Interactions

Much less calculated F values than the tabulated ones were obtained for Na, K, and Ca observed diffusivities, indicating that AA, CL, or FT interactions did not have any statistically significant effect on Na, K, and Ca observed diffusivities.

5.4.11.6 Conclusions

In conclusion:

1. The experimental variables (AA, CL, and FT) did not significantly affect Na, K, or Ca observed diffusivities.
2. The interactions of AA, CL, and FT did not significantly affect Na, K, or Ca observed diffusivities.

5.5. Evaluation of Three Center Points Experimental Design Between CFA-C, CFA-F and PCC Mixes

5.5.1. Compressive Strength

Results from compressive strength testing on the three center point prisms are listed in table 66 a, b, and c.

5.5.1.1 ANOVA

An ANOVA performed on data from the post-treatment samples revealed a difference between the mix types at the 99 percent confidence interval for which the reference F value was

⁸ ANOVA was carried out only on $D_{obs,3}$ (e.g., observed diffusivity only through the binder).

5.6 (see table L-1 in appendix L of volume II). The CFA-C samples had the highest compressive strengths, followed by the CFA-F, and then the PCC.

5.5.1.2 Tukey-Kramer Comparisons

The results from Tukey-Kramer testing on the (LLL) samples showed that PCC and CFA-C were significantly different at a 95.5 percent confidence level (see table L-2 in appendix L of volume II). CFA-F compressive strength values are between both groups and are not significantly different from the other two types.

At an age of 28-ds, PCC concrete compressive strengths were higher than both CFA-C and CFA-F concretes. It appears that at an age of 500 d, the CFA-C and CFA-F ashes had enough time to react and develop the late-term strengths brought about by their reactions with the hydration byproducts (Odler, 1991).

The slower strength increase of the CFA-F compared with the CFA-C is typical for these fly ashes (Popovics, 1982; Gebler and Klieger, 1986; and Naik et al., 1995). CFA-F can take more than a yr. to develop strengths equal to or greater than concrete with an equal proportion of CFA-C (Gebler and Klieger 1986).

5.5.1.3 Conclusions

In conclusion:

1. At an age of 500 d after LLL treatment, the CFA-C concrete was significantly stronger than the PCC at a 95 percent confidence level.
2. The CFA-C was not found to be significantly different than the CFA-F.
3. The CFA-F was not found to be significantly different than the PCC.
4. At higher ages, the higher strength of the CFA-C concrete can be attributed to the beneficial hydration of the fly ash.

5.5.2. Microcracking

5.5.2.1 ANOVA

The numerical results from the crack density traces are listed in table 67. The table includes the results from each of the three slices (two longitudinal and one transverse) for each prism in addition to the average of these three values and the average for each different mix design. The ANOVA for the prism crack density results is presented in table L-3 in appendix L of volume II.

Table 66a: Post-treatment compressive strength of CFA-C prisms.

Compressive Strength MPa	
C(LL) 01	28.6
C(LL) 02	29.8
C(LL) 03	32.9
C(LL) 17	26.1
C(LL) 18	34.2
C(LL) 19	31.5
C(LL) 33	33.9
C(LL) 34	27.7
C(LL) 35	28.8
Mean	30.4 ± 1.9

Table 66b: Post-treatment compressive strength of CFA-F prisms.

Compressive Strength MPa	
F(LL) 01	24.1
F(LL) 02	30.4
F(LL) 03	23.7
F(LL) 17	29.8
F(LL) 18	19.3
F(LL) 19	31.4
F(LL) 33	25.9
F(LL) 34	23.6
F(LL) 35	27.7
Mean	26.2 ± 2.6

Table 66c: Post-treatment compressive strength of PCC prisms.

Compressive Strength MPa	
P(LL) 01	24.6
P(LL) 02	15.7
P(LL) 03	24.7
P(LL) 17	17.2
P(LL) 18	22.2
P(LL) 20	18.1
P(LL) 33	24.9
P(LL) 34	14.6
P(LL) 35	19.4
Mean	20.2 ± 2.7

The corresponding tabular F values for this experiment are 10.9, 5.1, and 3.4 for 99, 95, and 90 percent confidence levels, respectively.

As can be seen from the crack density ANOVA results in table L-3 of appendix L in volume II, the main effect is that the difference between the three mixes is statistically significant at a 95 percent confidence level.

5.5.2.2 Tukey-Kramer Comparisons

Results of the differences between pairs of mixes as determined by the the Tukey-Kramer test are presented in table L-4 in appendix L of volume II.

Only the paired comparison of PCC and CFA-C is statistically different at a 95 percent confidence level, The paired comparisons of CFA-F and CFA-C and also CFA-F and PCC are not significantly different at a 95 percent confidence level.

The increased cracking in the PCC concrete when compared with the CFA-C concrete matches the strength results where the PCC concrete was found to be significantly weaker.

5.5.2.3 Conclusions

In conclusion:

1. The PCC concrete experienced significantly greater microcracking than the CFA-C concrete.
2. Microcracking was not significantly different between the PCC and the CFA-F nor between the CFA-F and the CFA-C concretes.
3. The PCC concrete had both more microcracks and lower strength than the CFA-C concrete.

5.5.3. Relative Dynamic Modulus

The results from the RDM analyses are summarized in table 68.

5.5.3.1 ANOVA

The ANOVAs tests for the low treated laboratory-created concrete are shown in table L-5 in appendix L of volume II.

Table 67: Crack density results (in percent) for prism specimens.

Specimen Name	Top	Center	Bottom	Specimen average	Mix average
C(LL)08	1.3	1.5	1.5	1.45	
C(LL)24	1.5	0.9	0.7	1.08	1.18
C(LL)40	0.8	1.3	0.9	1.00	
F(LL)08	1.4	2.2	2.3	1.94	
F(LL)24	1.7	2.4	2.0	2.03	1.89
F(LL)40	1.5	2.0	1.6	1.70	
P(LL)08	3.2	3.7	3.1	3.34	
P(LL)24	1.8	2.4	2.2	2.14	2.62
P(LL)40	2.5	2.8	1.9	2.39	

The ANOVAs showed significant differences between mix types. Freeze-thaw durability increases with greater amounts of air-entraining, lower saturation levels, less resistance to water movement (a coarser pore structure), and higher strength (see also section 5.4.3.) Entrained air volumes were roughly equivalent. The ash mixes did exhibit higher average strengths (see section 5.5.1), lower microcracking, and will be shown to have a finer pore structure (see section 5.5.4).

Though smaller pores increase resistance to water movement and thus can be expected to reduce freeze-thaw durability, a tighter pore structure also inhibits the re-saturation of concretes as concretes with ashes are known to exhibit reduced permeability. The concrete prisms tested here experienced a period of air drying before freeze-thaw exposure. If the prisms did not subsequently saturate during the freeze-thaw exposures, freeze-thaw deterioration would be inhibited.

Furthermore, higher strength and less microcracking would also increase FT durability. This correlates well with other research showing that concretes made with fly ash are generally reported to have good freeze-thaw durability (Kosmatka and Panarese 1988).

5.5.3.2 Tukey-Kramer Comparisons

Tukey-Kramer testing (see table L-6 in appendix L of volume II) found the CFA-C and CFA-F mixes had higher RDM values than the PCC mix though there were no significant differences between the performance of the CFA mixes themselves.

5.5.3.3 Conclusions

In conclusion:

1. The CFA-C and CFA-F mixes had greater FT durability than the PCC.
2. There was no significant difference in FT durability between the two ash mixes.
3. The greater FT durability of the ash mixes matches results found for microcracking and strength.

5.5.4. Effective Pore Size and Pore Size Distribution

The results from the MIP experiments are given in figures 87 and L-1 through L-8 of appendix L of volume II.

The porosity values of CFA-C concrete with low treatment varied from 8 to 10 percent, equating to a variance of 0.799 (see figure 88). This variance is consistent with other values on MIP related to concrete (Cook, 1991).

Table 68: Summary of RDM values for prisms subjected to LLL treatments.

	CFA-C	CFA-F	PCC
Minimum	30.6	22.1	18.4
Maximum	77.2	79.4	72.3
Average	59.8	64.0	49.7
95% confidence interval	22.0	25.5	28.0

The first intrusion peak of the low treatment samples was found to have a large variation of 0.34-0.6 μm (see figure 89). The second peak was found to have a consistent location, though a poorly defined weighted average threshold pore width of 0.01160 to 0.01180 μm .

The first peaks of intrusion for the CFA-F and PCC concretes were poorly defined. Sometimes numerous peaks were formed in the 1- μm region. These first multiple peaks ranged in pore width from 1 μm to 20 μm . In some cases minor peaks were observed to be almost as dominant as the first peak (see figure L-4).

In contrast, the first peaks generated by the CFA-C concrete were well-defined. It was therefore decided to limit the range used for the first peaks' nine-highest incremental intrusion values. This range was defined as the nine-highest incremental intrusions that occurred between the pore widths 0.1 to 2.5 μm . The second peaks also remained well-defined for all concretes and required no pore width constraints.

Tables 69 through 72 list the nine-highest values used in the calculation of uniformity indicators and weighted average threshold pore widths for each peak of the PCC and CFA-F concretes. Threshold pore widths have been underlined in these tables. The resulting uniformity indicators, weighted average threshold pore widths, and porosities are presented in table 73.

5.5.4.1 ANOVA

The ANOVAs for the low treated laboratory-created concrete prisms are shown in tables L-7 through L-11 in appendix L of volume II.

The ANOVAs for porosity, first peak uniformity indicator, and first peak weighted average threshold pore width found no significant differences between mix types. However, significant differences were identified for the second peak's uniformity indicator and weighted average threshold pore width.

As with the CFA-C specimens subjected to all levels of aging, the smaller pore size (0.01 μm) pores were more sensitive to aging.

The exact mechanism of interaction between the aging variables and the smaller pore structure is unknown.

The first and second peaks' critical threshold pore widths (as opposed to the weighted average threshold pore widths) were also analyzed for differences between mix types. Neither ANOVA calculated any significant differences (see tables L-12 and L-13 in appendix L of volume II).

These parameters were also not sensitive to aging in the CFA-C specimens subjected all levels of aging.

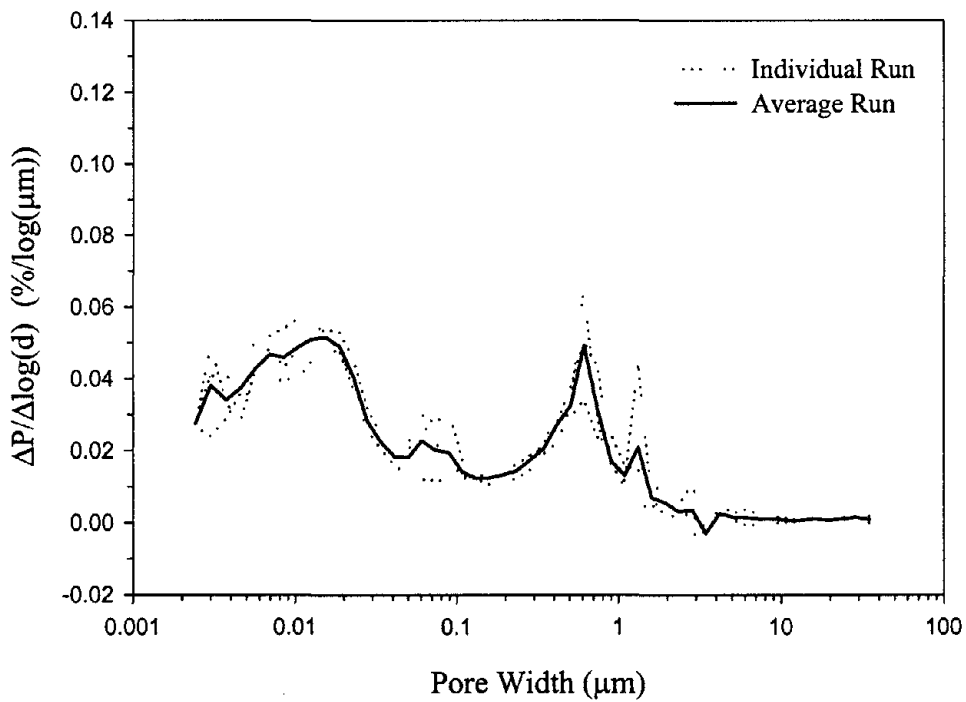
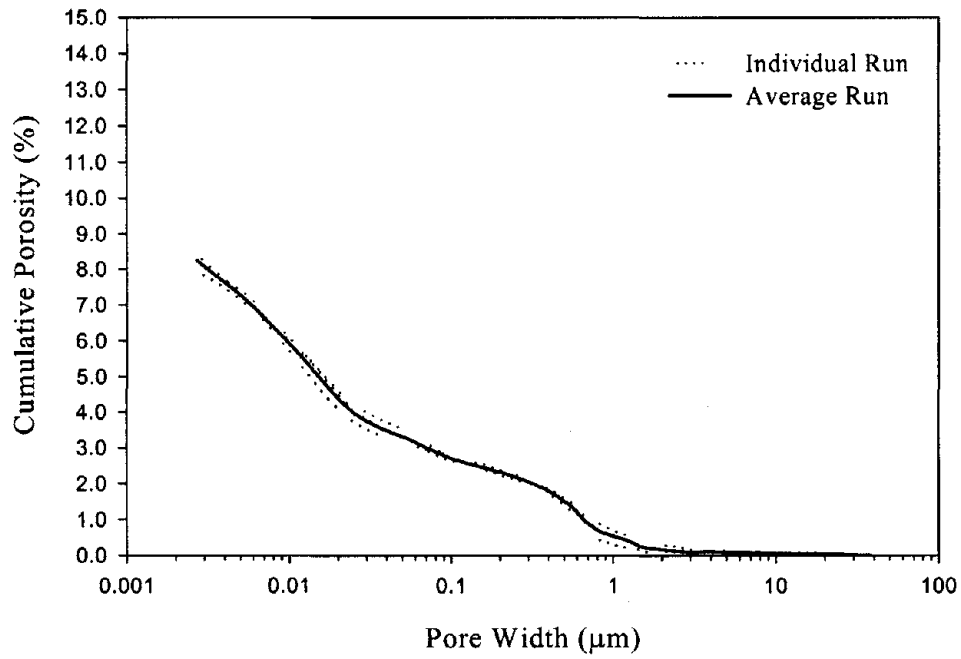


Figure 87: MIP results for C(LLL)09: (a) cumulative porosity vs. pore width; (b) average differential pore size distribution vs. pore width.

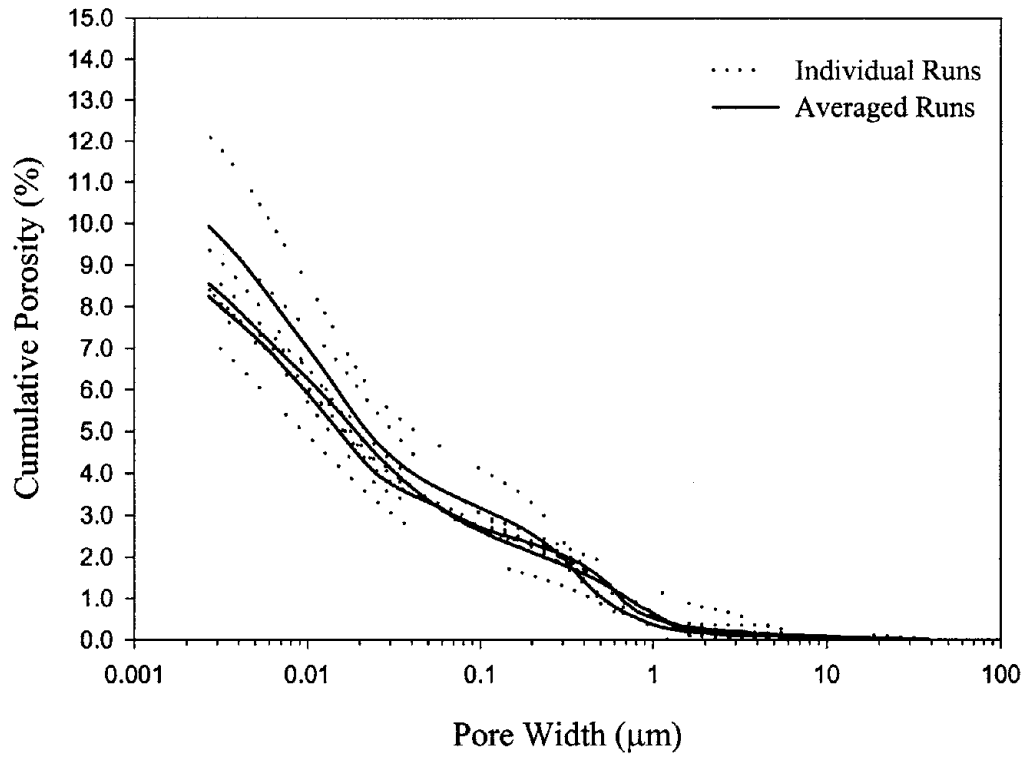


Figure 88: Cumulative porosity vs. pore width plot for CFA-C concrete low treatment samples.

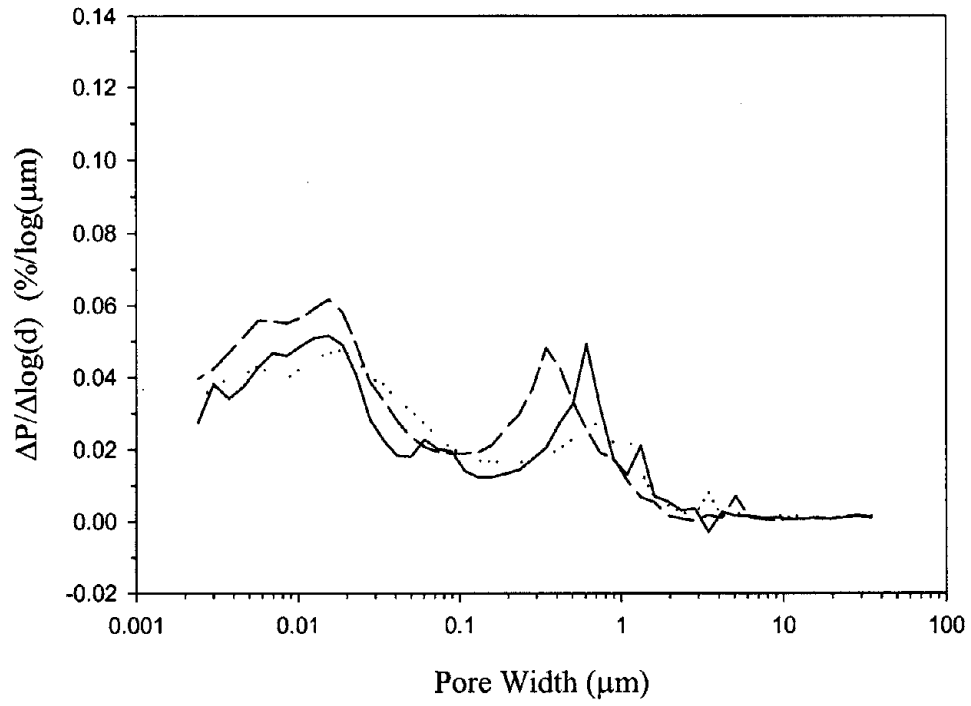


Figure 89: Average differential pore size distribution vs. pore width plot of CFA-C low treatment samples.

Table 69: CFA-F first peak nine highest $\Delta P/\Delta \log(d)$ values and their corresponding pore widths.

Sample ID	Parameter	1	2	3	4	5	6	7	8	9
F(LLL)09	$\Delta P/\Delta \log(d)$ (%/log(μm))	0.0175	0.0185	0.0211	0.0223	0.0230	0.0190	0.0188	0.0176	0.0154
	Pore Width (μm)	1.606	0.902	0.744	0.614	<u>0.506</u>	0.418	0.344	0.284	0.234
F(LLL)25	$\Delta P/\Delta \log(d)$ (%/log(μm))	0.0444	0.0548	0.0469	0.0312	0.0223	0.0228	0.0186	0.0177	0.0155
	Pore Width (μm)	0.902	<u>0.744</u>	0.614	0.506	0.418	0.344	0.284	0.234	0.193
F(LLL)41	$\Delta P/\Delta \log(d)$ (%/log(μm))	0.0680	0.0338	0.0326	0.0230	0.0336	0.0319	0.0279	0.0233	0.0208
	Pore Width (μm)	<u>1.325</u>	0.744	0.614	0.506	0.418	0.344	0.284	0.234	0.193

Table 70: PCC first peak nine highest $\Delta P/\Delta \log(d)$ values and their corresponding pore widths.

Sample ID	Parameter	1	2	3	4	5	6	7	8	9
P(LLL)09	$\Delta P/\Delta \log(d)$ ($\%/ \log(\mu\text{m})$)	0.0187	0.0224	0.0245	0.0235	0.0221	0.0216	0.0214	0.0200	0.0181
	Pore Width (μm)	1.325	1.093	<u>0.902</u>	0.744	0.614	0.506	0.418	0.344	0.284
P(LLL)25	$\Delta P/\Delta \log(d)$ ($\%/ \log(\mu\text{m})$)	0.0233	0.0341	0.0255	0.0245	0.0217	0.0212	0.0187	0.0177	0.0160
	Pore Width (μm)	1.093	<u>0.902</u>	0.744	0.614	0.506	0.418	0.344	0.284	0.234
P(LLL)41	$\Delta P/\Delta \log(d)$ ($\%/ \log(\mu\text{m})$)	0.0363	0.0248	0.0352	0.0417	0.0372	0.0325	0.0257	0.0224	0.0197
	Pore Width (μm)	2.360	1.325	1.093	<u>0.902</u>	0.744	0.614	0.506	0.418	0.344

Note: Threshold pore widths are underlined

Table 71: CFA-F second peak nine highest $\Delta P/\Delta \log(d)$ values and their corresponding pore widths.

Sample ID	Parameter	1	2	3	4	5	6	7	8	9
F(LLL)09	$\Delta P/\Delta \log(d)$ ($\%/ \log(\mu\text{m})$)	0.0373	0.0433	0.0467	0.0558	0.0574	0.0584	0.0529	0.0497	0.0425
	Pore Width (μm)	0.0127	0.0104	0.0085	0.0070	0.0057	<u>0.0046</u>	0.0037	0.0030	0.0024
F(LLL)25	$\Delta P/\Delta \log(d)$ ($\%/ \log(\mu\text{m})$)	0.0395	0.0419	0.0501	0.0591	0.0665	0.0696	0.0638	0.0575	0.0507
	Pore Width (μm)	0.0127	0.0104	0.0085	0.0070	0.0057	<u>0.0046</u>	0.0037	0.0030	0.0024
F(LLL)41	$\Delta P/\Delta \log(d)$ ($\%/ \log(\mu\text{m})$)	0.0355	0.0408	0.0476	0.0577	0.0629	0.0589	0.0568	0.0462	0.0441
	Pore Width (μm)	0.0127	0.0104	0.0085	0.0070	<u>0.0057</u>	0.0046	0.0037	0.0030	0.0024

Note: Threshold pore widths are underlined

Table 72: PCC Concrete Second Peak Nine Highest $\Delta P/\Delta \log(d)$ Values and Their Corresponding Pore Widths.

Sample ID	Parameter	1	2	3	4	5	6	7	8	9
P(LL)09	$\Delta P/\Delta \log(d)$ ($\%/ \log(\mu\text{m})$)	0.0397	0.0438	0.0490	0.0504	0.0520	0.0485	0.0471	0.0379	0.0376
	Pore Width (μm)	0.0339	0.0279	0.0230	0.0189	<u>0.0155</u>	0.0127	0.0104	0.0085	0.0070
P(LL)25	$\Delta P/\Delta \log(d)$ ($\%/ \log(\mu\text{m})$)	0.0414	0.0425	0.0445	0.0430	0.0432	0.0441	0.0449	0.0461	0.0435
	Pore Width (μm)	0.0339	0.0279	0.0230	0.0189	0.0155	0.0127	0.0104	<u>0.0085</u>	0.0070
P(LL)41	$\Delta P/\Delta \log(d)$ ($\%/ \log(\mu\text{m})$)	0.0505	0.0476	0.0487	0.0491	0.0475	0.0478	0.0468	0.0472	0.0454
	Pore Width (μm)	<u>0.0339</u>	0.0279	0.0230	0.0189	0.0155	0.0127	0.0104	0.0085	0.0070

Note: Threshold pore widths are underlined

Table 73: MIP results on CFA-C, CFA-F and PCC low treated concrete samples.

Sample	Porosity * (%)	First peak		Second peak	
		Uniformity indicator (μm) [†]	Weighted average threshold pore width (μm)	Uniformity indicator (μm)	Weighted average threshold pore width (μm)
C(LL)09	8.24	0.01095	0.607	0.00469	0.01180
C(LL)25	8.55	0.00394	0.606	0.00281	0.01160
C(LL)41	9.92	0.00974	0.337	0.00382	0.01181
F(LL)09	7.87	0.00245	0.628	0.00740	0.00622
F(LL)25	9.22	0.01460	0.565	0.01059	0.00604
F(LL)41	9.25	0.01411	0.642	0.00937	0.00616
P(LL)09	8.83	0.00211	0.699	0.00553	0.01760
P(LL)25	9.12	0.00535	0.618	0.00139	0.01734
P(LL)41	9.87	0.00764	0.985	0.00146	0.01774

* Porosity as measured by the volume of intrusion recorded at 207 MPa divided by the bulk volume of the sample

5.5.4.2 Tukey-Kramer Comparisons

The second peak uniformity indicators differ significantly (table L-14 in appendix L of volume II). CFA-C second peaks are less well-defined than CFA-F second peaks. Similarly, PCC second peaks are less well-defined than CFA-F second peaks. No difference is significant between the PCC and the CFA-C second peaks as shown in figure 90 and table L-17 in appendix L of volume II.

The weighted average threshold pore widths for the second peak for each mix type differ significantly (see tables L-7 and L-15 in appendix L of volume II). CFA-F concrete was shown to have the smallest weighted average threshold pore widths, followed by CFA-C, and then PCC (see table L-17).

These results are consistent with concretes containing these classes of fly ashes. Fly ashes in general produce finer pore size distributions than portland-cement-only concretes (Torii and Kawamura, 1992; Fraay et al., 1989).

5.5.4.3 Conclusions

In conclusion:

1. The three mixes did not differ significantly in traditional threshold pore widths, total porosities, or values associated with the coarser pore system in the laboratory concretes.
2. The three mixes did differ significantly with respect to descriptions of the finer pore system for which the CFA-F had the finest, most uniform pore system. The CFA-C had a somewhat larger system of fine pores and the PCC had the largest of the fine pore systems. Both the CFA-C and PCC mixtures exhibited less well-defined fine pore system widths.

5.5.5. Effective Surface Area

Effective surface area results are summarized in table 74.

5.5.5.1 ANOVA

An ANOVA performed on the low-treated samples from each mix found no differences between mix types as shown in tables L-18 and L-19 in appendix L of volume II.

5.5.5.2 Tukey-Kramer Comparisons

From the data found during this study, there are no apparent effects of mix design on surface area. This is likely due to the effect of unknown coarse aggregate contents in the experimental samples.

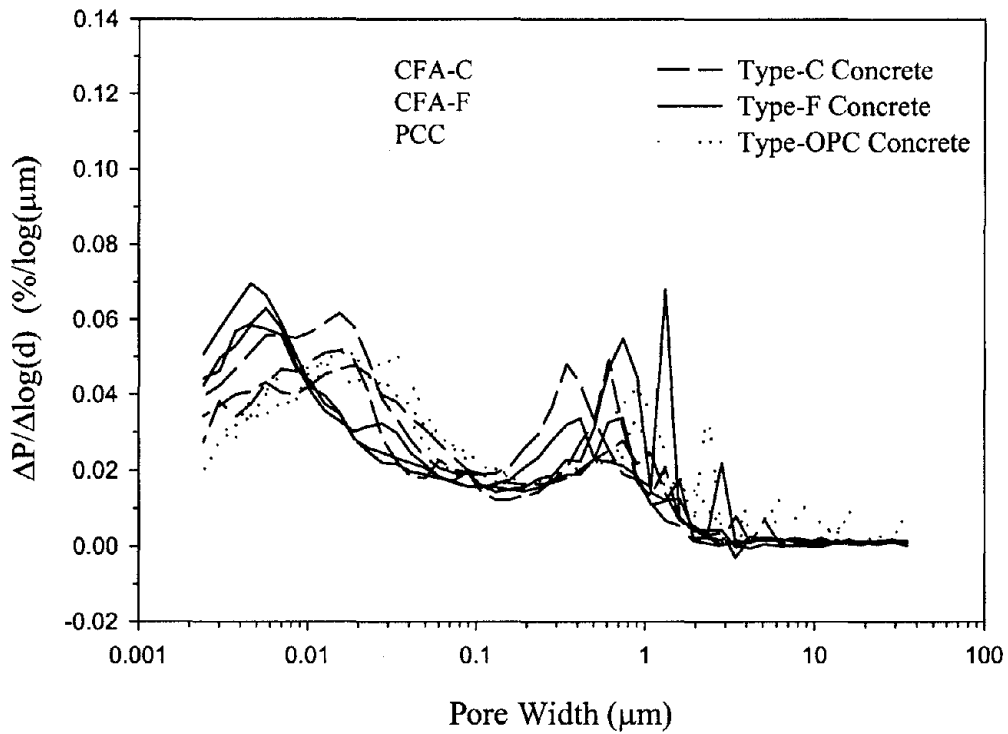


Figure 90: Average differential pore size distribution vs. pore width plot for the low treatment CFA-C, CFA-F, and PCC prisms.

Table 74: Results from BET-N₂ adsorption analysis of laboratory prisms.

Sample ID	Weighted surface area m ² /g
C(LL)09	2.53
C(LL)25	6.02
C(LL)41	9.81
F(LL)09	5.58
F(LL)25	7.79
F(LL)41	5.86
P(LL)09	10.83
P(LL)25	8.65
P(LL)41	11.09

5.5.5.3 Conclusions

In conclusion:

1. As with the slab concrete, for the laboratory concrete, surface area measurements were inconclusive due to the heterogeneous nature of concrete and the sample sizes relative to coarse aggregate sizes.

5.5.6. Elemental Composition

Total elemental composition analysis was performed on one sample from each of the three mix designs. Samples were analyzed for elemental composition after the 28-d curing process, but without having been subjected to any of the accelerated aging processes. The results are presented in tables L-20 through L-22 in appendix L of volume II and divided into major (greater than 10,000 ppm), minor (1,000 to 10,000 ppm), and trace (less than 1,000 ppm) components.

No significant difference was found between the elemental concentrations of the three types of prisms. Similarity between the elemental composition of the three concrete mixes was not surprising. The only difference between the contents and treatment of the three concrete mixes was the replacement, by weight, of 15 percent of the cement with CFA-C or CFA-F. This difference in 15 percent of the cementitious materials equals only a 2.2 weight percent difference in the concrete matrix. Since such a small fraction of the concrete weight was affected by the partial replacement of the portland cement with the CFA, differences in elemental concentrations were not seen.

In conclusion:

1. The slab concrete exhibited a lower Si concentration, perhaps because of the aging of the slab concrete.
2. The slab concrete exhibited a high concentration of S. This may correspond to the early distress experienced by the pavement.

5.5.7. Mineralogy

XRPD was performed in triplicate on three samples from each mix design to compare the bulk phase mineralogy. The PCC prisms analyzed were P(LLL)09, P(LLL)25, and P(LLL)41. The CFA-C prisms analyzed were C(LLL)09, C(LLL)25, and C(LLL)41. The CFA-F prisms that were analyzed were F(LLL)09, F(LLL)25, and F(LLL)41.

Quantification of mineral concentration by XRPD was performed for albite ($\text{NaAlSi}_3\text{O}_8$), calcite (CaCO_3), gypsum ($\text{CaSO}_4 \cdot 2\text{H}_2\text{O}$), ettringite ($\text{Ca}_6\text{Al}_2(\text{SO}_4)_3(\text{OH})_{12} \cdot 26\text{H}_2\text{O}$), portlandite ($\text{Ca}(\text{OH})_2$), and quartz (SiO_2) phases. Table 75 summarizes the quantitative XRPD results of the three concrete mixes.

Table 75: Mineral concentrations in the three types of experimental prisms quantified by XRPD.

PDFNo.	Mineral name	Chemical formula	RIR value	PCC prisms	
				Mean concentration ²	Concentration range ³
09-0466	Albite	NaAlSi ₃ O ₈	2.10	2.5%	0.4% - 5.7%
05-0586	Calcite	CaCO ₃	2.00	19.5%	12.1% - 30.4%
41-1451	Ettringite	Ca ₆ Al ₂ (SO ₄) ₃ (OH) ₁₂ • 26H ₂ O	1.00 ¹	0.2%	0% - 0.5%
33-0311	Gypsum	CaSO ₄ • 2H ₂ O	1.83	0.1%	0% - 0.7%
04-0733	Portlandite	Ca(OH) ₂	1.40	1.8%	1.4% - 3.0%
46-1045	Quartz	SiO ₂	3.41	5.6%	0.9% - 8.5%
PDFNo.	Mineral name	Chemical formula	RIR value	CFA-C prisms	
				Mean concentration ²	Concentration range ³
09-0466	Albite	NaAlSi ₃ O ₈	2.10	2.5%	0% - 5.9
05-0586	Calcite	CaCO ₃	2.00	20.5%	12.2% - 26.6%
41-1451	Ettringite	Ca ₆ Al ₂ (SO ₄) ₃ (OH) ₁₂ • 26H ₂ O	1.00 ¹	0.6%	0% - 1.6%
33-0311	Gypsum	CaSO ₄ • 2H ₂ O	1.83	0.4%	0.2% - 0.7%
04-0733	Portlandite	Ca(OH) ₂	1.40	1.2%	0.8% - 1.6%
46-1045	Quartz	SiO ₂	3.41	4.7%	2.1% - 8.1%
PDFNo.	Mineral name	Chemical Formula	RIR value	CFA-F prisms	
				Mean concentration ²	Concentration range ³
09-0466	Albite	NaAlSi ₃ O ₈	2.10	3.0%	0.6% - 5.8%
05-0586	Calcite	CaCO ₃	2.00	21.9%	17.1% - 28.2%
41-1451	Ettringite	Ca ₆ Al ₂ (SO ₄) ₃ (OH) ₁₂ • 26H ₂ O	1.00 ¹	0.5%	0% - 3.1%
33-0311	Gypsum	CaSO ₄ • 2H ₂ O	1.83	0.2%	0.1% - 0.4%
04-0733	Portlandite	Ca(OH) ₂	1.40	0.9%	0.3% - 3.0%
46-1045	Quartz	SiO ₂	3.41	6.7%	1.6% - 12.6%

1 The RIR value for ettringite was assumed to be 1.00

2 Mean of the nine diffractograms run for each center point mix design

3 Range of concentrations for the nine diffractograms run for each center point mix design

Similarities in mineral phases present in the three concrete mixes may be noted. Quartz (SiO_2), calcite (CaCO_3), and Mg Fe oxide were identified in each replicate of all three concrete mix types, all with low FOM or high certainty. Quartz was identified in the aggregate, the CFA-C, and the CFA-F as a major phase. Calcite was identified in the diffractograms of the portland cement paste and the aggregate. Mg Fe oxide was identified in the diffractogram of the combined aggregate sample. Since the aggregates are a significant source of these three minerals and the aggregate content of the three types of concrete were equal, similar concentrations of these mineral contents would be expected, as seen in table 75.

Ca oxide (CaO) was identified in all three concrete prisms types with good frequency, but the weighted average FOMs were lower in the PCC prisms and the CFA-F prisms than in the CFA-C prisms. CaO was identified as a trace mineral in the portland cement paste, as well as in one CFA-C diffractogram. Though most of the CaO in portland cement exists in a matrix of Si, Al and Mg oxides, a small residue of CaO as free lime is typical in portland cement (Neville, 1996), so that identification of CaO as a trace concrete mineral could be expected. CFA-C typically contains 1e to 3 percent free lime while CFA-F usually contains no free lime (FHWA, 1995). Since the untreated CFA-F typically contains no free lime, but CaO was still identified in those prisms it is likely the CaO phase identified in all three types of concrete results mainly from the portland cement matrix. CaO was not quantified by XRPD due to overlapping peaks with other significant mineral phases.

Portlandite (Ca(OH)_2) was identified by qualitative analysis with low FOMs in the CFA-C prisms and PCC prisms, but was not identified in the CFA-F prisms. Portlandite typically makes up 20 to 30 percent of fresh cement paste (Glasser, 1997). A mass balance revealed that portlandite might make up 3.9 to 5.9 percent of the experimental concrete, by weight. The quantification of portlandite in the PCC prisms resulted in a concentration range of 1.4 – 3.0 percent. Because of the high error associated with XRPD quantification at low concentration (McCarthy and Thedchanamoorthy, 1988), this concentration range agrees relatively well with the calculated portlandite concentration based on the mass balance. The quantification results show, as expected, that concentrations of portlandite in the CFA-C and CFA-F concrete prisms are not as high as in the PCC prisms. The CFA was used as a replacement for the portland cement in the concrete prisms. Since both the CFA-C and CFA-F are lower in Ca content than the portland cement, a decrease in the portlandite (Ca(OH)_2) concentration would be expected.

Albite ($\text{NaAlSi}_3\text{O}_8$) was detected at low levels in the three concrete mixes. Albite was shown to be part of the aggregate mineralogy and would be expected to occur in all three concrete mixes.

Gypsum ($\text{CaSO}_4 \cdot 2\text{H}_2\text{O}$) and ettringite ($\text{Ca}_6\text{Al}_2(\text{SO}_4)_3(\text{OH})_{12} \cdot 26\text{H}_2\text{O}$) were quantified at only trace levels in the three concrete mixes. In many diffractograms ettringite was not quantifiable at all. Trace phases are difficult to quantify because often only one peak is large enough and non-overlapping to be used for quantification work. The use of only one peak, as was often the case in the quantification of gypsum and ettringite, increases the uncertainty in the resulting concentration values.

5.5.7.1 ANOVA

An ANOVA was performed for each of the six mineral phases quantified by XRPD in the three concrete mixes. The ANOVA determines if there is a statistical difference between mineral concentrations in the different mix types, but does not specify which mix types exhibit a statistical difference. The ANOVA tables for mineral phase concentrations in the three types of concrete prisms are presented in tables L-23 through L-28 in appendix L of volume II. The tabular F values used to determine the level of statistical confidence were F of 2.54 at 90 percent confidence, F of 3.40 at 95 percent confidence, and F of 5.61 at 99 percent confidence (Kuehl, 1994).

No significant difference was found in the mineral concentrations of albite ($\text{NaAlSi}_3\text{O}_8$), calcite (CaCO_3), ettringite ($\text{Ca}_6\text{Al}_2(\text{SO}_4)_3(\text{OH})_{12}\cdot 26\text{H}_2\text{O}$), or quartz (SiO_2). Albite, calcite, and quartz were all identified as mineral phases in the aggregate. Since the same aggregate was used in the same proportion in all three mix types, it is logical that these minerals would not exhibit a difference between concrete mixes.

Finding no statistical difference in the ettringite ($\text{Ca}_6\text{Al}_2(\text{SO}_4)_3(\text{OH})_{12}\cdot 26\text{H}_2\text{O}$) concentration of the three concrete mixes was expected since ettringite was not identified by XRPD as a likely mineral phase in any of the nine prisms examined for this statistical comparison.

Statistical differences were found at a 95 percent confidence level in the concentrations of gypsum ($\text{CaSO}_4\cdot 2\text{H}_2\text{O}$) and portlandite (CaOH_2). The Tukey-Kramer Comparison of Means test was performed to identify specifically which mix types differ from one another.

5.5.7.2 Tukey-Kramer Comparisons

A Tukey-Kramer analysis was performed for gypsum ($\text{CaSO}_4\cdot 2\text{H}_2\text{O}$) and portlandite (CaOH_2) concentrations. A statistical difference between two concrete mixes is established if the absolute value of the intersecting box of the mix types is greater than the absolute value of the shaded boxes on the diagonal. These statistical comparisons were performed at a 95 percent confidence level.

Table L-29 in appendix L of volume II shows that the concentration of gypsum ($\text{CaSO}_4\cdot 2\text{H}_2\text{O}$) in the PCC samples was significantly different from the concentration of gypsum in the CFA-C concrete samples. The mean concentration of the nine diffractograms made for each mix type was 0.1 percent and 0.4 percent for the PCC and the CFA-C concrete mixes, respectively. Eight of nine diffractograms for the PCC samples were given a gypsum concentration of 0 percent; gypsum was not detected through quantification in these diffractograms. Gypsum was quantifiable in all nine of the CFA-C prisms with a range of 0.2 percent to 0.7 percent. There was not a statistical difference between the gypsum concentration in the CFA-F prisms and either of the PCC or CFA-C prisms.

Gypsum ($\text{CaSO}_4\cdot 2\text{H}_2\text{O}$) is added to portland cement during manufacturing in order to react with $3\text{CaO}\cdot \text{Al}_2\text{O}_3$, preventing the flash setting of the cement. Typically CFA-C contains

additional quantities of aluminates that would also react with the gypsum in the portland cement. Since gypsum is not added to account for the reactants in the CFA-C, the replacement of the cement with the ash can result in a gypsum deficit. Therefore it is not expected that the CFA-C concrete prisms would have more gypsum in them than the PCC prisms. Error associated with quantification of trace mineral by XRPD has been shown to be as high as 3.5 percent (McCarthy and Thedchanamoorthy, 1988). Use of only one resolved peak for quantification, as was the case with gypsum, also increases uncertainty in quantification results. Therefore, due to the trace concentrations of gypsum detected in the concrete prisms, the statistical difference between the CFA-C prisms and the PCC prisms is not considered reliable.

A statistical difference was found in the concentration of portlandite (CaOH_2) in PCC samples and CFA-F samples (see table L-30 in appendix L of volume II). The PCC prisms were found to be significantly higher in portlandite concentration than the CFA-F prisms. The difference in the design of these two mix types is the replacement of 15 percent of the portland cement with CFA-F, exchanging a high Ca material for a low Ca material. The lower Ca concentration in the CFA-F prisms requires that Ca be removed from the portlandite phase to increase the Ca content in the gel phase of the cement paste. The statistical difference between the concentrations of portlandite in the PCC prisms and the CFA-F prisms agrees with what would be expected.

Comparing these XRPD mineral concentration data between the slab and the laboratory concretes (see section 5.3.6, table 32) finds excellent correspondence.

5.5.7.3 Conclusions

In conclusion:

1. There were no significant differences in the concentrations of albite, calcite, ettringite, or quartz between the three laboratory concretes.
2. The gypsum level detected in the CFA-C was found to be significantly different than that of the PCC, but as the levels detected were quite low, the significance of this statistical difference is questionable.
3. The portlandite concentration was significantly higher in the PCC concrete as would be expected owing to the lack of CFA in the PCC.

5.5.8. pH-Dependent Leaching and Solid Phase Control

5.5.8.1 C(XXX)02, F(XXX)02, and P(XXX)02 Alkalinity and Constituent Solubility as a Function of pH

Acid neutralization capacity curves for the three 28-d cured material types prior to any aging (e.g., C(XXX)02, F(XXX)02, and P(XXX)02) are compared in figure 91.

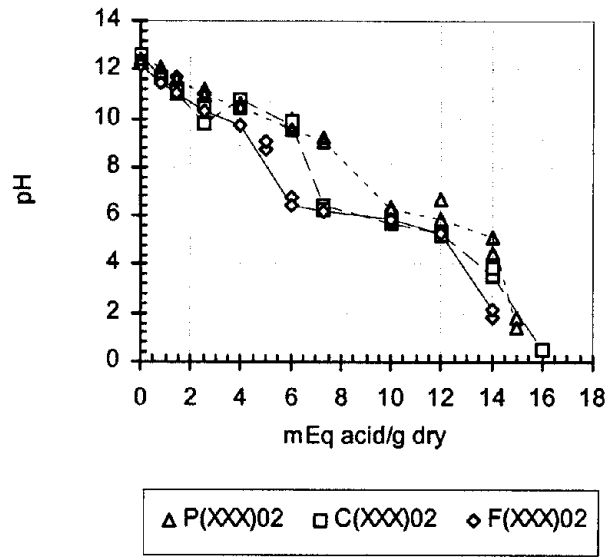


Figure 91: Acid neutralization capacity curves.

The acid neutralization capacity of PCC control was greater than the acid neutralization capacity of CFA-C mix and CFA-F mix. Indeed, 18 percent of portland cement was substituted by CFAs in the CFA mix. In addition, the acid neutralization capacity of CFA-C mix was greater than the acid neutralization capacity of CFA-F mix. This was consistent with a greater acid neutralization capacity of CFA-C compared with CFA-F. Thus, for PCC control, 10 mEq of acid/g of dry solid was needed to achieve pH 6 while 7 mEq was needed for CFA-C mix and 6 mEq for CFA-F mix.

For the three materials, the pH titration curves presented a plateau around pH 6 due to the buffering capacity of the aggregates (e.g., limestone type). Based on the acid required to reach pH 11.9, the quantity of Ca hydroxide produced during the hydration reactions of the cement was estimated at 22.6 g/kg of dry material (e.g., 57 kg /m³ of porous material) for C(XXX)02, 15.2 g/kg of dry material (e.g., 38.9 kg /m³ of porous material) for F(XXX)02, and 95.6 g/kg of dry material (e.g., 95.6 kg /m³ of porous material) for P(XXX)02.

The acid neutralization of the laboratory concretes matched well that of the slab concretes (see section 5.3.8.1 and figure 47).

Cd, Cu, Pb, Ni, and Zn solubility as a function of pH for the three material types after 28-d cure (e.g., C(XXX)02, F(XXX)02, and P(XXX)02) is compared in figure 92. Horizontal lines on each of the figures are used to indicate the FAAS detection limits.

No influence of the matrix (e.g., CFA-C mix, CFA-F mix, or PCC control) could be observed on Cd, Cu, Pb, Ni, and Zn solubility. For each of the metals of concern, the solubility increased as the pH decreased and no amphoteric behavior was observed.

At low pHs (e.g., less than 3), the concentration of the metals of concern reached a plateau. Leaching then seemed to be limited by an available content for Ni and Zn (e.g., less than 10 percent of Ni and 35 percent of Zn have been released) while exceeding the calculated total content in the case of Cd, Cu, and Pb. For pHs greater than 7, Ni and Zn solubility remained below FAAS detection limit (e.g., 0.01 mg/l and 0.001 mg/l, respectively).

In conclusion:

1. There was a slight difference between the three material types with respect to buffering capacity.
2. The PCC was more buffered than the CFA-F and the CFA-C.
3. The CFA-F was more buffered than the CFA-C.
4. There was no difference between the three material types with respect to solubility as a function of pH for each of the trace metals of concern.

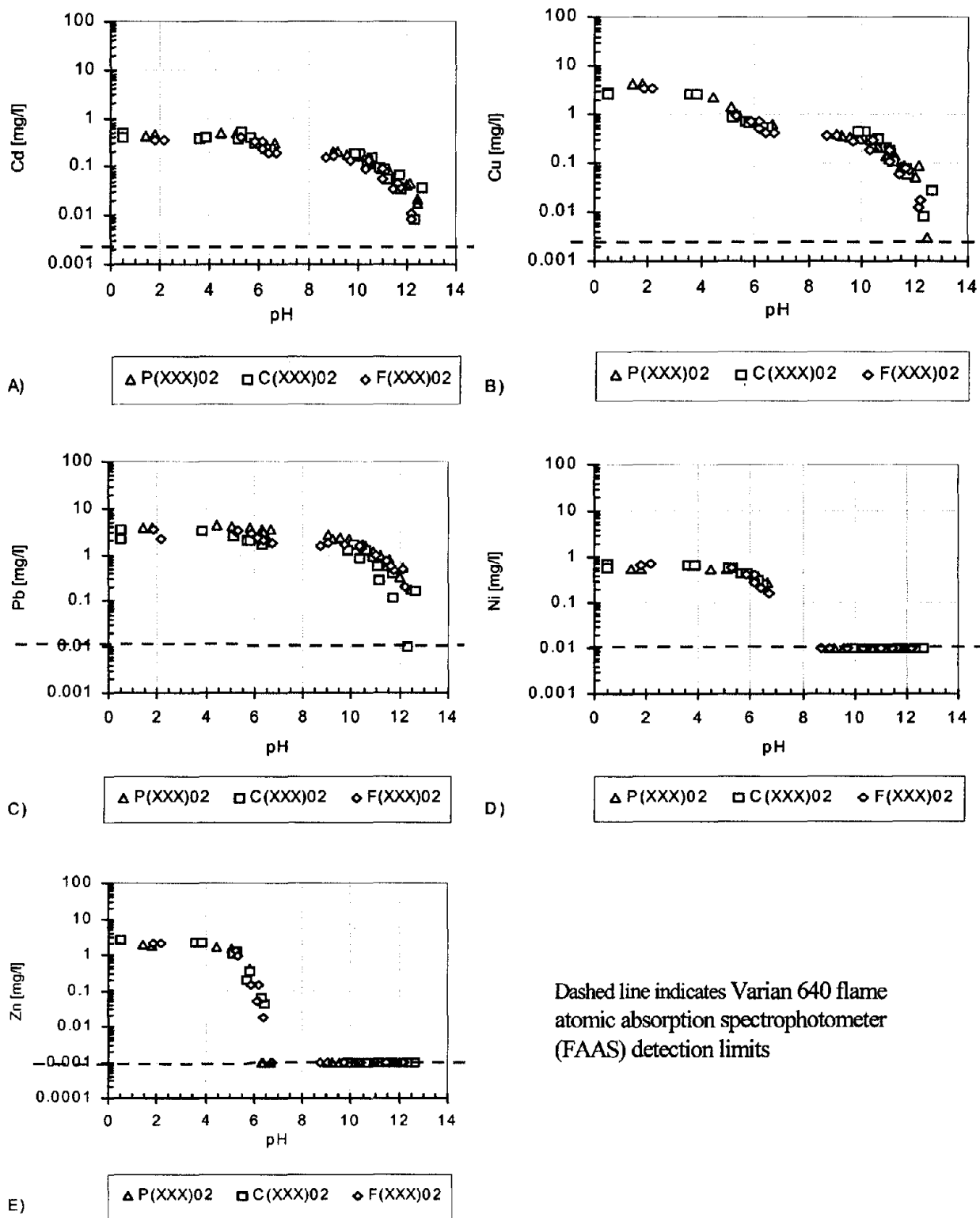


Figure 92: Solubility as a function of pH:
 A) Cd, B) Cu, C) Pb, D) Ni, E) Zn.

5.5.8.2 pH-Stat Leaching

Three concrete prisms from each mix type were subjected to pH-dependent leaching. Those samples were P(LL)09, P(LL)25, P(LL)41, C(LL)09, C(LL)25, C(LL)41, F(LL)09, F(LL)25, and F(LL)41. Each concrete sample was leached at four pH points, 5.0, 7.3, 9.7, and 12.0.

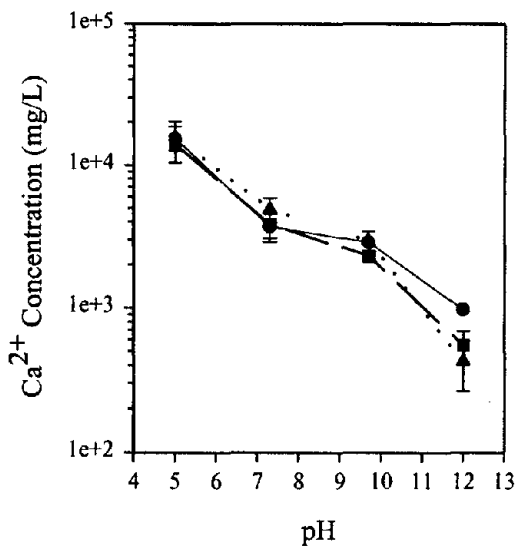
The resulting leachates were analyzed for Al, Ba, Ca, Cl, CO_3^{2-} , Cr, Fe, K, Mg, NO_3^- , Si, SO_4^{2-} , and Zn. NO_3^- was added as HNO_3 to the leaching system to maintain a constant pH. It was measured for the purposes of geochemical modeling. The other 12 species were measured to look for any differences in pH-dependent leaching behavior between the three concrete mixes as well as geochemical modeling.

Figures 93 through 95 show the average (+/- one standard deviation) of the leached concentrations of the 12 analytes for each of the three types of concrete.

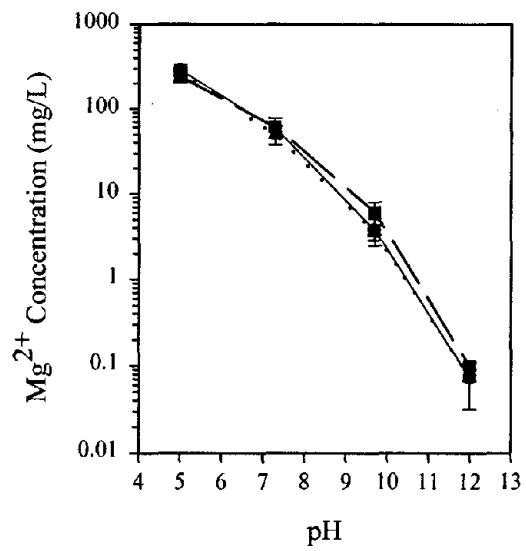
The general pH-dependent leaching behavior of Ca, Mg, Al, and Si were similar in the three concrete mixes (see figure 93). Ca and Mg demonstrated decreasing leachability with increasing pH over the entire pH range examined. Si leaching demonstrated a slight increase in concentration from a pH of 5.0 to a pH of 7.3 in the control and CFA-F concrete mixes, while a decrease in Si concentration was observed for the CFA-C concrete mix in the same range. For all three concrete mixes, Si concentration decreased from a pH of 7.3 to a pH of 12.0. Statistical significance of any differences is examined in section 5.5.8.3. Al showed typical amphoteric leaching behavior with a minimum solubility around a pH of 10.

Ba, Zn, Fe, and Cr leaching are depicted in figure 94. Ba leaching exhibited typical pH-dependent leaching behavior, with a minimum leachability around a pH of 10, for the CFA-C and control mixes. Behavior in Zn leaching for CFA-F concrete prisms differs from the other 2 mixes only at a pH of 9.7. The leached concentration of Zn at this pH is noticeably higher in the CFA-F mix than the other two mixes. At a pH of 9.7, the 3 concentrations of Zn from the CFA-F concrete prisms are 0.023 mg/L, 0.034 mg/L, and 0.27 mg/L. Exclusion of the highest of the three values would bring the trend for Zn leaching from the CFA-F mix in line with the leaching trend of the control and CFA-C mixes. Therefore it is likely that the general trend of Zn leaching is the same for all three types of prisms and that the Zn concentration in the CFA-F mix exhibits a deviation due to one unusually high result. Fe leaching decreased with increasing pH through the acidic and neutral pH ranges but leveled off in the basic pH range. Cr decreased in leachability with increasing pH for the entire pH range examined.

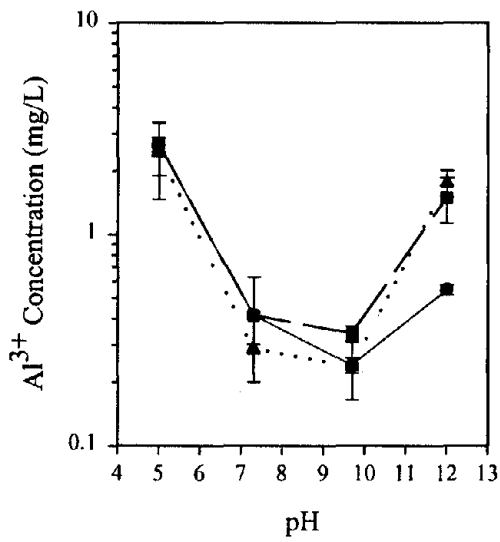
Figure 95 shows similar leaching between all three mixes for K^+ , Cl, CO_3^{2-} , and SO_4^{2-} . K^+ leachate concentration remained relatively constant over the pH range examined. Cl concentrations were often BDL and therefore leaching behavior was difficult to compare between the mixes. Species such as K^+ and Cl are expected to be pH-independent. CO_3^{2-} demonstrated pH-dependent leaching behavior, generally increasing in concentration with increasing pH for all



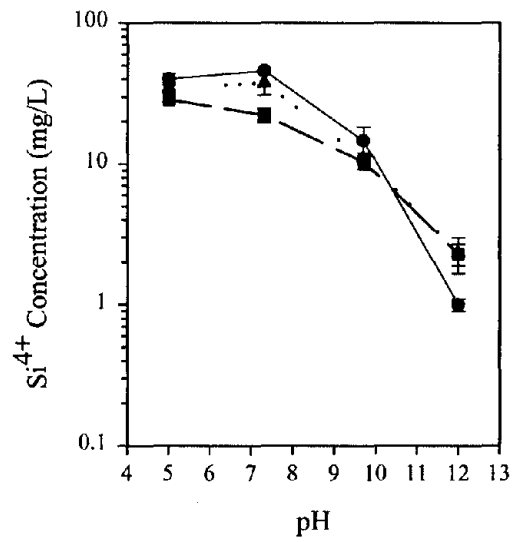
(a)



(b)



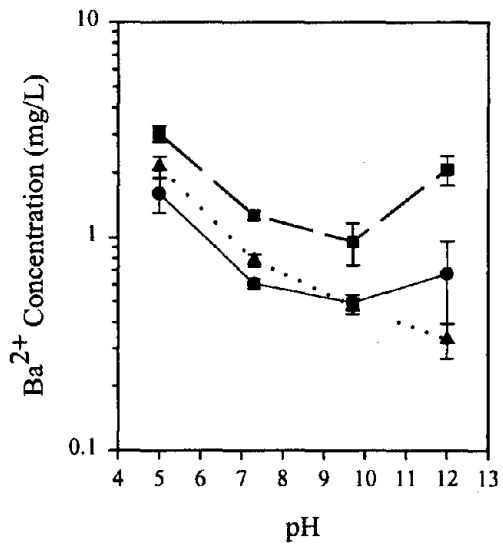
(c)



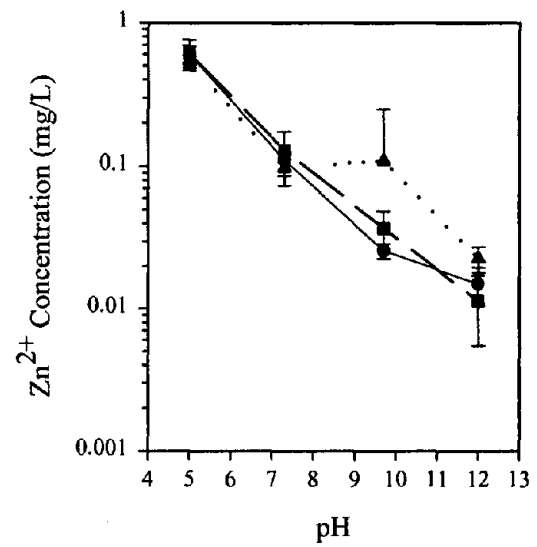
(d)

● PCC prisms ■ CFA-C prisms ▲ CFA-F prisms

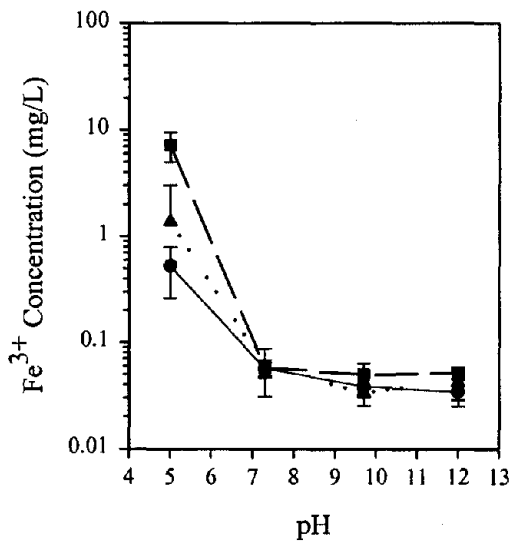
Figure 93: pH-dependent leaching of three types of concrete:
(a) Ca, (b) Mg, (c) Al, (d) Si.



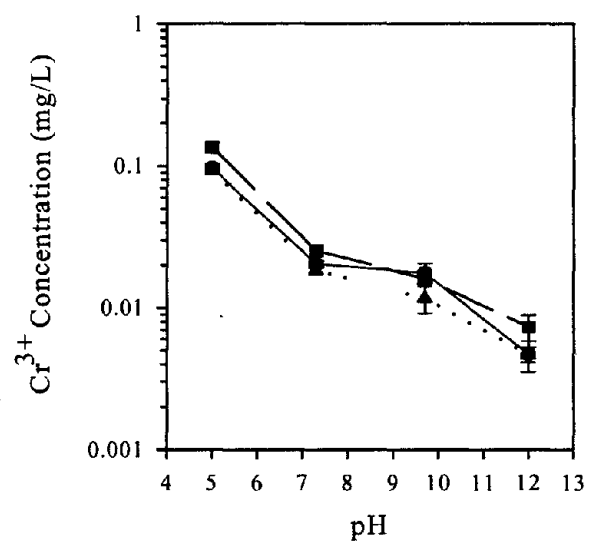
(a)



(b)



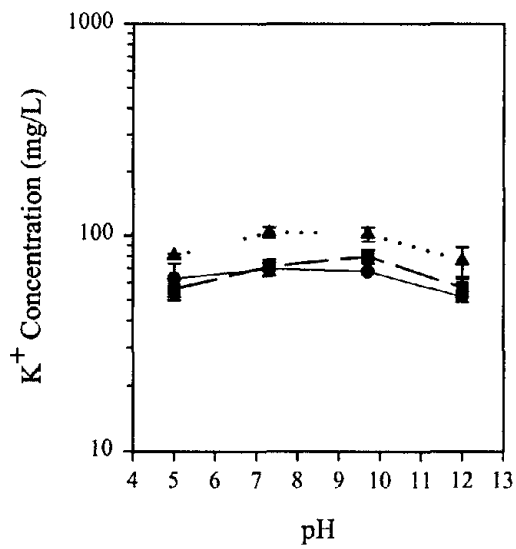
(c)



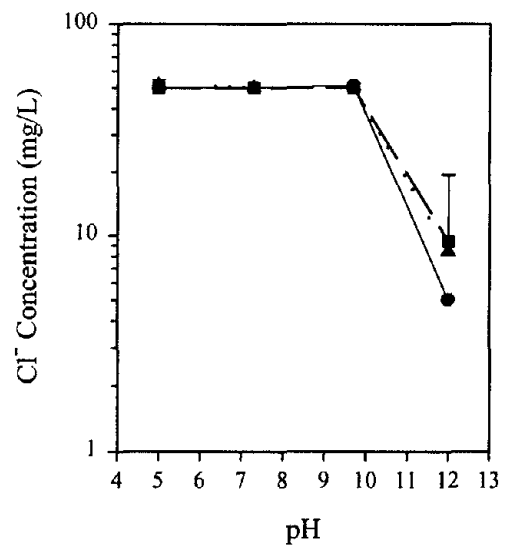
(d)

● PCC prisms ■ CFA-C prisms ▲ CFA-F prisms

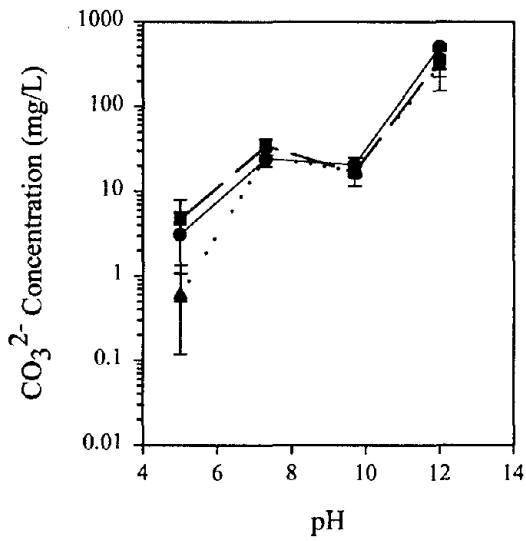
Figure 94: pH-dependent leaching of three types of concrete:
(a) Ba, (b) Zn, (c) Fe, (d) Cr.



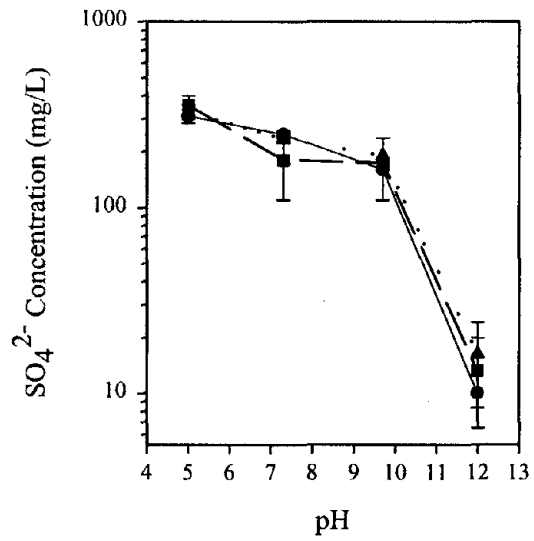
(a)



(b)



(c)



(d)

● PCC prisms ■ CFA-C prisms ▲ CFA-F prisms

Figure 95: pH-dependent leaching of three types of concrete:
 (a) K, (b) Cl, (c) CO₃²⁻, (d) SO₄²⁻.

three concrete mix types. SO_4^{2-} leachate concentrations were fairly constant from a pH of 5.0 to a pH of 9.7 and then decreased at the high end of the pH range examined.

5.5.8.3 ANOVA

ANOVAs were performed to determine if significant variation exists in the leachate concentrations of the three types of concrete. ANOVA for Cl^- concentration was only performed at pH of 12 because the majority of data points at the other pH levels were BDL. Selected ANOVA tables are presented in tables L-31 through L-33 in appendix L of volume II. Table 76 is a summary table of the ANOVA results of all analytes.

The ANOVA examines whether a statistical difference exists within the leaching data of the three mix types. If a statistical difference was found to exist with at least 90 percent confidence, the data was further analyzed by a Tukey-Kramer Comparison of Means to determine specifically which concrete mixes differ significantly from one another. The tabular F values used to determine statistical significance in the ANOVA were 3.46 at 90 percent confidence, 5.14 at 95 percent confidence, and 10.9 at 99 percent confidence (Kuehl, 1994).

Al, Ba, Ca, Cr, Fe, K, Si, and Zn all demonstrated significant differences in leaching between at least two mix types and at least at one pH level. Mg, Cl, CO_3^{2-} , and SO_4^{2-} did not demonstrate any differences in leachate concentration between any of the three concrete mix types.

5.5.8.4 Tukey-Kramer Comparisons

Tukey-Kramer tests were performed to determine which mix types exhibit a statistically significant difference in leached analyte concentrations at a particular pH level. The leaching results of different concrete mix types were considered significant if a difference was established with at least 90 percent confidence. A summary table of Tukey-Kramer testing is presented in table 77. Confidence levels at which statistical significance was established between mix types are noted in the summary table.

Leaching results of Ba showed the Ba concentrations were higher over the entire pH range in the CFA-C prism leachates than in the leachates of the CFA-F prisms and PCC prisms. Higher Ba leaching from the CFA-C prisms may be explained by the higher concentration of Ba in the CFA-C than in the CFA-F or portland cement. Total elemental composition showed the Ba concentration to be 5,249 ppm, while concentrations of Ba in the CFA-F and portland cement were 853 ppm and less than 43 ppm, respectively.

A similar explanation may be applicable to observed differences in K leaching. K leaching was found to be significantly greater in the CFA-F prisms than the CFA-C prisms and the control prisms over the entire pH range examined. This behavior corresponds to a higher total elemental concentration of K in the CFA-F than in the CFA-C or the portland cement. The total elemental composition of K in the CFA-F was 22,050 ppm. In the CFA-C, the total elemental composition of K was found to be 4,074 ppm and it was 5,726 ppm in the portland cement.

Table 76: Summary table of ANOVA for leaching of three types of concrete.

Species				
pH	Al	Ba	Ca	Cl ¹
5.0	none	>99%	none	--
7.3	none	>99%	none	--
9.7	>90%	>99%	none	--
12.0	>99%	>99%	>99%	none

Species				
pH	CO ₃	Cr	Fe	K
5.0	none	>99%	>99%	>95%
7.3	none	>99%	none	>99%
9.7	none	>95%	none	>99%
12.0	none	>95%	none	>95%

Species				
pH	Mg	Si	SO ₄ ²⁻	Zn
5.0	none	>99%	none	none
7.3	none	>99%	none	none
9.7	none	none	none	none
12.0	none	>95%	none	>90%

- 1 ANOVAs were not performed for chloride leaching at pH = 5.0, 7.9, or 9.7 because the majority of data values were BDL.

Table 77: Summary table of Tukey-Kramer tests for leaching of three types of concrete.

Species		Al			Ba		
pH		9.7	12.0	5.0	7.3	9.7	12.0
Mix types	CFA-C vs PCC	>90%	>99%	>90%	>95%	>95%	>99%
	CFA-F vs PCC	none	>99%	none	>95%	none	none
	CFA-C vs CFA-F	>90%	none	>90%	>95%	>95%	>99%
Species		Ca		Cr			
pH		12.0	5.0	7.3	9.7	12.0	
Mix types	CFA-C vs PCC	>95%	>99%	>95%	none	>90%	
	CFA-F vs PCC	>95%	none	none	>95%	none	
	CFA-C vs CFA-F	none	>99%	>95%	none	>90%	
Species		Fe		K			
pH		5.0	5.0	7.3	9.7	12.0	
Mix types	CFA-C vs PCC	>90%	none	none	>90%	none	
	CFA-F vs PCC	none	>90%	>99%	>90%	>90%	
	CFA-C vs CFA-F	>90%	>90%	>99%	>90%	>90%	
Species		Si		Zn			
pH		5.0	7.3	12.0	12.0		
Mix types	CFA-C vs PCC	>90%	>99%	>95%	none		
	CFA-F vs PCC	none	none	>95%	none		
	CFA-C vs CFA-F	>90%	>99%	none	>90%		

5.5.8.5 Geochemical Modeling

As done for mix components (see section 5.1.6.3) and the slab concrete (see section 5.3.8.3), geochemical modeling was performed using the modeling program MINTEQA2. To compare the modeling of the three mix types of concrete prisms, CFA-C, CFA-F and PCC prisms, the leaching data and modeling data for each mix type are presented side-by-side in figures L-9 through L-18 in appendix L of volume II. Results are summarized in table 78. Candidate controlling solids were selected for modeling of the leaching behavior of the analytes based on the XRPD data and the MINTEQA2 saturation indices of each solid.

Ca Modeling. Figure L-9 shows the modeling of Ca leaching for each of the concrete mixes. Agreement of candidate controlling solids with the experimental data was the same for each concrete mix. Calcite (CaCO_3), dolomite ($\text{CaMg}(\text{CO}_3)_2$), and gypsum ($\text{CaSO}_4 \cdot 2\text{H}_2\text{O}$) modeling had good agreement in concentration and curve shape over the entire pH range. Ettringite ($\text{Ca}_6\text{Al}_2(\text{SO}_4)_3(\text{OH})_{12} \cdot 26\text{H}_2\text{O}$) had reasonable agreement at a pH greater than 7.3. Portlandite (CaOH_2) modeling overestimated leached Ca concentrations over the entire pH range. Calcite, dolomite and gypsum are likely controlling solids for the Ca leaching from all three concrete mix types. (Calcite and dolomite were found as likely controlling solids for the hydrated cement paste (see section 5.1.6.3) and for the slab concrete (see section 5.3.8.3).

Mg Modeling. Figure L-10 shows the modeling for the leaching of Mg for controlling solids brucite ($\text{Mg}(\text{OH})_2$) and dolomite ($\text{CaMg}(\text{CO}_3)_2$). Brucite modeling did not show good agreement in any of the concrete mixes with regard to the shape of the leaching curve. Only at a pH of 12.0 was the predicted concentration a reasonable approximation of the observed data. At other pHs, the predicted concentrations for brucite modeling was too high. Dolomite provided good agreement for concentration for all three concrete mixes over the pH range. The shape of the curve for dolomite modeling deviated at a pH of 12.0 from the observed data for the CFA-C and CFA-F prisms, but matched well at this pH for the PCC prisms. Overall the modeling of dolomite was similar for the three concrete mixes and dolomite was determined to be a likely controlling solid for Mg leaching. The same was found for both the hydrated cement paste and the slab concrete.

Al Modeling. Figure L-11 shows the modeling of Al with ettringite ($\text{Ca}_6\text{Al}_2(\text{SO}_4)_3(\text{OH})_{12} \cdot 26\text{H}_2\text{O}$), gibbsite ($\text{Al}(\text{OH})_3$) and amorphous $\text{Al}(\text{OH})_3$ for all three concrete mixes. Similar results were found for the three concrete mixes. Ettringite was not a good model for Al leaching. Gibbsite was the best match of the modeled solids, but the range of minimum solubility was shifted to a lower pH than was demonstrated in all the experimental data. Al leaching in cement-based systems can be controlled by the hydrated Ca species (Glasser, 1997), which are not included in the MINTEQA2 database.

Si Modeling. Si was modeled for both crystalline and amorphous SiO_2 in figure L-12. Neither solid adequately described the leaching behavior of the Si observed in the three types of concrete prisms. Amorphous SiO_2 modeling agreed better with the CFA-F and PCC prisms at a pH less than 7.3 compared with the modeling of CFA-C prisms, but agreement was poor in all cases above a pH of 7.3.

Table 78: Geochemical modeling species for three types of concrete mixes.

Species	Solid phase	log K_{sp}	Well modeled pH range		
			CFA-C	CFA-F	PCC
Al	Gibbsite $Al(OH)_3$	-8.291	none	none	none
	$Al(OH)_3$ amorphous	-10.800	none	none	none
	Ettringite $(Ca_6Al_2(SO_4)_3(OH)_{12} \cdot 26H_2O)$	-56.700	none	none	none
Ba	$BaCrO_4$	9.670	5 - 10	none	none
	Barite ($BaSO_4$)	9.980	5 - 12	5 - 12	5 - 12
Ca	Gypsum ($CaSO_4 \cdot 2H_2O$)	4.610	5 - 12	5 - 12	5 - 12
	Portlandite ($Ca(OH)_2$)	-22.804	none	none	none
	Calcite ($CaCO_3$)	8.480	5 - 12	5 - 12	5 - 12
	Dolomite ($CaMg(CO_3)_2$)	16.540	5 - 12	5 - 12	5 - 12
	Ettringite $(Ca_6Al_2(SO_4)_3(OH)_{12} \cdot 26H_2O)$	-56.700	7 - 12	7 - 12	7 - 12
CO ₃	Calcite ($CaCO_3$)	8.480	7 - 10	7 - 10	7 - 10
	Dolomite ($CaMg(CO_3)_2$)	16.540	7 - 10	7 - 12	7 - 12
Cr	$BaCrO_4$	9.670	none	none	none
Fe	Ferrihydrite ($Fe(OH)_3$)	-3.191	none	none	none
	Maghemite (Fe_2O_3)	-6.386	none	none	none
Mg	Dolomite ($CaMg(CO_3)_2$)	16.540	5 - 10	5 - 10	5 - 12
	Brucite ($Mg(OH)_2$)	-16.844	~12	~12	~12
Si	Quartz (SiO_2)	4.000	none	none	none
	SiO_2 amorphous gel	2.710	5 - 7	5 - 7	5 - 7
SO ₄	Gypsum ($CaSO_4 \cdot 2H_2O$)	4.610	7 - 10	7 - 10	7 - 10
	Barite ($BaSO_4$)	9.980	5 - 12	5 - 12	5 - 12
Zn	Zincite ($Zn(OH)_2$)	-11.334	none	none	none

Ba Modeling. Figure L-13 depicts the modeling of Ba leaching by barium chromate (BaCrO_4) and barite (BaSO_4). For all three concrete mixes, the agreement with BaCrO_4 modeling was poor. Modeling results of barite were similar for the three concrete mix types. Barite modeling was in good agreement with the observed data of the three concrete mixes over the entire pH range, with regard to concentration and the shape of the leaching curve. Barite has been shown to be a possible controlling solid in all three concrete mixes, as well as in other work (Fruchter, 1990).

Zn Modeling. Figure L-14 shows that the leaching behavior of Zn was unsuccessfully modeled by Zincite (Zn(OH)_2) for all three concrete mix types. Other work has suggested that Zn sorbed to metal oxides, which then control the solubility of Zn (EPRI, 1987; van der Sloot et al., 1994).

Fe Modeling. Figure L-15 shows the geochemical modeling of Fe for all three concrete mixes. For each mix, the agreement of the modeled solids, ferrihydrite (Fe(OH)_3) and maghemite (Fe_2O_3), was poor in concentration and shape of the predicted and observed data curves. Difficulty in the modeling of Fe leaching has been shown previously (Fruchter, 1990).

Cr Modeling. Figure L-16 depicts the modeling of Cr with barium chromate ($\text{BaCr}^{6+}\text{O}_4$). The predicted leaching curve of this solid agreed well with the leaching observed leaching trends of Cr for all three concrete mix types, but the predicted concentrations were considerably higher than the observed data. Cr^{3+} has been shown to substitute for Al^{3+} in cement hydration products and is then part of the Ca Al hydrates matrix (Glasser, 1997). Cr^{3+} solubility is then limited by these cement species rather than more common Cr oxides and hydroxides that would be found in the MINTEQA2 database.

CO_3^{2-} Modeling. Figure L-17 depicts the leaching behavior of CO_3^{2-} modeled by controlling solids calcite (CaCO_3) and dolomite ($\text{CaMg}(\text{CO}_3)_2$). In all three mix types calcite and dolomite show reasonable agreement with the observed data at a pH of 7.3 and a pH of 9.7. At a pH of 12.0, the CFA-F and PCC prisms also modeled well for dolomite as a controlling solid, but there was poor agreement in the CFA-C concrete prisms. At a pH of 5.0, the observed CO_3^{2-} concentrations for all prisms were much lower than the modeled concentrations. Calcite had good agreement in the middle pH range for the three concrete mix types. Dolomite modeling showed better agreement over a greater pH range for the CFA-F and PCC prisms than the CFA-C prisms.

SO_4^{2-} Modeling. SO_4^{2-} leaching is modeled by gypsum ($\text{CaSO}_4 \cdot 2\text{H}_2\text{O}$) and barite (BaSO_4) (see figure L-18). Barite was a good match of the modeling of the leaching data over the entire pH range for the three concrete mixes. Gypsum modeling data was within concentration limits for most of the pH range but did not match well in the shape of the curve. Barite appears to be a controlling solid for SO_4^{2-} leaching (EPRI, 1987).

5.5.8.6 Comparison of the Three 28-d Cured Material Types with the Combined Aggregates

Acid neutralization capacity curves from the combined aggregates (e.g., 54.5 percent coarse aggregates and 45.5 percent fine aggregates) are compared in figure 96 with that from the three concrete products (e.g., C(XXX)02, F(XXX)02, and P(XXX)02). The acid neutralization capacity of the combined aggregates was less than that of the concrete products. However, for acid additions between 6 and 12 mEq acid/g of dry material, the pH titration curve of the combined aggregates and concrete products presented an identical plateau around pH 6, confirming that the plateau observed for the concrete products was due to the presence of the aggregates.

Cd, Cu, Pb, Ni, and Zn solubility as a function of pH obtained for the three concrete products (e.g., C(XXX)02, F(XXX)02, and P(XXX)02) and the combined aggregates are compared in figure 97. Horizontal lines on each of the figures are used to indicate the Varian 640 flame atomic absorption spectrophotometer (FAAS) detection limits. For pH greater than 6 and less than 11, Cd, Cu, and Pb solubility from the combined aggregates was lower than that from the concrete products. However, for pH less than 6 and greater than 11, the same concentration levels and behaviors were observed. Although the aggregates constituted the greatest source of metals in the concrete products, within the pH range 6 to 11, Cd, Cu, and Pb solubility from the aggregates only contributed for a small percentage in the Cd, Cu and Pb total solubility. No significant differences could be observed between Ni solubility from the combined aggregates and Ni solubility from the concrete products. Increased Zn solubility was observed for the combined aggregates over the entire pH range.

5.5.8.7 Conclusions

In conclusion :

5. The acid neutralization capacity of PCC control was greater than the acid neutralization capacity of CFA-C mix and CFA-F mix.
6. No influence of the matrix (e.g., CFA-C mix, CFA-F mix or PCC control) could be observed on Cd, Cu, Pb, Ni, and Zn solubility.
7. As with hydrated cement paste and the slab concretes, calcite (CaCO_3) and dolomite ($\text{CaMg}(\text{CO}_3)_2$) are likely controlling solids for Ca leaching from the three laboratory mixes. For the laboratory concrete, gypsum is also a likely controlling solid.
8. As with the hydrated cement paste and slab concrete, dolomite ($\text{CaMg}(\text{CO}_3)_2$) is a likely controlling solid for Mg leaching in the three laboratory mixes.
9. Unlike the hydrated cement paste for which barium chromate (BaCrO_4) was better, but like the slab concrete, barite (BaSO_4) is a likely controlling solid for Ba in the three laboratory mixes.

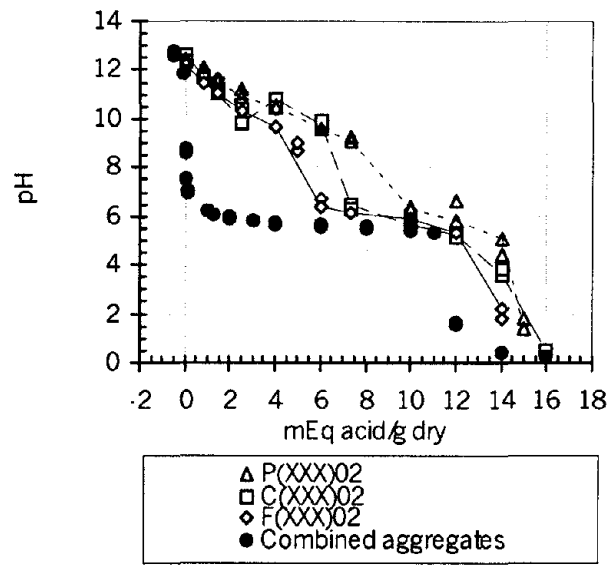
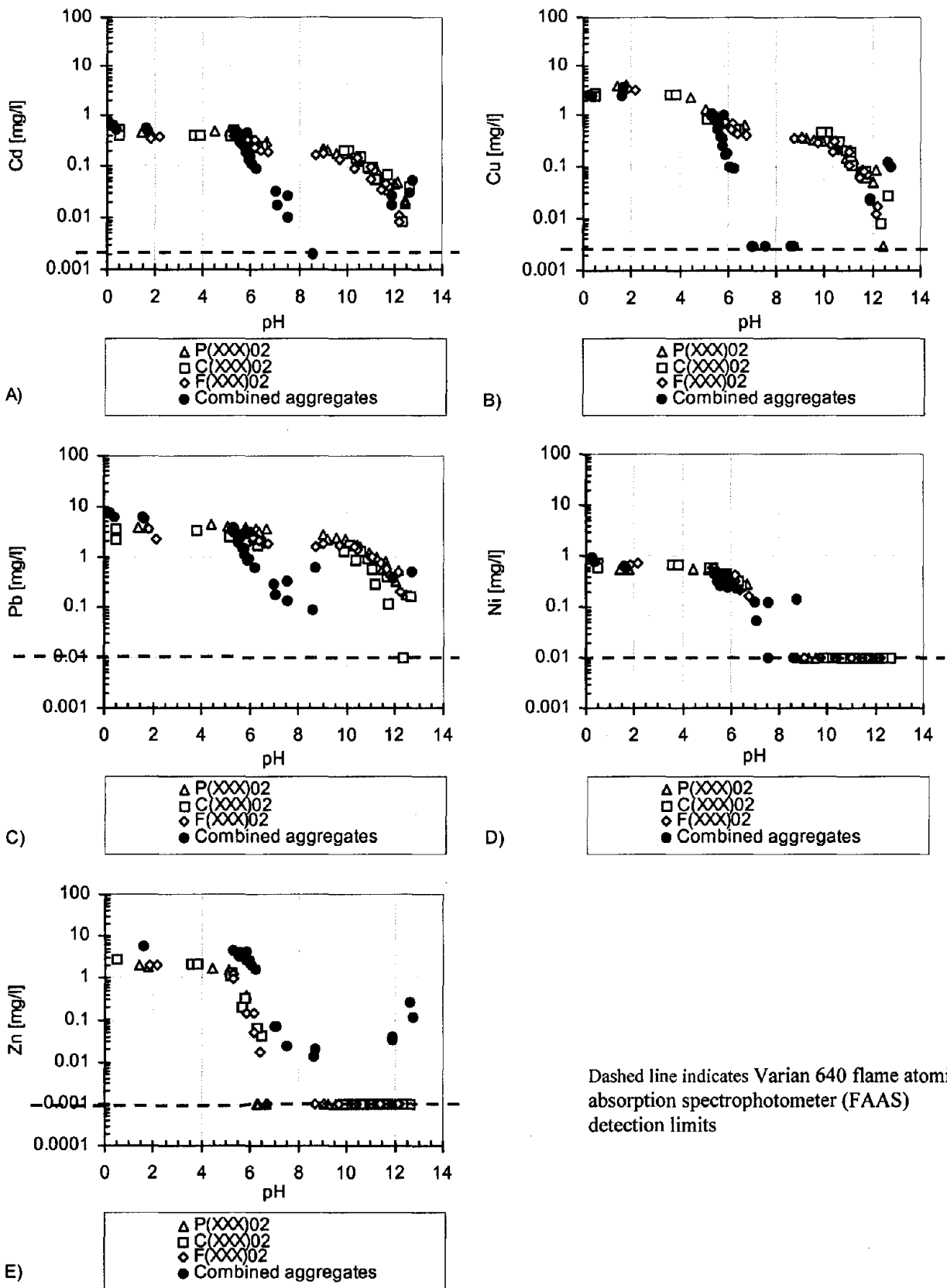


Figure 96: Acid neutralization capacity curves.



Dashed line indicates Varian 640 flame atomic absorption spectrophotometer (FAAS) detection limits

Figure 97: Solubility as a function of pH.:
A) Cd, B) Cu, C) Pb, D) Ni, E) Zn.

10. Like the slab concrete, barite (BaSO_4) is a likely controlling solid for SO_4^{2-} leaching in the three laboratory mixes.
11. As with the slab concrete, modeling was successful only at higher pH values for CO_3^{2-} and indicated dolomite ($\text{CaMg}(\text{CO}_3)_2$) and calcite (CaCO_3) as likely controlling solids. (Dolomite and barite were found for the hydrated cement pastes.)
12. As with the hydrated cement paste and slab concrete, geochemical modeling was not successful for Al, Si, Zn, Fe, Cr.
13. The controlling solids identified for the three types of concrete mixes appear to be typical of cement-based leaching.
14. Differences were seen in elemental leaching between the combined aggregates and the CFA-C prisms.

5.5.9. Low Liquid-Solid Ratio Leaching

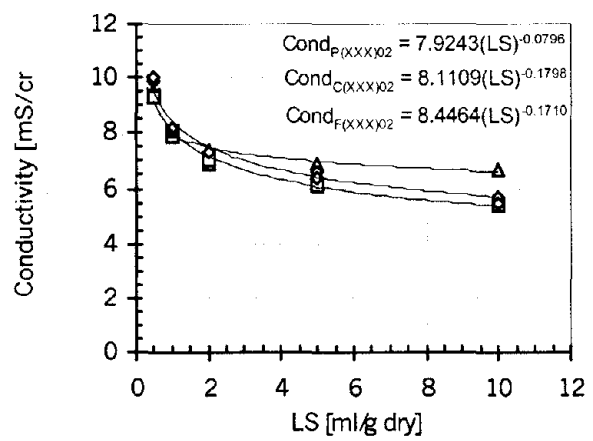
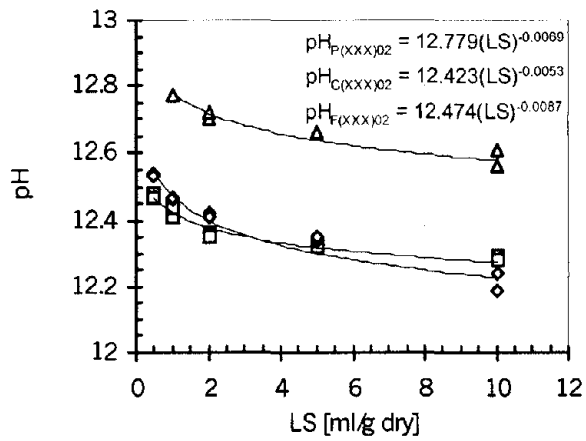
5.5.9.1 Low LS of CFA-C Mix, CFA-F Mix and PCC Control After 28 Days' Cure

pH and conductivity as a function of the liquid-solid ratio (e.g., LS ratio of 10, 5, 2, 1 and 0.5 ml/g of dry material) of 28-d cured CFA-C mix (e.g., C(XXX)02), CFA-F mix (e.g., F(XXX)02), and PCC control (e.g., P(XXX)02) are compared in figure 98. Concentration of the species of concern (e.g., Na, K, Cl, SO_4^{2-} , and Ca) as a function of the liquid-solid ratio are compared in figure 99.

pH data obtained for P(XXX)02 were 0.5 pH unit greater than the ones obtained for C(XXX)02 and F(XXX)02 (see figure 98), consistently with a higher cement percentage used in the mix design. When LS ratio decreased from 10 to 0.5 ml/g of dry material, pH slightly increased from 12.6 to 12.8 for P(XXX)02, 12.3 to 12.5 for C(XXX)02, and 12.2 to 12.6 for F(XXX)02.

No significant difference could be observed between the three materials from conductivity data (see figure 98), except at the LS ratio of 10 ml/g of dry material for which a slightly greater conductivity was found for P(XXX)02 (approximately 6.7 mS/cm for P(XXX)02 and 5.5 mS/cm for C(XXX)02 and F(XXX)02).

Na concentrations obtained for C(XXX)02 were greater than the ones obtained for P(XXX)02 and F(XXX)02, while the total contents in Na as provided by the cement, the aggregates and the CFAs were quite similar (e.g., 3,770 mg/kg, 3,240 mg/kg, and 3,900 mg/kg, for CFA-C mix, CFA-F mix and PCC control, respectively). However, when considering only the Na content provided by the cement and the CFAs (approximately 500 mg/kg, 120 mg/kg and 70 mg/kg for CFA-C mix, CFA-F mix, and PCC control, respectively), this result was consistent, suggesting that the Na provided by the aggregates was less available. In addition, no



A) △ P(XXX)02 □ C(XXX)02 ◇ F(XXX)02

B) △ P(XXX)02 □ C(XXX)02 ◇ F(XXX)02

Figure 98: A) pH and B) conductivity as a function of LS ratio.

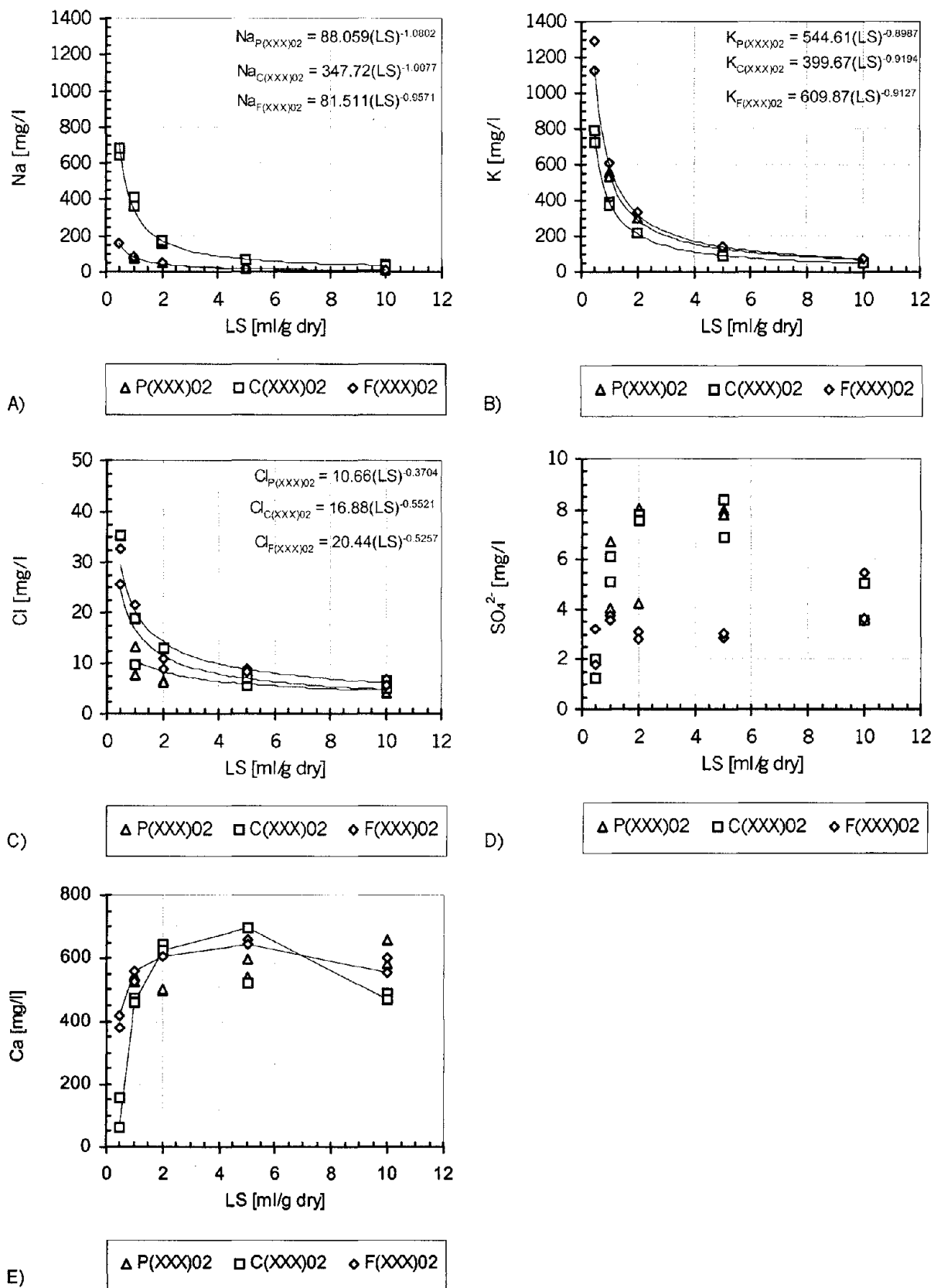


Figure 99: Major species concentration as a function of LS ratio:
 A) Na, B) K, C) Cl, D) SO_4^{2-} , E) Ca.

significant differences in Na concentrations could be observed between C(XXX)02 and F(XXX)02.

K concentrations obtained for P(XXX)02 and F(XXX)02 were slightly higher (e.g., two times) than that obtained for C(XXX)02, consistent with the K total content.

Similar Cl behavior as a function of the LS ratio could be observed for the three material types (see figure 99).

Low concentrations of SO_4^{2-} (e.g., less than 10 mg/l) were observed for the three material types (see figure 99). SO_4^{2-} concentrations obtained for F(XXX)02 were lower than that obtained for C(XXX)02 and P(XXX)02. When LS ratio decreased, a slight increase in SO_4^{2-} concentration was first observed, followed by a rapid decrease for LS ratio less than 2 ml/g of dry material.

Similar Ca leaching behavior as a function of the LS ratio could be obtained for the three material types (see figure 99).

Table 79 provides a comparison of the physical and chemical properties measured at LS of 5 ml/g dry for each material type and the estimated values for the pore water in each case. For C(XXX)02, an open porosity of 8.0 percent was estimated from the moisture content and density of the sample, assuming that the pores were completely filled with water (e.g., moisture of 3.0 percent and matrix density of 2.7 g wet/cm³). This resulted in an estimated pore water LS ratio of 0.03 ml/g dry. Empirical curve fits were then used to estimate pH and species concentrations to this LS ratio. Extrapolations resulted in estimated pH of 12.7 with concentrations of Na, K, Cl, SO_4^{2-} , and Ca of 11,900 mg/l, 10,050 mg/l, 120 mg/l, 0.8 mg/l, and less than 50 mg/l, respectively. Charge balances on the pore water of the matrix indicated that anionic species other than OH^- (as obtained from pH measurement), Cl^- , and SO_4^{2-} were likely present in the matrix pore water. These anionic species most likely were CO_3^{2-} due to the large quantities of limestone type aggregates (e.g., 78 percent) present in the sample. Therefore, the ionic strength of the pore water was estimated to be 1.2 mol/l, which corresponds to an activity coefficient of 0.73 for ions with a charge number of 1 and 0.29 for ions with a charge number of 2 (Hemond and Fechner, 1994).

For F(XXX)02, an open porosity of 8.2 percent was estimated from the moisture content and density of the sample, assuming that the pores were completely filled with water (e.g., moisture of 3.1 percent and matrix density of 2.7 g wet/cm³). This resulted in an estimated pore water LS ratio of 0.03 ml/g dry. Empirical curve fits were then used to estimate pH and species concentrations to this LS ratio. Extrapolations resulted in estimated pH of 12.9 with concentrations of Na, K, Cl, SO_4^{2-} , and Ca of 2,340 mg/l, 14,970 mg/l, 130 mg/l, less than 2 mg/l, and less than 300 mg/l, respectively. Charge balances on the pore water of the matrix indicated that anionic species other than OH^- (as obtained from pH measurement), Cl^- , and SO_4^{2-} were likely present in the matrix pore water. These anionic species most likely were CO_3^{2-} due to the large quantities of limestone type aggregates (e.g., 78 percent) present in the sample. Therefore, the ionic strength of the pore water

Table 79: Physical properties of the three 28-d cured material types (CFA-C, CFA-F and PCC) and chemical properties of leachates and pore water.

Physical or Chemical Property	Material type		
	C(XXX)02	F(XXX)02	P(XXX)02
Moisture content (%)	3	3.1	3
Density (g/cm ³)	2.7	2.7	2.6
Open porosity (%)	8	8.2	7.8
LS estimated for p.w. ^a (ml/g)	0.03	0.03	0.03
pH (standard units)			
at LS 5	12.3	12.3	12.7
Estimated for p.w.	12.7	12.9	13.0
Na (mg/l)			
at LS 5	63	19	17
Estimated for p.w.	11,900	2340	3890
K (mg/l)			
at LS 5	90	143	130
Estimated for p.w.	10,050	14,970	12,730
Cl (mg/l)			
at LS 5	6	9	6
Estimated for p.w.	120	130	40
SO ₄ ²⁻ (mg/l)			
at LS 5	8	3	8
Estimated for p.w.	0.8	<2	<2
Ca (mg/l)			
at LS 5	519	656	594
Estimated for p.w.	< 50	< 300	< 300
Ionic strength (mol/l)			
at LS 5	0.05	0.03	0.05
Estimated for p.w.	1.2	0.7	0.7
Activity coefficient			
charge ± 1			
at LS 5	0.85	0.87	0.85
Estimated for p.w.	0.73	0.71	0.71
charge ± 2			
at LS 5	0.53	0.58	0.53
Estimated for p.w.	0.29	0.26	0.26

^a p.w. – pore water

was estimated to be 0.7 mol/l, which corresponds to an activity coefficient of 0.71 for ions with a charge number of 1 and 0.26 for ions with a charge number of 2 (Hemond and Fechner, 1994). In contrast, the estimated ionic strength for an LS ratio of 5 (e.g., typical LS ratio for most equilibrium batch tests) was 0.03 mol/l, which corresponds to an activity coefficient of 0.87 for ions with a charge number of 1 and 0.58 for ions with a charge number of 2 (Linde, 1996).

For P(XXX)02, an open porosity of 7.8 percent was estimated from the moisture content and density of the sample, assuming that the pores were completely filled with water (e.g., moisture of 3.0 percent and matrix density of 2.6 g wet/cm³). This resulted in an estimated pore water LS ratio of 0.03 ml/g dry. Empirical curve fits were used to estimate pH and species concentrations to this LS ratio. Extrapolations resulted in estimated pH of 13 with concentrations of Na, K, Cl, SO₄²⁻, and Ca of 3,890 mg/l, 12,730 mg/l, 40 mg/l, less than 2 mg/l, and less than 300 mg/l, respectively. Charge balances on the pore water of the matrix indicated that anionic species other than OH⁻ (as obtained from pH measurement), Cl⁻, and SO₄²⁻ were likely present in the matrix pore water. These anionic species most likely were CO₃²⁻ due to the large quantities of limestone type aggregates (e.g., 78 percent) present in the sample. Therefore, the ionic strength of the pore water was estimated to be 0.7 mol/l, which corresponds to an activity coefficient of 0.71 for ions with a charge number of 1 and 0.26 for ions with a charge number of 2 (Hemond and Fechner, 1994). In contrast, the estimated ionic strength for an LS ratio of 5 (e.g., typical LS ratio for most equilibrium batch tests) was 0.05 mol/l, which corresponds to an activity coefficient of 0.85 for ions with a charge number of 1 and 0.53 for ions with a charge number of 2 (Linde, 1996).

5.5.9.2 Conclusions

In conclusion:

1. There were generally no significant differences between the three material types in terms of leaching behavior of primary matrix components as a function of LS ratio
2. Na release was much greater for C(XXX)02.
3. There was no significant difference with respect to the ionic strength at LS ratio of 5 ml/g dry (e.g., typical LS ratio for most equilibrium batch tests).
4. The pore water ionic strength of C(XXX)02 was much greater (e.g., 1.2 mol/l) than the pore water of F(XXX)02 and P(XXX)02 (e.g., 0.7 mol/l) due to a much greater Na release.
5. The estimated LS concentration and pH of the pore water in the slab concrete were 0.03 ml/dry gram and 12.7 to 13.0 respectively. (The slab concrete values were 0.03 and 13.7.)

5.5.10 Availability Leaching

5.5.10.1 Availability of C(XXX)02, F(XXX)02, and P(XXX)02

Cd, Cu, Ni, Pb and Zn availability for three 28-d cured material types prior to any aging (e.g., C(XXX)02, F(XXX)02, and P(XXX)02), as determined by the RU-AV002.0 protocol (e.g., EDTA extraction at pH 7.0), is presented in figure 100. In addition to availability results, total content and maximum release (e.g., maximum reached using the RU-SR002.0 protocol for pH less than 3) are provided for comparison.

Availability values of Cd, Cu, and Pb exceeded the total content for the three materials. This most likely was attributable to analytical errors associated with measurement of trace metals in extracts containing high concentration of total salts and analyses performed near the FAAS detection limit. For the three materials, availability values of Ni and Zn were found to be lower than the total contents (e.g., less than 10 percent of Ni and 35 percent of Zn were removed under RU-AV002.0 conditions). No significant difference between availability values and maximum of solubility was observed except for Cd and Pb.

5.5.10.2 Conclusions

In conclusion:

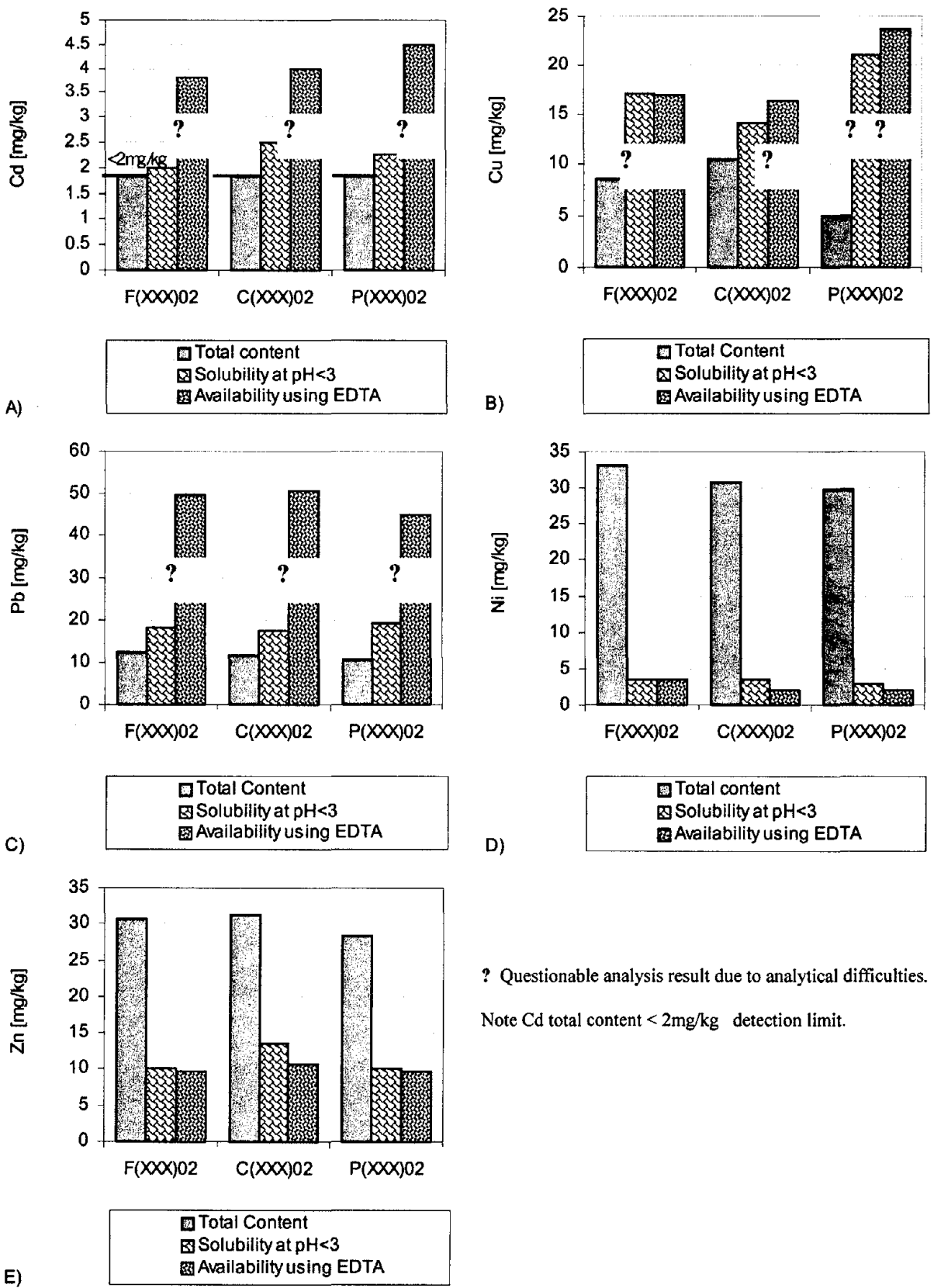
1. There was no difference between the three materials with respect to constituent availability.
2. For each of the three materials, only a fraction of Ni and Zn was available for leaching under the test conditions, while Cd, Pb, and Cu were completely available.
3. As with the slab concrete, availability values of Cd, Cu, and Pb by EDTA extraction at pH 7.0 exceeded the total content for the two locations as determined by NAA/XRF.
4. As with the slab concrete, availability of Ni and Zn by EDTA extraction at pH 7.0 were found to be lower than the total contents as determined by NAA/XRF

5.5.11. Monolithic Leaching on C(XXX)02, F(XXX)02, and P(XXX)02

Results presented here were obtained for the three 28-d cured material types prior to any aging (e.g., CFA-C mix, CFA-F mix, and PCC control after 28-ds of cure) for an overall cumulative leaching time of 20 mo with periodic renewals resulting in 18 extracts. Only one replicate of each material type was carried out.

5.5.11.1 pH and Conductivity

Final leachate pH obtained after each leaching interval for the three 28-d cured material types (e.g., C(XXX)02, F(XXX)02, and P(XXX)02) are compared in figures 101 a and b. Final



? Questionable analysis result due to analytical difficulties.
 Note Cd total content < 2mg/kg detection limit.

Figure 100: Comparison between constituent total content, solubility at pH<3, and availability using EDTA extraction at pH 7.

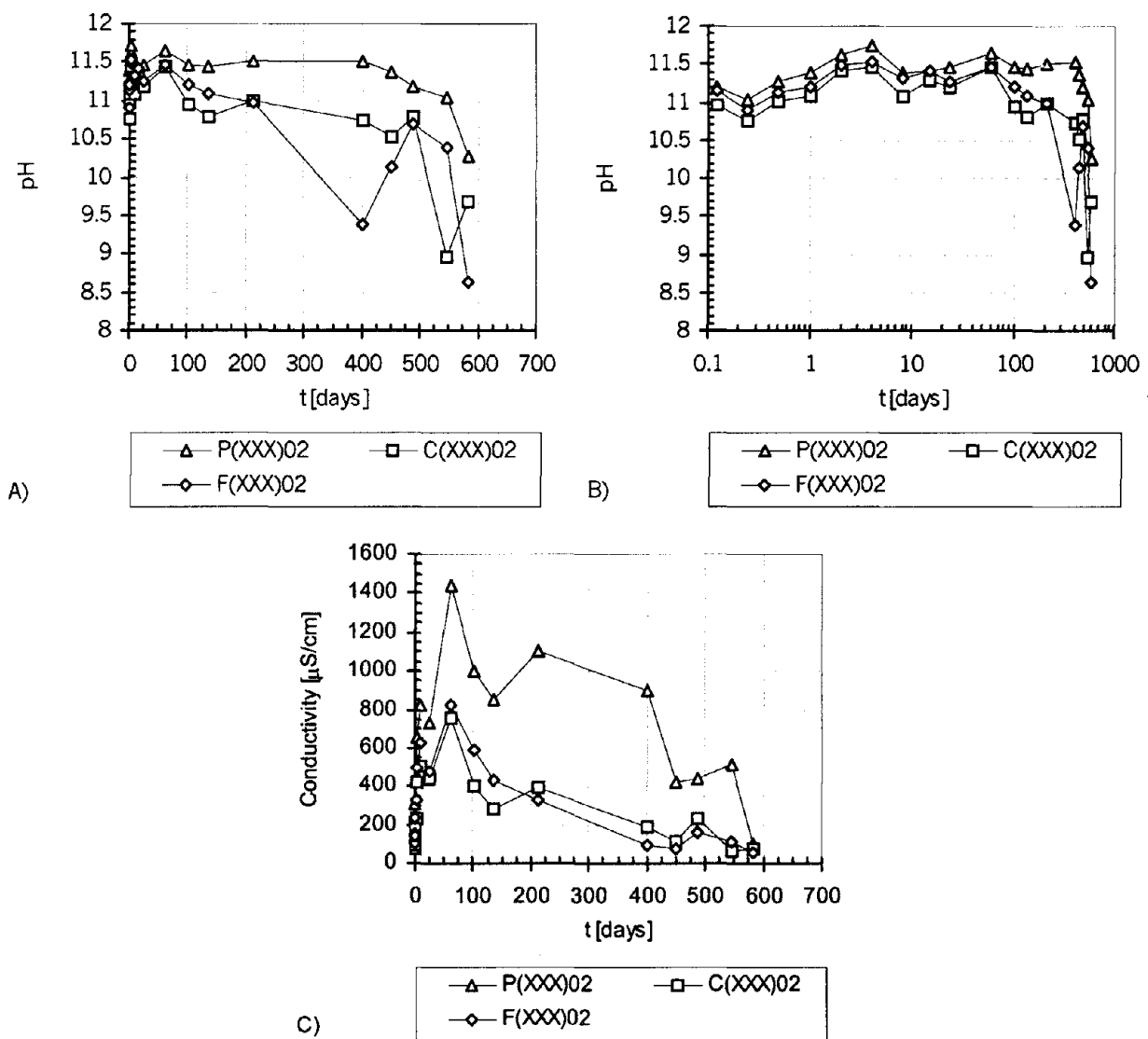


Figure 101: A) leachate pH, B) leachate pH, and C) leachate conductivity.

leachate pH was controlled by the release of hydroxides and the duration of the leaching period and ranged from 10.8 to 11.8 except for the last five extracts of C(XXX)02 and F(XXX)02 and the last extract of P(XXX)02. Indeed, the leachate pHs of these last renewals were observed to be abnormally low (e.g., pH ranging from 8.5 to 10.5) and showed scattering between the three samples. This suggests that reaction with atmospheric carbon dioxide infiltrating through leaching vessel seals might have occurred. Overall, final leachate pHs obtained for P(XXX)02 were higher by 0.3 pH unit than that obtained for both C(XXX)02 and F(XXX)02, consistent with the cement percentages used in the mix designs (e.g., 14.9 wt percent for the PCC control versus 12.7 wt percent for the CFA mix designs) and pH titration results. However, final leachate pHs obtained for F(XXX)02 were slightly higher (e.g., 0.1 pH unit) than that obtained for C(XXX)02, contrary to pH titration results (e.g., greater buffering capacity found for 28-d cured samples of CFA-C mix).

Final leachate conductivity obtained for the three 28-d cured material types is shown in figure 101. As with pH, final leachate conductivity obtained for P(XXX)02 was greater than that obtained for C(XXX)02 and F(XXX)02.

The pH behavior over time well matched that of the middle portion of the slab concrete (see section 5.3.11.1 and figure 65). The conductivity curves for the laboratory concrete bracketed the curves for the middle slab portion of the slab concrete.

5.5.11.2 Leaching Behavior of Major Species

Release and flux plots for major constituents are shown in figures 102 and L-19 through L-22 in appendix L of volume II.

Na Release. The cumulative release of Na (figure 102) observed over 20 mo of leaching was low for the three material types, compared with their respective total content. Thus, after 20 mo of leaching, only approximately 5 percent of the total content in Na was released from C(XXX)02 and only approximately 1 percent from F(XXX)02 and P(XXX)02. The release of Na from C(XXX)02 was significantly greater than the release of Na from F(XXX)02 and P(XXX)02 while the total content in Na⁹ (e.g., as provided by the cement, the aggregates, and the CFAs) and the porosity¹⁰ of the three materials were quite similar. Thus, the flux of Na from C(XXX)02 was about an order of magnitude greater than that of F(XXX)02 and P(XXX)02. Na was present in each mix component of the concrete products with more than 90 percent of the total content provided by the aggregates. The release rate of Na might vary by orders of magnitude depending on the matrix component. The release rate of Na from the aggregates was less than that from the other mix components. Therefore, assuming that the Na released during the 20 mo of leaching was only the Na from the cement and the CFAs, approximately 34 percent of Na was released from

9 Approximately 3,770 mg/kg, 3,240 mg/kg and 3,900 mg/kg, respectively as determined by NAA.

10 Approximately 8 percent for the three material types as estimated from moisture content and material density.

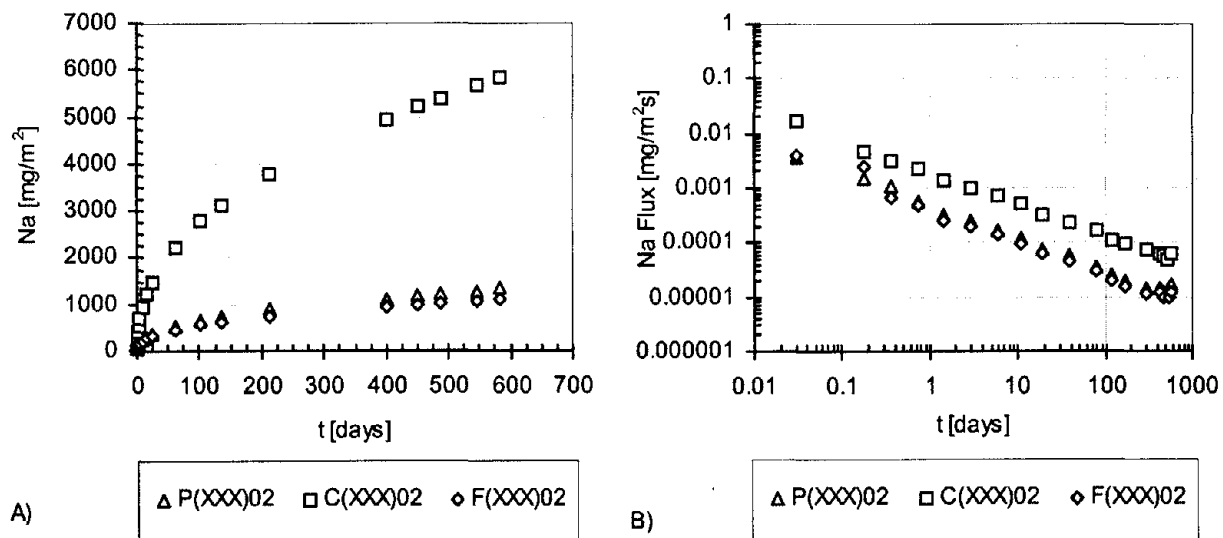


Figure 102: Na release from the three 28-d cured material types:
 A) cumulative mass released in mg/m²; B) flux released in mg/m²s.

C(XXX)02, approximately 27 percent from F(XXX)02 and approximately 57 percent from P(XXX)02. When considering that the Na released from the two CFA materials was only the Na provided by the CFAs (e.g., total of approximately 450 mg/kg and approximately 65 mg/kg for CFA-C mix and CFA-F mix, respectively), approximately 38 percent of Na was released from C(XXX)02 and approximately 50 percent from F(XXX)02.

K Release. Low release of K was observed for the three material types. Thus, after 20 mo of leaching, only 6.8 percent, 8.3 percent and 8.9 percent of the total content in K was released from C(XXX)02, F(XXX)02, and P(XXX)02, respectively. The cumulative release of K from P(XXX)02 was greater than from F(XXX)02 and greater than from C(XXX)02 (figure L-19). However, small differences in the release flux could be observed between the three materials. As with Na, K was present in each of the mix component of the concrete products with more than 80 percent of the total content in K provided by the aggregates. Thus, assuming that the K released during the 20 mo of leaching was only the K from the cement and the CFAs (e.g., total of 820 mg/kg, 1220 mg/kg and 850 mg/kg for CFA-C mix, CFA-F mix, and PCC control, respectively), approximately 26 percent of Na was released from C(XXX)02, approximately 23 percent from F(XXX)02, and approximately 43 percent from P(XXX)02. When considering that the K released from CFA-C mix was only the K provided by CFA-C (e.g., total of 90 mg/kg), the percentage released exceeded 100 percent. The K release was consistently less than that of the middle portion of the slab concrete.

Cl Release. Although Cl was found to be below the detection limits (e.g., 50 mg/kg) in each component of the concrete products (see figure L-20), Cl concentrations could be measured in the leachates at mg/l level. No influence of the material type (e.g., CFA-C mix, CFA-F mix, and PCC control), could be observed on the release of Cl. The Cl flux matched well the middle portion of the slab concrete.

SO₄²⁻ Release. After 60 d of leaching, the cumulative release of SO₄²⁻ appeared to be greater for F(XXX)02 than C(XXX)02, which was greater than P(XXX)02 (see figure L-21). After 17 mo of leaching, less than 0.8 percent of the total content S was released under SO₄²⁻ form for each material type. This constituent was present in each component of the concrete products with more than 75 percent of the total content provided by the cement. The same intensity of the flux was observed for the three material types. The CFA-C concrete best modeled the middle portion of the slab concrete.

Ca Release. The flux of Ca (figure L-22) was slightly greater for P(XXX)02 consistent with a greater total content in Ca for this material due to a higher cement percentage used in the mix design (e.g., 14.9 wt percent for the PCC control versus 12.7 wt percent for the CFA mix designs). The flux of Ca was slightly greater for F(XXX)02 than C(XXX)02, contrary to the total contents. However, these results were consistent with final leachate pHs. Ca was present in each component of the concrete products with more than 75 percent of the total content provided by the aggregates. After 13 mo of leaching the flux of Ca increased significantly. This behavior followed a long leaching period duration (e.g., 6 mo without renewals of the leaching solution). During a such long duration, several phenomena could have occurred such as accumulation of Ca in the finite bath reducing the driving force for leaching (e.g., saturation of the leaching solution) or carbonation phenomenon. From the leachate pH obtained at the end of the 14th leaching

period, it seems that the solution might have been carbonated, which would explain the low concentration of Ca found in the leachate and subsequent increase in the Ca released flux when more frequent renewals were used. The laboratory concrete curves for Ca release bracketed those of the middle portion of the slab concrete.

In conclusion:

1. Good correspondence was obtained between laboratory and slab concretes.
2. Na and SO_4^{2-} releases were best modeled by the CFA-C concrete.
3. The K release of the laboratory concretes was below that of the slab.

5.5.11.3 Leaching Behavior of Trace Metals

Flux and cumulative release as a function of time for Cu and Pb are presented in figures L-23 and figure L-24 in appendix L of volume II. Cu and Pb concentrations measured in the leachates are also shown and compared with graphite furnace detection limits. Only the initial seven extracts resulting in a cumulative leaching time of 8 d were analyzed. All the concentrations measured in the leachates were close to GFAAS detection limits. Therefore, no interpretation of the results was done due to large uncertainties in the analyses.

Average concentrations of major species and trace metals measured in the leachates are given in table 80. In all cases, the concentrations measured were close to or below average "natural" ground water concentration (e.g., data from van der Sloot et al., 1985). Although these ground water results are not from the vicinity of the test slab, they do indicate that the extract concentrations are of the same order of magnitude as unimpacted ground waters.

5.5.11.4 Conclusions

In conclusion:

1. Leachate pH and conductivity for the PCC were greater than that obtained for the CFA-C and CFA-F mixes.
2. Na fluxes were higher from the PCC mixes than from the CFA-C and CFA-F mixes.
3. K fluxes were similar between the three mixes.
4. Ca fluxes were higher in the PCC mixes than in the CFA-C and CFA-F mixes.
5. No observable trends were seen for Cu or Pb fluxes.

Table 80: Major species and trace metal concentrations in contact solutions of C(XXX)02, F(XXX)02 and P(XXX)02 – comparison with ground water.

	C(XXX)02	F(XXX)02	P(XXX)02	Ground water ^c
Ca [mg/l] ^a	9-70	9-80	15-140	20-120
Na [mg/l] ^a	0.5-12	0.2-2	0.2-0.5	20-70
K [mg/l] ^a	0.9-7	1-13	1.4-21	2-15
SO ₄ ²⁻ [mg/l] ^a	0.3-4	0.4-5	0.3-4	26-100
Cl [mg/l] ^a	0.1-1.2	0.1-1.2	0.6-1.2	30-100
pH ^a	9-11.5	9-11.6	10-11.7	3.2-7.7
Pb [µg/l] ^b	0.2-0.5	0.3-0.7	0.3-0.5	5-10
Cu [µg/l] ^b	<0.07-4	<0.07-12	<0.07-2	5-10

^a 20 mo (e.g., 21 extracts)

^b 8 d, 7 extracts

^c van der Sloot et al., 1985

5.5.12. Monolithic Leaching on F(XXX)02, F(LLL)13, F(LLL)30, and F(LLL)47

The effect of the low level of aging (e.g., low AA, CL, and FT) on CFA-F mix integrity was examined via pH, conductivity and the leaching behavior of primary matrix components (e.g., Na, K, SO_4^{2-} , Cl, and Ca). Three low level aged samples representing the center point replicates were examined. One of the three replicates (e.g., F(LLL)13) was leached for 10 mo with periodic renewals resulting in 16 extracts and the two other replicates (e.g., F(LLL)30 and F(LLL)47) were leached for 4 mo with periodic renewals resulting in 12 extracts. The 28-d cured sample was leached for 20 mo with periodic renewals resulting in 18 extracts. In all four materials were examined and only one replicate of each material was carried out.

5.5.12.1 pH and Conductivity

Final leachate pH and conductivity obtained after each leaching interval for 28-d cured CFA-F mix (e.g., F(XXX)02) and low level aged CFA-F mix (e.g., F(LLL)13, F(LLL)30, and F(LLL)47) are compared in figure 103. Leachate pH of the 28-d cured sample (e.g., F(XXX)02) was slightly greater (e.g., 0.3 pH unit) than that of the three center point replicates. Overall a good reproducibility was obtained between the three center point replicates although after 20 d of leaching a slightly lower pH was obtained for F(LLL)13.

Leachate conductivity of F(LLL)13 was slightly less, except for the last two extracts, than that of the 28-d cured sample and the two other center point replicates.(LLL)13.

5.5.12.2 Leaching Behavior of Major Species

Release and flux plots for major constituents are shown in figures 104 and L-25 through L-28 in appendix L of volume II.

Na Release. No significant difference in Na cumulative release could be observed during the initial 65 d of leaching (figure 104). Differences were observed after 65 d of leaching with a greater cumulative release of Na obtained for the three center point replicates. In addition, Na cumulative release from F(LLL)13 was slightly less than that from F(LLL)30 and F(LLL)47. Thus after 100 d of leaching, approximately 28 mg/kg (e.g., approximately 0.9 percent of Na total content) was released from F(LLL)13, approximately 40 mg/kg (e.g., approximately 1.2 percent of Na total content) from F(LLL)30 and F(LLL)47, and approximately 17 mg/kg (e.g., approximately 0.5 percent of Na total content) for F(XXX)02. In addition, no significant difference in Na flux could be observed between the four materials.

K Release. No significant difference in K release could be observed between the four materials (see figure L-25).

Cl Release. Cl analyses were carried out only on the leachates of F(XXX)02 and F(LLL)13 (see figure L-26). All of the concentrations measured in the leachates were close to

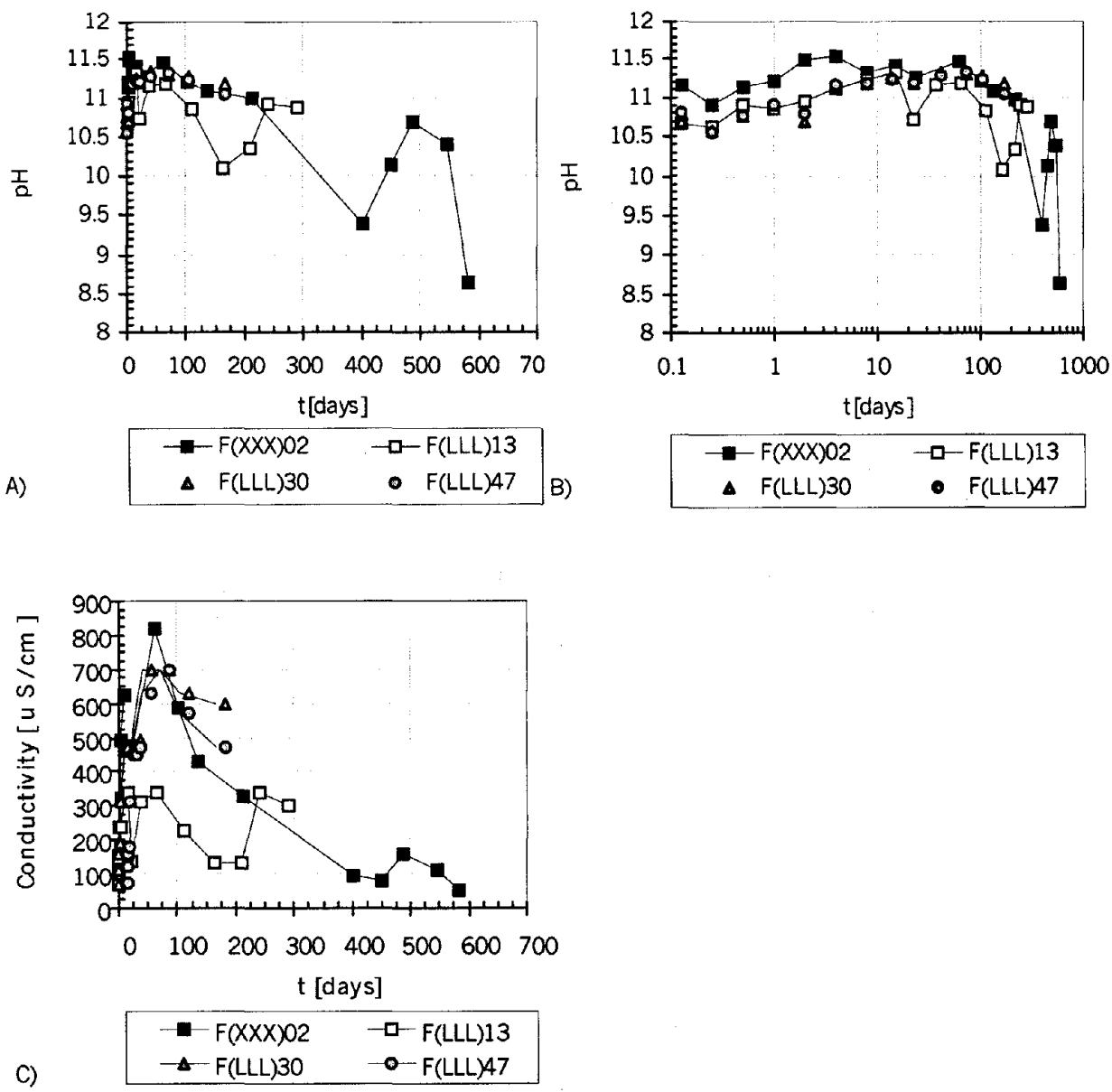


Figure 103: A) leachate pH, B) leachate pH and C) leachate conductivity obtained after each leaching interval for CFA-F mix.

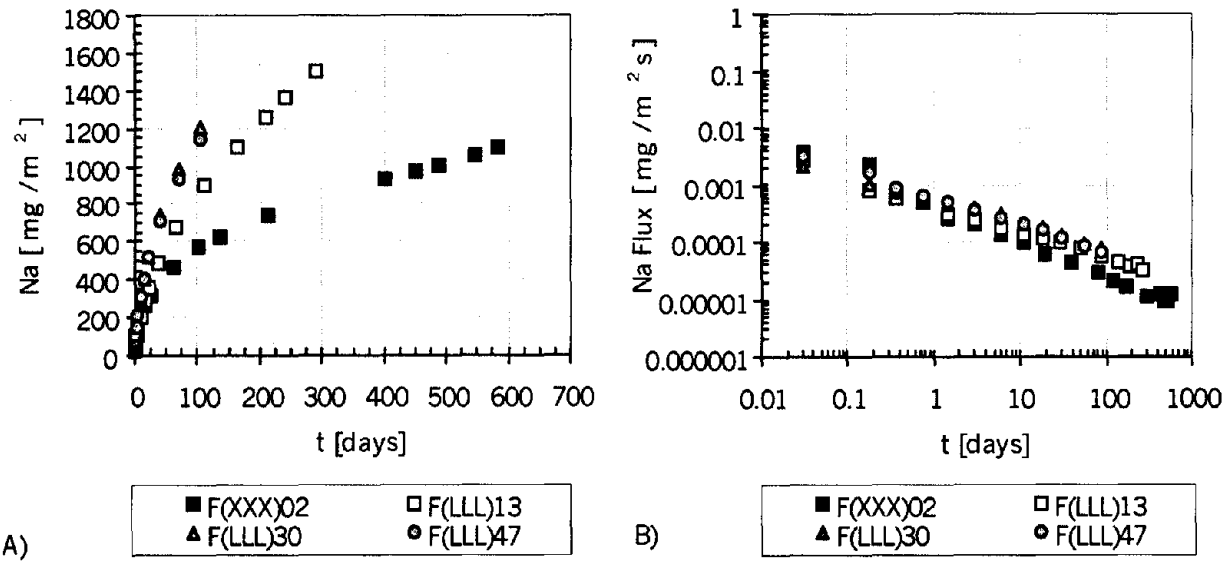


Figure 104: Na release for CFA-F mix:
 A) cumulative mass released in mg/m²; B) flux released in mg/m²s.

or below the detection limit (e.g., 1 mg/l). In addition, signals obtained during analyses were noisy. Therefore, no interpretation of the results could be done due to large uncertainties in the analyses.

SO₄²⁻ Release. SO₄²⁻ analyses were carried out only on the leachates of F(XXX)02 and F(LL)13. A greater SO₄²⁻ cumulative release (figure L-27) was observed for the low level aged material (e.g., F(LL)13). Thus after 100 d of leaching, 62 mg/kg were released for F(XXX)02 and 96 mg/kg for F(LL)13. During the initial 10 d of leaching the released flux of SO₄²⁻ from F(LL)13 was greater than that from F(XXX)02. However, after 10 d of leaching, no differences in the release flux of SO₄²⁻ could be observed between the two materials, suggesting that the initial difference could be due to surface wash-off.

Ca Release. While no significant difference in Ca cumulative release could be observed between F(XXX)02, F(LL)30, and F(LL)47, a much less Ca cumulative release was observed after 20 d of leaching for F(LL)13, consistent with leachate pH. However, no significant difference in Ca release flux could be observed between the four materials (see figure L-28).

5.5.12.3 Conclusions

In conclusion:

1. Leachate pH and conductivity were similar between CFA-F replicates.
2. Na fluxes were similar between the CFA-F replicates.
3. K fluxes were similar between the CFA-F replicates..
4. Ca fluxes were similar between the CFA-F replicates.

5.5.13. Monolithic Leaching of P(XXX)02, P(LL)13, P(LL)23, and P(LL)39

The effect of the low level of aging (low AA, CL, and FT) on PCC control matrix integrity was examined via pH, conductivity, and the leaching behavior of primary matrix components (e.g., Na, K, SO₄²⁻, Cl). Three low level aged samples representing the center point replicates were examined. One of the three replicates (e.g., P(LL)13) was leached for 10 mo with periodic renewals resulting in 16 extracts and the two other replicates (e.g., P(LL)23 and P(LL)39) were leached for 4 mo with periodic renewals resulting in 12 extracts. The 28-d cured sample was leached for 20 mo with periodic renewals resulting in 18 extracts. In all four materials were examined and only one replicate of each material was carried out.

5.5.13.1 pH and Conductivity

Final leachate pH and conductivity obtained after each leaching interval for 28-d cured PCC control (e.g., P(XXX)02) and the low level aged PCC control (e.g., P(LL)13, P(LL)23, and P(LL)39) are compared in figure 105.

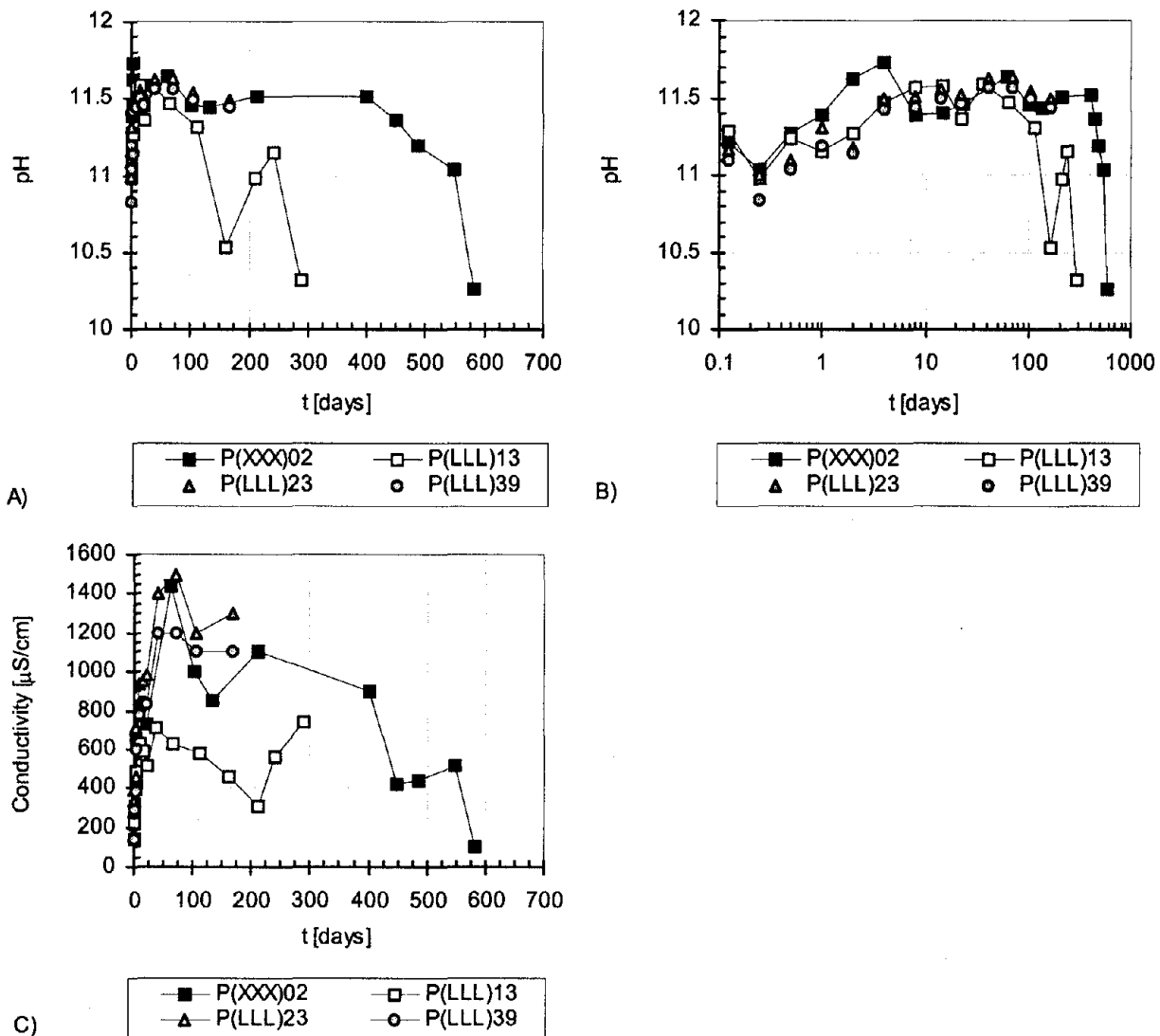


Figure 105: A) Leachate pH, and B) leachate conductivity obtained after each leaching interval for PCC control.

During the initial 100 d of leaching (11 extracts for P(XXX)02 and 12 extracts for P(LL)13, P(LL)23) and P(LL)39), no significant difference in leachate pH could be observed between the 28-d cured sample and the three center point replicates. Overall, a good reproducibility between the three center point replicates was obtained. A difference of approximately 0.5 to 1 pH unit between P(XXX)02 and P(LL)13 appeared after 100 d of leaching with a lower pH obtained for P(LL)13.

Leachate conductivity of P(LL)13 was slightly less than that of the 28-d cured sample and the two other center point replicates (P(LL)23 and P(LL)39).

5.5.13.2 Leaching Behavior of Major Species

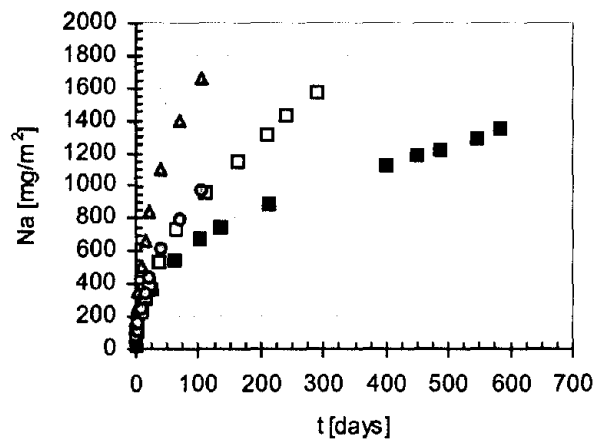
Release and flux plots for major constituents are shown in figures 106 and L-29 through L-32 in appendix L of volume II.

Na Release. A greater Na cumulative release was observed for the three center point replicates compared with the 28-d cured sample (figure 106). Thus after 100 d of leaching, approximately 53 mg/kg (e.g., approximately 1.4 percent of Na total content) was released for P(LL)23, approximately 28 mg/kg (e.g., approximately 0.8 percent of Na total content) for P(LL)13, approximately 31 mg/kg (e.g., approximately 0.8 percent of Na total content) for P(LL)39, and approximately 20 mg/kg (e.g., approximately 0.5 percent of Na total content) for P(XXX)02. In addition, Na released flux from P(LL)23 was slightly greater than that from P(XXX)02, P(LL)13, and P(LL)39.

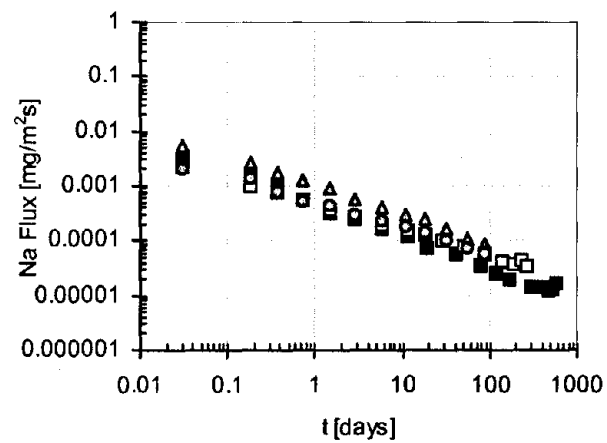
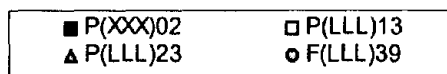
K Release. K cumulative release from P(XXX)02 and P(LL)23 was greater than that from P(LL)13 and P(LL)39 (figure L-29). Thus after 100 d of leaching, approximately 205 mg/kg (e.g., approximately 5 percent of K total content) was released for P(XXX)02 and P(LL)23 and approximately 120 mg/kg (e.g., approximately 2.9 percent of K total content) for P(LL)13 and P(LL)39. During the initial 10 d of leaching, the released flux of K from P(LL)13 and P(LL)23 was slightly lower than from P(XXX)02 and P(LL)39. However, after 10 d of leaching (e.g., at longer leaching intervals), no significant difference in the K released flux could be observed between the four materials.

Cl Release. Cl analyses were carried out only on the leachates of P(XXX)02 and P(LL)13 (figure L-30). All the concentration measured in the leachates was close to or below the Dionex ion chromatograph detection limit (e.g., 1 mg/l). In addition, signals obtained during analyses were pretty noisy. Therefore, no interpretation of the results could be done due to large uncertainties in the analyses.

SO₄²⁻ Release. SO₄²⁻ analyses were carried out only on the leachates of P(XXX)02 and P(LL)13. SO₄²⁻ cumulative release from P(XXX)02 was less than that from P(LL)13 (see figure L-31). Thus after 100 d of leaching, 43 mg/kg was released for P(XXX)02 and 90 mg/kg for P(LL)13. During the initial 10 d of leaching the released flux of SO₄²⁻ from P(LL)13 was greater than that from P(XXX)02. However, after 10 d of leaching, no differences in the



A)



B)



Figure 106: Na release for PCC control:
 A) cumulative mass released in mg/m^2 ; B) flux released in $\text{mg}/\text{m}^2\text{s}$.

released flux of SO_4^{2-} could be observed between the two materials, suggesting that the initial difference could be due to surface wash-off.

Ca Release. During the initial 20 d of leaching, no significant difference in Ca cumulative release could be observed between the four materials (figure L-32). After 20 d of leaching, the cumulative release of Ca from P(LLL)23 and P(LLL)39 was greater than that of P(XXX)02 and P(LLL)13. No significant difference in Ca released flux could be observed between the four materials.

5.5.13.3 Conclusions

In conclusion:

1. Leachate pH and conductivity were similar between PCC replicates.
2. Na fluxes were similar between the PCC replicates.
3. K fluxes were different between the PCC replicates..
4. Ca fluxes were similar between the PCC replicates.

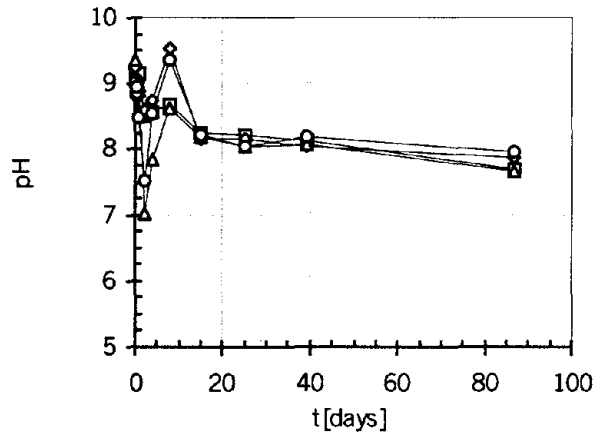
5.5.14. Monolithic Leaching of Coarse Aggregates

Examination of the total constituent content of the three concrete products (e.g., CFA-C mix, CFA-F mix, and PCC control) and relative contribution of constituents of concern from mix components to overall product composition indicated that the aggregates constituted the greatest source of the trace metals and major species of concern (see section 5.1). Therefore, the specific objectives of the evaluation here were to (i) measure the average flux that might be released by the aggregates for each major species of interest, (ii) compare the released flux obtained from the aggregates with that from the three material types and (iii) estimate intra-aggregate diffusivity for each constituent of interest.

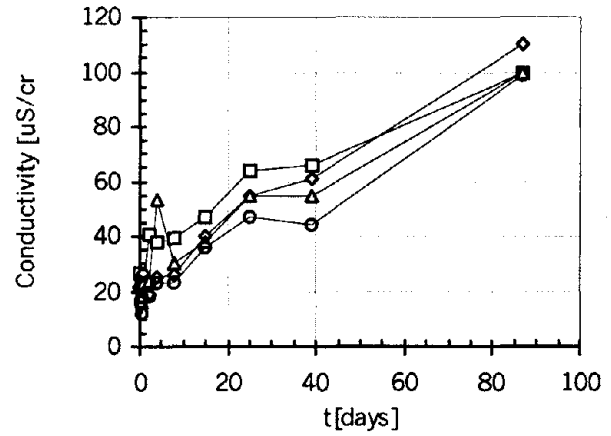
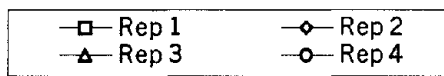
For this purpose, mass transfer leaching tests were carried out only on the coarse aggregates. Four replicates were used in order to ensure representativeness. For each replicate, two coarse aggregates with an average surface area of 60 cm^2 each were used. Results presented here were obtained for an overall cumulative leaching time of 86 d with periodic renewals resulting in 11 extracts.

5.5.14.1 pH and Conductivity

Final leachate pH and conductivity obtained after each leaching interval are shown in figure 107. Overall a good reproducibility of leachate pH and conductivity was observed between the four replicates. Final leachate pH ranged from 7 to 9.5, consistent with the low buffering capacity of the aggregates. Leachate conductivity consistently increased with increasing duration of the leaching period. Comparing this behavior with that of the slab and laboratory concretes,



A)



B)

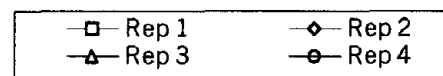


Figure 107: A) leachate pH, and B) leachate conductivity obtained after each leaching interval for the coarse aggregates.

as expected, coarse aggregates do not apparently control the pH and conductivity behavior of the concrete.

5.5.14.2 Leaching Behavior of Major Species

Release and flux plots for major constituents are shown in figures 108 and 109 as well as L-33 through L-35 in appendix L of volume II.

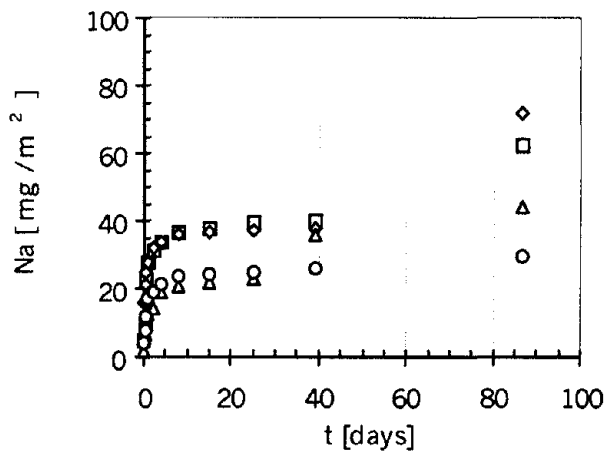
Na Release. The cumulative release of Na (see figure 108) from the four replicates was relatively low and showed some scatter between the replicates. After 86 d of leaching with periodic renewals, less than 3 percent of the total content of Na was released, indicating significant retention of Na in the coarse aggregates.

Reduced flux of Na was observed for the coarse aggregates compared with that observed for the three concrete products (see figure 109). The flux of Na from the coarse aggregates was as much as three orders of magnitude less than that from the CFA-C mix and as much as two orders of magnitude less than that from the CFA-F mix and PCC control. The cumulative release of Na from the aggregates obtained after 86 d of leaching represented less than 3 percent of the cumulative release obtained for the same leaching time from the CFA-C mix and less than 10 percent of the cumulative release obtained from CFA-F mix and PCC control. This result indicated that the release of Na from the coarse aggregates in the overall concrete products was negligible compared with the release of Na from the binder (e.g., cement and CFAs).

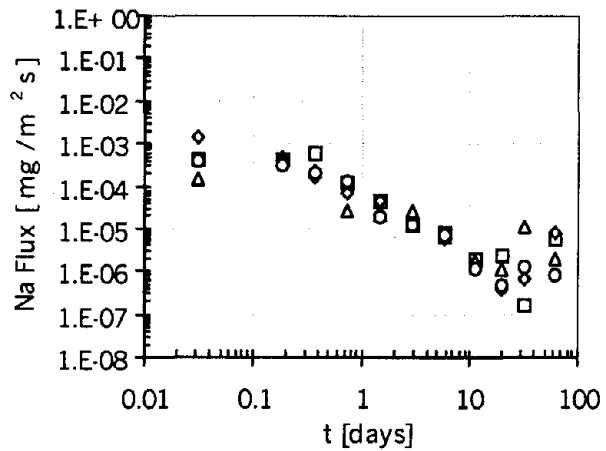
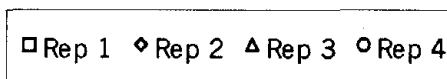
K Release. As with Na, the cumulative release of K (figure L-33) from the four replicates was relatively low and showed scattering between the replicates. After 86 d of leaching with periodic renewals, less than 3 percent of the total content in K was released, indicating significant retention of K in the coarse aggregates. Reduced flux of K (e.g., one to two orders of magnitude less) was observed for the coarse aggregates compared with that observed for the three concrete products (see figure 109). The cumulative release of K from the aggregates obtained after 86 d of leaching represented less than 3 percent of the cumulative release obtained for the same leaching time from the concrete products. This result indicated that the release of K from the coarse aggregates in the overall concrete products was negligible compared with the release of K from the binder (e.g., cement and CFAs).

Cl Release. For all replicates, all the Cl concentrations measured in the leachates were below the Dionex ion chromatograph detection limit (e.g., 1 mg/l).

SO₄²⁻ Release. The cumulative release of SO₄²⁻ (figure L-34) from the four replicates was relatively low and showed scattering between the replicates. SO₄²⁻ concentrations in all of the extracts were less than 3 mg/l. A similar intensity of the release flux of SO₄²⁻ was observed for the coarse aggregates and the three concrete products (figure 109). This result indicated that the release of SO₄²⁻ from the coarse aggregates in the overall concrete products was significant and therefore not negligible compared with the release of SO₄²⁻ from the binder (e.g., cement and CFAs).



A)



B)

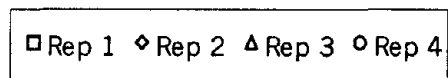


Figure 108: Na release from the coarse aggregates:
 A) cumulative mass released in mg/m^2 ; B) flux released in $\text{mg}/\text{m}^2\text{s}$.

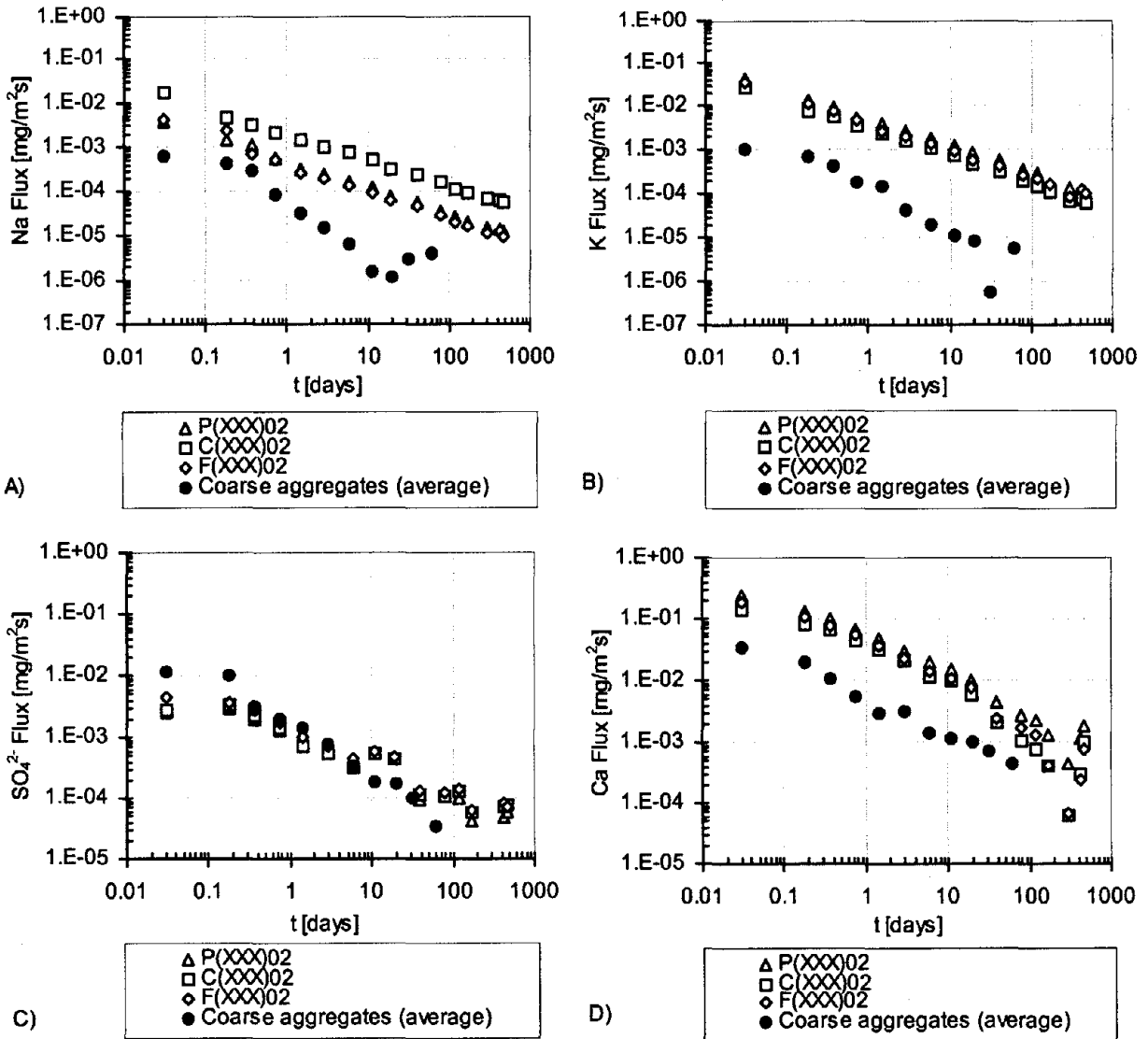


Figure 109: Comparison between the three 28-d cured material types and the coarse aggregates: A) Na flux; B) K flux; C) SO₄²⁻ flux; D) Ca flux.

Ca Release. Overall a good reproducibility of the release of Ca was observed between the four replicates (figure L-35). The flux of Ca from the coarse aggregates was five times less than from the three concrete products (figure 109). This result indicated that the release of Ca from the coarse aggregates in the overall concrete products was relatively negligible compared with the release of Ca from the binder (e.g., cement and CFAs).

5.5.14.3 Conclusions

In conclusion:

1. Leachate pH and conductivity were similar between PCC replicates.
2. Reduced fluxes of Na were observed for the coarse aggregates compared with that observed for the three concrete mixes.
3. Reduced fluxes of K were observed for the coarse aggregates compared with that observed for the three concrete products.
4. Fluxes of SO_4^{2-} for the coarse aggregates compared with those observed for the three concrete products.
5. Reduced fluxes of Ca were observed for the coarse aggregates compared with those observed for the three concrete products

5.5.15. Release Modeling

5.5.15.1 Release Modeling for C(XXX)02, F(XXX)02 and P(XXX)02

The one-dimensional diffusion model was used to interpret the release of Na, K, Cl, and Ca from the three 28-d cured material types (e.g., C(XXX)02, F(XXX)02, and P(XXX)02). During the time scale of the laboratory testing (e.g., 20 mo), no depletion of these species within the matrices was observed. For each species of concern, three different observed diffusivities (e.g., $D_{\text{obs } 1}$, $D_{\text{obs } 2}$ and $D_{\text{obs } 3}$) were determined. $D_{\text{obs } 1}$ was calculated assuming that the initial leachable concentration C_D was the total content of the species of concern. $D_{\text{obs } 2}$ was calculated assuming that the initial leachable concentration C_D was the species content provided only by the cement and the CFA. $D_{\text{obs } 3}$ was calculated assuming that (i) the initial leachable concentration C_D was the species content provided only by the cement and the CFA, (ii) the aggregates were inert and uniformly distributed within the matrix, and (iii) the flux was only provided by the fraction of the surface¹¹ of the sample not occupied by the aggregates. Thus, while $D_{\text{obs } 1}$ and $D_{\text{obs } 2}$ correspond to observed diffusivities through the overall matrix (e.g., binder and aggregates), $D_{\text{obs } 3}$

11 As a first approach, it was assumed that 57.5 percent of the surface of the material was non-occupied by the aggregates (42.5 percent of coarse aggregates were used in the mix design).

₃ corresponds to an observed diffusivity only through the binder (e.g., cement and CFA). Initial leachable concentrations and observed diffusivities of the three 28-d cured material types (e.g., C(XXX)02, F(XXX)02, and P(XXX)02) are compared in tables 81 through 84 for Na, K, Cl, and Ca, respectively. Ratios of observed diffusivity and molecular diffusivity are also compared with estimates of matrix tortuosity calculated using the Millington-Quirk relationship (Millington et al., 1971) (e.g., τ_{MQ} of $\epsilon^{-4/3}$, where τ and ϵ are tortuosity and matrix porosity, respectively).

Na Modeling. Low Na observed diffusivities were calculated (see table 81) using the Na total content, leading to ratios of observed diffusivity to molecular diffusivity for Na as much as five orders of magnitude greater than the estimated tortuosity using the Millington-Quirk relationship (e.g., τ_{MQ} of 30). This comparison indicated that significant retention of Na occurred within the concrete materials and the implied assumption of a homogeneous matrix was not appropriate. Na observed diffusivity of C(XXX)02 (e.g., $6.5 \cdot 10^{-15} \text{ m}^2/\text{s}$) was one order of magnitude greater than that of F(XXX)02 and P(XXX)02 (e.g., $3.0 \cdot 10^{-16} \text{ m}^2/\text{s}$ and $4.0 \cdot 10^{-16} \text{ m}^2/\text{s}$, respectively). When considering only the Na content provided by the cement and the CFA, the diffusivity results (e.g., $D_{obs,2}$ and $D_{obs,3}$) changed by two orders of magnitude for C(XXX)02, three orders of magnitude for F(XXX)02 and four orders of magnitude for P(XXX)02. Na observed diffusivity of P(XXX)02 (e.g., $1.3 \cdot 10^{-12} \text{ m}^2/\text{s}$) was then greater than that of C(XXX)02 and F(XXX)02 ($3.6 \cdot 10^{-13} \text{ m}^2/\text{s}$ and $2.0 \cdot 10^{-13} \text{ m}^2/\text{s}$, respectively). Diffusivity results slightly increased ($D_{obs,3}$ were three times greater than $D_{obs,2}$) when calculations were done by accounting only for the surface of the matrix not occupied by the aggregates. However, much greater ratios of observed diffusivity to molecular diffusivity for Na than the estimated tortuosity using the Millington-Quirk relationship were obtained.

K Modeling. K observed diffusivities of the same order of magnitude were calculated for the three 28-d cured material types (see table 82). Low K observed diffusivities (e.g., on the order of $10^{-14} \text{ m}^2/\text{s}$) were calculated from the K total content, leading to ratios of observed diffusivity to molecular diffusivity for K as much as three orders of magnitude greater than the estimated tortuosity using the Millington-Quirk relationship (e.g., τ_{MQ} of 30). This comparison indicated that significant retention of K occurred within the concrete materials. K observed diffusivity of C(XXX)02 (e.g., $2.2 \cdot 10^{-14} \text{ m}^2/\text{s}$) was 2 times less than that of F(XXX)02 and P(XXX)02. Similar K observed diffusivities were calculated for F(XXX)02 and P(XXX)02 (e.g., $3.5 \cdot 10^{-14} \text{ m}^2/\text{s}$ and $3.7 \cdot 10^{-14} \text{ m}^2/\text{s}$, respectively). When considering only the K content provided by the cement and the CFA-C, the diffusivity results (e.g., $D_{obs,2}$ and $D_{obs,3}$) changed by an order of magnitude. K observed diffusivity of P(XXX)02 (e.g., $8.7 \cdot 10^{-13} \text{ m}^2/\text{s}$) was then greater than that of C(XXX)02 (e.g., $3.3 \cdot 10^{-13} \text{ m}^2/\text{s}$) that was slightly greater than that of F(XXX)02 (e.g., $2.6 \cdot 10^{-13} \text{ m}^2/\text{s}$). Diffusivity results slightly increased ($D_{obs,3}$ were three times greater than $D_{obs,2}$) when calculations were done by accounting only for the surface of the matrix not occupied by the aggregates. However, much greater ratios of observed diffusivity to molecular diffusivity for K than the estimated tortuosity using the Millington-Quirk relationship were obtained.

Cl Modeling. Cl observed diffusivities of the same order of magnitude (e.g., $10^{-11} \text{ m}^2/\text{s}$) were calculated for the three 28-d cured material types (see table 83). Cl observed diffusivity of

Table 81: Parameter estimates for the release of Na from the one-dimensional diffusion model – comparison between the three 28-d cured material types (CFA-C, CFA-F and PCC).

	Material type		
	C(XXX)02	F(XXX)02	P(XXX)02
C_0^a [(mg elemental species from <u>cement, aggregates and CFA-C</u>) / (kg of concrete product)]	3770	3250	3900
$D_{obs 1}^b$ [m ² /s]	$6.5 \cdot 10^{-15}$	$0.3 \cdot 10^{-15}$	$0.4 \cdot 10^{-15}$
$\frac{D_{m,Na}^c}{D_{obs 1}}$	$0.2 \cdot 10^6$	$5.0 \cdot 10^6$	$3.3 \cdot 10^6$
C_0^d [(mg elemental species from <u>cement and CFA-C</u>) / (kg of concrete product)]	500	120	70
$D_{obs 2}^e$ [m ² /s]	$3.6 \cdot 10^{-13}$	$2.0 \cdot 10^{-13}$	$13.0 \cdot 10^{-13}$
$\frac{D_{m,Na}}{D_{obs 2}}$	3670	6600	1015
$D_{obs 3}^f$ [m ² /s]	$1.1 \cdot 10^{-12}$	$0.6 \cdot 10^{-12}$	$4.0 \cdot 10^{-12}$
$\frac{D_{m,Na}}{D_{obs 3}}$	1200	2200	330
$\tau_{MO} = \epsilon^{-4/3} g$	30	30	30

^a Total content in Na

^b Calculated assuming that the initial leachable concentration C_0 was the total content

^c $D_{m,Na} = 1.32 \cdot 10^{-9}$ m²/s (Linde, 1996)

^d Based on mix design and total content of individual mix components (e.g., cement and CFAs)

^e Calculated assuming that the initial leachable concentration C_0 was the species content provided only by the cement and the CFA

^f Calculated assuming that the initial leachable concentration C_0 was the species content provided only by the cement and the CFA and the flux was only provided by the fraction of the surface of the sample non-occupied by the aggregates

^g Millington-Quirk relationship (Millington et al., 1971). The porosity was estimated from moisture content and matrix density

Table 82: Parameter estimates for the release of K from the one-dimensional diffusion model – comparison between the three 28-d cured material types (CFA-C, CFA-F and PCC).

	Material type		
	C(XXX)02	F(XXX)02	P(XXX)02
^a C ₀ [(mg elemental species from <u>cement</u> , <u>aggregates</u> and <u>CFA-C</u>) / (kg of concrete product)]	3150	3340	4120
^b C ₀ [m ² /s]	2.2 10 ⁻¹⁴	3.5 10 ⁻¹⁴	3.7 10 ⁻¹⁴
^c C ₀	9.0 10 ⁴	5.7 10 ⁴	5.3 10 ⁴
^d C ₀ [(mg elemental species from <u>cement</u> and <u>CFA-C</u>) / (kg of concrete product)]	820	1220	850
^e C ₀ [m ² /s]	3.3 10 ⁻¹³	2.6 10 ⁻¹³	8.7 10 ⁻¹³
C ₀	5940	7540	2255
^f C ₀ [m ² /s]	1.0 10 ⁻¹²	0.7 10 ⁻¹²	2.6 10 ⁻¹²
C ₀	1960	2800	755
^g C ₀	30	30	30

^a Total content in K

^b Calculated assuming that the initial leachable concentration C₀ was the total content

^c C₀ = 1.96*10⁻⁹ m²/s (Linde, 1996)

^d Based on mix design and total content of individual mix components (e.g., cement and CFAs).

^e Calculated assuming that the initial leachable concentration C₀ was the species content provided only by the cement and the CFA

^f Calculated assuming that the initial leachable concentration C₀ was the species content provided only by the cement and the CFA and the flux was only provided by the fraction of the surface of the sample non-occupied by the aggregates

^g Millington-Quirk relationship (Millington et al., 1971). The porosity was estimated from moisture content and matrix density

Table 83: Parameter estimates for the release of Cl from the one-dimensional diffusion model – comparison between the three 28-d cured material types (CFA-C, CFA-F and PCC).

	Material type		
	C(XXX)02	F(XXX)02	P(XXX)02
C_0^a [(mg elemental species from cement, aggregates and CFA-C) / (kg of concrete product)]	120	100	110
$D_{obs, l}^b$ [m ² /s]	1.5 10 ⁻¹¹	2.8 10 ⁻¹¹	2.4 10 ⁻¹¹
$\frac{D_{m,Cl}^c}{D_{obs, l}}$	135	75	85
$\tau_{MO} = \epsilon^{-4/3 d}$	30	30	30

^a Total content in Cl

^b Calculated assuming that the initial leachable concentration C_0 was the total content

^c $D_{m,Cl} = 2.03 \cdot 10^{-9}$ m²/s (Linde, 1996)

^d Millington-Quirk relationship (Millington et al., 1971). The porosity was estimated from moisture content and matrix density

Table 84: Parameter estimates for the release of Ca from the one-dimensional diffusion model – comparison between the three 28-d cured material types (CFA-C, CFA-F and PCC).

	Material type		
	C(XXX)02	F(XXX)02	P(XXX)02
C_0^a [(mg elemental species from <u>cement, aggregates</u> and CFA-C) / (kg of concrete product)]	370,000	375,000	380,000
$D_{obs,1}^b$ [m ² /s]	$3.5 \cdot 10^{-16}$	$4.3 \cdot 10^{-16}$	$6.3 \cdot 10^{-16}$
$\frac{D_{m,Ca}^c}{D_{obs,1}}$	$2.3 \cdot 10^6$	$1.9 \cdot 10^6$	$1.3 \cdot 10^6$
C_0^d [(mg elemental species from <u>cement and CFA-C</u>) /(kg of concrete product)]	68,100	64,100	75,300
$D_{obs,2}^e$ [m ² /s]	$1.0 \cdot 10^{-14}$	$1.5 \cdot 10^{-14}$	$1.6 \cdot 10^{-14}$
$\frac{D_{m,Ca}}{D_{obs,2}}$	$7.9 \cdot 10^4$	$5.5 \cdot 10^4$	$5.0 \cdot 10^4$
$D_{obs,3}^f$ [m ² /s]	$3.1 \cdot 10^{-14}$	$4.4 \cdot 10^{-14}$	$4.9 \cdot 10^{-14}$
$\frac{D_{m,Ca}}{D_{obs,3}}$	$2.1 \cdot 10^4$	$1.8 \cdot 10^4$	$1.7 \cdot 10^4$
$\tau_{MO} = \varepsilon^{-4/3} g$	30	30	30

^a Total content in Ca

^b Calculated assuming that the initial leachable concentration C_0 was the total content

^c $D_{m,Ca} = 7.92 \cdot 10^{-10}$ m²/s (Linde, 1996)

^d Based on mix design and total content of individual mix components (e.g., cement and CFAs).

^e Calculated assuming that the initial leachable concentration C_0 was the species content provided only by the cement and the CFA

^f Calculated assuming that the initial leachable concentration C_0 was the species content provided only by the cement and the CFA and the flux was only provided by the fraction of the surface of the sample non-occupied by the aggregates

^g Millington-Quirk relationship (Millington et al., 1971). The porosity was estimated from moisture content and matrix density

F(XXX)02 and P(XXX)02 (e.g., $2.8 \cdot 10^{-11} \text{ m}^2/\text{s}$ and $2.4 \cdot 10^{-11} \text{ m}^2/\text{s}$, respectively) was slightly greater than that of C(XXX)02 (e.g., $1.5 \cdot 10^{-11} \text{ m}^2/\text{s}$). When considering only the Cl provided by the cement and the CFA-C, unrealistic diffusivity data (e.g., diffusivity data greater than the Cl molecular diffusivity) were obtained. This result might be due to the low total content in Cl (e.g., 100 mg/kg for the three material types) and the low Cl concentrations measured in the leachates (e.g., close to or below 1 mg/l, the instrument detection limit), leading to large uncertainties in the determination of the observed diffusivity.

Ca Modeling. Ca observed diffusivities of the same order of magnitude were calculated for the three 28-d cured material types (see table 84). Low Ca observed diffusivities (e.g., on the order of $10^{-16} \text{ m}^2/\text{s}$) were calculated from the Ca total content, leading to ratios of observed diffusivity to molecular diffusivity for Ca as much as 5 orders of magnitude greater than the estimated tortuosity using the Millington-Quirk relationship (e.g., τ_{MQ} of 30). Ca observed diffusivity of P(XXX)02 was slightly greater (e.g., $6.3 \cdot 10^{-16} \text{ m}^2/\text{s}$) than that of F(XXX)02 (e.g., $4.3 \cdot 10^{-16} \text{ m}^2/\text{s}$) that was slightly greater than that of C(XXX)02 (e.g., $3.5 \cdot 10^{-16} \text{ m}^2/\text{s}$). When considering only the Ca content provided by the cement and the CFA-C, the diffusivity results (e.g., $D_{\text{obs } 2}$ and $D_{\text{obs } 3}$) changed by two orders of magnitude. Diffusivity results slightly increased ($D_{\text{obs } 3}$ were three times greater than $D_{\text{obs } 2}$) when calculations were done by accounting only for the surface of the matrix non-occupied by the aggregates. Ratios of observed diffusivity to molecular diffusivity for Ca were then three orders of magnitude greater than the estimated tortuosity using the Millington-Quirk relationship. This discrepancy was consistent with the large interaction of Ca with the concrete matrix. Indeed Ca is found in the major products of cement hydration that include Ca hydroxide, Ca silicate hydroxide (CSH), and Ca sulfoaluminates and for which solubility differs by orders of magnitude.

In conclusion, the three different observed diffusivities calculated for each species of concern showed the importance of correctly selecting the initial leachable concentration C_D used in the diffusion model to estimate the observed diffusivity and highlighted the limits of the diffusion model in the case of heterogeneous porous materials. Thus, from the total content, much greater Na observed diffusivity and slightly less K and Cl observed diffusivities were obtained for C(XXX)02, while no significant difference in Na, K, and Cl observed diffusivities could be observed between F(XXX)02 and P(XXX)02. In contrast, when considering only the species content provided by the cement and the CFAs, no significant difference in Na and K observed diffusivities could be observed between C(XXX)02 and F(XXX)02 while greater observed diffusivities were obtained for P(XXX)02. In both cases (e.g., total content and content from the cement and the CFAs), Ca observed diffusivities were slightly less for C(XXX)02 than for F(XXX)02 and P(XXX)02.

In conclusion:

1. As with the slab concrete, there was significant retention of Na and K within the concrete materials and the implied assumption of a homogeneous matrix was not appropriate.
2. As with the slab concrete, diffusivity calculations involving Ca confirm its interaction with the concrete matrix.

5.5.15.2 Release Modeling for F(XXX)02 and the CFA-F Center Points

The one-dimensional diffusion model was used to interpret the release of Na, K, Cl, and Ca from the 28-d cured CFA-F mix sample (e.g., F(XXX)02) and the low level aged CFA-F mix samples (e.g., F(LLL)13, F(LLL)30, and F(LLL)47). During the time scale of the laboratory testing (e.g., 4 mo for F(LLL)30 and F(LLL)47, 10 mo for F(LLL)13, and 20 mo for F(XXX)02), no depletion of these species within the matrices was observed. For each species of concern, three different observed diffusivities (e.g., $D_{obs\ 1}$, $D_{obs\ 2}$, and $D_{obs\ 3}$) were determined. $D_{obs\ 2}$ was calculated assuming that the initial leachable concentration C_D was the total content of the species of concern. $D_{obs\ 2}$ was calculated assuming that the initial leachable concentration C_D was the species content provided only by the cement and the CFA-F. $D_{obs\ 3}$ was calculated assuming that (i) the initial leachable concentration C_D was the species content provided only by the cement and the CFA-F, (ii) the aggregates were inert and uniformly distributed within the matrix and (iii) the flux was only provided by the fraction of the surface¹² of the sample not occupied by the aggregates. Thus, while $D_{obs\ 1}$ and $D_{obs\ 2}$ correspond to observed diffusivities through the overall matrix (e.g., binder and aggregates), $D_{obs\ 3}$ corresponds to an observed diffusivity only through the binder (e.g., cement and CFA-F).

Initial leachable concentrations and observed diffusivities of the 28-d cured and low level aged CFA-F samples (e.g., F(XXX)02, F(LLL)13, F(LLL)30, and F(LLL)47) are compared in tables 85 through 88 for Na, K, Cl, and Ca, respectively.

Na Modeling. Slightly greater Na observed diffusivities were determined for the three low level aged CFA-F mix samples compared with the 28-d cured CFA-F mix sample (table 85). Thus, Na observed diffusivities of F(LLL)13, F(LLL)30, and F(LLL)47 were approximately 3 times to 6 times greater than that of F(XXX)02, independent of the method of calculation used (e.g., $D_{obs\ 1}$, $D_{obs\ 2}$, or $D_{obs\ 3}$). In addition, differences in Na observed diffusivities could be observed between the three low level aged CFA-F mix samples with Na observed diffusivities of F(LLL)30 and F(LLL)47 approximately 2 times greater than that of F(LLL)13.

K Modeling. As with Na, differences in K observed diffusivities could be observed between the three low level aged CFA-F mix samples. Thus, K observed diffusivities of two of the three low level aged CFA-F mix samples (e.g., F(LLL)30 and F(LLL)47) were slightly greater than that of the 28-d cured CFA-F mix sample (e.g., F(XXX)02) while K observed diffusivities of one of the three low level aged CFA-F mix samples (e.g., F(LLL)13) was slightly less (table 86).

Cl Modeling. Cl observed diffusivity of F(LLL)13 was approximately 2 times greater than that of F(XXX)02 (table 87).

12 As a first approach, it was assumed that 57.5 percent of the surface of the material was non-occupied by the aggregates (42.5 percent of coarse aggregates were used in the mix design).

Table 85: Parameter estimates for the release of Na from the one-dimensional diffusion model – CFA-F.

	F(XXX)02	F(LLL)13	F(LLL)30	F(LLL)47
C_0^a [(mg elemental species from <u>cement</u> , <u>aggregates</u> and <u>CFA-C</u>) / (kg of concrete product)]	3250	3250	3250	3250
$D_{obs,1}^b$ [m ² /s]	$0.3 \cdot 10^{-15}$	$0.9 \cdot 10^{-15}$	$1.7 \cdot 10^{-15}$	$1.7 \cdot 10^{-15}$
C_0^c [(mg elemental species from <u>cement</u> and <u>CFA-C</u>) /(kg of concrete product)]	120	120	120	120
$D_{obs,2}^d$ [m ² /s]	$2.0 \cdot 10^{-13}$	$6.7 \cdot 10^{-13}$	$12.0 \cdot 10^{-13}$	$12.0 \cdot 10^{-13}$
$D_{obs,3}^e$ [m ² /s]	$0.6 \cdot 10^{-12}$	$2.0 \cdot 10^{-12}$	$3.6 \cdot 10^{-12}$	$3.7 \cdot 10^{-12}$

^a Total content in Na

^b Calculated assuming that the initial leachable concentration C_0 was the total content

^c Based on mix design and total content of individual mix components (e.g., cement and CFA-F)

^d Calculated assuming that the initial leachable concentration C_0 was the species content provided only by the cement and the CFA-F

^e Calculated assuming that the initial leachable concentration C_0 was the species content provided only by the cement and the CFA-F and the flux was only provided by the fraction of the surface of the sample non-occupied by the aggregates

Table 86: Parameter estimates for the release of K from the one-dimensional diffusion model – CFA-F.

	F(XXX)02	F(LLL)13	F(LLL)30	F(LLL)47
C_0^a [(mg elemental species from <u>cement, aggregates</u> and <u>CFA-C</u>) / (kg of concrete product)]	3340	3340	3340	3340
$D_{obs,1}^b$ [m ² /s]	$3.5 \cdot 10^{-14}$	$3.0 \cdot 10^{-14}$	$4.6 \cdot 10^{-14}$	$5.1 \cdot 10^{-14}$
C_0^c [(mg elemental species from <u>cement and CFA-C</u>) /(kg of concrete product)]	1220	1220	1220	1220
$D_{obs,2}^d$ [m ² /s]	$2.6 \cdot 10^{-13}$	$2.3 \cdot 10^{-13}$	$3.5 \cdot 10^{-13}$	$3.9 \cdot 10^{-13}$
$D_{obs,3}^e$ [m ² /s]	$7.9 \cdot 10^{-13}$	$6.9 \cdot 10^{-13}$	$10.0 \cdot 10^{-13}$	$12.0 \cdot 10^{-13}$

^a Total content in K

^b Calculated assuming that the initial leachable concentration C_0 was the total content

^c Based on mix design and total content of individual mix components (e.g., cement and CFA-F)

^d Calculated assuming that the initial leachable concentration C_0 was the species content provided only by the cement and the CFA-F

^e Calculated assuming that the initial leachable concentration C_0 was the species content provided only by the cement and the CFA-F and the flux was only provided by the fraction of the surface of the sample non-occupied by the aggregates

Table 87: Parameter estimates for the release of Cl from the one-dimensional diffusion model – CFA-F.

	F(XXX)02	F(LLL)13
C_0^a [(mg elemental species from <u>cement</u> , <u>aggregates</u> and <u>CFA-C</u>) / (kg of concrete product)]	100	100
$D_{obs.}^b$ [m ² /s]	$2.8 \cdot 10^{-11}$	$4.6 \cdot 10^{-11}$

^a Total content in Cl

^b Calculated assuming that the initial leachable concentration C_0 was the total content

Table 88: Parameter estimates for the release of Ca from the one-dimensional diffusion model – CFA-F.

	F(XXX)02	F(LL)13	F(LL)30	F(LL)47
C_0^a [(mg elemental species from <u>cement</u> , <u>aggregates</u> and <u>CFA-C</u>) / (kg of concrete product)]	375,000	375,000	375,000	375,000
$D_{obs 1}^b$ [m ² /s]	4.3 10 ⁻¹⁶	2.3 10 ⁻¹⁶	2.7 10 ⁻¹⁶	2.8 10 ⁻¹⁶
C_0^c [(mg elemental species from <u>cement</u> and <u>CFA-C</u>) /(kg of concrete product)]	64,100	64,100	64,100	64,100
$D_{obs 2}^d$ [m ² /s]	15.0 10 ⁻¹⁵	8.0 10 ⁻¹⁵	9.3 10 ⁻¹⁵	9.6 10 ⁻¹⁵
$D_{obs 3}^e$ [m ² /s]	4.4 10 ⁻¹⁴	2.3 10 ⁻¹⁴	2.8 10 ⁻¹⁴	2.9 10 ⁻¹⁴

^a Total content in Ca

^b Calculated assuming that the initial leachable concentration C_0 was the total content

^c Based on mix design and total content of individual mix components (e.g., cement and CFA-F)

^d Calculated assuming that the initial leachable concentration C_0 was the species content provided only by the cement and the CFA-F

^e Calculated assuming that the initial leachable concentration C_0 was the species content provided only by the cement and the CFA-F and the flux was only provided by the fraction of the surface of the sample non-occupied by the aggregates

Ca Modeling. Ca observed diffusivities of the low level aged CFA-F mix samples were slightly less (e.g., approximately 2 times less) than that of the 28-d cured CFA-F mix sample (table 88). In contrast with Na and K, no significant difference in Ca observed diffusivities could be observed between the three low level aged CFA-F mix samples although slightly less Ca observed diffusivities were obtained for F(LL)13.

In conclusion:

1. Na diffusivity was 3 times greater and Cl was 2 times greater for the low-level CFA-F accelerated aged specimens than the 28-d specimens.
2. Ca diffusivity of the low-level aged CFA-F specimen was half that of the 28-d specimens

5.5.15.3 Release Modeling for P(XXX)02 and the PCC Center Points

The one-dimensional diffusion model was used to interpret the release of Na, K, Cl, and Ca from the 28-d cured PCC control sample (e.g., P(XXX)02) and the low level aged PCC control samples (e.g., P(LL)13, P(LL)23, and P(LL)39). During the time scale of the laboratory testing (e.g., 4 mo for P(LL)23 and P(LL)39, 10 mo for P(LL)13, and 20 mo for P(XXX)02), no depletion of these species within the matrices was observed. For each species of concern, three different observed diffusivities (e.g., $D_{obs\ 1}$, $D_{obs\ 2}$, and $D_{obs\ 3}$) were determined. $D_{obs\ 1}$ was calculated assuming that the initial leachable concentration C_0 was the total content of the species of concern. $D_{obs\ 2}$ was calculated assuming that the initial leachable concentration C_0 was the species content provided only by the cement. $D_{obs\ 3}$ was calculated assuming that (i) the initial leachable concentration C_0 was the species content provided only by the cement, (ii) the aggregates were inert and uniformly distributed within the matrix, and (iii) the flux was only provided by the fraction of the surface¹³ of the sample non-occupied by the aggregates. Thus, while $D_{obs\ 1}$ and $D_{obs\ 2}$ correspond to observed diffusivities through the overall matrix (e.g., binder and aggregates), $D_{obs\ 3}$ corresponds to an observed diffusivity only through the binder (e.g., cement). Initial leachable concentrations and observed diffusivities of the 28-d cured and low level aged PCC control samples (e.g., P(XXX)02 and P(LL)13, P(LL)23, and P(LL)39) are compared in tables 89 through 92, for Na, K, Cl and Ca, respectively.

Na Modeling. Slightly greater Na observed diffusivities were calculated for the three low level aged PCC control samples compared with the 28-d cured PCC control sample (table 89). Thus, Na observed diffusivities of P(LL)13, P(LL)23, and P(LL)39 were approximately 2 times to 9 times greater than that of P(XXX)02, independent of the method of calculation used (e.g., $D_{obs\ 1}$, $D_{obs\ 2}$, and $D_{obs\ 3}$). In addition, significant differences in Na observed diffusivities

13 As a first approach, it was assumed that approximately 57.5 percent of the surface of the material was non-occupied by the aggregates (42.5 percent of coarse aggregates were used in the mix design).

Table 89: Parameter estimates for the release of Na from the one-dimensional diffusion model – PCC.

	P(XXX)02	P(LL)13	P(LL)23	P(LL)39
C_0^a [(mg elemental species from cement, aggregates and CFA-C) / (kg of concrete product)]	3900	3900	3900	3900
D_{obs1}^b [m ² /s]	$0.4 \cdot 10^{-15}$	$0.9 \cdot 10^{-15}$	$3.5 \cdot 10^{-15}$	$0.8 \cdot 10^{-15}$
D_0^c [(mg elemental species from cement and CFA-C) /(kg of concrete product)]	70	70	70	70
D_{obs2}^d [m ² /s]	$1.3 \cdot 10^{-12}$	$2.6 \cdot 10^{-12}$	$11.0 \cdot 10^{-12}$	$2.5 \cdot 10^{-12}$
D_{obs3}^e [m ² /s]	$4.0 \cdot 10^{-12}$	$7.9 \cdot 10^{-12}$	$32.0 \cdot 10^{-12}$	$7.5 \cdot 10^{-12}$

^a Total content in Na

^b Calculated assuming that the initial leachable concentration C_0 was the total content

^c Based on mix design and total content of individual mix components (e.g., cement)

^d Calculated assuming that the initial leachable concentration C_0 was the species content provided only by the cement

^e Calculated assuming that the initial leachable concentration C_0 was the species content provided only by the cement and the flux was only provided by the fraction of the surface of the sample non-occupied by the aggregates

Table 90: Parameter estimates for the release of K from the one-dimensional diffusion model – PCC.

	P(XXX)02	P(LL)13	P(LL)23	P(LL)39
C_0^a [(mg elemental species from <u>cement</u> , <u>aggregates</u> and <u>CFA-C</u>) / (kg of concrete product)]	4120	4120	4120	4120
$D_{obs,1}^b$ [m ² /s]	$3.7 \cdot 10^{-14}$	$1.3 \cdot 10^{-14}$	$4.4 \cdot 10^{-14}$	$1.2 \cdot 10^{-14}$
C_0^c [(mg elemental species from <u>cement</u> and <u>CFA-C</u>) /(kg of concrete product)]	850	850	850	850
$D_{obs,2}^d$ [m ² /s]	$8.7 \cdot 10^{-13}$	$3.0 \cdot 10^{-13}$	$10.0 \cdot 10^{-13}$	$2.8 \cdot 10^{-13}$
$D_{obs,3}^e$ [m ² /s]	$2.6 \cdot 10^{-12}$	$0.9 \cdot 10^{-12}$	$3.1 \cdot 10^{-12}$	$0.9 \cdot 10^{-12}$

^a Total content in K

^b Calculated assuming that the initial leachable concentration C_0 was the total content

^c Based on mix design and total content of individual mix components (e.g., cement)

^d Calculated assuming that the initial leachable concentration C_0 was the species content provided only by the cement

^e Calculated assuming that the initial leachable concentration C_0 was the species content provided only by the cement and the flux was only provided by the fraction of the surface of the sample non-occupied by the aggregates

Table 91: Parameter estimates for the release of Cl from the one-dimensional diffusion model – PCC.

	P(XXX)02	P(LL)13
C_0^a [(mg elemental species from cement, aggregates and CFA-C) / (kg of concrete product)]	110	110
$D_{obs.}^b$ [m ² /s]	$2.4 \cdot 10^{-11}$	$1.0 \cdot 10^{-11}$

^a Total content in Cl

^b Calculated assuming that the initial leachable concentration C_0 was the total content

Table 92: Parameter estimates for the release of Ca from the one-dimensional diffusion model – PCC.

	P(XXX)02	P(LLL)13	P(LLL)23	P(LLL)39
C_0^a [(mg elemental species from <u>cement</u> , <u>aggregates</u> and <u>CFA-C</u>) / (kg of concrete product)]	380,000	380,000	380,000	380,000
$D_{obs 1}^b$ [m ² /s]	$6.3 \cdot 10^{-16}$	$8.0 \cdot 10^{-16}$	$15.0 \cdot 10^{-16}$	$12.0 \cdot 10^{-16}$
C_0^c [(mg elemental species from <u>cement</u> and <u>CFA-C</u>) /(kg of concrete product)]	75,300	75,300	75,300	75,300
$D_{obs 2}^d$ [m ² /s]	$1.6 \cdot 10^{-14}$	$2.0 \cdot 10^{-14}$	$3.9 \cdot 10^{-14}$	$3.1 \cdot 10^{-14}$
$D_{obs 3}^e$ [m ² /s]	$4.9 \cdot 10^{-14}$	$6.2 \cdot 10^{-14}$	$12.0 \cdot 10^{-14}$	$8.3 \cdot 10^{-14}$

^a Total content in Ca

^b Calculated assuming that the initial leachable concentration C_0 was the total content

^c Based on mix design and total content of individual mix components (e.g., cement)

^d Calculated assuming that the initial leachable concentration C_0 was the species content provided only by the cement

^e Calculated assuming that the initial leachable concentration C_0 was the species content provided only by the cement and the flux was only provided by the fraction of the surface of the sample non-occupied by the aggregates

could be observed between the three low level aged PCC control samples with Na observed diffusivities of P(LL)23 approximately 4 times greater than that of P(LL)13 and P(LL)39.

K Modeling. As with Na, differences in K observed diffusivities could be observed between the three low level aged PCC control samples. Thus, K observed diffusivities of two of the three low level aged PCC control samples (e.g., P(LL)13 and P(LL)39) were approximately 3 times less than that of the 28-d cured PCC control sample (e.g., P(XX)02) while K observed diffusivities of one of the low level aged PCC control samples (e.g., P(LL)23) was slightly greater (table 90).

Cl Modeling. Cl observed diffusivity of P(LL)13 was approximately 2.5 times less than that of P(XX)02 (table 91).

Ca Modeling. Slightly greater Ca observed diffusivities were calculated for the three low level aged PCC control samples compared with the 28-d cured PCC control sample (table 92). Thus, Ca observed diffusivities of P(LL)13, P(LL)23, and P(LL)39 were approximately 1.5 to 2.5 times greater than that of P(XX)02. Differences in Ca observed diffusivities could be observed between the three low level aged PCC control samples with Ca observed diffusivities of P(LL)13 approximately 2 times less than that of P(LL)23 and P(LL)39.

In conclusion:

1. Na diffusivity was 2 times greater and Cl was 1.5 times greater for the low-level PCC accelerated aged specimens than the 28-d specimens.
2. Ca and K diffusivity of the low-level aged PCC specimen was 1/3 that of the 28-d specimens.
3. Aging did affect diffusivity values for both the PCC and CFA-F concretes, generally increasing Na and Cl values and decreasing Ca and K values.

5.5.15.4 Release Modeling for Coarse Aggregates

The one-dimensional diffusion model was used to interpret the release of Na, K, and Ca from the coarse aggregates and estimate intra-aggregate diffusivity for each constituent of interest. Na, K, and Ca observed diffusivities obtained for the four replicates are presented in table 93. Averages of observed diffusivities and standard deviations are also shown. Na and K observed diffusivities were determined with large uncertainties because few leaching intervals presented a straight line with a slope between 0.35 and 0.65.

Low Na, K, and Ca observed diffusivities were obtained for the four replicates, indicating significant retention of these species in the coarse aggregates. Na and K observed diffusivities showed some scatter between the four replicates and ranged from $1.2 \cdot 10^{-15} \text{ m}^2/\text{s}$ to $27.0 \cdot 10^{-15} \text{ m}^2/\text{s}$ and $0.6 \cdot 10^{-15} \text{ m}^2/\text{s}$ to $5.4 \cdot 10^{-15} \text{ m}^2/\text{s}$, respectively. Good reproducibility of Ca

Table 93: Parameter estimates from the one-dimensional diffusion model – coarse aggregates.

	Rep 1	Rep 2	Rep 3	Rep 4	Average	Std
$D_{\text{obs,Na}}^b$ [m ² /s]	$1.2 \cdot 10^{-15}$	$27.0 \cdot 10^{-15}$	$1.3 \cdot 10^{-15}$	$8.2 \cdot 10^{-15}$	$9.4 \cdot 10^{-15}$	$12.0 \cdot 10^{-15}$
$D_{\text{obs,K}}^b$ [m ² /s]	$3.9 \cdot 10^{-15}$	$5.4 \cdot 10^{-15}$	$0.6 \cdot 10^{-15}$	$4.9 \cdot 10^{-15}$	$3.7 \cdot 10^{-15}$	$2.2 \cdot 10^{-15}$
$D_{\text{obs,Ca}}^b$ [m ² /s]	$2.8 \cdot 10^{-18}$	$3.4 \cdot 10^{-18}$	$2.6 \cdot 10^{-18}$	$2.5 \cdot 10^{-18}$	$2.8 \cdot 10^{-18}$	$0.4 \cdot 10^{-18}$

observed diffusivities was obtained between the four replicates with observed diffusivities ranging from $2.5 \cdot 10^{-18} \text{ m}^2/\text{s}$ to $3.4 \cdot 10^{-18} \text{ m}^2/\text{s}$. The obtained results showed that the release of Na, K, and Ca from the coarse aggregates in the overall concrete products was negligible compared with the release of these species from the binder (e.g., cement and CFAs). Indeed, Na, and K observed diffusivities through the coarse aggregates were three orders of magnitude less than that through the binder of the three material types (e.g., CFA-C mix, CFA-F mix and PCC control) and the U.S. 20 slab. Similarly, Ca observed diffusivities through the coarse aggregates were four orders of magnitude less.

5.5.15.5 ANOVA

ANOVA was carried out on two response variables of the three center point replicates of CFA-C mix, CFA-F mix, and PCC control. These response variables were the cumulative release of Na, K, and Ca at 22 d¹⁴ of leaching and the observed diffusivities¹⁵ of Na, K, and Ca. Calculated F values and tabulated F value at 95 percent are compared in tables L-34, L-35, and L-36 in appendix L of volume II for the cumulative release at 22 d of leaching and in L-37, L-38, and L-39 in appendix L of volume II for the observed diffusivities, respectively. A greater computed F value compared with the tabulated F value at 95 percent indicated that the values of the response variables of concern were significantly different at 95 percent. Tukey's paired comparison was also carried out to judge of the differences between the CFA-C mix, CFA-F mix and PCC control. Results of the Tukey's paired comparison are presented in tables L-40, L-41, and L-42 in appendix L of volume II and tables L-43, L-44, and L-45 in appendix L of volume II for Na, K and Ca cumulative release at 22 d of leaching and Na, K and Ca observed diffusivities, respectively.

ANOVA carried out on the cumulative release of Na and Ca at 22 d of leaching (table L-35) provided calculated F values that were greater than the tabulated F values at 95 percent, indicating significant differences at 95 percent in the examined values of Na and Ca cumulative release. In contrast, calculated F value from the cumulative release of K at 22 d of leaching (table L-36) was much less than the tabulated F value at 95 percent, indicating that the examined values of K cumulative release were not significantly different at 95 percent.

5.5.15.6 Tukey-Kramer Comparisons

Results of the Tukey's paired comparison showed that the CFA-C mix was significantly different at 95 percent from CFA-F mix and PCC control for Na and Ca cumulative release at 22 d of leaching (table L-41) while CFA-F mix, and PCC control were not significantly different. Additionally, the CFA-C mix, CFA-F mix, and PCC control were not significantly different at 95 percent for K cumulative release at 22 d of leaching (tables L-42 and L-43, respectively). The CFA-C mix, CFA-F mix, and PCC control were not significantly different at 95 percent for Na

14 22 d of leaching were chosen for ANOVA because they represented the greatest cumulative leaching time common to all samples.

15 ANOVA was carried out only on $D_{\text{obs } 3}$ (e.g., observed diffusivity only through the binder).

and K observed diffusivities (tables L-44 and L-45, respectively). Finally, the control was significantly different at 95 percent from CFA-C mix and CFA-F mix for Ca observed diffusivity (table L-46) while CFA-C mix and CFA-F mix were not significantly different.

5.5.15.7 Conclusions

In conclusion:

1. Chemical and mass transfer processes varied by orders of magnitude between the different components.
2. Observed diffusivities through the aggregates indicated that the release of Na, K, and Ca from the coarse aggregates in the overall concrete products was negligible compared with the release from the binder (e.g., cement and CFAs).
3. Na cumulative releases were significantly different between mix types.
4. Ca and K cumulative release were not significantly different between mix types.
5. Na and K observed diffusivities were not significantly different between mix types.
6. Ca observed diffusivities were significantly different between mix types.

5.6. Comparisons Between Slab and CFA-C Prism Specimens

In deciding to create laboratory concrete prisms with CFA-C for the purpose of developing an accelerated aging method for waste-containing pavements, it was desired to obtain a slab sample of a similar matrix that had been aged naturally and whose properties could be compared with the laboratory aged concrete. To compare the slab and laboratory concretes, the materials and mix used to make the 1987 Iowa pavement were replicated, as closely as possible, for the creation of the laboratory CFA-C concrete prisms.

It was hoped that the process of accelerated aging would produce laboratory prism concrete with physical characteristics, mineralogy, and leachability similar to the range of values found in the U.S. 20 slab concrete that had aged in the field for almost 10 yr..

5.6.1. Comparison of Materials Used

The mix design of the experimental CFA-C concrete was intended to replicate the materials and mix of the slab concrete as best as possible. Like the Iowa concrete the experimental CFA-C concrete mix included Type I portland cement, CFA-C from Ottumwa Power Station in Iowa, a quartz-based (SiO_2) fine aggregate, and a limestone-based coarse aggregate. The ratio of coarse aggregate to fine aggregate as well as amounts of aggregate, cement, and ash were the same for both concretes.

5.6.1.1 Portland Cement

The manufacturing sites for the cements were Lehigh Portland Cement Co. in Helena, Montana, for the laboratory concrete and the Lehigh Portland Cement Co. in Mason City, Iowa for the Iowa concrete. Oxide analysis of the two concretes are provided in table 94 with typical oxide concentrations in portland cement. The cement used for the laboratory concrete was slightly higher in Mg and Al oxides and slightly lower in S and Na. It is uncertain that these differences were significant.

5.6.1.2 CFA-C

The CFA-C for both concretes was acquired from the Ottumwa Power Generating Station in Iowa. The oxide analysis for both the CFA-C used in the Iowa concrete and the CFA-C used in the experimental concrete are provided in table 95. While some differences exist, it suggests that the CFA-C was similar. There is no data available on changes (if any) in the coal source or in combustion conditions at the Ottumwa Power Station over time. The C ash used for the laboratory concrete was slightly higher in Mg and slightly lower in Al and Na. It is uncertain if these differences were significant.

5.6.1.3 Coarse and Fine Aggregates

The source and supplier of the limestone coarse aggregate was the same for the Iowa concrete pavement and the experimental concrete mixes. The supplier of the quartz fine aggregate was also the same for the Iowa concrete as the laboratory concrete, but the pit from which the fine aggregate was mined had changed (though the geological formation was the same).

5.6.1.4 Conclusions

In conclusion:

1. Source materials for the CFA-C concrete were selected to be as close as possible in type and proportion to those used for the slab concrete.
2. Both the cement and the ash were slightly higher in MgO. Other differences in metal oxides may have been offsetting.
3. Aggregates for the slab and laboratory concretes were from the same geological formation and are likely to be quite similar.

5.6.2. Elemental Composition Analysis

Total elemental composition was analyzed in one CFA-C prism and in two slab specimens by neutron activation analysis/X-ray fluorescence (NAA/XRF). Tables 96 through 98 compare the results of these analyses. The tables are divided into major (greater than 10,000

Table 94: Oxide analysis of cements used in Iowa and laboratory concretes¹.

Species	Cement for Iowa concrete (%)	Cement for laboratory concrete (%)	Typical cement concentrations ² (%)
MgO	2.58	3.9	0.1 - 5.5
SO ₃	3.38	3	1 - 3
Al ₂ O ₃	4.87	5.4	3 - 8
3CaO • Al ₂ O ₃	9.05	11	N/A ³
Na ₂ O _e	0.07	N/A	N/A
K ₂ O	1.06	N/A	N/A
Na ₂ O _{e4}	0.77	0.52	N/A
SiO ₂	N/A	21.2	17 - 25
Fe ₂ O ₃	N/A	2.4	0.5 - 6

1 Chemical analyses provided by cement suppliers

2 Soroka, 1979

3 Test was not performed or results are unavailable

4 Equivalent alkali content equal to Na₂O + 0.658 K₂O

Table 95: Oxide analyses of CFA-C used in Iowa and in laboratory concretes.

Species	CFA-C for Iowa concrete ¹ (%)	CFA-C for laboratory concrete ² (%)	Typical CFA-C ³ (%)
Al ₂ O ₃	21.12	18.8	16.7
CaO	N/A ⁴	26.8	24.3
3CaO • Al ₂ O ₃	18.65	N/A	
Fe ₂ O ₃	N/A	6.3	5.8
K ₂ O	0.41	0.34	
MgO	4.61	5.6	4.6
Na ₂ O	2.55	2.0	
Na ₂ O _{e5}	2.81	2.22	
SiO ₂	N/A	32.8	39.9
SO ₃	2.27	2.2	3.3

1 Chemical analyses provided by cement suppliers

2 (Section 3.3.1)

3 FWHA, 1995

4 Results not provided or available

5 Equivalent alkali content equal to Na₂O + 0.658 K₂O

Table 96: Total elemental composition (+/- standard deviation) of major elements in CFA-C prism and U.S. 20 slab concrete (>10,000 ppm).

Element	CFA-C concrete prism (ppm)	Iowa slab concrete (ppm)
Al	18,200 +/- 340	19,985 +/- 375
Ca	363,900 +/- 45,800	372,200 +/- 46,900
Si	140,500 +/- 7,500	65,500 +/- 3,800

Table 97: Total elemental composition (+/- standard deviation) of minor elements in CFA-C prism and U.S. 20 slab concrete (1,000 - 10,000 ppm).

Element	CFA-C concrete prism (ppm)	Iowa slab concrete (ppm)
Fe	9,075 +/- 275	7,137 +/- 219
K	3,144 +/- 83	3,469 +/- 88
Na	3,771 +/- 57	3,573 +/- 54
S	3,801 +/- 18	5,993 +/- 23

Table 98: Total element composition (+/- standard deviation) of trace elements in prism CFA-C and U.S. 20 slab concrete (<1,000 ppm).

Element	CFA-C concrete prism (ppm)	Iowa slab concrete (ppm)
Ag	< ¹ 1	< 1
As	0.87 +/- 0.09	1.21 +/- 0.107
Au	< 2	< 1.50
Ba	138.38 +/- 9.28	148.73 +/- 11.607
Br	< 0.34	< 0.41
Cd	< 2.85	< 3.04
Ce	17.46 +/- 0.92	16.01 +/- 0.85
Cl	119.58 +/- 10.82	109.61 +/- 13.14
Co	4.65 +/- 0.24	2.98 +/- 0.16
Cr	278.71 +/- 7.20	20.60 +/- 0.75
Cs	0.40 +/- 0.05	0.37 +/- 0.05
Cu	14.00 +/- 1.40	8.75 +/- 1.30
Dy	0.67 +/- 0.07	0.67 +/- 0.08
Eu	0.32 +/- 0.02	0.25 +/- 0.02
Hf	0.97 +/- 0.06	1.48 +/- 0.09
Hg	< 1.00	< 1
I	3.99 +/- 1.66	3.66 +/- 1.59
In	< 0.06	< 0.06
La	6.16 +/- 0.11	6.40 +/- 0.13
Lu	0.08 +/- 0.01	0.10 +/- 0.01
Mg	< 230.00	< 333.00
Mn	37.77 +/- 0.51	211.79 +/- 2.78
Mo	< 1	< 1.50
Nd	8.59 +/- 1.02	8.9 +/- 1.11
Ni	0.80 +/- 0.10	81.6 +/- 1.30
P	< 100	< 100
Pb	13.30 +/- 2.20	11.70 +/- 2.15
Rb	18.67 +/- 2.03	15.71 +/- 1.74
Sb	0.45 +/- 0.05	0.37 +/- 0.05
Sc	2.18 +/- 0.11	2.33 +/- 0.11
Se	< 0.31	< 0.41
Sm	0.89 +/- 0.01	0.87 +/- 0.02
Sr	221.18 +/- 11.14	90.37 +/- 11.98
Ta	0.08 +/- 0.02	0.07 +/- 0.01
Tb	0.09 +/- 0.02	0.09 +/- 0.02
Th	2.57 +/- 0.14	2.31 +/- 0.13
Ti	< 544.08	< 214.95
U	0.37 +/- 0.13	0.50 +/- 0.16
V	< 4.14	21.16 +/- 2.30
W	< 1.00	< 2
Yb	< 0.60	< 1.10
Zn	18.00 +/- 1.30	13.80 +/- 1.30
Zr	20.90 +/- 7.2	30.6 +/- 8.05

1 < denotes detection limit

ppm), minor (1,000 to 10,000 ppm) and trace (less than 1,000 ppm) components. Comparison of these tables reveals that the concentrations of most elements were similar in the experimental CFA-C concrete and the slab concrete. Major, minor, and trace designations were the same for all elements.

The only element to show a large difference between the laboratory and slab concretes was Si. The Si concentration in the slab concrete was 6.6 percent, while in the experimental CFA-C concrete it was found to be 14.0 percent. Examination of table L-20 in appendix L of volume II also shows that the Si concentration of the experimental PCC concrete, which contained no CFA, was 13.9 percent. Therefore it is unlikely that the difference in the Si concentration in the slab and experimental CFA-C concrete was related to the CFA-C used and rather it was related to other materials such as the aggregate and/or the portland cement. In general the elemental composition of the slab concrete was duplicated in the experimental CFA-C prisms.

In conclusion:

1. Of the major elements, Al and Ca compare well while the Si concentration in the slab concrete is lower than that in the laboratory concretes (65,500 vs. 99,300 to 140,500 mg/kg).
2. Of the minor elements, Fe, K, and Na compare well while the S concentration in the slab concrete is higher than that in the laboratory concretes (5,993 vs. 3,801 to 4,940 mg/kg).
3. Trace elements compare well, though Cr in the CFA-C laboratory concrete is much higher than that of all the other concretes (279 vs. 21mg/kg for the slab), Mn is higher in the slab concrete (212 vs. 38 to 172), Ni is higher in the slab concrete (82 vs. 0.8 to 64), Sr is lower in the slab concrete (90 vs. 123 to 230), and V is higher in the slab concrete (21 vs. 4 to 16). It is unclear whether these differences are significant.
4. With respect to the low Si concentration in the slab concrete, it was noted in section 5.4.6.2 (concerning the mineralogy of the CFA-C laboratory concrete) that quartz concentrations were reduced by some unknown mechanism. The low Si concentration here would appear to confirm that observation as actual aging may have also reduced the Si concentration detected. (The accelerated aging methods did not result in chemical aging in excess of the true age of the slab concrete as shown in section 4.3.2.1 and table 19).
5. The high concentration of S in the slab concrete vs. the laboratory concrete is all the more remarkable in that the sulfate concentration in the source cement was already high (see section 5.1.5.2). This high concentration of S in the slab concrete correlates with unexpected amounts of gypsum found in the slab concrete (see section 5.3.6). These high S concentrations lend credence to the possibility that the deleterious hydration reaction may involve some sort of delayed ettringite reaction (see section 5.4.1.2).

5.6.3. Microcracking

The primary difference between the slab and prism specimens as evidenced from the neutron radiography crack density results is that, as a whole, the slab specimens experienced substantially more cracking than did their counterpart prism specimens. The crack densities of the slab specimen slices ranged from 0.3 to 6.6 percent with a mean of 2.3 percent, whereas those of the prism specimen slices ranged from 0.3 to 2.8 percent with a mean of only 0.9 percent.

In addition, the slab specimens experienced a gradation of cracking along their sections, as a result of their location in the slab. The top slices of the slab cores were cracked much more than the bottom slices in most cases. In fact, although the overall mean of the slab specimen slices was 2.3 percent, the mean of the bottom slices was only 1.7 percent.

With respect to crack density analysis, therefore, the laboratory-created prism specimens are not a good representation of the field-collected slab specimens, since the average crack densities of the slab and prism samples were not similar. A possibility is that the prism samples were not as detrimentally affected by the three aging conditions simulated in the laboratory as were the slab samples from exposure to field conditions.

In conclusion:

1. Microcracking was not as extensive in the laboratory prisms as it was in the slab concrete perhaps due to actual vs. accelerated aging.

5.6.4. Effective Pore Size and Pore Size Distribution

CFA-C concrete pore size distributions were similar to the U.S. 20 concrete with respect to shapes of the plots. Both slab and CFA-C concretes produced two distinct intrusion peaks and both had pore size distributions with little intrusion in the 0.1- μm region and in pores smaller than 0.01 μm (see figure 110).

The accelerated aging method recreated the second peak of the slab pore size distribution with samples that received high equivalent aging and no freeze-thaw deterioration, regardless of cyclic loading.

In conclusion:

1. The laboratory CFA-C mixture combined with high levels of heat aging resulted in differential pore size curves similar in nature to the slab concrete; both being a bimodal system of coarser and finer pore systems.
2. With respect to the coarser system of pores, the laboratory concretes exhibited smaller, more well-defined pore sizes.

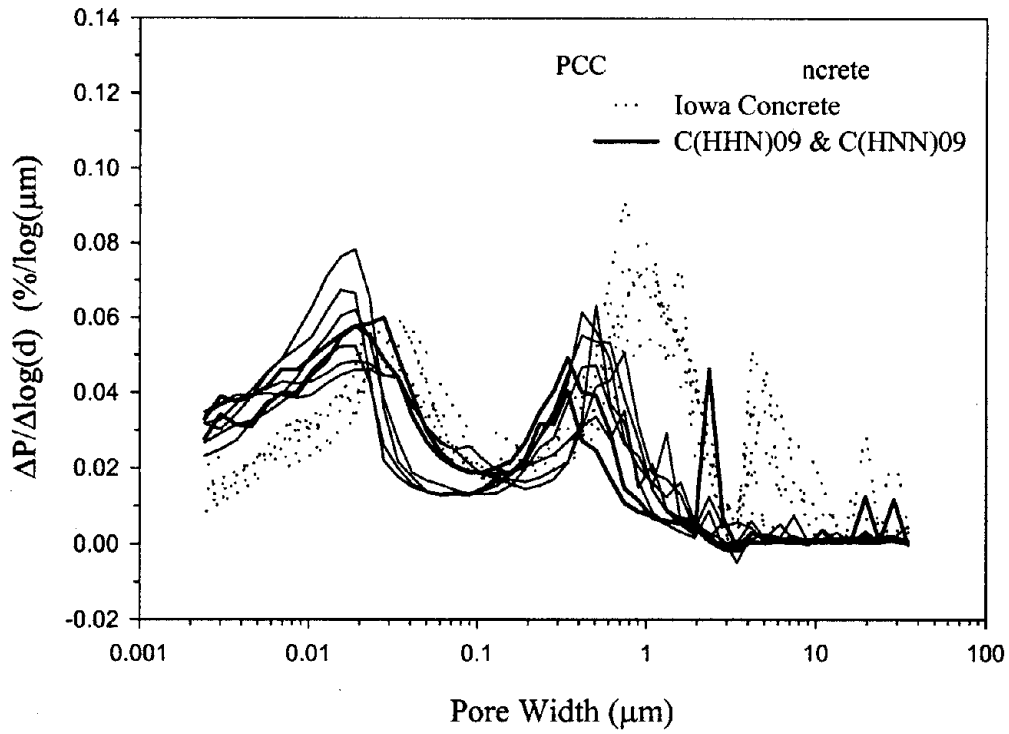


Figure 110: Average differential pore size distribution vs. pore width plot for laboratory-created CFA-C and Iowa U.S. 20 concrete.

3. With respect to the finer system of pores, the CFA-C concrete treated with high AA best modeled the slab concrete though the resulting pores were modestly finer than those of the slab concrete.

5.6.5. Effective Surface Area

The slab concrete's surface area results, though appearing less erratic than the laboratory concrete, varied as much as 50 percent for samples of the same age, materials, and location of removal from the slab. The cause of this variation was also attributed to the unknown coarse aggregate content.

In conclusion:

1. Attempts at measuring surface area were not consistent enough to allow a comparison between laboratory and slab concretes beyond the observation that measured values were of the same order of magnitude.

5.6.6. Mineralogy

Seven slab samples and 11 CFA-C prism samples were subject to XRPD. Table 99 lists phases that were identified with high certainty in both the slab concrete and the CFA-C prisms. No significant differences were seen in the types of phases identified in the two types of concrete or the number of times those phase were identified.

Albite ($\text{NaAlSi}_3\text{O}_8$), calcite (CaCO_3), gypsum ($\text{CaSO}_4 \cdot 2\text{H}_2\text{O}$), ettringite ($\text{Ca}_6\text{Al}_2(\text{SO}_4)_3(\text{OH})_{12} \cdot 26\text{H}_2\text{O}$), portlandite ($\text{Ca}(\text{OH})_2$), and quartz (SiO_2) were all successfully identified in the U.S. 20 slab concrete and the experimental CFA-C concrete prisms.

Comparisons of the abundance of each of these quantified phases in the slab and laboratory concretes can be found in figures 111 and 112. The comparisons are drawn using box plots. The dark line through the middle of the box represents the median value for all points in the data set. The top and bottom of the gray box represent the 75th and 25th percentiles of the data distribution, respectively. The extended line above the box indicates the 90th percentile and the similar line below the box indicates the 10th percentile. Data points outside the 10th and 90th percentiles are shown as individual points.

Figures 111 and 112 show that the range of values for each of the mineral phases quantified in the seven samples of the slab concrete are similar to the range of values found for the CFA-C concrete prisms that underwent various levels and combinations of the three accelerated aging methods. Albite ($\text{NaAlSi}_3\text{O}_8$), calcite (CaCO_3), ettringite ($\text{Ca}_6\text{Al}_2(\text{SO}_4)_3(\text{OH})_{12} \cdot 26\text{H}_2\text{O}$), and portlandite ($\text{Ca}(\text{OH})_2$) concentrations were not affected by any of the accelerated aging concentrations. Gypsum ($\text{CaSO}_4 \cdot 2\text{H}_2\text{O}$) was shown to have a decreased concentration due to the effect of heat aging and the effect of freeze-thaw treatment. Quartz (SiO_2) concentration showed a decrease in response to the freeze-thaw treatment.

Table 99: Phases identified in both CFA-C prism and U.S. 20 slab.

PDF No.	Name	Chemical formula
02-0083	Calcium Aluminum Oxide Hydrate	$\text{Ca}_3\text{Al}_2\text{O}_6 \cdot \text{H}_2\text{O}$
04-0733	Portlandite, syn	$\text{Ca}(\text{OH})_2$
05-0586	Calcite, syn	CaCO_3
09-0466	Albite, ordered	$\text{NaAlSi}_3\text{O}_8$
28-0775	Calcium Oxide	CaO
29-0287	Tacharanite	$\text{Ca}_{12}\text{Al}_2\text{Si}_{18}\text{O}_{51} \cdot 18\text{H}_2\text{O}$
29-1489	Halloysite-10A	$\text{Al}_2\text{Si}_2\text{O}_5(\text{OH})_4 \cdot 2\text{H}_2\text{O}$
33-0311	Gypsum, syn	$\text{CaSO}_4 \cdot 2\text{H}_2\text{O}$
36-0426	Dolomite	$\text{CaMg}(\text{CO}_3)_2$
41-1451	Ettringite, syn	$\text{Ca}_6\text{Al}_2(\text{SO}_4)_3(\text{OH})_{12} \cdot 26\text{H}_2\text{O}$
46-1045	Quartz, syn	SiO_2
46-1312	Wustite	FeO
48-0692	Potassium Iron Oxide	$\text{K}_6\text{Fe}_2\text{O}_5$
21-1258	Ringwoodite, ferroan	$(\text{Mg,Fe})_2\text{SiO}_4$
35-1393	Magnesium Iron Oxide	$\text{Mg}_{1-x}\text{Fe}_x\text{O}$

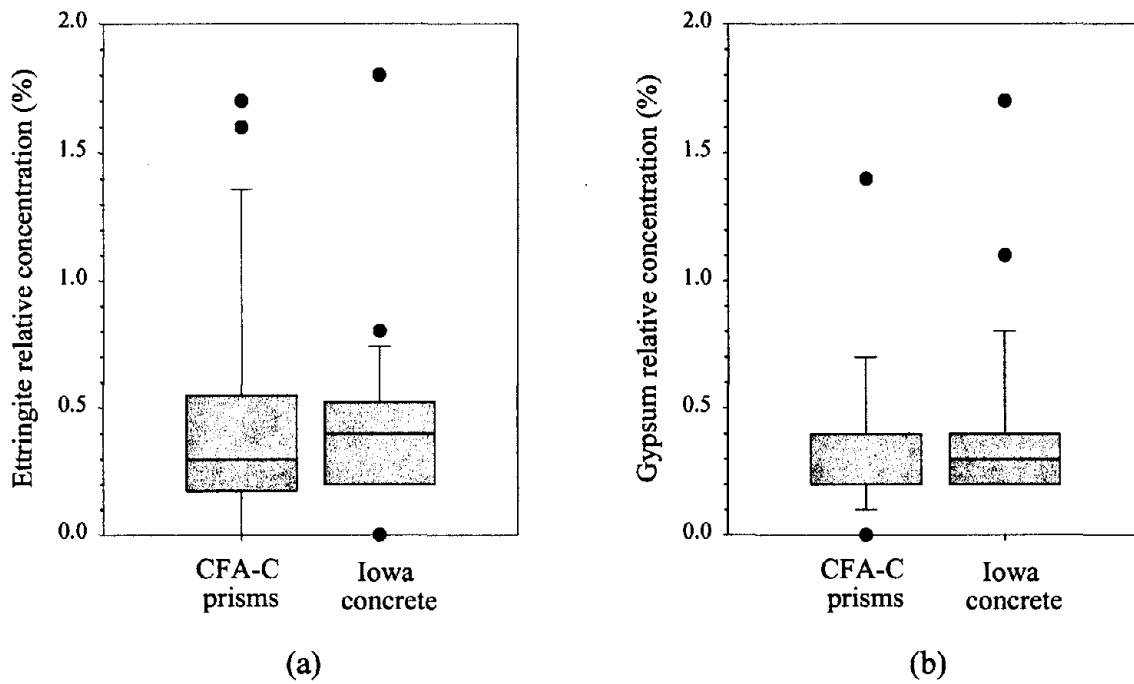
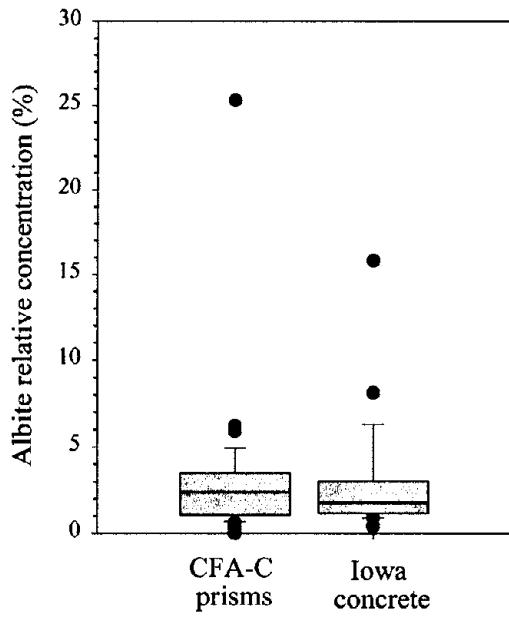
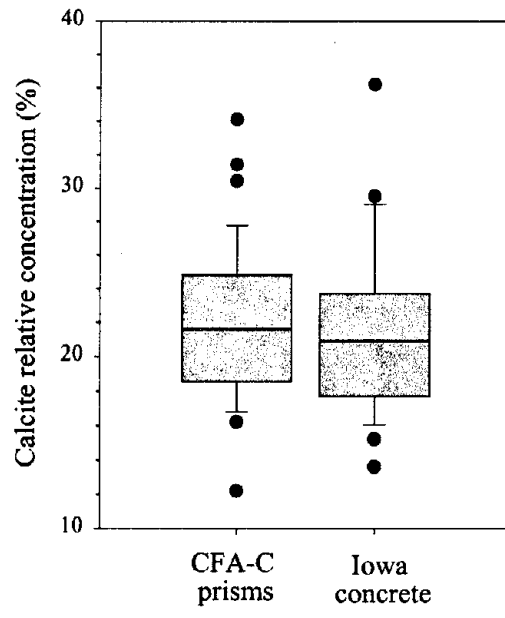


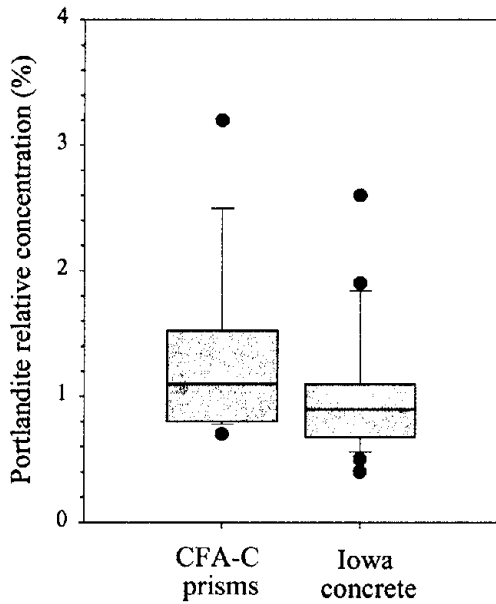
Figure 111: Comparison of mineral concentrations in U.S. 20 concrete and CFA-C prisms: (a) ettringite, (b) gypsum.



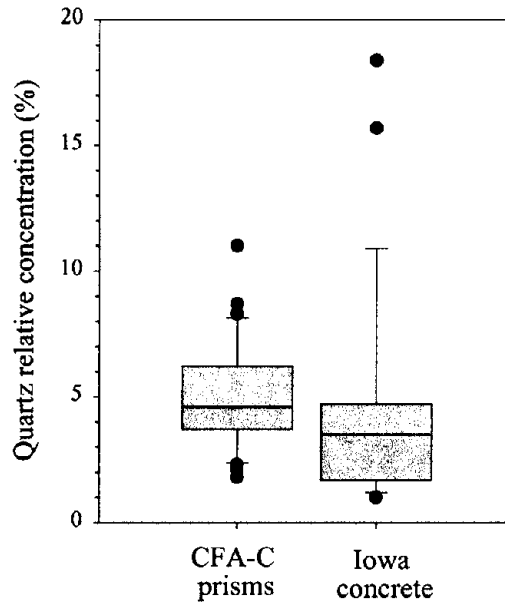
(a)



(b)



(c)



(d)

Figure 112: Comparison of mineral concentrations in U.S. 20 concrete and experimental CFA-C prisms: (a) albite, (b) calcite, (c) portlandite, (d) quartz.

The design of the laboratory concrete appropriately replicated the mineralogy found in the slab sample for the six mineral phases quantified. Effects of the accelerated aging on concentrations of gypsum ($\text{CaSO}_4 \cdot 2\text{H}_2\text{O}$) and quartz (SiO_2) produced results still within an agreeable range for concentrations found in the slab concrete. For these two mineral phases the accelerated aging process adequately reproduced concentrations found in the slab sample.

In conclusion:

1. Laboratory and slab concretes compared well to each other with respect to mineral composition (see sections 5.3.6 and 5.5.7.3).

5.6.7. pH-Dependent Leaching and Solid Phase Control

5.6.7.1 Alkalinity and Constituent Solubility as a Function of pH

Acid neutralization capacity curves from CFA-C mix (28-d cured sample) and U.S. 20 concrete samples at two locations (e.g., northwest region - sample I-JC - and southeast region - sample O-SC) are compared in figure 113. Differences in pH reached for the same amount of acid added were observed between the two slab samples and CFA-C mix sample within the pH range of 10 to 6. This may be due to sample heterogeneity in terms of aggregates. Based on the acid required to reach pH 11.9, the quantity of $\text{Ca}(\text{OH})_2$ produced during the hydration reactions of the cement was estimated at 18.6 g/kg of dry material (e.g., 41 kg/m³ of porous material) for sample I-JC, 16.7 g/kg of dry material (e.g., 37 kg/m³ of porous material) for sample O-SC, and 22.6 g/kg of dry material (e.g., 57 kg/m³ of porous material) for C(XXX)02.

No significant difference with respect to solubility as a function of pH for each of the trace metals of concern was observed between the two slab samples and 28-d cured CFA-C mix sample (see figure 114).

5.6.7.2 pH-Stat Leaching

Seven slab samples were subjected to pH-dependent leaching and the results are compared with the 11 CFA-C concrete prisms, which underwent the same leaching process. For each analyte, the range of leached concentrations of the slab concrete is compared with the range of leached concentration from the experimental CFA-C concrete prisms. Results of the geochemical modeling of the slab and laboratory concrete are compared as well.

Comparisons of Ca, Mg, Al, and Si leaching in the slab concrete and the experimental CFA-C concrete prisms can be found in figure 115. Ca, Mg, and Si pH-dependent leaching behavior was similar in both concretes. The range of concentrations leached from the laboratory concrete matched well the range of leached values from the slab samples for these three analytes. The leaching of Al from the slab concrete was BDL at the low range of leaching for pH of 5.0, 7.3, and 9.7. In this pH range, the distribution of leached concentrations of Al from the slab concrete extended to lower concentrations than seen in the experimental CFA-C prisms. The

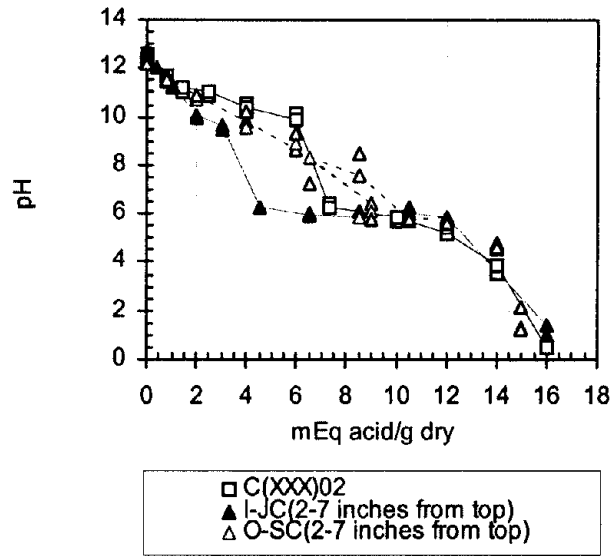


Figure 113: Acid neutralization capacity curves.

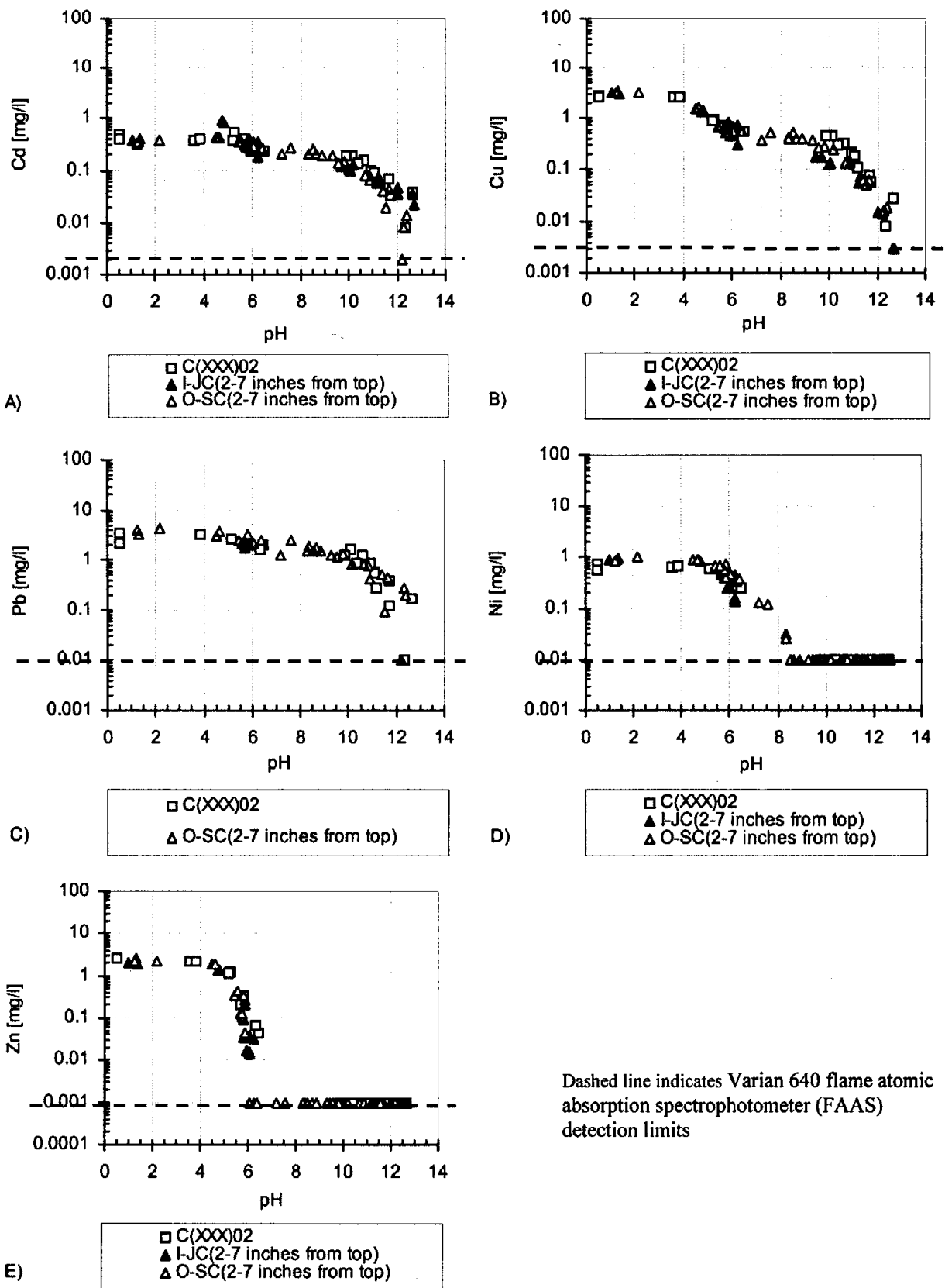
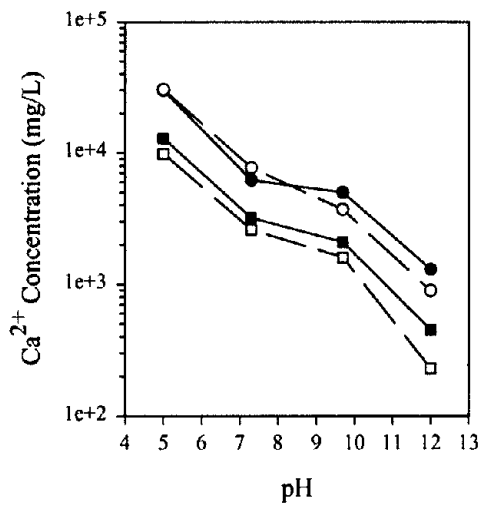
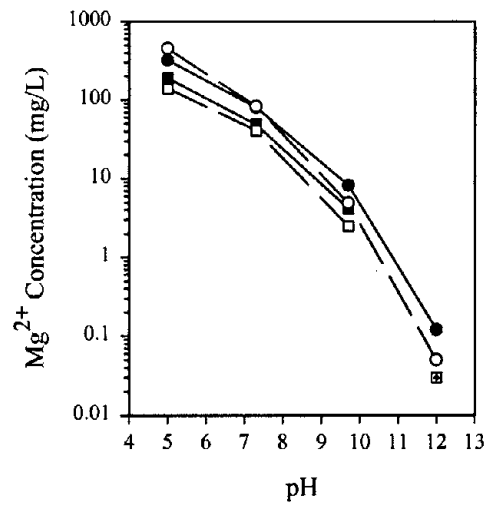


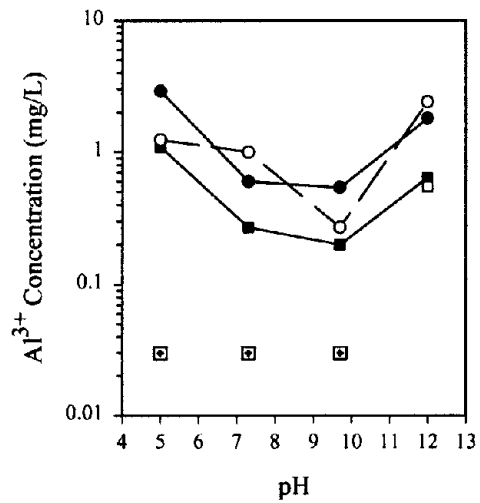
Figure 114: Solubility as a function of pH:
 A) Cd, B) Cu, C) Pb, D) Ni, E) Zn.



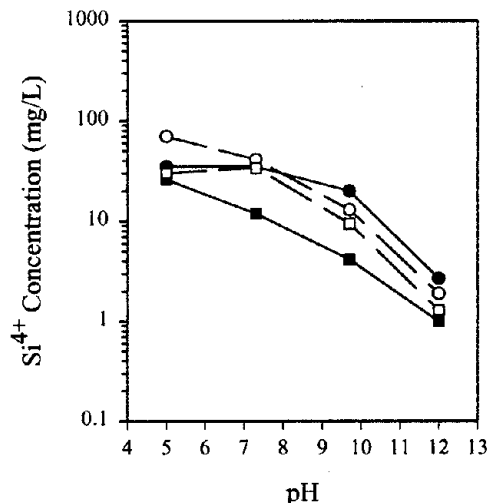
(a)



(b)



(c)



(d)

Figure 115: Comparison of pH-dependent leaching of the experimental CFA-C prism concrete and the U.S. 20 slab concrete:

(a) Ca, (b) Mg, (c) Al, (d) Si.

Experimental Prism Concrete:

- highest value
- highest value BDL
- lowest value
- lowest value BDL

Iowa Slab Concrete:

- highest value
- ⊙ highest value BDL
- lowest value
- ⊠ lowest value BDL

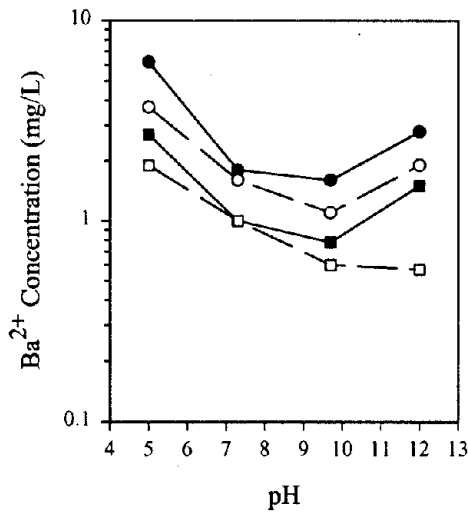
highest values of Al leaching from the slab concrete matched well with the range of leached concentrations from the experimental CFA-C concrete prisms.

Figure 116 depicts the leaching behavior of Ba, Zn, Fe, and Cr in the slab concrete and the experimental CFA-C concrete prisms. The ranges of Ba leaching for the two concretes overlapped throughout the entire pH range and both exhibit a typical amphoteric curve with a minimum around pH of 10. The lowest values of Zn leached from the slab concrete with BDL at pH of 5.0, 7.3, and 9.7. While the highest concentration of Zn leached from the slab concrete generally agreed with the range of leached concentration from the laboratory concrete, the curve of the highest values from the slab concrete exhibited an amphoteric curve, typical for Zn leaching (van der Sloot et al., 1994), not seen in the high or low curves of the experimental prism concrete leaching. Comparison of the leaching curves for Fe and Cr in the two types of concrete is not possible due to a high number of BDL samples at various pHs. In general the leaching of Fe from the slab concrete was lower at pH of 5.0 and pH of 7.3, but similar in concentration at pH of 9.7 and pH of 12.0 to the CFA-C concrete. The leaching of Cr from the slab concrete cannot be compared with the laboratory concrete at the lower pH points, but at the high pH points Cr^{3+} leaching appears to be greater in the slab concrete than the experimental concrete.

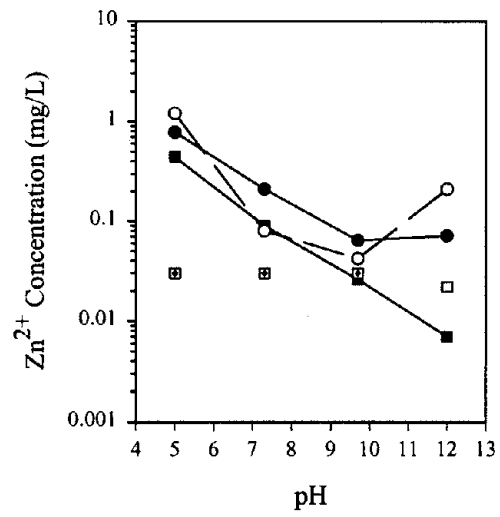
Figure 117 shows the leaching ranges for K, Cl, CO_3^{2-} , and SO_4^{2-} from the slab concrete and the experimental CFA-C concrete. K exhibited pH-independent leaching for both concretes. The range of leached concentration from the slab concrete was much larger than the experimental concrete concentration ranges, but the ranges were in general agreement. The data for Cl⁻ leaching is incomplete due to BDL values for the entire lower range of leaching for both the slab and experimental concretes. Where data were available at the highest concentration, there was good agreement between the two types of concrete. The concentrations of CO_3^{2-} from the two concretes exhibit adequate agreement in concentration and behavior at pH of 7.3 and 9.7. At a pH of 5.0 the detection of CO_3^{2-} from the two concretes do not agree in behavior and show only minimal overlap in concentration. The slab concrete generally decreased in leached CO_3^{2-} concentration from pH 5.0 to pH of 7.3 while the experimental CFA-C concrete showed a general increase in concentration over the same pH range. The range of CO_3^{2-} concentrations in the slab concrete at pH of 12.0 was quite large, but did not overlap with the concentration range of the experimental concrete. These differences in CO_3^{2-} concentration may be explained by difficulty experienced in attaining accuracy with the Total Alkalinity Method used to quantify CO_3^{2-} concentration. The leaching behavior and concentrations of SO_4^{2-} in the slab and experimental CFA-C concretes showed good agreement at the high end of the range of leached values. At pH of 5.0, the lowest values of SO_4^{2-} concentration leached from the concrete agreed, but at high pHs the SO_4^{2-} levels in slab concrete leachates were BDL.

5.6.7.3 Geochemical Modeling

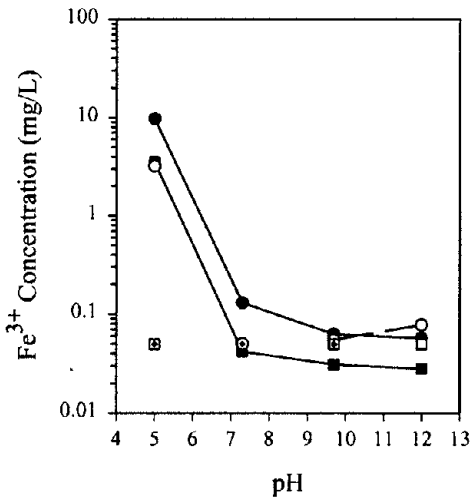
Geochemical modeling of Ca, Mg, Al, Si, Ba, Zn, Fe, Cr, CO_3^{2-} and SO_4^{2-} leaching from the slab concrete and the experimental CFA-C concrete prisms are summarized in table 100. Figures M-1 through M-10 in appendix M of volume II show side-by-side comparisons of the two concretes and reveal that geochemical modeling resulted in similar modeling of candidate controlling solids.



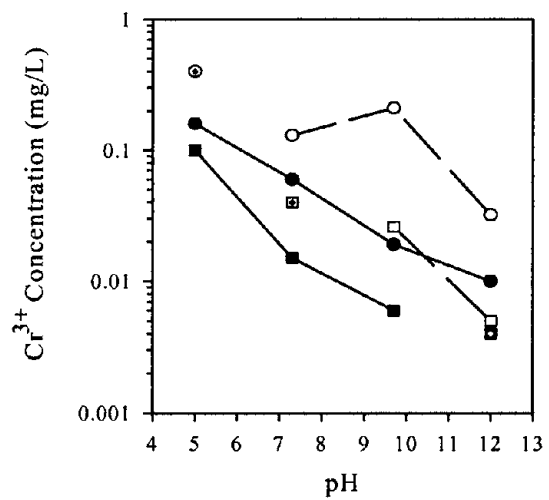
(a)



(b)



(c)



(d)

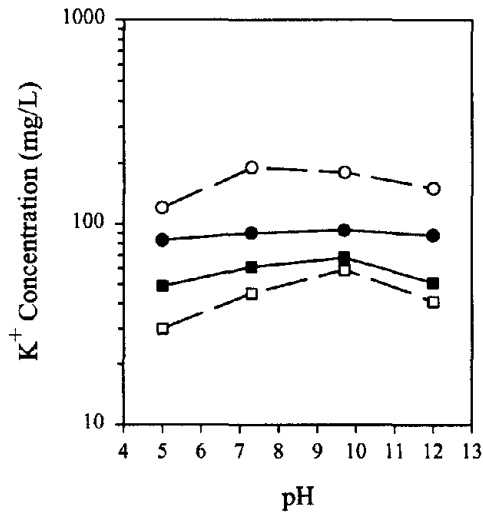
Figure 116: Comparison of pH-dependent leaching of the experimental CFA-C prism concrete and the U.S. 20 slab concrete: (a) Ba, (b) Zn, (c) Fe, (d) Cr.

Experimental Prism Concrete:

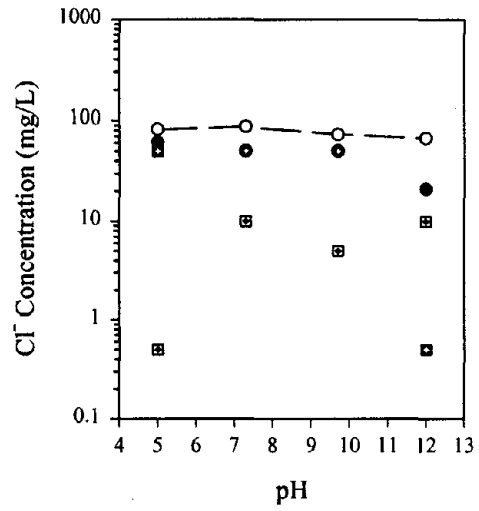
- highest value
- highest value BDL
- lowest value
- lowest value BDL

Iowa Slab Concrete:

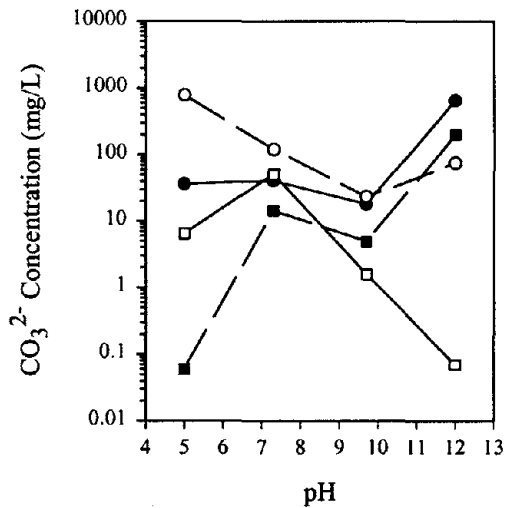
- highest value
- ⊙ highest value BDL
- lowest value
- ⊠ lowest value BDL



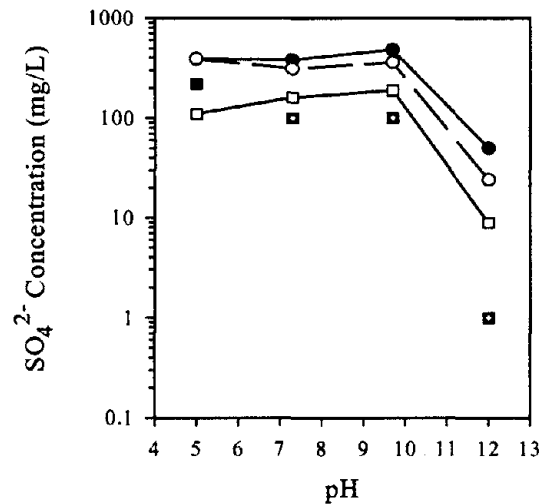
(a)



(b)



(c)



(d)

Figure 117: Comparison of pH-dependent leaching of the experimental CFA-C prism concrete and the U.S. 20 slab concrete: (a) K, (b) Cl, (c) CO₃²⁻, (d) SO₄²⁻.

Experimental Prism Concrete:

- highest value
- highest value BDL
- lowest value
- lowest value BDL

Iowa Slab Concrete:

- highest value
- ⊙ highest value BDL
- lowest value
- lowest value BDL

Table 100: Geochemical modeling species for the CFA-C prism and U.S. 20 slab concrete.

Species	Solid Phase	log K_{sp}	Well modeled pH range	
			CFA-C prisms	Iowa slab
Al	Gibbsite $Al(OH)_3$	-8.291	none	none
	$Al(OH)_3$ amorphous	-10.800	none	none
	Ettringite $(Ca_6Al_2(SO_4)_3(OH)_{12} \cdot 26H_2O)$	-56.700	none	none
Ba	$BaCrO_4$	9.670	5 - 10	none
	Barite ($BaSO_4$)	9.980	5 - 12	5 - 12
Ca	Gypsum ($CaSO_4 \cdot 2H_2O$)	4.610	5 - 12	5 - 12
	Portlandite ($Ca(OH)_2$)	-22.804	none	none
	Calcite ($CaCO_3$)	8.480	5 - 12	5 - 12
	Dolomite ($CaMg(CO_3)_2$)	16.540	5 - 12	5 - 12
	Ettringite $(Ca_6Al_2(SO_4)_3(OH)_{12} \cdot 26H_2O)$	-56.700	7 - 12	7 - 12
CO ₃	Calcite ($CaCO_3$)	8.480	7 - 10	7 - 12
	Dolomite ($CaMg(CO_3)_2$)	16.540	7 - 10	7 - 12
Cr	$BaCrO_4$	9.670	none	none
Fe	Ferrihydrite ($Fe(OH)_3$)	-3.191	none	none
	Maghemite (Fe_2O_3)	-6.386	none	none
Mg	Dolomite ($CaMg(CO_3)_2$)	16.540	5 - 10	5 - 12
	Brucite ($Mg(OH)_2$)	-16.844	~12	~12
Si	Quartz (SiO_2)	4.000	none	none
	SiO_2 amorphous gel	2.710	5 - 7	5 - 7
SO ₄	Gypsum ($CaSO_4 \cdot 2H_2O$)	4.610	7 - 10	7 - 10
	Barite ($BaSO_4$)	9.980	5 - 12	5 - 12
	Ettringite $(Ca_6Al_2(SO_4)_3(OH)_{12} \cdot 26H_2O)$	-56.700	10 - 12	none
Zn	Zincite ($Zn(OH)_2$)	-11.334	none	none

Ca Modeling. As shown in figure M-1, Ca leaching was well modeled over the entire pH range by calcite (CaCO_3), dolomite ($\text{CaMg}(\text{CO}_3)_2$), and gypsum ($\text{CaSO}_4 \cdot 2\text{H}_2\text{O}$). Ettringite ($\text{Ca}_6\text{Al}_2(\text{SO}_4)_3(\text{OH})_{12} \cdot 26\text{H}_2\text{O}$) modeled well as a possible controlling solid at pH greater than 7.3. Portlandite (CaOH_2) modeling concentrations were higher than the observed Ca concentrations in both concretes. Calcite, dolomite, and gypsum are likely controlling solids for Ca leaching from the CFA-C concrete prisms and the slab concrete.

Mg Modeling. Figure M-2 shows the geochemical modeling of Mg with candidate controlling solids dolomite ($\text{CaMg}(\text{CO}_3)_2$) and brucite ($\text{Mg}(\text{OH})_2$). Brucite can be a reaction product of MgO often found in CFA-C. Brucite modeling was only adequate at pH of 12.0. At other pHs the predicted Mg concentration was much greater than the observed data. Dolomite modeled showed satisfactory agreement from pH of 5.0 to pH of 9.7 in the CFA-C concrete prisms. The predicted concentration of Mg and the shape of the dolomite modeling curve deviated from the observed data at pH of 12.0. Good agreement was seen for dolomite in the slab concrete over the entire pH range for both concentration and shape of the leaching curve.

Al Modeling. Figure M-3 shows the modeling of Al with ettringite ($\text{Ca}_6\text{Al}_2(\text{SO}_4)_3(\text{OH})_{12} \cdot 26\text{H}_2\text{O}$), gibbsite ($\text{Al}(\text{OH})_3$), and amorphous $\text{Al}(\text{OH})_3$ for the CFA-C concrete prisms and the slab concrete. Results for the two concretes were similar. Ettringite was not a good model for the leaching of Al from either concrete. Gibbsite was the best match of the three controlling solids, but the range of minimum solubility was shifted to a lower pH than was demonstrated for the experimental data. Al leaching in cement-based systems can be controlled by the hydrated Ca species, which are not included in the MINTEQA2 database (Glasser, 1997).

Si Modeling. Si was modeled for both crystalline and amorphous SiO_2 in figure M-4. Neither solid adequately described the leaching behavior of Si observed in the slab concrete or the CFA-C concrete prisms. Similar difficulties in Si modeling have been reported previously (Eighmy et al., 1994, Fruchter 1990). The Ca-Al-silicates abundant in the concrete matrix may be a source of controlling solids for Si leaching, but these species are not present in the MINTEQA2 database and therefore were not modeled.

Ba Modeling. Figure M-5 depicts the modeling of Ba leaching by barium chromate (BaCrO_4) and barite (BaSO_4). BaCrO_4 demonstrated a reasonable match in concentration between the predicted and observed data for the entire pH, but the shape of the modeled curve was in good agreement only from pH of 5.0 to pH of 9.7. Barite modeling agreed well with the observed leaching data for both concretes over the entire pH range examined. Barite is a likely controlling solid in the CFA-C concrete prisms and the slab concrete.

Zn Modeling. Figure M-6 shows that the leaching behavior of Zn was unsuccessfully modeled by zincite for the CFA-C concrete prisms and the slab concrete. Other work has suggested that Zn sorbs to metal oxides which then control the solubility of Zn (EPRI, 1987; van der Sloot et al., 1994).

Fe Modeling. Geochemical modeling of Fe leaching was performed for candidate controlling solids ferrihydrite ($\text{Fe}(\text{OH})_3$) and maghemite (Fe_2O_3) (see figure M-7). Neither solid adequately modeled the leaching of Fe from the CFA-C concrete prisms or the slab concrete.

Fe(OH)₃ has been identified as a likely controlling solid based on thermodynamic data (EPRI, 1987), but in modeling applications problems of agreement between observed and predicted data have been shown (Fruchter, 1990).

Cr Modeling. Figure M-8 depicts the modeling of Cr with barium chromate (BaCr⁶⁺O₄). The predicted leaching curve of this solid agreed well with the leaching observed leaching trends of Cr from the CFA-C concrete prisms, but the predicted concentrations were considerably higher than the observed data. Cr leaching from the slab concrete could not be fully modeled due to a high number of data points that were BDL. In the pH range where modeling was possible BaCrO₄ modeling showed poor agreement with the concentration and leaching trends of the observed data. Cr³⁺ has been shown to substitute for Al³⁺ in cement hydration products and is then part of the Ca Al hydrates matrix (Glasser, 1997). Cr³⁺ solubility is then limited by these cement species rather than more common Cr oxides and hydroxides that would be found in the MINTEQA2 database. Since Cr leaching may be controlled by Ca Al species, related differences between the concretes, though not discernable in these analyses, may contribute to observed differences in the leaching behaviors.

CO₃²⁻ Modeling. Figure M-9 depicts the leaching behavior of CO₃²⁻ in the CFA-C concrete prisms and the slab concrete modeled by controlling solids calcite (CaCO₃) and dolomite (CaMg(CO₃)₂). Calcite and dolomite produced better agreement with the observed data from the slab concrete than from the observed data of the CFA-C concrete prisms. This difference may be related to differences in cracking and carbonation of the concretes. It may also reflect the difficulty in attaining accuracy in the total alkalinity measurement of the leached concrete samples from which the CO₃²⁻ concentration is derived.

SO₄²⁻ Modeling. SO₄²⁻ leaching is modeled by gypsum (CaSO₄•2H₂O), barite (BaSO₄), and ettringite (Ca₆Al₂(SO₄)₃(OH)₁₂•26H₂O) (see figure M-10). Similar results were seen for the CFA-C concrete prisms and the slab concrete. Barite was a good match of the modeling of the leaching data over the entire pH range for both types of concrete. Gypsum modeling data was within concentration limits for most of the pH range but did not match well in the shape of the curve. Ettringite was not a well-modeled solid. Barite appears to be a controlling solid for SO₄²⁻ leaching (EPRI, 1987).

5.6.7.4 Conclusions

In conclusion:

1. The acid neutralization of the laboratory concretes matched well that of the slab concretes (see section 5.3.8.1 and figure 47).
2. Solubility curves matched well in shape and magnitude to those of the slab concrete (see section 5.3.8.1 and figure 48).
3. General agreement in the leaching was found for Ca, Mg, Al, Si, Ba, Zn, Fe, Cl, K, CO₃²⁻ and SO₄²⁻.

4. Cr leaching was not in good agreement between the two sample types
5. Similar results were observed for modeling solid phase control of the CFA-C concrete prisms and the slab concrete.
6. The controlling solids identified for the CFA-C concrete prisms and the slab concrete appear similar to and typical of cement-based leaching.
7. As with hydrated cement paste and the slab concretes, calcite and dolomite are likely controlling solids for Ca leaching from the slab concrete. For the laboratory concrete, gypsum is also a likely controlling solid.
8. As with the hydrated cement paste and slab concrete, dolomite is a likely controlling solid for Mg leaching.
9. Unlike the hydrated cement paste for which barium chromate was better, but like the slab concrete, barite is a likely controlling solid for Ba.
10. Like the slab concrete, barite is a likely controlling solid for SO_4^{2-} leaching.

5.6.8. Low Liquid-Solid Ratio Leaching

pH and conductivity as a function of the liquid-solid ratio (e.g., LS ratio of 10, 5, 2, 1 and 0.5 ml/g of dry material) of the 28-d cured CFA-C mix (e.g., C(XXX)02), a high AA aged CFA-C mix (e.g., C(HNN)13) and the U.S. 20 concrete sample (e.g., O-SC) are compared in figure 118.

pH data obtained for the U.S. 20 concrete sample were overall slightly greater (e.g., 0.2 to 0.4 pH unit) than that for C(XXX)02 and C(HNN)13. Slightly greater conductivities were also observed for the U.S. 20 concrete sample at LS less than 2 ml/g dry.

Much greater Na and K concentrations (see figure 119 a and b, respectively) were observed for the U.S. 20 concrete sample at LS less than 5 ml/g dry. However, no significant differences in Cl, SO_4^{2-} , and Ca concentrations were observed between the three materials.

Table 101 provides a comparison of the physical and chemical properties measured at LS of 5 ml/g dry for each sample and the estimated values for the pore water in each case. Similar physical properties were obtained for the three materials. Although much greater Na and K concentrations were experimentally observed at low LS for the U.S. 20 concrete sample, similar ionic strength of the pore water was estimated for both the 28-d cured CFA-C sample and the U.S. 20 concrete sample. However, a much lower ionic strength of the pore water was estimated for the high AA aged CFA-C sample.

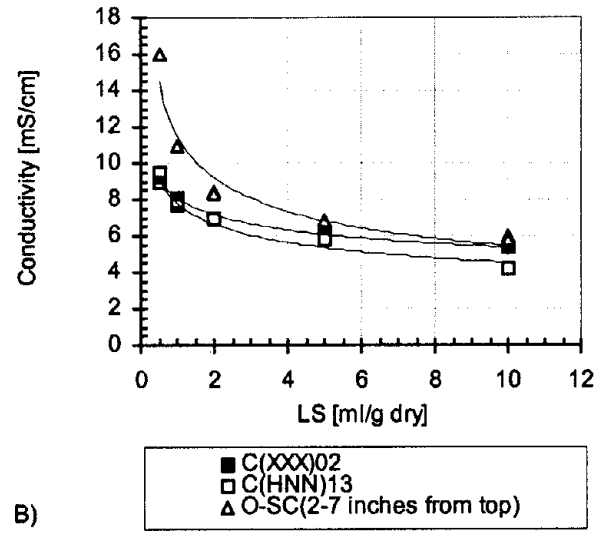
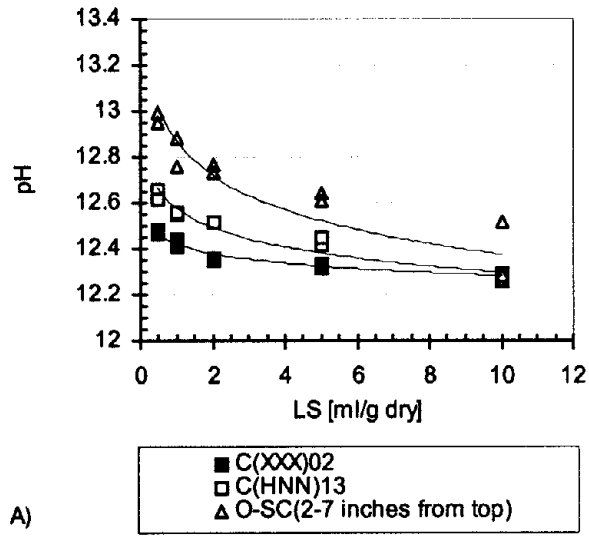


Figure 118: A) pH and B) conductivity as a function of LS ratio.

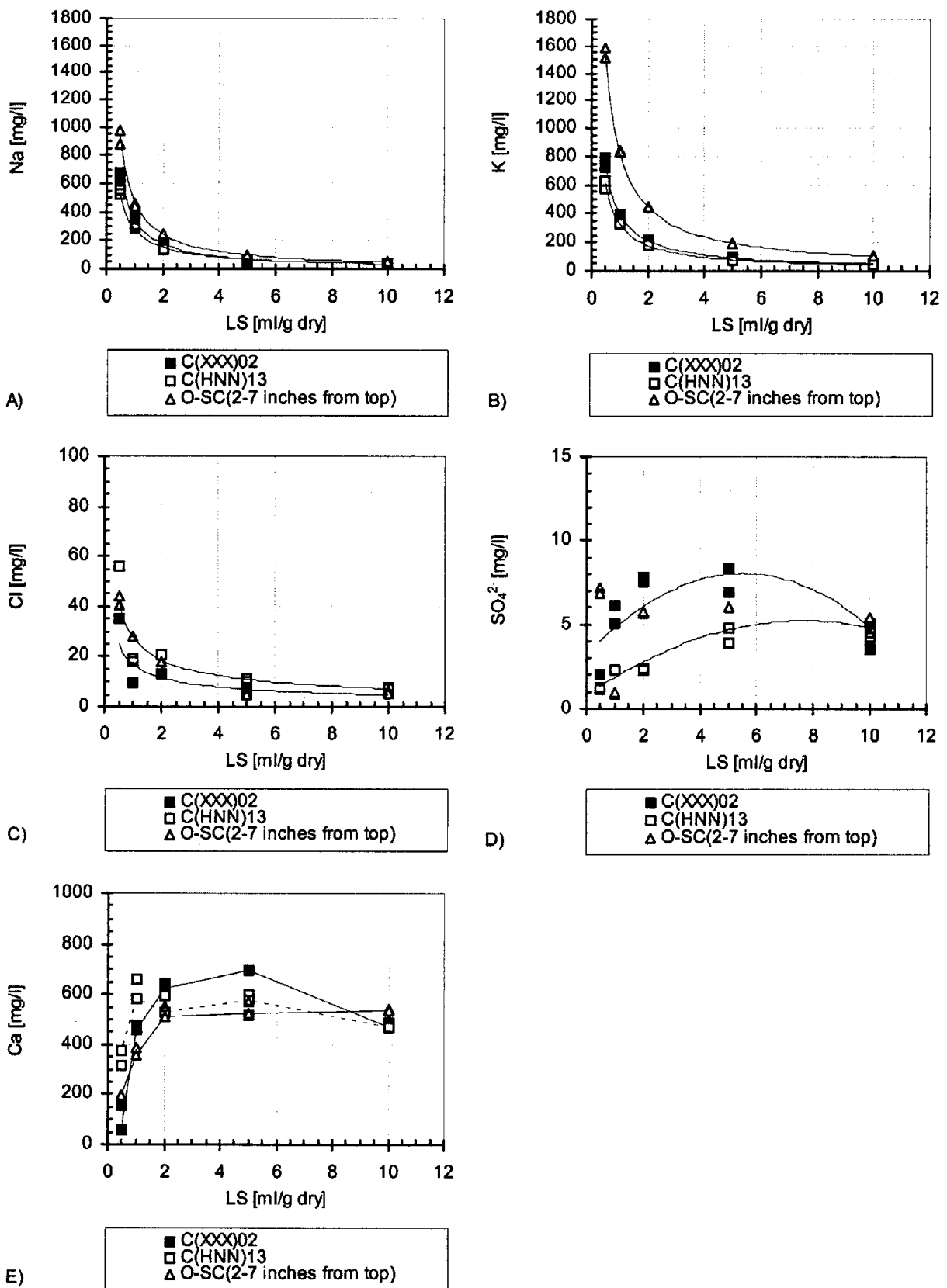


Figure 119: Major species concentration as a function of LS ratio:
 A) Na, B) K, C) Cl, D) SO_4^{2-} , E) Ca.

Table 101: Physical properties of 28-d cured CFA-C, high temperature-aged CFA-C, and U.S. 20 slab concrete sample and chemical properties of leachates and pore water.

Physical or chemical property	Material type		
	C(XXX)02	C(HNN)13	O-SC (Southeast region)
Moisture content (%)	3	3	3.2
Density (g/cm ³)	2.7	2.5	2.3
Open porosity (%)	8	7.4	7.4
LS estimated for p.w. ^a (ml/g)	0.03	0.03	0.03
pH (standard units)			
at LS 5	12.3	12.5	12.6
Estimated for p.w.	12.7	13	13.7
Na (mg/l)			
at LS 5	63	62	94
Estimated for p.w.	11,908	6,477	12,005
K (mg/l)			
at LS 5	90	80	193
Estimated for p.w.	10,043	7,597	19,783
Cl (mg/l)			
at LS 5	6	11	4.9
Estimated for p.w.	117	221	410
SO ₄ ²⁻ (mg/l)			
at LS 5	8	4.5	6
Estimated for p.w.	0.8	0.8	6
Ca (mg/l)			
at LS 5	519	591	548
Estimated for p.w.	< 50	< 50	108
Ionic strength (mol/l)			
at LS 5	0.05	0.05	0.06
Estimated for p.w.	1.2	0.7	1.3
Activity coefficient			
charge ± 1			
at LS 5	0.85	0.85	0.82
Estimated for p.w.	0.73	0.71	0.74
charge ± 2			
at LS 5	0.53	0.53	0.46
Estimated for p.w.	0.29	0.26	0.30

^a p.w. – pore water

In conclusion:

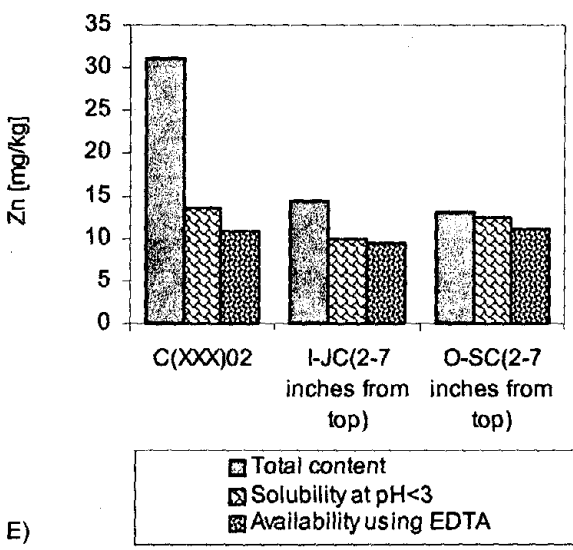
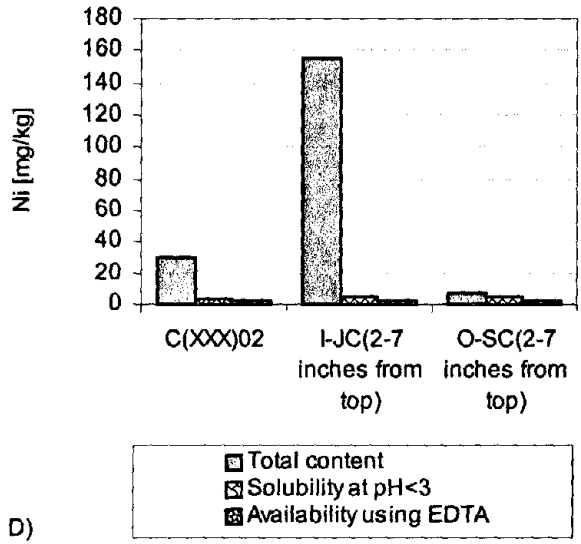
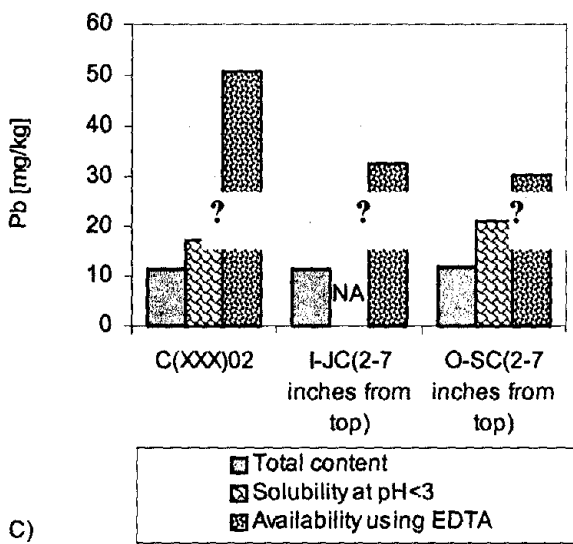
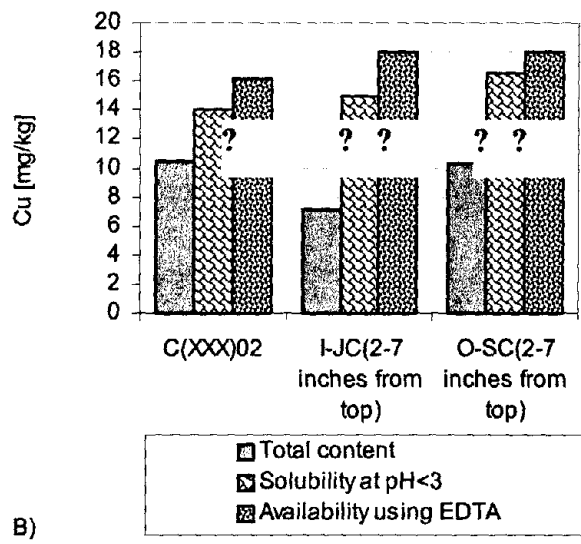
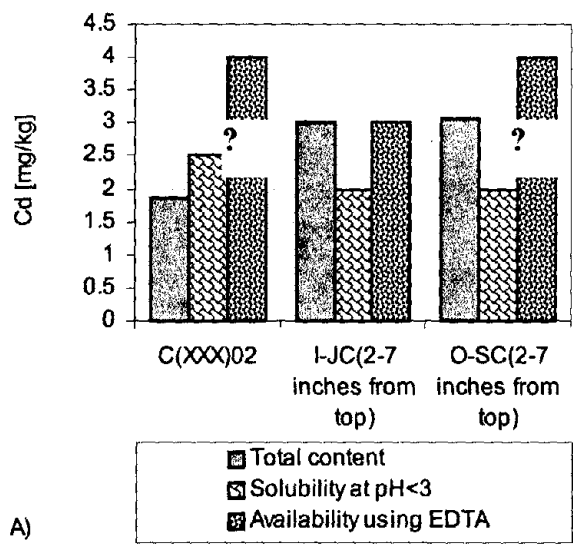
1. As with the slab concrete, conductivity and Na, Cl, and K concentrations increase significantly with decreasing LS ratios.
2. pH increases from approximately 12.2 to 12.5 for the CFA-C and CFA-F concrete and from 12.6 to 12.8 for the PCC, whereas for the slab concrete, pH increased from 12.4 to 13 with decreasing LS ratios.
3. As with the slab concrete, SO_4^{2-} concentration appeared to be independent of the LS ratio.
4. Consistent with pH changes, Ca concentration (see figure 63) decreased with the LS ratio.
5. The estimated LS concentration and pH of the pore water in the slab concrete were 0.03 ml/dry gram and 12.7 to 13.0, respectively. (The slab concrete values were 0.03 and 13.7.)

5.6.9. Availability Leaching

Cd, Cu, Ni, Pb and Zn availability for 28-d cured CFA-C sample (e.g., C(XXX)02), I-JC sample (e.g., from the northwest region), and O-SC sample (e.g., from the southeast region), as determined by the RU-AV002.0 protocol (e.g., EDTA extraction at pH 7.0), are compared in figure 120. In addition to the availability results, total content as determined by neutron activation analyses or X-ray fluorescence (e.g., NAA or XRF) and maximum release (e.g., maximum reached using the RU-SR002.0 protocol for pH less than 3) are provided for comparison.

In conclusion:

1. No significant difference between the 28-d cured CFA-C mix and U.S. 20 slab was observed with respect to Cd, Cu, Ni, Pb, and Zn availability.
2. For both materials, only a fraction of Ni and Zn was available for leaching under the test conditions, while Cd, Pb, and Cu were completely available.
3. As with the slab concrete, availability values of Cd, Cu, and Pb by EDTA extraction at pH 7.0 exceeded the total content for the two locations as determined by NAA/XRF.
4. As with the slab concrete, availability of Ni and Zn by EDTA extraction at pH 7.0 were found to be lower than the total contents as determined by NAA/XRF.



? Questionable analysis result due to analytical difficulties.

NA Not available.

Figure 120: Comparison between total content, maximum of solubility at pH<3, and availability using EDTA extractions at pH 7.

5.6.10. Monolithic Leaching

5.6.10.1 pH and Conductivity

Final leachate pH and conductivity obtained after each leaching interval for the 28-d cured CFA-C sample (e.g., C(XXX)02), the four high level- aged CFA-C samples (e.g., C(HNN)13, C(NHN)13, C(NNH)13 and C(NNN)13), the three cores taken from the bulk of the U.S. 20 slab (e.g., 7-C (2.5 to 6.5 in from top), 8-C (2.5 to 6.5 in from top) and 9-C (2.5 to 6.5 in from top)) and the core taken from the surface of the U.S. 20 slab (e.g., 9-C (0 to 1.6 in from top)) are compared in figures 121 a, b, and c, respectively. After 10 d of leaching, final leachate pH of the three samples representing the bulk of the U.S. 20 slab appeared to be overall slightly greater than that of CFA-C mix samples (e.g., 28-d cured and high level aged samples). After 60 d of leaching, final leachate pH of the sample representing the surface of the slab was much less than that of CFA-C mix samples and samples representing the bulk of the slab.

As with pH, after 10 d of leaching, conductivity data obtained for the three samples representing the bulk of the U.S. 20 slab were greater overall than that of CFA-C mix samples (e.g., 28-d cured and high level aged samples). However, similar leachate conductivities were observed between the four high level- aged CFA-C samples and the sample representing the surface of the slab.

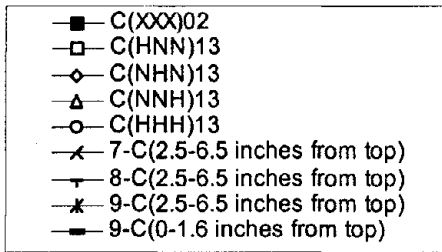
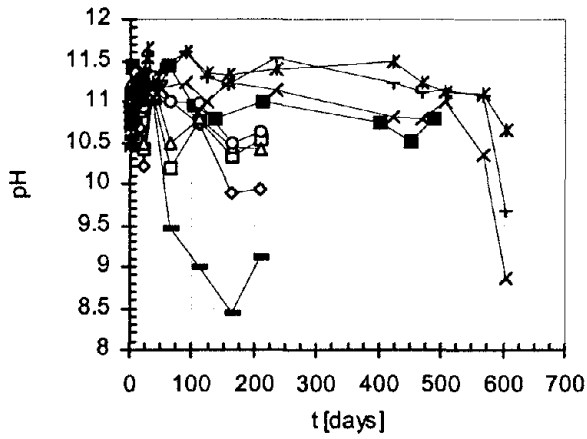
5.6.10.2 Leaching Behavior of Major Species

Release and flux plots for major constituents are shown in figures 122 and M-11 through M-14 in appendix M of volume II.

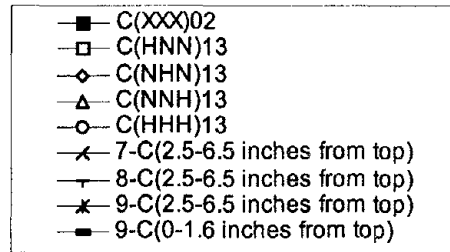
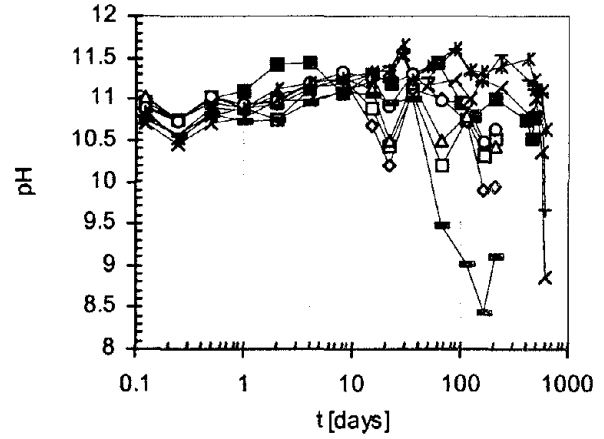
Na Release. A much greater cumulative release of Na was observed for the U.S. 20 concrete samples (figure 122). During the initial 10 d of leaching, the flux of Na from the U.S. 20 concrete samples representing the bulk of the slab was 3 times greater than that from CFA-C mix samples. This result was consistent with a greater Na pore water concentration estimated for the U.S. 20 concrete samples (approximately 12,000 mg/l for the U.S. 20 sample, 11,900 mg/l for the 28-d cured CFA-C sample, and 6,500 for the high temperature-aged CFA-C sample). However, after 10 d of leaching, no significant differences in Na release flux could be observed between the four high level- aged CFA-C samples and the three samples representing the bulk of the U.S. 20 slab. In addition, the flux of Na from the sample representing the surface of the slab was much greater than that from the U.S. 20 bulk samples (e.g., three times greater) and CFA-C mix samples (e.g., six times greater). This may be a result from the use of road salt on the surface of the U.S. 20 slab.

K Release. A much greater cumulative release of K was observed for the U.S. 20 concrete samples (see figure M-11). The flux of K from the U.S. 20 concrete samples was four times greater than that from CFA-C mix samples. This result was consistent with a greater K pore water concentration estimated for the U.S. 20 concrete samples (approximately 20,000 mg/l for the U.S. 20 samples and 10,000 mg/l for the CFA-C mix samples).

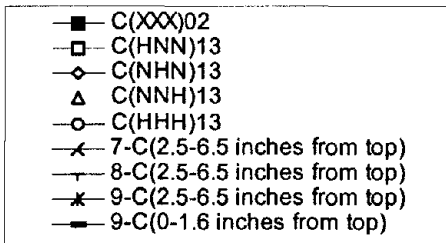
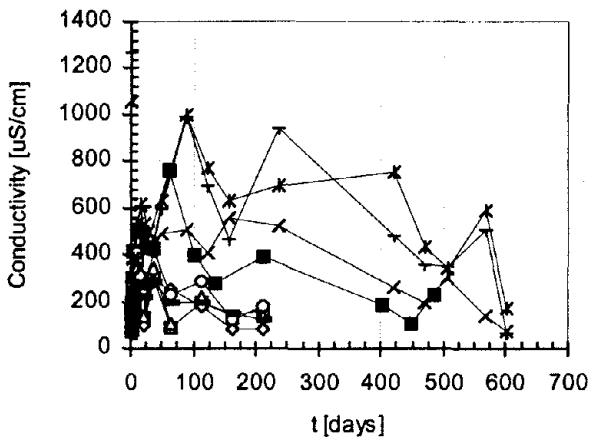
Cl Release. No significant difference in the released flux of Cl could be observed between the U.S. 20 concrete bulk samples and the CFA-C mix samples (see figure M-12).



A)

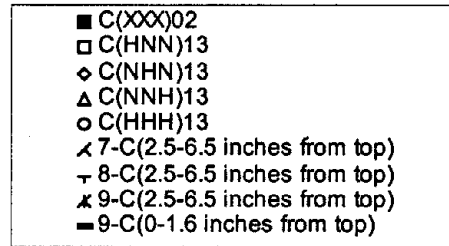
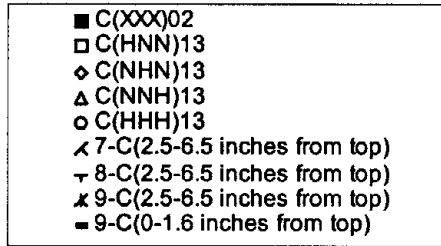
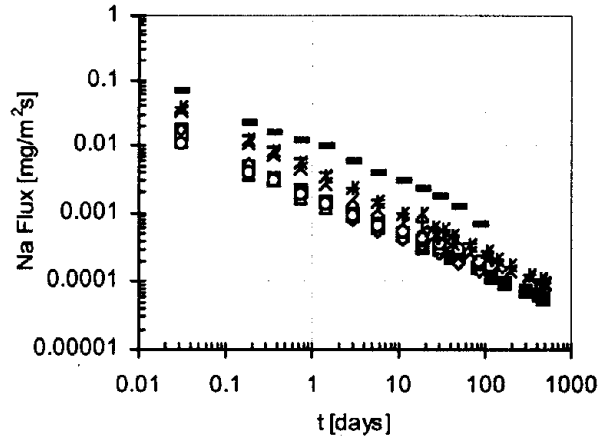
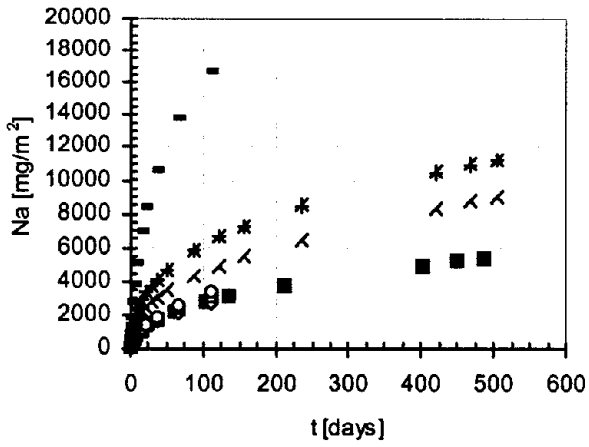


B)



C)

Figure 121: A) leachate pH, B) leachate pH, and C) leachate conductivity.



A)

B)

Figure 122: Na release:
 A) cumulative mass released in mg/m^2 ; B) flux released in $\text{mg}/\text{m}^2\text{s}$.

However, a much greater flux of Cl was observed for the sample representing the surface of the U.S. 20 slab. This also may be a result from the use of road salt on the surface of the U.S. 20 slab.

SO₄²⁻ Release. No significant differences in the cumulative release of SO₄²⁻ could be observed between the 28-d cured CFA-C mix sample and the U.S. 20 concrete bulk samples (see figure M-13). Similarly, no significant differences in the cumulative release of SO₄²⁻ could be observed between the four high level- aged CFA-C samples (e.g., C(HNN)13, C(NHN)13, C(NNH)13, and C(NNN)13) and the sample representing the surface of the U.S. 20 slab. However, a much greater cumulative release of SO₄²⁻ was obtained from the four high level- aged CFA-C samples and the U.S. 20 surface sample than for the unaged CFA-C sample (e.g., C(XXX)02) and the samples from the interior of the slab. Indeed, during the initial 10 d of leaching, the released flux of SO₄²⁻ from these samples was 4 times greater. However, after 10 d of leaching (e.g., at longer leaching intervals), no significant differences in the released flux of SO₄²⁻ could be observed between the materials.

Ca Release. The cumulative release of Ca (figure M-14) from the CFA-C mix samples was much greater than that from the U.S. 20 concrete samples. During the initial 10 d of leaching, the flux of Ca from the CFA-C mix samples was 5 times greater than that from the U.S. 20 concrete samples. After 30 d of leaching, similar flux of Ca could be observed for the U.S. 20 concrete samples and the CFA-C mix samples.

5.6.10.3 Conclusions

In conclusion:

1. The pH behavior over time well matched that of the middle slab portion of the slab concrete (see section 5.3.11.1 and figure 65). The conductivity curves for the laboratory concrete bracketed the curves for the middle slab portion of the slab concrete.
2. Good correspondence was obtained between laboratory and slab concretes.
3. The K release of the laboratory concretes was below that of the slab.
4. Differences were seen in the monolith leaching of Na and K between the two materials.
5. No differences were seen in the monolith leaching of Cl, SO₄²⁻ and Ca between the two materials.
6. U.S. 20 slab surface samples exhibited different monolith leaching than interior samples.

5.6.11. Release Modeling

Na, K, Cl, and Ca observed diffusivities obtained for the CFA-C mix samples (e.g., 28-d cured and high level aged CFA-C mix samples) and the U.S. 20 concrete samples are compared in tables 102 through 105, respectively. For each species of concern, three different observed diffusivities (e.g., $D_{obs\ 1}$, $D_{obs\ 2}$, and $D_{obs\ 3}$) are presented. $D_{obs\ 1}$ was calculated assuming that the initial leachable concentration C_D was the material total content of the species of concern. $D_{obs\ 2}$ was calculated assuming that the initial leachable concentration C_D was the species content provided only by the cement and the CFA-C. $D_{obs\ 3}$ was calculated assuming that (i) the initial leachable concentration C_D was the species content provided only by the cement and the CFA-C, (ii) the aggregates were inert and uniformly distributed within the matrix, and (iii) the flux was only provided by the fraction of the surface of the sample not occupied by the aggregates. Thus, while $D_{obs\ 1}$ and $D_{obs\ 2}$ correspond to observed diffusivities through the overall matrix (e.g., binder and aggregates), $D_{obs\ 3}$ corresponds to an observed diffusivity only through the binder (e.g., cement and CFA-C). For the CFA-C mix samples, only a range of the obtained observed diffusivities is given. For the U.S. 20 concrete samples, the average of observed diffusivities of the three samples representing the bulk of the slab is presented.

Significant differences in Na, K, and Cl observed diffusivities could be observed between the CFA-C mix samples and the U.S. 20 concrete samples. Thus, Na observed diffusivities (see table 102) of the U.S. 20 concrete samples were greater than that of the CFA-C mix samples (e.g., 1 order of magnitude greater for $D_{obs\ 1}$ and $D_{obs\ 2}$ and 4 times greater for $D_{obs\ 3}$). As with Na, much greater K observed diffusivities (e.g., 1 order of magnitude greater) were obtained for the U.S. 20 concrete samples (see table 103) while slightly lower Cl observed diffusivities (see table 104) were obtained (e.g., 4 times lower). However, no significant difference in Ca observed diffusivities could be observed between the CFA-C mix samples and the U.S. 20 concrete samples (see table 105).

In conclusion:

1. Irrespective of the type of D_{obs} , significant differences were seen in diffusivities of Na, K and Cl between the CFA-C and slab samples.
2. Irrespective of the type of D_{obs} , there were no differences in diffusivities of Ca between the CFA-C and slab samples.

5.7. Modeling of Heterogeneous Materials

Increased interest in utilization of recycled materials in civil engineering works (e.g., coal fly ash in concrete, incineration slag in road construction) and concern about the long-term environmental performance of systems utilizing such secondary materials has resulted in the need for more accurate assessments of constituent leaching. This includes understanding the leaching behavior of primary matrix components that may be indicative of both structural and environmental performance. Currently, most models, based on diffusion controlled release or coupled dissolution and diffusion, use laboratory leaching data to estimate long-term slab

Table 102: Parameter estimates for the release of Na from the one-dimensional diffusion model – comparison between CFA-C and U.S. 20 slab.

	28-d cured and high level aged CFA-C mix	Bulk of the Iowa U.S. 20 slab (average)
$D_{obs 1}^a$ [m ² /s]	6.5 10 ⁻¹⁵ - 11.0 10 ⁻¹⁵	4.7 10 ⁻¹⁴
$D_{obs 2}^b$ [m ² /s]	3.6 10 ⁻¹³ - 5.9 10 ⁻¹³	2.4 10 ⁻¹²
$D_{obs 3}^c$ [m ² /s]	1.1 10 ⁻¹² - 1.8 10 ⁻¹²	7.3 10 ⁻¹²

- ^a Calculated assuming that the initial leachable concentration C_0 was the total content
- ^b Calculated assuming that the initial leachable concentration C_0 was the species content provided only by the cement and the CFA
- ^c Calculated assuming that the initial leachable concentration C_0 was the species content provided only by the cement and the CFA and the flux was only provided by the fraction of the surface of the sample non-occupied by the aggregates

Table 103: Parameter estimates for the release of K from the one-dimensional diffusion model – comparison between CFA-C and U.S. 20 slab.

	28-d cured and high level aged CFA-C mix	Bulk of the Iowa U.S. 20 slab (average)
$D_{obs 1}^a$ [m ² /s]	1.4 10 ⁻¹⁴ - 2.2 10 ⁻¹⁴	20.0 10 ⁻¹⁴
$D_{obs 2}^b$ [m ² /s]	2.0 10 ⁻¹³ - 3.3 10 ⁻¹³	3.6 10 ⁻¹²
$D_{obs 3}^c$ [m ² /s]	6.2 10 ⁻¹³ - 10.0 10 ⁻¹³	1.1 10 ⁻¹¹

- ^a Calculated assuming that the initial leachable concentration C_0 was the total content
- ^b Calculated assuming that the initial leachable concentration C_0 was the species content provided only by the cement and the CFA
- ^c Calculated assuming that the initial leachable concentration C_0 was the species content provided only by the cement and the CFA and the flux was only provided by the fraction of the surface of the sample non-occupied by the aggregates

Table 104: Parameter estimates for the release of Cl from the one-dimensional diffusion model – comparison between CFA-C mix and U.S. 20 slab.

	28-d cured and high level aged CFA-C mix	Bulk of the Iowa U.S. 20 slab (average)
$D_{obs,1}^a$ [m ² /s]	1.5 10 ⁻¹¹ - 2.6 10 ⁻¹¹	0.6 10 ⁻¹¹

^a Calculated assuming that the initial leachable concentration C_0 was the total content

Table 105: Parameter estimates for the release of Ca from the one-dimensional diffusion model – comparison between CFA-C mix and U.S. 20 sSlab.

	28-d cured and high level aged CFA-C mix	Bulk of the Iowa U.S. 20 slab (average)
$D_{obs,1}^a$ [m ² /s]	3.0 10 ⁻¹⁶ - 3.9 10 ⁻¹⁴	3.3 10 ⁻¹⁶
$D_{obs,2}^b$ [m ² /s]	0.9 10 ⁻¹⁴ - 11.0 10 ⁻¹⁴	9.3 10 ⁻¹⁵
$D_{obs,3}^c$ [m ² /s]	2.6 10 ⁻¹⁴ - 3.3 10 ⁻¹⁴	2.8 10 ⁻¹⁴

- ^a Calculated assuming that the initial leachable concentration C_0 was the total content
- ^b Calculated assuming that the initial leachable concentration C_0 was the species content provided only by the cement and the CFA
- ^c Calculated assuming that the initial leachable concentration C_0 was the species content provided only by the cement and the CFA and the flux was only provided by the fraction of the surface of the sample non-occupied by the aggregates

performance assuming the constituents of concern in cement stabilized systems are uniformly dispersed in a homogeneous matrix. However, the actual physical system often comprises distinct components such as coarse or fine aggregates in a cement concrete or waste encapsulated in a stabilized matrix (e.g., slag incorporated in a cement-based matrix). Constituents of concern may be present in either or both of the physical components (e.g., binder or aggregate). Rates of chemical and mass transfer processes can vary by orders of magnitude between the components. Misrepresentation of the physical system may result in erroneous long-term performance assessments. Thus, it is necessary to consider a multi-regime transport model for accurate long-term leaching assessments.

The specific objectives of the modeling study presented here were to (i) develop a one-dimensional, multi-regime transport model (e.g., model) to account for the different components of heterogeneous porous materials, and (ii) evaluate simple limit cases using the model for species when release is not dependent on pH, to illustrate the impact of heterogeneous porous materials on contaminant release.

The porous solid matrix was modeled as two distinct homogeneous compartments (e.g., aggregates and binder): (i) a compartment made of binder in which mass transport of the species of interest toward the leaching solution occurs by diffusion and (ii) a compartment made of a uniform distribution of aggregates that acted as sources or sinks for the species of interest. The aggregates were modeled as spheres within which transport occurred by diffusion. The model assumes that there is no interface reaction between the aggregates and the binder. In this stage of development, the model is only valid to describe the release from a heterogeneous porous material of species when leaching behavior is not a function of pH (e.g., Na, Cl) or when no pH gradient within the material is generated during the leaching. For these cases, species release is controlled only by diffusion.

Two different model systems were evaluated using the model:

- Model System 1. Porous material (binder) contaminated with the species of interest and containing inert aggregates (e.g., the species of interest is initially only found in the binder); and,
- Model System 2. Porous material containing the contaminant of interest only in the aggregates.

These model systems were used to examine the effect of three factors on the contaminant release: (i) volume fraction of material occupied by the aggregates compared with a homogeneous porous material, (ii) aggregate size, and (iii) differences in mass transfer rates between the binder and the aggregates. For these purposes, three different volume fractions of aggregates (e.g., 0 percent, 30 percent and 70 percent) and four different aggregate sizes (e.g., spheres of 0.15, 2.5, 5, and 10-mm radius) were used. Three different diffusivity ratios ($D_{e,Binder}/D_{e,agg}$) were used to simulate the cases where the diffusion in the aggregates was (i) much slower than in the binder, (ii) much faster than in the binder, and (iii) the same as in the binder. Simulations were carried out considering blocks of 10- by 10- by 10-cm in contact with water on only one face in a liquid-solid ratio of 10-cm and periodic renewals of the leaching solution at intervals of 3, 5, 16, 24, 48,

96, 168, and 168 h (e.g., typical leaching intervals used in laboratory testing) resulting in a cumulative leaching time of 5 wk.

5.7.1. Effect of the Volume Fraction of Material Occupied by the Aggregates

Simulation results obtained using three different volume fractions of aggregates (e.g., 0 percent, 30 percent, and 70 percent) and considering the aggregates as spheres of 10-mm radius are shown in figure 123 for Model System 1 and Model System 2, respectively. The diffusivity ratio ($D_{e,Binder}/D_{e,agg}$) was set to one. Zero percent represented the case of a homogeneous porous material uniformly contaminated with the species of interest. The simulations for Model System 1 exhibited expected patterns that were similar for all cases, including the homogeneous case (e.g., straight line with a slope of -0.5) with the intensity of the flux decreasing as the volume fraction of aggregates increased. The simulations for Model System 2 exhibited an initial delay in the release flux as a result of mass transport through the binder and the overall flux intensity increased as the volume fraction of aggregates increased.

5.7.2. Effect of Aggregate Size

Simulation results obtained for Model System 1 and Model System 2 using four different aggregate sizes (e.g., spheres of 0.15, 2.5, 5, and 10-mm radius) and considering a volume fraction of aggregates of 30 percent are shown figure 124 for both model systems. The diffusivity ratio ($D_{e,Binder}/D_{e,agg}$) was set to one. For Model System 1, no effect of aggregate size was observed. Model System 2 showed lower release flux as aggregate size increased until mass transfer through the binder was no longer the limiting factor.

5.7.3. Effect of Differences in Mass Transfer Rate Between the Components

Simulations were carried out on the Model System 2 considering a volume fraction of aggregates of 30 percent and four different aggregate sizes (e.g., spheres of 0.15, 2.5, 5, and 10-mm radius). Three diffusivity ratios (e.g., ($D_{e,Binder}/D_{e,agg}$) equal to 10^5 ; 10^{-5} and 1) were used to simulate, respectively, the cases where the diffusion within the aggregates was (i) much slower, (ii) much faster, and (iii) the same as in the binder. When diffusion in the aggregates was much slower than in the binder, a significant increase in the released flux was observed followed by a constant flux (see figure 125). The same behavior of the flux was observed when diffusion in the aggregates was much faster than in the binder but shifted in time and intensities. When diffusion in the aggregates was the same as in the binder, the released flux showed an initial delay due to the initial mass transport through the binder followed by a similar pattern as the flux obtained for the homogeneous material.

5.7.4. Conclusions

The theoretical results obtained using the model showed that in the case of a porous material contaminated with the species of interest and containing inert aggregates (e.g., the

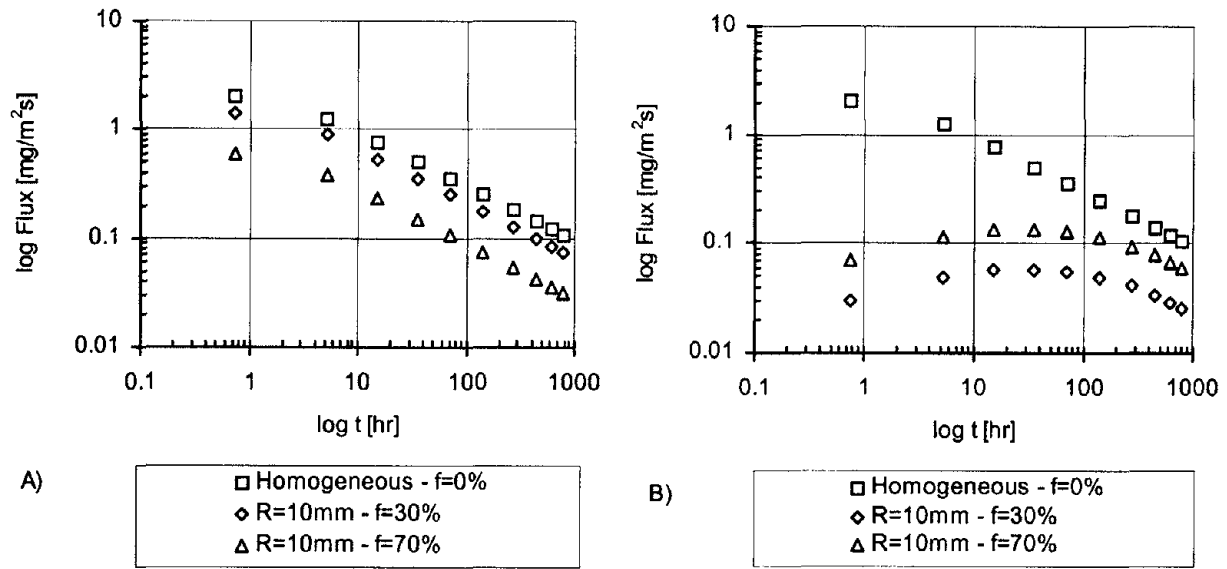


Figure 123: Release flux as a function of volume fraction of material occupied by the aggregates: A) Model System 1, and B) Model System 2.

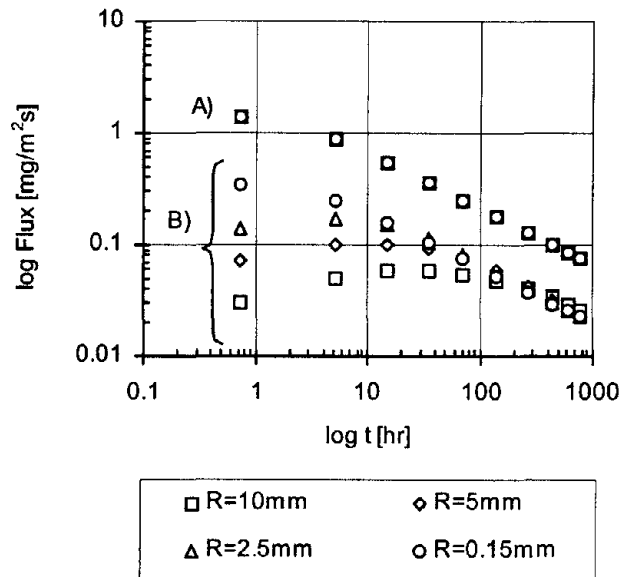
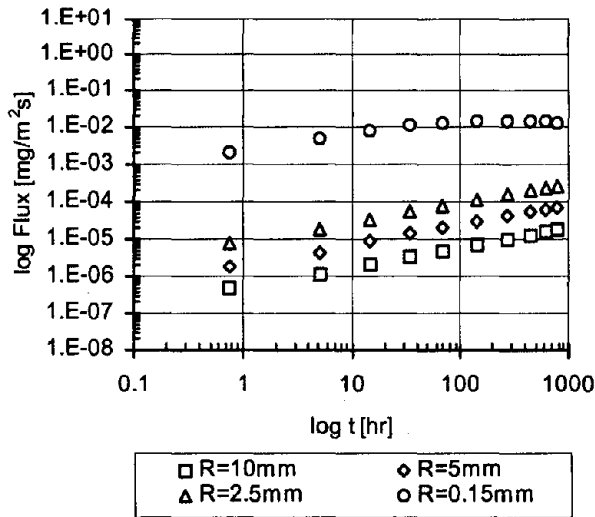
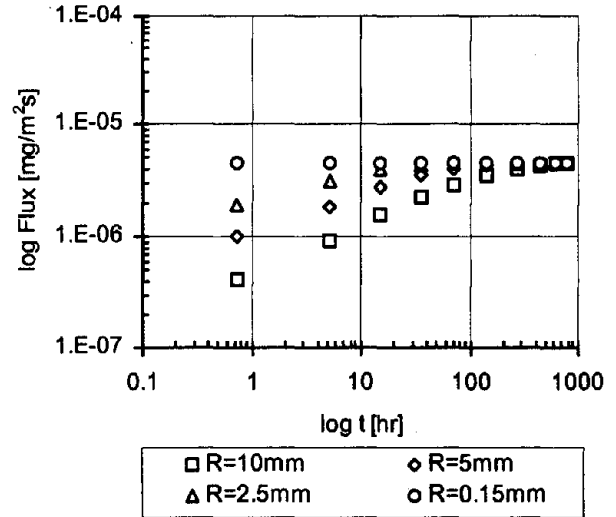


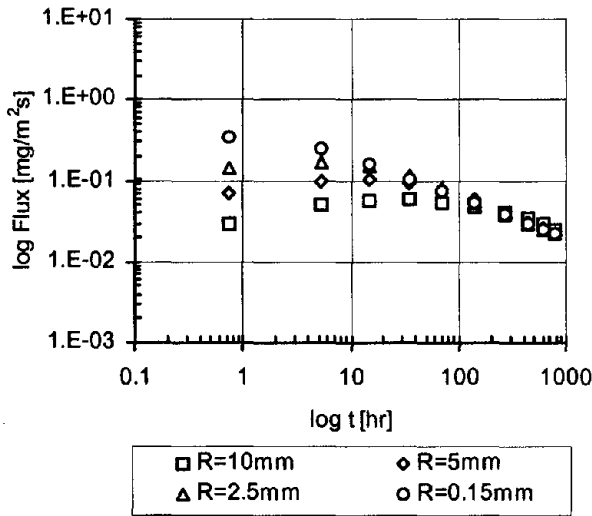
Figure 124: Release flux as a function of aggregate size: A) Model System 1, and B) Model System 2.



A) $D_{e,Binder}/D_{e,Agg} = 10^5$



B) $D_{e,Binder}/D_{e,Agg} = 10^{-5}$



C) $D_{e,Binder}/D_{e,Agg} = 1$

Figure 125: Release flux when diffusion in the aggregates was
 A) much slower than in the binder; B) much faster than in the binder; and
 C) the same as in the binder.

species of interest is initially only found in the binder), the released flux is a fraction of the flux obtained in the homogeneous case and is proportional to the volume fraction of material occupied by the binder. However, in the case of a porous material containing contaminated aggregates (e.g., the species of interest is initially only found in the aggregates), an initial delay in release as well as increases in the released flux or constant flux could be observed, indicating that prediction of species release based on the assumption of an homogeneous porous material may result in significant errors. In that case, long-term release prediction cannot be done by using a simple correction factor to compensate for matrix heterogeneity, and it is necessary to use a multi-regime transport model.

CHAPTER 6: CONCLUSIONS

6.1. Summary of Findings

The following summary of significant findings can be drawn from this research:

Mix Components Characterization

CFA-C.

1. The elemental composition of the CFA-C used here was generally in line with published values.
2. MgO concentrations were found to be about 5 percent in the CFA-C. Such concentrations have been shown to cause deleterious reactions in concrete.
3. CFA-C morphologies were typical.
4. Surface concentrations of elements varied widely from particle to particle in CFA-C.
5. Compared with total compositional analyses by NAA/XRF, surface concentrations of Al, Si, and Mg were higher and Fe and S were lower than bulk concentrations in the CFA-C.
6. Typical mineral phases were found in the CFA-C.
7. The CFA-C had a relatively high acid neutralization capacity with a natural pH around 12.
8. The leaching behavior of the CFA-C was consistent with its cementitious properties.
9. Solubility levels as well as leaching behaviors of trace metals (e.g., Zn, Ni) and elements of concern (e.g., Pb, Cd) that were observed were consistent with the ash type.
10. Availability values of Cu, Ni, and Zn were found to be lower than the total contents in the CFA-C, indicating that only a fraction of these trace metals was available for leaching under extraction conditions.

CFA-F.

1. The elemental composition of the CFA-F used here was higher in Al, Si, and Ti and lower in Fe, and Ca.
2. The CFA-F was enriched in Al, Si, and Ti and lower in Fe and Ca compared with other Class F ashes.
3. CFA-F morphologies were typical.

4. Surface concentrations of elements varied widely from particle to particle in CFA-F.
5. Compared with total compositional analyses by NAA/XRF, surface concentrations of Al, Si, and Mg were higher and Fe and S were lower than bulk concentrations in the CFA-F.
6. Typical mineral phases were found in the CFA-F.
7. The CFA-F had a very low acid neutralization capacity with a natural pH around 4.
8. The leaching behavior of the CFA-F was consistent with its pozzolanic properties.
9. Solubility levels as well as leaching behaviors of trace metals (e.g., Zn, Ni) and elements of concern (e.g., Pb, Cd) that were observed were consistent with the ash type.
10. Availability values of Cu, Ni, and Zn were found to be lower than the total contents in the CFA-F, indicating that only a fraction of these trace metals was available for leaching under extraction conditions.

Aggregates.

1. The combined aggregates presented very low concentrations of trace metals (e.g., less than 50 mg/kg) and relatively high levels of Al, Ca, Na, and K (e.g., ranging from 5,000 mg/kg to 300,000 mg/kg).
2. The elemental composition of the aggregates was as expected for limestone- and quartz-based aggregates.
3. The combined aggregates (e.g., 54.5 percent coarse aggregates and 45.5 percent fine aggregates corresponding to the ratio used in the mix design) had trace metal and elements of concern solubility levels on the same order of magnitude or greater than that of CFA-C or CFA-F.
4. The total content in Cd, Cu, and Zn for the aggregates was found to be available for leaching under extraction conditions.
5. Coarse aggregate porosity was found to be approximately 1 percent, which would contribute less than 0.5 percent to the concrete porosity in a CFA mix.
6. Coarse and fine aggregate porosity and pore size distributions were not expected to substantially affect those of the concrete as a whole.
7. Surface areas of the aggregates were found to be 12 to 25 percent of the surface areas of the concretes in the CFA mixes.
8. Surface areas of the aggregates were expected to be consistent between all concretes

examined here and therefore would not have any effect on differences noted between the concretes.

9. Calcite (CaCO_3) and dolomite ($\text{CaMg}(\text{CO}_3)_2$) were identified in the coarse aggregate mix. This is expected for a limestone-based aggregate.
10. Quartz (SiO_2) was identified in the fine aggregate. This was expected for sand-like materials found in the fines.

Portland Cement.

1. There are indications that the portland cement used for these experiments was unusually high in sulfates. A high level of sulfates can result in a deleterious expansive reaction in hardened concrete through the formation of ettringite ($\text{Ca}_6\text{Al}_2(\text{SO}_4)_3(\text{OH})_{12}\cdot 26\text{H}_2\text{O}$).
2. Typical cement mineral phases were found in month-old hydrated cement pastes made from the portland cement.
3. Gypsum ($\text{CaSO}_4\cdot 2\text{H}_2\text{O}$) was also detected in the pastes, but this was unexpected as gypsum was expected to have completely reacted by the age of 1 month.
4. The presence of gypsum in the hydrated pastes may correspond to the unexpectedly high level of sulfates detected in the portland cement.

Relative Contributions of Three Materials Types to Expected Environmental Behavior.

1. The aggregates were the greatest source of the trace metals (e.g., Mo, As, Se, Ni) and major species of concern (e.g., Pb, Cd).
2. The trace metals of concern were present at very low concentrations (e.g., less than 0.01 wt percent).

U.S. 20 Slab Characterization

1. The compressive strength of the slab (35.1 ± 4.7 MPa) was in excess of expected values.
2. Visual inspection revealed macrocracking in the tire path.
3. Microcracking was more extensive in cores taken from near the tire path and least in cores taken from near the shoulders. This correlates to the supposition that localized stresses due to traffic contributed to microcracking.
4. Microcracking was more extensive near the top of cores than near the bottom. This corresponds to placement compaction, placement curing, density changes, and cycles of freezing and thawing, heating and cooling, and drying and wetting.

5. Slab concrete porosities as measured by MIP ranged from 10 to 13 percent.
6. Slab concrete exhibited two distinct pore system microstructures: the first with an interconnecting pore width in the 1- μm range, the second in the 0.03- μm range.
7. Surface areas of the slab concrete ranged from 1.4 to 2.9 m^2/g with poor reproducibility.
8. The surface area of the slab concrete was low but reasonable when compared with known paste surface areas and probable aggregate fractions.
9. Expected minerals such as portlandite ($\text{Ca}(\text{OH})_2$), calcite (CaCO_3), and quartz (SiO_2) were found in the slab concrete.
10. Portlandite ($\text{Ca}(\text{OH})_2$) concentrations in the slab concrete were low as was expected for older concretes containing fly ash.
11. Unexpected amounts of gypsum ($\text{CaSO}_4 \cdot 2\text{H}_2\text{O}$) were found in the slab concrete possibly corresponding to high sulfate contents in the source cement and the related high gypsum content in month-old laboratory pastes.
12. Quartz (SiO_2) concentrations were found higher in the top of the slab than in the bottom, perhaps due to a higher concentration of fine aggregate there.
13. The slab showed no difference in the concentrations of albite ($\text{NaAlSi}_3\text{O}_8$), calcite (CaCO_3), or portlandite ($\text{Ca}(\text{OH})_2$) between the top, middle, and bottom of the slab.
14. The upper surface of the slab was carbonated only to a very limited depth (<0.5 mm), although it was exposed to traffic and climatic conditions for 10 yr.
15. The lower surface (e.g., in contact with the base soils), the shoulder edge, and part of the joint edge also appeared to be carbonated, but only to a very limited depth (<0.5 mm).
16. The macrocracks and or microcracks on the upper surface did not seem to have influenced the carbonation rate.
17. There was no carbonation within the interior region of the slab cores that were tested.
18. There was a slight difference in the buffering capacity of the slab according to the sample location (e.g., northwest region or southeast region).
19. There was no influence of sample location within the slab with respect to extract concentration and solubility as a function of pH for each of the trace metals of concern (e.g., Pb, Cd)..
20. Extractions at different low LS ratios to approximate the saturated solution within the

pore water of the slab confirmed that there was no carbonation of the slab core at the southeast region.

21. The determination of constituent availability showed that only a fraction of the Ni and Zn was available for leaching under the test conditions while Cd, Cu, and Pb were completely available.
22. As with the hydrated cement paste, calcite (CaCO_3) and dolomite ($\text{CaMg}(\text{CO}_3)_2$) were likely controlling solids for Ca leaching from the slab concrete.
23. As with the hydrated cement paste, dolomite ($\text{CaMg}(\text{CO}_3)_2$) was a likely controlling solid for Mg leaching.
24. Unlike the hydrated cement paste for which barium chromate (BaCrO_4) was better, barite (BaSO_4) is a likely controlling solid for Ba in the slab concrete.
25. Modeling was successful only at higher pH values for CO_3^{2-} and indicated dolomite ($\text{CaMg}(\text{CO}_3)_2$) and calcite (CaCO_3) as likely controlling solids.
26. As with the hydrated cement paste, geochemical modeling of pH-stat leaching was not successful for Al, Si, Zn, Fe, and Cr.
27. The controlling solids identified for the slab concrete appear to be typical of cement-based leaching systems.
28. There were significant differences in monolithic leaching behavior of major species between the two studied vertical locations within the slab (e.g., bulk and top): much greater release of the highly soluble species (e.g., Na, K, Cl) and less release of Ca obtained for the surface of the slab, suggesting possible species accumulation at the surface, a higher level of microcracking, partial carbonation of the slab surface, or a combination of these.
29. All the concentrations of the trace metals of concern measured in the monolith leach test were very close to or below detection limits.
30. Surface carbonation will likely have a potential effect on trace metal release.
31. Release modeling showed significant differences in observed diffusivities of major species between the two studied vertical locations within the slab (e.g., bulk and top): much greater Na, K, and Cl observed diffusivities and lower Ca observed diffusivity obtained for the surface of the slab.
32. A model study on the release rate of Na, K, and Ca from the coarse aggregates used in the mix design showed that the release of Na, K, and Ca from the coarse aggregates in the overall concrete products was negligible compared with the release of these species from the binder in the slab.

Effects of AA, CL and FT on Physical and Environmental Performance of CFA-C Laboratory Prisms in the $2^3 + 3$ Experimental Design

Table 106 summarizes the data obtained in the $2^3 + 3$ experimental design for the CFA-C prisms for each of the experimental variables that was analyzed. For each of the main effects, two way interactions and three-way interactions, a significance level is shown, the type of effect (negative or positive) is noted where available, and the level of significance of the curvature effect is provided.

Some highlights from Table 106 are as follows:

Compressive Strength.

1. AA treatment lowered concrete strength, indicating that a deleterious chemical reaction was present in addition to the normal hydration reactions.
2. FT treatment produced an expected decrease in compressive strength.
3. CL treatment had no consistent net effect due to conflicting tendencies for CL to increase strength when applied at low levels and to decrease strength when applied at high levels.
4. No interactions between aging treatments on compressive strength were observed.

Microcracking.

1. Of the aging treatments, only CL resulted in increased levels of microcracking.
2. Likely as a result of increased microcracking, CL resulted in interactions of the pore sizes of the fine pore system with the AA and FT aging methods and in the Ca cumulative release and observed diffusivity monolithic leaching data (see below).

Relative Dynamic Modulus.

1. AA caused an increase in vulnerability to FT deterioration, which is likely the result of a deleterious chemical reaction during accelerated aging which then resulted in a loss of tensile strength in the matrix.
2. The increase in vulnerability to FT deterioration, as revealed by relative dynamic modulus, was apparent in all the tested specimens, even though statistical testing could not be used.

Table 106: Summary of results of response variables in the 2³ + 3 experimental design for the CFA-C prisms.

Response variable	Units	Main effects							Two way interactions			Three way interaction	Curvature
		AA	CL	FT	AA & CI	AA & FT	CL & FT	AA & CL & FT					
Compressive Strength	MPa	>99% (neg)	NS	>99% (neg)	NS	NS	NS	NS	NS	NS	NS	NS	>99%
Microcracking	%	NS	90% (pos)	NS	NS	NS	NS	NS	NS	NS	NS	NS	NS
Relative Dynamic Modulus	%	>99% (neg)	NS	Not Appl.	NS	Not Appl.	NS	Not Appl.	Not Appl.	Not Appl.	Not Appl.	Not Appl.	>99%
Large Pore (0.1 to 1.0 µm) Uniformity Indicator	µm	NS	NS	NS	NS	NS	NS	NS	NS	NS	NS	NS	NS
Large Pore (0.1 to 1.0 µm) Weighted Average Threshold Pore Width	µm	NS	NS	NS	NS	NS	NS	NS	NS	NS	NS	NS	NS
Small Pore (0.01µm) Uniformity Indicator	µm	>95% (neg)	>90% (neg)	>95% (neg)	NS	NS	NS	NS	NS	NS	NS	NS	>95%
Small Pore (0.01µm) Weighted Average Threshold Pore Width	µm	>99% (pos)	>90% (neg)	>99% (neg)	>99% (neg)	>99% (neg)	>99% (neg)	>99% (neg)	NS	>95% (pos)	>99% (pos)	>99% (pos)	>99%
Porosity	%	NS	NS	NS	NS	NS	NS	NS	NS	NS	NS	NS	NS
Effective Surface Area	m ² /g	NS	NS	NS	NS	NS	NS	NS	NS	NS	NS	NS	NS
Albite Concentration	%	NS	NS	NS	NS	NS	NS	NS	NS	NS	NS	NS	NS
Calcite Concentration	%	NS	NS	NS	NS	NS	NS	NS	NS	NS	NS	NS	NS
Etringite Concentration	%	NS	NS	NS	NS	NS	NS	NS	NS	NS	NS	NS	NS
Gypsum Concentration	%	>95% (neg)	NS	>95% (neg)	NS	NS	NS	NS	NS	NS	NS	NS	NS
Portlandite Concentration	%	NS	NS	NS	NS	NS	NS	NS	NS	NS	NS	NS	NS
Quartz Concentration	%	NS	NS	>90% (neg)	NS	NS	NS	NS	NS	NS	NS	NS	NS
Al pH-Stat Leaching (pH 12)	mg/L	NS	NS	NS	NS	NS	NS	NS	NS	NS	NS	NS	NS
Ba pH-Stat Leaching (pH 12)	mg/L	> 90% (neg)	NS	NS	NS	NS	NS	NS	NS	NS	NS	NS	NS

Table 106: Summary of results of response variables in the 2³ + 3 experimental design for the CFA-C prisms (continued).

Response variable	Units	Main effects							Two way interactions			Three way interaction	Curvature
		AA	CL	FT	AA & CI	AA & FT	CL & FT	AA & CL & FT					
Ca pH-Stat Leaching (pH 12)	mg/L	> 90% (neg)	> 95% (neg)	NS	NS	NS	NS	NS	NS	NS	NS	NS	> 90%
Cl pH-Stat Leaching (pH 12)	mg/L	NS	NS	NS	NS	NS	NS	NS	NS	NS	NS	NS	NS
CO ₃ ²⁻ pH-Stat Leaching (pH 12)	mg/L	NS	NS	NS	NS	NS	NS	NS	NS	NS	NS	NS	NS
Cr pH-Stat Leaching (pH 12)	mg/L	NS	NS	NS	NS	NS	NS	NS	NS	NS	NS	NS	NS
Fe pH-Stat Leaching (pH 12)	mg/L	NS	NS	NS	NS	NS	NS	NS	NS	NS	NS	NS	NS
K pH-Stat Leaching (pH 12)	mg/L	> 90% (neg)	NS	NS	NS	NS	NS	NS	NS	NS	NS	NS	> 90%
Mg pH-Stat Leaching (pH 12)	mg/L	> 90% (neg)	> 90% (pos)	NS	> 95% (pos)	NS	NS	NS	NS	> 90% (neg)	NS	NS	NS
Si pH-Stat Leaching (pH 12)	mg/L	NS	NS	NS	NS	NS	NS	NS	NS	NS	NS	NS	NS
SO ₄ ²⁻ pH-Stat Leaching (pH 12)	mg/L	NS	NS	NS	NS	NS	NS	NS	NS	NS	NS	NS	NS
Zn pH-Stat Leaching (pH 12)	mg/L	> 95% (neg)	NS	> 95% (pos)	NS	NS	NS	NS	NS	> 90% (neg)	NS	NS	> 95%
Na Monolith Cumulative Flux (Release)	mg/kg	NS	NS	NS	NS	NS	NS	NS	NS	NS	NS	NS	NS
K Monolith Cumulative Flux (Release)	mg/kg	NS	NS	NS	NS	NS	NS	NS	NS	NS	NS	NS	NS
Ca Monolith Cumulative Flux (Release)	mg/kg	> 99% (pos)	> 99% (pos)	> 99% (pos)	> 90% (pos)	> 99% (pos)	> 90% (neg)	> 90% (neg)	> 99% (neg)	> 90% (neg)	> 99% (neg)	> 99% (neg)	> 99%
Na Observed Diffusivity Through Binder (D _{obs3})	m ² /s	NS	NS	NS	NS	NS	NS	NS	NS	NS	NS	NS	NS
K Observed Diffusivity Through Binder (D _{obs3})	m ² /s	NS	NS	NS	NS	NS	NS	NS	NS	NS	NS	NS	NS

Table 106: Summary of results of response variables in the $2^3 + 3$ experimental design for the CFA-C prisms (continued).

Response variable	Units	Main effects			Two way interactions			Three way interaction		Curvature
		AA	CL	FT	AA & CI	AA & FT	CL & FT	AA & CL & FT		
Ca Observed Diffusivity Through Binder ($D_{obs,2}$)	m^2/s	NS	> 90% (neg)	NS	NS	NS	NS	NS	NS	> 90%

Effective Pore Size and Pore Size Distribution.

1. No effects on porosity by aging methods could be discerned due to the variability of the porosity measurements. AA and FT were not expected to have an effect whereas CL was.
3. CFA-C concretes exhibited two distinct pore networks: a coarser pore network centered on connection pore widths of approximately 0.5 μm , and a finer network centered on approximately 10 to 20 nm.
4. Aging treatments had no discernable effect on the coarser pore network.
5. AA caused the finer pore network to coarsen and become less uniform
6. CL had no apparent effect on the finer pore network.
7. FT caused the finer pore network to shift to a smaller average pore width of a less uniformly defined nature. This may be due to expansive pressures in the coarser pores having squeezed and narrowed the finer pores.
8. There were significant interactive effects on the finer pore system between AA and CL, CL and FT, and all three of the aging treatments.

Effective Surface Area.

1. Surface area measurements were inconclusive due to the heterogeneous nature of concrete and the sample sizes relative to coarse aggregate sizes.

Mineralogy.

1. Gypsum ($\text{CaSO}_4 \cdot 2\text{H}_2\text{O}$) concentrations were reduced by AA and FT treatments probably due to increased reaction and dissolution during these treatments, respectively.
2. Quartz (SiO_2) concentrations were reduced by FT aging, the mechanism is unknown.

Prism Alkalinity and Constituent Solubility as a Function of pH.

1. There was a slight difference between the 28-d cured material and the high temperature-aged material with respect to buffering capacity, suggesting possible sample carbonation during the temperature aging.
2. There was no difference between the 28-d cured material and the high temperature-aged material with respect to solubility as a function of pH for Cd, Ni, and Zn.

3. There was a significant decrease of Pb solubility as a function of pH for the high temperature-aged material and a slight decrease of Cu solubility for pHs greater than 8, suggesting possible sample carbonation during AA.

pH-Stat Leaching.

1. Species concentrations in leachate were not typically affected by aging mechanisms.
2. When species concentrations were affected, AA had the greatest effect.
3. Many analytes were successfully modeled over some or part of the pH range examined.
4. The controlling solids identified for the CFA-C concrete prisms appear to be typical of cement-based leaching.
5. There was excellent correspondence of apparent controlling solids between the slab and the laboratory concretes.
6. As with the slab concrete, geochemical modeling was not successful for Al, Si, Zn, Fe, and Cr.

Low LS Leaching.

1. AA did not result in a significant change in the leaching behavior of primary matrix components (e.g., Ca, Na, K, SO_4^{2-} , Cl) as a function of LS ratio.
2. AA did not affect the ionic strength at an LS ratio of 5 ml/g dry (e.g., typical LS ratio for most equilibrium batch tests) but resulted in a decrease in pore water ionic strength.
3. There was very good agreement of low LS leaching behaviors between slab and laboratory concretes.

Monolithic Leaching

1. Although slight differences in the leaching behavior of primary matrix components (e.g., Na, K, SO_4^{2-} , Cl, and Ca) could be observed, no clear tendency resulting from aging could be observed.
2. Much greater differences were observed for Na and K release between the three center point replicates than the different aged samples, indicating that the observed differences between the aged samples were more likely the result of experimental uncertainties than aging effect.
3. Over the time scale of the laboratory testing, there was no substantial effect of the three types of aging (e.g., AA, CL, FT) on leachate pH, leachate conductivity, and leaching behavior of primary matrix components.

4. Release modeling showed greater differences in Na, K, and Ca observed diffusivities between the three center point replicates than between the aged and non-aged samples, indicating that there was no substantial effect of the three types of aging on observed diffusivities.
5. No statistically significant effect of the three types of aging or interactions were observed for Na and K cumulative release at 22 d of leaching.
6. No statistically significant effect of the three types of aging or interactions were observed for Na and K observed diffusivities at 22 d of leaching.
7. Statistically significant effects of the three types of aging and the interactions were observed on Ca cumulative release at 22 d of leaching.
8. Statistically significant effects were observed for Ca observed diffusivities at 22 d of leaching. This result may be significant in understanding the material durability, because Ca (unlike Na and K) is a primary matrix constituent. This result may relate to observed loss of strength, changes in microcracking, and changes in fine pore structure from accelerated aging.

Comparison of CFA-C, CFA-F, and PCC Laboratory Prisms in the Three Center Points Experimental Design

Table 107 summarizes the data obtained in the Tukey-Kramer comparisons between the CFA-C, CFA-F, and PCC experimental prisms from the three center points experimental design for each of the experimental variables that was analyzed. For each comparison, a significance level is shown.

Some highlights from Table 107 are as follows:

Compressive Strength.

1. At an age of 500 d after LLL treatment, the CFA-C concrete was significantly stronger than the PCC at a 95 percent confidence level.
2. The CFA-C was not found to be significantly different than the CFA-F.
3. The CFA-F was not found to be significantly different than the PCC.
4. At higher ages, the higher strength of the CFA-C concrete can be attributed to the beneficial hydration of the fly ash.

Table 107: Summary of results of Tukey-Kramer comparisons in the three center point experimental design for the CFA-C, CFA-F and PCC prisms.

Response variable	Units	Comparison		
		CFA-C & CFA-F	CFA-C and PCC	CFA-F and PCC
Compressive Strength	MPa	NS	>95%	NS
Microcracking	%	NS	>95%	NS
Relative Dynamic Modulus	%	NS	>95%	>95%
Large Pore (0.1 to 1.0 μm) Uniformity Indicator	μm	NS	NS	NS
Large Pore (0.1 to 1.0 μm) Weighted Average Threshold Pore Width	μm	NS	NS	NS
Small Pore (0.01 μm) Uniformity Indicator	μm	> 95% (CFA-F > CFA-C)	NS	> 95% (CFA-F > PCC)
Small Pore (0.01 μm) Weighted Average Threshold Pore Width	μm	> 95% (CFA-C > CFA-F)	> 95% (PCC > CFA-C)	> 95% (PCC > CFA-F)
Porosity	%	NS	NS	NS
Effective Surface Area	m ² /g	NS	NS	NS
Albite Concentration	%	NS	NS	NS
Calcite Concentration	%	NS	NS	NS
Etringite Concentration	%	NS	NS	NS
Gypsum Concentration	%	NS	> 95% (CFA-C > PCC)	NS
Portlandite Concentration	%	NS	NS	> 95% (PCC > CFA-F)
Quartz Concentration	%	NS	NS	NS
Acid Neutralizing Capacity to pH 4.3	meq/g	NS	> 95% (PCC > CFA-C)	> 95% (PCC > CFA-F)
Al pH-Stat Leaching (pH 12)	mg/L	NS	> 99% (CFA-C > PCC)	> 99% (CFA-F > PCC)
Ba pH-Stat Leaching (pH 12)	mg/L	> 99% (CFA-C > CFA-F)	> 99% (CFA-C > PCC)	NS
Ca pH-Stat Leaching (pH 12)	mg/L	NS	> 95 % (PCC > CFA-C)	> 95% (PCC > CFA-F)

Table 107: Summary of results of Tukey-Kramer comparisons in the three center point experimental design for the CFA-C, CFA-F and PCC prisms (continued).

Response variable	Units	Comparison		
		CFA-C & CFA-F	CFA-C and PCC	CFA-F and PCC
Cl pH-Stat Leaching (pH 12)	mg/L	NS	NS	NS
CO ₃ ²⁻ pH-Stat Leaching (pH 12)	mg/L	NS	NS	NS
Cr pH-Stat Leaching (pH 12)	mg/L	> 90 % (CFA-C > CFA-F)	> 90 % (CFA-C > PCC)	NS
Fe pH-Stat Leaching (pH 12)	mg/L	NS	NS	NS
K pH-Stat Leaching (pH 12)	mg/L	> 90 % (CFA-F > CFA-C)	NS	> 90 % (CFA-F > PCC)
Mg pH-Stat Leaching (pH 12)	mg/L	NS	NS	NS
Si pH-Stat Leaching (pH 12)	mg/L	NS	> 95% (CFA-C > PCC)	> 95% (CFA-F > PCC)
SO ₄ ²⁻ pH-Stat Leaching (pH 12)	mg/L	NS	NS	NS
Zn pH-Stat Leaching (pH 12)	mg/L	> 90% (CFA-F > CFA-C)	NS	NS
Na Monolith Cumulative Flux (Release)	mg/kg	> 95% (CFA-F > CFA-C)	> 95% (PCC > CFA-C)	NS
K Monolith Cumulative Flux (Release)	mg/kg	NS	NS	NS
Ca Monolith Cumulative Flux (Release)	mg/kg	> 95% (CFA-C > CFA-F)	> 95% (CFA-C > PCC)	> 95 % (CFA-F > PCC)
Na Observed Diffusivity Through Binder (D _{obs,3})	m ² /s	NS	NS	NS
K Observed Diffusivity Through Binder (D _{obs,3})	m ² /s	NS	NS	NS
Ca Observed Diffusivity Through Binder (D _{obs,3})	m ² /s	NS	> 95% (PCC > CFA-C)	> 95 % (CFA-F > PCC)

Microcracking.

1. The PCC concrete experienced significantly greater microcracking than the CFA-C concrete matching the observed and corresponding lower strength.
2. Microcracking was not significantly different between the PCC and the CFA-F nor between the CFA-F and the CFA-C concretes.

Relative Dynamic Modulus.

1. The CFA-C and CFA-F mixes had greater FT durability than the PCC.
2. There was no significant difference in FT durability between the two ash mixes.
3. The greater FT durability of the ash mixes matches results found of less microcracking and higher strength.

Effective Pore Size and Pore Size Distribution.

1. The three mixes did not differ significantly in traditional threshold pore widths, total porosities, or values associated with the coarser pore system in the laboratory concretes.
2. The three mixes did differ significantly with respect to descriptions of the finer pore system for which the CFA-F had the finest, most uniform pore system. The CFA-C had a somewhat larger system of fine pores and the PCC had the largest of the fine pore systems. Both the CFA-C and PCC mixtures exhibited less well-defined fine pore system widths.

Effective Surface Area.

1. As with the slab concrete, for all the laboratory concretes, surface area measurements were inconclusive due to the heterogeneous nature of concrete and the sample sizes relative to coarse aggregate sizes.

Elemental Composition.

2. No significant differences were seen.

Mineralogy.

1. There were no significant differences in the concentrations of albite ($\text{NaAlSi}_3\text{O}_8$), calcite (CaCO_3), ettringite ($\text{Ca}_6\text{Al}_2(\text{SO}_4)_3(\text{OH})_{12}\cdot 26\text{H}_2\text{O}$), or quartz (SiO_2) between the three laboratory concretes.
2. The gypsum ($\text{CaSO}_4\cdot 2\text{H}_2\text{O}$) level detected in the CFA-C was found to be significantly higher than that of the PCC, but as the levels detected were quite low, the significance of

this statistical difference is questionable.

3. The portlandite ($\text{Ca}(\text{OH})_2$) concentration was significantly higher in the PCC concrete as would be expected owing to the lack of CFA in the PCC.

Prism Alkalinity and Constituent Solubility as a Function of pH.

1. There was a slight, but insignificant difference between the three material types with respect to buffering capacity.
2. There was no difference between the three material types with respect to solubility as a function of pH for each of the trace metals of concern (e.g., Cd, Cu, Pb, Ni, and Zn).

pH-Stat Leaching.

1. Species concentrations in leachate were different between mix types for select constituents (Al, Ba, Ca, Cr, K, Si, Zn).
2. As with hydrated cement paste and the slab concretes, calcite (CaCO_3) and dolomite ($\text{CaMg}(\text{CO}_3)_2$) are likely controlling solids for Ca leaching from the three laboratory mixes. For the laboratory concrete, gypsum ($\text{CaSO}_4 \cdot 2\text{H}_2\text{O}$) is also a likely controlling solid.
3. As with the hydrated cement paste and slab concrete, dolomite ($\text{CaMg}(\text{CO}_3)_2$) is a likely controlling solid for Mg leaching in the three laboratory mixes.
4. Unlike the hydrated cement paste for which barium chromate (BaCrO_4) was better, but like the slab concrete, barite (BaSO_4) is a likely controlling solid for Ba in the three laboratory mixes.
5. Like the slab concrete, barite (BaSO_4) is a likely controlling solid for SO_4^{2-} leaching in the three laboratory mixes.
6. As with the slab concrete, modeling was successful only at higher pH values for CO_3^{2-} and indicated dolomite ($\text{CaMg}(\text{CO}_3)_2$) and calcite (CaCO_3) as likely controlling solids. (Dolomite and barite were found for the hydrated cement pastes.)
7. As with the hydrated cement paste and slab concrete, geochemical modeling was not successful for Al, Si, Zn, Fe, and Cr.
8. The controlling solids identified for the three types of concrete mixes appear to be typical of cement-based leaching.

Low LS Leaching.

1. There were no significant differences between the three material types in terms of

leaching behavior of primary matrix components as a function of LS ratio, with nevertheless a much greater Na release for C(XXX)02.

2. There was no significant difference with respect to the ionic strength at LS ratio of 5 ml/g dry (e.g., typical LS ratio for most equilibrium batch tests).
3. The pore water ionic strength of C(XXX)02 was much greater (e.g., 1.2 mol/l) than the pore water of F(XXX)02 and P(XXX)02 (e.g., 0.7 mol/l) due to a much greater NA release.

Availability Leaching.

1. There was no difference between the three materials with respect to constituent availability.
2. For each of the three materials, only a fraction of Ni and Zn was available for leaching under the test conditions, while Cd, Pb and Cu were completely available.

Monolithic Leaching

1. There were slight differences in leaching behavior of major species (e.g., Na, K, and Ca) between the three material types: a much greater release of Na was obtained for the CFA-C mix, a greater release of K release was obtained for PCC control and a lesser release for CFA-C mix, and a greater Ca release was obtained for PCC control, consistent with its greater Ca total content.
2. All the concentrations of the trace metals of concern measured in the monolith leach test leachates were very close to or below the detection limits.
3. The CFA-C mix was significantly different at 95 percent from CFA-F mix and PCC control for Na cumulative release.
4. The PCC control was significantly different at 95 percent from CFA-C mix and CFA-F mix for Ca observed diffusivity.
5. There was no significant difference at 95 percent between CFA-C mix, CFA-F mix, and PCC control for Na and Ca cumulative release at 22 d of leaching.
6. There was no significant difference at 95 percent between CFA-C mix, CFA-F mix and PCC control for Na and Ca observed diffusivities at 22 d of leaching

Comparison of Laboratory-Aged CFA-C Laboratory Prisms to the Field Aged U.S. 20 Pavement Slab

Table 108 summarizes the data obtained from the analyses of the CFA-C prisms and the U.S. slab for each of the experimental variables that was analyzed. Additional noteworthy

Table 108: Summary of results comparing the CFA-C prisms to the U.S. 20 slab.

		Range of values (mean of values)	
Category or response variable	Units	Laboratory aged CFA-C prisms (from 2 ³ +3 experimental design)	Field aged U.S. 20 slab samples
CFA-C	-	Ottumwa CFA-C (1997)	Ottumwa CFA-C (1987)
Portland cement	-	Type 1 (Lehigh, Iowa)	Type 1 (Lehigh, Montana)
Coarse Aggregate	-	Limestone (Iowa source)	Limestone (Iowa source)
Fine Aggregate	-	Quartz-based (Iowa Source)	Quartz-based (Iowa Source)
Air Content	%	2.9 - 4.1 (at mixing)	2 - 6 (in petrographic analyses)
Mean Equivalent Age (by f_c)	Yr	1.0 to 2.9	Not Applicable (approximately 10 yr. of field aging with early distress after 3 to 4 yr)
Mean Equivalent Age (by p-wave)	Yr	1.0 to 2.9	Not Applicable (approximately 10 yr. of field aging with early distress after 3 to 4 yr)
Mean Equivalent Age (by non-evaporable water content)	Yr	1.1 to 4.8	Not Applicable (approximately 10 yr. of field aging with early distress after 3 to 4 yr)
Total Compositional Differences	-	Si content of 14% (from cement)	Si content of 6.6%
Compressive Strength	MPa	25.9 to 56.1 (mean of 40.2)	29.2 to 40.8 (mean of 35.1)
Microcracking	%	0.3 to 2.8 (mean of 0.9)	0.3 to 6.6 (mean of 2.3)
Large Pore (0.1 to 1.0 μ m) Uniformity Indicator	μ m	0.0039 to 0.0152 (mean of 0.0102)	0.0105 to 0.0185 (mean of 0.0146)
Large Pore (0.1 to 1.0 μ m) Weighted Average Threshold Pore Width	μ m	0.321 to 0.669 (mean of 0.491)	0.982 to 1.075 (mean of 1.029)
Small Pore (0.01 μ m) Uniformity Indicator	μ m	0.0023 to 0.0136 (mean of 0.0063)	0.0064 to 0.0103 (mean of 0.0086)
Small Pore (0.01 μ m) Weighted Average Threshold Pore Width	μ m	0.0116 to 0.0212 (mean of 0.0147)	0.0265 to 0.0374 (mean of 0.0312)
Porosity	%	8.2 to 10.2 (mean of 9.1)	10.0 to 13.4 (mean of 11.7)
Effective Surface Area	m ² /g	2.3 to 11.5 (mean of 5.5)	1.4 to 2.9 (mean of 2.1)
Albite Concentration	%	0 to 2.53 (mean of 3.1)	0.4 to 15.8 (mean of 3.0)

Range of values (mean of values)				
Category or response variable	Units	Laboratory aged CFA-C prisms (from 2 ³ +3 experimental design)	Field aged U.S. 20 slab samples	
Calcite Concentration	%	12.2 to 34.1 (mean of 22.2)	13.6 to 36.2 (mean of 21.7)	
Etringite Concentration	%	0 to 1.7 (mean of 0.4)	0 to 1.8 (mean of 0.4)	
Gypsum Concentration	%	0 to 1.4 (mean of 0.3)	0.2 to 1.7 (mean of 0.4)	
Portlandite Concentration	%	0.7 to 3.2 (mean of 1.3)	0.4 to 2.6 (mean of 1.0)	
Quartz Concentration	%	1.8 to 11.0 (mean of 5.1)	1.0 to 18.4 (mean of 4.4)	
Acid Neutralizing Capacity to pH 4.3	meq/g	13.5 to 14	13.5	
Al pH-Stat Leaching (pH 12)	mg/L	0.64 to 1.8 (mean of 1.2)	0.55 to 2.4 (mean of 1.2)	
Ba pH-Stat Leaching (pH 12)	mg/L	1.5 to 2.8 (mean of 2.2)	0.57 to 1.9 (mean of 1.2)	
Ca pH-Stat Leaching (pH 12)	mg/L	450 to 1,300 (mean of 750)	230 to 890 (mean of 520)	
Cl pH-Stat Leaching (pH 12)	mg/L	BDL of 0.5 to 21 (mean of 4.4)	1.6 to 67 (mean of 24)	
CO ₃ ²⁻ pH-Stat Leaching (pH 12)	mg/L	190 to 650 (mean of 350)	0.07 to 75 (mean of 26)	
Cr pH-Stat Leaching (pH 12)	mg/L	BDL of 0.004 to 0.01 (mean of 0.007)	0.005 to 0.032 (mean of 0.024)	
Fe pH-Stat Leaching (pH 12)	mg/L	0.028 to 0.057 (mean of 0.046)	0.050 to 0.078 (mean of 0.063)	
K pH-Stat Leaching (pH 12)	mg/L	51 to 88 (mean of 67)	41 to 150 (mean of 100)	
Mg pH-Stat Leaching (pH 12)	mg/L	BDL of 0.03 to 0.12 (mean of 0.09)	0.03 to 0.05 (mean of 0.04)	
Si pH-Stat Leaching (pH 12)	mg/L	1.0 to 2.7 (mean of 1.8)	1.3 to 1.9 (mean of 1.5)	
SO ₄ ²⁻ pH-Stat Leaching (pH 12)	mg/L	BDL of 1.0 to 13 (mean of 7.1)	8.9 to 24 (mean of 21)	
Zn pH-Stat Leaching (pH 12)	mg/L	0/007 to 0.071 (mean of 0.029)	0.022 to 0.21 (mean of 0.06)	
Al Controlling Solid (applicable pH range)	-	none	none	
Ba Controlling Solid (applicable pH range)	-	BaSO ₄ (5-12), BaCrO ₄ (5-10)	BaSO ₄ (5-12)	
Ca Controlling Solid (applicable pH range)	-	CaSO ₄ ·2H ₂ O (5-12), CaMg(CO ₃) ₂ (5-12), CaCO ₃ (5-12), Ca ₆ Al ₂ (SO ₄) ₃ (OH) ₁₂ ·26H ₂ O (7-12)	CaSO ₄ ·2H ₂ O (5-12), CaCO ₃ (5-12), CaMg(CO ₃) ₂ (5-12), Ca ₆ Al ₂ (SO ₄) ₃ (OH) ₁₂ ·26H ₂ O (5-12)	

Range of values (mean of values)				
Category or response variable	Units	Laboratory aged CFA-C prisms (from 2 ³ +3 experimental design)	Field aged U.S. 20 slab samples	
CO ₃ ²⁻ Controlling Solid (applicable pH range)	-	CaCO ₃ (7-10), CaMg(CO ₃) ₂ (7-10)	CaCO ₃ (7-12), CaMg(CO ₃) ₂ (7-12)	
Cr Controlling Solid (applicable pH range)	-	None Identified	None Identified	
Fe Controlling Solid (applicable pH range)	-	None Identified	None Identified	
Mg Controlling Solid (applicable pH range)	-	CaMg(CO ₃) ₂ (5-10)	CaMg(CO ₃) ₂ (5-12)	
Si Controlling Solid (applicable pH range)	-	SiO ₂ (5-7)	SiO ₂ (5-7)	
SO ₄ ²⁻ Controlling Solid (applicable pH range)	-	BaSO ₄ (5-12), Ca ₆ Al ₂ (SO ₄) ₃ (OH) ₁₂ •26H ₂ O (10-12), CaSO ₄ •2H ₂ O (7-10)	BaSO ₄ (5-12), CaSO ₄ •2H ₂ O (7-10)	
Zn Controlling Solid (applicable pH range)	-	None Identified	None Identified	
Cd Availability Leaching	mg/kg	1.9	3.1	
Cu Availability Leaching	mg/kg	10.5	7.2 to 10.3	
Ni Availability Leaching	mg/kg	31	7.8 to 155.3	
Pb Availability Leaching	mg/kg	11.6	11.4 to 12	
Zn Availability Leaching	mg/kg	31.3	13.2 to 14.4	
Low L/S (Pore Water) pH	pH	12.7 to 13	13.7	
Pore Water Ionic Strength	molal	0.7 to 1.2	1.3	
Na Monolith Cumulative Flux After 22 d (Release)	mg/m ²	1,270 to 2,850	2,490 to 3,395 (bulk) 8,430 (surface)	
K Monolith Cumulative Flux After 22 d (Release)	mg/m ²	1,370 to 3,100	4,960 to 6,240 (bulk) 8,235 (surface)	
Cl Monolith Cumulative Flux After 22 d (Release)	mg/m ²	Not quantifiable	615 to 665 (bulk) 4,685 (surface)	
SO ₄ ²⁻ Monolith Cumulative Flux After 22 d (Release)	mg/m ²	Not quantifiable	730 to 800 (bulk) 2,140 (surface)	
Ca Monolith Cumulative Flux After 22 d (Release)	mg/m ²	16,990 to 27,520	23,270 to 25,200	

Range of values (mean of values)			
Category or response variable	Units	Laboratory aged CFA-C prisms (from 2 ³ +3 experimental design)	Field aged U.S. 20 slab samples
Na Observed Diffusivity Through Binder ($D_{obs,3}$)	m ² /s	1.1 x 10 ⁻¹² to 6.2 x 10 ⁻¹²	5.0 x 10 ⁻¹² to 8.8 x 10 ⁻¹² (bulk) 63.0 x 10 ⁻¹² (surface)
K Observed Diffusivity Through Binder ($D_{obs,3}$)	m ² /s	0.7 x 10 ⁻¹² to 2.7 x 10 ⁻¹²	6.1 x 10 ⁻¹² to 15.0 x 10 ⁻¹² (bulk) 25.0 x 10 ⁻¹² (surface)
Cl Observed Diffusivity Through Binder ($D_{obs,3}$)	m ² /s	1.5 x 10 ⁻¹¹ to 2.6 x 10 ⁻¹¹	4.8 x 10 ⁻¹² to 8.1 x 10 ⁻¹² (bulk) 1.7 x 10 ⁻¹⁰ (surface)
Ca Observed Diffusivity Through Binder ($D_{obs,3}$)	m ² /s	2.6 x 10 ⁻¹⁴ to 3.4 x 10 ⁻¹⁴	2.5 x 10 ⁻¹⁴ to 3.1 x 10 ⁻¹⁴ (bulk) 0.7 x 10 ⁻¹⁴ (surface)
Tortuosity (τ_{MO})	unitless	30	30

comparisons about age, material components, and mix characteristics are given.

Some highlights from Table 108 are as follows:

Component Sources.

1. It is difficult to ascertain how similar or different the CFA-C was between the 1987 and 1998 samples. The samples were both obtained from the same power station. From oxide analyses, they are not markedly different.
2. The coarse aggregate came from the same supplier and same quarry.
3. The fine aggregate came from a different supplier and quarry, but the same geologic formation.
4. The portland cement came from the same supplier, but a different production facility. It likely had a higher Si content.

Air Content

1. Air contents in the CFA-C mix during batching ranged from 2.9 to 4.1 percent based on air voids testing. Petrographic analyses of failed Iowa pavements suggested air voids of <2 to 6 percent.

Age.

1. The equivalent age of the CFA-C prisms ranged from 1.0 to 4.8 yr.(with chronological ages of less than 2 mo when accelerated aging began and about 7 mo at the end of accelerated aging).
2. The slab was about 10 yr old when collected, but had exhibited signs of early distress after about 3 yr.

Compositional Differences.

1. Si was the only element that showed differences in content between the CFA-C prisms and the slab. It was higher in the CFA-C prism mix and the source was the cement.

Compressive Strength.

1. Compressive strengths of the CFA-C prisms (after equating to cylinder cores) were shown to be similar to slab cores.

Microcracking.

1. Microcracking was not as extensive in the laboratory prisms as it was in the slab concrete.

Effective Pore Size and Pore Size Distribution.

1. The laboratory CFA-C mixture combined with high levels of heat aging resulted in differential pore size curves similar in nature to the slab concrete; both were a bimodal system of coarser and finer pore systems.
2. With respect to the coarser system of pores, the laboratory concretes exhibited smaller, more well-defined pore sizes.
3. With respect to the finer system of pores, the CFA-C concrete treated with high AA best modeled the slab concrete though the resulting pores were modestly finer than those of the slab concrete.

Effective Surface Area.

1. Attempts at measuring surface area were not consistent enough to allow a comparison between laboratory and slab concretes beyond the observation that measured values were of the same order of magnitude.

Mineralogy.

1. Laboratory and slab concretes compared well to each other with respect to mineral composition for the six minerals that were examined.

Prism Alkalinity and Constituent Solubility as a Function of pH.

1. There was no difference between the two material types with respect to buffering capacity.
2. There was no difference between the two material types with respect to solubility as a function of pH for trace metals of concern (e.g., Cd, Cu, Pb, Ni, and Zn).

pH-Stat Leaching.

1. General agreement in the leaching was found for Ca, Mg, Al, Si, Ba, Zn, Fe, Cl, K, CO_3^{2-} , and SO_4^{2-} .
2. Cr leaching was not in good agreement between the CFA prisms and slab concretes.
3. Similar results were observed for modeling solid phase control of the CFA-C concrete prisms and the slab concrete.
4. The controlling solids identified for the CFA-C concrete prisms and the slab concrete were similar and typical of cement-based leaching.
5. As with hydrated cement paste and the slab concretes, calcite (CaCO_3) and dolomite

(CaMg(CO₃)₂) were likely controlling solids for Ca leaching from the slab concrete. For the laboratory concrete, gypsum (CaSO₄•2H₂O) was also a likely controlling solid.

6. As with the slab concrete, dolomite (CaMg(CO₃)₂) was a likely controlling solid for Mg leaching in the CFA-C concrete.
7. Unlike the hydrated cement paste for which barium chromate (CaCrO₄) was better, but like the slab concrete, barite (BaSO₄) was a likely controlling solid for Ba in the CFA-C concrete.
8. Like the slab concrete, barite (BaSO₄) was a likely controlling solid for SO₄²⁻ leaching in the CFA-C concrete.

Low LS Leaching.

1. Although much greater Na and K concentrations were experimentally observed at low LS for the slab concrete sample, similar ionic strengths of the pore water were estimated for both the 28-d cured CFA-C sample and the slab concrete sample.
2. A much lower ionic strength of the pore water was estimated for the high AA aged CFA-C sample than the slab concrete.

Availability Leaching.

1. There was no significant difference between the 28-d cured CFA-C mix and the slab with respect to Cd, Cu, Ni, Pb, and Zn availability.
2. For both materials, only a fraction of Ni and Zn was available for leaching under the test conditions, while Cd, Pb, and Cu were completely available.

Monolithic Leaching.

1. Comparison of the results obtained from mass transfer leaching tests carried out on the slab concrete samples and the CFA-C mix samples showed a much greater Na, K, and Cl release and a much lower release of Ca for the slab samples compared with the CFA-C prism samples.
2. The high Cl fluxes seen, especially from the slab surface specimens, may be related to road salting.
3. Release modeling showed significant differences in Na, K, and Cl observed diffusivities between the slab concrete samples and the CFA-C samples: greater Na and K observed diffusivities and lower Cl observed diffusivities were seen for the slab samples. However, no significant difference in Ca observed diffusivities could be observed between the slab and prism samples.

4. The slab surface specimens exhibited more pronounced differences than the prism samples. The observed higher level of microcracking in the surface portions of the slab in the slab concrete may help to explain this.
5. Bulk tortuosities were found to be similar between the two materials.

Utility of Accelerated Aging and Evaluation Approach

1. An accelerated aging protocol was developed that looked at the individual and interactive effects of one developmental and two degradative aging methods on the physical and environmental performance of PCC made with a coal fly ash.
2. The aging protocol impacted both physical and chemical properties of the monoliths.
3. Generally speaking, the main effects were more important than the interactive effects. This was unexpected.
4. It took about a 9 mo of elapsed time to age specimens to an equivalent age of up to 4 yr.using AA.
5. The equivalent ages matched well with the time frame seen in the field for the onset of early distress and also matched well the chronological age of the field pavement.
6. The use of a factorial design was useful in exploring the possibilities of this method; however, given the limited interactions that were seen, the use of experimental variables themselves may be appropriate.
7. AA significantly reduced the compressive strength of the concrete, possibly indicating an onset of a deleterious reaction in the mix.
8. CL affected the microcracking in the concrete.
9. All aging variables affected the fine pore structure of the concrete.
10. CL affected the Ca diffusional leaching from the monoliths.
11. Logically, there appears to be a linkage between strength loss, microcracking, and leaching behavior of a major matrix constituent in the concrete (Ca).
12. Most response variables were similar between the aged laboratory prisms and the field samples suggesting that the method did a reasonable job of producing an aged pavement of similar age and distress.
13. Certain field aging phenomena could not be recreated in the laboratory specimens. These phenomena include more extensive microcracking from unknown sources, road salting, and carbonation.

6.2 Conclusions

1. The accelerated aging method appeared successful in possibly recreating phenomena that may have contributed to the failure of the field slab. The AA treatment produced an unexpected loss of strength that suggests the accelerated aging promoted the onset of a deleterious reaction.
2. Comparisons between CFA-C prism performance and CFA-F and PCC control performance showed expected differences.
3. The use of both physical and environmental response variables shows the linkage between such variables as compressive strength, microcracking, fine pore structure, Cl diffusive leaching (an efflux related to road salting increasing the concentration of Cl in the monolith), and Ca diffusive leaching (related to change in matrix structure and loss of Ca).
4. The use of CFA as a model recycled material in a portland cement matrix was only partially useful in exploring the interaction of physical and environmental performance: the trace metal content and contaminants of concern were present in similar concentrations in the CFA, portland cement, and the aggregates. These constituents leached at very low levels. It was impossible to describe which source term contributed to the low signals that were measured.
5. When evaluating field specimens that have undergone early distress and field aging, it is important to consider samples that have been exposed to additional aging phenomena related to road traffic, road salting, CO₂ uptake, etc. These sub-samples may behave very differently from bulk samples that have aged less drastically.
6. Comparisons to earlier accelerated aging methods for bituminous asphaltic pavements is useful: in hydrophobic monoliths with little chemical reactivity, loss of tortuosity dramatically impacts the diffusive leaching behavior of many constituents on concerns contained in recycled materials. In portland cement concrete, the matrix is hydrophilic, contains a much more elaborate fine pore structure, and the matrix is chemically reactive (e.g., sorption, acid-base reactions, exchange reactions can occur). Despite significant aging, the matrix may be able to still control contaminant release. Aging in a portland cement matrix is a much more complex system to describe and model.
7. A diffusion model that explored monolith heterogeneity was developed and proved useful in evaluating diffusive leaching data. Care should be taken in using diffusion models where components of widely different tortuosity are present.

6.3 Suggestions for Future Work

1. As further data are developed about the failure of the U.S. 20 pavement, relate that work to this work.

2. Further explore this accelerated aging method with other recycled materials in a portland cement matrix, particularly ones that might contribute a more significant signature for contaminants of concern.
3. Explore means to speed up the accelerated aging approach to make it more utilitarian. A method that takes 1 or 2 mo may be better applied than one that takes many months.
4. Further explore other aging phenomena (Cl intrusion/release, carbonation, etc.) as these aging variables may also contribute to environmental behaviors (either beneficial or detrimental).
5. Develop a shortened list of physical and environmental response variable test methods that may be coupled with an aging protocol to be used in an accelerated aging procedure or method for evaluating future uses of recycled materials in portland cement matrices.
6. Consider development of an accelerated aging protocol for other highway applications: flowable fill, stabilized base, granular fill, etc.

CHAPTER 7: REFERENCES

- AASHTO TP17-93, *Standard Test Method for Resistance of Concrete to Rapid Freezing and Thawing*, American Association of State Highway Transportation Officials, Washington, D.C., 1993.
- Allison Geoscience Consultants and HydroGeoLogic, *MINTEQA2/PRODEFA2, A Geochemical Assessment for Environmental Systems: User Manual Supplement for Version 4.0*, National Exposure Research Laboratory, Ecosystems Research Division, U.S. EPA, Athens, GA, 1998.
- Allison, J.D., Brown, D.S., and Novo-Gradac, K.J., *MINTEQA2/PRODEFA2, A Geochemical Assessment for Environmental Systems: Version 3.0 User's Manual.*, Environmental Research Laboratory, U.S. EPA, Athens, GA, 1991.
- APHA, *Standard Methods for the Examination of Water and Wastewater*, APHA, Washington, D.C., 1995.
- ASTM C 215, Standard Test Method for Fundamental Transverse, Longitudinal, and Torsional Frequencies of Concrete Specimens, *Annual Book of ASTM Standards*, American Society for Testing and Materials, Philadelphia, PA, 1976.
- ASTM C 305, Standard practice for mechanical mixing of hydraulic cement paste and mortars of plastic consistency, *Annual Book of ASTM Standards*, 04.01/2, 205-207, 1998.
- ASTM C 618, Standard specification for coal fly ash and raw or calcined natural pozzolan for use as a mineral admixture in concrete, *Annual Book of ASTM Standards*, 04.02, 298-300, 1988.
- Barna, R., Sanchez, F., Moszkowicz, and P., Méhu, J., Leaching behaviour of pollutants in stabilized/solidified wastes, *J. Haz. Matl.* 52, 287-310, 1997.
- Barrett, E.P., Joyner, L.G., and Halenda, P.P., The determination of pore volume and area distributions in porous substances, I. computations from nitrogen isotherms, *J. Amer. Chem. Soc.* 73, 373-380, 1951.
- Batchelor, B., A numerical leaching model for solidified/stabilized wastes, *Water Sc. Tech.* 26, 107-115, 1992.
- Baverman, C., Moreno, L., and Neretnieks, I., Using Chemfronts: a geochemical transport program to simulate leaching from waste materials, pp: 437-446. In: (J.J.M. Goumans, H.A. van der Sloot, and G.J. Senden, eds.) *Environmental Aspects of Construction with Waste Materials. Putting Theory into Practice*, Elsevier Science B.V., Amsterdam, 1997.
- Bisaillon, S. and Malhotra, V.M., Permeability of concrete using a uniaxial water-flow method, pp. 175-193. In: (V. Whiting and J. Walitt, eds.) *Permeability of Concrete*, ACI SP-108, American Concrete Institute, Washington, D.C., 1988.

Brodersen, K., Glasser, F.P., Longomanizo, N., Monine, J.C., Van Iseghem, P., and Wang, J., Chemical and thermodynamic stability of waste products. In: *Proceedings of the International Conference of Luxembourg*, October, 1990.

Byfors, J., *Plain Concrete at Early Ages*, CBI Research Report No. 3:80, Swedish Cement and Concrete Research Institute, Stockholm, 1980.

Carlson, E.D., Keynote Address, p. 9-11. In: *Symposium Proceedings: Recovery and Effective Reuse of Discarded Materials and By-Products for Construction of Highway Facilities*, FHWA, Washington, D.C., 1993.

Cody, R.D., Spry, P.G., Cody, A.M., and Gan, G.L., *The Role of Magnesium in Concrete Deterioration*, Final Report to the Iowa DOT, Project Number HR-355, November, 1994.

Cook, R.A., *Fundamentals of Mercury Intrusion Porosimetry and its Application to Concrete Materials Science*, Master's thesis, Cornell University, Ithaca, NY, 1991.

Cook, R.A., *A Generalized Form of the Powers Model of Cement Microstructure and its Evaluation Via Mercury Porosimetry and Related Techniques*, Ph.D. Dissertation, Cornell University, Ithaca, NY, 1992.

Cook, R.A. and Hover, K.C., Mercury porosimetry of cement-based materials and associated correction factors, *ACI Materials J.* March-April, 152-161, 1993.

Copeland, L.E. and Hayes, J.C., Porosity of hardened portland cement pastes, *J. Amer. Concrete Inst.* 52, 633-640, 1956.

Crank, J., *The Mathematics of Diffusion*, Clarendon Press, Oxford, 1986.

de Groot, G.J. and van der Sloot, H.A., Determination of leaching characteristics of waste materials leading to environmental product certification, pp. 149-161. In: (T.M. Gilliam and C.C. Wiles, eds) *Solidification/Stabilization of Hazardous, Radioactive and Mixed Wastes*, ASTM, Philadelphia, PA, 1992.

Eighmy, T.T. and van der Sloot, H.A., A unified approach to leaching behavior of waste materials, pp. 979-988. In: (J.J.J.M. Goumons, H.A. van der Sloot, and Th.G. Aalbers, eds.) *Environmental Aspects of Construction with Waste Materials*, Elsevier Science B.V., Amsterdam, 1994.

Eighmy, T.T., Eusden, J.D., Marsella, K., Hogan, J., Domingo, D., Krzanowski, J.E., and Stampfli, D., Particle petrogenesis and speciation of elements in MSW incineration bottom ashes, pp: 111-136. In: (J. J. J. M. Goumans, H. A. van der Sloot, and T. G. Aalbers, eds.) *Environmental Aspects of Construction With Waste Materials*, Elsevier Science B.V., Amsterdam, 1994.

Eighmy, T.T., Crimi, D., Hasan, S., Zhang, X., and Gress, D.L., The influence of void change,

cracking, and bitumen aging on diffusional leaching behavior of pavement monoliths constructed with MSW combustion bottom ash, *Trans. Research Rec.* 1489, 42-48, 1995.

Eighmy, T.T., Eusden, J.D. Jr., Krzanowski, J.E., Domingo, D., Stämpfli, D., Martin, J.R., and Erickson, P.M., Comprehensive approach towards understanding element speciation and leaching behavior in municipal solid waste electrostatic precipitator ash, *Environ. Sci. Technol.* 29, 629-646, 1995.

Eighmy, T.T., Gress, D.L., Crimi, D., Hasan, S.L., and Karpinski, S.J., *The Laconia, N.H. Bottom Ash Paving Project- Volume 1: Environmental Testing Report*, Environmental Research Group, University of New Hampshire, Durham, N.H., 1996.

Eighmy, T.T., Crannell, B.S., Butler, L.G., Cartledge, F.K., Emery, E.K., Oblas, D., Krzanowski, J.E., Eusden, J.D. Jr., Shaw, E.L. and Francis, C.A., Heavy metal stabilization in municipal solid waste combustion dry scrubber residue using soluble phosphate, *Environ. Sci. Technol.* 31, 3330-3338, 1997.

Eighmy, T.T., Crimi, D., Whitehead, I.E., Zhang, X., and Gress, D.L., The influence of monolith physical properties and integrity on diffusional leaching behavior of asphaltic pavements constructed with MSW combustion ash, pp. 125-147. In: (J.J.J.M. Goumans, G.J. Senden, and H.A. van der Sloot, eds.) *Waste Materials in Construction*, Elsevier Science Publ., B.V., Amsterdam, 1997.

EPRI, *Extraction Procedure and Utility Industry Solid Wastes*, EPRI EA-1667, EPRI, Palo Alto, CA, 1981.

EPRI, *Trace Element and Phase Relations in Fly Ash*, EPRI EA-1822, EPRI, Palo Alto, CA, 1981.

EPRI, *Pilot Study of Time Variability of Elemental Concentrations in Power Plant Ash*, EPRI EA-2959, EPRI, Palo Alto, CA, 1983.

EPRI, *Time Variability of Elemental Concentrations in Power Plant Ash*. EPRI EA-3610, EPRI, Palo Alto, CA, 1984.

EPRI, *Leaching Studies on Utility Solid Wastes: Feasibility Experiments*, EPRI EA-4215, EPRI, Palo Alto, CA, 1985.

EPRI, *Mobilization and Attenuation of Trace Elements in Artificially Weathered Fly Ash*, EPRI EA-4747, EPRI, Palo Alto, CA, 1986.

EPRI, *Limestone Dissolution Studies*, EPRI CS-4845, EPRI, Palo Alto, CA, 1986.

EPRI, *Chemical Form and Leachability of Inorganic Trace Elements in Coal Ash*, EPRI EA-5115, EPRI, Palo Alto, CA, 1987.

EPRI, *Evaluation of the Toxicity Characteristics Leaching Procedure (TCLP) on utility wastes*, EPRI CS-5355, EPRI, Palo Alto, CA, 1987.

EPRI, *Micro-surface-analytical Techniques for Characterizing Fly Ash*, EPRI EA-4820, EPRI, Palo Alto, CA, 1987.

EPRI, *Inorganic and Organic Constituents in Fossil Fuel Combustion Residues*, EPRI EA-5176, EPRI, Palo Alto, CA, 1987.

EPRI, *Chemical Characterization of Fossil Fuel Combustion Wastes*, EPRI EA-5321, Palo Alto, CA, 1987a.

EPRI, *Inorganic and Organic Constituents in Fossil Fuel Combustion Residues; Volume 1: A Critical Review*, EPRI EA-5176, EPRI, Palo Alto, CA, 1987b.

EPRI, *Trace Elements in Coal and Coal Wastes*, EPRI GS-6575, EPRI, Palo Alto, CA, 1989.

EPRI, *Detailed Physical, Chemical, and Mineralogical Analyses of Selected Coal and Oil Combustion Ashes*, EPRI TR-101785, EPRI, Palo Alto, CA, 1993.

FHWA, *Fly Ash Facts For Highway Engineers*, FHWA-SA-94-081, FHWA, Washington, D.C., 1995.

FHWA, *Early Distress in Concrete Pavements*, FHWA-SA-97-045, FHWA, Washington, D.C., 1997.

Fraay, A.L.A., Bijen, J.M., and de Haan, Y.M., The reaction of fly ash in concrete—a critical examination, *Cement Concrete Res.* 19, 235–246, 1989.

Freiesleben-Hansen, P. and Pedersen, E. J., Maturity computer for controlled curing and hardening of concrete, *Nordisk Betong.* 1, 21-25, 1997.

Fruchter, J. S., Rai, D., and Zachara, J. M., Identification of solubility-controlling solid phases in a large fly ash field lysimeter, *Env. Sci. Tech.* 24, 1173-1179, 1990.

Fuhrmann, R.F., Pietrzak, R.F., Franz, E.M., Heiser, J.H. III, and Colombo, P., *Optimization of the Factors that Accelerate Leaching*, U.S. DOE-BNL-52204, 1989.

Garrabrants, A.C., *Development and Application of Fundamental Leaching Property Protocols for Evaluating Inorganic Release from Wastes and Soils*, Master thesis, Rutgers, The State University of New Jersey, Piscataway, NJ, 1998.

Garrabrants, A.C., Kosson, D.S., Use of chelating agent to determine the metal availability for leaching from soils and wastes, *Waste Manage.* 20 (1), 155-165, 2000.

Garrabrants, A.C., Sanchez, F., Gervais, C., Moszkowicz, P., and Kosson, D.S., The effect of

storage in an inert atmosphere during intermittent wetting on the release of inorganic constituents from a cement-based material, *J. Haz. Matl.*, in press, 2001.

Gebler, S.H. and Klieger, P., Effect of fly ash on physical properties of concrete, pp: 1 - 50. In: *Proceedings, 2nd International Conference on Fly Ash, Silica Fume, Slag, and Natural Pozzolans in Concrete*, ACI SP-91, ACI, Detroit, 1986.

Gervais, C., Garrabrants, A., Sanchez, F., Barna, R., Moszkowicz, P., and Kosson, D., Leaching of inorganic contaminants from cement-based waste materials as a result of intermittent wetting, pp:97-103, In: *Stabilisation des Dechets et Environnement 99*, Societe Alpine de Publications, Grenoble, France., 1999.

Gimblett, F.G.R., Lawrence, C.D., and Sing, K.S.W., Sorption studies of the microstructure of hydrated cement, *Langmuir* 5, 1217-1222, 1989.

Glasser, F. P., Chemistry of cement-solidified waste forms, pp: 1 -38. In: (R.D. Spence, ed.) *Chemistry and Microstructure of Solidified Waste Forms*, Lewis Publishers, Boca Raton, Florida, 1993.

Glasser, F. P., Fundamental aspects of cement solidification and stabilization, *J. Haz. Matl.* 52, 151-170, 1997.

Guadard, M. and Schoof, J., *A Design of Experiments Situation*, Class Notes, Mathematics Department, University of New Hampshire, Durham, NH, 1995.

Hemond, H.F. and Fechner, F.J., *Chemical Fate and Transport in the Environment*, Academic Press, San Diego, 1994.

Hinsenveld, M., *A Shrinking Core Model as a Fundamental Representation of Leaching Mechanisms in Cement Stabilized Waste*, Ph.D. Dissertation, University of Cincinnati, Cincinnati, OH, 1992.

Hsu, T.T.C., Fatigue of plain concrete, *J. Amer. Concrete Inst.* 78, 292-305, 1981.

Jones, K. and Putherickal, J., *Evaluation of Deterioration on U.S. 20 in Webster County*, Final Report for Iowa DOT, Project MIR-91-1, January, 1991.

Kosmatka S.H. and Panarese, W.C., *Design and Control of Concrete Mixtures*, Portland Cement Association, Skokie, IL, 1988.

Kosson, D.S., van der Sloot, H.A., and Eighmy, T.T., Estimation of contaminant release during utilization and disposal of municipal waste combustion residues, *J. Haz. Matl.* 47, 43-75, 1996.

Kuehl, R. O., *Statistical Principles of Research Design and Analysis*, Duxbury Press, Belmont, CA, 1994.

Ladd, M. F. C. and Lee, W. H., *Introduction to Physical Chemistry*, Cambridge University Press, Cambridge, UK, 1986.

Laidler, K. J., *Chemical Kinetics*, Harper and Row Publishers, New York, 1987.

Landsberger, S., Delayed instrumental neutron activation analysis, pp 121 -142, In: (Z. B. Alfassi, ed.), *Chemical Analysis by Nuclear Methods*, John Wiley and Sons, New York, 1994.

Lea, F. M., *The Chemistry of Cement and Concrete*, Chemical Publishing Company, Inc., New York, 1971.

Linde, D.R., *CRC Handbook of Chemistry and Physics*, CRC press, Inc., Boca Raton, FL, 1996.

Malhotra, V.M. and Ramezaniapour, A.A., *Fly Ash in Concrete*, Natural Resources Canada MSL-94-45(1R), CANMET, Ottawa, Canada, 1994.

Markowicz, A. A. and Grieken, R.E.V., X-ray spectrometry, *Anal. Chem.* 62, 101R-113R, 1990.

Marks, V.J. and Debberke, W.G., *Investigation of PCC Pavement Deterioration A Few Facts are Worth More Than 100 Opinions*, Interim Report for Iowa DOT Research Project HR-2074, presented to Committee A2EO1, Transportation Research Board 74th Annual Meeting, Washington, D.C., 1995.

Marks, V.J. and Debberke, W.G., *A Different Perspective for Investigation of PCC Pavement Deterioration*, Interim Report for Iowa DOT Research Project HR-2074, presented to Committee A2EO1, Transportation Research Board 75th Annual Meeting, Washington, D.C., 1996.

Martin, T. D., Brockhoff, C. A., Creed, J. T., and Group, E. M. W., *Method 200.7: Determination of Metals and Trace Elements in Water and Wastes by Inductively Coupled Plasma-Atomic Emissions Spectrometry*, Environmental Monitoring Systems Laboratory, Office of Research and Development, U.S. EPA, Cincinnati, Ohio, 1994.

Massry, I.W., *The impact of Micropore Diffusion on Contaminant Transport and Biodegradation Rates in Soils and Aquifer Materials*, Ph.D. dissertation, Rutgers The State University of New Jersey, New Jersey, Piscataway, NJ, 1997.

Mehta, P.K., Influence of fly ash characteristics on the strength of portland-fly ash mixtures, *Cement Concrete Res.* 15, 669-674, 1985.

Meima, J. A. and Comans, R. N. J., Geochemical modeling of weathering reactions in municipal solid waste incinerator bottom ash, *Env. Sci. Tech.* 31, 1269-1276, 1997.

Mikhail, R.S., Copeland, L.E., and Brunauer, S., Pore structure and surface areas of hardened Portland cement pastes by nitrogen adsorption, *Can. J. Chem.* 42, 426-438, 1964.

Millington, R.J. and Shearer, R.C., Diffusion in aggregated porous media, *Soil Sci. Soc. Amer. J.*

111, 372-378, 1971.

Moszkowicz, P., Sanchez, F., Barna, R., and Méhu, J., Pollutants leaching behaviour from solidified wastes: a selection of adapted various models, *Talanta* 46, 375-383, 1998.

Najjar, W.S., Aderhold, H.C., and Hover, K.C., The application of neutron radiography to the study of microcracking in concrete, *Cement, Concrete & Aggregates* 8(2), 103-109, 1986.

Naik, T.R., Ramme, B.W., and Tews, J.H., Pavement construction with high-volume class C and class F fly ash concrete, *J. Amer. Concrete Inst.* 92, 200-210, 1995.

Nelson, E.L., Carrasquillo, R.L., and Fowler, D.W., Behavior and failure of high-strength concrete subjected to biaxial-cyclic compression loading, *J. Amer. Concrete Inst.*, 85, 248-253, 1988.

Neville, A.M., *Properties of Concrete*, John Wiley and Sons, Inc., New York, 1996.

Odler, I., Strength of cement, final report of task group 1, 68-MMH technical committee, *Matériaux et Constructions*, 24, 143-157, 1991.

Odler, I. and Köster, H., Investigations on the structure of fully hydrated portland cement and tricalcium silicate pastes. III. specific surface area and permeability, *Cement Concrete Res.* 21, 975-982, 1991.

OECD, *Recycling for Road Improvements*, OECD EIR1 Scientific Expert Group on Recycling for Road Improvements, OECD, Paris, France, 1996.

Pfaff, J. D., *Method 300.0: Determination of Inorganic Anions by Ion Chromatography*, Environmental Monitoring Systems Laboratory, Office of Research and Development, U.S. EPA, Cincinnati, OH, 1993.

Pons, G. and Maso, J.C., Microstructure evolution of concrete under low-frequency cyclic loading: determination of the porosity variations, pp: 2817 - 2824, In: *Advances in Fracture Research, Proceedings, 6th International Conference on Fracture*, New Delhi, India, 1984.

Popovics, S., Strength relationships for fly ash concrete, *J. Amer. Concrete Inst.* 79, 43-49, 1982.

Potgieter, J.H. and Strydom, C.A., An investigation into the correlation between different surface area determination techniques applied to various limestone-related compounds, *Cement Concrete Res.* 26, 1613-1617, 1996.

Powers, T. C. and Brownyard, T. L., *Studies of the Physical Properties of Hardened Cement Paste*, Research Laboratories of the Portland Cement Association, Bulletin 22, Chicago, 1948.

Powers, T.C., The nonevaporable water content of hardened portland-cement paste—its significance for concrete research and its method of determination, *ASTM Bulletin* 158, 68-76,

1949.

RILEM Recommendations CPC-18, Measurement of hardened concrete carbonation depth. *Materials and Structures* 21, 453-455, 1988.

Rößler, M. and Odler, I., Investigations on the relationship between porosity, structure and strength of hydrated cement pastes. I. effect of porosity, *Cement Concrete Res.* 15, 320-330, 1985.

Rostásy, F.S., Weiß, R., and Wiedemann, G., Changes of pore structure of cement mortars due to temperature, *Cement Concrete Res.* 10, 157-164, 1980.

Rusch, H., Research toward a general flexural theory for structural concrete, *J. Amer. Concrete Inst.* 57, 1-28, 1960.

Sanchez, F., Barna, R., Garrabrants, A., Kosson, D., and Moszkowicz, P., Environmental assessment of a cement-based solidified soil contaminated with lead, *Chem. Eng. Sci.* 55, 113-128, 1999.

Sasse, H. R. and Schrage, I., A proposed method for aging polymers used in buildings under simultaneous action of artificial weathering and mechanical stress, *Durability of Building Materials* 2, 45-48, 1983.

Schlörholtz, S. and Amenson, J., *Evaluation of Microcracking and Chemical Deterioration in Concrete Pavements*, Final Report to the Iowa DOT, Project Number HR-358, October 31, 1995.

Schreurs, J.P.G.M., van der Sloot, H.A., and Hendriks, Ch. F. Verification of laboratory-field leaching behavior of coal fly ash and MSWI bottom ash as a roadbase material, pp: 415 - 428. In: (J.J.J.R. Goumans, H.A. van der Sloot, and Th.G. Aalbers, eds.) *Waste Materials in Construction*, Elsevier Science Publ., B.V., Amsterdam, 1997.

Sersale, R., Cioffi, R., Frigione, G., and Zenone, F., Relationship between gypsum content, porosity, and strength in cement. I. effect of SO₃ on the physical microstructure of portland cement mortars, *Cement Concrete Res.* 21, 120-126, 1991.

Sims, I., Assessment of concrete carbonation, *Concrete* 28 (6), 33-38, 1994.

Soroka, I., *Portland Cement Paste and Concrete*, Chemical Publishing Co., Inc., NY, 1979.

Stegemann, J.A., Shi, C., and Caldwell, R.J., Response of various solidification systems to acidic addition, pp: 803-814, In: (J.J.M. Goumans, H.A. van der Sloot and G.J. Senden, eds.) *Environmental Aspects of Construction with Waste Materials. Putting Theory into Practice*, Elsevier Science B.V., Amsterdam, 1997.

Taylor, H. F. W., *Cement Chemistry*, Thomas Telford, London, 1997.

Tishmack, J. K., Olek, J., and Diamond, S., Characterization of high-calcium fly ashes and their potential influence on ettringite formation in cementitious systems, *Cement, Concrete, and Aggregates* 21(1), 82-92, 1999.

Torii, K. and Kawamura, M., Pore structure and chloride permeability of concretes containing fly ash, blast-furnace slag and silica fume, pp: 135 - 150. In: *Proceedings, 4th International Conference on Fly Ash, Silica Fume, Slag, and Natural Pozzolans in Concrete*, ACI SP-132, ACI, Detroit, 1992.

van der Hoek, E., *Speciation of Arsenic and Selenium During Leaching of Fly Ash*. Ph.D. Dissertation, University of Utrecht, Utrecht, the Netherlands, 1995.

van der Sloot, H.A., Systematic leaching behavior of trace metals from construction materials and waste materials, p. 19-36. In: (J.J.J.R. Goumons, H.A. van der Sloot & Th.G. Aalbers, eds.) *Waste Materials in Construction*, Elsevier Science Publ., B.V., Amsterdam, 1991.

van der Sloot, H.A., Hjelm, O., Aalbers, T.G., Wahlstrom, M., and Fallman, A.-M. *Proposed Leaching Test for Granular Solid Wastes*, ECN-C-93-012, Netherlands Energy Research Foundation, Petten, The Netherlands, 1993.

van der Sloot, H.A., Comans, R.N.J., and Hjelm, O., Similarities in the leaching behavior of trace contaminants from waste, stabilized waste, construction materials and soils, *Sci. Total Environ.* 196, 111-126, 1994a.

van der Sloot, H.A., Hoede, D., De Groot, G.E., van der Wegen, G.J.L., and Quevauviller, P., *Intercomparison of Leaching Tests for Stabilized Wastes*, ECN-C-94-062, Netherlands Energy Research Foundation, Petten, The Netherlands, 1994b.

van der Sloot, H.A., Kosson, D.S., Eighmy, T.T., Comans, R.N.J., and Hjelm, O., Approach towards international standardization: a concise scheme for testing of granular waste leachability, pp. 453-466. In: (J.J.J.M. Goumons, H.A. van der Sloot, and Th.G. Aalbers, eds.) *Environmental Aspects of Construction with Waste Materials*, Elsevier Science B.V., Amsterdam, 1994c.

van der Sloot, H.A., Weyers, E.G., Hoede, D., and Wijkstra, J., *Physical and chemical characterization of pulverized-coal ash with respect to cement-based applications*, ECN-178, Netherlands Energy Research Foundation, Petten, The Netherlands, 1985.

van der Sloot, H. A., *Characterization of the Leaching Behavior of Cement Mortars to Assess Long-term Environmental Behavior During Their Service Life and Their Recycling Stage*, (draft manuscript), 1998.

van der Wegen, G. and van der Plas, C., Validation of leaching model on actual structures, pp. 55-62. In: (J.J.J.M. Goumons, H.A. van der Sloot, and Th.G. Aalbers, eds.), *Environmental Aspects of Construction with Waste Materials*, Elsevier Science B.V., Amsterdam, 1994.

Washburn, E.W., Note on a method of determining the distribution of pore sizes in a porous material, *Proc. Nat. Acad. Sci.* 7, 115-116, 1921.

Young, J.F., Capillary porosity in hydrated tricalcium silicate pastes, *Powder Tech.* 9,173-179, 1974.

Zhang, B., Relationship between pore structure and mechanical properties of ordinary concrete under bending fatigue, *Cement Concrete Res.* 28, 699-711, 1998.